Design and Synthesis of Radioactive Metal Complexes for the Diagnosis and Treatment of Disease

Katherine Morgan

ORCID: 0000-0002-2874-8737

July 2023

School of Chemistry

Faculty of Science

The University of Melbourne

Submitted in total fulfilment of the requirements of the degree of Doctor of Philosophy

I. Declaration

I certify that the thesis comprises my original work towards the PhD and that due acknowledgement has been made to all other material used in the text. The thesis is less than 100,000 words in length.

Katherine Anne Morgan

July 2023

II. Abstract

Personalised medicine is becoming increasingly important in the treatment of various cancers and diseases. Early diagnosis is important for patient outcomes, and radiation therapy offers a molecular treatment option that allows for highly specific targeting of cancer cells *in vivo*. The overarching theme of the research described in this thesis relates to the design and synthesis of new radiopharmaceuticals designed to better diagnose or treat various malignancies, including renal cancer, Alzheimer's disease and cancers that are associated with suppression of the immune system, known as immune checkpoint inhibitors.

Selective and targeted delivery of the radionuclide to sites of disease is essential. Radionuclide therapy is possible with radionuclides that emit α particles. Actinium-225 emits α particles with a radioactive half-life of 9.9 days. Targeted delivery of actinium-225 to tumours has the potential to treat tumours. Chapters Two to Five of this thesis describe new approaches to incorporate actinium-225 into targeting molecules.

Chapters, Two, Three and Four discuss the design and synthesis of a new bifunctional ligand, H_2MacropaSqOEt designed to form stable complexes with actinium-225. Monoclonal antibodies that target Carbonic Anhydrase IX were chemically modified to incorporate the ligand H_2MacropaSqOEt. Carbonic Anhydrase IX is an enzyme that is overexpressed on the surface of cancers such as clear cell renal cell carcinoma. These antibody conjugates were radiolabelled with actinium-225, and [^{225}Ac]Ac(MacropaSq-hG250) was evaluated in a murine model of cancer that overexpresses Carbonic Anhydrase IX. The research presented in these three chapters highlight the future potential of targeted alpha therapy with monoclonal antibodies.

The work in Chapter Five focused on the concept of antibody-based pre-targeting. The synthesis of [^{225}Ac]Ac(Macropa-Tetrazine) was a preliminary investigation into the

possibilities of pre-targeted α therapy, and future work will involve exploring the potential of the iEDDA reaction between [^{225}Ac]Ac(Macropa-Tetrazine) and TCO-modified antibodies.

Copper-64 is a positron emitting radionuclide with a half-life of 12.7 hours. Copper-64 is used as a diagnostic radionuclide in positron emission tomography. Chapter Six focused on developing a copper-64-based diagnostic imaging agent for Alzheimer's disease. The aim of this research project was to develop a proof-of-concept strategy to enable antibody-targeted positron emission tomography imaging *via* the preparation of small copper-containing molecules designed to cross the blood brain barrier and react with specifically modified Amyloid-β antibodies. Finally, the research presented in Chapter Seven focused on the development of a new peptide-based imaging agent for the diagnosis of PD-L1-positive tumours. This chapter explored the copper-64 radiochemistry and stability of this new peptide complex.

III. Preface

This thesis comprises original work; it also involved research done in collaboration with other laboratories at the Olivia Newton John Cancer Research Institute (ONJCRI), The Peter MacCallum Cancer Centre (PMCC), Monash Biomedical Imaging, The Florey Institute of Neuroscience and Mental Health and Collaborative Research and Innovation @ Bio21.

The *in vivo* longitudinal therapy study of [^{225}Ac]Ac(MacropaSq-hG250) was performed at the ONJCRI by the skilled Nancy Guo. Thanks to Dr Laura Osellame for your expertise in confocal microscopy, and for quantification of radiation damage from tumour sections. Positron Emission Tomography was performed at a National Imaging Facility (an NCRIS facility) and Monash Biomedical Imaging. The *in vitro* binding assay by flow cytometry of [^{64}Cu]Cu(Sar-CLP003) was performed at PMCC under the supervision of Kelly Waldeck.

The monoclonal antibody Girentuximab, both humanised and its derivatives, were provided by Telix Pharmaceuticals. The monoclonal antibody, Aducanumab, was provided by Luke Miles and Colin Masters at The Florey Institute of Neuroscience and Mental Health. Brain tissue of Alzheimer's Patients was provided by the Victorian Brain Bank Network thanks to Dr Catriona McLean.

It should be noted that part of the text presented on pages on pages, 21 – 24, 27 – 31, 169 – 171 has appeared in a publication that I co-authored with Professor Paul Donnelly titled: Metallic Radionuclides for diagnostic imaging and cancer radiotherapy: the development of theragnostic matched pairs and targeted alpha therapy. Part of the text presented on pages 1 – 19, and 224 – 247 has appeared in a submitted manuscript that I co-authored with Professor Paul Donnelly, Dr Stacey Rudd and Dr Asif Noor titled Theranostic Nuclear Medicine with Gallium-68, Lutetium-177, Copper-64/67, Actinium-225, and Lead-212/203 Radionuclides (Chemical Reviews). The text presented on pages 184 – 219 has appeared in a publication that

I co-authored titled: Pre-Targeting Amyloid-β with Antibodies: Toward Antibody Targeted Molecular Imaging of Alzheimer's Disease. All text used for this publication is my own original writing. The work presented under the sub-heading (previous work) on page 197 was completed prior to the commencement of this degree.

This research was funded in part by the Australian Research Council, Australian Cancer Research Foundation, National Health and Medical Research Council, the Victorian Cancer Council, and Telix Pharmaceuticals.

IV. Acknowledgements

I would like to sincerely thank my supervisor, Professor Paul Donnelly, for allowing me to be part of his research group for the last seven years. You have instilled a love of all things radiochemistry in me and have allowed me to pursue some exciting chemistry. Thank you for your constant encouragement and belief in my abilities. You have created such a wonderful research group and I have learnt so much from you. I am very glad that I gave the PhD a go. To my panel, Professor Brendan Abrahams and Professor Craig Hutton, your guidance during my candidature was always insightful. Thank you both for helping me stay on track and for making me feel so supported during my studies.

I would like to thank all the Donnelly lab members, past and present, but I especially thank Dr Stacey Rudd and Dr Asif Noor. You are both inspiring chemists and have not only taught me so much but have been role models to me. I feel very privileged to be working alongside such great scientists. There are so many previous Donnelly Group lab members that have not only helped me in my research but made great friends along the way, especially Dr Jackie Lange, Dr Hui Jing Koay, Dr Lachlan McInnes, Dr Ben Spyrou, Dr Jack Rowan and Kathryn Szostak. Also, a big thanks to Emily, La'El, Ellanor, Janelle and Crystal, who have kept me sane(ish) the last year. A special thanks to Professor Jonathon White, for his expertise in X-ray crystallography which made it possible to solve many of these structures and his generosity with his time over the last six years.

To all the excellent scientists at ONJCRI, especially Dr Christian Wichmann, thank you for teaching me everything I know about actinium-225. It was a pleasure to learn from you. To Professor Andrew Scott, Nancy Guo, Dr Laura Osellame, Dr Zhipeng Cao and Fiona Scott, thank you for all the guidance and work during my time at ONJCRI.

I would like to thank Associate Professor Brett Paterson, Dr Michael De Veer, Dr Cormac Keldermann, Dr Ekaterina Salimova and the facilities and scientific and technical assistance of the National Imaging Facility, a National Collaborative Research Infrastructure Strategy capability at Monash Biomedical Imaging. Thanks to Dr Ben Blyth, Kelly Waldeck and Jess Van Zuylekom for their work on the *in vitro* binding assays of the immune checkpoint peptides and their insightful impacts on the project.

To Associate Professor Nick Williamson, Dr Ching-Seng Ang and Dr Shuai Nie at the Mass Spectrometry and Proteomics Facility, thank you for running such an excellent facility and for the insightful conversations during my studies at Bio21.

I would like to give a special thanks to my beautiful family. Mum, Dad, James, Dave, Kes, Poppy and Clover, you have all helped me in such a significant way and made this journey so meaningful. Thank you to my parents for your constant support and unwavering love; I will always appreciate everything you have done for me, big and small. Thank you to all my beautiful friends; your kindness always made me feel so loved and appreciated. Finally, I would like to thank Jordan, thank you for being my person, I couldn't have done it without you.

V. COVID-19 Impact Statement

The PhD candidate started in August 2019. In March 2020, the COVID-19 pandemic led to repeated laboratory closures and restricted access to the research laboratory. Over the next two years, Melbourne experienced 264 days of lockdown, and during this time, the candidate had restricted/ no access to the laboratory. The research detailed in this thesis is entirely laboratory-based. There were further restrictions to access to biochemical/radiochemical laboratories based within the Hospitals (Olivia Newton John Cancer Research Institute, Austin Hospital and Peter MacCallum Cancer Centre) during this time.

VI. List of Abbreviations

AD	Alzheimer's Disease
APP	Amyloid Precursor Protein
ATSM	Diacetyl*bis*(N(4)-methyl-3-thiosemicarbazonato)
Aβ	Amyloid Beta
CAIX	Carbonic Anhydrase IX
ccRCC	Clear cell Renal Cell Carcinoma
$CHCl_3$	Dichloromethane
CHX-A''-DTPA	N-[(R)-2-amino-3-(p-aminophenyl)propyl]trans-(S,S)-cyclohexane-1,2-diamine-N,N,N',N",N"-pentaacetic acid
COSY	Correlation Spectroscopy
CT	Computed Tomogrpahy
CuAAC	Copper(I) Azide-Alkyne Cycloaddition
DIPEA	N,N-Diisopropylethylamine
DMF	Dimethylformamide
DMSO	Dimethylsulfoxide
EDC.HCl	N′-ethylcarbodiimide hydrochloride
EDTA	Ethylenediaminetetraacetic acid
ESI-TOF-MS	Electrospray Ionisation Time of Flight Mass Spectrometry
FBS	Fetal Bovine Serum
HATU	1-[Bis(dimethylamino)methylene]-1*H*-1,2,3-triazolo[4,5-*b*]pyridinium 3-oxid hexafluorophosphate
hG250	Girentuximab
hG250-FcRn	Girentuximab - Modified Biodistribution
HIFα	Hypoxia Induible Factor-α
HMBC	Heteronuclear Multiple Bond Correlation

HRMS	High Resolution Mass Spectrometry
HSQC	Heteronuclear Single Quantum Coherence
iEDDA	Inverse Electron Demand Diels Alder
LET	Linear Energy Transfer
m.p.i	Minutes Post Injection
mAb	Monoclonal Antibody
Me	Methyl
MeCN	Acetonitrile
MeOH	Methanol
MTD	Maximal Tolerated Dose
NHS	N-hydroxysuccinimide
OEG	Oligo(ethylene Glycol)
ORTEP	Oak Ridge Thermal Ellipsoid Plot
p.i.	post injection
PBS	Phosphate Buffered Saline
PD-1	Programmed Death - 1
PD-L1	Programmed Death - Ligand 1
PEG	Poly(ethylene Glycol)
PET	Positron Emission Tomography
PSMA	Protstate Specific Membrane Antigen
RCP	Radiochemical Purity
RCY	Radiochemical Yield
RP-HPLC	Reverse-Phase High Performance Liquid Chromatography
RPMI	Roswell Park Memorial Institute Medium
SE-HPLC	Size exclusion high performance liquid chromatography
SPECT	Single Photon Emission Computed Tomography
SqOEt	Squaramide Ethyl Ester

SSTR2	Somatostatin subtype 2a receptor
TAT	Targeted Alpha Therapy
TBTA	Tris(benzyltriazolylmethyl)amine
TCO	*Trans*-cyclooctene
TFA	Trifluoroactetic acid
THF	Tetrahydrofuran

VII. Table of Contents

1 Introduction to Nuclear Medicine 1

1.1.1 Toward the Personalization of Medicine 1

1.1.2 Understanding the Effects of Ionising Radiation on DNA 5

1.2 The FDA Approval of Four Radiopharmaceuticals Stimulates Interest in Radiotheranostics 6

1.2.1 Theranostics for Somatostatin-positive Tumours 6

1.2.2 Theranostics for Prostate Cancer using Peptidomimetics 13

1.2.3 Treatment of Cancer with Lutetium-177 18

2 H_2MacropaSqOEt, a New Ligand for Targeted Alpha Therapy with Actinium-225 Labelled Antibodies 21

2.1 Understanding the Coordination Chemistry of Actinium 21

2.2 The Production of Actinium-225 24

2.3 The Practical Challenges of Using Actinium-225 27

2.4 The Clinical Potential of Actinium-225 Radiotherapy 28

2.5 The Search for Metal Chelators that Form Stable Complexes with Actinium-225 30

2.5.1 The Phosphate Derivate of DOTA, H_8DOTP, Forms Complexes with Actinium 32

2.5.2 DOTA Forms Complexes with Actinium-225 at High Temperatures, the FDA Approval of DOTA Chelators has Paved the Way for New Radionuclides 33

2.5.3 Actinium-225 is Rapidly Radiolabelled with H_2Macropa 35

2.5.4 Second-Generation H_2Macropa Chelators Are Not More Stable 36

2.5.5 The PSMA-Targeting Peptidomimetic, [^{225}Ac]Ac(RPS-074) Elicits a Complete Tumour Response 41

2.6 Aims 42

2.7 Results and Discussion 45

2.7.1 Synthesis and Characterisation of the Bifunctional Chelator, H_2MacropaSqOEt 45

2.7.2 A One-pot Synthesis of Compound *12* 50

2.7.3 Using a Squaramide Ethyl Ester as a Functional Group that Reacts with Antibodies 52

2.7.4 Synthesis of H_2MacropaSqOEt Through a Copper(I) Catalysed Click Reaction 56

2.7.5 Concluding Remarks and Improvements on the Synthesis of H_2Macropa 60

2.8 The Coordination Chemistry of Monofunctional H_2Macropa with Lanthanum(III) 61

2.8.1 X-ray Crystallography of H_4Macropa$(CF_3CO_2)_2(H_2O)$ 61

2.8.2 X-ray Crystallography of [La(HMacropa)(H_2O)].$(CF_3SO_3)_2$. 62

2.8.3 Investigating the Role 1,2,3-Triazoles Play in Complex Formation using Lanthanum as a Non-Radioactive Surrogate 65

2.9 Concluding remarks 73

2.10 Experimental 75

2.10.1 Materials and Reagents 75

2.10.2 Instrumentation 75

2.10.3 Synthesis and Characterisation of H_2MacropaSqOEt 76
2.10.4 Dimethylpyridine-2,6-dicarboxylate (2) 76
2.10.5 Methyl 6-(hydroxymethyl)picolinate (3) 77
2.10.6 Methyl-6-chloromethyl-pyridine-2-carboxylate (4) 77
2.10.7 Diethyl-4-hydroxypyridine-2,6-carboxylate (6) 78
2.10.8 Diethyl 4-(prop-2-yn-1-yloxy)pyridine-6-dicarboxylate (7) 78
2.10.9 2-Hydroxymethyl 4-(prop-2-yn-1-yloxy)pyridine-6-ethylcarboxylate (8) 79
2.10.10 2-Chloromethyl 4-(prop-2-yn-1-yloxy)pyridine-6-ethylcarboxylate (9) 80
2.10.11 Methyl 6-((1,4,10,13-tetraoxa-7,16-diazacyclooctadecan-7-yl)methyl)picolinate (11) 80
2.10.12 Ethyl 4-(prop-2-yn-1-yloxy)-6-((16-((6-(methoxycarbonyl)pyridin-2-yl)methyl)-1,4,10,13-tetraoxa- 7,16- diazacyclooctadecan-7-yl)methyl)picolinate (12) 81
2.10.13 4-(prop-2-yn-1-yloxy)-6-((16-((6-carboxypyridin-2-yl)methyl)-1,4,10,13-tetraoxa-7,16-diazacyclooctadecan-7-yl)methyl)picolinic acid (13) 82
2.10.14 $N_3(OEG)_3$SqOEt (16) 83
2.10.15 H_2MacropaSqOEt (17) 84
2.10.16 Compound 18 85
2.10.17 Compound 19 86
2.10.18 Compound 20 86
2.10.19 [La(MacropaTz$_2$Bn$_2$)]CO_3 (21) 87
2.10.20 [La(HMacropa)(H_2O)].(CF_3SO_3)$_2$ 88

3 The Bifunctional Ligand, H_2MacropaSqOEt, is Easily Conjugated to Monoclonal Antibodies 89

3.1 Targeting Carbonic Anhydrase IX 89

3.2 Girentuximab: A Monoclonal Antibody that Selectively Binds to Carbonic Anhydrase IX to Treat Renal Cell Carcinoma 92
3.2.1 Renal Cell Carcinoma 92
3.2.2 Targeting Cancer with Monoclonal Antibodies 93
3.2.3 Girentuximab, a Monoclonal Antibody that Binds CAIX 95
3.2.4 Targeted Alpha Therapy Can Overcome the Radioresistance Observed in Hypoxic Tumours 97
3.2.5 Chemical modification of monoclonal antibodies 99

3.3 Aims 100

3.4 Results and Discussion 101
3.4.1 Characterising the Conjugation of H_2Macropa-SqOEt to Girentuximab by Native Protein Mass Spectrometry 101
3.4.2 The Synthesis and Characterization of H_4DOTA-NCS-hG250 104
3.4.3 Size Exclusion High-Performance Liquid Chromatography of Antibody Conjugates 106
3.4.4 Enzyme-Linked Immunosorbent Assay (ELISA) 108

3.5 Concluding Remarks 110

3.6 Experimental 111
3.6.1 Instrumentation 111

3.6.2 H_2MacropaSq-hG250 and H_2MacropaSq-hG250-FcRn 111
3.6.3 H_2MacropaSq-IgG1 Control 112
3.6.4 H_4DOTA-pBn-NCS-hG250 (CAR 1:1) 112
3.6.5 H_4DOTA-pBn-NCS-hG250 (CAR 3:1) 112
3.6.6 ELISA 112

4 Radiolabelling Monoclonal Antibodies with Actinium-225 114

4.1 The Challenges of Detecting Actinium-225 114

4.2 Aims 116

4.3 Results and Discussion 117
4.3.1 Radiolabelling H_2MacropaSq-Antibodies with Actinium-225 117
4.3.2 Determining the Radiochemical Yield of [^{225}Ac]Ac-radioimmunoconjugate Formation by Radio-Thin Layer Chromatography 120
4.3.3 [^{225}Ac]Ac(MacropaSq-hG250) Retains its Immunoreactivity Toward SKRC-52 Cells 122
4.3.4 [^{225}Ac]Ac(MacropaSq-hG250) Complexes are Stable in Challenge Experiments 125
4.3.5 [^{225}Ac]Ac(MacropaSq-hG250) Outperforms [^{225}Ac]Ac(DOTA-NCS-hG250) 126
4.3.6 [^{225}Ac]Ac(MacropaSq-hG250) is Stable in Human Serum 129
4.3.7 [^{225}Ac]Ac(MacropaSq-hG250) and [^{225}Ac]Ac(MacropaSq-hG250-FcRn) Reduce the Viability of SKRC-52 cells 130
4.3.8 [^{225}Ac]Ac(MacropaSq-hG250) Inhibits the Ability of SKRC-52 Cells to Form New Colonies 134
4.3.9 [^{225}Ac]Ac(MacropaSq-hG250) Accumulates in SKRC-52 Tumours in Evaluation of Biodistribution 135
4.3.10 [^{225}Ac]Ac(MacropaSq-hG250) Delays Tumour Growth in Longitudinal Therapy Study 139
4.3.11 γH2AX Microscopy Determines the Number of Double-Strand Breaks in Actinium-225 Treated Tumour Sections 143

4.4 Concluding Remarks 150

4.5 Experimental 151
4.5.1 Instrumentation 151
4.5.2 Cell culture and tumour models 151
4.5.3 Radiolabelling of H_2MacropaSq Antibodies with Actinium-225 151
4.5.4 Radiolabelling of H_4DOTA-NSC-hG250 with Actinium-225 152
4.5.5 Flow Cytometry of hG250 Antibodies and Conjugates 152
4.5.6 Lindmo-Scatchard Assay 153
4.5.7 MTS Cell Viability Assay 153
4.5.8 Colony Formation (Clonogenic) Assay 156
4.5.9 Biodistribution Study in BALB/c Nude Mice bearing Established SKRC-52 Xenografts 157
4.5.10 *In vivo* Longitudinal Studies with [^{225}Ac]Ac(MacropaSq-hG250) 160
4.5.11 γH2AX Confocal Microscopy to Determine the Double-Strand Breaks in Tumour Sections 162

5 Adapting [^{225}Ac]Ac(Macropa) for use in Bioorthogonal Click Reactions 164

5.1 Reducing Off-target Toxicity *via* Pretargeted Tetrazine and *Trans*-cyclooctene Click Chemistry 164

5.2 Leveraging Click Chemistry for *In Vivo* Reactions 165

5.3 Harnessing the iEDDA Click Reaction for Antibody Pretargeting 167

5.3.1 Pretargeted Radioimmunotherapy with Copper-64/67 Delays Tumour Growth in Murine Models of Cancer 167

5.3.2 Pretargeted Radioimmunotherapy is possible with Actinium-225 169

5.4 Aims 171

5.5 Results and Discussion 172

5.5.1 Synthesis of a Crown Ether Macrocycle with an Appended Tetrazine, H_2Macropa-Tetrazine 172

5.5.2 Characterising the Conjugation of *Trans*-cyclooctene to Girentuximab by Native Protein Mass Spectrometry 176

5.5.3 Radiolabelling of H_2Macropa-Tetrazine with Actinium-225 178

5.6 Conclusions and Future work 179

5.7 Experimental 181

5.7.1 (4-(1,2,4,5-tetrazin-3-yl)phenyl)methanamine hydrochloride (20) 181

5.7.2 Tetrazine glutaric acid (21) 182

5.7.3 Tetrazine NHS ester (22) 182

5.7.4 Compound 23 183

5.7.5 H_2Macropa-Tetrazine (24) 184

5.7.6 Proof of concept *in vitro* 'click' reaction quantified by mass spectrometry. 185

5.7.7 Radiolabelling H_2Macropa-Tetrazine 185

6 Pre-Targeting Amyloid-β with Antibodies: Toward Antibody Targeted Molecular Imaging of Alzheimer's Disease 187

6.1 Introduction 187

6.1.1 The Pathology of Alzheimer's Disease 187

6.1.2 Diagnostic Imaging of the Amyloid-β Burden 189

6.1.3 [^{64}Cu]Cu^{II}-based complexes of *bis*(thiosemicarbazones) are Stable 190

6.1.4 Monoclonal Antibodies Gain Approval for the Treatment of Alzheimer's Disease 192

6.1.5 Antibody Pretargeting may Overcome Challenges of Brain ImmunoPET 192

6.2 Aims 193

6.3 Results and Discussion 195

6.3.1 Previous Work 195

6.3.2 Synthesis of Non-symmetrical *Bis*(thiosemicarbazones) 195

6.3.3 Synthesis of copper(II) *bis*(thiosemicarbazone) complexes 196

6.3.4 Cyclic Voltammetry of Cu(atsm-Tz) and Cu(dtse-Tz) 197

6.3.5 X-ray Crystallographic data of Cu(dtse-Tz)$_2$(C_2H_2OS)$_3$ and [Cu(H_2atsm-Tz)](ClO_4)$_2$. 199

6.3.6 Characterising the Conjugation of *Trans*-cyclooctene to Aducanumab and 6E10 by Native Protein Mass Spectrometry 203

6.3.7 H_2atsm-Tz and H_2dtse-Tz can be Radiolabelled with Copper-64 207

6.3.8 In Vitro 'Click' Reaction with Trans-cyclooctene Functionalised Amyloid-β Antibodies 209
6.3.9 *In Vivo* Analysis of [^{64}Cu]Cu(atsm-Tz) and [^{64}Cu]Cu(dtse-Tz) 210

6.4 Concluding Statements and Future Work 212

6.5 Experimental 214
6.5.1 Instrumentation 214
6.5.2 Diacetyl-4,4-dimethyl-4'-methyl*bis*(thiosemicarbazone) (1) 214
6.5.3 Diethyl-4,4-dimethyl-4'-ethyl*bis*(thiosemicarbazone) (2) 215
6.5.4 H_2atsm-Tz 215
6.5.5 Cu(atsm-Tz) 216
6.5.6 H_2dtse-Tz 216
6.5.7 Cu(dtseTz) 217
6.5.8 Conjugation of TCO-PEG$_4$-NHS to aducanumab and 6E10 antibodies 217
6.5.9 Immunohistochemistry 218
6.5.10 Radiochemistry 218
6.5.11 Stability studies with cysteine and histidine. 218
6.5.12 Stability study with glutathione (GSH). 218
6.5.13 In vitro click reaction with aducanumab-TCO and 6E10-TCO. 219
6.5.14 PET/CT of [^{64}Cu]Cu(atsm-Tz) and [^{64}Cu]Cu(dtse-Tz) in Balb/c mice 220
6.5.15 Biodistribution of [^{64}Cu]Cu(atsm-Tz) and [^{64}Cu]Cu(dtse-Tz) in Balb/c mice 221

7 Toward Molecular Imaging of PD-L1 Positive Targets with Copper-64 Labelled Peptides 223

7.1 The Cancer Immunity Cycle 223

7.2 The PD-1 /PD L1 Checkpoint 225

7.3 The Development of Chelators that Form Complexes with Copper 228
7.3.1 The Chelator Makes the Difference for Copper 228
7.3.2 'Sarcophagine' Ligands form Stable Complexes with Copper 230
7.3.3 Bifunctional Sarcophagines allow Conjugation to Antibodies and Peptides 232
7.3.4 Preclinical evaluation of [$^{64/67}$Cu]Cu(SarTATE) shows promise 237
7.3.5 [$^{64/67}$Cu]Cu(SarTATE) Moves to Clinical Studies 240
7.3.6 [$^{64/67}$Cu]CuSar-bombesin used in breast and prostate cancer 242

7.4 Imaging Immune Checkpoint Regulators 247
7.4.1 Diagnostic Imaging of PD-L1 Positive Tumours with Antibodies 247
7.4.2 Peptides that Interact with PD-1/ PD-L1 Show Promise in Preclinical Therapy Studies 248
7.4.3 Diagnostic Imaging of PD-L1 positive NSCLC Tumours with [^{68}Ga]GaNOTA-WL12 250

7.5 Aims 252

7.6 Results and Discussion 253
7.6.1 Synthesis of the Fluorescent Peptide, FITC-CLP003 253
7.6.2 Synthesis of a Fluorescent Peptidomimetic, FITC-SNuKK 255
7.6.3 Flow Cytometry of a Fluorescently Labelled Peptide and Peptidomimetic 257
7.6.4 Synthesis of a Peptide that Contains the Copper Chelator, MeCOSar 258

7.6.5 Radiolabelling of Peptides with Copper-64 260
7.6.6 Investigating the Stability of [^{64}Cu]Cu(Sar-CLP003) in human serum 261
7.6.7 Investigating the Stability of [^{64}Cu]Cu(Sar-CLP003) in a Cysteine and Histidine Challenge 263
7.7 Concluding remarks and Future work 264
7.8 Experimental 266
7.8.1 General procedure for peptide synthesis 266
7.8.2 NH_2-PEG_4-CLP003 266
7.8.3 FITC-PEG_4-CLP003 267
7.8.4 Boc-Ser(tBu)-NH-NH_2 267
7.8.5 FITC-SNuKK 268
7.8.6 Sar-CLP003 270
7.8.7 Flow cytometry of fluorescent PD-L1 peptides 270
7.8.8 Radiolabelling of Sar-CLP003 270
7.8.9 Stability of [^{64}Cu]Cu(Sar-CLP003) in human serum 271
7.8.10 Stability studies with cysteine and histidine 271
8 Conclusions, Challenges and Future Opportunities 272
9 References 277

VIII. Table of Figures

Figure 1: Schematic of a PET scanner used to generate an image of activity. The annihilation between a positron (β^+) and an electron generates two γ-ray photons detected by gamma ray detectors. Created with biorender.com. 4

Figure 2: Schematic representation of a radiopharmaceutical, consisting of a radioactive compound, and a targeting molecule that is typically connected by a linker. The targeting molecule binds to a receptor on the tumour cell. Created with biorender.com. 5

Figure 3: (a) Structure of the transmembrane receptor SSTR2;[34] (b) chemical structure of [Tyr^3]-octreotide and (c) [Tyr^3]-octreotate. 7

Figure 4: (a) Chemical structure of pentetreotide and (b) ball and stick representation of the complex anion present in $Na_2[In(DTPA)]\cdot 7H_2O$ as determined by X-ray crystallography.[43] 8

Figure 5: The chemical structure of DOTA-Tyr^3-octreotate (DOTATATE). 10

Figure 6: (a) Ball and stick representation of the complex anion present in $Na[Lu(DOTA)(H_2O)]\cdot 4H_2O$ as determined by X-ray crystallography,[61] (b) ORTEP representation of [Ga(DOTA-D-Phe-NH_2)] as determined by X-ray crystallography, thermal ellipsoids are shown at 50% probability.[62] 12

Figure 7: (a) PET image of a patient with high-grade metastatic renal NETs using [^{68}Ga]Ga(DOTATATE) as the diagnostic imaging agent. The patient received four cycles of [^{177}Lu]Lu(DOTATATE); (b) [^{68}Ga]Ga(DOTATATE) PET/CT obtained three months later shows near complete imaging response (black arrow).[69] 13

Figure 8: (a) Ribbon diagram of the PSMA ectodomain homodimer as determined by X-ray crystallography, (b) structure of the binuclear zinc active site in the protease domain of PSMA.[83] 14

Figure 9: (a) Chemical structure of HBED, where R^1, R^2 = H & HBED-CC where R^1, R^2 = $CH_2CH_2CO_2H$, (b) chemical structure of PSMA-11, (c) ORTEP representation of the neutral [Ga(HBED)(H_2O)] as determined by X-ray crystallography, thermal ellipsoids shown at 50% probability;[93] (d) PET/CT of a patient representative for disseminated lymph node and bone metastases of prostate cancer imaging using [^{68}Ga]Ga(PSMA-11).[97] 17

Figure 10: (a) Chemical structure of PSMA-617; (b) [^{68}Ga]Ga(PSMA-11) PET maximum intensity projection (MIP) images before (left) with PSA 967 ng/mL and three months after (right) [^{177}Lu]Lu(PSMA-617) radionuclide therapy, PSA 7 ng/ mL.[108] 19

Figure 11: Illustration of an X-ray absorption spectrum, showing the characteristic absorption of the X-ray absorption near-edge structure (XANES) and extended X-ray absorption fine structure (EXAFS regions). The XANES region is characterised by the absorption edge, that provides information of the electronic structure and oxidation state. The EXAFS region has a higher energy than the XANES region.[118] 23

Figure 12: Decay pathway of actinium-225 from ^{237}Np to stable ^{205}Tl. 25

Figure 13: Alpha spectra of purified actinium-225 produced *via* cyclotron irradiation (top) and actinium-225 extracted from thorium-229 (bottom).[127] 26
Figure 14: [^{68}Ga]Ga(PMSA-11) PET/CT scans of a patient treated with [^{225}Ac]Ac(PSMA-617) at University Hospital Heidelberg. (a) shows the metastatic and marrow infiltration of mCR prostate cancer, (b) shows scans 2 months following 3 treatments of [^{225}Ac]Ac(PSMA-617), (c) shows scans two months after additional consolidation therapy.[140] 29
Figure 15: Chemical structures of chelators studied to probe actinium-225 complex stability. 31
Figure 16: (a) Comparison of ^{31}P NMR spectrum of $DOTP^{8-}$ (δ 0 – 80 ppm, D_2O, pD 10) which is shown in the black trace, compared with the spectra of various metal complexes, $M(DOTP)^{5-}$ where M= La^{III}, Ac^{III} and Am^{III}. (b) X-ray crystal structure of the anion of $(NH_4)_5La(DOTP)(H_2O)$. Thermal ellipsoid are shown at 30%.[148] 32
Figure 17: Chemical structures of (a) H_4DOTA and (b) H_4DOTA-pBn-SCN. 34
Figure 18: Chemical Structures of (a) H_2Macropa and (b)H_2Macropa-NCS, an asymmetric bifunctional derivate of H_2Macropa. 36
Figure 19: Chemical structures of (a) H_2CHX-Macropa, (b) H_2BZMacropa, (c) H_2BZ_2Macropa, (d) H_2macrodipa (e) H_2py-macrodipa and (f) H_2py_2-macrodipa. 37
Figure 20: (a) Radio-thin layer chromatography of [^{225}Ac]Ac(GC33-BZM) after 7 days in human serum (37°C). Intact [^{225}Ac]Ac(BZM-GC33) stays at the baseline (retention ~ 20 mm). [^{225}Ac]Ac^{III} that has been trans chelated exists as [^{225}Ac]Ac(EDTA) (retention ~ 110 mm); (b) the stability over time of [^{225}Ac]Ac(GC33-BZM) and [^{225}Ac]Ac(GC33-M) in human serum as a function of time.[162] 38
Figure 21: Radiochemical yields at different concentrations of [^{225}Ac]Ac(macrodipa), [^{225}Ac]Ac(py-macrodipa), [^{225}Ac]Ac(Macropa) and [^{225}Ac]Ac(DOTA). Radiolabelling was performed at 25 °C for [^{225}Ac]Ac(py-macrodipa), [^{225}Ac]Ac(Macropa), 40 °C for [^{225}Ac]Ac(macrodipa), and 80 °C for [^{225}Ac]Ac(DOTA); pH 5.5 – 6; 60 min reaction time.[165] 39
Figure 22: Chemical structures of (a) H_2macropquin-SO_3, (b) H_2Macropaquin and (c) H_2macrophopho. 40
Figure 23: Chemical structure of [^{225}Ac]Ac(RPS-074). 41
Figure 24: The relative electronegativities of carbon, sulphur and oxygen.[176] 45
Figure 25: Analytical RP-HPLC of the crude reaction mixture of compound ***12*** when the product was formed by (a) reflux and (b) microwave irradiation. HPLC conditions for both traces: 0 –100 % CH_3CN in MilliQ with 0.1% TFA over 25 minutes (214 nm). Blue arrows indicate the retention time of starting material, red stars indicate the retention time of compound ***12*** formed. 50
Figure 26: The preparative RP-HPLC/MS trace of the one-pot reaction of ***12***. Highlighted peaks were collected and used in future reactions. (5 – 95 % CH_3CN in MilliQ with 0.1% formic acid over 23 minutes (15 mL/ min, 280 nm). All fractions were collected and used for further synthesis. 51

Figure 27: (a) RP-HPLC of compound ***16,*** showing a single peak (R_t = 7.33 min, column B), (b) HR-MS of compound 16, $[M+H]^+$ = 343.1613, $[2M+H]^+$ = 685.3155. 53
Figure 28: (a) The restricted rotation around the vinylogous amide means that two isomers (a and b) are present in ^{1}H NMR, (b) chemical structure of compound ***16***, blue arrow indicates the hydrogen (c) ^{1}HNMR (d_6-DMSO) between 4 – 10 ppm of compound ***16*** (room temperature). 54
Figure 29: ^{1}H NMR (d_6-DMSO) between δ 1 – 4 ppm of compound ***16*** (room temperature) with corresponding assignments. 55
Figure 30: ^{13}C NMR (d_6-DMSO) between ~170 – 195 ppm of compound ***16,*** showing the carbon environments of the squaramide ethyl ester with corresponding assignments. 56
Figure 31: RP-HPLC (280nm) of H_2MacropaSqOEt (R_t = 10.07 mins; column A), with an inset of the mass spectrum; $[M+2H]^{2+}$ = 465.2161 57
Figure 32: (a) Chemical structure and assignments of H_2Macropa-SqOEt, (b) ^{1}H NMR, D_2O) between δ 7 – 7.5 ppm, (c) Correlated spectroscopy of H_2Macropa-SqOEt between δ 7.1 – 8.5 ppm. 58
Figure 33: ^{1}H NMR (D_2O) of H_2MacropaSqOEt between δ 4.2 – 5.8 ppm at (a) room temperature and (b) 40 °C. 59
Figure 34: ^{1}H NMR (D_2O) of H_2MacropaSqOEt with assignments. 60
Figure 35: X-ray crystal structure of H_4Macropa$(CF_3CO_2)_2(H_2O)$. The asymmetric unit consists of a half cation, trifluoracetic acid counter anion, and one H_2O molecule. The trifluoracetic acid counter anion and H_2O are emitted for clarity. 61
Figure 36: X-ray structure of the cation $[La^{III}(HMacropa)(H_2O)]_2(CF_3SO_3)_2$ Solvent molecules and counter ions are omitted for clarity. 63
Figure 37: X-ray crystal structure of the cation present in $[La(HMacropa)(H_2O)].(CF_3SO_3)_2$. Thermal ellipsoids are shown at 50 % probability. 65
Figure 38: The chemical structures of (a) $[La^{III}(Macropa)(H_2O)]^+$, (b) the model compound $[La^{III}(MacropaTz_2Bn_2)(H_2O)]^+$ with two 1,2,3-triazole functional groups that have the potential to coordinate to La^{III} (R = benzyl). 66
Figure 39: (a) Chemical structure of semi-rigid and conjugating triazole-pyridine-amido based ligand (TPA) that contains two 1,2,3-triazole groups, (b) The single crystal X-ray structure of the mono-bridged dinuclear $La_2(TPA)_3$ complex.[182] 67
Figure 40: X-ray crystal structure of $(H_2MacropaTz_2Bn_2)(H_2O)$. 69
Figure 41: X-ray of the zwitterionic form of $H_2MacropaTz_2Bn_2$. 69
Figure 42: High-resolution mass spectrometry of (a) the singly protonated $[M+H]^+$ adduct of compound ***20***, $H_2MacropaTz_2Bn_2$ and (b) the charged $[M]^+$ cation of $[La(MacropaTz_2Bn_2)]CO_3$. 71
Figure 43: Chemical structure and assignment of (a) $H_2MacropaBn_2Tz_2$ and (b) $[La(MacropaTz_2Bn_2)]CO_3$ ^{1}HNMR spectra of compound 19 and complex $LaMacropaTz_2Bn_2$ in deuterated methanol. 72

Figure 44: An illustration of the proposed role of CAIX in the acidification of the extracellular space. Adapted from Pastorekova[194] and created with BioRender.com. 90
Figure 45: (a) The proposed structure of the arrangement of CAIX dimer on the cell membrane adapted from De Simone[211] and (b) the tetrahedral zinc active site of CAIX.....92
Figure 46: (a) A schematic illustration of an antibody and (b) a crystal structure of an antibody.[227] ..94
Figure 47: Maximum intensity projection of patient with a ccRCC tumour localised in the left kidney (red arrow). The tumour is visible from 0.5 h post-injection, and the tumour-to-background ratio increases up to 168 hours.[239] 97
Figure 48: (a) An illustration of a monoclonal antibody (IgG) with a solvent-accessible lysine residue and H_2MacropaSqOEt; (b) after H_2MacropaSqOEt has reacted with the primary amine on lysine, forming a disquaramide. 100
Figure 49: ESI-TOF deconvoluted mass spectra of (a) unmodified Girentuximab (hG250), (b) H_2MacropaSq-hG250 showing between 1 – 8 chelator attachments and (c) La^{III}(MacropaSq-hG250) showing between 1 – 8 chelator attachments. 102
Figure 50: ESI-TOF deconvoluted mass spectra of (a) unmodified Girentuximab (hG250-FcRn), (b) H_2MacropaSq-hG250-FcRn showing between 1–8 chelator attachments and (c) La^{III}(MacropaSq-hG250-FcRn) showing between 1–8 chelator attachments. 104
Figure 51: (a) The structure of H_4DOTA-pBn-SCN and (b) schematic of [^{225}Ac]Ac(DOTA-*p*Bn-NCS) conjugated to a monoclonal antibody via a surface lysine residue (exact coordination geometry unknown). 105
Figure 52: ESI-TOF deconvoluted mass spectra of (a) unmodified Girentuximab (hG250) and (b) H_4DOTA-NCS-hG250 showing between 0-2 chelator attachments, (c) H_4DOTA-NCS-hG250 showing 0-5 attachments. 106
Figure 53: SE-HPLC of constructs (a) hG250, (b) hG250-FcRN (c) H_2MacropaSq-hG250 and (d) H_2MacropaSq-hG250-FcRN, (e) H_4DOTA-NCS-hG250 (CAR 1:1) and (f) H_4DOTA-NCS-hG250 (CAR 3:1). 107
Figure 54: (a) Elisa Assay demonstrates that only Girentuximab has any binding efficacy against the antigen carbonic anhydrase IX. Elisa Assay demonstrates that modifying the antibody with H_2MacropaSq functional groups does not impact the binding of hG250 to carbonic anhydrase IX (CAIX). The IgG1 control shows no binding to CAIX and is a suitable control antibody for further in vitro work.....109
Figure 55: The actinium-225 decay pathway. Actinium-225 emits four daughter alpha particles and two beta particles to reach the stable isotope bismuth-209. Adapted from [145]. 114
Figure 56: (a) An annotated radioTLC of an actinium-225 labelled IgG, (b) diagram of a TLC. The arrow points to the direction of flow of the mobile phase when placed in the developing tank. 116

Figure 57: SE-HPLC chromatograms of (a) [^{225}Ac]Ac(MacropaSq-hG250) and (b) fast clearing [^{225}Ac]Ac(MacropaSq-hG250-FcRn). Radioactive fractions in red, compared to the UV trace of H_2MacropaSq-hG250 and H_2MacropaSq-hG250-FcRn in blue (λ = 280 nm). 119
Figure 58: SE-HPLC chromatograms of [^{225}Ac]Ac(MacropaSq-IgG1). Radioactive fractions in red, compared to the UV trace of H_2MacropaSq-IgG1 in blue (λ = 280 nm).....120
Figure 59: Radio Thin Layer Chromatography of (left) 'free' [^{225}Ac]Ac^{III} (right) [^{225}Ac]Ac-MacropaSq-hG250, radioTLC mobile phase: 0.05 M citrate buffer pH 5.0 120
Figure 60: The radiochemical yield of [^{225}Ac]Ac(MacropaSq-hG250) as a function of time (measured at 1, 5, 15, 30 minutes) at an antibody concentration 1.5×10^{-6} M and 1.5×10^{-7} M. 121
Figure 61: (a) RCY as a function of time at various concentrations of H_2MacropaSq-hG250 with [^{225}Ac]Ac^{III} (b) RCY at the reaction endpoint with increasing concentrations of H_2MacropaSq-hG250. 122
Figure 62: Flow Cytometry of hG250 antibodies, including H_2MacropaSq-hG250, against SKRC-52 cells. 122
Figure 63: (a) Lindmo Assay showing the fraction of [^{225}Ac]Ac(MacropaSq-hG250) binding to SKRC-52 cells as a function of cell number, (b) the inverse of specific binding plotted against the inverse of SKRC-52 cell number.....123
Figure 64 : Scatchard Assay of [^{225}Ac]Ac(MacropaSq-hG250) binding to SKRC-52 cells. 124
Figure 65: (a) The radiochemical yield of [^{225}Ac]Ac(DOTA-NCS-hG250) and (b) [^{225}Ac]Ac(MacropaSq-hG250) as a function of time at different antibody concentrations in the same buffer and pH (sodium acetate buffer, pH 5.5).....127
Figure 66: RadioTLC showing radiochemical yield of [^{225}Ac]Ac(MacropaSq-hG250), [^{225}Ac]Ac(MacropaSq-hG250-FcRn) and [^{225}Ac]Ac(DOTA-NCS-hG250) when incubated in human serum at at 37°C over seven days. 129
Figure 67: (a) The enzymatic reduction of MTS to Formazan in the presence of living cells, (b) the formazan product is detected colourimetrically (λ = 490 nm). 131
Figure 68: Effect on viability of SKRC-52 cells following incubation with increasing dose of [^{225}Ac]Ac(MacropaSq-hG250), [^{225}Ac]Ac(MacropaSq-hG250-FcRn) as determined by MTS assay. 132
Figure 69: (a) Clonogenic assay performed in six-well plates, with clones produced by SKRC-52 cells. Representative image (n = 6) of colonies formed after seeding 5000 cells, with increasing activity of [^{225}Ac]Ac(MacropaSq-hG250), colonies were stained with crystal violet; (b) a number of colonies incubated for 24 hours with increasing radioactivity of [^{225}Ac]Ac(MacropaSq-hG250) (n = 3). 135
Figure 70: Biodistribution in BALB/c nude mice bearing SKRC-52 tumours (n = 5). Mice were injected with 14.8 kBq of [^{225}Ac]Ac(MacropaSq-hG250) and sacrificed at Days 0, 1, 2, 3, 5, 7.....137
Figure 71: Biodistribution in Balb/c nude mice bearing SKRC-52 tumours (n = 5). Mice were injected with 14.8 kBq (0.4 μCi) of [^{225}Ac]Ac(MacropaSq-IgG1) control and sacrificed at Days 0 and 3.....138

Figure 72: (a) Tumour volume (mm^3) as a function of time post-treatment with [^{225}Ac]Ac(MacropaSq-hG250) (14.8 kBq, 30 μg), [^{225}Ac]Ac(MacropaSq-IgG1) (14.8 kBq, 30 μg) or hG250 (30 μg) in mice with SKRC-52 tumour xenografts. 141
Figure 73: (a) Kaplan Meier plot shows the percentage survival of the cohort as a function of time (days); (b) Percentage body weight change after treatment with [^{225}Ac]Ac(MacropaSq-hG250) (14.8 kBq), [^{225}Ac]AcMacropaSq-hIgG1(14.8 kBq) or hG250(30 μg) over 84 days. 142
Figure 74: DNA is unravelled, it exists as nucleosomes; 145 base pairs of DNA tightly wrapped around histone proteins. These histones are an octamer of four proteins. One of the proteins is called H2AX; (b) when DNA experiences a double-strand break (DSB), the amino acid residue of H2AX serine-139 is phosphorylated, initiating downstream repair mechanisms. 144
Figure 75: [^{225}Ac]Ac(MacropaSq-G250) induces double-strand DNA breaks in an SKRC-52 tumour model. Confocal microscopy of SKRC-52 tumours harvested on day 8 post-treatment were stained with DAPI (nuclei – blue) and immunostained with antibodies against γH2AX (ds DNA breaks – green) and F-actin (actin – red). 146
Figure 76: [^{225}Ac]Ac(MacropaSq-hG250) induces double-strand DNA breaks in an SKRC-52 tumour model. Average foci per nuclei from each treatment group (mean ± SEM). Nuclei quantitated for [^{225}Ac]Ac(MacropaSq-hG250) = ≥55. Nuclei quantitated for [^{225}Ac]Ac-MacropaSq-IgG1 and hG250 = ≥36 ****p= ≤0.0001.....148
Figure 77: Flow Cytometry of hG250 antibodies against SKRC-52 cells 153
Figure 78: (a) Concerted [4+2] cycloaddition of 1,2,4,5-tetrazine with *trans*-cyclooctene. The highly strained bicyclic adduct (b) is rapidly converted in a retro-Diels–Alder step (upon release of nitrogen) to the corresponding 4,5-dihydro-pyridazine (c) subsequent isomerisation leads to the corresponding 1,4-dihydro-isomers; (d) Electron-rich tetrazines can aromatise to give (e) under ambient conditions.[311] 166
Figure 79: HOMO-LUMO energy gap can be tuned by incorporating an electron donating group (EDG) on the dienophile and electron-withdrawing groups (EWG) on the diene. Adapted from Knall *et al.*[306] 167
Figure 80: (a) A *trans*-cyclooctene modified antibody is injected into the bloodstream and allowed time to localise at the tumour site, after an appropriate time period when the antibody has reached its optimal biodistribution *in vivo*, a small molecule radioligand is introduced, (b) where it reacts with the modified antibody and excess radioactivity is excreted. 168
Figure 81: Chemical structure of [^{225}Ac]Ac(DOTA-peg$_7$-Tz).....170
Figure 82: (a) Reverse phase HPLC of H_2Macropa-tetrazine (H_2L^3) showing a single peak at 10.88 minutes (λ = 280 nm), and (b) HR-MS of H_2L^3 showing the singly, doubly and triply protonated adducts. 174
Figure 83: ^{1}H NMR of H_2Macropa-Tetrazine. 175

Figure 84: Schematic of TCO-PEG_4-hG250, which has undergone an iEDDA reaction with H_2Macropa-tetrazine (monoclonal antibody not drawn to scale). 176
Figure 85: ESI-TOF deconvoluted mass spectra of (a) unmodified Girentuximab (hG250), (b) TCO-Peg_4-hG250 showing between 1-6 trans-cyclooctene attachments and (c) H_2Macropa-Tz-TCO-Peg_4-hG250 showing reaction between the tetrazine and the trans-cyclooctene. 177
Figure 86: RadioTLC of [^{225}Ac]AcMacropa-Tetrazine (91 nmol, 1.5 μM) 178
Figure 87: (a) Non-amyloidogenic processing of APP by α-secretase then ɣ-secretase releasing the p3 soluble fragment; (b) amyloidogenic processing of APP by BACE1 followed by cleavage by ɣ -secretase, releasing 39-42 amino acid Aβ peptide. Adapted from O'Brien.[335, 340] Created with biorender.com. 188
Figure 88: (a) Schematic representation of Aβ monomers sacking to form a cross β-sheet structure; (b) protofilaments twist together in a helical geometry to form protofibrils, which further aggregate into senile plaques.[344] 189
Figure 89: Chemical structure of (a) [^{18}F]Florbetaben, (b) [^{18}F]Florabetapir, (c) [^{18}F]flutemetamol, (d) Sagittal (left) and axial (right) PET image of a patient after administration of [^{18}F]Florabetapir. Maximum colour corresponds to a standard uptake value (SUV, the concentration of the tracer in tissue typically divided by the injected activity and body weight) approximately 2.2.[350] 190
Figure 90: Chemical structure of (a) Cu(atsm), where $R^1 = R^2 = CH_3$; (b) Cu(atsm-stilbene), which binds to amyloid-β plaques.[359] 191
Figure 91: Schematic representation of in vivo inverse-electron-demand Diels-Alder 'click' reaction between tetrazines and strained trans-cyclooctene (TCO). In step 1) the small, radiolabelled probe is administered, and step 2) *in vivo* click between the *trans*-cyclooctene. 194
Figure 92: HPLC chromatogram of (a) Cu(atsm-Tz) and (b) Cu(dtse-Tz) incubated with an excess of glutathione in MilliQ /acetonitrile mobile phase containing 0.1% TFA. 197
Figure 93: Cyclic voltammetry of Cu(atsm-Tz) (1mM) in DMF (versus Ag/Ag^+), referenced to Fc/Fc+ couple E°' = 0V) with $(Bu)_4NPF_6$ supporting electrolyte 0.1M. 198
Figure 94: Cyclic voltammetry of Cu(dtse-Tz) (1mM) in DMF (versus Ag/Ag^+), referenced to Fc/Fc+ couple E°' = 0V) with $(Bu)_4NPF_6$ supporting electrolyte 0.1M. 198
Figure 95: Cyclic voltammetry of (a) H_2atsm-Tz and (b) H_2dtse-Tz (1mM) in DMF (versus Ag/Ag^+), referenced to Fc/Fc+ couple E°' = 0V) with $(Bu)_4NPF_6$ supporting electrolyte 0.1M. 199
Figure 96: ORTEP representations (with ellipsoids at 50% probability) of the X-ray crystal structure of Cu(dtse-Tz), selected bond lengths (Å): Cu-N3 1.966(3); Cu-N4 1.965(3); Cu-S1 2.2430(11); Cu-S2 2.2453(10). 200
Figure 97: ORTEP representations (with ellipsoids at 50% probability) of the X-ray crystal structure of $[Cu(H_2atsm\text{-}Tz)](ClO_4)_2$ selected bond lengths (Å): Cu-N3 1.968(3); Cu-N4 1.957(3); Cu-S1 2.2413(8); Cu-S2 2.2489(9); Cu-O3 2.505(3). 201

Figure 98: Thermal ellipsoid plot (50% ellipsoids) of the asymmetric unit of Cu(dtse-Tz) showing the hydrogen bonding interaction between the two complexes and with the three molecules of the DMSO solvate: N1-H···N18 (N1···N18 3.000(5) Å, N1-H···N18 173(5)°); N6-H···O1 (N6···O1 2.792(5) Å, N6-H···O1 164(5)°); N16-H···O2 (N16···O2 2.824(5) Å, N16-H···O2 157(5)°); N11-H···O3 (N11···O3 2.986(5) Å, N11-H···O3 153(6)°).....202
Figure 99: Thermal ellipsoid plot (50% ellipsoids) showing centrosymmetric CuH_2atsm-Tz dimers bridged by N-H···O hydrogen bonds: N1-H···O4 (N1···O4 2.955(5) Å, N1-H···O4 143(5)°); N2-H···O4 (N2···O4 2.731(5) Å, N2-H···O4 157(4)°); N5-H···O5 (N5···O5 2.863(4) Å, N5-H···O5 172(4)°); N6-H···O8: (N6···O8 2.878(4) Å, N6-H···O8 174(4)°); O3-Cu1 2.504(3) Å 202
Figure 100: Deconvoluted ESI mass spectra of (a) unconjugated aducanumab and (b) aducanumab-TCO_x conjugate where x = 2 – 7. 204
Figure 101: Deconvoluted ESI mass spectra of (a) unconjugated 6E10 and (b) 6E10-TCO_x conjugate where x = 3-8. 205
Figure 102: Sections of human brain tissue from an AD-affected subject. (a) Immuno-stained with 6E10-TCO antibody (1:400 dilution), (b) immuno-stained with 6E10 antibody (1:200 dilution). The staining shows that there is the retention of antigen-binding sites and comparable binding between the unmodified 6E10 antibody and the 6E10-TCO conjugate. black scale bar = 100 μm. 206
Figure 103: Size exclusion HPLC chromatograms for (a) unmodified Aducanumab, and (b) Aducanumab-TCO, (c) Aducanumab-TCO + Cu(atsm-Tz) click, and (d) Aducanumab-TCO + Cu(dtse-Tz) click. Eluent: 1x PBS pH 7.4, flow rate: 0.35 mL/min, UV detection: 220 nm. 207
Figure 104: Radio HPLC of (a) [^{64}Cu]Cu(atsm-Tz) (scintillation detector, red trace) Cu(atsm-Tz) (λ = 280 nm, blue trace). Retention time = 10.8 min and 10.6 min, respectively; (b) [^{64}Cu]Cu(dtse-Tz) (scintillation detector, red trace) Cu(dtse-Tz) (λ = 280 nm, blue trace). Retention time = 13.2 min and 13.0 min, respectively. 208
Figure 105: HPLC chromatograms of (a) [^{64}Cu]Cu(atsm-Tz) and (b) [^{64}Cu]Cu(dtse-Tz) at 0, 2, 4 hours incubation times with an excess of cysteine and histidine. 0.05% TFA in the mobile phases instead of 0.1% TFA accounts for the slight shift in the retention times for both copper-64 complexes. 209
Figure 106: Normalised, smoothed radioTLC traces of (a) [^{64}Cu]Cu(atsm-Tz) and (b) [^{64}Cu]Cu(dtse-Tz) (red) >95% RCY, when reacted with aducanumab-TCO or 6E10-TCO (blue) for 1 h, in 0.1M sodium acetate, pH 5.5, 10^{-6} M. 210
Figure 107: microPET/CT images of the brain region in Balb/c mice at (a) 1-5 m.p.i. and (b) 5-30 m.p.i of [^{64}Cu]Cu(atsm-Tz). 212
Figure 108: RadioTLC of [^{64}Cu]Cu(atsm-Tz) and [^{64}Cu]Cu(dtse-Tz) incubation with unmodified aducanumab control. 219
Figure 109: Radio TLC of ^{64}Cu]Cu(atsm-Tz) and [^{64}Cu]Cu(dtse-Tz) incubation with unmodified 6E10 control 220

Figure 110: Illustration of the cancer immunity cycle. Adapted from Chen *et al.*[385] Created with biorender.com. 225
Figure 111: Illustration of PD-1 mediated inhibition of T cells. Prolonged T cell receptor (TCR) activation can result in the upregulation of PD-1. Tumour cells often express PD-L1 and PD-L2, and binding to PD-1 decreases T cell proliferation and survival by inhibition of TCR-mediated positive signalling. PD-1 or PD-L1 antibodies reactive to the immune response.[389] Created with biorender.com 227
Figure 112: Synthesis of $(NH_2)_2$Sar. 231
Figure 113: Chemical structures of sarcophagine-based chelators. 233
Figure 114: (a) Synthesis of Cu(COSar) and Cu(bisCOSar) (b) ORTEP representation of the cation present in [Cu(bisCOSar)](CF_3SO_3)Cl as determined by X-ray crystallography.[432] 236
Figure 115: Synthesis of methyl-capped bifunctional Sar ligand, MeCOSar. 237
Figure 116: (a) ORTEP representation of the cation present in $[Cu^{II}(MeCOSar)](ClO_4)_2 \cdot 0.5MeCN$ as determined by X-ray crystallography, thermal ellipsoids shown at 30% probability.[435] (b) Chemical structure of [^{nat}Cu]Cu(SarTATE) (c) PET/CT maximum intensity projection images of AR42J tumour bearing female Balb/c nude mice following injection of [^{64}Cu]Cu(SarTATE) at 1 and 4 h p.i, reproduced with permission.[436] (d) Efficacy of fractionated [^{67}Cu]Cu(SarTATE) PRRT compared to [^{177}Lu]Lu(TATE). Mice were treated with vehicle (day 1), 30 MBq [^{177}Lu]Lu(TATE) (day 1) or 30 MBq [^{67}Cu]Cu(SarTATE) (day 2). For fractionated dosing 15 MBq [^{177}Lu]Lu(TATE) (day 1 + 15) or 15 MBq [^{67}Cu]Cu(SarTATE) on (day 2 + 16) were administered; n = 8 mice/group, reproduced with permission.[436] 239
Figure 117: (a) Maximum intensity projection PET/CT images show excellent lesion detection and contrast with [^{64}Cu]Cu(SarTATE) at 4 hours p.i. in a patient with pancreatic primary tumour, (b) Maximum intensity projection PET/CT imaging also shows clear visualisation of primary tumour in the gastrointestinal tract.[354] Images kindly provided by Prof. Rodney J. Hicks. 241
Figure 118: Side by side PET and SPECT at equivalent time points of [^{64}Cu]Cu(SarTATE) and [^{67}Cu]Cu(SarTATE), respectively, shows that changing the radionuclide does not affect tumour targeting.[438] 242
Figure 119: (a) Chemical structure of [^{nat}Cu]Cu(Sar-BBN), (b) MIP of [^{64}Cu]Cu(Sar-BBN) with PC3 tumour xenografts at 1, 4, 24 hours p.i.,[170] (c) Therapeutic results of 6 × 24 MBq of [^{67}Cu]Cu(Sar-BBN) in PC3 tumour-bearing mice (injected on days 0, 2, and 4, then 14, 16, and 18) delayed tumour growth.[445] 245
Figure 120: PET images of a patient with ER/PR+ HER2-negative metastatic breast cancer administered with [^{64}Cu]Cu(Sar-BBN) (200 MBq) at 1, 4, 24 hours p.i. Reproduced with permission.[446] 246
Figure 121: (a) A comparison of the 3D spheroid penetration (MDA-MB-231 cells) of CLP002 peptide and anti-PD-L1 antibody. (BioXcell, 29E.2A3). Cy5-labelled peptide and antibody were incubated with

the tumour spheroids (~ 700 μm) for 2 and 6 h, followed by confocal microscopy analysis to evaluate tumour penetration (z -stacked confocal images of the spheroids (50 μm; scale bar = 200 μm); (b) CT26 tumour-bearing Balb/C mice (n = 10) were intraperitoneally injected with the anti-PD-L1 peptides (2 mg/Kg) daily for a total of 10 injections and the anti-mouse PD-L1 antibody (10 mg/Kg) every other day for a total of 5 injections. Tumour volume measured over time and represented as the mean ± SE (n = 10). and (c). Image of tumours harvested at day 14.[465] 250
Figure 122: (a) Chemical structure of [^{68}Ga]Ga-NOTA-WL12; (b) [^{68}Ga]Ga-NOTA-WL12 has been investigated preclinically in mice bearing PD-L1 positive tumour xenografts (CHO) and showed clear tumour uptake. (c) Recently, [^{68}Ga]Ga-NOTA-WL12 has been used to image patients with PD-L1 positive non-small cell Lung Cancer.[472] 251
Figure 123: RP-HPLC of compound FITC-CLP003**,** showing a single peak (R_t = 14.47 min, column B, method A) with an inset of the HR-MS of compound FITC-CLP003. 255
Figure 124: Chemical structure of (a) the peptidomimetic from Aurigene and (b) the peptidomimetic compound with a C-terminal lysine for functionalisation with fluorophore and metal chelators. 256
Figure 125: Synthesis of FITC-SNuKK. i) Fmoc-Lys(Alloc)-OH, HATU/DIPEA; Piperidine (20%) in DMF/NMP, Fmoc-Lys(Boc)-OH, HATU/DIPEA; Piperidine (20%) in DMF/NMP ii) carbonyldiimidazole, H-Asn(Trt)-OH iii) Boc-Ser(tBu)-$NHNH_2$ HATU/DIPEA iv) $Pd(PPh_3)_4$, morpholine, dichloromethane then fluorescein isothiocyanate v) TFA/TIPS/DODT/H_2O (92.5: 2.5: 2.5: 2.5) 257
Figure 126: Flow Cytometry showing the (a) fluorescence intensity propidium iodide (PI) of FITC-SNuKK and FITC-CLP003 against HCC-827 cells; (b) the fluorescence intensity (FITC) of FITC-SNuKK and FITC-CLP003 against HCC-827 cells. 258
Figure 127: RP-HPLC of compound Sar-CLP003**,** showing a single peak (R_t = 8.59 min, column B, method B) with an inset of the HR-MS of compound Sar-CLP003. 260
Figure 128: Radio HPLC of [^{64}Cu]Cu(Sar-CLP003) (scintillation detector, red line) and [^{nat}Cu]Cu(Sar-CLP003) (λ = 280 nm, blue line). Retention time = 8.23 min and 8.41 min, respectively. 261
Figure 129: Radio HPLC of [^{64}Cu]Cu(Sar-CLP003) after 120 min incubation with human serum with an inset of the radiochemical yield (%) calculated by RP-HPLC of [^{64}Cu]Cu(Sar-CLP003) up to 120 minutes incubation time with an excess of human serum. Blue arrow represents the retention time of [^{64}Cu]Cu(Sar-CLP003), 8.21 mins. 263
Figure 130: Radio HPLC of [^{64}Cu]Cu(Sar-CLP003) after incubation with cysteine and histidine (5 mM, 6 hours) with an inset of radiochemical yield (%) calculated by radioTLC of [^{64}Cu]Cu(Sar-CLP003) at 0, 1, 4 hours incubation time with an excess of cysteine and histidine. 264

IX. List of Schemes

Scheme 1: (a) Chemical structure of H_2Macropa-SCN, (b) This work: the retrosynthesis and important components in the ligand design of H_2MacropaSqOEt. 42

Scheme 2: Different reaction conditions: including reaction time, solvent volume and reported yields. (a) Published synthesis and reaction conditions reported by Wilson[160], (b) The original synthetic strategy used in this thesis with sequential N-alkylation, method **A** used reflux, method **B** used microwave irradiation (μwave), (c) An improved one-pot microwave-assisted synthesis.....46

Scheme 3: Synthetic pathway of (i) catalytic H_2SO_4, methanol, 16 hours, 85°C, 3.94 g, 80% (ii) $NaBH_4$ in methanol, 0 °C 8 hours, purified via silica chromatography (1% MeOH in DCM), 3.37 g, 57% (iii) $SOCl_2$ 2 hours, 0°C, 2.42 g, 90%.....47

Scheme 4: Synthetic pathway of (i) catalytic H_2SO_4, ethanol, 16 hours, 85°C, 3.98 g, 76% (ii) K_2CO_3 Dimethylformamide (DMF) 2 hours, 70 °C, recrystallised from ethyl acetate, 2.47 g, 68% (iii) $NaBH_4$ in ethanol, 16 hours, 0 °C, purified via silica chromatography (0-2 % MeOH in DCM), 1.20 g, 75% (iv), $SOCl_2$, 4 hours, 80°C, 0.33 g, 77%.....48

Scheme 5: Synthesis of the $N_3(OEG)_3$SqOEt (***16***); i) ethanol, RT, 4 hours. 52

Scheme 6: Copper(I) catalysed azide-alkyne cycloaddition between $N_3(OEG)_3$-SqOEt and ***13*** (i) $CuSO_4$, sodium ascorbate, TBTA, DMF: H2O (4:1), RT, 1 hour.....57

Scheme 7: Synthesis of H_2MacropaTz_2Bn_2. (i) Synthesis of the starting material ***18*** was also collected in a one-pot synthesis (*vide supra*). DIPEA, 85°C and μwave, 1.5 hours; (ii) $CuSO_4$, sodium ascorbate, NaN_3, benzyl bromide, Na_2CO_3 DMF: H_2O 4:1, RT, 1 hour (iii) NaOH in a solution of MeOH and dichloromethane (9:1), RT, 0.5 hours.....68

Scheme 8: The investigation of actinium-225 labelled antibodies comprises of three sections; developing and optimising the radiochemistry, an evaluation of the stability and cytotoxicity of [^{225}Ac]Ac^{III}-labelled antibody conjugates, and finally preclinical studies involving the biodistribution and therapeutic efficacy in a CAIX-positive tumour xenograft model. 117

Scheme 9: The retrosynthesis and important components in the ligand design of H_2Macropa-Tetrazine. 172

Scheme 10: Synthesis of a 1,2,4,5-tetrazine containing an N-hydroxysuccinimidyl activated ester; (i) DIPEA, dichloromethane, 50°C overnight, 76% (ii) N-hydroxysuccinimide, EDC.HCl and DIPEA, room temperature, 65%. 173

Scheme 11: Synthesis of compound 24. (i) $CuSO_4$, Sodium Ascorbate, DMF: H_20 4:1, (ii) followed by ester hydrolysis with NaOH in MeOH. 173

Scheme 12: The synthesis of H_2Macropa-Tetrazine, (i) CH_3CN, 4 hours, purification *via* semi-preparative HPLC, 53%.....174

Scheme 13: The retrosynthesis and important components in the ligand design of H_2atsm-Tz and H_2dtse-Tz. 194

Scheme 14: General synthetic pathway of asymmetric bis(thiosemicarbazones), i) H_2O and HCl (36%); and ii) NN-dimethylformamide, CH_3COOH. 195
Scheme 15: General synthetic pathway of the ligands H_2atsm-Tz and H_2dtse-Tz; i) CH_3CN, N,N-diisopropylethylamine, using μwave heating (64 –67%). For H_2atsm-tz: $R^1 = R^2 = CH_3$; and for H_2dtse-tz: $R^1 = R^2 = CH_2CH_3$. 196
Scheme 16: Copper(II) complexation of H_2atsm-Tz and H2dtse-Tz; i) copper(II) acetate in DMF (Cu(atsm-Tz)) or CH_3OH (Cu(dtse-Tz)) (88%). 196
Scheme 17: Chemical structure the fluorescently labelled peptide FITC-CLP003. Relevant amino acid residue protecting groups omitted for clarity. i) Sequential SPPS on resin with HATU/DIPEA; deprotection of Fmoc protecting groups with Piperidine (20%) in DMF/NMP; ii) Fmoc-PEG_4-OH, HATU/DIPEA; Piperidine (20%) in DMF/NMP followed by cleavage with TFA/TIPS/DODT/H_2O (92.5: 2.5: 2.5: 2.5). FITC and NH_2-PEG_4-CLP003 (DMF, RT), to give FITC-PEG_4-CLP003, FITC-CLP003 (30 %). 254
Scheme 18: Synthesis of Sar-CLP003 on 2CT resin. Relevant amino acid residue protecting groups omitted for clarity. i) Sequential SPPS on resin with HATU/DIPEA; deprotection of Fmoc protecting groups with Piperidine (20%) in DMF/NMP; ii) Fmoc-PEG_4-OH, HATU/DIPEA; Piperidine (20%) in DMF/NMP followed by cleavage with TFA/TIPS/DODT/H_2O (92.5: 2.5: 2.5: 2.5). MeCOSar-NHS and NH_2-PEG_4-CLP003 (DMF, RT), to give MeCOSar-PEG_4-CLP003, Sar-CLP003 (63 %). 259

X. List of Tables

Table 1: Summary of the properties of alpha, beta and Auger decay. 2

Table 2: Crystallographic Table of $(H_4Macropa(TFA)_2(H_2O))_2$ and $[La(HMacropa)(H_2O)]\cdot(CF_3SO_3)_2$. 63

Table 3: Selected bond length of the cation present in $[La(HMacropa)(H_2O)].(CF_3SO_3)_2$. 65

Table 4: Crystallographic Table of $(H_2MacropaTz_2Bn_2)(H_2O)$. 70

Table 5: Calculated EC50 values of monoclonal antibodies by ELISA. 109

Table 6: Immunoreactivity of [^{225}Ac]Ac(Macropa-Sq) conjugated antibodies incubated in human serum over seven days. 125

Table 7: Competition experiment of [^{225}Ac]Ac(MacropaSq-hG250) over seven days. 126

Table 8: Radiochemical yield of [^{225}Ac]Ac(DOTA-NCS-hG250) when heated to 60°C. 128

Table 9: Different ratios of [^{225}Ac]Ac(MacropaSq-hG250) in organs of interest at day seven p.i 139

Table 10: Radiolabelling conditions of H_4DOTA-NCS-hG250. 152

Table 11: Details of the MTS assay 154

Table 12: Results of the MTS assay, including cell viability (%) at different antibody concentrations. 155

Table 13: Dilutions used in the clonogenic assay. 157

Table 14: Biodistribution data of [^{225}Ac]Ac(MacropaSq-hG250). 158

Table 15: Biodistribution of [^{225}Ac]Ac(MacropaSq-IgG1). 160

Table 16: Response to targeted alpha therapy with actinium-225. 161

Table 17: Average tumour volumes of mice receiving [^{225}Ac]Ac(MacropaSq-hG250). 161

Table 18 Average tumour volumes of mice receiving [^{225}Ac]Ac(MacropaSq-IgG1) and hG250. 162

Table 19: Radiolabelling conditions of [^{225}Ac]Ac(Macropa-Tetrazine) and [^{225}Ac]Ac(DOTA-peg$_7$-Tz). 179

Table 20: Crystallographic Data for $Cu(H_2atsm\text{-}Tz)(ClO_4)_2$ and $Cu(dtse\text{-}Tz)(C_2H_2OS)_3$. 203

Table 21: Brain uptake of [^{64}Cu]Cu(atsm-Tz) and [^{64}Cu]Cu(dtse-Tz) at 2 minutes and 60 minutes, expressed as % IA g^{-1}. 211

Table 22: Biodistribution data for [^{64}Cu]Cu(atsm-Tz), and [^{64}Cu]Cu(dtse-Tz). 222

Table 23: Amino acid sequence of peptides investigated in this work. 253

Table 24: Radiochemical yield (%) calculated by radioTLC of [^{64}Cu]Cu(SarCLP003) up to 120 minutes incubation time with an excess of human serum. 262

Table 25: The percentage of radioactivity in soluble and insoluble fractions of human serum. 271

1 Introduction to Nuclear Medicine

1.1.1 Toward the Personalization of Medicine

Nuclear medicine uses molecules labelled with radionuclides, called radiopharmaceuticals, to assist in the diagnosis and treatment of disease. The field is playing an increasing role in clinical practice.[1] Radionuclides are characterised by their inherent instability and their tendency to achieve stability by emitting excess energy in the form of gamma radiation, emitting a new particle from the nucleus, or releasing an electron as a conversion electron. The ability to use diagnostic imaging to quantify where a particular drug goes within an individual patient offers the potential for personalised medicine, where patient selection for treatment with targeted radionuclide therapy is determined by the corresponding imaging results.[1] Radionuclide therapy for cancer is possible by irradiating cancerous tissue with either alpha (α^{2+}), beta (β^{-}) or Auger emitting radionuclides capable of causing irreversible damage to DNA (Table 1). Radionuclides possess unique properties that can be exploited for various applications in nuclear medicine.

The decay energy refers to the amount of energy that is released as an unstable isotope undergoes nuclear decay and transitions to a lower energy state. The biological effects of radiation are dependent on the absorbed dose and the rate at which the dose is delivered. The biological response of a tumour treated with radionuclides also depends on the intrinsic mechanisms of biological repair. Some tumours are more susceptible to radiation than others. The absorbed dose and ability of the tissue to repair is also an important consideration for non-target tissue and organs such as the kidneys and liver.[1] The range of the particles emitted by radionuclides in tissue depends on their Linear Energy Transfer (LET), a measure of the amount of energy transferred per unit length along the track of an ionising particle (keV/μm) and the kinetic energy of the particle. Particles that penetrate a relatively long distance in tissue

can be useful for treating larger tumours as the effects can extend beyond the targeted cell(s), but this can also lead to increased off-target radiological toxicity. Particles with a relatively short range within tissue minimise the impact on off-target tissue, provided they can be selectively delivered to metastatic disease.

Table 1: Summary of the properties of alpha, beta and Auger decay.

Decay Type	*Decay Energy*	*Distance travelled in biological tissue*	*LET (keV/μM)*
Alpha (α^{2+})	5 – 9 MeV	40 – 90 μm	80
Beta (β^-)	0.05 – 2.3 MeV	0.05 – 12 mm	0.2
Auger	~ 80 keV	1 – 20 μm	4 – 26

Radioactive decay by α-emission involves the emission of helium nuclei (two protons and two neutrons) from the nucleus. α particles are emitted when elements are unstable; and occurs commonly with elements that have atomic numbers greater than 82.[2] Radionuclides emitting α particles have an energy between 5 – 9 MeV and a LET of approximately 80 keV/μm. Depending on their emission energy, α particles travel on average 40 – 90 μm in tissue,[3-5] which is about 5 – 10 cell diameters.

Beta decay is a nuclear decay process whereby the atomic number of an element changes while the overall mass number remains the same. This includes the use of β^- (negatron) emission for radiation therapy, whereby the decay process produces a negatron (β^-), a daughter nucleus, and an electron antineutrino. Compared to α-decay, radionuclides that emit β^- particles have energies between 50 – 2200 keV and can travel up to 12 mm within body tissue. This results in a LET of approximately 0.2 keV/μm, meaning the energy of an α particle is approximately 400 times greater than the corresponding β-emissions. This results in high doses of radioactivity capable of causing double-stranded breaks in DNA across short distances.

Auger electrons have short-range emissions in the range of 1 – 20 μm.[6] Therefore, although the energy of the emissions is typically less than 80 keV, the short range over which they travel results in a large LET. Auger-emitting radiopharmaceuticals typically work best

when they are localised at the tumour DNA and can target micro-metastases *via* double-stranded DNA breaks. Auger-emitting radionuclides need to localise very close to DNA within the cell nucleus, and this requirement has impeded their clinical development.[1]

In nuclear medicine, diagnostic imaging with radioisotopes typically uses either Single Photon Emission Tomography (SPECT) or Positron Emission Tomography (PET). In SPECT imaging, a γ-emitting radionuclide is used as a tracer administered to the patient, and the photons emitted are detected by an external camera.[7] Recent interest has focused on increasing the applications of PET as it offers the potential for superior resolution and quantitation than SPECT. Both PET and SPECT imaging has the limitation of approximately millimetre resolution.[8, 9]

Positron-emitting radionuclides are neutron deficient and achieve stability through the nuclear transmutation of a proton into a neutron, leading to the emission of a positron (β^+) and an electron neutrino (ν_e).[10] As the positron travels through tissue and loses kinetic energy, it can interact with an electron, forming an unstable, hydrogenic atom known as a positronium. Positroniums rapidly annihilate, producing a pair of γ-ray photons that move in approximately opposite directions and are detected in coincidence by detectors (Figure 1).[11]

The increased interest in PET has largely been stimulated by the success of a glucose derivative [flourine-18]fluorodeoxyglucose ([^{18}F]FDG), radiolabelled with positron-emitting fluorine-18, which can probe the expression of glucose transporters providing useful diagnostic information in oncology, neurology and inflammation. Recent advancements in radiopharmaceuticals utilising PET technology have sparked extensive research into the radiolabelling of various molecules with fluorine-18, as well as positron-emitting metallic radionuclides such as gallium-68 and copper-64. These developments provide valuable information on a range of indications.

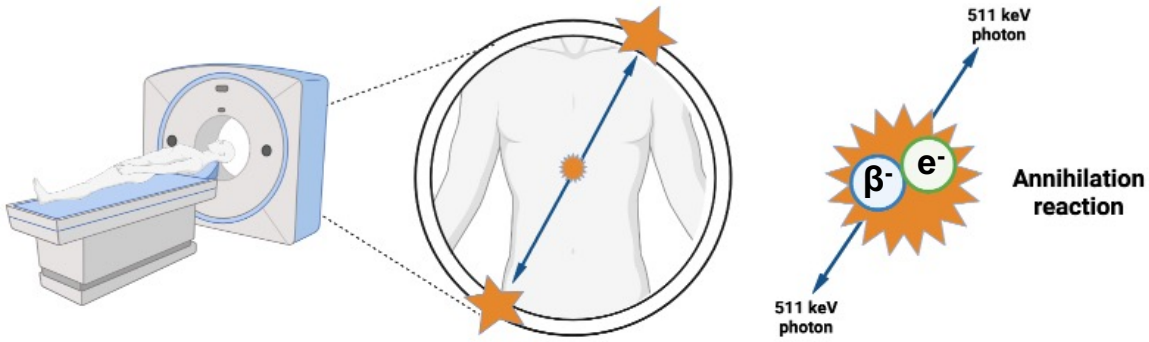

Figure 1: Schematic of a PET scanner used to generate an image of activity. The annihilation between a positron (β^+) and an electron generates two γ-ray photons detected by gamma ray detectors. Created with biorender.com.

The use of a single material or chemical compound for a combination of diagnostic imaging and therapy is referred to as either 'theranostics' or 'theragnostics'.[12, 13] Early clinical applications of radiotheranostics include the use of various isotopes of iodine to diagnose and treat thyroid disorders.[14-16] More recent developments in the ability to target malignancies with molecules that selectively interact with receptors or enzymes over-expressed in cancerous tissue, coupled with the increasing availability of appropriate radionuclides, has reignited interest in radiotheranostics. Several metallic radionuclides with radioactive emissions are well-suited for either imaging or therapy or even simultaneous imaging and therapy. Innovative advances in manufacturing metallic radionuclides with sufficient purity in economically viable processes have combined exciting clinical results and clinical approvals, which have resulted in a surge of interest in radiotheranostics.[17] Radiopharmaceuticals comprise three main components: the radionuclide of interest, a chelating ligand responsible for encapsulating the radiometal and a targeting molecule designed to selectively deliver the radiation to the specific site of disease (Figure 2). This structure forms the basis for the rational design and development of radiopharmaceuticals and enables precise control of the delivery of radiation to diseased tissue while minimising off-target effects. This selectivity is provided by the development of a targeting molecule that binds with high affinity to and is often internalised by a receptor that is overexpressed on the surface of the tumour cells.

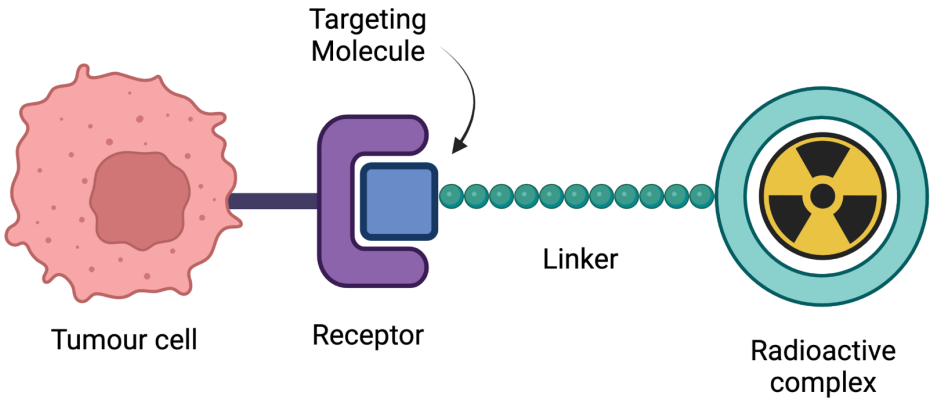

Figure 2: Schematic representation of a radiopharmaceutical, consisting of a radioactive compound, and a targeting molecule that is typically connected by a linker. The targeting molecule binds to a receptor on the tumour cell. Created with biorender.com.

Of the radionuclides with suitable energies and decay profiles for therapy and imaging, metallic radionuclides have become of particular interest due to the ability to form stable coordination complexes that can be functionalised with targeting molecules. In both diagnostic imaging and systemic radiation therapy, it is important to choose a radionuclide with suitable physical properties that allow for precise, sensitive imaging or the selective destruction of cancerous cells.

1.1.2 Understanding the Effects of Ionising Radiation on DNA

Therapeutic outcomes require that ionising radiation causes DNA damage to an extent beyond the capacity of the cell to repair it.[18-20] Direct exposure of DNA and proteins to ionising radiation can cause lesions to the DNA that include single/double-strand breaks, modifications of the DNA bases, DNA-protein conjugates and multiply damaged sites.[21] The damage to cells is proportional to the radiation dose and can occur as a direct or indirect interaction with DNA. A direct interaction involves radiation exposure where DNA or proteins are exposed to an ionising dose of radiation, and this either kills or mutates the DNA.[22] These DNA lesions can initiate downstream cellular signalling and ultimately apoptosis.[22] Ionising radiation also leads to the formation of free radicals, such as the hydroxyl radical that can hydroxylate

biomacromolecules. The formation of reactive free radical species is enhanced in the presence of oxygen, therefore hypoxic cells are more radioresistant than oxygenated cells. Actively dividing/mitotic cells (such as stomach mucosa, bone marrow, stem cells and basal layer skin cells) are more radiosensitive than mature and differentiated cells such as neurons.[23-26]

The decision to treat cancer with either α or β-emitting radionuclides depends on the type of tumour and extent of disease. High LET α particles exhibit an extraordinary degree of efficacy. Only 1 – 4 particles are necessary to traverse a nucleus and induce cell death.[27] Conversely, β^- particles possess a low LET (0.2 keV/μm). Therefore, thousands of β^- particles must travel through a cell nucleus in order to achieve an equivalent outcome. The range of β^- particles in tissue can extend beyond the targeted tumour, referred to as 'cross-fire', and is important for nuclear sterilisation. This has increased interest in radionuclides that emit relatively low energy β^- particles with a shorter penetration range in tissue. A potential advantage of the crossfire effect is that it is not essential to target each individual cell, provided the malignant environment falls within the ionising radius of particle-induced cell death.[28-30]

1.2 The FDA Approval of Four Radiopharmaceuticals Stimulates Interest in Radiotheranostics

At least part of the resurgence in interest in radiotheranostic approaches can be attributed to significant clinical and commercial successes in agents that target neuroendocrine tumours and prostate cancer. The intelligent design strategy and consequent clinical implementation of radiopharmaceuticals that contain radionuclides that emit β^- particles have laid the foundation for the development of treatments utilising α-emitting radionuclides like actinium-225.

1.2.1 Theranostics for Somatostatin-positive Tumours

Neuroendocrine tumours (NETs) are a heterogeneous group of neoplasms arising predominantly from endocrine cells in the gastrointestinal tract, pancreas or bronchial tree. Somatostatin receptors, especially the somatostatin subtype 2a receptor (SSTR2), are G-

coupled protein receptors which are highly overexpressed in neuroendocrine tumours compared to relatively low levels of expression in other tissues and organs. The SSTR2 receptor is also overexpressed in other malignancies such as medulloblastoma, neuroblastoma and meningioma (Figure 3, a).[31-33]

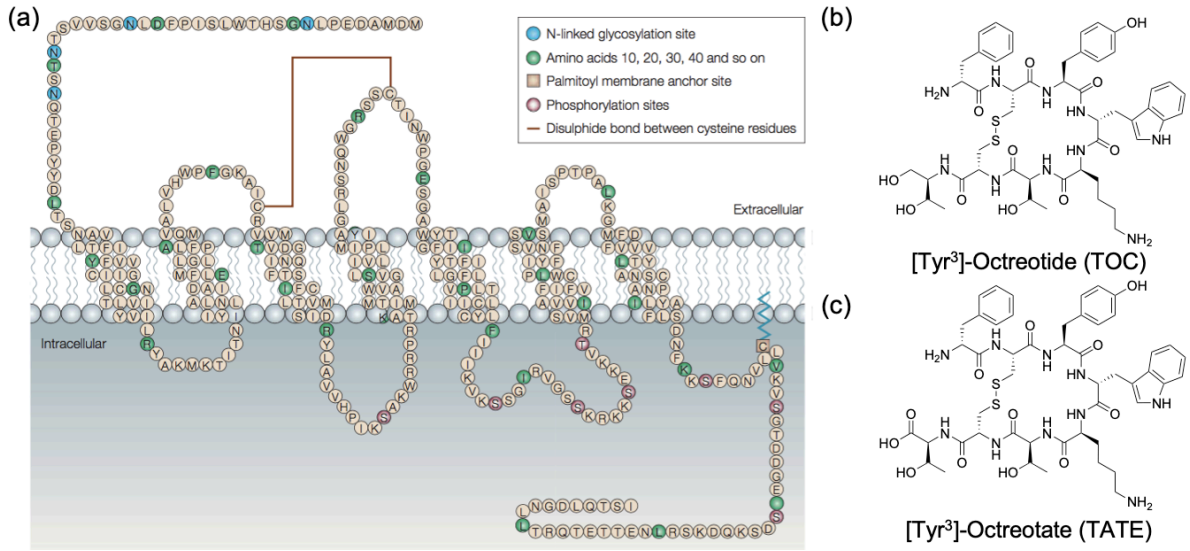

Figure 3: (a) Structure of the transmembrane receptor SSTR2;[34] (b) chemical structure of [Tyr^3]-octreotide and (c) [Tyr^3]-octreotate.

There are two forms of the natural somatostatin hormone that are either 14 or 28 amino acids in length, and they play a role in the regulation of the endocrine system affecting cell proliferation and neurotransmission. The somatostatin analogues octreotide and octreotate are cyclic peptides with 8-amino acid residues that have improved plasma stability compared to endogenous somatostatin but still retain a high affinity for SSTR2. Octreotide (D-Phe-c[Cys-Phe-D-Trp-Lys-Thr-Cys]-Thr-ol) maintains the crucial β-turn induced by D-tryptophan and lysine residues with low nanomolar affinity for SSTR2 (2- 22 nM).[35-37] Further improvements on the peptide were later made, including the development of [Tyr^3]-octreotide (TOC), where the third phenylalanine residue is replaced with tyrosine (Figure 3, b). The C-terminal threoninol was then replaced with threonine to give [Tyr^3]-octreotate (TATE, D-Phe-c[Cys-Tyr-DTrp-Lys-Thr-Cys]-Thr, Figure 3, c), which exhibited a nine-fold increase in binding affinity to the SSTR2 receptor.[38 39, 40 41 42]

Some of the first SPECT diagnostic imaging of SSTR2 positive tumours used [^{111}In]In-pentetreotide, a tracer prepared by conjugation of the metal chelator diethylenediaminepentaacetic acid (DTPA) to octreotide (Figure 4, a). The chelator forms a stable complex with In^{III} (Figure 4, b),[43] allowing the pentetreotide to be radiolabelled with γ-emitting [^{111}In]In^{III} (half-life ($t_{1/2}$) = 67.2 hours, EC (100%); two low energy γ emissions, E_γ (mean) 171 keV (Iγ = 91%) and 245 keV (Iγ = 94%).[44] Early attempts to translate this diagnostic approach to peptide-targeted therapy of SSTR2 positive tumours examined using the Auger electron emission properties of indium-111 to reduce tumour burden. Auger emissions are observed in nuclei that decay by electron capture as low-energy electron emissions that travel over extremely short distances (<10 μm, often in the nm range) and generally exhibit very high LET. This required the administration of relatively high amounts of radioactivity (up to 18.5 GBq) of [^{111}In]In-pentetreotide per cycle).[17, 45-47] This approach proved to have limited efficacy, presumably partly due to the short tissue penetration range of the Auger emissions and insufficient localisation of the agent in the respective cell nuclei.

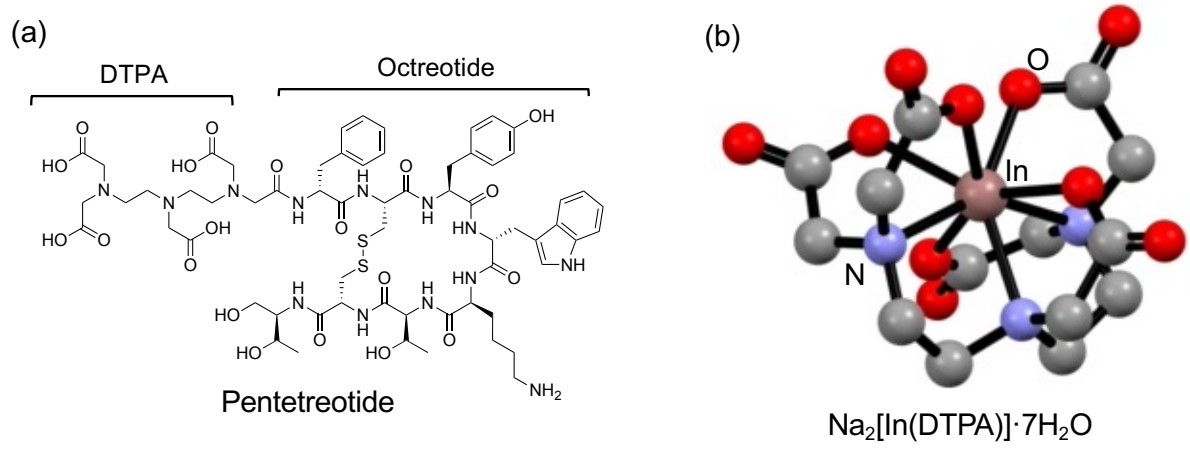

Figure 4: (a) Chemical structure of pentetreotide and (b) ball and stick representation of the complex anion present in $Na_2[In(DTPA)]\cdot 7H_2O$ as determined by X-ray crystallography.[43]

The limited success afforded by indium-111 Auger therapy meant that the focus of peptide-targeted radiotherapy then shifted to the β^--emitting radionuclide, yttrium-90 ($t_{1/2}$ = 2.67 days, β^- 100%, E_β (mean) 934 keV).[48] Yttrium-90 is produced either by the neutron irradiation of

natural yttrium or by chemical separation from its parent isotope, strontium-90, which is available from nuclear waste because strontium-90 is a major fission product of uranium-235. Yttrium-90 produced by (n,γ) activation requires a high flux nuclear reactor, and the product is of low specific activity due to the small neutron cross-section of natural strontium.[49] The difficulty of separating no carrier-added yttrium-90 from strontium-90 ($t_{1/2}$ = 28.8 years) has hampered the clinical implementation of yttrium-90 radiopharmaceuticals. The presence of strontium-90 impurities results in the deposition of the radionuclide in bone due to the chemical similarities of strontium and calcium. Although it has been proposed that $^{90}Sr/^{90}Y$ generators could allow for convenient on-site production of yttrium-90, the technology is yet to be translated to a level that could be applied to a clinical setting.[50]

Somatostatin targeted radiotherapy with yttrium-90 based agents is associated with moderate nephrotoxicity due to the relatively high energy of the β^- particles, which have a relatively long range in tissue (up to 12 mm).[51] Dose-limiting nephrotoxicity is common as radiolabelled peptides are filtered by the glomerulus, followed by reabsorption in the renal proximal tubuli.[52, 53] The co-infusion of an amino acid solution (lysine and arginine) can be administered to protect the kidneys against the effects of radiation without the induction of hyperkalaemia.[54-56]

The complications associated with the nephrotoxicity of yttrium-90 based agents contributed to a switch in focus to lutetium-177 ($t_{1/2}$ = 6.65 days, β^- 100%, E_β (mean) 134 keV) with less energetic β^- particle emissions. Initial investigations identified that the peptide-targeted radionuclide therapy with lutetium-177 based agents was capable of achieving a similar therapeutic efficacy to ytrrium-90 based agents but with less toxicity.[57, 58] These comparatively short-range β^- particle emissions from lutetium-177 (up to 3 mm) result in higher doses being delivered to tumours with less effect on the dose-limiting organs when compared to therapy with yttrium-90 based molecules. The improved toxicity profile of

lutetium-177 based somatostatin targeting agents coupled with the challenges associated with the production of yttrium-90 have seen lutetium-177 become the radionuclide of choice for peptide receptor radionuclide therapy (PRRT).

For therapeutic applications with cytotoxic radionuclides, it is important that the radioactive metal ion remains bound to the targeting agent to maximise therapeutic effects whilst minimising off-target toxicity. The increased importance of using stable metal complexes contributed to a change in the metal chelator used from the acyclic polyamine carboxylate ligand DTPA to the macrocyclic tetraamine ligand 1,4,7,10-tetraazacyclododecane-1,4,7,10-tetracetic acid (DOTA) prepared by the introduction of carboxymethyl groups into the tetraaza macrocycle 1,4,7,10-tetraazacyclododecane (cyclen). Conjugation of DOTA to the 8-amino acid peptide octreotate to give DOTATATE (Figure 5) results in a ligand that forms sufficiently stable complexes with $[^{68}Ga]Ga^{III}$ for diagnostic PET imaging and $[^{177}Lu]Lu^{III}$ for targeted peptide radionuclide therapy.

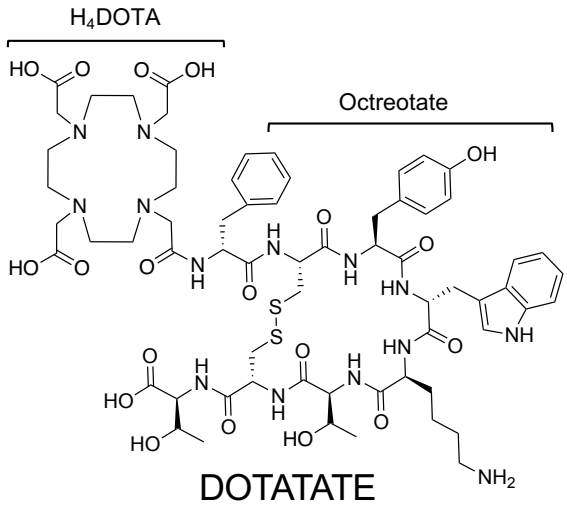

Figure 5: The chemical structure of DOTA-Tyr^3-octreotate (DOTATATE).

The increased availability of the β^+-emitting radionuclide gallium-68 ($E\beta^+_{max}$ = 1,899 keV $E\beta^+_{mean}$ = 829 keV $t_{1/2}$ = 68 minutes) due to the development of small portable generators based on germanium-68, as well as the increased resolution of PET imaging compared to SPECT imaging, has seen increased adoption of PET imaging with gallium-68 labelled peptides for

the diagnosis and staging of disease suitable for somatostatin targeted radiotherapy. The effective radiation dose of a gallium-68 PET scan is also lower than that of an indium-111 SPECT scan due to the shorter half-life and lower particle energy of gallium-68.[59]

Although [^{68}Ga]Ga^{III} and [^{177}Lu]Lu^{III} both form complexes with DOTATATE, they have different coordination geometries and chemical structures and consequently different binding affinities for somatostatin receptors.[60] The difference in chemical structures can be inferred by examination of the structures of [Lu(OH_2)(DOTA)]$^-$ and the Ga^{III} complex of a DOTA-D-Phe-NH_2 conjugate, [Ga(DOTA-D-Phe-NH_2)] as determined by single crystal X-ray crystallography. In the structure of Na[Lu(DOTA)(H_2O)]·4H_2O, the Lu^{III} is nine coordinate and in a capped square prismatic environment (Figure 6, a) with the DOTA ligand acting as an octadentate N_4O_4 donor with one coordinated water molecule completing the coordination sphere.[61] The different coordination environments may have significant implications for biodistribution as peptide-metal complex assemblies prepared with different metal ions do not have the same binding and internalisation.[60]

The Ga^{III} complex of DOTA-D-Phe-NH_2 was investigated as a small molecule analogue of octreotate, where the first amino acid is D-Phe (Figure 6, b). In this complex, the Ga^{III} is in a six-coordinate distorted octahedral geometry with the ligand acting as a hexadentate N_4O_2 donor. The equatorial plane is formed by two *trans*annular nitrogens in the cyclen ring and two oxygens from the carboxylate groups, both *cis* to each other. One of the carboxylate functional groups is not involved in coordination to the metal ions and is deprotonated at physiological pH, which likely contributes to rapid renal excretion of these peptide conjugates.[62] The different coordination environments may have significant implications for biodistribution as peptide-metal complex assemblies prepared with different metal ions do not have the same binding and internalisation.[60]

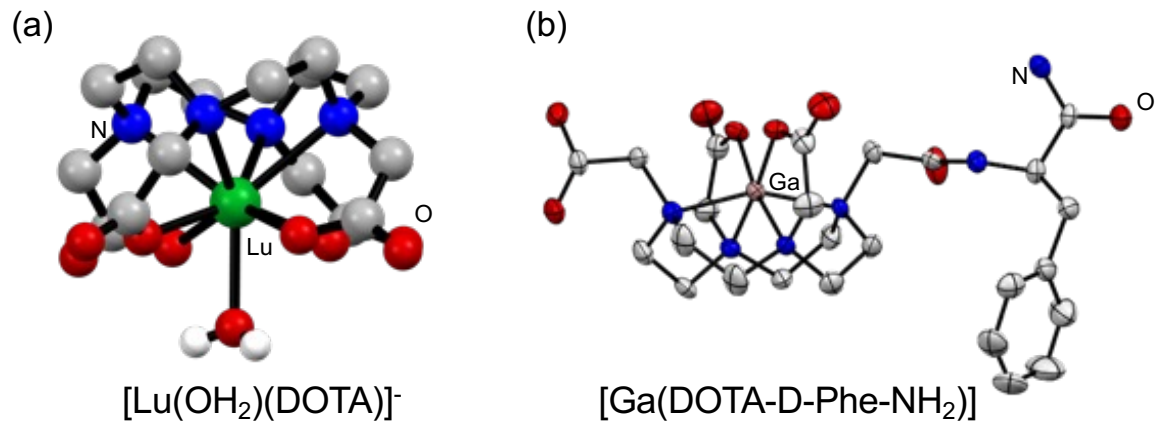

Figure 6: (a) Ball and stick representation of the complex anion present in $Na[Lu(DOTA)(H_2O)]\cdot 4H_2O$ as determined by X-ray crystallography,[61] (b) ORTEP representation of $[Ga(DOTA\text{-}D\text{-}Phe\text{-}NH_2)]$ as determined by X-ray crystallography, thermal ellipsoids are shown at 50% probability.[62]

Despite the differences in the coordination chemistry of Ga^{III} and Lu^{III} an effective approach for the treatment of somatostatin positive tumours has been established where diagnostic PET imaging with the [^{68}Ga]Ga(DOTATATE) (or the closely related [^{68}Ga]Ga(DOTATOC)) is used to guide therapy with [^{177}Lu]Lu(DOTATATE).[38, 42, 63-68]

In a significant clinical example of this approach, PET imaging using [^{68}Ga]Ga(DOTATATE) in a patient with high-grade metastatic renal NET clearly showed uptake in locoregional nodal and diffuse hepatic metastases (Figure 7, a). After receiving four cycles of [^{177}Lu]Lu(DOTATATE) combined with the radio-sensitising agent (5-fluorouracil), a repeat scan using [^{68}Ga]Ga(DOTATATE) shows a near complete imaging response (Figure 7, b). PRRT with [^{177}Lu]Lu(DOTATATE) is now a part of the current treatment guidelines for patients with advanced locoregional disease or distant metastases for NETs in the gastrointestinal tract.[55]

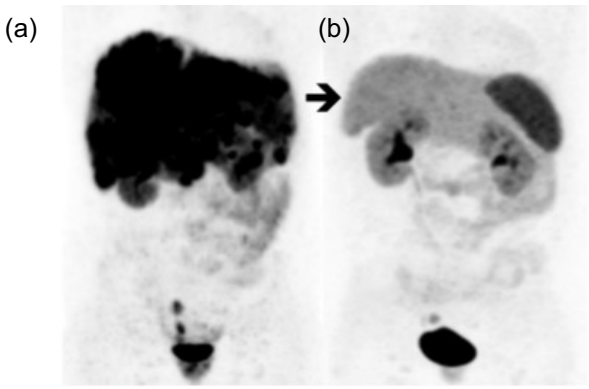

Figure 7: (a) PET image of a patient with high-grade metastatic renal NETs using [^{68}Ga]Ga(DOTATATE) as the diagnostic imaging agent. The patient received four cycles of [^{177}Lu]Lu(DOTATATE); (b) [^{68}Ga]Ga(DOTATATE) PET/CT obtained three months later shows near complete imaging response (black arrow).[69]

The clinical approvals by the Food and Drug Administration (FDA) of [^{68}Ga]Ga(DOTATATE) for the 'for localisation of somatostatin receptor-positive NETs' in 2016 and of [^{177}Lu]Lu(DOTATATE) for the 'treatment of somatostatin receptor-positive gastroenteropancreatic NETs' in 2018 are significant milestones in the field of theranostics and the culmination of decades of pioneering research across multiple disciplines.[70, 71 72-77]

Targeted radionuclide therapy with [^{177}Lu]Lu(DOTATATE) is useful for the treatment of grade 1 and 2 neuroendocrine neoplasms and for patients with progressive disease. This type of peptide receptor radionuclide therapy can also be useful for controlling symptomatic disease in hormone-secretory syndromes or tumour-related pain.[78] Neuroendocrine neoplasms that over-express somatostatin receptors are relatively rare, but the success in targeting these tumours has provided the foundations for radiotheranostic approaches for the treatment of other cancers. In particular, this approach has proven successful for the diagnosis and treatment of prostate cancer, a much more common malignancy.

1.2.2 Theranostics for Prostate Cancer using Peptidomimetics

This pioneering work to develop diagnostic imaging and radiation therapy for SSTR2 tumours stimulated the development of molecular agents to target prostate cancer. Prostate Specific Membrane Antigen (PSMA), also known as glutamate carboxypeptidase II and folate

hydrolase I is a membrane-bound zinc metalloenzyme overexpressed in 90% of prostate carcinomas.[79, 80] It is an integral membrane-bound glycoprotein with a 707 amino-acid extracellular C-terminal domain, 24 amino acid transmembrane portion and 19 amino acid internal domain (Figure 8, a).[81, 82] The overexpression of PSMA in prostate cancers is especially pronounced in metastatic and castration-resistant prostate cancer (mCRPC). Although PSMA is present in normal epithelium, there is significantly lower expression in healthy tissue, making it a promising target for imaging and therapy.

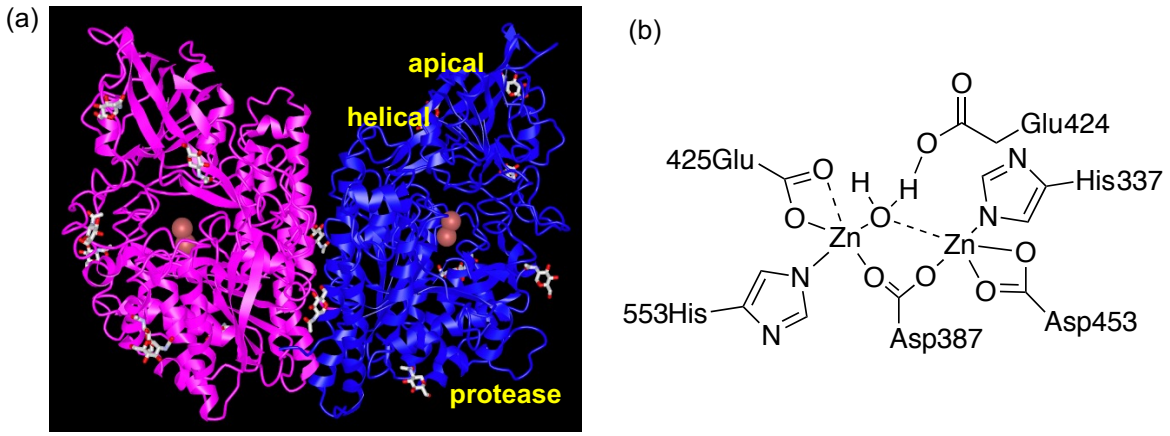

Figure 8: (a) Ribbon diagram of the PSMA ectodomain homodimer as determined by X-ray crystallography, (b) structure of the binuclear zinc active site in the protease domain of PSMA.[83]

The enzymatic activity of PSMA has allowed for the development of selective inhibitors that bind to the enzyme with high affinity and undergo internalisation after ligand binding. Several different structural motifs were identified as effective PSMA inhibitors, with the original focus on developing inhibitors of *N*-acetyl-α-linked acidic dipeptidase I in brain tissue.[84-86] These initial studies identified urea-based (and phosphonic acid–based) amino acid containing small molecules as potent ligands for PSMA. These pharmacophores were refined to achieve maximum uptake and retention for diagnostic imaging and radionuclide therapy. The gallium-68 and lutetium-177 PSMA agents that have reached clinical approval feature the urea-linked amino acid dimer glutamate-ureido-lysine (Glu-NH-CO-NH-Lys). The importance of retaining the glutamate amino acid is unsurprising, considering the physiological role of PSMA is to hydrolyse polyglutamated folate and other carboxyterminated glutamates.

Molecules containing the tricarboxylate Glu-NH-CO-NH-Lys motif often retain an impressive selectivity for the active site, but the urea linkage serves as a bioisosteric replacement of an amide that is resistant to hydrolysis. The active site and substrate-binding cavity of PSMA lie deep within the protein and feature two Zn^{II} atoms similar to other binuclear zinc exopeptidases (Figure 8, b). For Ga^{III} and Lu^{III} complexes that bind to PSMA, the Glu-NH-CO-NH-Lys functional group is separated from the metal complex by a hydrophobic spacer to promote access of the pharmacophore to the active site that is buried within the enzyme. This following discussion will focus on two metal-based PSMA targeting radiopharmaceuticals, [^{68}Ga]Ga(PSMA-11) and [^{177}Lu]Lu(PSMA-617), but it is acknowledged that other molecules have been developed that are either in clinical use or in clinical development.[87, 88 89]

A significant development in PET imaging of PSMA in prostate cancer was the design and synthesis of a molecule given the name of [^{68}Ga]Ga(PSMA-11). PSMA-11 includes a HBED-CC chelator (HBED-CC = N,N'-bis-[2-hydroxy-5-(carboxyethyl)benzyl]ethylenediamine-N,N'-diacetic acid, Figure 9, a) which forms stable complexes with [^{68}Ga]Ga^{III}. The HBED-CC chelator is attached to a Glu-NH-CO-NH-Lys pharmacophore through an aminohexanoic acid (Ahx) linker (Figure 9, b).[90] The parent phenolic aminocarboxylate chelator, N,N-bis(2-Hydroxybenzyl)ethylenediamine-N,N-diacetic acid (HBED) was originally investigated as a ligand for Fe^{III} and [Fe(HBED)]- complexes were developed as liver-enhancing agents for magnetic resonance imaging (MRI).[91, 92]

The PSMA-11 ligand forms complexes with [^{68}Ga]Ga^{III} at room temperature, but complexation at room temperature leads to the formation of multiple isomers similar to what is observed for complexes of HBED with Fe^{III}.[91-93] Increasing the reaction temperature to 95 °C favours the formation of the thermodynamically favoured product (RR), the major geometric isomer.[94, 95]

Some insight into the molecular structure of [^{68}Ga]Ga(PSMA-11) can be inferred from the molecular structure of the Ga^{III} complex of the parent HBED ligand, [Ga(OH_2)HBED] as determined by X-ray crystallography (Figure 9, c).[93] The Ga^{III} is in a six-coordinate distorted octahedral environment with the HBED ligand acting as a pentadentate N_2O_3 donor with the two carboxylate groups *trans* to each other and the two secondary amines *cis* to each other. A coordinated water molecule occupies the remaining coordination site, and only one of the two phenolic groups is coordinated to the Ga^{III}. The non-coordinating phenolic group is protonated and uncharged. Other isomers are present, where the phenol groups and the carboxylates exchange coordination around the Ga^{III} centre, as shown in NMR experiments (^{1}H, ^{13}C,[96] COSY, HSQC and ^{71}Ga spectra).[93]

An early clinical study with [^{68}Ga]Ga(PSMA-11) was in a 67-year-old patient who had undergone previous radiotherapy of the prostate due to carcinoma. PET imaging with [^{68}Ga]Ga(PSMA-11) was able to identify a lesion adjacent to the urinary bladder that was not detected by PET imaging with [^{18}F]-fluoromethylcholine.[90, 97] These initial clinical studies were followed by several large-cohort, multi-centre clinical trials that confirmed that [^{68}Ga]Ga(PSMA-11) is an excellent tracer to assist in the diagnosis of prostate cancer and was superior to PET imaging with choline based tracers (Figure 9, d).[87, 97, 98]

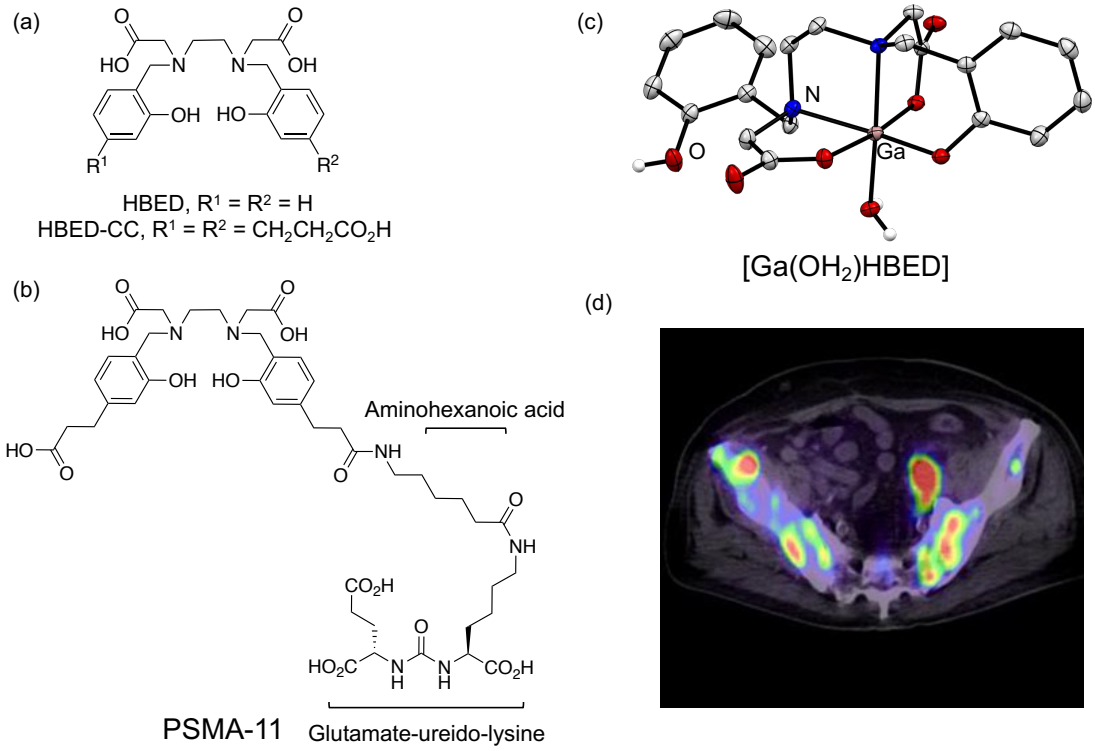

Figure 9: (a) Chemical structure of HBED, where R^1, R^2 = H & HBED-CC where R^1, R^2 = $CH_2CH_2CO_2H$, (b) chemical structure of PSMA-11, (c) ORTEP representation of the neutral [Ga(HBED)(H_2O)] as determined by X-ray crystallography, thermal ellipsoids shown at 50% probability;[93] (d) PET/CT of a patient representative for disseminated lymph node and bone metastases of prostate cancer imaging using [^{68}Ga]Ga(PSMA-11).[97]

In 2020, [^{68}Ga]Ga(PSMA-11) was approved by the Food and Drug Administration (USA) for 'the initial diagnosis and staging of prostate cancer patients with suspected metastases and the imaging of patients with suspected biochemical recurrence after prostatectomy or radiation therapy'.[99] The FDA approval of [^{68}Ga]Ga(PSMA-11) was made possible through an interesting academic partnership between two Universities who collaborated to conduct a bicentric phase 3 clinical trial for PET imaging of prostate cancer where the trials were specifically designed to achieve clinical approval.[100] The ligand required to synthesise [^{68}Ga]Ga(PSMA-11) is now available in convenient 'kit' formulations that are commercially available.[101] The agent has become important in selecting patients for radionuclide therapy with PSMA targeting agents labelled with lutetium-177.

1.2.3 Treatment of Cancer with Lutetium-177

Considering the clinical success of radionuclide therapy with [^{177}Lu]Lu(DOTATATE), it was an obvious extension to pursue a therapeutic partner to PET imaging of prostate cancer with [^{68}Ga]Ga(PSMA-11). Unfortunately, the HBED-CC chelator used in PSMA-11 does not form complexes with [^{177}Lu]Lu^{III} that were of sufficient stability for *in vivo* applications. This led to the development of PSMA targeting molecules containing the Glu-NH-CO-NH-Lys motif, but where the HBED-CC chelator (Figure 9, a) was replaced with DOTA, which forms stable complexes with [^{177}Lu]Lu^{III} (Figure 10, a). In 2022, the FDA (USA) approved [^{177}Lu]Lu(PSMA-617) (also known as lutetium-177 vipivotide tetraxetan and Pluvicto®) for the 'treatment of adult patients with prostate-specific membrane antigen (PSMA)-positive metastatic castration-resistant prostate cancer (mCRPC) who have been treated with androgen receptor pathway inhibition and taxane-based chemotherapy'.[102] [^{177}Lu]Lu(PSMA-617) was originally developed by researchers at The German Cancer Research Center and University Hospital Heidelberg, Germany.[103] The molecule contains a glutamate-ureido-lysine motif, but the linker between the pharmacophore and the DOTA chelator was systematically optimised to improve tumour uptake and internalisation as well as pharmacokinetic properties. Therapeutic applications benefit from both high tumour uptake and retention of the radionuclide in the tumour. Tumour retention is related to internalisation. The tumour uptake and internalisation of Glu-NH-CO-NH-Lys containing derivatives depends on molecular features outside the Glu-NH-CO-NH-Lys motif that interact with the Zn^{II}-containing active site. Intelligent exploratory synthetic chemistry and thorough structure-activity studies led to the selection of PSMA-617 where the Glu-NH-CO-NH-Lys motif is separated from the DOTA chelator by 2-naphthyl-L-alanine (NaI) and tranexamic acid, TXA (Figure 10, a).[103, 104]

The FDA approval of [^{177}Lu]Lu(PSMA-617) in 2022 followed a phase III clinical trial that established an increase in progression-free and overall survival in patients with mCRPC.[80,

[105-107] The efficacy of [^{177}Lu]Lu(PSMA-617) radionuclide therapy is highlighted in images obtained from the phase II investigation. [^{68}Ga]Ga(PSMA-11) PET images were taken before and after [^{177}Lu]Lu(PSMA-617) radionuclide therapy (up to 4 cycles every 6 weeks) in patients with mCRPC, who were non-responsive to the standard care (Figure 10, b). [^{68}Ga]Ga(PSMA-11) imaging before and after treatment with 6 ± 2 GBq of [^{177}Lu]Lu(PSMA-617), adjusted according to tumour burden, showed an incredible response and an associated decline in the prostate-specific antigen (PSA) levels, a common serum biomarker for PC (967 ng/ mL to 7 ng/mL).[108]

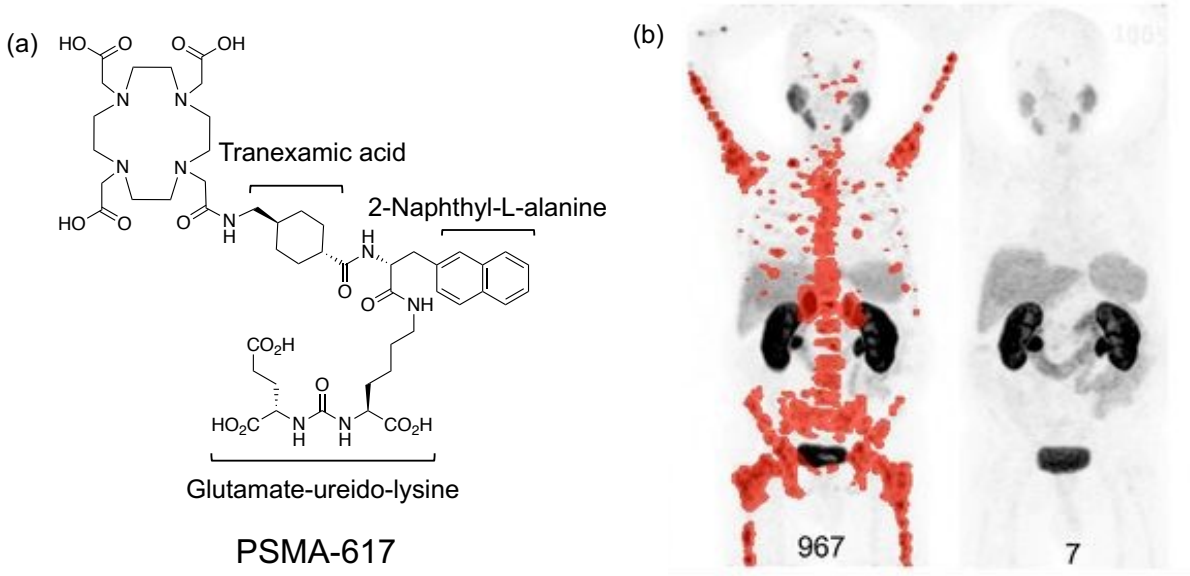

Figure 10: (a) Chemical structure of PSMA-617; (b) [^{68}Ga]Ga(PSMA-11) PET maximum intensity projection (MIP) images before (left) with PSA 967 ng/mL and three months after (right) [^{177}Lu]Lu(PSMA-617) radionuclide therapy, PSA 7 ng/ mL.[108]

With the advent of new imaging technologies and the production of radionuclides, diagnostic imaging and systemic radiation therapy are becoming more widely available. While external beam radiation therapy is considered a pillar in oncologic treatment, systemic radiation therapy is still considered a 'last resort'.[1] There are still some challenges and limitations that are impeding widespread adoption in clinical cancer care. One of these challenges is the relatively narrow scope of the indications for which the agents have gained clinical approval. For example, to be eligible for treatment with [^{177}Lu]Lu(PSMA-617) patients must have

already been treated with androgen receptor pathway inhibition and taxane-based chemotherapy and are no longer responding to this treatment. It is possible that these restrictions are limiting the number of patients who could benefit and supports the notion of radionuclide therapy being a last resort.[109] Despite these impressive results, which have culminated in the FDA approval of a select few diagnostic imaging and radionuclide therapeutics, overall, the success rate of cancer drugs from first trials to FDA approval is only 3.4%.[110] This highlights the challenges of bringing a drug from 'benchtop to bedside'.

The dramatic responses seen in some patients treated with radionuclide therapy, when compared to other treatments, point to tantalising opportunities. The relative success in radiotheranostics that target malignancies that over-express somatostatin receptors or prostate specific membrane antigen is highly dependent on the differential expression of these targets on cancerous tissue when compared to comparatively low expression in other tissues and organs. The successful engagement of these molecular targets also relied on creative synthetic chemistry to develop metabolically stable peptides or peptidomimetics that bind to the target with high affinity leading to high tumour uptake but also retention. The FDA approval of these molecular agents marks a significant milestone in the advancement of systemic radionuclide therapy and is promising in the development of systemic radionuclide therapy with other nuclides. These approvals are the result of more than two decades of research and the collaborative efforts of numerous research groups and institutions. These achievements underscore the potential of using other radionuclides, such as α-emitting actinium-225.

2 H_2MacropaSqOEt, a New Ligand for Targeted Alpha Therapy with Actinium-225 Labelled Antibodies

André Louis Debierne claimed the discovery of elemental actinium in 1899 after supposedly separating actinium from uranium ore pitchblende. It was 'rediscovered' in 1902 by Friedrich Oskar Giesel. It is now believed that Debierne's original discovery in 1899 likely contained no actinium, and what followed in his 1900 preparation was actually a mixture of several radioisotopes that perhaps only contained trace elements of actinium.[111] Although there have been 32 isotopes of actinium discovered or synthetically produced, actinium-227 is the most stable isotope ($t_{1/2.}$ = 21.77 years) and the only isotope that occurs in nature as part of the long decay series of uranium-235.[112] The lack of non-radioactive isotopes of actinium and the scarcity of the element add further complications. One gram of natural uranium estimated to contain at most 2×10^{-10} gram of actinium due to the low isotopic abundance of uranium-235 (0.72%).[111]

2.1 Understanding the Coordination Chemistry of Actinium

Actinium has [Rn] $6d^1$ $7s^2$ electronic configuration, with the +III oxidation state being the most common ionic form similar to the other actinoid and lanthanoid elements. The challenges of actinium coordination chemistry are further amplified by the ground state configuration of trivalent actinium ion being $5f^0$ $6d^0$, which are silent to conventional spectroscopic techniques such as ultraviolet-visible, fluorescence and electron paramagnetic resonance.[112] The fundamental knowledge of actinium coordination chemistry is limited, with only a handful of complexes characterised by X-ray powder diffractions on a microgram scale (2 – 10 μg).[113-115] The compounds AcF_3, $AcCl_3$, $AcBr_3$, AcOF, AcOCl, AcOBr, Ac_2O_3, $AcPO_4.0.5H_2O$, and Ac_2S_3 were all synthesised by Fried *et al.*[113] and compared with the corresponding lanthanum complexes. The nine complexes were confirmed to be isostructural

with lanthanum, which is the second-largest trivalent cation in the periodic table. Notably, the unit cell dimensions were consistently larger for the actinium compounds when compared to the corresponding lanthanum complexes, presumably due to the larger ionic radius of the actinium cation.[113]

The earliest spectroscopic and computational investigations of actinium coordination chemistry used X-ray absorption fine structure (XAFS) and L_3-edge X-ray absorption near-edge structure (XANES) spectroscopy to evaluate the coordination chemistry of trivalent $[^{227}Ac]Ac^{III}$ and Am^{III} with binding to chloride ions. This process utilised Ac^{III} and Am^{III} in concentrated HCl (11 M) to make comparisons to the Am^{III}-aqua ion (Am^{III} in HO_3SCF_3, 0.11 M).[112]

In XAFS spectroscopy, as the wavelength (λ) of the X-rays decreases, the absorption coefficient (μ) also decreases until a critical wavelength is reached when there is a sharp rise in the extinction coefficient for the absorption of X-rays, classified as the 'edge', which represents the ejection of a core electron.[116] The constructive and destructive interactions of the photoelectron with the backscattering from adjacent atoms allow the measurement of well-known oscillations and is useful for extracting information of the local atomic structure. These spectra undergo a Fourier transformation, providing information on coordination number and metal-ligand (M–L) bond lengths.[117] XAFS oscillations are typically only observed for atoms within approximately 5 Å of the absorbing atom (Figure 11).[118]

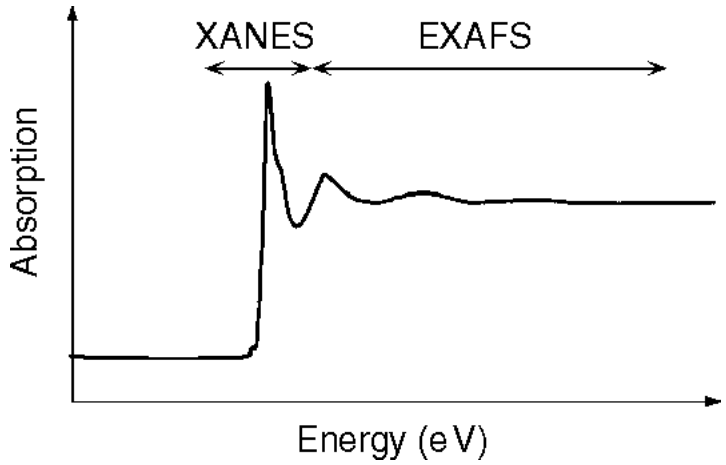

Figure 11: Illustration of an X-ray absorption spectrum, showing the characteristic absorption of the X-ray absorption near-edge structure (XANES) and extended X-ray absorption fine structure (EXAFS regions). The XANES region is characterised by the absorption edge, that provides information of the electronic structure and oxidation state. The EXAFS region has a higher energy than the XANES region. [118]

Ferrier demonstrated that the three spectra of $[^{227}Ac]Ac(HCl)_x$, and $Am(HCl)_x$, and $Am(OH_2)_x$, showed a pronounced edge peak, which was explained to be an electric-dipole-allowed transition[119] from the 2p orbital to an unoccupied 6d orbital such as $2p^6…5f^0\ 6d^0$ to $2p^5\ …5f^0\ 6d^1$. Both americium spectra looked very similar, suggesting the H_2O molecules dominated the inner coordination sphere. In contrast, the $[^{227}Ac]Ac(HCl)_x$ spectrum had two different contributions. The $[^{227}Ac]Ac(HCl)_x$ spectrum indicated that both Cl^- and H_2O molecules were in the inner coordination sphere.

The extended X-ray absorption fine structure (EXAFS) is characterised by oscillations that arise from constructive and destructive interferences of the X-rays scattered by neighbouring atoms. Analysis of the EXAFS spectra suggested the primary coordination sphere included 6.6 ± 1.8 water molecules with a bond distance of 2.59 (3) Å and 3.2 ± 1.1 chlorido ligands with an estimated bond distance of 2.95(3) Å.[120] Computational modelling predicted Ac–O H_2O and Ac–Cl bond lengths of 2.76 ± 0.08 and 3.04 ± 0.13 Å, respectively, agreeing with experimentally determined values from two unique scattering paths. This was done with molecular dynamic density functional theory (MD-DFT) calculations conducted on a box containing one $[^{227}Ac]Ac^{III}$, three Cl^- ligands and 64 H_2O molecules for 1 ps. The MD-DFT

revealed 3 Cl^- and 6.14 ± 0.34 H_2O ligands within the first coordination sphere of the [^{227}Ac]Ac^{III} ion (4 Å) for the duration of the DFT calculation. The Ac–O H_2O and Ac–Cl calculated distances agreed with the EXAFS analysis at 2.76 ± 0.08 and 3.04 ± 0.13 Å, respectively.

Characterisation of the [^{227}Ac]Ac-aqua ion aimed to further understand fundamental actinium chemistry, which is necessary to understand the thermodynamic constants that predict metal complexation, aqueous speciation, and equilibria in biological systems.[120, 121] The microgram quantity of radioactive [^{227}Ac]Ac available for experimental work made the synthesis of the [^{227}Ac]Ac-aqua ion exceptionally challenging. It was not possible to separate actinium-227; therefore, lutetium was required as a macroscopic carrier. The products were then centrifuged and redissolved in dilute aqueous triflic acid.

EXAFS spectroscopy analysed the [^{227}Ac]Ac-aqua ion, suggesting the inner coordination sphere contains 10.9 ± 0.5 water molecules with an average bond distance of 2.63(1) Å. The [^{227}Ac]Ac-aqua ion coordination number is slightly higher than other actinide and lanthanide aqua ions and is the only example of an 11-coordinate aqua complex. The relatively long Ac−O H_2O bond lengths further illustrate that actinium is the largest trivalent cation in the periodic table. Although some coordination chemistry can be extrapolated from La^{III} chemistry, there are limitations due to its smaller ionic radius La^{III} (1.03 Å) when compared to Ac^{III} (1.12 Å).

2.2 The Production of Actinium-225

The isotope [^{225}Ac]Ac^{III} ($t_{1/2}$ = 9.9 days) has shown the most promise as a potential actinium radiopharmaceutical.[122] [^{225}Ac]Ac^{III} decays to the near stable isotope bismuth-209 ($t_{1/2} = 1.9 \times 10^{19}$ years) *via* the release of four α particles and two β particles, and it is a member of the neptunium decay series ($t_{1/2} = 2.14 \times 10^6$ years, Figure 12). Actinium-225 is most readily produced by 'milking' a sample of thorium-229 ($t_{1/2}$ = 7340 years)[123, 124] that is generated *via*

neutron bombardment of naturally abundant thorium or from uranium-233 decay extracted from nuclear stockpiles.[125]

There are three sources of thorium-229 globally, the Oak Ridge National Laboratory (USA), the Directorate for Nuclear Safety and Security of the Joint Research Centre (JRC, Germany) and the Institute of Physics and Power Engineering (IPPE, Russia). The separation and purification of actinium-225 from radium-225 as well as the thorium-229 parent nuclide ($t_{1/2}$ = 7340 years) are based on ion exchange methods in aqueous HNO_3. The thorium-229 source (214.5 mg) produces approximately 1.68 GBq (45.6 mCi), and based on the half-life of actinium-225, approximately 1.46 GBq (39.4 mCi) can be isolated from the thorium source every 9 weeks.[123]

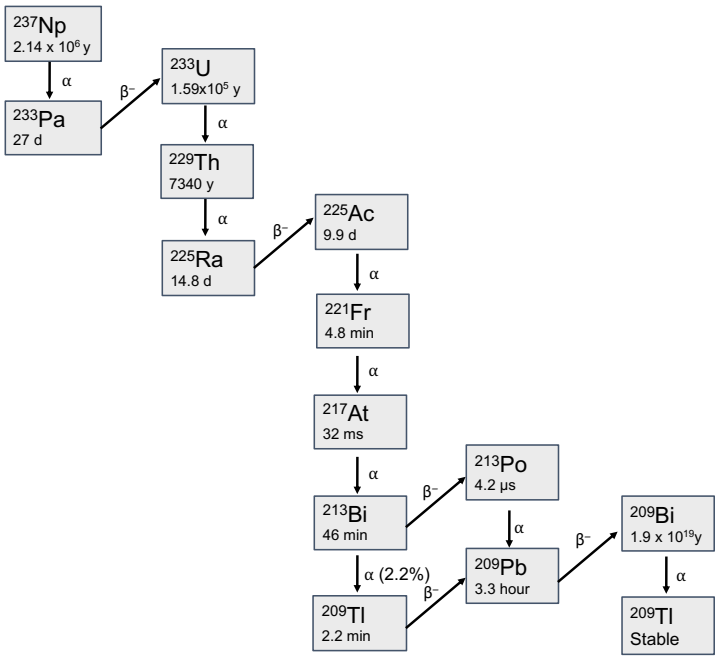

Figure 12: Decay pathway of actinium-225 from ^{237}Np to stable ^{205} Tl.

With current production of actinium-225 only approximately 75 GBq,[126] it is widely recognised that new techniques are necessary to increase the production of actinium-225 so that the supply is not heavily restricted at a cost that is not prohibitive to advances in research. This includes proton irradiation of radium-226 targets in a cyclotron through the ^{226}Ra (p,2n) ^{225}Ac reaction. Radium targets (30.1 mg) were irradiated with a 16 MeV proton beam for 45.3

hours with a proton current of 50 mA yielding 0.48 GBq (13.1 mCi) of actinium-225. This new technique showed no significant differences in radiochemical purity compared to clinical grade actinium-225, as shown in the alpha spectra of the two samples (Figure 13), providing promising results for potential strategies to ease the bottleneck on global actinium-225 production.[127]

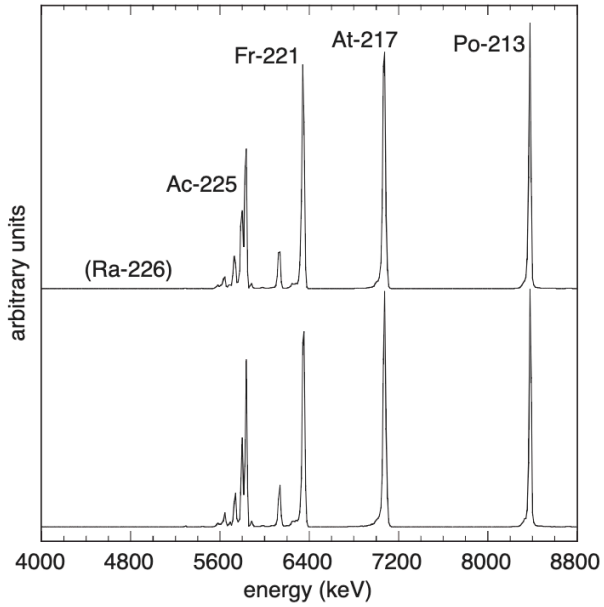

Figure 13: Alpha spectra of purified actinium-225 produced *via* cyclotron irradiation (top) and actinium-225 extracted from thorium-229 (bottom).[127]

Another production strategy that has been investigated recently the irradiation of natural thorium targets with high-energy protons (> 70 MeV). This $^{232}Th(p, x)^{225}Ac$ spallation reaction may provide an alternative production route of actinium-225.[125] Unfortunately, the co-production of unwanted actinium-227, which has a significantly longer half-life ($t_{1/2}$ = 21.77 years), occurs at a low percentage of the total actinium-225 activity (0.1 – 0.3%). This limits the potential application of the actinium-225 production method by high-energy spallation. This is primarily due to the strict measures in place for the injection of radionuclides with longer half-lives and the disposal strategies for actinium-227. In a more recently developed process using a radium-225/actinium-225 generator derived from irradiated thorium (438 ± 2 MeV), actinium-225 was produced with quantities of actinium-227 that are 2000-fold lower

than the first $^{232}Th(p, x)^{225}Ac$ spallation reaction.[128] It is possible to obtain actinium-225 with a total percentage of actinium-227 of 7.5×10^{-5} % by conducting another extraction chromatography step from the radium-225 fraction.

2.3 The Practical Challenges of Using Actinium-225

As actinium decays, it emits four daughter α particles and two β particles, some of which may decomplex with the metal chelator. These daughter radionuclides have different decay characteristics and therefore are detected differently from actinium.[129]

The recoil energy associated with the decay of α particles is in the range of 0.05 –0.1 MeV, which is far greater than any chemical binding energy (the Ac-O bond dissociation energy was estimated to be approximately 8 eV).[130] As a result, the energy associated with the alpha particle emission is sufficient to break any coordinate bonds.[131, 132] It is also important to consider the binding efficacy of the metal chelators used for actinium for its daughter nuclides. Francium-221 ($t_{1/2}$ = 4.8 minutes) is the first daughter in the decay chain. Francium exists mainly in monocationic form, unlike the majority of lanthanide and actinide elements, which are present as trivalent cations. H_4DOTA does not form complexes with $[^{221}Fr]Fr^{I}$.[133] The highly radioactive nature of all decay products until reaching $[^{209}Bi]Bi^{III}$ poses a significant challenge in the development of a metal chelator that can form complexes with a variety of metals. For example, bismuth exists commonly in the +III oxidation state; however, -III, +I, +II, and +V oxidation states are also accessible.[134]

An enormous body of work has focused on developing a ligand that has the ‘breadth’ to coordinate metals with varied characteristics. It appears that this always comes at a trade-off for reduced stability for the parent radionuclide $[^{225}Ac]Ac^{III}$.

2.4 The Clinical Potential of Actinium-225 Radiotherapy

One methodology to targeting [^{225}Ac]Ac^{III} in tumours is to use the same approach that has been successful with β^- particle emitting radionuclides; that is to use stable coordination complexes that are attached to tumour-targeting molecules such as octreotate or PSMA targeting peptidomimetics. Significant interest in [^{225}Ac]Ac^{III} chemistry has been stimulated by the emergence of α-emitting [^{225}Ac]Ac^{III} targeted radionuclide therapy. The higher particle energy and LET of α-emission when compared to β-emission leads to the potential of delivering very high doses of radioactivity capable of causing double-strand breaks in DNA across short distances. In contrast with β-emission, α-emissions often travel only a few cell diameters in distance; this may reduce off-target radiotoxicity to adjacent healthy tissue.[3-5] The moderate LET and longer distances travelled by β^- particles often result in single-strand DNA breaks that tumour cells more readily repair and may lead to radio-resistance in more aggressive cancers. Owing to the clinical successes of [^{177}Lu]Lu^{III} agents Pluvitco® and Lutathera®, H_4DOTA was investigated as an [^{225}Ac]Ac^{III} ligand.

The high LET and small particle range of radionuclides that emit α particles have shown promise to treat more malignant forms of cancer. In a study of 148 advanced prostate cancer patients, 40% did not respond to [^{177}Lu]Lu(PSMA-617) β-radiotherapy (based on biochemical PSA decline)[135] despite showing favourable tolerability and presented with progressive, diffuse metastatic disease, including bone marrow infiltration.[136] This poses a major treatment challenge due to the risks of dose escalation of β-radiotherapy related to the long-range penetration of β^- particles, namely, the significant risk of haematologic toxicity with bone marrow failure and the associated morbidity from various blood cell cytopenias.

Although early-stage prostate cancer generally has a good prognosis, patients with inoperable disease or extensive metastases and marrow infiltration suffer poor survival outcomes. In this light, actinium-225 has been developed as a salvage therapy for conventional

treatment-resistant advanced prostate cancer.[137-141] In the first human trial of [^{225}Ac]Ac^{III} in two patients with metastatic castration-resistant prostate cancer (mCRPC), 100 kBq activity of [^{225}Ac]Ac(PSMA-617) per kilogram of body weight was administered bi-monthly.[140] Biochemical response was assessed monthly with serum prostate-specific antigen (PSA) levels and the radiological response was evaluated with [^{68}Ga]Ga(PMSA-11) PET/CT imaging (Figure 14).

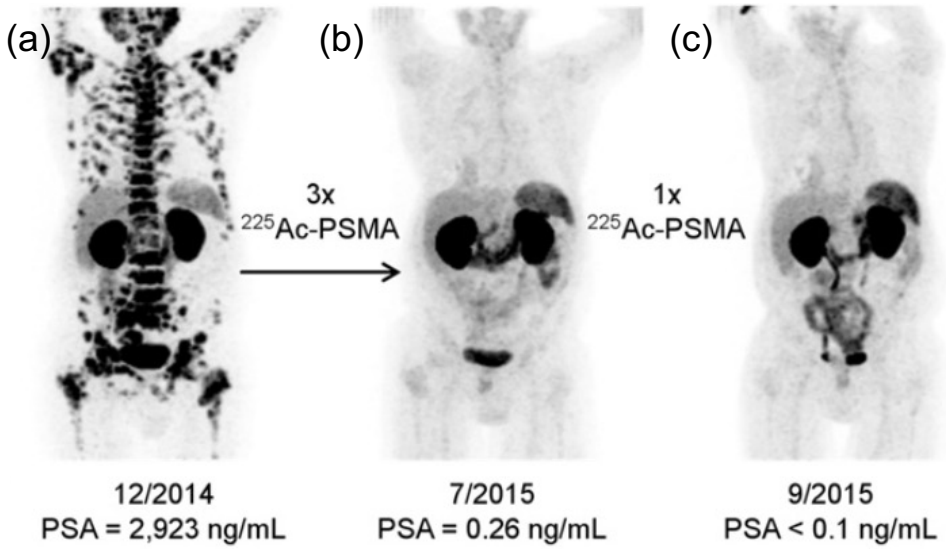

Figure 14: [^{68}Ga]Ga(PMSA-11) PET/CT scans of a patient treated with [^{225}Ac]Ac(PSMA-617) at University Hospital Heidelberg. (a) shows the metastatic and marrow infiltration of mCR prostate cancer, (b) shows scans 2 months following 3 treatments of [^{225}Ac]Ac(PSMA-617), (c) shows scans two months after additional consolidation therapy.[140]

The synthesis of [^{225}Ac]Ac(PSMA-617), which incorporates H_4DOTA as its chelator, required heating to 95°C for 5 min in a microwave-assisted reaction with a final radiochemical purity of 98. 8 ± 0.8 % and specific activity of 0.17 ± 0.05 Mbq/nmol. The treatment of two patients who had exhausted all surgical and chemotherapeutic options, including 6 cycles of endoradiotherapy with α-emitter [^{223}Ra]$RaCl_2$ (Figure 14, a), showed a significant response to the actinium-225-based therapy with four doses of [^{225}Ac]Ac(PSMA-617) leading to a decline in the prostate-specific antigen (PSA) to < 0.1 ng/mL in combination with a complete imaging

response (Figure 14, c). Despite these impressive responses with [^{225}Ac]Ac(PSMA-617), severe xerostomia (oral dryness) became the dose-limiting toxicity.[142]

2.5 The Search for Metal Chelators that Form Stable Complexes with Actinium-225

A radiopharmaceutical must be specific for the target tissue and have sufficient stability to avoid loss of the metal ion and its accumulation in off-target tissue. Specifically, the incorporation of a bioactive targeting vector must exhibit a high degree of selectivity in targeting cancerous cells and effectively delivering the radiation payload. Moreover, the radionuclide must be encapsulated by a metal chelator that is both kinetically and thermodynamically stable, thereby preventing any potential damage to healthy tissue.

Ac^{III} is defined as a hard Lewis acid due to the lack of polarizability of the frontier orbitals. Consequently, the ion is likely to prefer chelators with hard oxygen and carboxylate donors.[143] Electrostatic interactions, defined as the sum of the attractive forces between positively charged nuclei and the negatively charged electrons of two molecules;[144] decrease with the ratio of charge over a distance. As such, the large ionic radius and low charge density of the Ac^{III} ion result in kinetically labile complexes.[145] The accumulation of 'free' [^{225}Ac]Ac^{III} in the liver and bone can cause significant radiotoxicity, highlights the necessity for radioactive metal complexes of [^{225}Ac]Ac^{III} that exhibit high kinetic stability.[146] In this context, the stability of actinium-225 complexes with different macrocyclic and acyclic ligands has been the subject of extensive research.

The metal chelator CHX-A"-DTPA (N-[(R)-2-amino-3-(p-aminophenyl)propyl]trans-(S,S)-cyclohexane-1,2-diamine-N,N,N',N",N"-pentaacetic acid, Figure 15, a) was investigated for [^{225}Ac]Ac^{III} therapy because the ligand forms stable complexes with the α-emitting [^{213}Bi]Bi^{III} that are stable *in vivo*.[147] CHX-A"-DTPA was compared with the aminopolycarboxylic acid chelator ethylenediaminetetraacetic acid (EDTA, Figure 15, b) and

[^{225}Ac]Ac(CH_3CO_2)$_3$.[146] Administration of both [^{225}Ac]Ac(CHX-A"-DTPA) and [^{225}Ac]Ac(EDTA) resulted in a different biodistribution in major organs such as the liver, skeleton, kidney and heart when compared to administration of 'free' actinium-225 in the form of [^{225}Ac]Ac(CH_3CO_2)$_3$. The organ with the highest radioactivity after treatment with [^{225}Ac]Ac(CH_3CO_2)$_3$ was the liver (>120 % IA g^{-1}), which had rapid and persisting accumulation for the duration of the study. Both complexes could not mitigate the toxicity associated with releasing free actinium into the body. The radiotoxicity of the [^{225}Ac]Ac(CHX-A"-DTPA) was evaluated by maximum tolerated dose (MTD) and toxicity studies of organ system damage with increasing activity (92, 185, 370, and 740 kBq). [^{225}Ac]Ac(CHX-A"-DTPA) caused significant but repairable toxicity at the lowest dose range, including bone marrow suppression and cellular liver and kidney damage. However, mice receiving doses greater than 185 kBq of [^{225}Ac]Ac(CHX-A"-DTPA) suffered an acute decrease in white blood cell count and was accompanied by severe organ damage with 100% morbidity after 5 days and 100% mortality 8 days post-injection. This demonstrated that CHX-A"-DTPA is an unsuitable chelator for actinium-225 therapy, with the release of free actinium-225 responsible for significant tissue and organ damage.

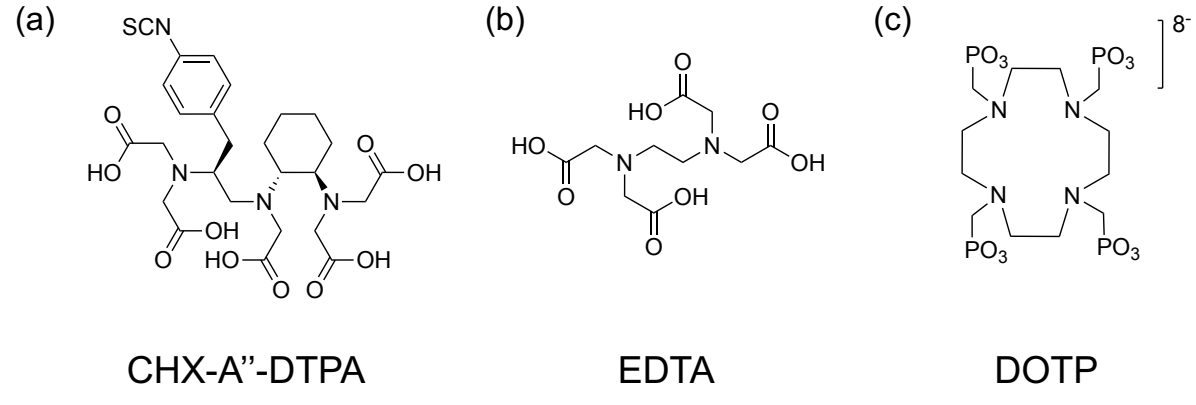

Figure 15: Chemical structures of chelators studied to probe actinium-225 complex stability.

2.5.1 The Phosphate Derivate of DOTA, H_8DOTP, Forms Complexes with Actinium

A phosphonate derivative of DOTA, 1,4,7,10-tetraaza- cyclododecane-1,4,7,10-tetra(methylene)phosphonic acid ($DOTP^{8-}$, Figure 15, c), was investigated as a potential ligand for $[^{227}Ac]Ac^{III}$ and the trivalent f-block elements La^{III} and Am^{III}. These complexes were characterised *via* EXAFS, DFT calculations and ^{31}P Nuclear Magnetic Resonance (NMR, Figure 16, a).[148] Basic conditions (pH > 10) ensured all phosphonate functional groups are deprotonated, and the corresponding $[^{227}Ac]Ac^{III}$, La^{III} and Am^{III} complexes were heated at 40 °C for 30 minutes. The microscopic quantities available of $[^{227}Ac]Ac^{III}$ available made X-ray crystallography untenable. Instead, the X-ray crystal structure of the corresponding $(NH_4)_5La(DOTP)(H_2O)$ complex was used as a model (Figure 16, b). The X-ray crystal structure of the anion of $(NH_4)_5La(DOTP)(H_2O)$ gave average La–O and La–N bond distances of 2.46(3) and 2.84(2) Å, respectively. The bond distances demonstrated that the $DOTP^{8-}$ complex had a larger binding pocket compared to $DOTA^{4-}$, which is especially important for the formation of stable complexes with the large Ac^{III} cation.

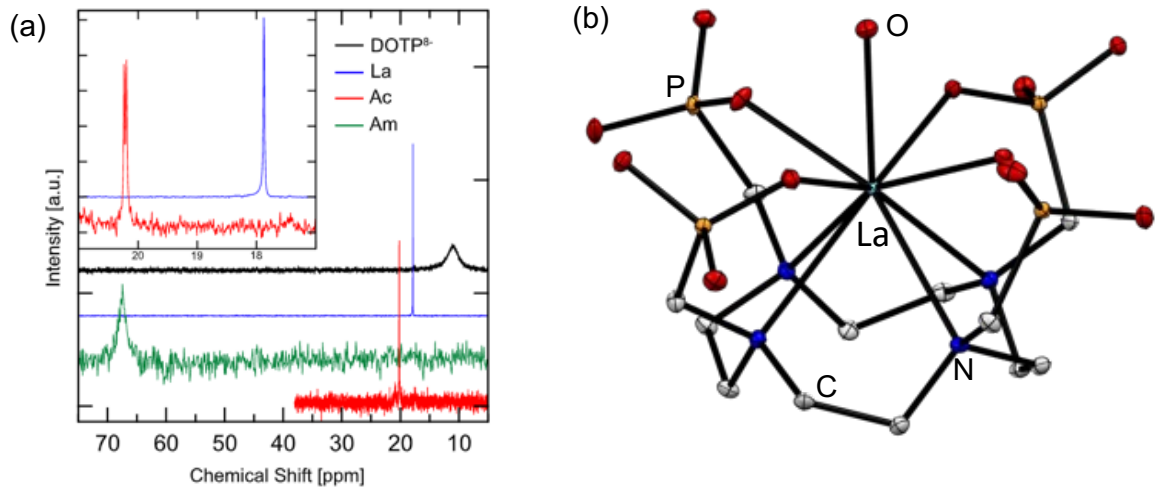

Figure 16: (a) Comparison of ^{31}P NMR spectrum of $DOTP^{8-}$ (δ 0 – 80 ppm, D_2O, pD 10) which is shown in the black trace, compared with the spectra of various metal complexes, $M(DOTP)^{5-}$ where $M= La^{III}$, Ac^{III} and Am^{III}. (b) X-ray crystal structure of the anion of $(NH_4)_5La(DOTP)(H_2O)$. Thermal ellipsoid are shown at 30%.[148]

The ^{31}P NMR spectrum of the various metal complexes provided important insight into the binding interactions and similarities between metal cations. The ligand $DOTP^{8-}$ spectrum (black) shows a single broad peak, which is a result of fluxional processes whereby atoms can chemically interchange between symmetry-equivalent positions. The peak is shifted downfield upon complexation with La^{III} (blue), $[^{227}Ac]Ac^{III}$ (red) and Am^{III} (green). The addition of La^{III} resulted in a sharpening of the peak accompanied by a downfield shift (δ_P = 17.9 ppm) as the formation of the complex limits the rotational freedom of the $DOTP^{8-}$ ligand. The $Ac(DOTP)^{5-}$ spectrum exhibited a similar line sharpening and downfield shift (δ_P = 20.2 ppm) and contained an unequal doublet (3:1 ratio in area) that Stein *et. al.* attributed to the slow exchange of two $Ac(DOTP)^{5-}$ isomeric species. Investigation of $DOTA^{4-}$ complexes with lanthanoid metals identified these two isomers as the square antiprism and twisted square antiprism complexes.[149] Further studies on the stability of $[^{225/227}Ac]Aa(DOTP)^{5-}$ are required to assess its kinetic inertness *in vivo*.

2.5.2 DOTA Forms Complexes with Actinium-225 at High Temperatures, the FDA Approval of DOTA Chelators has Paved the Way for New Radionuclides

1,4,7,10-Tetraazacyclododecane-1,4,7,10-tetraacetic acid (DOTA) is often used to chelate the trivalent metal cations Ga^{III}, Lu^{III}, and Y^{III} for use as radiopharmaceuticals (Figure 17, a). The 12-membered tetraaza-macrocycle contains four nitrogen donor groups and four pendant carboxylic acid arms and is the ligand in both Pluvitco® and Lutathera® (*vide supra, 1.2*). The thermodynamic stability of metal ion complexes of DOTA is inversely related to the ionic radius of the metal ion, meaning that larger cations such as actinium are likely to form less stable complexes with DOTA.[150] Complexation of $[^{225}Ac]Ac^{III}$ with H_4DOTA requires heating above 50°C for 45 minutes. The stability of the $[^{225}Ac]Ac(DOTA)^-$ and $[^{225}Ac]Ac(DOTP)^{5-}$ complexes (Figure 15, c) were measured in 25% human serum at 37 °C over 53 days.

[^{225}Ac]Ac(DOTA)$^{-}$ maintained superior stability compared to [^{225}Ac]Ac(DOTP)$^{5-}$, with only 10 % dissociation of [^{225}Ac]Ac^{III} within one half-life ($t_{1/2}$ = 9.9 days).

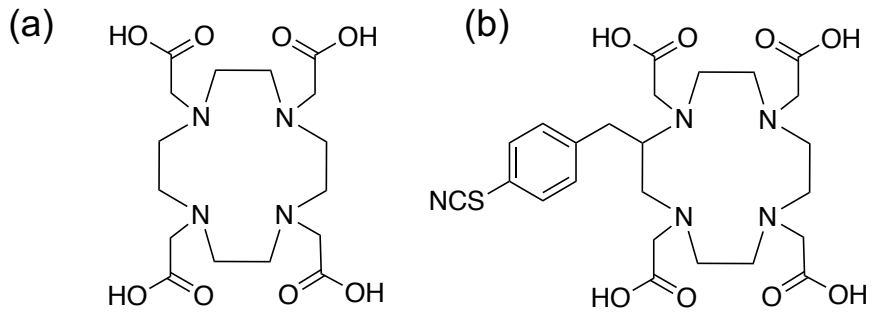

Figure 17: Chemical structures of (a) H_4DOTA and (b) H_4DOTA-pBn-SCN.

The potential of using actinium-225 for radioimmunotherapy was realised in seminal preclinical work developing antibody conjugates using actinium-225.[151-154] This initial work used DOTA as a chelator for actinium-225. In an early study, the therapeutic efficacy of [^{225}Ac]Ac(DOTA-lintuzumab), an anti-CD33 monoclonal antibody, was investigated as a treatment of acute myeloid leukaemia (AML, NCT02575963).[155-157] Clinical studies of radionuclide complexes conjugated to monoclonal antibodies are also underway for prostate cancer, with a phase I study investigating the efficacy of [^{225}Ac]Ac(DOTA-J591), a monoclonal antibody that targets PSMA for the treatment of mCRPC.[158]

The above radiolabelling conditions are incompatible with the viability of an antibody, where temperatures above 37 °C result in the denaturation of the biomolecule. Therefore, the radiolabelled actinium-225 antibody construct was synthesised in two steps. The [^{225}Ac]Ac(DOTA-NCS) chelation was performed first and required heating to 50 – 60°C for up to one hour, then reacted with the antibody or another targeting agent *via* the isothiocyanate group, which reacts with the primary amines on surface lysine residues to form a thiourea bond (Figure 17, b). The two-step procedure resulted in modest radiochemical yields of 9.9 %, likely due to the hydrolysis of the isothiocyanate functional group and thus required further optimisation.

In 2014, Maguire *et al.* published an optimised one-step procedure for radiolabelling antibody-DOTA construct, which reduced the effects of the hydrolysis of the isothiocyanate and conserved the therapeutic activity.[154] Directly radiolabelling these monoclonal antibodies with sufficiently high yields required a chelator-to-antibody ratio greater than 10, which may significantly impact the immunoreactivity of the monoclonal antibodies towards their antigen. Nevertheless, this technique improved the radiochemical yield of $[^{225}Ac]Ac^{III}$ labelling with DOTA and effectively increased the clinical application of using $[^{225}Ac]Ac^{III}$ in targeted alpha therapy.

The early-stage clinical studies involving $[^{225}Ac]Ac^{III}$ peptide and peptidomimetic conjugates are very promising, but radiolabelling DOTA with $[^{225}Ac]Ac^{III}$ requires heating at high-temperature (~ 95 °C/microwave assisted) and this is not possible with proteins or antibodies. Additionally, the prolonged radiolabelling times and low yields associated with the use of DOTA for actinium-225 remain an ongoing challenge. The potential limitations of using DOTA for actinium-225 are also consistent with XAFS investigations, which determined actinium-225 forms 11-coordinate complexes.[112] These limitations stimulated the search for alternative ligands.

2.5.3 Actinium-225 is Rapidly Radiolabelled with H_2Macropa

Functionalisation of the diaza crown ether, 4,13-diaza-18-crown-6 ether with two picolinate pendant arms, to give the ligand, N,N'-bis[(6-carboxy-2-pyridil)methyl]-4,13-diaza-18-crown-6, called H_2Macropa, increased the binding affinity towards larger lanthanoid(III) ions (Figure 18, a).[159] Potentiometric titrations demonstrated a drop in the stability of complexes as the ionic radii decreased across the lanthanide row, distinctly different from typical macrocyclic polydentate chelators that experience an increase in stability as a result of the increased charge density of metal cations. The larger lanthanide metals, such as La^{III} and Ce^{III}, exhibited the highest logK values, with a sharp decrease in the stability from Ce^{III} to Lu^{III}.[159]

In 2017, Wilson and Radchenko demonstrated that H_2Macropa could be labelled with [^{225}Ac]Ac^{III} at room temperature. H_2Macropa could form complexes with [^{225}Ac]Ac^{III} (26 kBq) within 5 minutes at sub-micromolar concentrations (0.59 μM). The stability of the [^{225}Ac]Ac(Macropa)$^+$ complex was evaluated in competition experiments, where 50 equivalents of La^{III} was unable to displace actinium over 7 days, and 98% of the complex remained intact. The addition of an isothiocyanate functional group onto one of the picolinate units of H_2Macropa provides a ready point of functionalisation to attach peptides or proteins to the macrocyclic framework (Figure 18, b).[160]

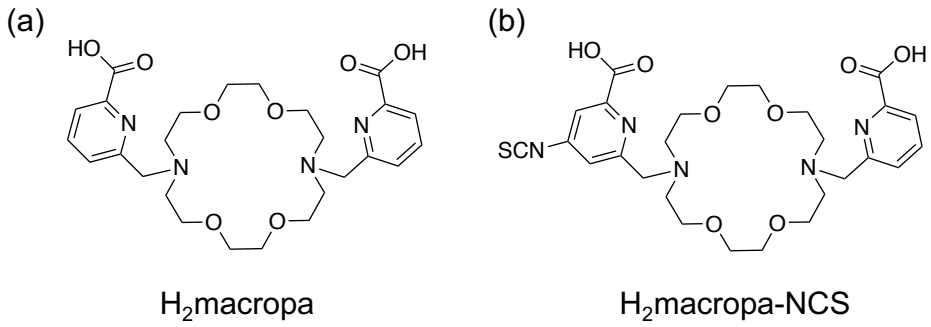

Figure 18: Chemical Structures of (a) H_2Macropa and (b)H_2Macropa-NCS, an asymmetric bifunctional derivate of H_2Macropa.

Comparing the complexation of [^{225}Ac]Ac^{III} with H_4DOTA and H_2Macropa revealed significant differences. Under the same reaction conditions as [^{225}Ac]Ac(Macropa)$^+$, the [^{225}Ac]Ac(DOTA)$^-$ did not radiolabel even at temperatures of 80°C in the same timeframe. With these promising results, the ligand was conjugated to the targeting vectors, PMSA and Trastuzumab, which is an antibody specific for HER2-positive breast cancer cells. The radiolabelled constructs maintained their integrity with no release of actinium *in vivo* and demonstrated selective targeting to tumour tissue.[160]

2.5.4 Second-Generation H_2Macropa Chelators Are Not More Stable

There has been a significant interest in developing new metal chelators based on H_2Macropa that can form stable complexes with a range of radionuclides. The work pioneered by Wilson *et al*. has focused on expanding the potential theranostic toolkit for radiochemists. This has

also catalysed an interest in developing macrocyclic chelators with dual-size selectivity that are capable of binding multiple metallic radionuclides.[148, 161, 162]

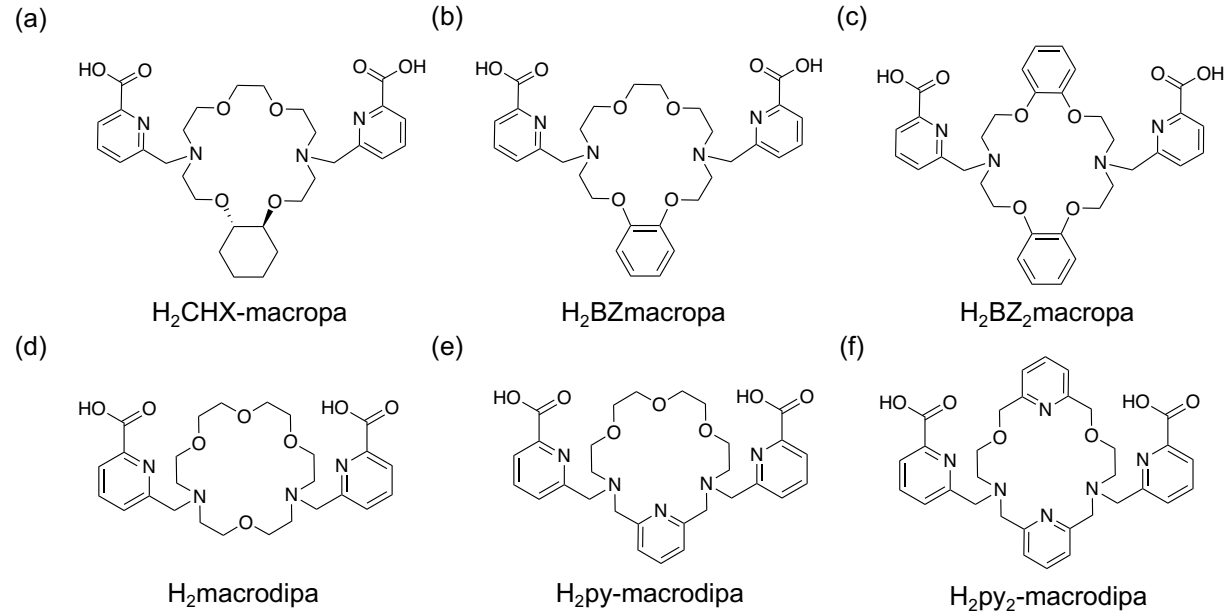

Figure 19: Chemical structures of (a) H_2CHX-Macropa, (b) H_2BZMacropa, (c) H_2BZ_2Macropa, (d) H_2macrodipa (e) H_2py-macrodipa and (f) H_2py_2-macrodipa.

The ligand H_2CHX-Macropa (Figure 19, a) exhibited an increase in the thermodynamic selectivity of large lanthanide metals such as La^{III} over smaller metals such as Lu^{III}, in part due to the incorporation of a cyclohexyl moiety into the 18-membered macrocycle.[163] This reduced the stability of the complexes with smaller lanthanide metals, as the macrocycle could not distort appropriately to facilitate ligand binding. This change in ligand design did not translate into greater complex stability, with complexes exhibiting poor thermodynamic and kinetic stability of f-block elements.

The ligands H_2BZMacropa and H_2BZ_2Macropa were designed to increase the rigidity of the macrocycle *via* the addition of one or two phenyl rings (Figure 19, b, c).[162] Interestingly, although the phenyl groups introduce some degree of preorganisation of the ligand which results in a favourable entropic contribution, the reduction in donor atom strength actually reduces the stability of the La^{III} complexes. H_2BZMacropa-SCN is a bifunctional chelator of

H_2BZMacropa that was synthesised and conjugated to a monoclonal antibody GC33, [^{225}Ac]Ac(GC33-BZM), which targets the GPC3 receptor. The serum stability was investigated, showing significant decomplexation of [^{225}Ac]Ac^{III} from the chelator (Figure 20).[162]

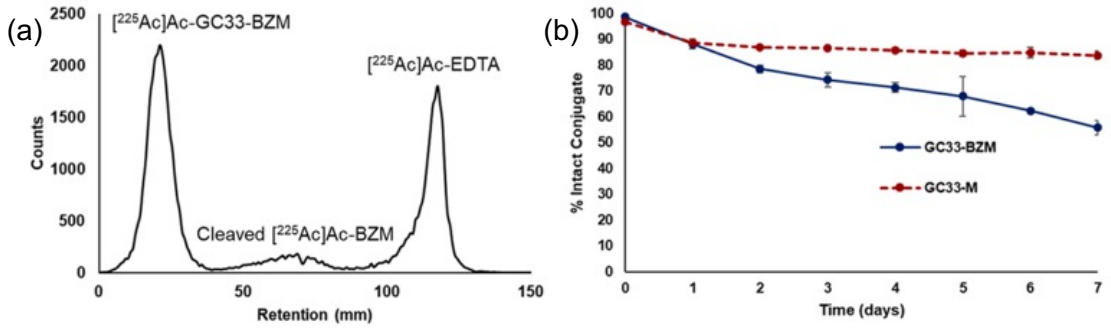

Figure 20: (a) Radio-thin layer chromatography of [^{225}Ac]Ac(GC33-BZM) after 7 days in human serum (37°C). Intact [^{225}Ac]Ac(BZM-GC33) stays at the baseline (retention ~ 20 mm). [^{225}Ac]Ac^{III} that has been trans chelated exists as [^{225}Ac]Ac(EDTA) (retention ~ 110 mm); (b) the stability over time of [^{225}Ac]Ac(GC33-BZM) and [^{225}Ac]Ac(GC33-M) in human serum as a function of time.[162]

Modifying the 4,13-diaza-18-crown-6 macrocycle to rearrange the N_2O_4 backbone so that the secondary amines of the backbone were not symmetrical in the macrocylic core produced a new class of macrocyclic chelator.[164] The first-generation chelator, H_2macrodipa, experienced dual-size selectivity with respect to lanthanoid metals (Figure 19, d). Large cations such as La^{III} exist in a ten-coordinate conformation with the macrocycle encapsulating the metal. In contrast, small lanthanoids exist in an eight-coordinate, asymmetric complex where the metal forms coordinate bonds with the picolinate arms but only partially coordinates with the macrocyclic backbone oxygens.

This was later derivatised to yield H_2py-macrodipa, where the macrocyclic core was modified to contain a pyridyl nitrogen donor, which replaced a single backbone oxygen donor to provide N_3O_3 coordination. (Figure 19, e).[165, 166] The 'conformational toggle', which allowed these ligands to change conformations based on radiometal size, allows the targeting of a broader range of clinically relevant isotopes, such as [$^{132/135}$La]La^{III} and [$^{44/47}$Sc]Sc^{III}. H_2py-macrodipa is also a promising candidate for targeted alpha therapy with [^{213}Bi]Bi^{III} owing to

its high radiolabelling efficiency and high stability in kinetic challenge experiments with EDTA. Although H_2py-macrodipa can complex [^{225}Ac]Ac^{III} with an overall radiochemical yield (RCY) of 75% at a concentration of 10^{-6} M, the complex was very labile in a human serum challenge, with greater than 90% of the complex dissociating after one day. Although it is a suitable ligand for [^{213}Bi]Bi^{III}, these second-generation ligands exhibit poorer long-term stability when coordinating [^{225}Ac]Ac^{III} compared with the non-rigid H_2Macropa. H_2Macropa forms complexes with [^{225}Ac]Ac^{III} in quantitative yield at concentrations of 10^{-6} M while [^{225}Ac]Ac^{III} complexes of H_2macrodipa and H_2py-macrodipa are formed at lower radiochemical yields (Figure 21).

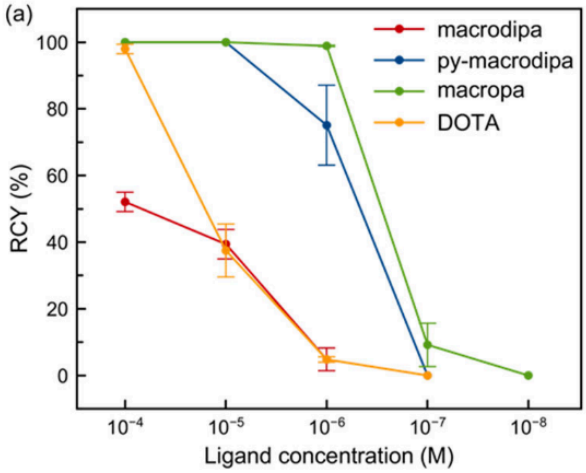

Figure 21: Radiochemical yields at different concentrations of [^{225}Ac]Ac(macrodipa), [^{225}Ac]Ac(py-macrodipa), [^{225}Ac]Ac(Macropa) and [^{225}Ac]Ac(DOTA). Radiolabelling was performed at 25 °C for [^{225}Ac]Ac(py-macrodipa), [^{225}Ac]Ac(Macropa), 40 °C for [^{225}Ac]Ac(macrodipa), and 80 °C for [^{225}Ac]Ac(DOTA); pH 5.5 – 6; 60 min reaction time.[165]

In another iteration of H_2macrodipa, the chelator H_2py$_2$-macrodipa (Figure 19, f) built on prior work by increasing the number of pyridyl groups fused into the macrocyclic core.[161] Modifying the crown ether macrocycle to induce rigidity has allowed for the complexation of both [^{225}Ac]Ac^{III} and [^{213}Bi]Bi^{III}. The bismuth complexes exist in a pentagonal pyramidal conformation. The binding efficacy remains several orders of magnitude lower for small lanthanoid cations when compared to H_4DOTA. Nevertheless, room temperature radiolabelling is not possible with H_4DOTA. These complexes, such as those in PSMA-617 and DOTATATE, require heating above 80°C for quantitative radiolabelling.

By altering the donor atoms on the pendant arms of the diaza-18-crown-6 macrocycle, the binding affinity for different metals can be modified (Figure 22). This includes [^{213}Bi]Bi^{III}, a daughter nuclide of [^{225}Ac]Ac^{III}. The basicity of the donor ligands plays a crucial role in this process. In a trans-chelation challenge, the phosphate ligands were shown to be the most labile in an excess of DPTA, with a calculated half-life of only 8.9 ± 1.7 minutes. The Bi^{III} complexes with H_2Macropa and its more rigid derivative H_2CHX-Macropa with picolinate donor arms performed marginally better with experimentally determined half-lives of Bi(CHX-Macropa)$^+$ 40.4 ± 4.3 minutes and Bi(Macropa)$^+$ 46.6 ± 0.9 minutes. Bi(Macropaquin)$^+$ had a longer half-life of 14.3 ± 1.4 hours, but it was [^{213}Bi]Bi(macroquin-SO_3)$^-$ that was most stable to DPTA challenge, with a half-life of greater than 21 days.[167]

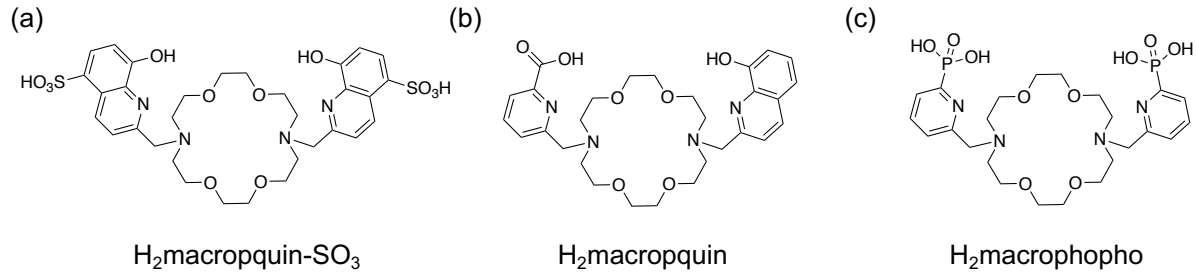

Figure 22: Chemical structures of (a) H_2macropquin-SO_3, (b) H_2Macropaquin and (c) H_2macrophopho.

The creative ligand design of these second-generation metal chelators based on H_2Macropa has demonstrated that these chelators can form complexes with more than one metallic radionuclide in the emerging field of radiotheranostics. However, it remains to be seen if there is a ligand that forms complexes with [^{225}Ac]Ac^{III} of greater stability than H_2Macropa (Figure 21). It appears that there is a trade-off between increasing the potential scope and the number of radiometals that form complexes with the ligand that comes at a sacrifice to the specificity and long-term stability. Nevertheless, this diligent investigation into varied ligand design has proved insightful in understanding the coordination chemistry and stability of [^{225}Ac]Ac^{III} complexes.

2.5.5 The PSMA-Targeting Peptidomimetic, [^{225}Ac]Ac(RPS-074) Elicits a Complete Tumour Response

H_2Macropa, the albumin binding motif 4-(p-iodophenyl)butyric acid, and the Glu-NH-CO-NH-Lys pharmacophore were combined in a trifunctional chelator designed to increase the *in vivo* circulatory half-life of the actinium-225 complex ([^{225}Ac]Ac(RPS-074), Figure 23). A preclinical investigation in mice bearing LNCaP xenograft tumours demonstrated significant tumour inhibition. The i*n vivo* biodistribution of [^{225}Ac]Ac(RPS-074) showed tumour uptake of 12.7 ± 1.5 % IA g^{-1} at 24 hours p.i. and activity in the tumours remained high (11.9 ± 1.5 5 % IA g^{-1}) at 14 days p.i. In the longitudinal therapy study, mice injected with 148 kBq of radiotracer showed a full biochemical response from a single treatment.[138]

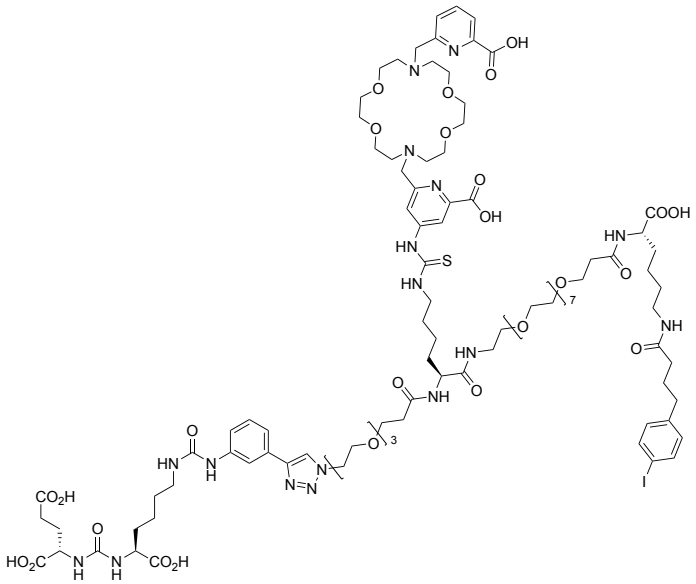

Figure 23: Chemical structure of [^{225}Ac]Ac(RPS-074).

Pioneering work has developed peptidomimetic compounds that target metastatic castration-resistant prostate cancer with the 18-membered macrocycle H_2Macropa, yet it remains to be seen if radionuclide-conjugated monoclonal antibodies will also experience this surge in clinical translation. The long circulation time of monoclonal antibodies as targeting vectors necessitates the formation of extremely stable complexes. For a radionuclide as cytotoxic as actinium-225, the potential risk of decomplexation *in vivo* is too great.

2.6 Aims

Actinium-225 based radiopharmaceuticals have shown impressive results in treating late-stage cancers in patients that are refractory to traditional β therapy. This targeted alpha therapy may be especially advantageous in the management of hypoxic tumours. Pioneering work has shown that the 18-membered macrocycle, H_2Macropa-NSC (Scheme 1, a), forms complexes with $[^{225}Ac]Ac^{III}$ at room temperature. When H_2Macropa-NSC was conjugated to a peptidomimetic that targets the prostate-specific membrane antigen (PSMA), it formed stable complexes with $[^{225}Ac]Ac^{III}$.

The research described in this chapter aims to develop a bifunctional chelator that could rapidly radiolabel monoclonal antibodies with actinium-225. This strategy would harness the excellent selectivity of monoclonal antibodies to deliver an ionising dose of radiation to tumours (Scheme 1, b).

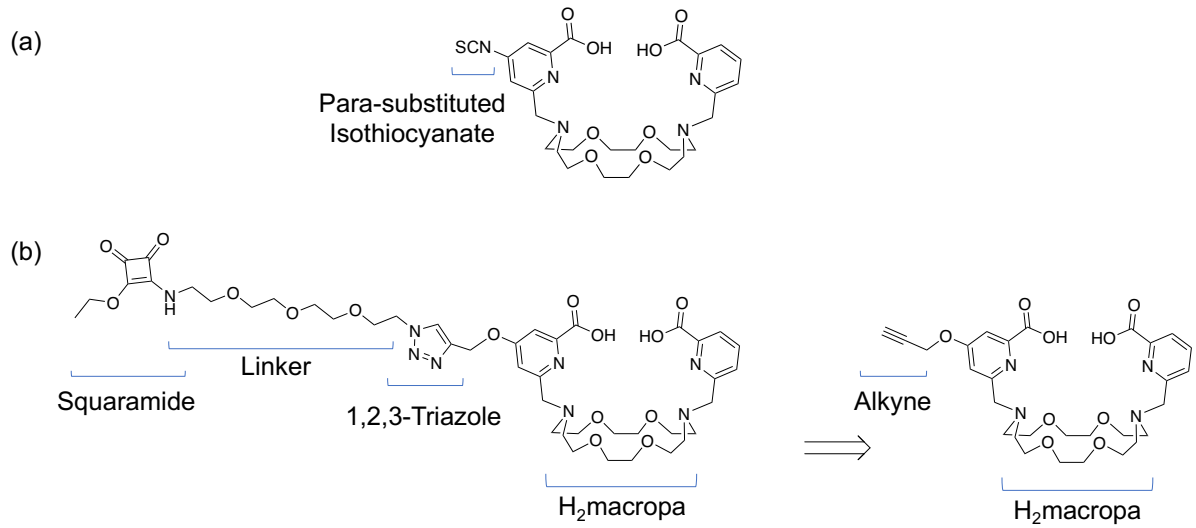

Scheme 1: (a) Chemical structure of H_2Macropa-SCN, (b) This work: the retrosynthesis and important components in the ligand design of H_2MacropaSqOEt.

The *para*-isothiocyanate substituted pyridine (Scheme 1, a) is susceptible to hydrolysis and the electron withdrawing *ortho*-carboxylic acid functional group significantly increases the reactivity of the isothiocyanate functional group. This vulnerability to hydrolysis may limit its potential in the clinic. In particular, this functional group is prone to radiolysis (due to the

formation of activated hypochlorite species in the presence of chloride species). The stability issues that are present in antibody conjugates that use thiourea bonds stems in part due to the radiolysis of water molecules. In the presence of chloride ions (such as in saline solution), radiolysis products react to form OCl^- ions, and these are known to react with the SH-group of the enolised thiourea unit. Therefore, intermediary sulphenyl chloride bonds are formed, and upon further oxidation, the sulphonyl chloride bonds are highly reactive, undergoing reactions such as the cleavage of methionyl peptide bonds.[168] This is highlighted in the comparison of *p*-NCS-Bn-DOTA, where the isothiocyanate group resides on an adjacent phenyl ring and H_2Macropa-NCS. H_2Macropa-NCS undergoes hydrolysis 10 times faster.[169] The rapid hydrolysis of the isothiocyanate functional group in both solid and solution state has made the shipping and storage of H_2Macropa-SCN a challenge.[162]

In our design strategy of a bifunctional metal chelator that was optimised for actinium-225 radioimmunotherapy, the following components were integral:

1. H_2Macropa was the ideal choice as the metal chelator for $[^{225}Ac]Ac^{III}$. It was chosen due to the formation of highly stable complexes with $[^{225}Ac]Ac^{III}$ with reaction conditions suited to antibody conjugations, namely rapid complexation of $[^{225}Ac]Ac^{III}$ at room temperature.

2. An alkyne functional group was incorporated into the H_2Macropa scaffold to allow the use of Cu^I-catalysed click chemistry. This would increase the scope and variability of the potential linkers. Any linker with an aliphatic azide can be easily incorporated into the bifunctional chelator. This bioorthogonal functional group has excellent stability and reacts with high selectivity with azides. The formation of the corresponding 1,2,3-triazole is a suitably stable functional group.

3. The presence of metal chelators on antibodies and peptides can compromise biological activity. This can be minimised by inserting a molecular spacer between the coordination

complex and the antibody. In this work, we elected to insert an oligo(ethylene glycol) spacer into the metal chelator framework as similar work has demonstrated that they serve as an adequate spacer without significantly increasing hydrophobicity.[170, 171] Incorporation of oligo(ethylene glycol) and, more commonly, higher molecular weight poly(ethylene glycol) chains are well-established techniques to alter the pharmacokinetic properties of a pharmaceutical and their effects on the structure and stability of these modified proteins has been studied.[172, 173]

4. Squaramide ethyl esters react selectively with amines, particularly lysine residues of proteins and antibodies. Squaramide ethyl esters are stable with respect to hydrolysis and have a long shelf life.[174] The squaramides formed by the reaction of squaramide esters with an amine occurs under mild conditions; room temperature and aqueous solutions. Selective mono-amidation of squarate diesters can be conducted by controlling pH due to the changes in aromaticity that occur. The first amidation gives a monoamide, and under slightly more basic conditions, this monoamide is deprotonated, favouring the second reaction with an amine. The resulting diamide is very stable due to the aromaticity of the final functional groups and the vinylogous amides. Squaramide functional groups are considered isosteres for a variety of carboxylate groups, including carboxylic acids and amino acids.[175]

This leads to bioconjugates of increased stability when compared to thioureas formed from the isothiocyanate coupling. It is also important to note that the squaramide functional group has a similar dipole moment to a conventional amide which contributes to the improved solubility in aqueous mixtures when compared to thiourea groups that tend to be significantly more hydrophobic (Figure 24).

Figure 24: The relative electronegativities of carbon, sulphur and oxygen.[176]

Macromolecules such as antibodies cannot tolerate heating above biological temperatures and require a conjugation strategy that will prevent aggregation. When a bifunctional metal chelator is conjugated onto an antibody, it should satisfy the following qualities: it must be stable to hydrolysis and radiolysis when labelled with a metallic radionuclide, the linker should increase the distance between the chelator and the antibody surface without increasing hydrophobicity, and ideally contain functional groups that will expand its versatility. We have developed a bifunctional chelator that fulfils these requirements. In this work, a new chelator, H_2MacropaSqOEt, was characterised.

2.7 Results and Discussion

2.7.1 Synthesis and Characterisation of the Bifunctional Chelator, H_2MacropaSqOEt

This thesis was motivated to optimise the synthesis of the macrocycle with an appended alkyne, (***13***). The initial synthesis of the macrocycle and hydrolysis of the corresponding methyl and ethyl esters was based on the work of Wilson and Radchenko (Scheme 2, a).[160] Following on from the literature, we attempted two synthetic strategies, summarised in (Scheme 2, route one, method ***A*** or ***B***). Finally, we developed an efficient one-pot synthesis of ***12***, which was facilitated with microwave irradiation (Scheme 2, route two). This work increased the overall yield with a greater than >68-fold improvement in reaction time.

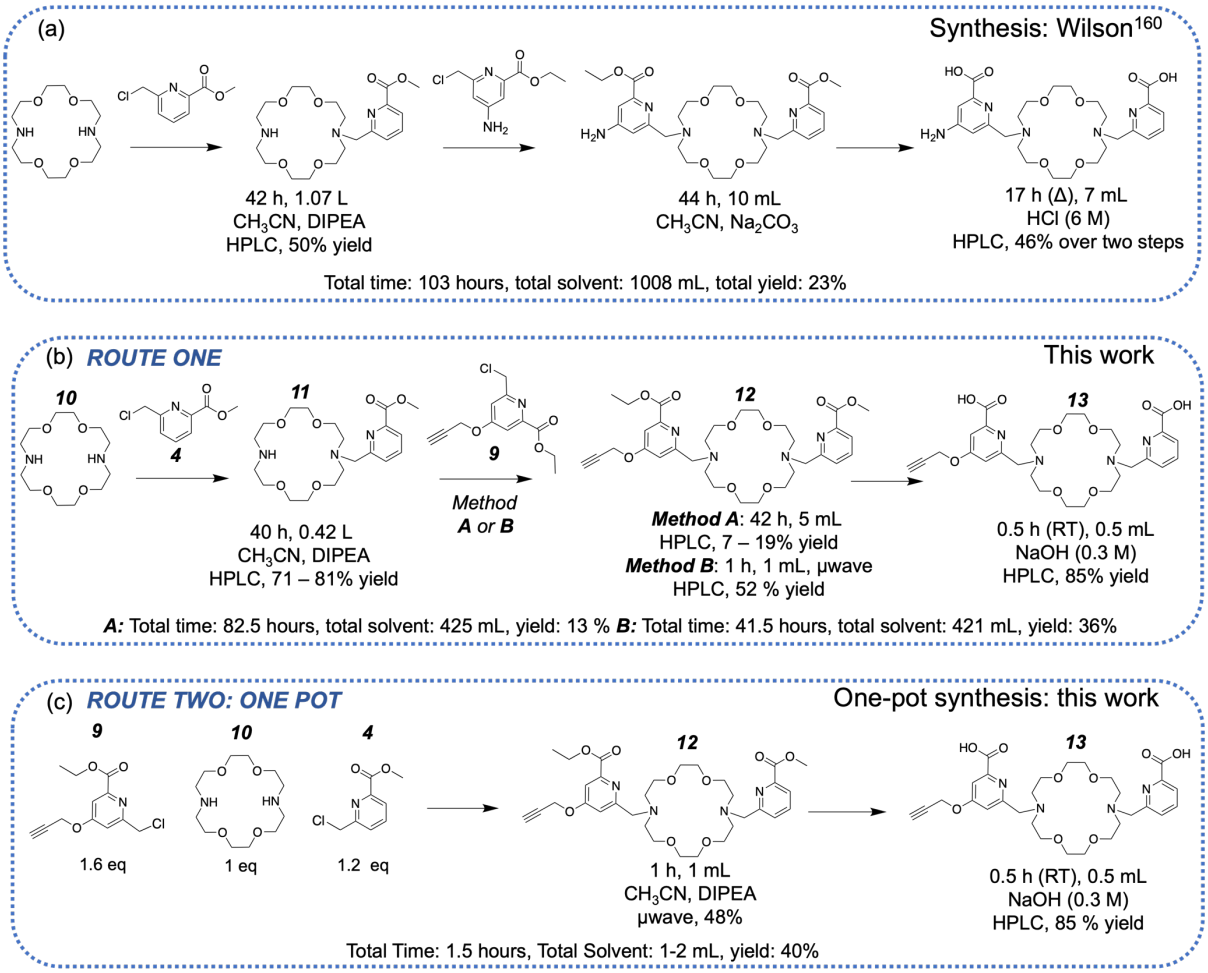

Scheme 2: Different reaction conditions: including reaction time, solvent volume and reported yields. (a) Published synthesis and reaction conditions reported by Wilson[160], (b) The original synthetic strategy used in this thesis with sequential N-alkylation, method **A** used reflux, method **B** used microwave irradiation (μwave), (c) An improved one-pot microwave-assisted synthesis.

The synthesis of a macrocycle ideally suited to conjugation to antibodies required the synthesis of a ligand with only one point for conjugation. Methyl-6-chloromethyl-pyridine-2-carboxylate was prepared for *N*-alkylation of a diaza-18-crown-6 over three steps (Scheme 3). Dipicolinic acid was esterified in the presence of methanol and catalytic sulphuric acid, yielding colourless crystals (80%). One of the methyl esters of dimethylpyridine-2,6-dicarboxylate was then reduced with sodium borohydride to give the methyl 6-(hydroxymethyl)picolinate in 57 % yield. The primary alcohol was then converted to an alkyl halide by treatment with thionyl chloride (90%).

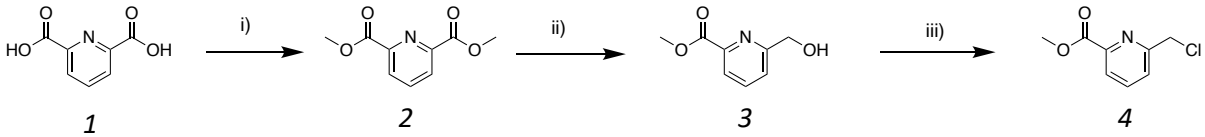

1 *2* *3* *4*

Scheme 3: Synthetic pathway of (i) catalytic H_2SO_4, methanol, 16 hours, 85°C, 3.94 g, 80% (ii) $NaBH_4$ in methanol, 0 °C 8 hours, purified via silica chromatography (1% MeOH in DCM), 3.37 g, 57% (iii) $SOCl_2$ 2 hours, 0°C, 2.42 g, 90%.

Ideally, a bifunctional chelator is easily conjugated into a range of targeting vectors. The Huisgen1,3-dipolar cycloaddition forms a 1,4-disubstituted [1,2,3]-triazole between a terminal alkyne and an aliphatic azide in the presence of copper(I). Many commercially available building blocks contain azide functional groups that react with the terminal alkyne in the metal chelator, thus increasing the versatility of the metal chelator.

The synthesis of ***9*** proceeded in four steps and followed a similar synthesis as ***4*** (Scheme 4). The carboxylic acid functional groups of chelidamic acid (***5***) were esterified. Ethyl esters were chosen based on the solubility of ***5*** in ethanol (76%). To incorporate an alkyne functional group into the metal chelator, propargyl bromide was reacted with the hydroxyl group at the 4-position of the chelidamic acid. Purification of the reaction mixture by silica chromatography and recrystallization from ethyl acetate afforded colourless crystals (68%). After incorporating the alkyne functional group, a reduction with sodium borohydride and chlorination of the resulting primary alcohol (***8***) with thionyl chloride yielded **9** (58% yield over two steps) which would be reacted with diaza-18-crown-6. The alkyne functional group is stable in the presence of both acid and $NaBH_4$.

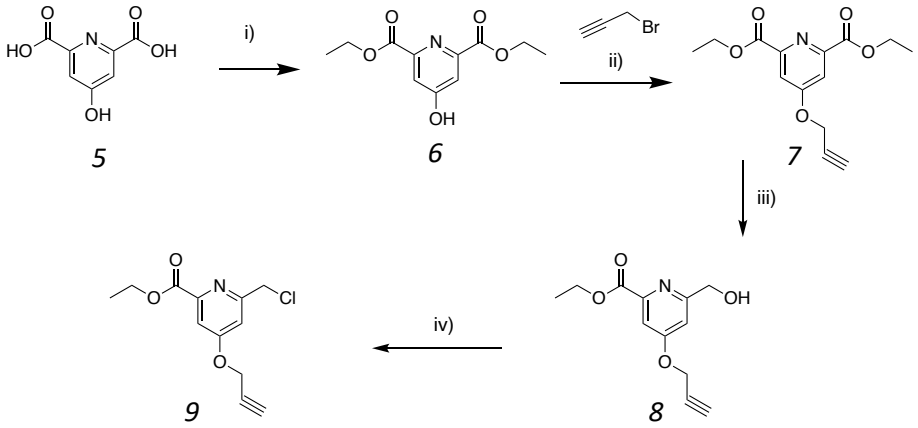

Scheme 4: Synthetic pathway of (i) catalytic H_2SO_4, ethanol, 16 hours, 85°C, 3.98 g, 76% (ii) K_2CO_3 Dimethylformamide (DMF) 2 hours, 70 °C, recrystallised from ethyl acetate, 2.47 g, 68% (iii) $NaBH_4$ in ethanol, 16 hours, 0 °C, purified via silica chromatography (0-2 % MeOH in DCM), 1.20 g, 75% (iv), $SOCl_2$, 4 hours, 80°C, 0.33 g, 77%.

In the reported synthesis (Scheme 2, a),[160] the diaza-18-crown-6 macrocycle was dissolved in anhydrous CH_3CN under a nitrogen atmosphere and high dilution (1.9 g of diaza-18-crown-6 dissolved in 1.07 L of CH_3CN). Methyl-6-chloromethyl-pyridine-2-carboxylate (***4***) was added dropwise over a period of two hours before heating at reflux for 42 hours.[160] Despite the use of high dilution conditions the symmetrically substituted *N*-alkylated macrocycle containing two picolinate functional groups was still isolated (H_2Macropa, Figure 18, a), as well as the singly substituted compound ***11***.

In this work, we developed two different synthetic routes to form non-symmetrically substituted diaza-18-crown-6, route one and route two. In route one, the two-step, sequential N-alkylation of the diaza-18-crown-6 with compounds ***4*** and ***9*** also required long reaction times (> 40 hours per reaction). The first *N*-alkylation of diaza-18-crown-6 with compound ***4*** produced slightly improved yields compared to those reported by Wilson under similar conditions (71 – 81% vs 50%). Conversely, the long reaction heating times (>40 hours) necessary in the second N-alkylation to form compound ***12*** proceeded in lower yields (Scheme 2, b, method ***A***: 7 – 19 %), presumably due to the hydrolysis of compound ***9***.

The mono substituted compound, ***11***, was purified by reverse phase HPLC (0.1% TFA mobile phase), which led to its isolation as the protonated trifluoroacetate salt. Potassium

carbonate, sodium carbonate and cesium carbonate were investigated as potential non-nucleophilic bases (Scheme 2, a). These bases were suspended in either anhydrous acetonitrile or dimethylformamide (DMF). These conditions led to low yields of the disubstituted compound ***12*** (Scheme 2, b, method ***A***) and required the separation of compound ***12*** from a complex mixture containing unreacted starting material and multiple side products *via* semi-preparative HPLC (Figure 25, a). The analytical RP-HPLC of the crude mixture clearly indicates that even when an excess of compound ***9*** was used, the reaction did not reach completion after 40 hours. Notably, the starting material, which has a retention time of 15.9 minutes, was not present (Figure 25, a: blue arrow), suggesting degradation of ***9***. This synthesis was sub-optimal, as the non-nucleophilic base was not suitable, while prolonged reaction times with stronger bases such as N,N-diisopropylethylamine (DIPEA) also caused decomposition of ***9***, both of which resulted in low yields.

Considering the low yields an alternative approach using microwave irradiation (method ***B***) was pursued. The microwave-assisted secondary N-alkylation of ***11*** in the presence of DIPEA proceeded with superior yields (Scheme 2, b, method ***B***). The accelerated reaction time by microwave irradiation achieved significantly higher yields without any detectable breakdown of the starting material (Figure 25, b, blue arrow). Purification of this reaction mixture by semi-preparative HPLC allowed recovery of precious starting material and compound ***12*** in 52% yield.

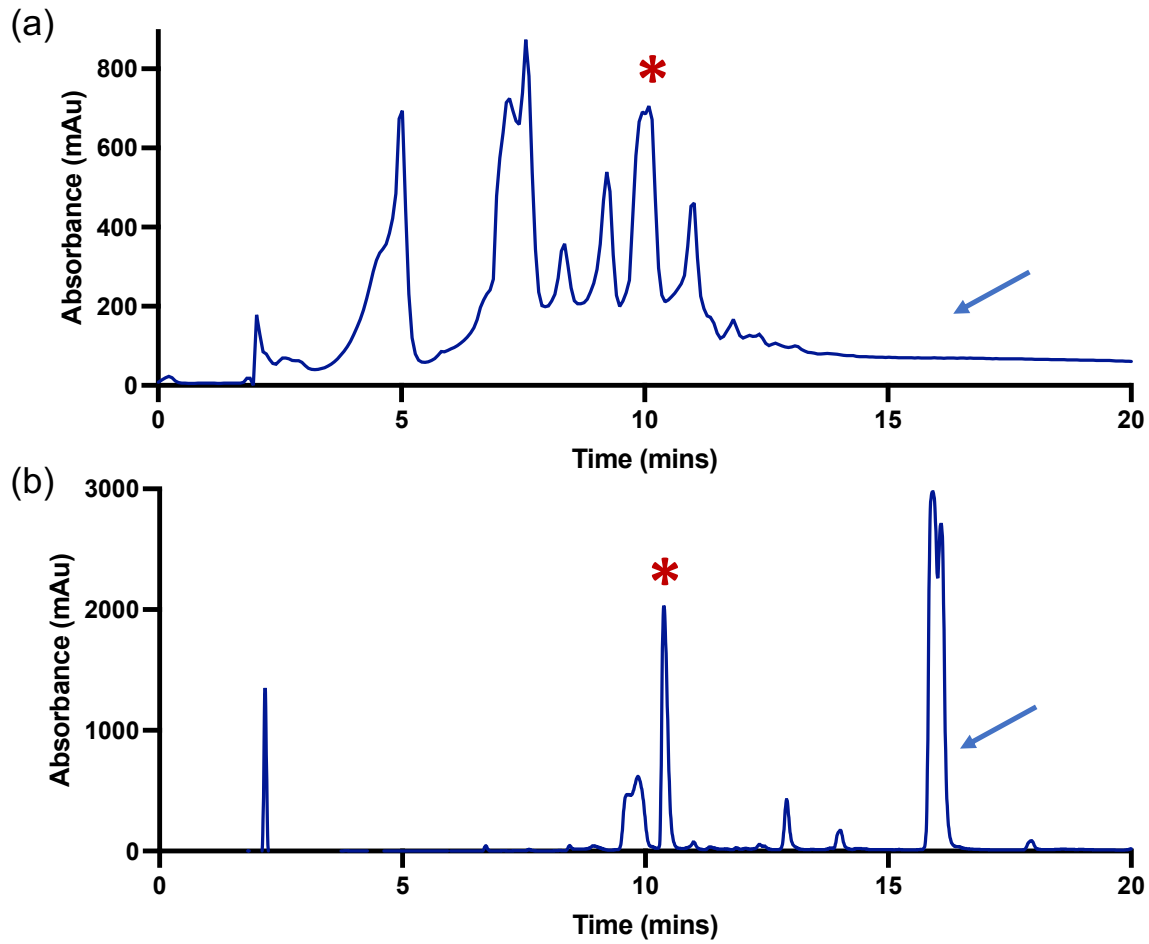

Figure 25: Analytical RP-HPLC of the crude reaction mixture of compound ***12*** when the product was formed by (a) reflux and (b) microwave irradiation. HPLC conditions for both traces: 0 –100 % CH_3CN in MilliQ with 0.1% TFA over 25 minutes (214 nm). Blue arrows indicate the retention time of starting material, red stars indicate the retention time of compound ***12*** formed.

2.7.2 A One-pot Synthesis of Compound *12*

The synthesis of compound ***12*** was further optimised in a one-pot synthesis (route two). Microwave irradiation of all the three starting materials for 1 hour at 85 °C, followed by purification by RP-HPLC, isolated the compound ***12*** in 48 % yield. Semi-preparative HPLC of the crude reaction mixture (Figure 26) allowed for the straightforward separation of the macrocycle ***12***, as well as an analogue that contains two alkyne functional groups (***18***). Compound ***18*** was important in the synthesis of ligands that required the attachment of two functional groups by 1,3-dipolar cycloaddition (see section 2.8.3).

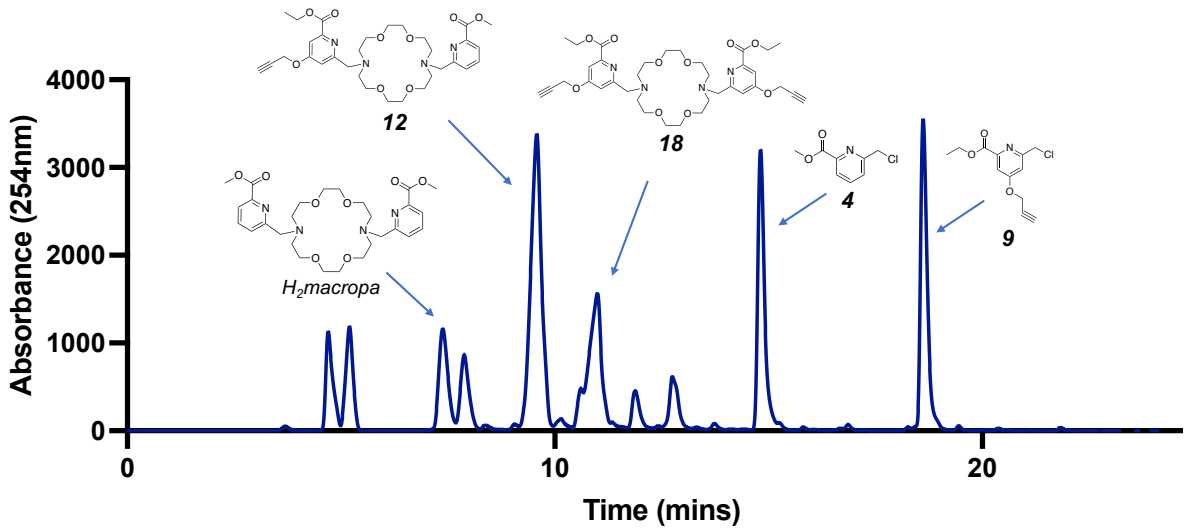

Figure 26: The preparative RP-HPLC/MS trace of the one-pot reaction of ***12***. Highlighted peaks were collected and used in future reactions. (5 – 95 % CH_3CN in MilliQ with 0.1% formic acid over 23 minutes (15 mL/ min, 280 nm). All fractions were collected and used for further synthesis.

In this work, microwave irradiation was used to facilitate significantly faster reaction times (1 vs 80 + hours). Subsequently, this synthetic strategy also removed the need for one purification step. The yields were superior to the corresponding compounds, where the reagents were heated at reflux for 42 hours (Scheme 2, route one vs two).

During the preparation of this thesis, Reissig *et al.* published the macrocycle ***12***, for use as a metal chelator for actinium-225.[177] Their work also recognised the versatility of the alkyne functional group to form a more stable bifunctional derivative of H_2Macropa-SCN and focused on using the PSMA as a targeting vector. Their work to obtain compound ***12*** proceeded in 28% yield over two steps and required purification by silica chromatography (ethyl acetate/ethanol + 1% triethylamine).

The methyl and ethyl esters were hydrolysed quantitively with NaOH in a mixture of dichloromethane and methanol. The crude solution was neutralised and then purified by semi-preparative HPLC, which allowed for the isolation of the diacid, compound ***13*** in > 85% yield (Scheme 2, route one and two). In the literature (Scheme 2, a), the esters were hydrolysed in HCl (6 M, 90 °C) for 17 hours and reported a 46% yield over two steps.[160] In our work, the base-assisted hydrolysis of the methyl and ethyl esters was conducted at room temperature and

was complete within 30 minutes. This is an improvement in the overall synthesis time of the diacid, ***13***.

This work has identified a superior synthetic methodology for the preparation of non-symmetrically substituted 'Macropa' derivatives (route two). The advantages of this technique include a one-pot synthesis of ***12*** which was facilitated with microwave irradiation. This strategy increased the overall yield (40% vs 23%) with a greater than > 68-fold improvement in the reaction time and reduction of one purification step. The optimisation of the synthesis of these macrocycles may have positive implications for the development of this compound on large-scale synthesis. It is possible that this approach could be extended to other alkylation reactions, where microwave irradiation may facilitate better yields and increased reaction speed.

2.7.3 Using a Squaramide Ethyl Ester as a Functional Group that Reacts with Antibodies

Diethyl squarate is formed from squaric acid by reflux in ethanol (Scheme 5, ***14***). The reaction of diethyl squarate with a slight excess of a primary amine (***15***) in ethanol at room temperature for four hours gave the corresponding squaric amide esters (***16***). This reaction is effectively selective as the reaction rate of the second ester of diethyl squarate is slower than the formation of the first vinylogous amide. This limits the formation of the symmetrical diamide.[174, 178]

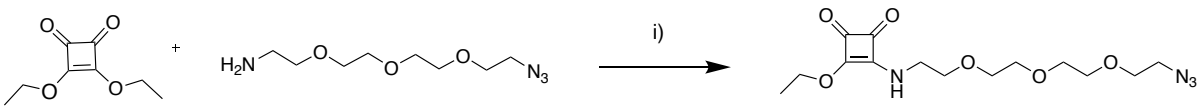

14 *15* *16*

Scheme 5: Synthesis of the $N_3(OEG)_3SqOEt$ (***16***); i) ethanol, RT, 4 hours.

Isolation of compound **16** as a colourless oil (49%) and analysis by RP-HPLC determined a single peak with a retention time of 7.33 minutes. High-resolution ESI-MS determined the signal of highest intensity as the singly protonated adduct, $[M+H]^+$, m/z =

343.1613 with a second, smaller peak corresponding to the $[2M+H]^+$ adduct with an m/z = 685.3155 (Figure 27).

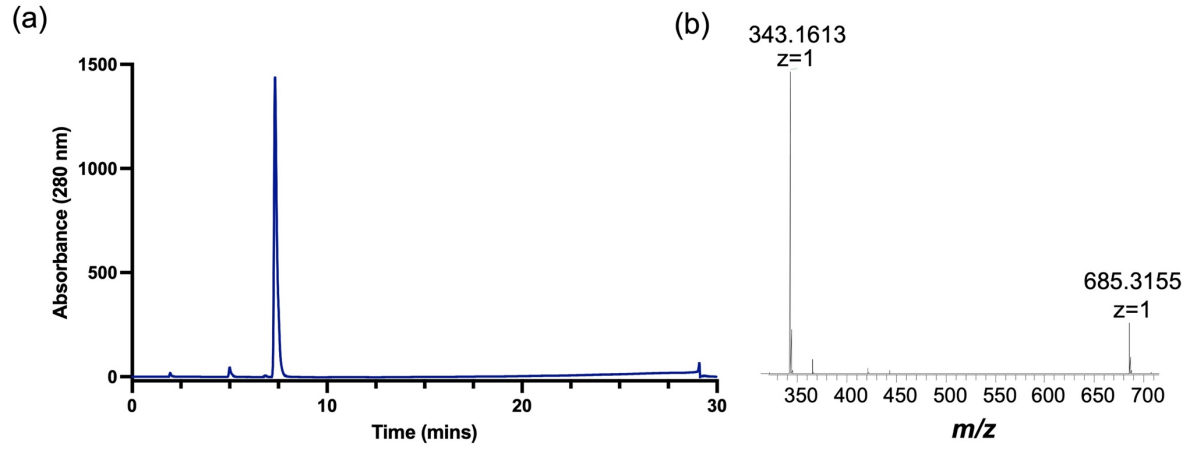

Figure 27: (a) RP-HPLC of compound ***16,*** showing a single peak (R_t = 7.33 min, column B), (b) HR-MS of compound 16, $[M+H]^+$ = 343.1613, $[2M+H]^+$ = 685.3155.

Investigation of the ^{1}H NMR environments of compound ***16*** indicated that there are two environments present on the NMR time scale in d_6-DMSO. This is due to two geometric isomers (Figure 28, a) formed through restricted rotation around the vinylogous amide N–C in the squaramide (Figure 28, b). This is evident in the interesting splitting and multiplicity in the hydrogen environments visible in the ^{1}H NMR spectrum (Figure 28, c). Notably, there are two downfield resonances at δ 8.79 ppm and δ 8.62 ppm that integrate to approximately 0.5 hydrogen environments each, which can be assigned to the two isomers of the squaramide hydrogen (7). It appears that one isomer (denoted as ***a*** in Figure 28, a) is slightly more abundant than the other isomer (b). This can be rationalised in terms of the syn versus anti configuration of the planar squaramide ethyl ester. Further investigation of the ^{1}H NMR spectrum demonstrated that the –CH_2– environments of the ethoxy group (2) present at δ 4.62 –4.67 ppm appear as a multiplet as a result of the two overlapping triplet signals. The splitting of these signals suggests there may be multiple isomers on the NMR timescale. Assignment of these peaks was made possible through 2D experiments (COSY, HSQC and HMBC).

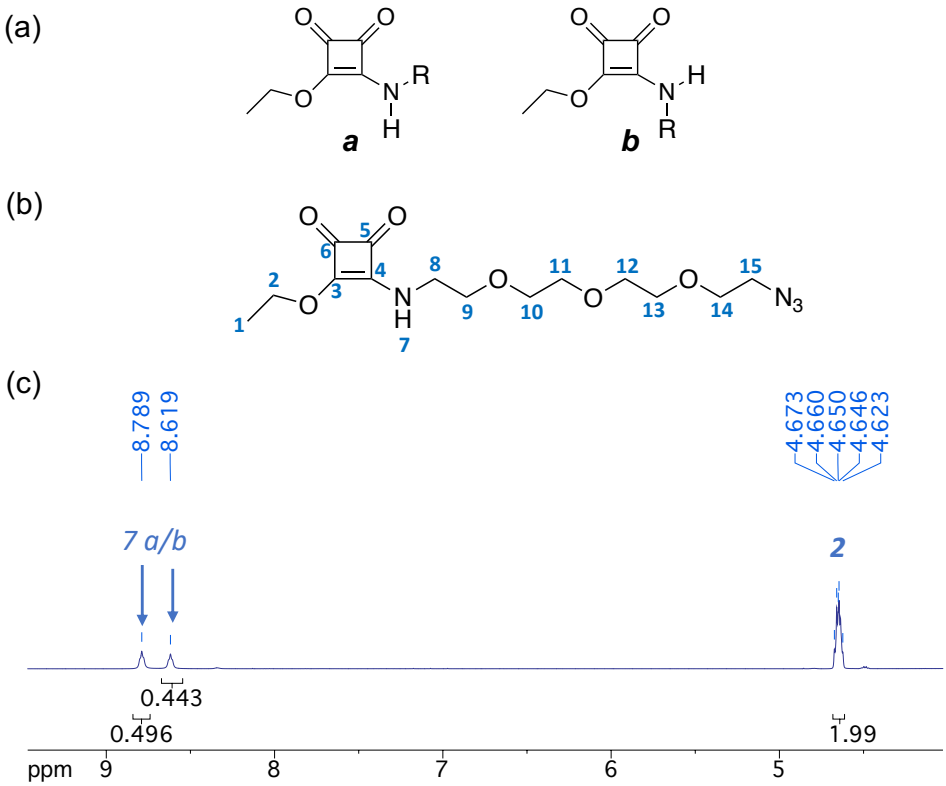

Figure 28: (a) The restricted rotation around the vinylogous amide means that two isomers (a and b) are present in ^{1}H NMR, (b) chemical structure of compound ***16***, blue arrow indicates the hydrogen (c) ^{1}HNMR (d_6-DMSO) between 4 – 10 ppm of compound ***16*** (room temperature).

These two geometric isomers are evident in the split resonances of the methylene group HN–CH_2 adjacent to the vinylogous amide of the squaramide (denoted as 8a/b). These environments are present as two triplets at δ 3.42 (a) and 3.62 ppm (b), which integrate for approximately one hydrogen each and show cross peaks with the corresponding hydrogen environments of the vinylogous amide hydrogen (7) in 2D-correlated spectroscopy analysis. The hydrogen environments of the methylene group, –CH_2–N_3, closest to the azide (15), are present as a single triplet at δ 3.38 ppm. The remaining –CH_2–O methylene peaks are unresolved and appear as a complex multiplet at δ 3.51 – 3.53 ppm, which integrates for ten hydrogens (Figure 29).

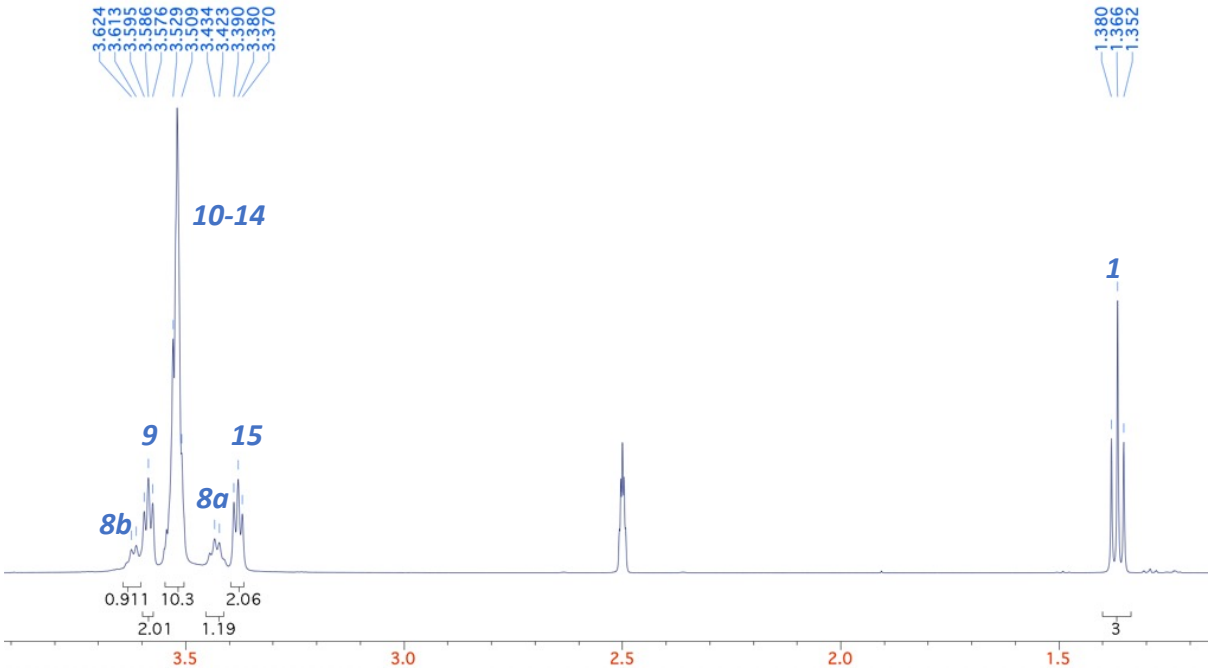

Figure 29: ^{1}H NMR (d_6-DMSO) between δ 1 – 4 ppm of compound ***16*** (room temperature) with corresponding assignments.

The ^{13}C NMR of compound ***16*** is also consistent with the presence of isomers (Figure 30).[179] There is a characteristic shift of the carbonyl carbon vinylogous ester moiety (6) at δ 189.17 – 189.31 ppm, and the corresponding β-carbon (3) has a shift of δ 176.65 – 176.94 ppm. The carbonyl carbon of the vinylogous amide functional group (5) experiences a shift of δ 182.05 – 182.21 ppm, whilst its corresponding β-carbon (4) has a shift of δ 172.50 – 172.97 ppm. The carbon environments of the corresponding isomers are very close but still resolved. The carbon environment (4) exhibits the largest difference in the shift of the carbon signals Δ 0.47 ppm, presumably due to its vicinity to the vinylogous amide.

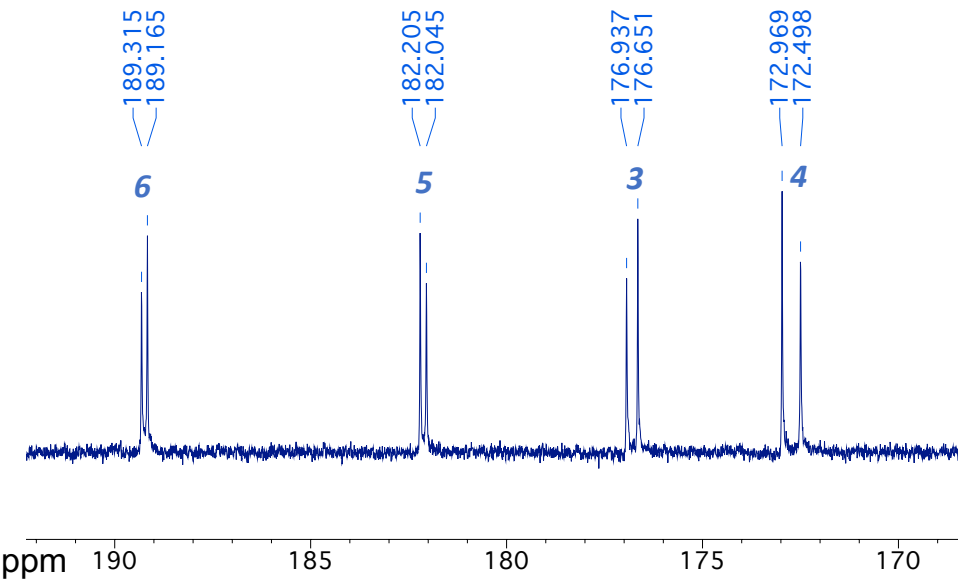

Figure 30: ^{13}C NMR (d_6-DMSO) between ~170 – 195 ppm of compound ***16***, showing the carbon environments of the squaramide ethyl ester with corresponding assignments.

The interesting behaviour of diethyl squarate functional groups means that only a single amidation reaction takes place with an incoming amide due to changes in the overall aromaticity of the squarate that makes it less reactive to a second amine. Compound ***16*** is synthesised in high purity, confirmed by both the RP-HPLC and ESI-MS. Two geometric isomers are present on an NMR timescale.

2.7.4 Synthesis of H_2MacropaSqOEt Through a Copper(I) Catalysed Click Reaction

The terminal alkyne on the metal chelator (***13***) was reacted with the aliphatic azide on the short oligo(ethylene glycol) chain with a pendant squaramide ethyl ester (***16***) proceeded using a copper(I) catalysed Huisgen's 1,3-dipolar cycloaddition (Scheme 6).[180, 181] Copper(II) sulphate pentahydrate was reduced with sodium ascorbate *in situ* to the active copper(I) species in the presence of tris((1-benzyl-4-triazolyl)methyl)amine (TBTA) as an additive to facilitate the quantitative, regioselective formation of the 1,2,3-triazole. The remaining copper(I/II) was removed with excess EDTA, and the crude reaction mixture was purified *via* semi-preparative HPLC to give the final compound (***17***, H_2MacropaSqOEt) in 40 % yield.

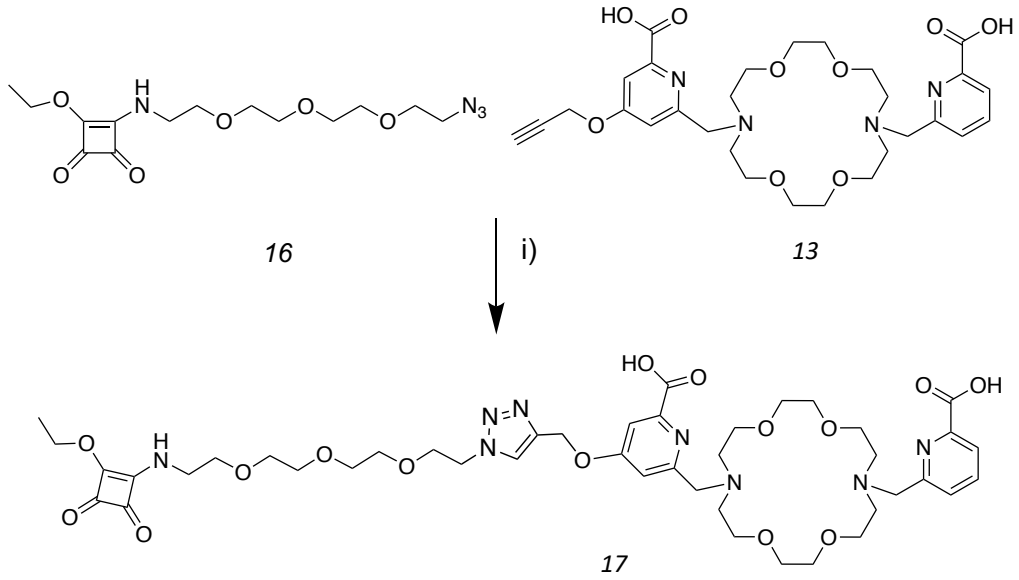

Scheme 6: Copper(I) catalysed azide-alkyne cycloaddition between $N_3(OEG)_3$-SqOEt and ***13*** (i) $CuSO_4$, sodium ascorbate, TBTA, DMF: H2O (4:1), RT, 1 hour.

Analytical RP-HPLC gave a single peak corresponding to the ligand, H_2MacropaSqOEt, with a retention time of 10.07 minutes. High-resolution ESI-MS presented the major peak corresponding to the doubly protonated $[M+2H]^{2+}$ adduct with an m/z = 465.2161 (Figure 31).

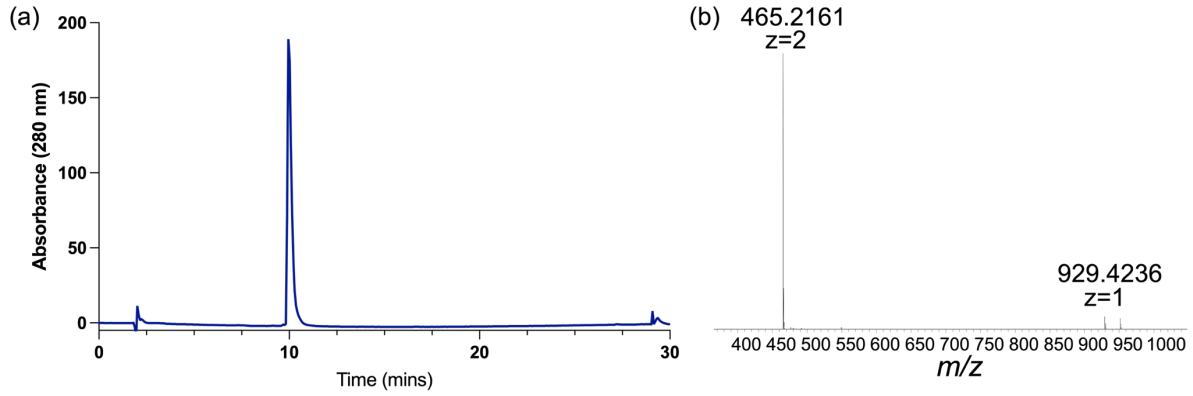

Figure 31: RP-HPLC (280nm) of H_2MacropaSqOEt (R_t = 10.07 mins; column A), with an inset of the mass spectrum; $[M+2H]^{2+}$ = 465.2161.

The ^{1}H NMR spectrum of H_2MacropaSqOEt (Figure 32, a) has six downfield resonances corresponding to the five aromatic hydrogen atoms as part of the two pyridyl rings and one hydrogen at the 5-position of the 1,2,3-triazole (Figure 32, b). These signals each integrate for one hydrogen atom. The assignment of hydrogen environments was aided by 2D-

correlated spectroscopy (COSY, Figure 32, c). The hydrogen atom at δ 8.1 ppm (3) is present as a triplet and is adjacent to two hydrogen environments (2 and 4) which are present at δ 7.75 ppm and δ 8.04 ppm of the corresponding pyridyl ring, as evidenced by the shared cross peaks. This allows for the assignment of the remaining hydrogen environments (22 and 24) further upfield observed at δ 7.42 ppm and δ 7.67 ppm. The most deshielded resonance arises from the hydrogen atom of the triazole (29). Before the 1,3-dipolar cycloaddition, the resonance attributed to the terminal hydrogen of the alkyne functional group in compound ***13*** was present at δ 2.61 ppm. Upon formation of the triazole, this hydrogen environment exhibits a significant downfield shift to a resonance at δ 8.24 ppm (29). This is also evident in the ^{13}C NMR spectrum with a shift from δ 77.20 ppm to δ 128.55 ppm.

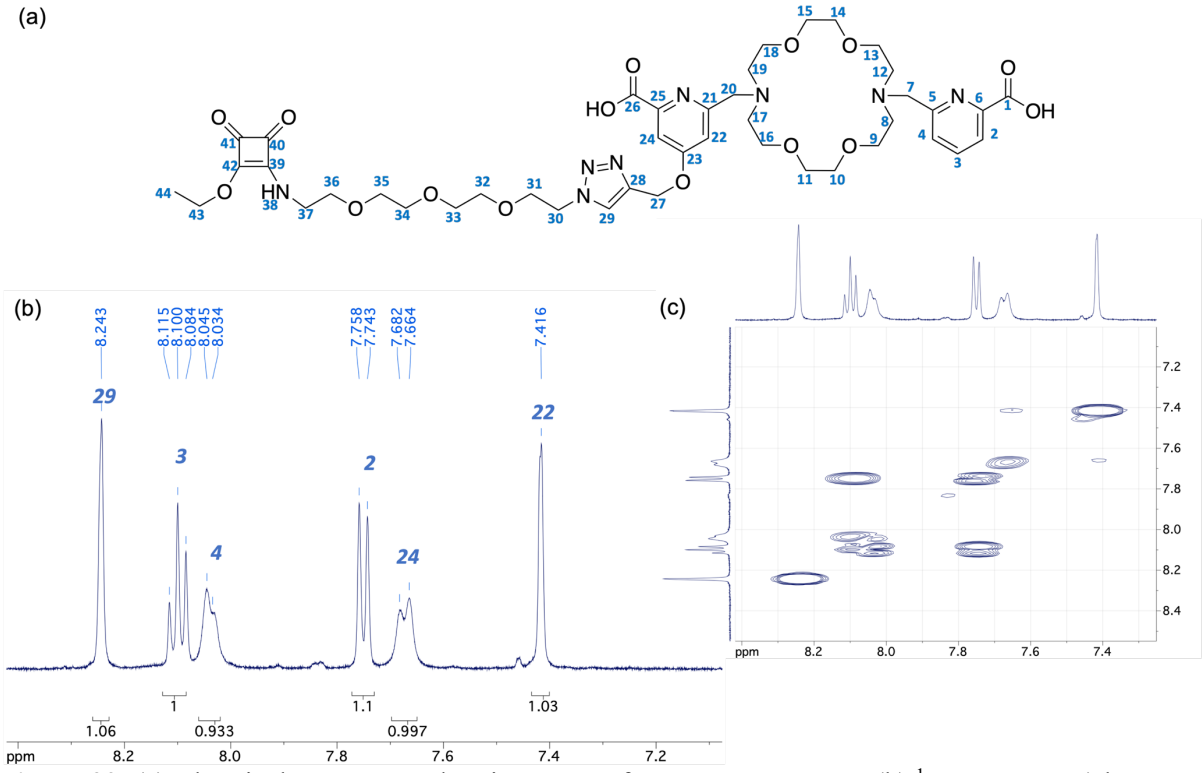

Figure 32: (a) Chemical structure and assignments of H_2Macropa-SqOEt, (b) ^{1}H NMR, D_2O) between δ 7 – 7.5 ppm, (c) Correlated spectroscopy of H_2Macropa-SqOEt between δ 7.1 – 8.5 ppm.

The presence of isomers due to the vinylogous ethyl ester also led to the resonances attributed to the –CH_2–CH_3 (43) at δ 4.61 ppm, which integrates for four hydrogens appearing

as a multiplet as a consequence of the two overlapping quartets, as well as one resonance that can be attributed to the –CH_2– group (20, Figure 33, a). Variable temperature ^{1}H NMR (40 °C) made it possible to resolve the resonances from the hydrogen atoms (7, 20 and 43, Figure 33, b).

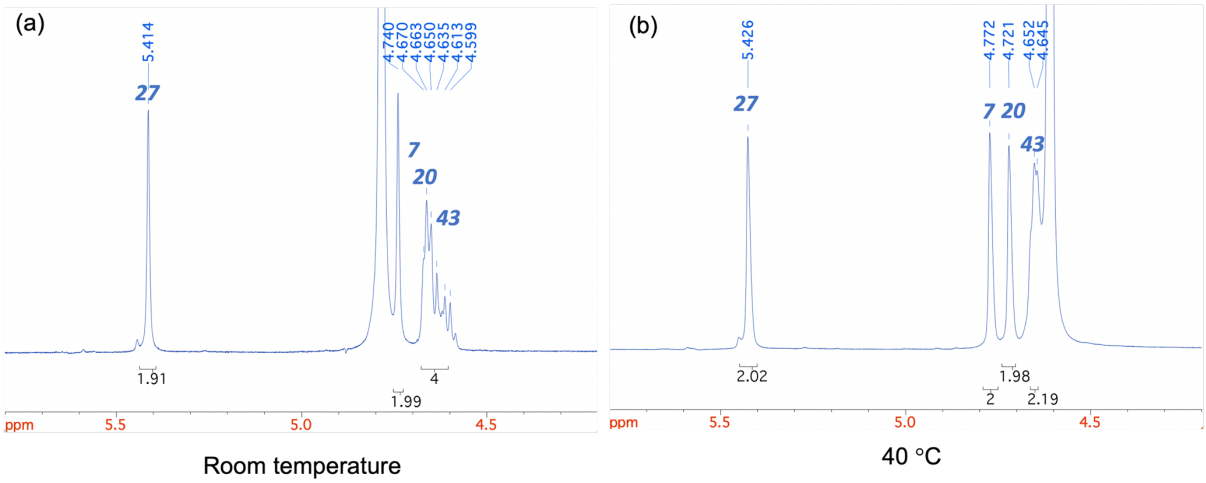

Figure 33: ^{1}H NMR (D_2O) of H_2MacropaSqOEt between δ 4.2 – 5.8 ppm at (a) room temperature and (b) 40 °C.

The corresponding –CH_3 environment (44) integrates for three hydrogens but exists as a multiplet of two overlapping triplet signals at δ 1.52 – 1.55 ppm (Figure 34). The complexity of the ^{1}H and ^{13}C NMR required 2D spectra to assign the environments. There are 40 hydrogens in two complex multiplets at δ 3.55 – 3.68 and δ 3.94 – 3.98 ppm, and as discussed, these multiplicities arise from the isomerism at the NMR timescale. Comparison of the spectra of the macrocycle as well as the linker N_3(OEG)$_3$SqOEt (***17***) in D_2O makes it possible to assign the resonances from the hydrogen environments from methylene peaks within the macrocycle. The three different hydrogen resonances from the diaza-crown ether appear at δ 3.94 ppm (8H, 9, 13, 16, 18), δ 3.69 ppm (8H, 10, 11, 14, 15) and δ 3.64 ppm (8, 12, 17, 19). The resonances δ 3.64 ppm overlap with the hydrogen environments that are assigned as –CH_2–O from the (OEG)$_3$SqOEt linker (32, 33, 34, 35).

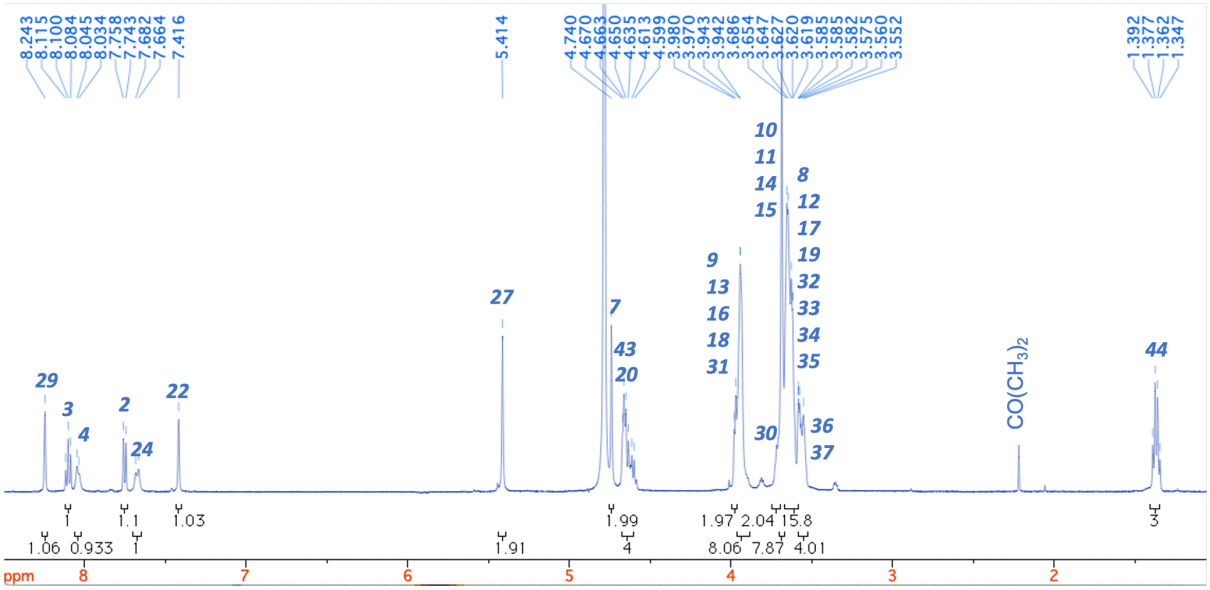

Figure 34: ^{1}H NMR (D_2O) of H_2MacropaSqOEt with assignments.

2.7.5 Concluding Remarks and Improvements on the Synthesis of H_2Macropa

Pioneering work has shown that a crown ether macrocyclic ligand functionalised with two picolinic acid arms, H_2Macropa forms stable complexes with actinium-225.[160] In this work, a new bifunctional variant of H_2Macropa with a pendant diethyl squarate ester, H_2MacropaSqOEt, was synthesised and characterised. This new bifunctional chelator will allow for the conjugation of the macrocycle to monoclonal antibodies.

The p*ara*-isothiocyanate substituted pyridine present in H_2Macropa-NCS is highly reactive and consequently more prone to hydrolysis. We designed our metal chelator, H_2MacropaSqOEt, in an attempt to circumvent these issues *via* the incorporation of the squaramide ethyl ester functional group. Squaramide ethyl esters are stable with respect to hydrolysis and have a long shelf life and improved solubility in aqueous mixtures. The ligand H_2MacropaSqOEt is compatible with aqueous buffers, and this will likely reduce the perturbation imposed on any monoclonal antibody conjugates.

2.8 The Coordination Chemistry of Monofunctional H_2Macropa with Lanthanum(III)

2.8.1 X-ray Crystallography of H_4Macropa$(CF_3CO_2)_2(H_2O)$

Crystals of [H_4Macropa$(CF_3CO_2)_2(H_2O)$] of sufficient quality for structure determination by X-ray crystallography were isolated from the slow evaporation of tetrahydrofuran into an aqueous solution of the ligand (Figure 35). The ligand was purified by RP-HPLC in a mobile phase containing 0.1 % trifluoracetic acid (TFA, CF_3COOH) and therefore was isolated as the TFA salt (Table 2). The ligand is protonated at the tertiary nitrogens on the diaza-crown ether backbone (N1). Analysis of the X-ray crystal structure confirms the connectivity of the ligand and its similarity to the previously published X-ray crystal structure by Thiele *et al.* of H_2Macropa·2HCl·4H_2O.[160] In the crystal structure of H_4Macropa$(CF_3CO_2)_2(H_2O)$ the molecule lies on a centre of inversion and the picolinate arms are in a *trans* configuration with respect to the macrocyclic core. It is worth noting that the *trans* disposition of the picolinate arms requires reorganisation to accommodate a metal cation as shown by the X-ray crystal structure of the La^{III} complex, (Figure 37) but it is not known if the *trans* disposition is retained in solution.

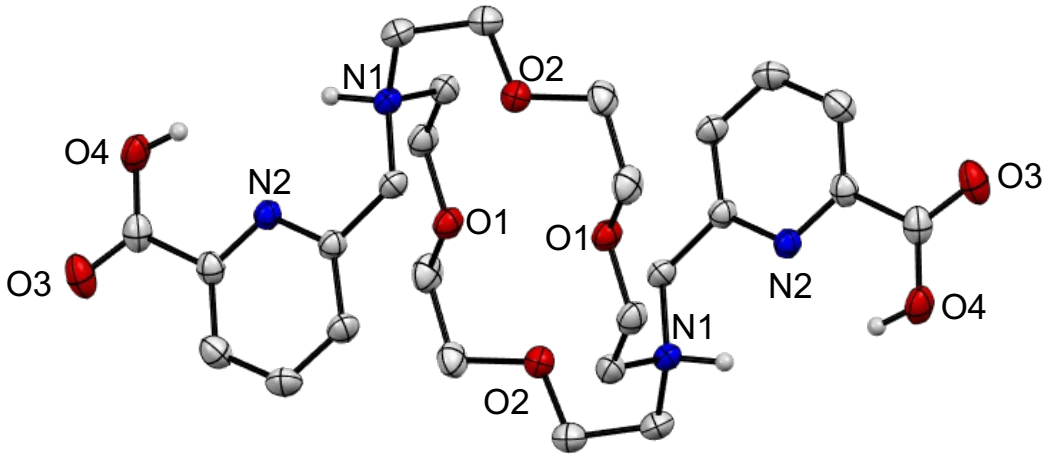

Figure 35: X-ray crystal structure of H_4Macropa$(CF_3CO_2)_2(H_2O)$. The asymmetric unit consists of a half cation, trifluoracetic acid counter anion, and one H_2O molecule. The trifluoracetic acid counter anion and H_2O are emitted for clarity.

The TFA -CF_3 group is disordered. This gives rise to F(1) and F(1A) configuration. The bond lengths of O(2)-C(4) and O(2)-C(5) are 1.4210(16) Å and 1.4181(17) Å, respectively. The O(1)-C(2) (1.4268(16) Å) and O(1)-C(3) (1.4260(16) Å) bond lengths are similar. The bond lengths of the protonated tertiary nitrogen (N1) to adjacent carbon atoms within the ring (C1, C6) are 1.5044(17) Å and 1.5049(15) Å, respectively.

2.8.2 X-ray Crystallography of [La(HMacropa)(H_2O)].(CF_3SO_3)$_2$.

La^{III} is often used as a non-radioactive surrogate for [^{225}Ac]Ac^{III} as it is a +III cation with a relatively large atomic radius. EXAFS studies with [^{227}Ac]Ac^{III} determined an optimal coordination number of 11, and X-ray crystallography was used to examine the coordination geometry of La^{III} complexes of H_2Macropa (Table 2).[112, 120, 121]

The La^{III} complex was formed by adding lanthanum triflate to an aqueous solution of the ligand, after which the solution was acidified to pH approximately 4. Crystals suitable for X-ray crystallography were formed by vapour diffusion of THF into the aqueous solution of the complex. The unit cell contains two THF molecules, four $CF_3SO_3^-$ anions and two [La^{III}(HMacropa)(H_2O)]$^{2+}$ complexes that share an internal hydrogen bond between the O(8) and O(8A) oxygen atoms (Figure 36). This close intermolecular contact O(8)-H'-O(8A) (2.20(18) Å) results in a coordination polymer that forms between O(8) and O(8A) on the neighbouring complexes.

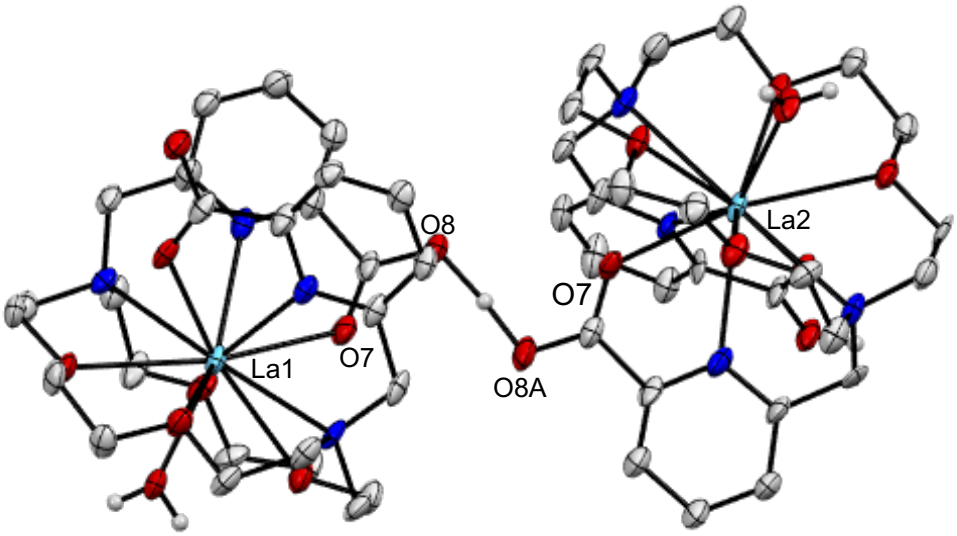

Figure 36: X-ray structure of the cation $[La^{III}(HMacropa)(H_2O)]_2(CF_3SO_3)_2$ Solvent molecules and counter ions are omitted for clarity.

Table 2: Crystallographic Table of $(H_4Macropa(TFA)_2(H_2O))_2$ and $[La(HMacropa)(H_2O)]\cdot(CF_3SO_3)_2$.

Empirical Formula	$C_{30}H_{38}F_6N_4O_{12}$	$C_{32}H_{41}F_6LaN_4O_{16}S_2$
Formula Weight	768.58	1054.72
Crystal System	Triclinic	Triclinic
Space Group	$P\bar{1}$	$P\bar{1}$
***a*/Å**	7.4829(2)	13.3112(7)
***b*/Å**	11.5882(3)	15.7099(7)
***c*/Å**	11.7829(3)	19.8270(11)
α/(°)	113.461(3)	92.917(4)
β/(°)	100.127(2)	96.551(5)
γ/(°)	106.309(2)	96.351(4)
***V*/Å^3**	850.19(4)	4085.3(4)
Z	1	4
Temperature/K	100.0(2)	100.0(3)
λ/Å	1.54184	1.54184
Refinement method	Full-matrix least-squares on F2	Full-matrix least-squares on F2
R-Factor/%	4.1	11.5

The La^{III} complex is 11 coordinate and in an all-faced capped trigonal prism coordination environment (Figure 37). This is derived from the symmetrical position of the La^{III} within the macrocycle. The La^{III} sits above the plane of the macrocycle with two picolinic acid arms on the same face in a syn arrangement and each acting as bidentate donors. A coordinated water molecule completes the coordination sphere and is positioned on the other side of the macrocycle with respect to the picolinic acid arms (Table 2).

Interestingly, one carboxylic acid of the ligand remains protonated, giving the dicationic structure. This is consistent with a previously published crystal structure of the perchlorate salt, $[La(HMacropa)(H_2O)](ClO_4)_2$.[160] Their work also described a close intermolecular contact with the corresponding O(6) and O(8) in neighbouring molecules in the crystal structure (2.468 Å).

The La^{III} forms coordinate bonds with the four oxygen atoms (O(1A) – O(4A)) within the macrocycle, ranging in length between 2.718(11) Å for O(3A)-La(2) and 2.802(9) Å for O(2A)-La(2). The coordinate bonds of La^{III} to the nitrogens of the diaza-crown ether (N(1A) – N(2A) range from N(1A)-La(2) 2.980(11) Å to N(2A)-La(2) 2.921(11) Å. The bond lengths of nitrogen atoms within the picolinate arms (N(3A) and N(4A)) were 2.800(13) Å for N(3A)-La(2) and 2.751(12) Å for the bond between N(4A)-La(2). An inner sphere H_2O, which has penetrated from below the macrocycle, forms a coordinate bond (O(9A)-La(2) – 2.516(11) Å). Comparison to the published structure determined by Thiele *et al.*[160] show similarities in the corresponding metal-ligand bond lengths (Table 3).

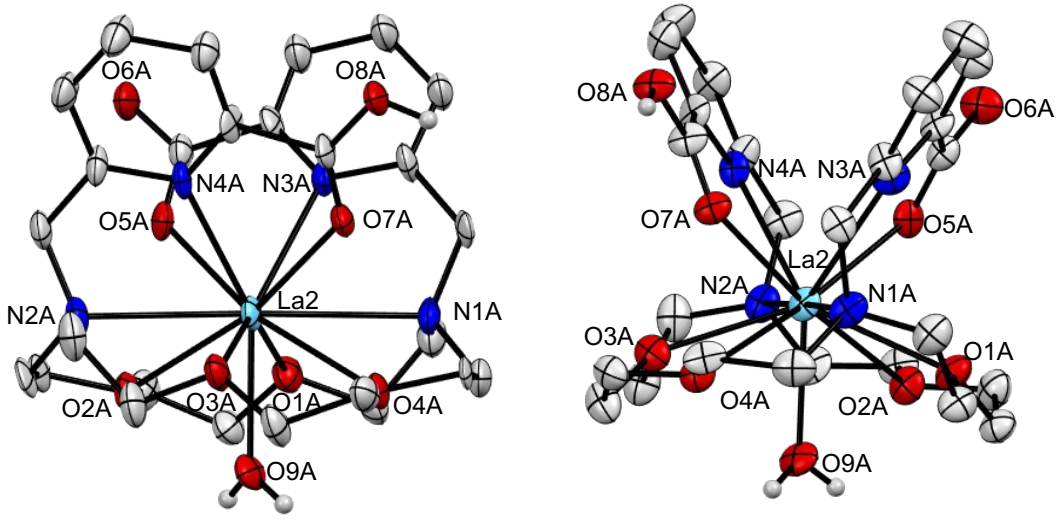

Figure 37: X-ray crystal structure of the cation present in [La(HMacropa)(H_2O)].(CF_3SO_3)$_2$. Thermal ellipsoids are shown at 50 % probability.

Table 3: Selected bond length of the cation present in [La(HMacropa)(H_2O)].(CF_3SO_3)$_2$.

La(1) Bond Lengths (Å)		La(2) Bond Lengths (Å)		Thiele *et al.*[160]	
N(1)-La(1)	2.915(11)	N(1A)-La(2)	2.980(11)	N(1)-La	2.942(4)
N(2)-La(1)	2.898(11)	N(2A)-La(2)	2.921(11)	N(2)-La	2.898(4)
N(3)-La(1)	2.742(12)	N(3A)-La(2)	2.800(13)	N(3)-La	2.759(4)
N(4)-La(1)	2.741(13)	N(4A)-La(2)	2.751(12)	N(4)-La	2.776(4)
O(1)-La(1)	2.726(10)	O(1A)-La(2)	2.784(11)	O(1)-La	2.791(2)
O(2)-La(1)	2.805(8)	O(2A)-La(2)	2.802(9)	O(2)-La	2.701(4)
O(3)-La(1)	2.672(10)	O(3A)-La(2)	2.718(11)	O(3)-La	2.794(3)
O(4)-La(1)	2.837(9)	O(4A)-La(2)	2.781(9)	O(4)-La	2.732(3)
O(5)-La(1)	2.549(9)	O(5A)-La(2)	2.515(9)	O(5)-La	2.527(3)
O(7)-La(1)	2.535(9)	O(7A)-La(2)	2.522(9)	O(7)-La	2.552(2)
O(9)-La(1)	2.493(11)	O(9A)-La(2)	2.516(11)	O(9)-La	2.558(3)

2.8.3 Investigating the Role 1,2,3-Triazoles Play in Complex Formation using Lanthanum as a Non-Radioactive Surrogate

One structural difference in the design of our chelator, H_2MacropaSqOEt, is the presence of a 1,2,3-triazole, a five-membered ring of two carbon atoms and three nitrogen atoms (Figure 39, a). The triazole is a product of the cycloaddition between the terminal alkyne and the aliphatic azide and was part of the ligand design, which aimed to use click chemistry to increase the number of potential targeting vectors that could be ‘clicked’ onto the macrocycle.

Heterocyclic 1,2,3-triazoles are good ligands and form complexes with a wide range of metal ions. The presence of a coordinated H_2O and the protonation of one of the carboxylic acid arms in our crystal structure, $[La(HMacropa)(H_2O)].(CF_3SO_3)_2$ (Figure 38, a) prompted us to investigate whether the triazole functional group present in our bifunctional ligand, H_2MacropaSqOEt could coordinate to La^{III}. This would provide some inferences about similar interactions in $[^{225}Ac]Ac^{III}$. This was inspired by the enhancement in radiochemical yields at low concentrations reported by Reissig *et al.*[177] in their $[^{225}Ac]Ac(Macropa)^+$ derivative that contained an additional triazole moiety. They attributed this phenomenon to the presence of an additional nitrogen donor atom. Therefore, we designed a H_2Macropa derivative (Figure 38, b) that contained two 1,2,3-triazole functional groups to investigate whether a triazole could coordinate La^{III} in preference of an inner sphere coordinated H_2O.

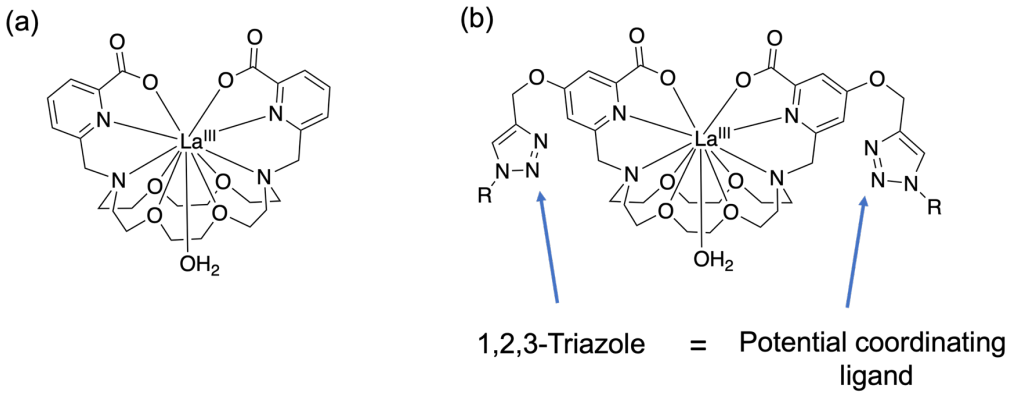

Figure 38: The chemical structures of (a) $[La^{III}(Macropa)(H_2O)]^+$, (b) the model compound $[La^{III}(MacropaTz_2Bn_2)(H_2O)]^+$ with two 1,2,3-triazole functional groups that have the potential to coordinate to La^{III} (R = benzyl).

In this context, the semi-rigid and conjugating triazole-pyridine-amido-based ligand, TPA, serves as an excellent example (Figure 39, a). This ligand incorporates two 1,2,3,-triazole moieties that coordinate to metal centres such as La^{III} (Figure 39, b).[182, 183] The X-ray structure of the cation reveals a trans-ligand bridged dinuclear $La_2(TPA)_3$, in which one La^{III} cation is clamped by a ligand with the cis-conformation and bridged together with the other through a ligand with a trans-conformation. Consequently, each La^{III} centre exhibits coordination by one

whole and one half-ligand, TPA.[182] Notably, the mono-bridged dinuclear $La_2(TPA)_3$ exists as a mesomer, with both La^{III} metal centres adopting opposite configurations (Δ versus Λ). Most importantly, this X-ray crystal structure provides evidence of La^{III}-triazole bond formation.

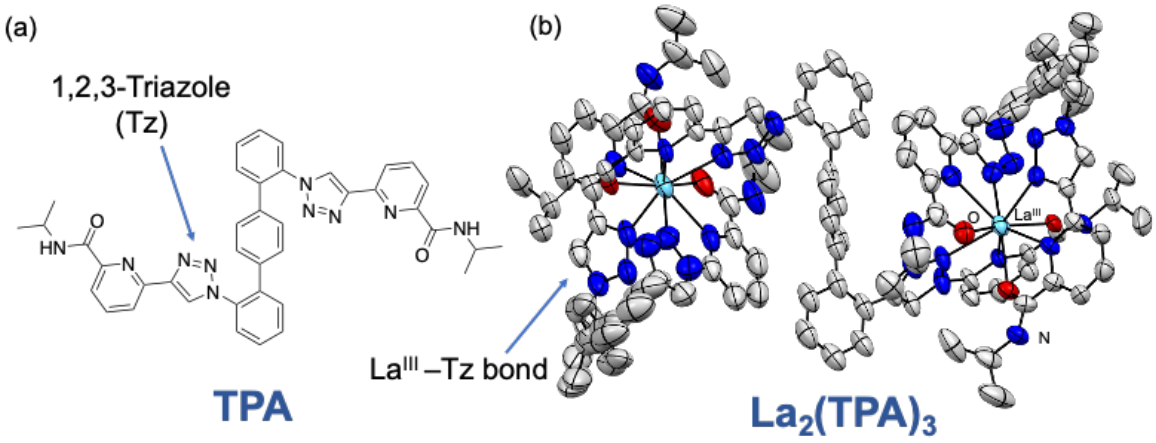

Figure 39: (a) Chemical structure of semi-rigid and conjugating triazole-pyridine-amido based ligand (TPA) that contains two 1,2,3-triazole groups, (b) The single crystal X-ray structure of the mono-bridged dinuclear $La_2(TPA)_3$ complex.[182]

We chose to use La^{III} as the non-radioactive surrogate of actinium-225. This is partly due to the comparable ionic radii of the two trivalent cations (1.12 Å vs. 1.06 Å), though La^{III} is smaller, but also because of the electron configuration of lanthanum ($5d^1$ $6s^2$):[184] La^{III} complexes are diamagnetic and can be analysed by ^1H NMR. A model compound, ***20***, was designed that contained two 1,2,3-triazole groups with the same structural backbone as H_2Macropa would allow us to see if either one of the triazoles would form a coordinate bond to La^{III} (Figure 38, b).

The synthesis of the metal chelator ***20*** proceeded in three steps (Scheme 7). Compound ***18*** was collected in high purity from the one-pot synthesis of compound ***12*** (Figure 26) or alternatively, was achieved by microwave irradiation of 2.5 equivalents of **9**, with 2 equivalents of DIPEA and diaza-18-crown-6 for 1 hour at 85°C, the ethyl-ester protected macrocycle **18** was purified by semi-preparative HPLC and isolated in 75 % yield. The two corresponding 1,2,3-triazoles were synthesised in a one-pot reaction (of compound ***19***), where the azide was generated *in situ* from bromobenzyl. Aliphatic azides can be readily prepared

from the corresponding halides by nucleophilic displacement.[185] A benzyl group was chosen to occupy the 1-position of the triazole as this functional group with a view to promote crystallisation without adding any potential ligands that could coordinate to the La^{III} metal. Compound ***19*** was isolated without further purification, and the immediate hydrolysis of ethyl esters was performed as previously described, which gave the ligand ***20*** as a colourless powder. Compound ***20*** was purified by RP-HPLC, which gave a single peak in 69 % yield.

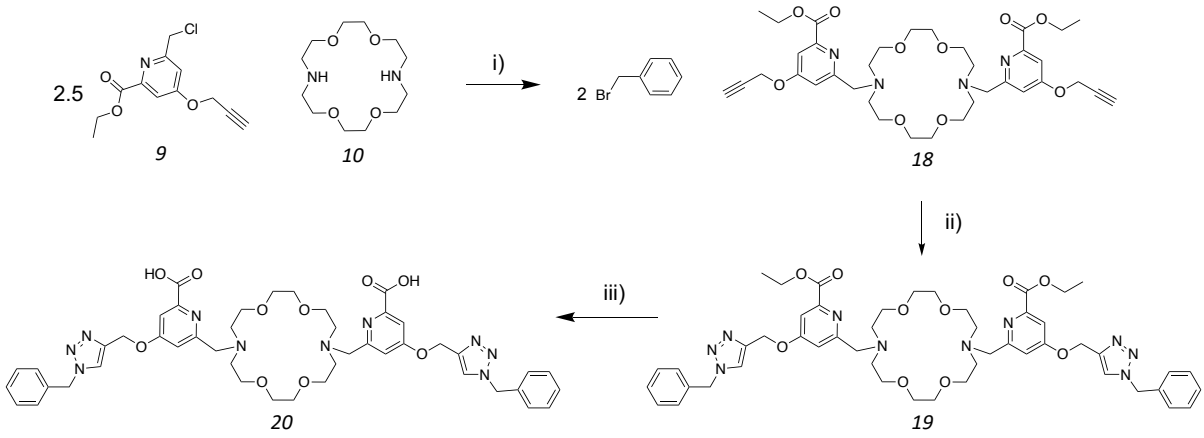

Scheme 7: Synthesis of $H_2MacropaTz_2Bn_2$. (i) Synthesis of the starting material ***18*** was also collected in a one-pot synthesis (*vide supra*). DIPEA, 85°C and μwave, 1.5 hours; (ii) $CuSO_4$, sodium ascorbate, NaN_3, benzyl bromide, Na_2CO_3 DMF: H_2O 4:1, RT, 1 hour (iii) NaOH in a solution of MeOH and dichloromethane (9:1), RT, 0.5 hours.

Crystals of the ligand $H_2MacropaTz_2Bn_2$ of suitable quality for X-ray crystallography were grown from the slow evaporation of methanol (Figure 40). The ligand exhibits symmetry with respect to the two picolinic acid 'arm' derivatives, which are trans to each other with respect to the macrocyclic ring. Although the ligand was purified by RP-HPLC, it was not isolated as the $CF_3O_2^-$ salt. Instead, the ligand exists as a zwitterion, N(1) is protonated, and O(4) carboxylic acid is deprotonated. The X-ray crystal structure of $(H_2MacropaTz_2Bn_2)(H_2O)$ confirms the connectivity of the atoms (Table 4). Bond lengths within the diaza-crown ether macrocycle are similar to those X-ray crystal structure of $H_4Macropa(CF_3CO_2)_2(H_2O)_2$. As is also the case in the X-ray crystal structure of $(H_2MacropaTz_2Bn_2)(H_2O)$, reorganisation of the picolinate arms will be required to form a complex such as the La^{III} complex, previously

described. The C(13)O(4) bond length (1.253 Å) is slightly longer than the C(13)O(3) bond of 1.242 Å, indicative of the carbonyl double bond.

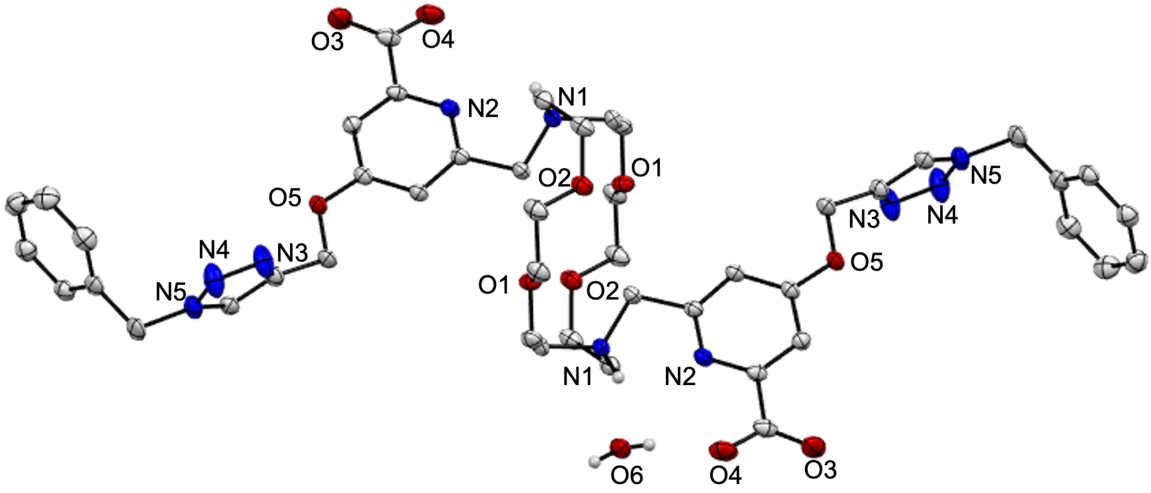

Figure 40: X-ray crystal structure of (H_2MacropaTz$_2$Bn$_2$)(H_2O).

Examination of the interaction between N(1)···O(6) and H(6C)···O(4) shows hydrogen bonding (Figure 41). This facilitates the presence of a protonated N(1) and deprotonated carboxylic acid C(4) in the X-ray crystal structure. Picolinic acid derivatisation to diaza crown ethers is well established. These functional groups are recognised for their ability to coordinate transition metals such as Zn^{II} and Cu^{II}. In a published investigation of the Zn^{II}(Macropa)$^{2+}$ complex, the Zn^{II} coordinates exocyclicly by the corresponding N(2) O(4) atoms of the picolinate arms, while the donor atoms of the crown ether remain uncoordinated.[186]

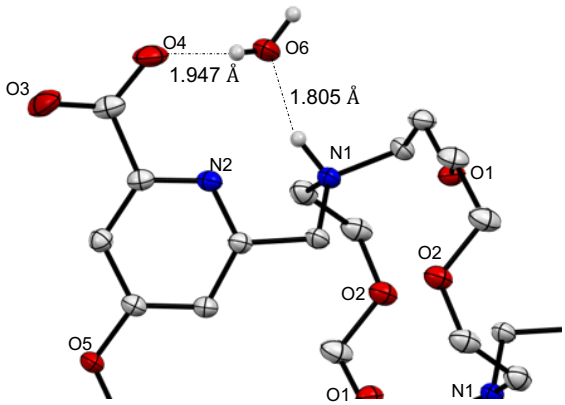

Figure 41: X-ray of the zwitterionic form of H_2MacropaTz$_2$Bn$_2$.

Table 4: Crystallographic Table of (H_2MacropaTz$_2$Bn$_2$)(H_2O).

Empirical Formula	$C_{46}H_{58}N_{10}O_{12}$
Formula Weight	943.02
Crystal System	Monoclinic
Space Group	P 1 21/n 1
***a*/Å**	13.6601(2)
***b*/Å**	9.88900(10)
***c*/Å**	17.3628(3)
α/(°)	90
β/(°)	99.0500(10)
γ/(°)	90
***V*/Å^3**	2316.25(6)
Z	2
Temperature/K	130.00(10)
λ/Å	1.54184
Refinement method	Full-matrix least-squares on F2
R-Factor/%	4.1%

Complexation of ligand ***20*** with lanthanum carbonate ($La_2(CO_3)_3.xH_2O$) in a solution of methanol and H_2O gave the corresponding complex in quantitative yield. Both the ligand and the complex, [La(MacropaTz$_2$Bn$_2$)]CO_3, were characterised by high-resolution mass spectrometry (Figure 42). The ligand was present as both the singly and doubly protonated adducts, $[M+H]^+$ and $[M+2H]^{2+}$, with an observed m/z = 907.4095 and m/z = 454.2093, respectively. The positive charge of the metal complex [La(MacropaTz$_2$Bn$_2$)]CO_3 determined

the peak of highest abundance as the cation of $[M]^+$ of m/z = 1043.2932. The singly protonated, doubly charged $[M+H]^{2+}$ species was also present with a m/z = 522.1509.

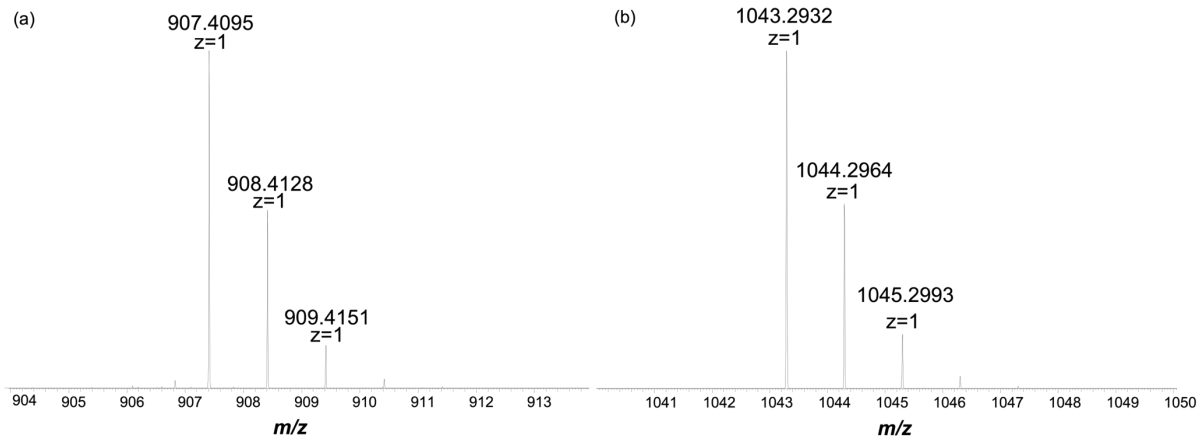

Figure 42: High-resolution mass spectrometry of (a) the singly protonated $[M+H]^+$ adduct of compound ***20***, $H_2MacropaTz_2Bn_2$ and (b) the charged $[M]^+$ cation of $[La(MacropaTz_2Bn_2)]CO_3$.

The ^1H NMR spectra of the ligand ***20*** and the complex $[La(MacropaTz_2Bn_2)]CO_3$ were compared (Figure 43). The phenyl hydrogen atoms have overlapping chemical shifts between δ 7.31 and 7.38 ppm. This signal integrates for 12 hydrogen atoms because of the overlapping resonances of the phenyl hydrogen atoms (1-3) and the hydrogen atom (7). The more deshielded hydrogen atom of the picolinate functional group (6) has a resonance at δ 7.72 ppm. There are three signals associated with three methylene groups that exist as singlets in compound ***20***. These signals each integrate for 4 hydrogen atoms due to the symmetry of ***20*** and exhibit chemical shifts of δ 4.68, 5.37, and 5.61 ppm, for N–CH_2 (17), O–CH_2 (10), and Bn–CH_2 (7), respectively. The hydrogen atom at the 4-position of the 1,2,3-triazole in the ligand has a characteristic shift and is the most downfield signal. It is present as a singlet at δ 8.16 ppm.

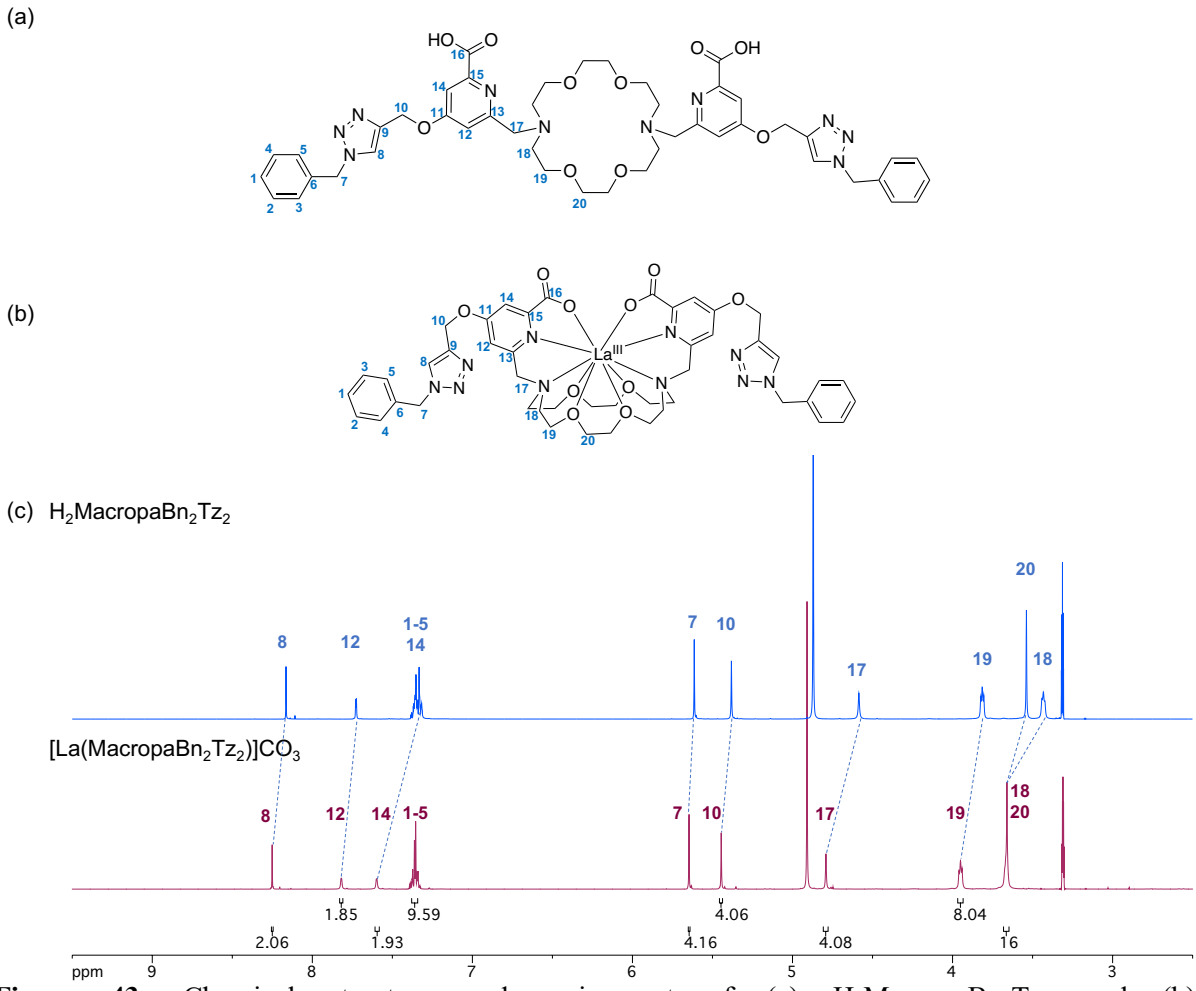

Figure 43: Chemical structure and assignment of (a) $H_2MacropaBn_2Tz_2$ and (b) $[La(MacropaTz_2Bn_2)]CO_3$ ^{1}HNMR spectra of compound 19 and complex $LaMacropaTz_2Bn_2$ in deuterated methanol.

Following complexation with La^{III}, there are shifts in some of the hydrogen environments. There is a significant downfield shift of the hydrogen atom (14) from δ 7.31-7.38 ppm to δ 7.60 ppm as it is no longer hidden under the complex benzyl hydrogen atom multiplet. The more deshielded aromatic hydrogen atom (12) has a slight downfield shift to δ 7.82 ppm. Upon coordination to La^{III}, the methylene hydrogens of the crown ether backbone were effectively locked into a single chemical environment.

The hydrogen atom that is most indicative of the formation of a triazole-metal coordinate bond is at the 4-position of the 1,2,3-triazole. In the ^{1}H NMR of the ligand, it exists as a singlet at δ 8.16 ppm. Upon the formation of $[La(MacropaTz_2Bn_2)]CO_3$, the signal exhibits a moderate downfield shift to δ 8.25 ppm. In the ^{1}HNMR analysis of $La_2(TPA)_3$, coordination

of the 1,2,3-triazole to La^{III} caused a significant shift of resonance for the triazole hydrogen from δ 8.1 ppm to δ 8.8 pm.[182] Therefore, we would expect a significant downfield shift to approximately δ 8.5 – 9.5 ppm.

It was postulated that only one of the 1,2,3-triazoles present within the ligand, H_2MacropaBn$_2$Tz$_2$, would form a coordinate bond to La^{III}. This was based on the presence of only one coordinated water as determined by previous X-ray crystallographic analysis of [La(HMacropa)(H_2O)].(CF_3SO_3)$_2$ (Figure 37). Therefore, if one 1,2,3-triazole functional group were coordinating to the La^{III} metal centre, we would expect to see a splitting of the 1,2,3-triazole resonance at δ 8.25 ppm, with each environment integrating for one hydrogen resonance and as a consequence the complex would lose symmetry. It appears that the 1,2,3-triazole did not participate in coordination to La^{III}, as evident in the absence of a large downfield shift of the characteristic triazole resonance.

2.9 Concluding remarks

The work in this chapter has focused on the design of a bifunctional metal chelator, H_2MacropaSqOEt, specifically optimised for actinium-225 radioimmunotherapy. Each component of H_2MacropaSqOEt has been tailored to create a ligand that is compatible with antibody labelling. The incorporation of the H_2Macropa-based ligand was integral due to its ability to form highly stable complexes with [^{225}Ac]Ac^{III}. These rapid complexation kinetics at room temperature are necessary for antibody labelling.

The inclusion of an alkyne functional group into the H_2Macropa scaffold offers flexibility in the linker section while maintaining excellent stability and high selectivity with azides. The formation of the corresponding 1,2,3-triazole provides a suitably stable functional group. Additionally, the incorporation of an oligo(ethylene glycol) linker serves as an adequate spacer without significantly increasing hydrophobicity.[170, 171] Finally, the inclusion of a pendant squaramide ethyl ester was chosen due to its stability with respect to hydrolysis[174] and

its increased aqueous solubility when compared to thioureas formed from the isothiocyanate coupling. These design considerations collectively contribute to the development of a stable bifunctional chelator, H_2MacropaSqOEt optimised for antibody conjugates and suitable for actinium-225 radioimmunotherapy.

The investigation of H_2Macropa-based ligands and complexes has provided valuable insights into the interesting coordination chemistry of lanthanoids with which we aim to draw inferences to with [^{225}Ac]Ac^{III} coordination chemistry. The X-ray crystal structure of the ligand, H_4Macropa$(CF_3CO_2)_2(H_2O)$, and the corresponding La^{III} complex, $[La(Hacropa)(H_2O)]_2(CF_3SO_3)_2$ showed similarities with the published structures by Wilson *et al.*[160] The X-ray crystal structure of $[La(Hacropa)(H_2O)]_2(CF_3SO_3)_2$ determined the complex to be 11 coordinate and in an all-faced capped trigonal prism coordination environment. The La^{III} sits above the plane of the macrocycle with two picolinic acid arms in a syn arrangement and a coordinated water molecule completes the coordination sphere.

The interesting coordination of the La^{III} complex prompted us to investigate whether the 1,2,3-triazole in our ligand, H_2MacropaSqOEt, was potentially coordinating to La^{III}. The synthesis and characterisation of a model ligand, H_2MacropaTz$_2$Bn$_2$, contains two 1,2,3-triazole groups. The ligand was characterised by X-ray crystallography, and formation of the complex [La(MacropaTz$_2$Bn$_2$)]CO_3 allowed us to probe the La^{III} coordination environment by ^{1}H NMR, ultimately determining that the 1,2,3-triazoles were likely not coordination to La^{III}.

2.10 Experimental

2.10.1 Materials and Reagents

All solvents and reagents were purchased from standard commercial suppliers and were used as received.

2.10.2 Instrumentation

^{1}H, ^{13}C, COSY, HSQC, HMBC were all recorded using a Varian FT-NMR 400 or FT NMR 500 spectrometer with a cryoprobe (Bruker). All ^{1}H NMR spectra were acquired at 400 MHz or 500 MHz and ^{13}C spectra were acquired at 101 MHz or 126 MHz. The reported peaks were all referenced to solvent peaks in the order of parts per million at 25°C. Microwave reactions were performed on a Biotage Initiator. Non-radioactive analytical HPLC were performed on Agilent 1200 series HPLC system fitted with an Alltech Hypersil BDS-C18 (4.6 x 150 nm, 5um, column A) or a Phenomonex Luna C18(2) column (4.6 mm x 150 mm, 5 µm, column B) and Phenomenex SecurityGuard™ C18 guard cartridge (4 mm x 30 mm) with a 1 mL/min flow rate; system A: gradient elution of Buffer A = 0.1% TFA in H_2O and Buffer B = 0.1% TFA in acetonitrile (0 to 100% B in A over 25 min) and UV detection at λ 214, 254, 280 nm and 350 nm. System A: System B with the following gradient 0 to 100% B in A over 17 min). Several chromatographic systems were used for purification steps. Semipreparative RP- HPLC (1260 Infinity II Preparative LC System with mass detector on a Lunar C18 column, 100Å, 21.2 x 250 mm, 5 µm) with a 15 mL/min flow rate. Gradient elution of Buffer B = 0.1% FA in H_2O and Buffer B= 0.1% FA in acetonitrile. Method C (5 to 95% B in A at 23 min, 95 % B in A at 25 min, 5 % B at 26 min) and detection at 214, 280 nm and 254 nm. Method D: Method B with the following gradient (5 to 60 % B in A at 20 min, 60 to 95% B at 26 min, 95 to 5 % B in A at 30 min). Method E: Method B with the following gradient (15 to 60 % B in A at 22 min, 60 to 95% B at 28 min, 95 to 15 % B in A at 31 min). Radio-radioTLC were analysed using a Raytest Rita-Star TLC scanner. X-ray crystallography were mounted in low temperature oil

then cooled to 130 K using an Oxford low temperature device. Intensity data were collected at 130 K with an Oxford XCalibur X-ray diffractometer with Sapphire CCD detector using Cu Kα radiation (graphite crystal monochromators λ = 1.54184 Å) or Rigaku Oxford X-ray diffractometer. Data were reduced and corrected for absorption. The structures were solved by direct methods and difference Fourier synthesis using the SHELX suite of programs as implemented within the WINGX2 3.38 software. Thermal ellipsoid plots were generated using the programs ORTEP-3 integrated with the SHELX suite of programs.

2.10.3 Synthesis and Characterisation of H_2MacropaSqOEt

2.10.4 Dimethylpyridine-2,6-dicarboxylate (2)

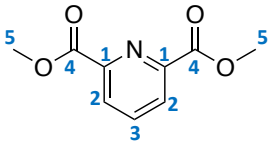

Dimethylpyridine-2,6-dicarboxylate was prepared according to an adaption of a literature procedure.[187] Pyridine-2,6-dicarboxylic acid (4.23 g, 25.3 mmol) and sulfuric acid (1 mL) in methanol (30 mL) were heated at reflux for 6 h. The solid was filtered as colourless crystalline solid. A second crop was obtained by removing the solvent under reduced pressure, dissolved in dichloromethane (100 mL), and washed with saturated $NaHCO_3$ solution (2 x 50 mL) and water (50 mL). The combined organic layers were dried over $MgSO_4$ and the solvent was removed under reduced pressure to give colourless solid (3.94 g, 80 %). Rt= 9.70 min (method A, column B). ESI-MS $[M+H]^+$: 196.0599 calculated for $(C_9H_{10}NO_4)^+$: 196.0605. ^{1}H NMR (400 MHz, $CDCl_3$) δ 8.30 (d, J = 7.8 Hz, 2H, 2), 8.01 (t, J = 7.8 Hz, 1H, 3), 4.01 (s, 6H, 5). ^{13}C NMR (101 MHz, $CDCl_3$) δ 165.0 (4), 148.2 (1), 138.4 (3), 128.0 (2), 53.2 (5).

2.10.5 Methyl 6-(hydroxymethyl)picolinate (3)

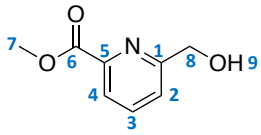

Methyl 6-(hydroxymethyl)picolinate was synthesised using an adapted literature protocol.[188] To dimethyl 2,6-pyridine-2,6-dicarboxylate (6.0 g, 30.6 mmol) in methanol (200 mL) at 0 °C was added sodium borohydride (2.32 g, 62 mmol) over 1 hour. The reaction mixture was stirred for 5 h at room temperature. The solution was quenched using saturated NH_4Cl (100 mL) at 0°C and methanol was removed under reduced pressure. The aqueous layer was extracted with dichloromethane (3 × 100 mL). The combined organic layers were dried over $MgSO_4$, filtered and the solvent was removed under reduced pressure. The colourless solid was purified by column chromatography (0-2 % MeOH in DCM) to give compound **3** (3.37 g, 57%). R_t = 6.67 min (method A, column A). ESI-MS $[M+H]^+$: 168.0652 calculated for $(C_8H_{10}NO_3)^+$: 168.0655. ^{1}H NMR (500 MHz, $CDCl_3$) δ 8.01 (d, *J* = 7.6 Hz, 1H, 4), 7.84 (t, *J* = 7.7 Hz, 1H, 3), 7.56 (d, *J* = 7.9 Hz, 1H, 2), 4.87 (s, 2H, 8), 3.98 (s, 4H, 7). ^{13}C NMR (126 MHz, $CDCl_3$) δ 165.66 (6), 160.58 (1), 147.02 (5), 137.80 (3), 124.16 (2), 123.85 (4), 64.75 (8), 52.97 (7). ×

2.10.6 Methyl-6-chloromethyl-pyridine-2-carboxylate (4)

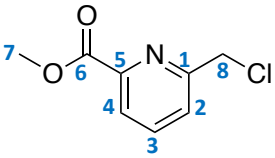

Methyl-6-chloromethyl-pyridine-2-carboxylate was synthesised using an adapted literature protocol.[188] Thionyl Chloride (6 mL) was slowly added to methyl-6-hydroxymethyl-2-pyridine carboxylate (2.5 g, 15 mmol) at 0 °C under an atmosphere of N_2 and stirred for 1 hour. After 1 hour, the thionyl chloride was removed *in vacuo*. The residue was dissolved in toluene (50 mL) and washed with saturated $NaHCO_3$ (50 mL). The organic fractions were dried over $MgSO_4$, filtered, and the solvent was removed under reduced pressure to give an oil that precipitated

out to yield an off-white solid (2.42g, 90%). R_t = 7.65 mins (method A, column A). ESI-MS $[M+H]^+$: 186.0319 calculated for $(C_8H_9ClNO_2)^+$: 186.0244. ^1H NMR (500 MHz, cdcl$_3$) δ 8.09 (d, *J* = 6.6 Hz, 1H, 4), 7.91 (t, *J* = 7.8 Hz, 1H, 3), 7.74 (d, *J* = 6.7 Hz, 1H, 2), 4.79 (s, 2H, 4), 4.02 (s, 3H, 7). ^{13}C NMR (101 MHz, $CDCl_3$) δ 165.3 (6), 157.2 (1), 147.5 (5), 138.1 (3), 126.2 (2), 124.5 (4), 53.1 (8), 46.3 (7).

2.10.7 Diethyl-4-hydroxypyridine-2,6-carboxylate (6)

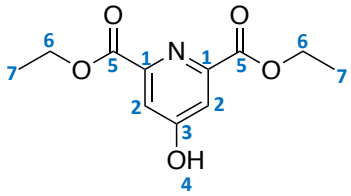

Diethyl-4-hydroxypyridine-2,6-carboxylate was synthesised using an adapted literature protocol.[189] Chelidamic acid (4.0 g, 21.8 mmol) was dissolved in ethanol (150 mL) and sulfuric acid (6 drops) was added and refluxed for 16 hours. The ethanol was removed under reduced pressure and used in the next reaction without further purification (3.98g, 76%). R_t = 7.85 mins (method A, column A). ESI-MS $[M+H]^+$: 240.0866 calculated for $(C_{11}H_{14}NO_5)^+$: 240.0867. 124°C. ^1H NMR (400 MHz, $CDCl_3$): δ 9.40 (br, 1H, 4), 7.45 (s, 2H, 2), 4.45 (q, 4H, 6), 1.41(t, 6H, 7).

2.10.8 Diethyl 4-(prop-2-yn-1-yloxy)pyridine-6-dicarboxylate (7)

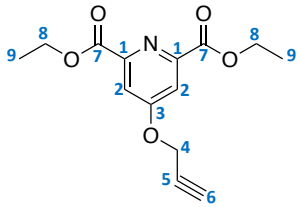

Diethyl 4-(prop-2-yn-1-yloxy)pyridine-2,6-dicarboxylate was synthesised using an adapted literature protocol.[190] To a suspension of diethyl chelidamate (4) (3.15 g, 13.2 mmol) and K_2CO_3 (3.6 g, 26.4 mmol) in DMF (30 ml) was added propargyl bromide solution (80 wt. % in toluene – 4.69 mL, 52.3 mmol). The mixture was heated at 80 °C for 3 h to aid solubility then stirred at room temperature overnight. Then the mixture was filtered, and the filtrate was concentrated under reduced pressure. The residue was purified by column chromatography (0-

2 % MeOH in DCM) to give compound **5** as either pale yellow or brown solid which was recrystallised from ethyl acetate to yield colourless crystals (2.47 g, 68%). R_t = 8.75 mins (method A, column A). ESI-MS $[M+H]^+$: 278.1021 calculated for $(C_{14}H_{16}NO_5)^+$: 278.1023 ^{1}H NMR (400 MHz, DMSO-d_6) δ 7.78 (s, 2H, 2), 5.09 (d, *J* = 2.4 Hz, 2H, 4), 4.36 (q, *J* = 7.1 Hz, 4H, 8), 3.73 (t, *J* = 2.3 Hz, 1H, 6), 1.32 (t, *J* = 7.1 Hz, 6H, 9).^{13}C NMR (101 MHz, DMSO-d_6) δ 165.11 (7), 164.01 (3), 149.68 (1), 114.44 (2), 79.86 (5), 77.65 (6), 61.69 (8), 56.52 (4), 39.52, 14.10 (9).

2.10.9 2-Hydroxymethyl 4-(prop-2-yn-1-yloxy)pyridine-6-ethylcarboxylate (8)

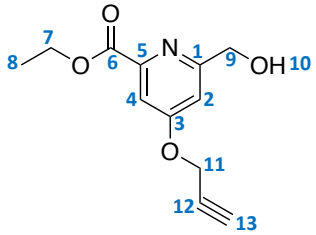

2-Hydroxymethyl 4-(prop-2-yn-1-yloxy)pyridine-6-ethylcarboxylate was synthesised using an adapted literature protocol.[188] To Diethyl 4-(prop-2-yn-1-yloxy)pyridine-2,6-dicarboxylate (1.81 g, 6.49 mmol) in ethanol (100 mL) at 0 °C was added sodium borohydride (0.319 g, 8.44 mmol) over 0.5 hours. The reaction mixture was stirred for 3 h at room temperature and monitored via MS until no starting material remained. The solution was quenched using saturated NH_4Cl (50 mL) at 0°C and ethanol was removed under reduced pressure. The aqueous layer was extracted with ethyl acetate (3 x 70 mL). The combined organic layers were dried over $MgSO_4$, filtered and the solvent was removed under reduced pressure to give the off-white compound **6**, which was purified by column chromatography (0 – 2 % MeOH in DCM) to yield a colourless powder (1.2 g, 75 %). ESI-MS $[M+H]^+$: 236.0919 calculated for $(C_{12}H_{14}NO_4)^+$: 236.0918. ^{1}H NMR (500 MHz, $CDCl_3$) δ 7.63 (d, *J* = 2.4 Hz, 1H, 4), 7.08 (d, *J* = 2.3 Hz, 1H, 2), 4.83 – 4.78 (m, 4H, 9), 4.45 (q, *J* = 7.1 Hz, 2H, 7), 2.60 (t, *J* = 2.4 Hz, 1H, 13), 1.42 (t, *J* = 7.1 Hz, 4H, 8).^{13}C NMR (126 MHz, $CDCl_3$) δ 165.28 (6), 165.01 (3), 162.11

(1), 149.18 (5), 111.51 (2), 109.81 (4), 77.21 (12), 76.84 (13), 64.74 (9), 62.21 (7), 56.14 (11), 14.41 (17).

2.10.10 2-Chloromethyl 4-(prop-2-yn-1-yloxy)pyridine-6-ethylcarboxylate (9)

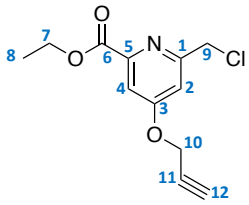

Thionyl Chloride (6 mL) was slowly added to 2-Hydroxymethyl 4-(prop-2-yn-1-yloxy)pyridine-6-ethylcarboxylate (0.4 g, 1.7 mmol) at 0 °C under an atmosphere of N_2 and stirred for 3 hours. After 3 hours, the thionyl chloride was removed in vacuo to yield a pale-yellow residue, which was dissolved in ethyl acetate (20 mL) and washed with saturated $NaHCO_3$ (30 mL) and water (30 mL). The organic fractions were dried over $MgSO_4$, filtered and the solvent was removed under reduced pressure to yield a pale-yellow powder (0.33g, 77%). R_t = 15.94 mins (method A, column B). ESI-MS $[M+H]^+$: 254.0578 calculated for $(C_{12}H_{14}NO_4)^+$: 236.0918. ^{1}H NMR (500 MHz, $CDCl_3$) δ 7.69 (d, *J* = 2.4 Hz, 1H, 4), 7.33 (d, *J* = 2.4 Hz, 1H, 2), 4.85 (d, *J* = 2.4 Hz, 2H, 9), 4.77 (s, 2H, 10), 4.50 (q, *J* = 7.1 Hz, 2H, 7), 2.64 (t, *J* = 2.4 Hz, 1H, 12), 1.46 (t, *J* = 7.1 Hz, 3H, 8).^{13}C NMR (126 MHz, $CDCl_3$) δ 165.50 (6), 164.82 (3), 159.04 (1), 149.60 (5), 112.44 (2), 111.68 (4), 77.36 (11), 76.67 (12), 62.37 (7), 56.21 (10), 46.42 (9), 14.41 (8).

2.10.11 Methyl 6-((1,4,10,13-tetraoxa-7,16-diazacyclooctadecan-7-yl)methyl)picolinate (11)

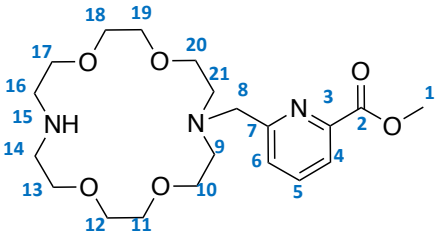

Methyl 6-((1,4,10,13-tetraoxa-7,16-diazacyclooctadecan-7-yl)methyl)picolinate was synthesised using an adapted literature protocol.[160] To a solution of 1,7,10,16-tetraoxa- 4,13-

diazacyclooctadecane (0.77 g, 3.02 mmol) and DIPEA (0. 34 g, 3.93 mmol) in dry CH_3CN (350 mL) at 75 °C was added dropwise a solution of **3** (0.37 g, 2.03 mmol) in dry CH_3CN (80 mL) over 4 hours under an atmosphere of nitrogen and was heated at reflux for 40 h. The solution was concentrated at 60 °C under reduced pressure to a pale-yellow oil. To the crude oil was then purified by *via* semi-preparative HPLC (method C), and appropriate fractions were combined and lyophilised to give a pale oil (626 mg, 76%). R_t = 7.26 min (method A, column A). ESI-MS $[M+2H]^{2+}$: 206.6257 calculated for $(C_{20}H_{33}N_3O_6)^{2+}$: 206.6257. ^{1}H NMR (500 MHz, D_2O) δ 8.36 (d, *J* = 7.7 Hz, 1H, 6), 8.27 (t, *J* = 7.8 Hz, 1H, 5), 7.92 (d, *J* = 7.7 Hz, 1H, 4), 4.88 (s, 2H, 8), 4.05 (dd, *J* = 6.2, 3.7 Hz, 4H, 10, 20), 3.99 (s, 3H, 1), 3.98 – 3.91 (m, 4H, 13, 17), 3.86 – 3.81 (m, 4H, 12, 18), 3.78 (q, *J* = 5.2 Hz, 8H, 9, 21, 11, 19), 3.49 (t, *J* = 4.9 Hz, 4H, 14, 16).^{13}C NMR (126 MHz, D_2O) δ 167.74 (2), 149.70 (7), 147.49 (3), 140.08 (5), 128.20 (6), 125.58 (4), 69.68 (11, 19), 69.52 (12, 18), 65.14 (10, 20), 63.98 (13, 17), 57.37 (8), 54.43 (9, 21), 46.69 (14, 16).

2.10.12 Ethyl 4-(prop-2-yn-1-yloxy)-6-((16-((6-(methoxycarbonyl)pyridin-2-yl)methyl)-1,4,10,13-tetraoxa-7,16-diazacyclooctadecan-7-yl)methyl)picolinate (12)

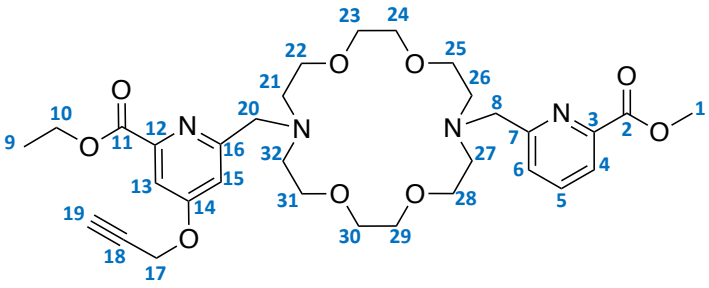

Two-step synthesis: Methyl 6-((1,4,10,13-tetraoxa-7,16-diazacyclooctadecan-7-yl)methyl)picolinate (0.149 g, 0.4 mmol), 2-chloromethyl 4-(prop-2-yn-1-yloxy)pyridine-6-ethylcarboxylate (0.138 g, 0.54 mmol) and DIPEA (0.14 mL, 0.8 mmol) in CH_3CN (2 mL) were combined and the reaction was heated with microwave irradiation at 85°C for 1 hour. The resulting solution was taken to dryness under reduced pressure to yield a pale-yellow oil, which

was purified *via* semi-preparative HPLC (method D), and appropriate fractions were combined and lyophilised to give a colourless oil (131 mg, 52%). *One-pot synthesis:* Diaza-18-crown-6 (50 mg, 0.19 mmol), compound **4** (46 mg, 0.24 mmol), compound **9** (76.2 mg, 0.31 mmol), DIPEA (70 μL 0.4 mmol) were dissolved in CH_3CN (2 mL) and heated with microwave irradiation at 90 °C for 1 hour. The resulting solution was diluted to a final ratio of MilliQ:CH_3CN of 2:1 and lyophilised. The resulting crude product was purified *via* semipreparative HPLC (method D). Pure fractions of compounds ***12***, ***18***, and ***H_2Macropa*** were separated and lyophilised, compound ***12*** (57 mg, 48%). R_t = 10.38 min (method A, column B). ESI-MS $[M+2H]^{2+}$: 315.1627 calculated for $(C_{32}H_{46}N_4O_9)^{2+}$: 315.1627, $[M+H]^+$: 629.3172 calculated for $(C_{32}H_{44}N_4O_9)^+$: 629.3181. ^{1}H NMR (500 MHz, D_2O) δ 8.20 – 8.17 (m, 1H, 6), 8.15 – 8.09 (m, 1H, 5), 7.79 (d, *J* = 2.3 Hz, 1H, 4), 7.77 (dd, *J* = 7.8, 1.1 Hz, 1H, 6), 7.39 (d, *J* = 2.3 Hz, 1H, 15), 4.97 (d, *J* = 2.4 Hz, 2H, 17), 4.75 (s, 2H, 8), 4.69 (d, *J* = 1.2 Hz, 2H, 20), 4.42 (q, *J* = 7.2 Hz, 2H, 10), 3.96 (s, 3H, 1), 3.93 (t, *J* = 4.9 Hz, 8H, 22, 25, 28, 31), 3.67 (s, 8H, 18, 23, 24, 29, 30), 3.64 (t, *J* = 5.1 Hz, 8H, 21, 26, 27, 32), 3.08 (td, *J* = 2.4, 1.0 Hz, 1H, 19), 1.38 (t, *J* = 7.2 Hz, 3H, 9). ^{13}C NMR (126 MHz, D_2O) δ 166.39 (2), 166.06 (14), 165.58 (11), 151.74 (3), 150.05 (12), 149.19 (16), 147.08 (7), 140.09 (5), 128.60 (6), 125.96 (4), 115.02 (15), 112.90 (13), 78.10 (18), 77.20 (19), 69.95 (23, 24, 29, 30), 64.11 (22, 25, 28, 31), 63.41 (10), 58.15 (8), 58.01 (20), 56.72 (17), 54.49 (21, 26, 27, 32), 53.39 (1), 13.47 (9).

2.10.13 4-(prop-2-yn-1-yloxy)-6-((16-((6-carboxypyridin-2-yl)methyl)-1,4,10,13-tetraoxa-7,16-diazacyclooctadecan-7-yl)methyl)picolinic acid (13)

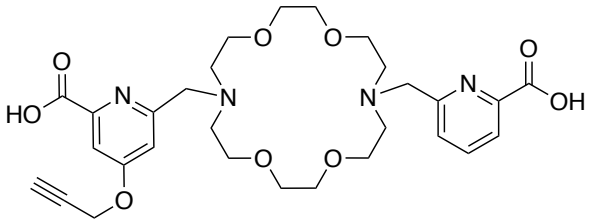

4-(prop-2-yn-1-yloxy)-6-((16-((6-carboxypyridin-2-yl)methyl)-1,4,10,13-tetraoxa-7,16-diazacyclooctadecan-7-yl)methyl)picolinic acid was synthesised using an adapted literature

protocol.[191] To a solution of **9** (18.5 mg, 0.03 mmol) in DCM (450 µL), was added a suspension of NaOH in methanol (50 µL, 3 M), so the final concentration of NaOH was 0.3 M and the final DCM:MeOH ratio was 9:1. The reaction mixture was stirred at room temperature for 1 hour, the reaction mixture was neutralised and the solvent was removed under reduced pressure. R_t = 8.54 mins (method A, column A). ESI-MS $[M+2H]^+$: 294.1393 calculated for $(C_{29}H_{40}N_4O_9)^{2+}$: 294.1393.

2.10.14 $N_3(OEG)_3SqOEt$ (16)

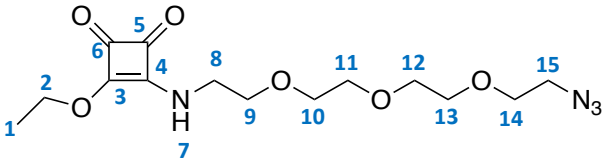

Freshly prepared diethyl squarate (0.23g, 1.32 mmol) was dissolved in ethanol (4 mL) before adding 1-Amino-11-azido-3,6,9-trioxaundecane (0.28g, 1.29 mmol) and DIPEA (1 eq) under nitrogen. The mixture was stirred at room temperature for 8 hours; then the colourless solution was taken to dryness under reduced pressure and purified *via* semi-preparative HPLC (method C). Fractions were combined and lyophilised to yield a colourless oil (209 mg, 49%). ESI-MS $[M+H]^+$: 343.1613 calculated for $(C_{14}H_{23}N_4O_6)^+$: 343.1612 R_t = 7.33 mins (method A, column B). ^{1}H-NMR (500 MHz; DMSO-d_6): δ 8.80 (s, 0.5 H, 7a), 8.63 (s, 0.5 H,7b), 4.66 (dd, *J* = 6.8, 4.6 Hz, 2H, 2), 3.63 (d, *J* = 5.4 Hz, 1H, 8b), 3.59 (t, *J* = 4.8 Hz, 2H, 9), 3.53 (t, *J* = 8.6 Hz, 10H, 10-14), 3.44 (d, *J* = 5.4 Hz, 1H, 8a), 3.39 (t, *J* = 4.9 Hz, 2H, 15), 1.37 (t, *J* = 7.1 Hz, 3H, 1). ^{13}C NMR (126 MHz; DMSO-d_6): δ 189.31 (5b), 189.16(5a), 182.20(6a), 182.04 (6b), 176.9 (3b), 176.6 (3a), 173.0 (4a), 172.5 (4b), 69.82, 69.78, 69.74, 69.69, 69.61, 69.25, 69.21, 68.79 (9-14), 68.74 (2), 50.0 (15), 43.7 (8a), 43.3(8b), 15.6 (1).

2.10.15 H_2MacropaSqOEt (17)

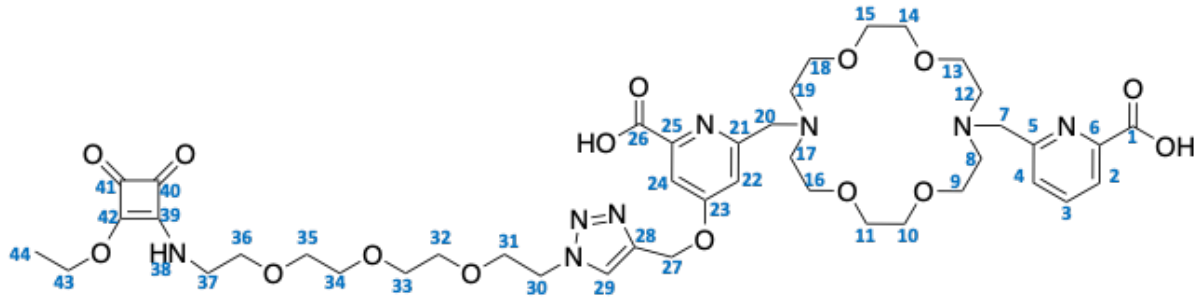

$CuSO_4$ (0.22 mg, 0.0014 mmol, 8% mmol) and Sodium Ascorbate (0.64 mg, 0.0032 mmol, 18% mmol) were combined and shaken for 2 minutes to ensure complete reduction to copper (I) species. TBTA (2.8 mg, 0.0057 mmol, 32% mmol in DMF) was added as a stabilising ligand with $N_3(OEG)_3$SqOEt (6.42 mg, 0.016 mmol) and reacted for 10 minutes. **13** (11 mg, 0.018 mmol) was added, and the reaction mixture was purged for 15 minutes with a stream of nitrogen to reduce the oxygen content in the reaction mixture. The reaction was monitored by RP-HPLC to ensure complete removal of azide species (280 nm). Na_2EDTA was added to the reaction species to remove the catalytic copper. The pale green solution was taken to dryness under reduced pressure and dried *in vacuo*. The resulting precipitate was purified *via* semi-preparative HPLC (method D), and fractions were combined and lyophilised to yield an off-white powder (5 mg, 40 %). ESI-MS $[M+2H]^{2+}$: 465.2161 calculated for $(C_{43}H_{62}N_8O_{15})^{2+}$: 465.2162. Rt = 10.07 mins (method A, column A). ^{1}H NMR (500 MHz, D_2O) δ 8.24 (d, J = 2.3 Hz, 1H, 29), 8.10 (t, J = 7.8 Hz, 1H, 3), 8.04 (s, 1H,4), 7.75 (d, J = 7.8 Hz, 1H, 2), 7.67 (d, J = 9.0 Hz, 1H, 24), 7.42 (d, J = 2.2 Hz, 1H, 22), 5.41 (s, 2H, 27), 4.74 (s, 2H, 7), 4.63 (m, 4H, 43, 20), 3.98 (d, J = 4.9 Hz, 2H, 31), 3.94 (t, J = 4.8 Hz, 8H, 9, 13, 16, 18), 3.72 (t, J = 5.0 Hz, 2H, 30), 3.69 (s, 8H, 10, 11, 14, 15), 3.64 (dq, J = 15.1, 5.0 Hz, 16H, 32, 33, 34, 35, 8, 12, 17, 19), 3.59 – 3.52 (m, 4H, 36, 37), 1.37 (q, J = 7.4 Hz, 3H, 44). ^{13}C NMR (126 MHz, D_2O) δ 191.20 (41), 185.60 (40), 179.69 (42), 179.47 (42), 176.04 (39), 175.99 (39) 169.48 (1, 23), 168.73 (26), 165.81 – 164.96, (q, TFA), 153.90 (25), 153.85 (25), 152.35 (6), 150.78 (21),

148.92 (5), 144.34 (28), 142.60 (3), 130.59 (2), 128.55 (29), 128.53 (29), 127.75 (4), 116.77 (22), 122.29 – 115.32 (q, TFA), 114.88 (24), 114.80 (24), 73.08 (43), 73.02 (43), 72.39 (10, 11, 14, 15), 72.22, 72.11, 72.01, 71.85 (m, 32, 33, 34, 35, 36), 71.15 (31), 66.39 (9, 13, 16, 18), 64.34 (27), 59.82 (7), 59.69, (20) 57.20 (17, 19 or 8, 12), 57.13 (17, 19 or 8, 12), 52.72 (30), 46.47 (37), 46.33 (37), 17.51 (44), 17.46 (44).

2.10.16 Compound 18

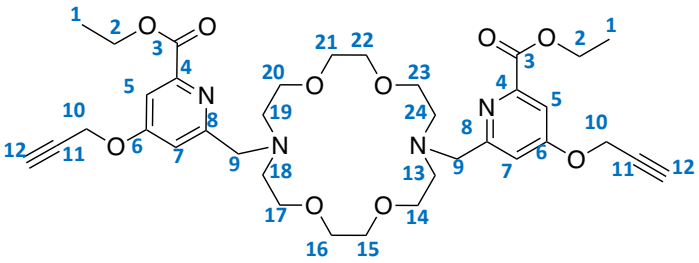

To a solution of 1,7,10,16-tetraoxa-4,13-diazacyclooctadecane (50 mg, 0.19 mmol) and DIPEA (66 µL, 0.38 mmol) in CH_3CN (2 mL) was added **9** (100 mg, 0.4 mmol). The reaction mixture was heated at 85 °C for 1 hour with microwave radiation. The solvent was removed under reduced pressure to yield an off-white powder. The resulting precipitate was purified *via* semi-preparative HPLC (method D), and fractions were combined and lyophilised to yield an off-white powder (97 mg, 75 %). R_t = 12.35 min (method A, column B) ESI-MS $[M+2H]^{2+}$: 349.1767 calculated for $(C_{36}H_{50}N_4O_{10})^{2+}$: 349.1759. ^{1}H NMR (500 MHz, $CDCl_3$) δ 7.54 (d, *J* = 2.5 Hz, 2H, 5), 7.50 (d, *J* = 2.6 Hz, 2H, 7), 4.79 (d, *J* = 2.4 Hz, 4H, 10), 4.44 (q, *J* = 7.1 Hz, 4H, 2), 3.95 (s, 4H, 9), 3.65 (t, *J* = 5.5 Hz, 8H, 14, 17, 20, 23), 3.60 (s, 8H, 15, 16, 21, 22), 2.90 (s, 8H, 13, 18, 19, 24), 2.60 (t, *J* = 2.3 Hz, 2H, 12), 1.40 (t, *J* = 7.1 Hz, 6H, 1). ^{13}C NMR (126 MHz, $CDCl_3$) δ 165.15 (3), 149.17 (6), 148.22 (4), 138.40 (8), 111.91 (7), 110.91 (5), 77.14 (11), 76.80 (12), 70.74 (14, 17, 20, 23), 61.98 (15, 16, 21, 22), 61.04 (2), 55.95 (10), 54.40 (13, 18, 19, 24), 14.30 (1).

2.10.17 Compound 19

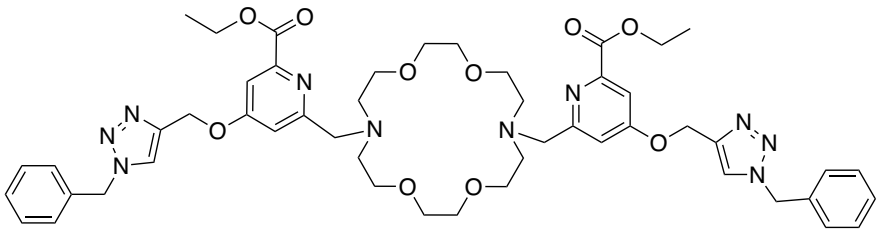

Sodium Ascorbate (17 mg, 0.086 mmol, 77 µL in H_2O) and $CuSO_4$ (2 mg, 0.008 mmol, 28 µL in H_2O) were combined and allowed time for the copper(II) to reduce to copper(I). NaN_3 (6 mg, 0.086 mmol, 24 µL in H_2O), benzyl bromide (12 µL, 0.09 mmol), and Na_2CO_3 (19 mg 0.18 mmol) was added to the reaction mixture and stirred for 0.5 hours to form the azide *in situ*. Then **18** (30mg, in 200µL DMF) was added to the reaction mixture and heated to 37°C for 1 hour. Na_2S (3 mg, 0.038 mmol) was added to precipitate the copper species, which formed a black precipitate and was removed *via* centrifugation. Ice cold water (6 mL) was added to the supernatant to precipitate the product, washed (5 mL x 1) then dilute NH_4OH (ATTENTION: this step is important, as copper azides are explosive when dry, and their traces should be removed before the product is dried), then dried in vacuo and used without further purification. ESI-MS $[M+2H]^{2+}$: 482.2407 calculated for $(C_{50}H_{64}N_{10}O_{10})^{2+}$: 482.2398.

2.10.18 Compound 20

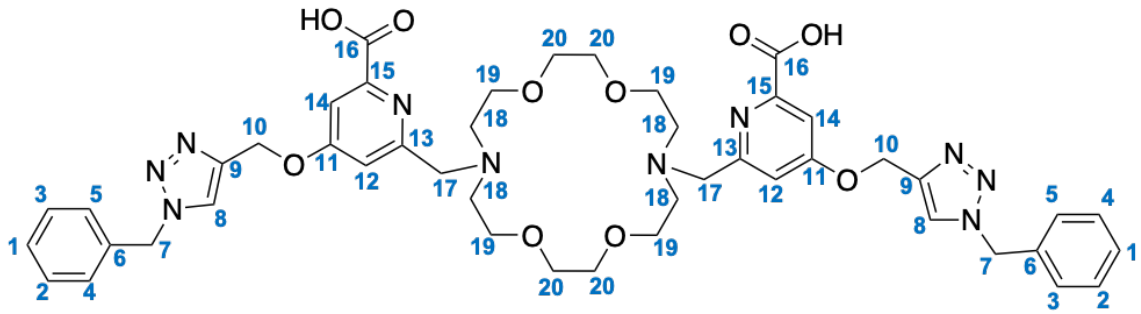

To a solution of **18** (20 mg 0.021 mmol) in DCM (450 µL), was added a suspension of NaOH in methanol (50 µL, 3 M), so the final concentration of NaOH was 0.3 M and the final DCM:MeOH ratio was 9:1. The reaction mixture was stirred at room temperature for 1 hour,

the NaOH was neutralised, and the solvent was removed under reduced pressure. The crude mixture was purified *via* semi-preparative HPLC (method E) to yield a white powder (13 mg, 69 %). R_t = 9.35 min (column B, method B). ESI-MS $[M+H]^+$: 907.4095, $[M+2H]^{2+}$: 454.2085 calculated for $(C_{46}H_{55}N_{10}O_{10})^+$: 907.4097, $(C_{46}H_{56}N_{10}O_{10})^{2+}$: 454.2085. ^{1}H NMR (500 MHz, MeOD) δ 8.16 (s, 2H, 8), 7.72 (d, *J* = 2.3 Hz, 2H, 12), 7.38 – 7.30 (m, 12H, 1-5, 14), 5.61 (s, 4H, 7), 5.38 (s, 4H, 10), 4.58 (s, 4H, 17), 3.81 (t, *J* = 4.8 Hz, 8H, 19), 3.54 (s, 8H, 20), 3.43 (t, *J* = 4.9 Hz, 8H, 18). ^{13}C NMR (126 MHz, MeOD) δ 167.70 (11), 166.77 (16), 153.11 (13), 142.26 (15), 135.37 (6), 128.02 (1-5), 127.78 (9), 124.28 (8), 111.67 (14) , 110.74 (12) , 69.65 (20), 65.92 (19) 61.71 (10) 57.04 (17) 54.71 (18) 53.31 (7)

2.10.19 [La(MacropaTz$_2$Bn$_2$)]CO$_3$ (21)

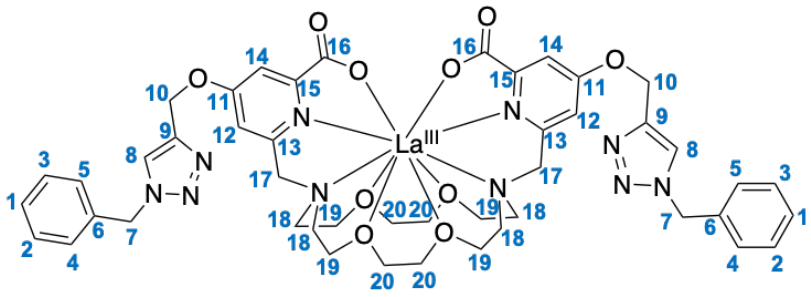

To a solution of ***20*** (13mg, 0.0143 mmol) in CH_3OH (300 µL) was added $La_2(CO_3)_3.xH_2O$ (3.3 mg, 0.007 mmol) in H_2O (300 µL) and the reaction was heated to 37°C overnight. Upon concentration of the reaction mixture to remove CH_3OH, a white precipitate formed and was collected, and washed with cold H_2O (3 x 1 mL) to give a colourless powder. ESI-MS $[M]^+$: 1043.2932, $[M+H]^{2+}$: 522.1509 calculated for $(C_{46}H_{52}LaN_{10}O_{10})^+$: 1043.2931, calculated for $(C_{46}H_{53}LaN_{10}O_{10})^{2+}$: 522.1500 ^{1}H NMR (500 MHz, MeOD) δ 8.27 (s, 2H, 8), 7.84 (d, *J* = 2.3 Hz, 2H, 12), 7.62 (d, *J* = 2.4 Hz, 2H, 14), 7.42 – 7.35 (m, 10H, 1-5), 5.67 (s, 4H, 7), 5.46 (s, 4H, 10), 4.81 (s, 4H, 17), 3.97 (t, *J* = 4.9 Hz, 8H, 19), 3.68 (d, *J* = 4.0 Hz, 16H, 18, 20). ^{13}C NMR (126 MHz, MeOD) δ 167.46 (11), 165.02 (16), 151.72 (13), 148.70 (15), 141.87 (9), 135.05 (6), 128.71 (4, 5), 128.37 (1), 127.88 (2, 3), 124.99 (8), 113.75 (14), 112.66 (12), 70.01 (20), 64.55 (19), 61.75 (10), 57.15 (17), 54.17 (18), 53.87 (7).

2.10.20 [La(HMacropa)(H_2O)].(CF_3SO_3)$_2$.

H_2Macropa was prepared according to a literature procedure[159] or obtained as a product in the one-pot synthesis of ***12.*** To an aqueous solution of H_2Macropa (11.8 mg, 0.022 mmol) was added lanthanum(III)tris(trifluoromethanesulfonate) (13 mg, 0.022 mmol) and the reaction was stirred at room temperature until a precipitate formed and was collected yielding a colourless powder. R_t = 9.1 minutes (method B, column B). ESI-MS $[M]^{2+}$: 335.0754 calculated for $(C_{26}H_{35}LaN_4O_8)^{2+}$: 335.0754, $[M]^{+}$: 669.1437 calculated for $(C_{26}H_{34}LaN_4O_8)^{+}$: 669.1440. Crystals of [La(HMacropa)(H_2O)]·(TFA) suitable for X-ray crystallography were grown *via* vapour diffusion of THF into an aqueous solution of the complex.

3 The Bifunctional Ligand, H_2MacropaSqOEt, is Easily Conjugated to Monoclonal Antibodies

3.1 Targeting Carbonic Anhydrase IX

Carbonic anhydrases (CA) are a family of enzymes responsible for the catalysis of the reversible hydration of carbon dioxide to produce protons and bicarbonate anions, according to the equation:

$$H_2O + CO_2 \rightleftharpoons H^+ + HCO_3^-$$

Fifteen isoforms of CA exist and are named CA I – CA XV. Carbonic anhydrases differ widely in their cellular localization: CA I, II, III, VII and XIII reside in the cytosol, CA IV, IX, XII and XIV are associated with the cell membrane.[192] All isoforms of CA rely on a zinc(II) active site. The four-coordinate zinc(II) is tetrahedral, with three conserved histidine residues bound to the zinc(II) and one H_2O molecule or a $^-$OH ligand. CAIX expression is induced in response to low oxygen levels and is upregulated in hypoxic environments. Therefore, it is an important process in solid tumour acidification and is correlated to a hypoxic phenotype.[193] CAIX is postulated to play a role in the bicarbonate transport metabolon acting in tumour cells. The expression of CAIX is essential in the growth of solid tumours and is responsible for converting CO_2 from the cytoplasm of hypoxic cells into bicarbonate anions and protons. Protons remain outside of the cell and contribute to extracellular acidification. Bicarbonate ions are taken into bicarbonate transporters (BT) and transported to the cytoplasm, where they are converted to CO_2 in a reaction that consumes intracellular protons. This leads to the neutralization of intracellular pH (Figure 44).[194-197]

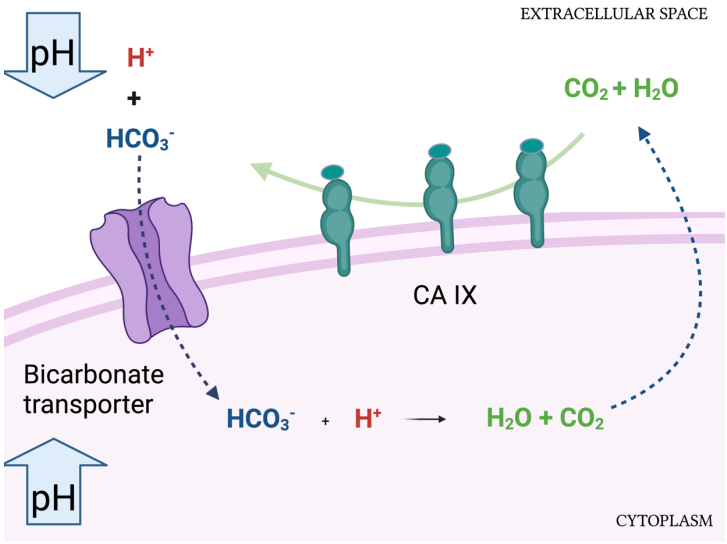

Figure 44: An illustration of the proposed role of CAIX in the acidification of the extracellular space. Adapted from Pastorekova[194] and created with BioRender.com.

Several tumours, such as clear cell renal cell carcinoma, glioblastoma, triple-negative breast cancer, ovarian cancer and colorectal cancer, overexpress carbonic anhydrase isoform IX on the tumour surface/ cell membranes.[198] In contrast, CAIX is not expressed in the normal proximal tubular epithelium. There are low levels of endogenous expression localised in the bile duct epithelium of the gastrointestinal tract and the mucus cells of the stomach.[199] The sequencing and characterisation of the CAIX gene showed that it encodes for a signal peptide region (which is removed during protein maturation), N-terminal proteoglycan-related domain (PG), which is only present in the isoform IX, a highly conserved CA catalytic site, a transmembrane anchor (TM) and an intracytoplasmic portion (IC).[200]

CAIX possesses an intramolecular proton shuttle that facilitates the rapid exchange of protons between the catalytic centre and the surrounding bulk solution. Among the CA family, CAIX is the only member that features a proteoglycan-like (PG) domain. It is 59 amino acid residues long and consists of 18 glutamate and eight aspartate residues, which serve as an intramolecular proton buffer.[201] This buffer is crucial for supporting CAIX's catalytic activity in an acidic environment.[202]

Typically, the most aggressive and invasive tumour cells rely on glycolysis to meet their high energy requirements.[203] Increased glucose consumption due to upregulated glycolysis is a nearly universal attribute of primary and metastatic cancers. This underpins the utility of [^{18}F]fluorodeoxyglucose PET, which relies on this principle to observe increased cellular uptake of glucose as a radiological marker of cancer cell metabolism.[204] As a result, highly glycolytic tumour cells produce large amounts of lactate and protons *via* monocarboxylate transporters (MCT). This further increases extracellular acidification. Protons must be removed from the cell to prevent acidosis. The PG domain of CAIX may serve as a 'proton antenna' to facilitate MCT transport activity.[205-208]. High cell density within tumour tissues combined with inadequate vascularisation cause a hypoxic cellular environment. This, in turn increases glycolytic activity.

Crystals of 2.2 Å resolution have been obtained for the catalytic domain of CAIX both with and without the known inhibitor, Acetazolamide (AZM).[209] The crystal structure shows the zinc active site at the bottom of a large cone-shaped cavity where the site is surrounded by both hydrophobic and hydrophilic pockets (Figure 45, a). CAIX is reported to exist as a homodimer, and the formation of a disulphide bond at Cys-41 facilitates dimerisation.[210, 211] Even with mutation of the Cys-41 to a Ser residue, crystallographic data shows the protein still exists in its dimeric form (Figure 45). Both active sites of the dimer are clearly exposed to the extracellular medium and allow for the efficient hydration of CO_2.[211]

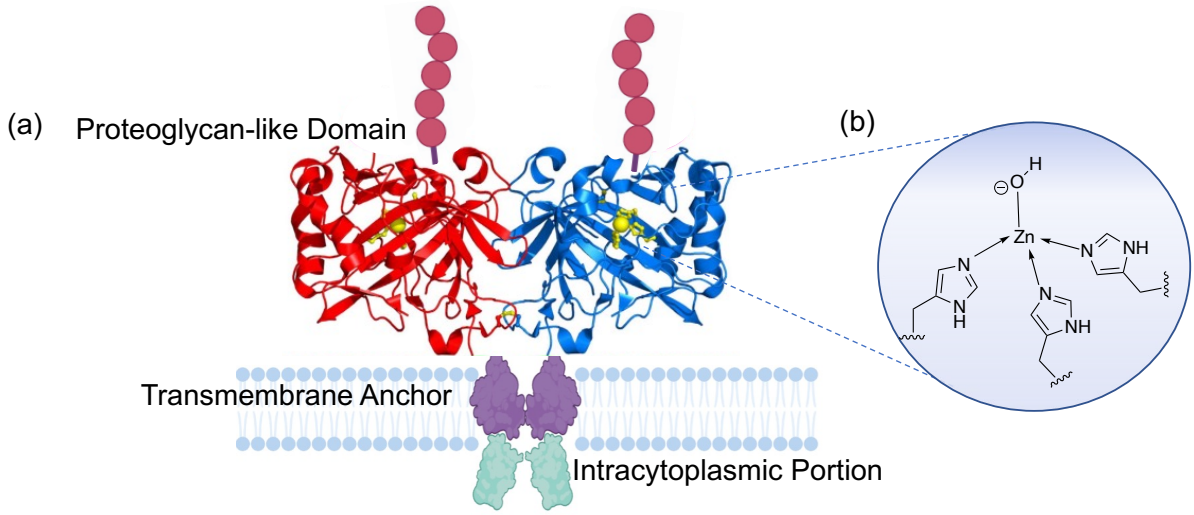

Figure 45: (a) The proposed structure of the arrangement of CAIX dimer on the cell membrane adapted from De Simone[211] and (b) the tetrahedral zinc active site of CAIX.

3.2 Girentuximab: A Monoclonal Antibody that Selectively Binds to Carbonic Anhydrase IX to Treat Renal Cell Carcinoma

3.2.1 Renal Cell Carcinoma

Renal cell carcinoma (RCC), a type of genitourinary cancer, represents 2 – 3% of adult cancers and is responsible for 80 – 90% of renal malignancies. Renal cell carcinoma originates in the proximal tubular epithelium[212] and has the highest mortality rate among such cancers.[213, 214] Clear cell carcinoma (ccRCC) is the most common histological subtype and accounts for 80 – 90% of cases. It is characterised by the abundant clear cytoplasm due to the presence of intracytoplasmic glycogen.[215] One-third of renal cell carcinoma (RCC) patients present with de novo metastatic disease, whilst over 30% with initially localised disease will develop metastatic progression. In the case of metastatic disease present (mRCC), the prognosis and rates of long-term survival are poor.[214, 216]

The inactivation of the Von Hippel-Lindau (VHL) gene is indicated in the pathogenesis of ccRCC.[217] Hereditary ccRCC contains bi-allelic mutations in the VHL gene on chromosome 3p and has also been shown in sporadic RCC. The VHL protein is part of a ubiquitin ligase, a protein complex responsible for the ubiquitination of specific substrates, thus promoting

proteasome degradation.[218, 219] The transcription factor hypoxia-inducible transcription factor 1α (HIF1α) is the substrate for VHL ubiquitin ligase. HIF1α binds VHL in normoxic environments. HIF1α is hydroxylated, which causes its consequent ubiquitination and the degradation of the protein.[220, 221] In hypoxic cells, the hydroxylation of HIF1α does not occur, and instead, HIF1α accumulates in hypoxic cells, switching on genes such as vascular endothelial growth factor and glucose transporters, both of which cause the downstream effects of many angiogenic growth factors and changes in the cellular environment.[222-224]

The incidence of RCC has increased at a rate of 2% per year over the last 65 years.[225] Over 270,000 new cases of kidney cancer are diagnosed annually, and globally 116,000 people die from the disease.[213] Therefore, a way to effectively target RCC for appropriate treatment of the disease is needed.

3.2.2 Targeting Cancer with Monoclonal Antibodies

Antibodies (also known as immunoglobulins) are proteins that range in molecular weight from 150 to 1000 kDa, and are produced by B-lymphocytes to recognise a unique molecule, known as an antigen, *via* the fragment of antigen binding region (also known as the complementary determining region; CDR).[226] Antibodies are characterised by incredible variability and diversity in binding foreign molecules of interest. The order of 10^{12} possible combinations includes but is not limited to proteins, receptors, lipids and small organic molecules.[227] Upon antigen binding to the surface of a B-cell, it stimulates the proliferation and maturation of millions of unique antibody clones. Each B-lymphocyte is monospecific, yet collectively can recognise and bind an almost infinite number of antigens.[226]

Antibodies consist of two heavy chain (H) and two light (L) chain molecules linked *via* disulphide bonds (Figure 46, a, b). The light and heavy chains comprise constant (C_L, C_{H1}, C_{H2}, C_{H3}) and variable (V_L, H_L) regions. The incredible affinity and specificity of antibodies to bind a target is determined from six 'hypervariable' CDR regions on the V_L, H_L domains that contain

high levels of sequence variability resulting in the ability to target an almost infinite number of antigens.[228] Antibody engineering using recombinant DNA technology makes it possible to target specific antigens present as receptors on the surface of cancer cells.

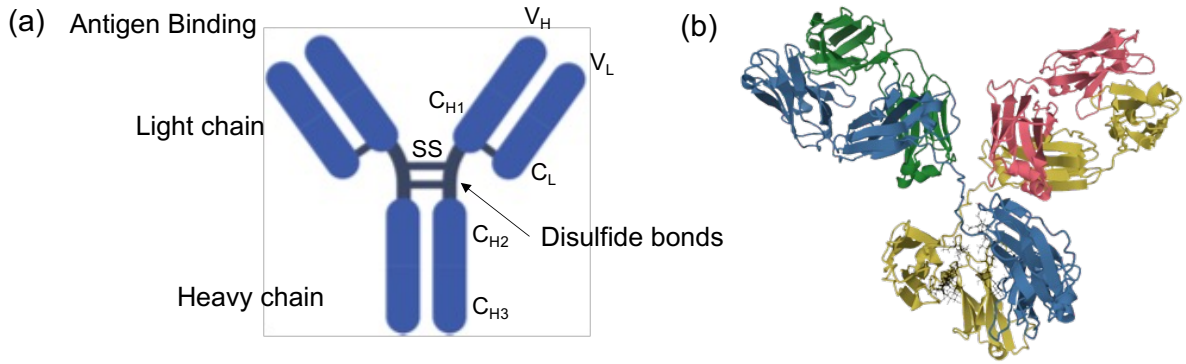

Figure 46: (a) A schematic illustration of an antibody and (b) a crystal structure of an antibody.[227]

Antibodies have a long circulation time *in vivo*. This is partly due to the neonatal FcRn receptor, which plays an important role in protecting the antibody from rapid intracellular catabolism. In the context of antibodies, catabolism can lead to their destruction and removal from the body. Therefore, the role of the FcRn receptor in preventing catabolism is crucial for the effective functioning of antibodies in the immune system.[229, 230]

The FcRn protein selectively binds to the IgG region of antibodies, with the strength of the interaction being contingent on the pH of the surrounding milieu. The highest affinity is observed at a pH range of 6.0 – 6.5, which corresponds to the acidic conditions present in early endocytic vesicles. Conversely, the binding affinity decreases at a neutral pH range of 7.0 – 7.5. Remarkably, the IgG-FcRn complex is safeguarded from intracellular degradation and is transported back to the cell membrane, where the neutral pH conditions trigger the dissociation of the antibody and its subsequent release into circulation. This recycling mechanism is believed to underlie the extended half-life of certain antibodies, which can persist for 11 – 30 days in the human body.[231]

3.2.3 Girentuximab, a Monoclonal Antibody that Binds CAIX

A monoclonal antibody, G250, was raised against human renal cell carcinoma. The RCC-associated antigen was shown to be the same as the carcinoma-associated antigen CAIX.[232, 233] Immunohistochemical analysis demonstrated that greater than 75% of primary and metastatic renal cell carcinomas express the CAIX protein,[234] and CAIX is over-expressed in 94% of clear cell RCC tumours due to the mutational loss of VHL protein.[233, 235, 236] G250, also known as Girentuximab, was developed for cancer immunotherapy by the German biotechnology company Wilex to target CAIX.

Historically, G250 was first developed as a murine antibody, after which the chimeric form cG250, which was derived from the murine variable region of G250 (Rencarex: 68% human, 32% murine) was developed. cG250 binds to the extracellular proteoglycan (PG)-like domain (Figure 45). This is unique to carbonic anhydrase isoform IX and was able to induce natural killer cells to kill tumour cells *in vitro* due to antibody-dependent cellular cytotoxicity.[237] cG250 was fully humanised to reduce the risk of adverse immune reactions. In a final iteration, the humanised antibody was modified so that the biodistribution of the antibody changed. This is presumably due to changes in the Fc region of the antibody.

Girentuximab has been investigated in multiple clinical trials over the past twenty years, first for immunotherapy, as well as in combinatorial therapy and radioimmunotherapy.[238-242] A landmark phase III clinical trial probed the efficacy of the chimeric monoclonal antibody Girentuximab (Rencarex). The randomised, controlled clinical trial was conducted in patients with non-metastatic RCC who had undergone surgery (NCT00087022). cG250 failed to meet its primary endpoint. Although it did not show clinical benefit in the adjuvant treatment for all high-risk patients, cG250-treated patients that had a high CAIX score appeared to have a significantly improved disease-free survival. It was

indicated that the CAIX score could stratify patients who may benefit from cG250 adjuvant therapy.[243, 244]

In the last decade, the therapeutic radionuclide lutetium-177 has also been investigated for targeted radioimmunotherapy.[242, 245] The chimeric radioimmunoconjugate [^{177}Lu]Lu(DOTA-cG250) demonstrated a promising response in patients with progressive metastatic ccRCC. Unfortunately, the clinical implementation of this treatment has been hindered so far due to extensive bone marrow depletion and, consequently, myelotoxicity.[240]

In addition to immunotherapy, cG250 has been investigated as a diagnostic imaging agent. Using monoclonal antibodies as the targeting vector requires the incorporation of radionuclides with relatively long half-lives, such as zirconium-89 ($t_{1/2}$ = 72 hours).[219, 246-249] Most recently, the Australian biotechnology company, Telix acquired the exclusive rights for the development and commercialisation of diagnostic and therapeutic radionuclide conjugates of Girentuximab. This has led to the development of another variant of the humanised Girentuximab with a different biodistribution.

A phase I study evaluated the safety and tolerability of [^{89}Zr]Zr(DFO-G250) (37 MBq) in 10 patients with suspected ccRCC. Investigation of the radiotracer *via* PET/CT was monitored over 168 hours, with one patient's lesions visible after only 0.5 hours post-injection. There was negligible uptake in tumours that were histologically confirmed to be ccRCC negative, illustrating a high specificity (Figure 47). Following these promising results, a phase III kidney cancer imaging study (NCT03849118) in patients with ccRCC, demonstrated a high degree of consistency with very high sensitivity and specificity overall.[239]

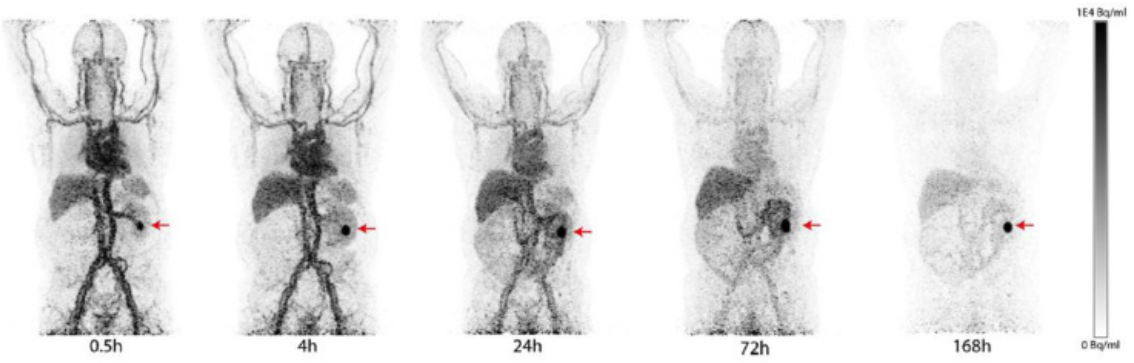

Figure 47: Maximum intensity projection of patient with a ccRCC tumour localised in the left kidney (red arrow). The tumour is visible from 0.5 h post-injection, and the tumour-to-background ratio increases up to 168 hours.[239]

Recently, the efficacy of CAIX-directed radiotherapy with the humanised Girentuximab (hG250) was investigated in preclinical mouse models.[250] [^{177}Lu]Lu^{III} and [^{225}Ac]Ac^{III}-labelled conjugates were studied in a murine xenograft model with high CAIX expression to compare the efficacy of alpha radionuclide therapy with [^{225}Ac]Ac^{III} to traditional beta therapy with [^{177}Lu]Lu^{III}. This work provides evidence that TAT may be a viable and effective treatment option for RCC that is confirmed to be CAIX positive. Treatment of mice bearing SKRC-52 tumour xenografts with [^{225}Ac]Ac(DOTA-hG250) (15 – 25 kBq activity) significantly prolonged survival. Of note, non-tumour-bearing mice that received [^{225}Ac]Ac(DOTA-hG250) exhibited weight loss and nephrotoxicity as a result of treatment with [^{225}Ac]Ac^{III}, highlighting the fine line between clinical benefit and significant off-target toxicity.

3.2.4 Targeted Alpha Therapy Can Overcome the Radioresistance Observed in Hypoxic Tumours

Hypoxic tumours, which are characterised by insufficient oxygen supply relative to tumour size, present a formidable challenge to cancer treatments due to their inherent resistance to radiation and chemotherapy. Indeed, tumour hypoxia is hypothesised to be mechanistically linked to poorer treatment response and prognosis. The hypoxic tumour microenvironment induces dysfunctional vascularisation and angiogenesis and can lead to the phenotypic characteristics of the epithelial-to-mesenchymal transition with acquisition of abnormal tumour

cell mobility, which enables locally invasive tumour growth, as well as increased metastatic potential. Therapeutic resistance is postulated to be pathogenically linked to altered cancer cell metabolism caused by hypoxia, with stimulation of a complex cellular signalling network involving the HIFα, PI3K, MAPK, and NFκB pathways. The upshot of hypoxic tumour cell metabolism may be induction of cell quiescence and thus resistance to traditional cancer treatment mechanisms which target vulnerabilities of cells with a high rate of proliferation. All of these processes taken together are central to the occurrence of tumour radioresistance and present significant challenges in the treatment of cancer.[251]

The emissions from β particles more frequently cause single-strand breaks in tumour DNA and rely on the crossfire effect of the emissions to damage DNA. In a hypoxic tumour microenvironment, low levels of oxygen can mean that the indirect effects of ionising radiation are less pronounced, as reactive oxygen species are not formed. This reduces the cytotoxicity of using radioimmunotherapy with β-emitting radionuclides. This is typified in the phase II results of using [^{177}Lu]Lu(DOTA-cG250) for the treatment of metastatic ccRCC, where the high radioactive doses required to necessitate a therapeutic effect caused too significant off-target toxicity.[240] This is likely due to the decreased efficacy of β-therapy in characteristically hypoxic tumours.

By contrast, the high LET (~80 keV / μm) delivered to tumour cells by α-emitting radionuclides may enhance the cytotoxic effect of these immunoconjugates. Radionuclides that emit α particles can target hypoxic environments independently of oxygen levels in solid tumours, and it has been demonstrated that as few as two α particles must traverse a cell nucleus to induce lethal lesions.[252] Therefore, our strategy involved specifically targeting the receptor CAIX with [^{225}Ac]Ac^{III} aiming to selectively deliver α particles to hypoxic tumour cells that are characteristically radioresistant. This is especially important as the expression of CAIX is directly regulated by HIFα, and the metalloenzyme CAIX plays an integral role in stabilising

hypoxia within the tumour microenvironment, as CAIX facilitates the adaption to low-oxygen environments. The energy of α particles is also sufficient to directly damage DNA without cellular oxygenation, so α−emitting radionuclides are more toxic to hypoxic tumours than β^--emitting radionuclides.[253] Therefore, targeting CAIX with α-emitting radioimmunoconjugates holds promise as a solution to classical radioresistant tumours as well as being able to target the direct downstream factor of HIFα. In this work, we chose to investigate the efficacy of CAIX-directed radioimmunotherapy with targeted α-therapy.

3.2.5 Chemical modification of monoclonal antibodies

In general, antibodies have over 80 lysine residues within their primary structure. More than 20 of these lysine residues are found at highly solvent-accessible sites.[254, 255] Therefore, antibody functionalisation often relies on chemical modification of the primary amine group of lysine residues to form a new amide bond.[172] These reactions are not site-specific, and the covalent modification of antibodies to attach a number of chelators of interest is based on a number of factors, such as the reaction time, temperature, concentration and the number of equivalents of the bifunctional chelator.

The number of chelators covalently bound to the antibody surface has significant implications for the immunoreactivity of the antibodies to their target antigen; it can affect how the antibody conjugates behave *in vitro*. The majority of the solvent-accessible lysine residues are in the C_{H2} domain. Excessive conjugation in this region can destabilise the antibody and may lead to aggregation.[256, 257] Retaining the solubility of these large biomolecules after the introduction of small molecular metal chelators is a challenge. Previous work in the Donnelly group showed that the chelator-to-antibody ratio (CAR) of 3 – 4:1 is optimal for *in vivo* performance.[174] Similarly, an systematic investigation of the optimal chelator ratio for immunoPET imaging with desferrioxamine (DFO)-conjugated [^{89}Zr]Zr-antibodies determined an optimal CAR 1 – 3:1 (which relies on the aqueous solubility of the ligand and impacts the

solubility of the antibody conjugate).[258] Therefore, the characterisation of these constructs and the calculation of the CAR is necessary. The CAR also impacts the overall biodistribution *in vivo*. The covalent attachment of bifunctional metal chelators to the primary amine lysine residues leads to a wide range of possible ratios at varying conjugation sites. [259]

3.3 Aims

In this chapter, we aimed to develop a straightforward and reproducible strategy for covalently attaching H_2Macropa-SqOEt onto monoclonal antibodies, with a view to evaluate the binding efficacy of Girentuximab conjugates that have been chemically modified to contain H_2Macropa-Sq. Targeted α therapy may be particularly advantageous in the treatment of hypoxic tumours. The work in chapter two (see section 2.6) focused on the motivations behind the utilisation of the squarate as a stable, aqueous solvent compatible, functional group. Herein, we highlight the advantages of using pendant squaramide ethyl esters to chemically modify antibodies through solvent accessible lysine residues (Figure 48, a).

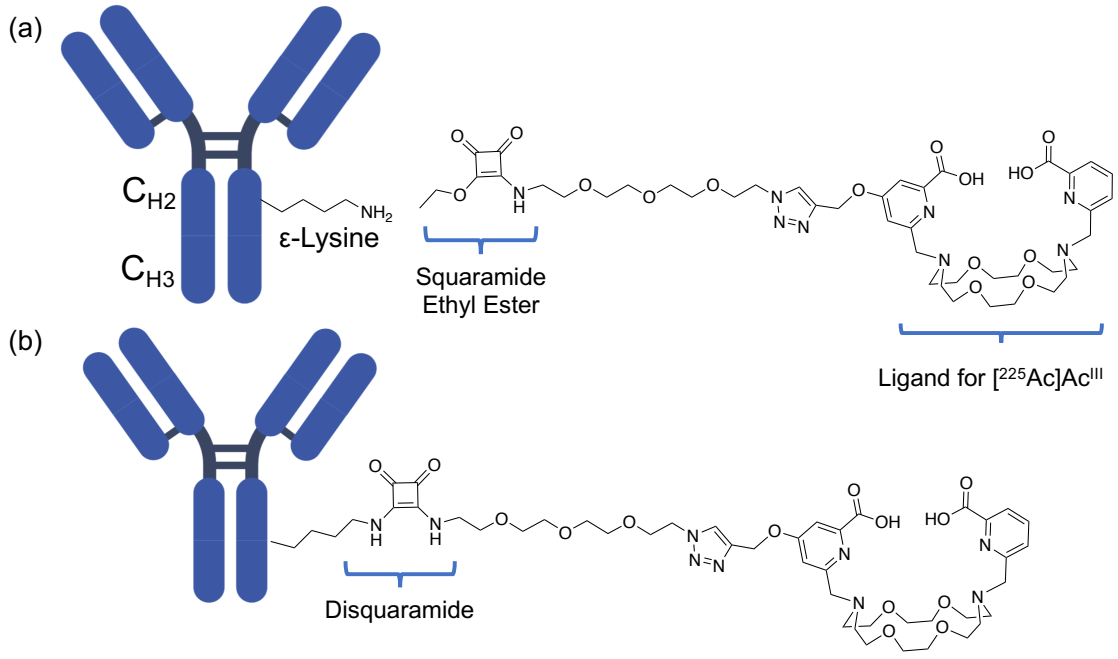

Figure 48: (a) An illustration of a monoclonal antibody (IgG) with a solvent-accessible lysine residue and H_2MacropaSqOEt; (b) after H_2MacropaSqOEt has reacted with the primary amine on lysine, forming a disquaramide.

The inclusion of a squaramide ethyl esters allows for control over the number of additions based on the antibody: ligand stoichiometry. Due to the excellent aqueous solubility of the corresponding disquaramide (Figure 48, b), it is possible to achieve a CAR 3 – 4:1, which does not cause protein aggregation and is advantageous for radiolabelling.

3.4 Results and Discussion

3.4.1 Characterising the Conjugation of H_2Macropa-SqOEt to Girentuximab by Native Protein Mass Spectrometry.

Intact native protein mass spectroscopy provides valuable information on both antibody conjugates. The deconvoluted mass spectrum of hG250 antibody (Figure 49, a) shows the antibody has a molecular weight of 147,568 Daltons. There are three peaks, presumably due to the different degrees of glycosylation on the antibody surface. There is an increase of +160 Daltons (Da), consistent with the addition of a sugar group onto the antibody surface.

The conjugation of H_2MacropaSqOEt to surface lysine residues by reaction of the pendant squaramide ethyl ester with the primary amine was achieved in borate buffer (pH 9.0). Humanised Girentuximab, hG250, and hG250-FcRn were incubated with 15 equivalents of H_2MacropaSqOEt (dissolved in dimethyl sulfoxide, DMSO, then added to borate buffer so that the DMSO < 4 %) for 4 hours, resulting in the attachment of between 1 and 8 H_2MacropaSq chelators per antibody (Figure 49, b) and a CAR of approximately 4:1. The number of additions onto the antibody surface were monitored by the change in mass between peaks of highest intensity in the deconvoluted MS each peak corresponds to a mass difference of 882 Da, which is consistent with the attachment of the ligand H_2MacropaSq onto the antibody surface through the disquaramide linkage.

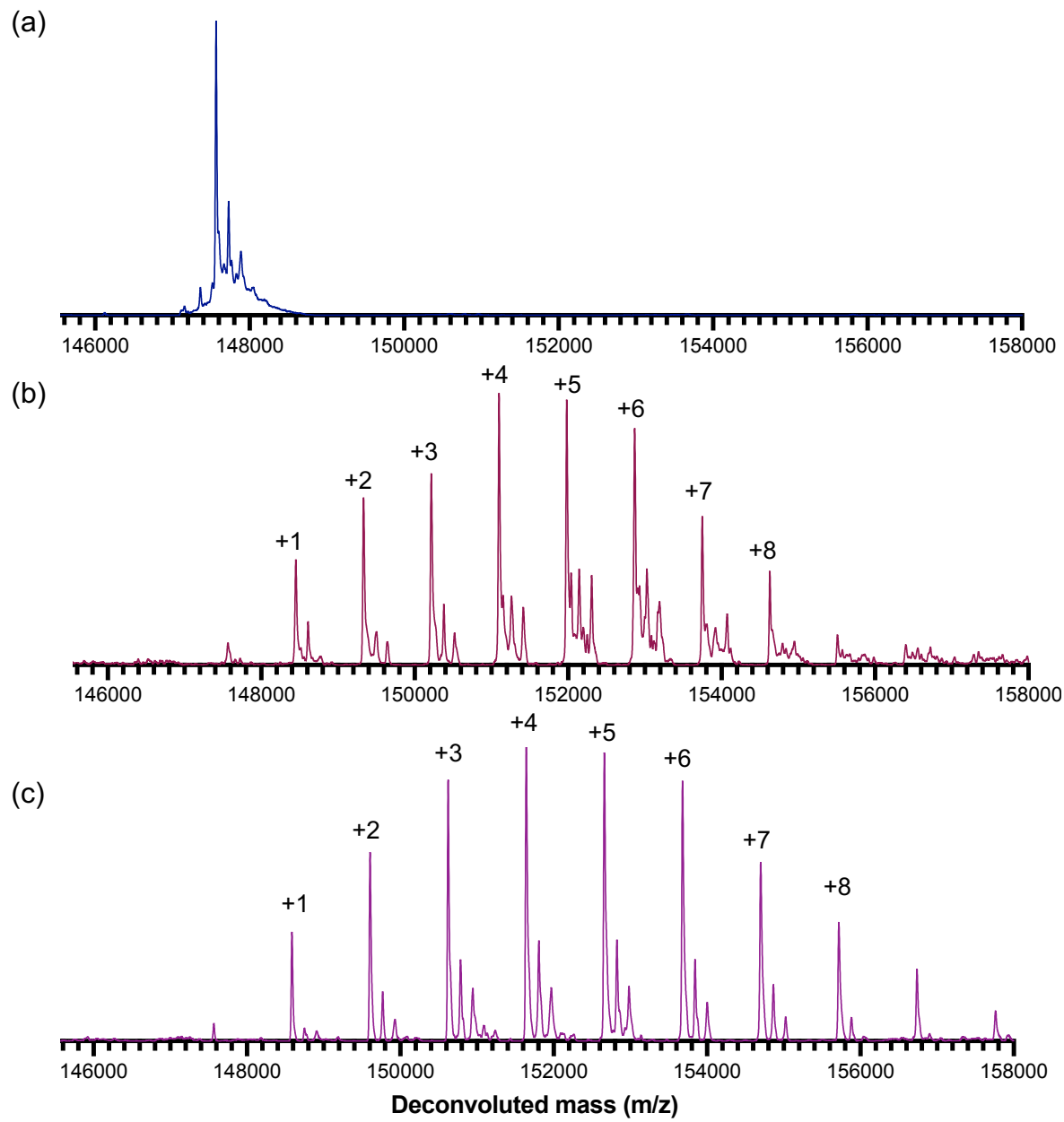

Figure 49: ESI-TOF deconvoluted mass spectra of (a) unmodified Girentuximab (hG250), (b) H_2MacropaSq-hG250 showing between 1 – 8 chelator attachments and (c) La^{III}(MacropaSq-hG250) showing between 1 – 8 chelator attachments.

Any further increase in the number of metal chelators per antibody may interfere with the antigen binding site or alter the pharmacokinetic properties of the antibody. The unreacted H_2MacropaSqOEt was removed *via* spin filtration with a size exclusion filter. This purification technique also allowed the antibody to be reconstituted in the radiolabelling buffer sodium acetate (pH 5.5). The affinity of H_2MacropaSq for large trivalent metal cations was investigated with the addition of 12 equivalents of a solution of $La_2(CO_3)_3.xH_2O$ for one hour at room

temperature (Figure 49, c). There is complete complexation of the La^{III}, evident in the change in the mass difference from 888 Da to 1020 Da. The H_2MacropaSq ligands deprotonate to give the complex that is singly charged. This is presumably why the conjugate is deconvoluted better in the mass spectrum.

Therefore, the synthesis and characterisation of the antibody conjugate with hG250-FcRn followed the same protocol. hG250-FcRn has a molecular weight of 147,418 Da (Figure 50, a). When compared to the humanised hG250, there is less glycosylation of hG250-FcRn.

The purified conjugate H_2MacropaSq-hG250-FcRn had a CAR of 4:1, and the same mass difference (888 Da) was observed between the peaks of maximum intensity (Figure 50, b), demonstrating that the bifunctional chelator H_2MacropaSqOEt was easily attached onto the surface of antibodies, even those with post-translational modifications such as hG250-FcRn. The complexation of H_2MacropaSq-hG250-FcRn with lanthanum(III) showed comparable results (Figure 50, c), thus highlighting that this conjugation strategy could be applied to any monoclonal antibody in a reproducible manner. An isotype control, H_2MacropaSq-IgG1, was synthesised under the same conditions to be used for *in vivo* and *in vitro* work.

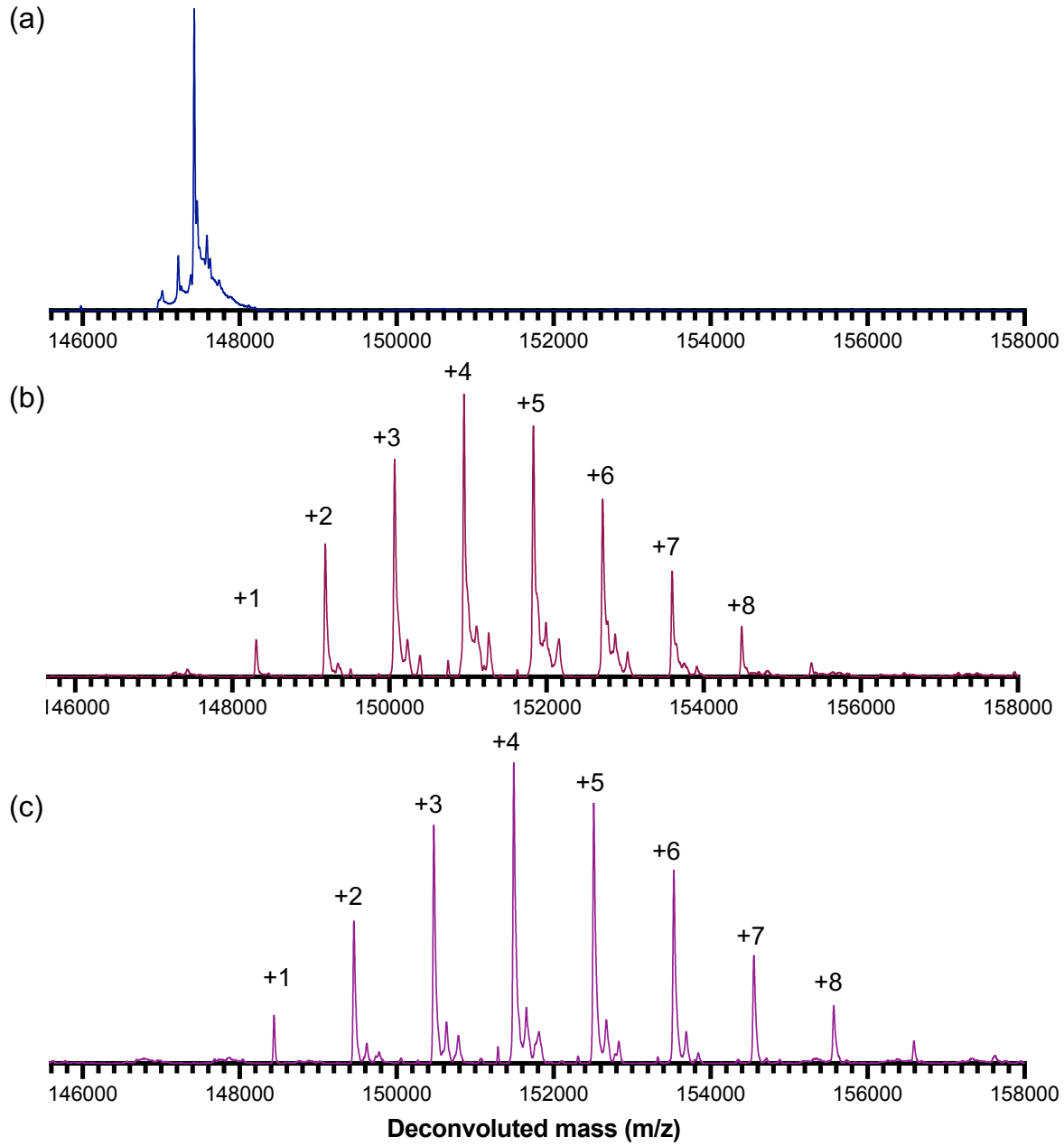

Figure 50: ESI-TOF deconvoluted mass spectra of (a) unmodified Girentuximab (hG250-FcRn), (b) H_2MacropaSq-hG250-FcRn showing between 1–8 chelator attachments and (c) La^{III}(MacropaSq-hG250-FcRn) showing between 1–8 chelator attachments.

3.4.2 The Synthesis and Characterization of H_4DOTA-NCS-hG250

H_4DOTA-pBn-SCN is commercially available (Macrocyclics) and provides bifunctional reactivity through a *para*-benzyl group of the macrocyclic backbone (Figure 51, a). The isothiocyanate group reacts with primary amines on the antibody surface (present as lysine side

chain residues) and forms thiourea bonds (Figure 51, b). Two H_4DOTA-NCS-hG250 conjugates were prepared, one with a CAR of 1:1 and one with a CAR of 3:1. (Figure 51, b).

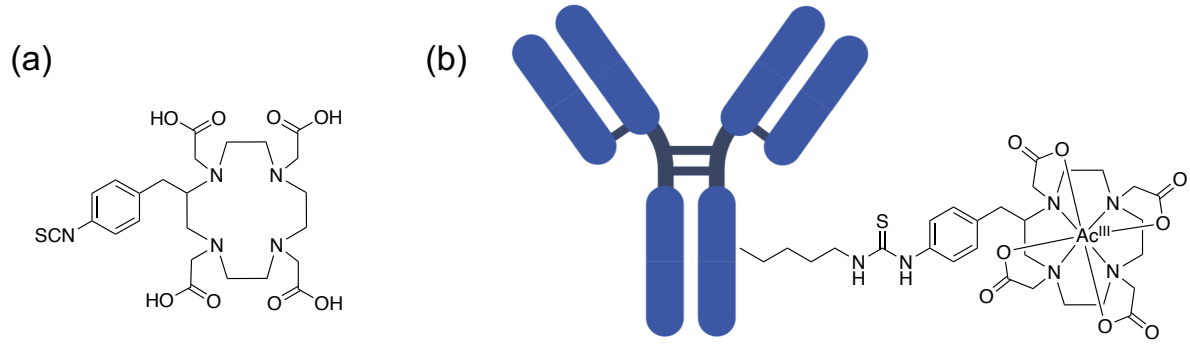

Figure 51: (a) The structure of H_4DOTA-pBn-SCN and (b) schematic of [^{225}Ac]Ac(DOTA-*p*Bn-NCS) conjugated to a monoclonal antibody via a surface lysine residue (exact coordination geometry unknown).

These conjugates were purified and characterised *via* ESI-TOF-MS (Figure 52, b, c) and SE-HPLC (Figure 53, e, f). The mass spectrum of both conjugates shows a characteristic mass difference of 588 Da between peaks of the highest intensity. Unfortunately, it was not possible to achieve a comparable CAR 4:1 for H_4DOTA-NSC-hG250, due to a poor recovery of the antibody conjugate when higher equivalents of H_4DOTA-NSC were used. This is presumably due to precipitation or aggregation of the protein. Therefore, we elected to use the H_4DOTA-NSC-hG250 conjugate with a CAR 3:1 for future radiochemical experiments.

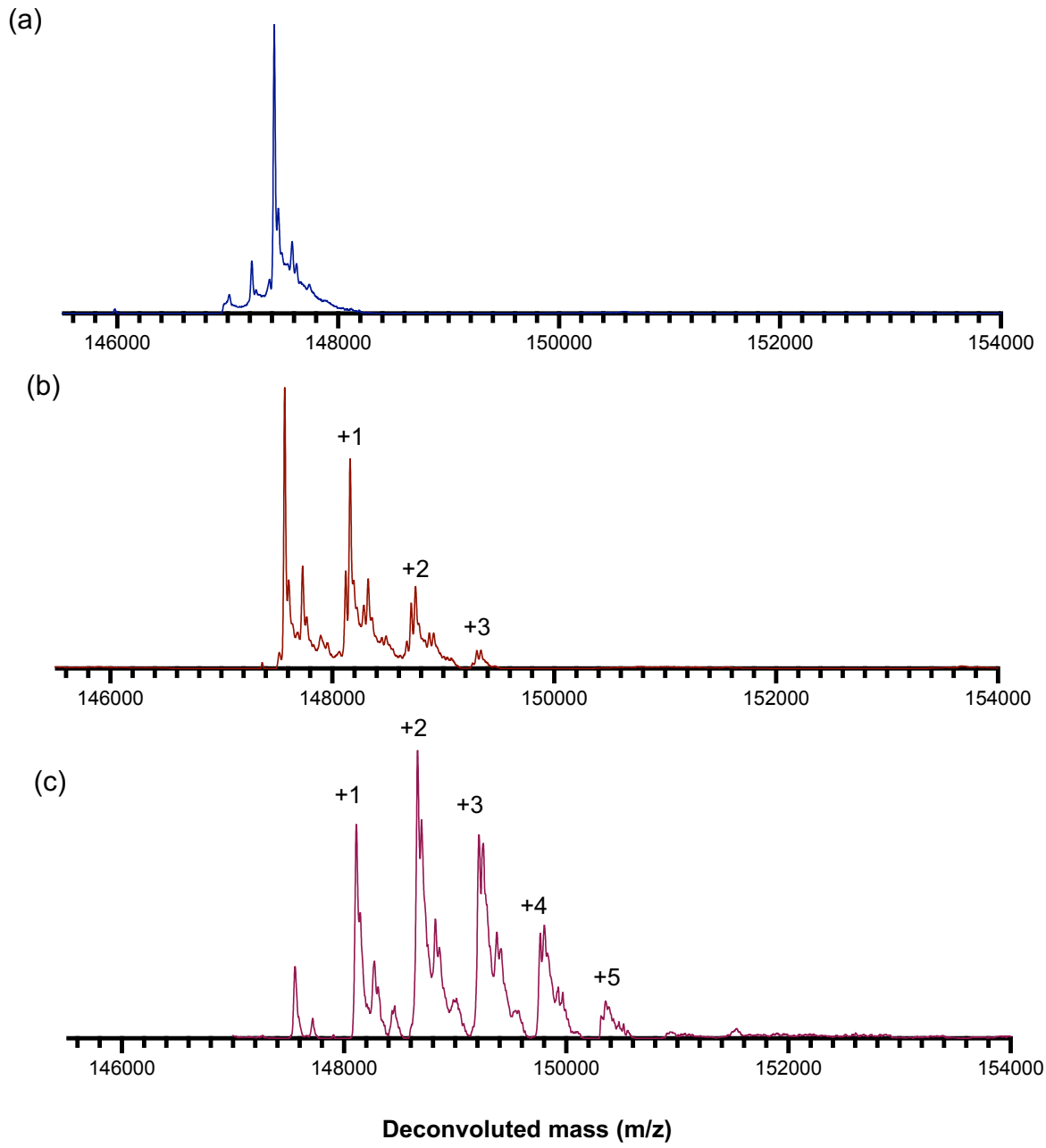

Figure 52: ESI-TOF deconvoluted mass spectra of (a) unmodified Girentuximab (hG250) and (b) H_4DOTA-NCS-hG250 showing between 0-2 chelator attachments, (c) H_4DOTA-NCS-hG250 showing 0-5 attachments.

3.4.3 Size Exclusion High-Performance Liquid Chromatography of Antibody Conjugates

Size exclusion chromatography is a reliable technique to estimate of antibody size. In size exclusion chromatography, a stationary phase consists of porous beads that act as molecular sieves, allowing smaller molecules to enter the beads and thus travel through the column more slowly than larger molecules. More importantly, SE-HPLC quantifies the amount of antibody

that has aggregated after modification (Figure 53). There are no significant changes in the SE-HPLC of both H_2MacropaSq-hG250 and H_2MacropaSq-hG250-FcRn, when compared to the parental antibodies. All antibodies have a retention time of ~10 minutes. Protein aggregates are typically larger and, therefore, will elute at earlier time points. There is apparent tailing of the antibody samples in all chromatograms. Instead, we are interested in the presence of aggregation (Figure 53, a, blue arrow) that may occur after chemical modification of the antibody with either H_2MacropaSqOEt or H_4DOTA-NCS. Therefore, the modification of both antibodies with H_2MacropaSq did not cause the conjugates to aggregate.

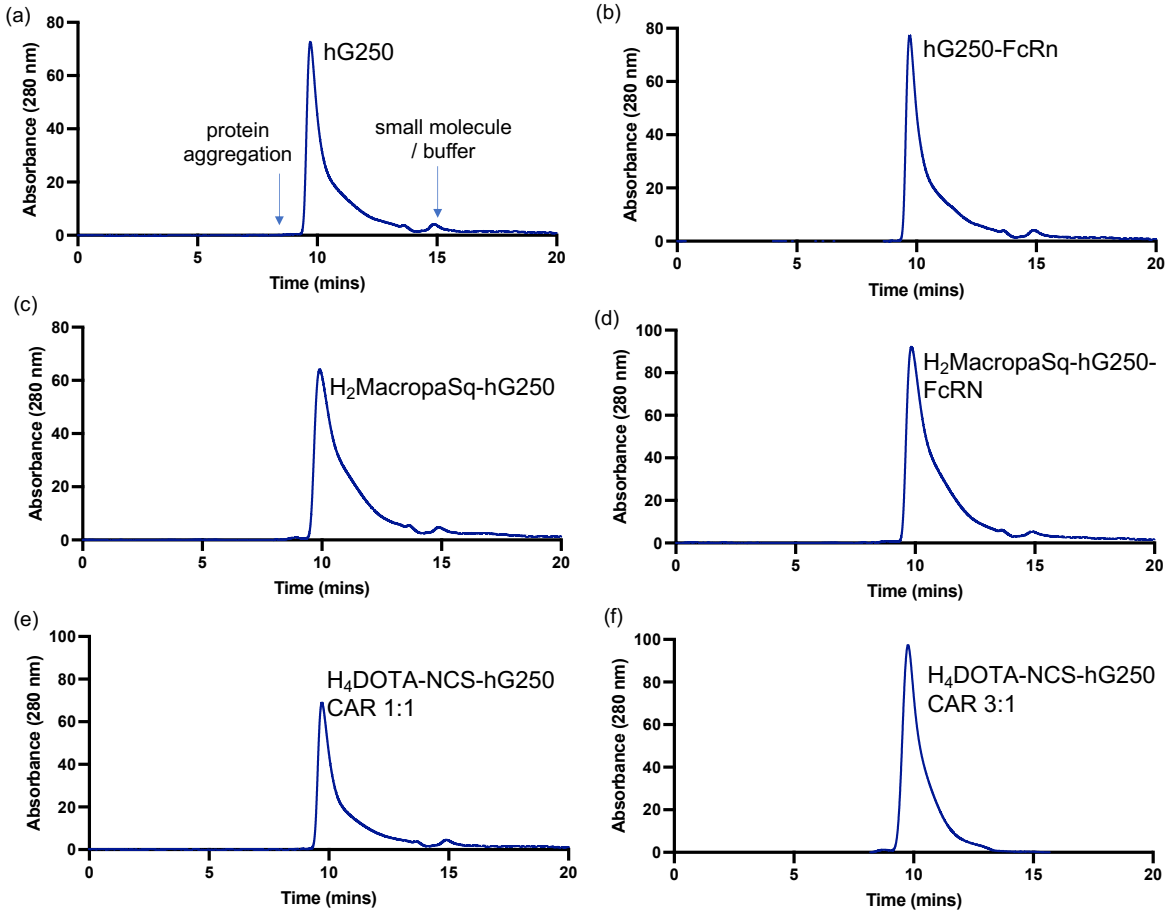

Figure 53: SE-HPLC of constructs (a) hG250, (b) hG250-FcRN (c) H_2MacropaSq-hG250 and (d) H_2MacropaSq-hG250-FcRN, (e) H_4DOTA-NCS-hG250 (CAR 1:1) and (f) H_4DOTA-NCS-hG250 (CAR 3:1).

The antibody conjugates H_2MacropaSq-hG250 and H_2MacropaSq-hG250-FcRn were stored at -20°C in sodium acetate radiolabelling buffer (0.15 M). There was no change in the intact protein mass spectrum and SE-HPLC for both antibody conjugates in over 10 months.

3.4.4 Enzyme-Linked Immunosorbent Assay (ELISA)

An ELISA assay is a versatile and sensitive biochemical technique used to probe the binding efficacy of monoclonal antibodies and their respective antigens. Therefore, it is an excellent assay to analyse the binding efficacy of the monoclonal antibody, hG250, to its antigen CAIX. It is also important to compare how the modification of hG250 with H_2MacropaSq affects antigen recognition.[260, 261] This assay is also used to confirm that antibody isotype controls do not bind to the antigen CAIX (in addition to flow cytometry). Briefly, the antigen is immobilised onto the plate, before a sample containing the antibody of interest is added. Unbound antibody is removed. Next, an enzyme-conjugated secondary antibody that binds to the primary antibody is added. Any unbound molecules are removed, and a substrate for the enzyme is added. If the enzyme is present, it will catalyse the conversion of the substrate into a colorimetric signal, which can be quantified spectrophotometrically.

A standard curve is generated using the serial dilutions of the antibodies. The optical density values obtained from the assay were plotted against the corresponding concentrations of hG250, and a sigmoidal dose-response curve was observed. The data showed a typical sigmoidal shape (between approx. 80 and 800 ng/mL) where optical density increases with antibody concentration. This suggests that hG250 specifically recognises and binds to CAIX in a concentration-dependent manner (Figure 54).

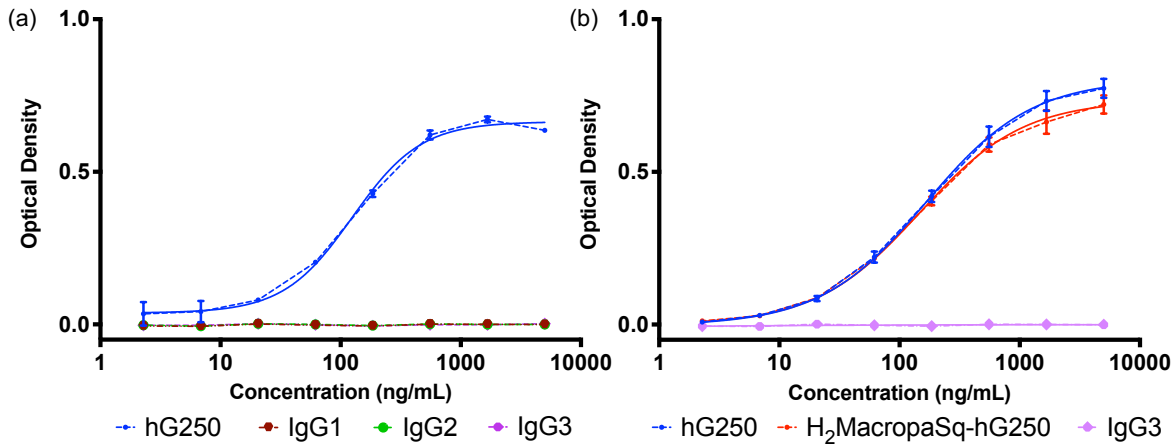

Figure 54: (a) Elisa Assay demonstrates that only Girentuximab has any binding efficacy against the antigen carbonic anhydrase IX. Elisa Assay demonstrates that modifying the antibody with H_2MacropaSq functional groups does not impact the binding of hG250 to carbonic anhydrase IX (CAIX). The IgG1 control shows no binding to CAIX and is a suitable control antibody for further in vitro work.

The EC_{50} values represent the concentration of antibodies that results in 50% of the maximal response. It is determined by plotting the optical density obtained again the concentration of the antibodies and calculating the midpoint of the sigmoidal dose-response curve. The value is the half-maximal effective concentration is the antibody concentration that produces a response that is measured to be halfway (50%) between the maximal response and the baseline. The calculated EC_{50} values for the unmodified hG250 antibody and H_2MacropaSq-hG25 are 166 ± 23 nM and 148 ± 20 nM, highlighting that there is no significant change in the overall binding affinity of these antibodies for their antigen CAIX.

Table 5: Calculated EC50 values of monoclonal antibodies by ELISA.

Antibody	*EC_{50} (nM)*
hG250	166 ± 23
H_2MacropaSq-hG250	148 ± 20
IgG1	N/A

These preliminary studies are particularly important in the selection of a tumour cell line that will have appropriate levels of CAIX expression that our radioimmunoconjugates can target. This assay demonstrated a reliable and specific binding of hG250 and H_2MacropaSq-hG250 to CAIX in a dose-dependent manner. A range of antibodies were screened to ensure

there was no cross-reactivity with CAIX, and IgG1 was chosen as an isotope control for *in vivo* analysis. The quantitative determination of the half-maximal binding concentrations for both constructs was calculated and compared. Both hG250 and H_2MacropaSq-hG250 show strong and reproducible binding to the antigen CAIX, which is overexpressed in 94% of ccRCC, making it an ideal target for alpha therapy with actinium-225.

3.5 Concluding Remarks

The new bifunctional chelator, H_2MacropaSqOEt outlined in Chapter Two was used to add the chelator to antibodies hG250 and hG250-FcRn. These antibodies are selective for CAIX which is overexpressed in ccRCC. This reproducible strategy covalently attaches H_2Macropa-SqOEt onto the surface exposed primary amines on monoclonal antibodies through the formation of a stable squaramide linkage through the reaction of H_2MacropaSqOEt with lysine residues of antibodies. The conjugation reaction occurs in four hours, meaning that the synthesis and characterisation of the antibody conjugate can be performed on the same day. This protocol typically attaches between 1 to 8 H_2Macropa-Sq chelators onto the antibody surface, with an average CAR of 4:1. H_2Macropa-SqOEt was designed with a linker that would not increase the hydrophobicity of the chelator so as to minimise the disturbance of the overall structure. When the modified antibodies have a CAR of approximately 4:1, the metal chelator does not impact the overall solubility of the antibody conjugate, and there is no aggregation of the antibody.

Moreover, the antibody constructs H_2MacropaSq-hG250, and H_2MacropaSq-hG250-FcRn are both stable at -20°C for over 10 months. This further highlights the stability and minimal disturbance the chelator has on the antibody. The binding efficacy of H_2MacropaSq-hG250 to its antigen, CAIX, was measured. When H_2MacropaSq-hG250 had a CAR of 4:1, the conjugate had an EC_{50} of 148 ± 20 nM. We are confident that the addition of H_2Macropa-Sq does not compromise the activity of the antibody to specifically bind to CAIX.

3.6 Experimental

3.6.1 Instrumentation

ESI-QTOF MS was collected on an Exactive Plus Orbitrap Infusion mass spectrometer (Exactive Series, 2.8 Build 268801, ThermoFisher Scientific). Analysis was performed using Xcalibur 4.0.27.10 (ThermoFisher Scientific). Protein samples were analysed on Agilent 6220 ESI-TOF LC/MS Mass Spectrometer coupled to an Agilent 1200 LC system (Agilent, Palo Alto, CA). All data were acquired, and reference mass corrected *via* a dual-spray electrospray ionisation (ESI) source. Acquisition was performed using the Agilent Mass Hunter Acquisition software version B.02.01 (B2116.30). Ionisation mode: Electrospray Ionisation; Drying gas flow: 7 L/min; Nebuliser: 35 psi; Drying gas temperature: 325°C; Capillary Voltage (Vcap): 4000 V; Fragmentor: 300 V; Skimmer: 65 V; OCT RFV: 250 V; Scan range acquired: 300–3200 m/z Internal Reference ions: Positive Ion Mode = m/z = 121.050873 & 922.009798. Protein desalting and chromatographic separation was performed using an Agilent Poroshell C18 2.1 x 75 mm, 5µm column using 5% (v/v) acetonitrile ported to waste (0 – 5min). Upon desalting of the sample, the flow was ported back into the ESI source for subsequent gradient elution with (5% (v/v) to 100% (v/v)) acetonitrile / 0.1% formic acid over 8 min at 0.25 mL/min. Analysis was performed using Mass Hunter version B.06.00 with BioConfirm software using the maximum entropy protein deconvolution algorithm; mass step 1 Da; Baseline factor 3.00; peak width set to uncertainty. ELISA assay measurements were performed on a FLUOstar Omega microplate reader (BMG Labtech) and analysed with MARS data analysis software.

3.6.2 H_2MacropaSq-hG250 and H_2MacropaSq-hG250-FcRn

Humanised Girentuximab, hG250 (5.03 mg/ mL, 200 µL) and hG250-FcRn antibodies (5.0 mg/mL) in PBS were buffer exchanged into borate buffer (0.25 M, pH 9.0) and reconstituted to a final concentration of 5 mg/ mL. To the reaction mixture was added H_2MacropaSqOEt (15

mg / mL stock solution in DMSO – final DMSO concentration less than 4 %, 15 equivalents) and shaken at room temperature for four hours. Excess reagents were removed, and buffer was exchanged (Sodium Acetate, 0.15 M, pH 5.5) *via* spin filtration (50 KDa MW cut-off).

3.6.3 H_2MacropaSq-IgG1 Control

IgG1 (3.0 mg/mL) in PBS was buffer exchanged into borate buffer (0.25 M, pH 9.0) to a final concentration of 5 mg/ mL. To the reaction mixture was added H_2MacropaSqOEt (10 mg / mL stock solution in DMSO, 10 equivalents) and shaken at room temperature for four hours. Excess reagents were removed, and buffer was exchanged (Sodium Acetate, 0.15 M, pH 5.5) *via* spin filtration (50 KDa MW cut-off). H_2MacropaSq-IgG1 required further purification due to excess aggregation above suitable levels (> 4%). SE-HPLC was performed with the antibody conjugate collected at 15-second aliquots to separate aggregated protein.

3.6.4 H_4DOTA-pBn-NCS-hG250 (CAR 1:1)

hG250 (5.03 mg/mL) in PBS was buffer exchanged into carbonate buffer (1 M, pH 9.0) to a final concentration of 5 mg/ mL. To the reaction mixture was added pNCS-Bn-DOTA (Macrocyclic, 10 mg / mL stock solution in DMSO, 5 or 10 equivalents) and shaken at 37 °C for 1 hour. The product was purified by a PD-10 desalting column.

3.6.5 H_4DOTA-pBn-NCS-hG250 (CAR 3:1)

To a solution of hG250 (5.03 mg/mL, 100 µL) in PBS was added carbonate buffer (1 M, pH 9.0, 12 µL) and MilliQ (6 µL). To the reaction mixture was added pNCS-Bn-DOTA (Macrocyclic, 10 mg / mL stock solution in DMSO, 3.3 µL) and 3 µL more DMSO, and shaken at room temperature for 3 hours. Excess reagents were removed, and buffer was exchanged (Sodium Acetate, 0.15 M, pH 5.5) *via* spin filtration (50 KDa MW cut-off).

3.6.6 ELISA

The ELISA protocol was adapted from Pantheon Biologics.[262] Human CAIX protein (50 µg) was reconstituted in MilliQ (stock concentration of 200 µg/mL), then diluted (3µg/ mL), then

coat a 96-well plate (100 µL), sealed, and incubated overnight at 2-8 °C before washing with PBST wash solution (1x, 4 x 300 µL). Blocking buffer (1% BSA in PBS) was added, and the plate was sealed and incubated (60 mins), then washed with PBST wash solution. hG250, H_2MacropaSq-hG250, and the isotype controls IgG1, IgG2 and IgG3 were diluted to 100 µg/mL in assay diluent. The dilutions were performed in a deep well dilution plate from a maximum concentration of 5000 ng/ mL to 2.28 ng/mL before 100 µL of the appropriate dilution was used for the assay. The assay plate was sealed and incubated (75 min) before washing with PBST wash solution. Secondary antibody-HRP conjugate was diluted to a (15 ng/mL) and added to the assay plate (100 µL), then incubated darkness (75 min) before washing with PBST wash solution. Ensure the TMB substrate has sufficient time to equilibrate to room temperature in the absence of light. After at least 60 minutes, TMB substrate was added to the assay plate and incubated for 15 minutes in darkness before stop solution (2M H_2SO_4, 100 µL) was added to stop the reaction. The plate was checked to ensure no air bubbles, and then samples were run on a FLUOstar Omega microplate reader (BMG Labtech) and analysed with MARS data analysis software.

4 Radiolabelling Monoclonal Antibodies with Actinium-225

4.1 The Challenges of Detecting Actinium-225

Actinium-225 undergoes radioactive decay through a series of decay steps, ultimately reaching the near stable isotope bismuth-209. The long radioactive half-life of actinium-225 ($t_{1/2}$ = 9.9 days) means that it decays relatively slowly when compared to some of its daughter nuclei. As actinium-225 decays, it produces several daughter radionuclides, including francium-221, astatine-217, bismuth-213, polonium-213 and lead-209 (Figure 55). These daughter nuclides, in turn, undergo further radioactive decay until reaching bismuth-209.

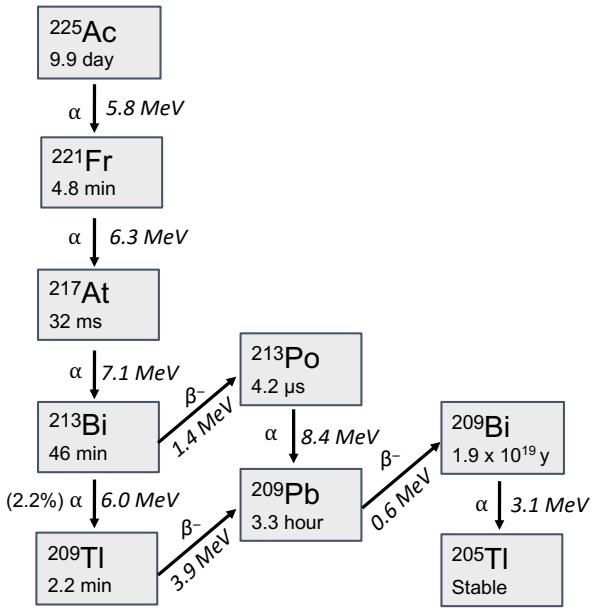

Figure 55: The actinium-225 decay pathway. Actinium-225 emits four daughter alpha particles and two beta particles to reach the stable isotope bismuth-209. Adapted from [145].

Secular radioactive equilibrium can occur when the parent nucleus has a long half-life. The rate of decay of actinium-225 is much slower than its daughter nuclides. As a result, actinium-225 accumulates over time, and the concentration of the daughter radionuclides in the decay chain will reach an equilibrium where the rate of production and decay is at a steady state. Considering secular equilibrium is necessary to make inferences about the coordination

of actinium-225 into the targeting molecule. Actinium-225 is in secular equilibrium with its progeny after approximately eight hours. Therefore, on average, samples were left for eight hours before they were analysed. Quantification of yield at time points before can lead to the over or underestimation of the radiochemical yield.[129]

Radio-thin layer chromatography (TLC) is a rapid and efficient technique used in radiochemistry to separate and quantify radioactive species in a sample based on their chemical properties. It involves the separation of compounds based on the differential affinity for a stationary phase/mobile phase. The stationary phase is a thin layer of inert material. Typically, a silica-impregnated glass microfiber plate is commonly used for antibodies and peptides and aluminium-backed plates are more commonly used for small molecules. This process separates the unlabelled [^{225}Ac]Ac^{III} from [^{225}Ac]Ac-conjugates (small molecules, peptides or antibodies) based on their differential migration on the TLC plate, which serves as a medium for the separation of compounds based on their affinity for the stationary phase (Figure 56, a). The mobile phase (50 mM citrate buffer, pH 5.0 for monoclonal antibodies, or 40 mM citrate pH 4 + 10% MeOH for small molecules) interacts with the radiolabelled compounds that have been immobilised onto the stationary phase based on their polarity, size and charge, leading to differential migration (Figure 56, b). Quantification of the radiochemical yield is challenging due to the presence of daughter radionuclides. The large recoil energy of alpha emissions as well as the different chemical qualities of the progeny as they decay means that these daughters may not be complexed to H_2Macropa-Sq. Therefore, measuring the activity of the TLC plates before secular equilibrium has been reached may mean daughter nuclides distribute across the chromatographic plate.

After secular equilibrium has been reached, the radioactivity in the samples is measured with a γ-detector. The radioactivity associated with each of the separated radioactive

compounds is then converted into a radio-chromatogram where the radiochemical yield of the reaction can be quantified.

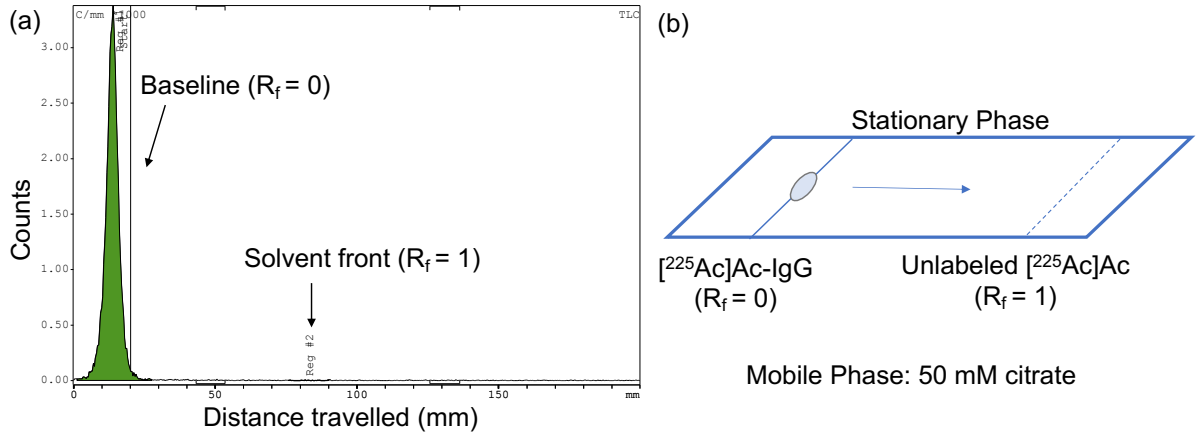

Figure 56: (a) An annotated radioTLC of an actinium-225 labelled IgG, (b) diagram of a TLC. The arrow points to the direction of flow of the mobile phase when placed in the developing tank.

4.2 Aims

The primary objective of this chapter is to develop a highly reproducible method for radiolabeling antibody conjugates with actinium-225. The evaluation of [^{225}Ac]Ac(MacropaSq-hG250) as a suitable therapeutic for radioimmunotherapy of CAIX-positive cancers can be divided into three sections; the initial radiochemistry, an *in vitro* evaluation of the cytotoxicity and finally, an *in vivo* preclinical evaluation in mice bearing CAIX-positive tumours (Scheme 8).

Specifically, we aim to explore the radiochemistry of antibody conjugates H_2MacropaSq-hG250 and H_2MacropaSq-hG250-FcRn, and to compare the complexation kinetics and stability with DOTA-conjugated counterparts. The cytotoxicity of the conjugates will be assessed in cell-based assays. Subsequently, we aim to evaluate the biodistribution profiles of [^{225}Ac]Ac(MacropaSq-hG250) in a CAIX-positive murine tumour xenograft model. This will provide valuable information about the pharmacokinetic properties of [^{225}Ac]Ac(MacropaSq-hG250) compared to an [^{225}Ac]Ac^{III}-labelled isotype control. Finally, a longitudinal therapy study will investigate the effects of α radiation on tumours that

overexpress CAIX. Through these investigations, we seek to gain valuable insights into the potential of using [^{225}Ac]Ac(MacropaSq-hG250) to treat CAIX-positive cancers.

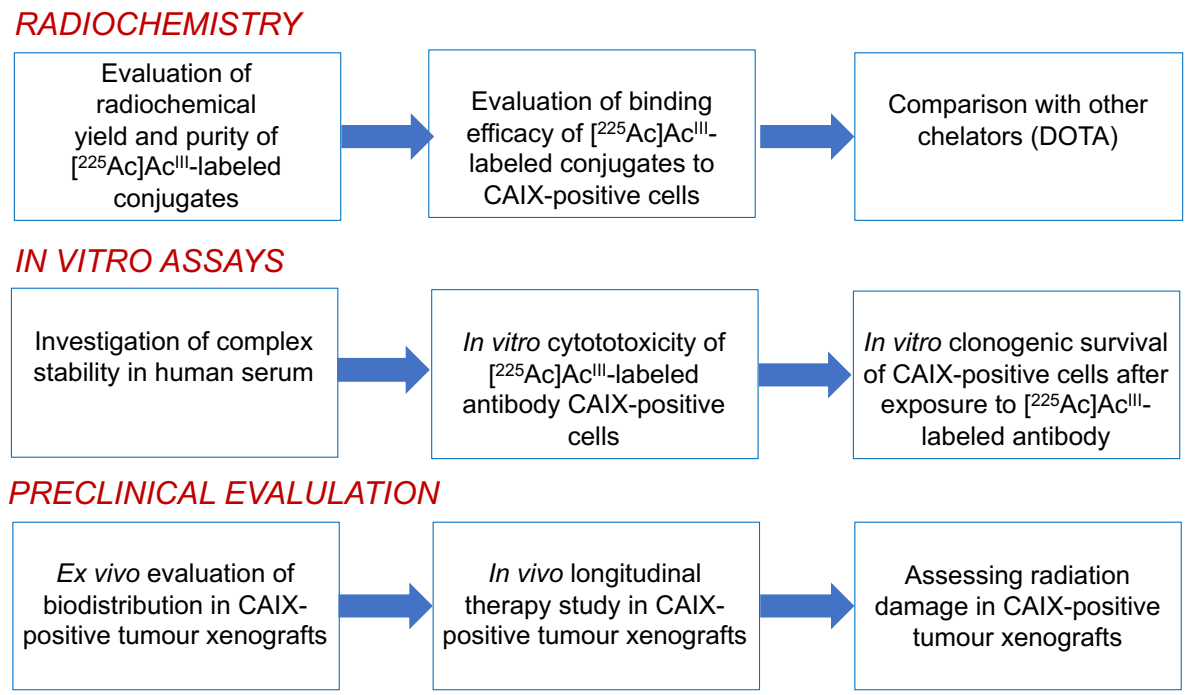

Scheme 8: The investigation of actinium-225 labelled antibodies comprises of three sections; developing and optimising the radiochemistry, an evaluation of the stability and cytotoxicity of [^{225}Ac]Ac^{III}-labelled antibody conjugates, and finally preclinical studies involving the biodistribution and therapeutic efficacy in a CAIX-positive tumour xenograft model.

4.3 Results and Discussion

4.3.1 Radiolabelling H_2MacropaSq-Antibodies with Actinium-225

Actinium-225 was obtained from Oak Ridge National Laboratory as [^{225}Ac]Ac$(NO_3)_3$. The nitrate film was reconstituted in HCl (0.2 M) and then neutralised with $NaCH_3CO_2$ buffer (0.15 M, pH 5.5). The radioimmunoconjugates [^{225}Ac]Ac(MacropaSq-hG250), [^{225}Ac]Ac(MacropaSq-hG250-FcRn), and [^{225}Ac]Ac(MacropaSq-IgG1) were synthesised accordingly. Initial radiochemical experiments reacted 370 kBq (10 µCi) of neutralised [^{225}Ac]Ac^{III} with H_2MacropaSq-hG250 (10 µg). At an approximate concentration of 10^{-6} M (final antibody concentration of 1.2 – 1.5 µM), quantitative radiolabelling was achieved within 5 minutes. The radiolabelled constructs were used without further purification.

Size exclusion high-performance liquid chromatography (SE-HPLC) is useful chromatographic technique used for the separation of compounds based on their size and provides important structural information about the antibody conjugates, primarily the level of antibody aggregation. They were characterised by comparing their respective SE-HPLC traces with the unlabelled antibody conjugates (λ = 280 nm, Figure 57).

In a typical SE-chromatogram, after the sample has been separated based on size, it is analysed by a UV detector coupled with a radiation detector. Due to the complex nature of the actinium decay pathway, analysis of the chromatogram with a radiation detector would show a complex mixture of signals from the radioactive progeny. Instead, the [^{225}Ac]Ac-MacropaSq-conjugates are separated by SE-HPLC, with fractions being collected in 15-second intervals over 20 minutes (80 fractions per chromatogram). The use of SE-HPLC to characterise [^{225}Ac]Ac-antibody-conjugates is time-consuming and manually demanding as 80 independent fractions have to be individually quantified in a γ-counter eight hours after they are separated by size exclusion column. Consequently, radioTLC was predominantly employed to calculate the radiochemical yields of actinium-225 conjugates.

Both [^{225}Ac]Ac(MacropaSq-hG250) and [^{225}Ac]Ac(MacropaSq-hG250-FcRn) have comparable retention times compared to the non-radioactive control. Fractions of both [^{225}Ac]Ac(MacropaSq-hG250) and [^{225}Ac]Ac(MacropaSq-hG250-FcRn) were collected in 15-second intervals. This method separated aggregated antibodies, labelled antibody conjugates, and unlabelled actinium. Therefore 15-second intervals provided sufficient resolution when investigating the purity of the conjugates. [^{225}Ac]Ac(MacropaSq-hG250) and [^{225}Ac]Ac(MacropaSq-hG250-FcRn) showed a maximum number of counts of actinium in the fraction at 8.25 minutes. This closely matches the retention time of H_2MacropaSq-hG250 and H_2MacropaSq-hG250-FcRn, which were 8.23 minutes and 8.21 minutes, respectively.

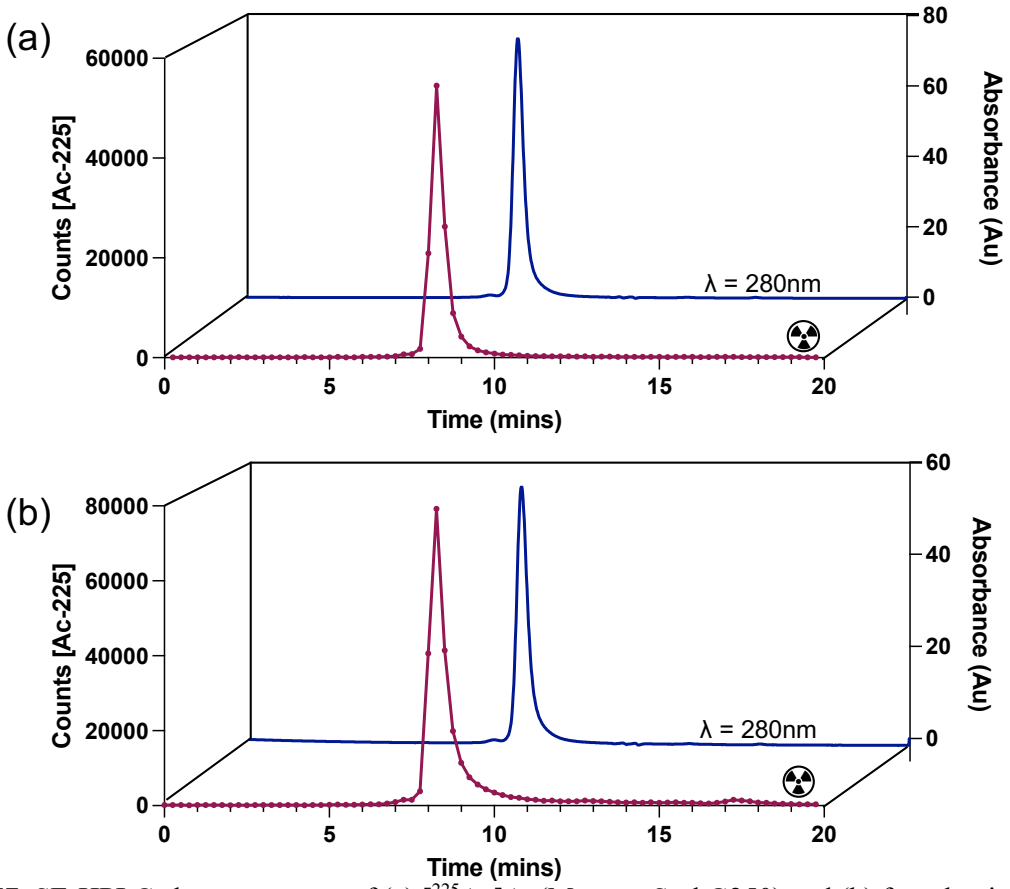

Figure 57: SE-HPLC chromatograms of (a) [^{225}Ac]Ac(MacropaSq-hG250) and (b) fast clearing [^{225}Ac]Ac(MacropaSq-hG250-FcRn). Radioactive fractions in red, compared to the UV trace of H_2MacropaSq-hG250 and H_2MacropaSq-hG250-FcRn in blue (λ = 280 nm).

The antibody IgG1 had evidence of more aggregation when compared to both girentuximab constructs. After SE-HPLC purification, the aggregation levels were less than 4%, and the conjugates were radiolabelled under existing protocol conditions. [^{225}Ac]Ac(MacropaSq-IgG1) showed a maximum number of counts in the fraction at 7.50 and 8.75 minutes. The sample measured at a wavelength of 280 nm had retention times of 7.53 and 8.70 minutes. The peak with a retention time of 7.5 minutes corresponds to the aggregated antibody conjugate, and the retention time of 8.75 minutes corresponds to the peak of [^{225}Ac]Ac(MacropaSq-IgG1).

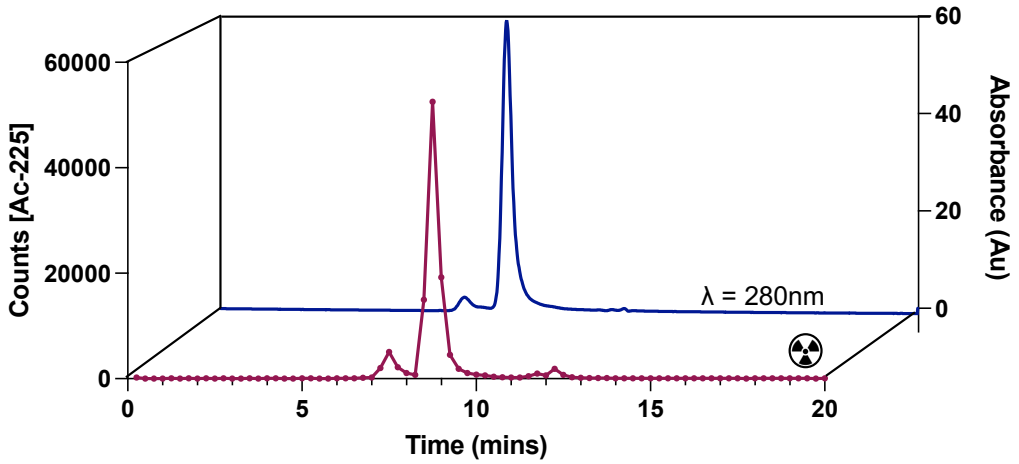

Figure 58: SE-HPLC chromatograms of [^{225}Ac]Ac(MacropaSq-IgG1). Radioactive fractions in red, compared to the UV trace of H_2MacropaSq-IgG1 in blue (λ = 280 nm).

4.3.2 Determining the Radiochemical Yield of [^{225}Ac]Ac-radioimmunoconjugate Formation by Radio-Thin Layer Chromatography

When radiolabelling H_2MacropaSq-hG250 with [^{225}Ac]Ac^{III}, the use of 0.05 M citrate buffer (pH 5.0) as a mobile phase gave excellent separation of the complex from the free radionuclide by TLC. Unlabelled [^{225}Ac]Ac^{III}, which presumably exists as the citrate complex, travels to the solvent from (8 cm, R_f = 1), while complexed [^{225}Ac]Ac-IgGs stay at the baseline (R_f = 0), allowing for the easy quantification of radiochemical yield (Figure 59). The most accurate results were achieved when secular equilibrium was reached before the analysis of samples. The radiochemical yield was then calculated by the 218 keV γ-emission of [^{221}Fr]Fr^{I} and 440 keV window of [^{213}Bi]Bi^{III}.

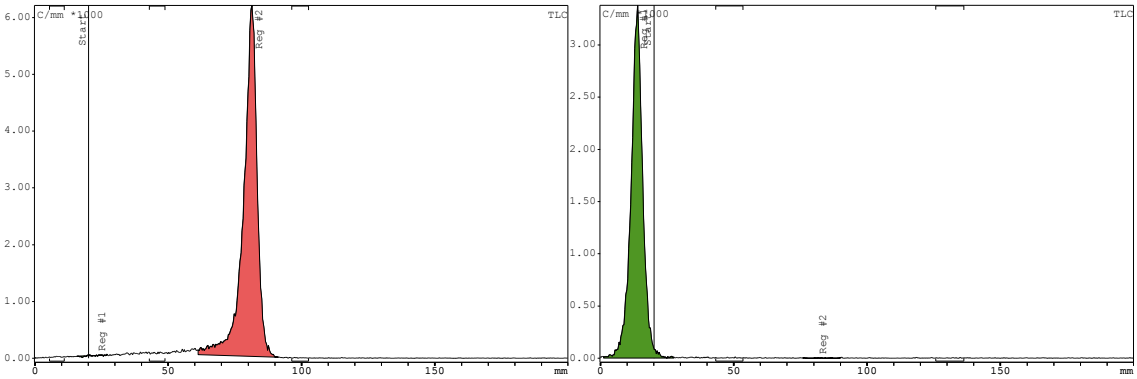

Figure 59: Radio Thin Layer Chromatography of (left) 'free' [^{225}Ac]Ac^{III} (right) [^{225}Ac]Ac-MacropaSq-hG250, radioTLC mobile phase: 0.05 M citrate buffer pH 5.0

The radiochemical yield (RCY) is the amount of activity in the product expressed as a percentage of the related starting activity.[263] The RCY of [^{225}Ac]Ac(MacropaSq-hG250) was measured after reaction times of 1, 5, 15 and 30 minutes, at an antibody concentration of both 1.5×10^{-6} M and 1.5×10^{-7} M in sodium acetate buffer (pH 5.5, Figure 60). At an antibody concentration of 1.5×10^{-6} M, quantitative radiolabeling was achieved within 1 minute. At a concentration of 1.5×10^{-7} M, quantitative radiolabeling was achieved within 5 minutes.

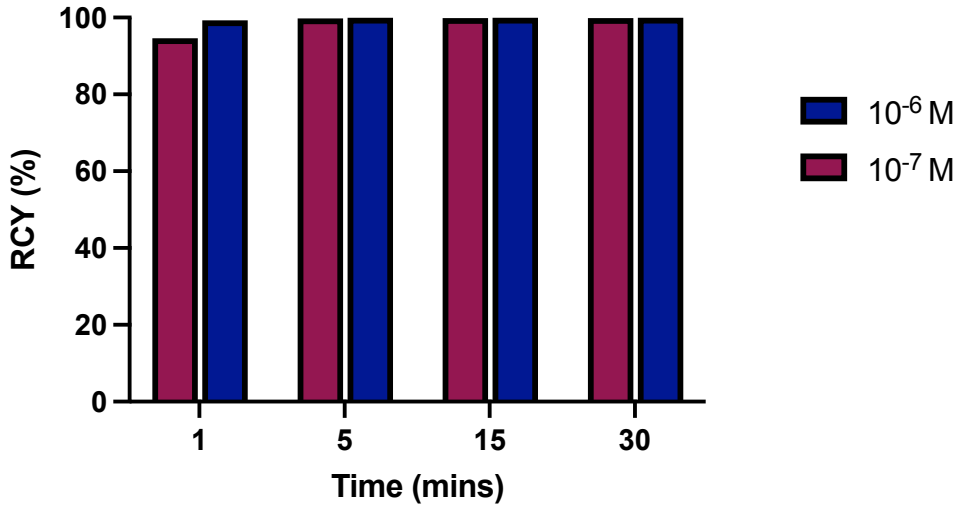

Figure 60: The radiochemical yield of [^{225}Ac]Ac(MacropaSq-hG250) as a function of time (measured at 1, 5, 15, 30 minutes) at an antibody concentration 1.5×10^{-6} M and 1.5×10^{-7} M.

The radiochemical yield was then investigated at decreasing concentrations of H_2MacropaSq-hG250, in the range of 10^{-6} M to 10^{-8} M over a reaction time of 30 minutes (Figure 61, a). There is negligible (<1%) [^{225}Ac]Ac(MacropaSq-hG250) complex formation at concentrations of $10^{-7.5}$ M and below. At a concentration of $10^{-7.1}$ M, the RCY increases from 17.9 % at 1 minute to 96.6 % at the final time point of 30 minutes. Extrapolation of the radiochemical yields of the different concentrations at 30 minutes reaction time shows the minimum concentration required to reach near quantitative labelling (Figure 61, b).

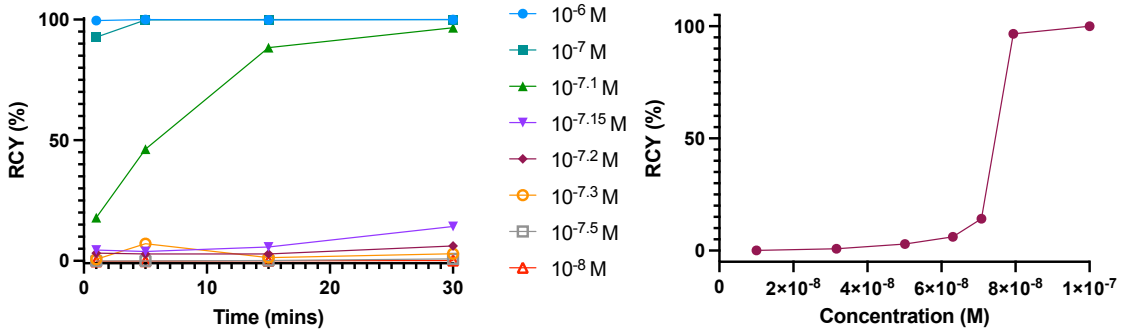

Figure 61: (a) RCY as a function of time at various concentrations of H_2MacropaSq-hG250 with [^{225}Ac]Ac^{III} (b) RCY at the reaction endpoint with increasing concentrations of H_2MacropaSq-hG250.

4.3.3 [^{225}Ac]Ac(MacropaSq-hG250) Retains its Immunoreactivity Toward SKRC-52 Cells

The binding of hG250, as well as the conjugate H_2MacropaSq-hG250 (Figure 62) to SKRC-52 cells was confirmed by flow cytometry. There is no change in binding between the unmodified hG250 antibody and the H_2MacropaSq-hG250 conjugate, indicating that the addition of H2Macropa-Sq did not interfere with antigen binding.

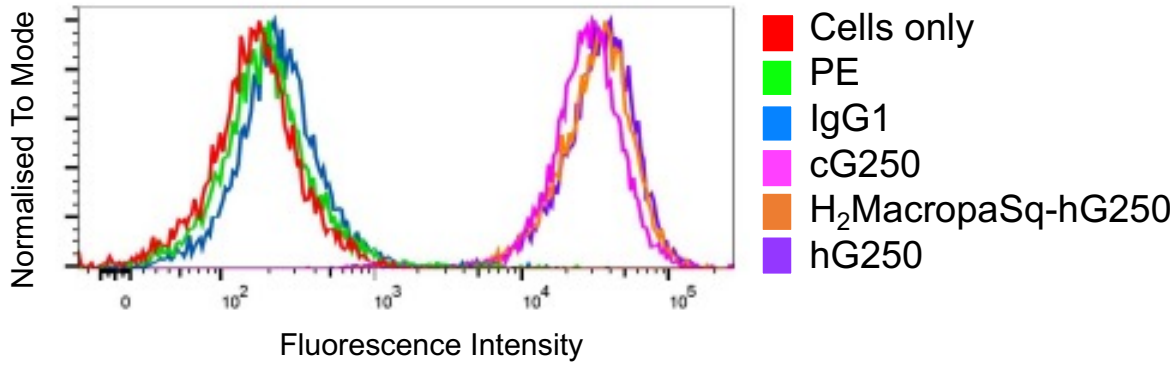

Figure 62: Flow Cytometry of hG250 antibodies, including H_2MacropaSq-hG250, against SKRC-52 cells.

This cell line is derived from clear-cell renal cell carcinoma metastatic lesions and overexpresses CAIX, and is, therefore, a suitable cell line to test [^{225}Ac]Ac(MacropaSq-hG250). In the radioactive Lindmo assay, [^{225}Ac]Ac(MacropaSq-hG250) was incubated with an increasing number of SKRC-52 cells (0 – 5 x10^6 cells/ mL). To determine the amount of radioactivity bound to SKRC-52 cells, the cells were washed to remove the unbound antibody and then counted in a gamma counter. The radioactivity is proportional to the amount of

antibody that has bound to the cells, indicating the presence of a specific binding response to the antigen. The fraction of immunoreactive antibody is determined by linear extrapolation with conditions that represent an infinite antigen excess. A more reliable determination is obtained if the binding is measured at a series of increasing antigen concentrations so that the fraction of bound antibody is seen to approach a plateau value. Therefore, a more accurate value of the immunoreactive fraction is obtained instead of an apparent immunoreactive fraction under conditions of limited antigen excess. The data reaches a plateau above the cell number of approximately 3×10^6 cells/ mL (Figure 63, a).

A double-inverse plot of the radiolabelled antibody construct over the specific binding (Figure 63, b), yields a straight line. The immunoreactive fraction can be calculated by linear extrapolation to the x-intercept, that is:

$$\frac{1}{x} = \frac{1}{1.01} = 0.99$$

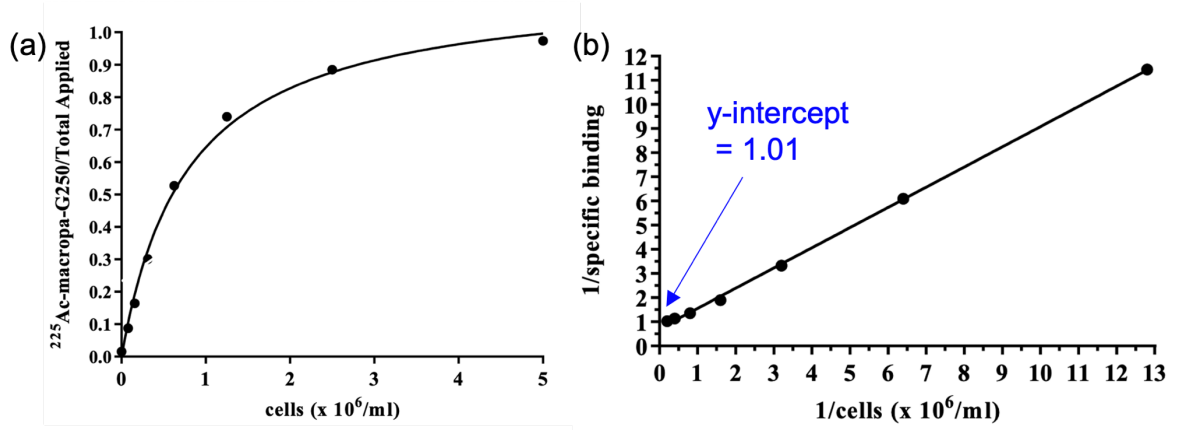

Figure 63: (a) Lindmo Assay showing the fraction of [^{225}Ac]Ac(MacropaSq-hG250) binding to SKRC-52 cells as a function of cell number, (b) the inverse of specific binding plotted against the inverse of SKRC-52 cell number.

The immunoreactive fraction was effectively 1, meaning that, just as the addition of the H_2MaropaSq chelators had not impacted the overall antigen recognition, measured by ELISA assay (see section 3.4.4), the radiolabelling of [^{225}Ac]Ac(MacropaSq-hG250) did not affect binding to SKRC-52 cells.

The Scatchard assay is used to determine the number of antibody molecules bound per cell and to extrapolate the association constant of the antibody-antigen binding interaction. The resulting plot is a straight line, the negative slope of which represents the binding constant or affinity of the antibody; calculated $K_a = 2.5 \times 10^9$ M^{-1}, while the x-intercept represents the maximum binding capacity to the antigen, determined to be 5.1×10^5 /cell. (Figure 64).

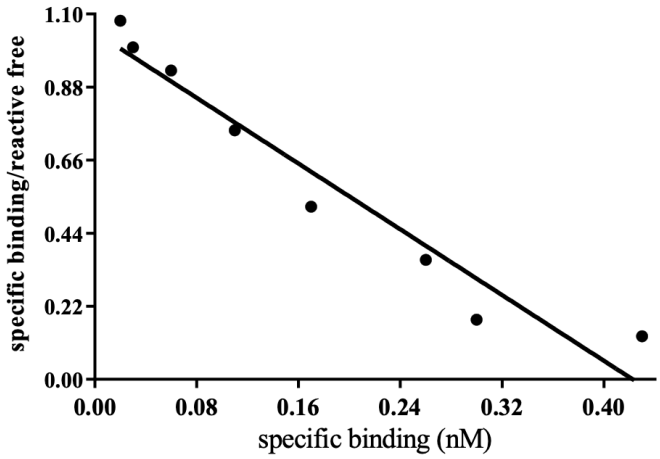

Figure 64 : Scatchard Assay of [^{225}Ac]Ac(MacropaSq-hG250) binding to SKRC-52 cells.

The immunoreactivity of the two actinium-labelled antibodies, [^{225}Ac]Ac(MacropaSq-hG250) and [^{225}Ac]Ac(MacropaSq-hG250-FcRn), was measured over seven days (day 0, 2, 7) in human serum (37 °C, Sigma Aldrich) and expressed as a percentage of the immunoreactivity towards SKRC-52 cells (Table 6). The non-specific binding, when the antibodies bind to non-target proteins in the cell suspension sample, was measured using an excess of unlabelled antibodies. The immunoreactivity of both antibodies decreased over 7 days, with [^{225}Ac]Ac(MacropaSq-hG250) decreasing from 99.9% to 86.9% and [^{225}Ac]Ac(MacropaSq-hG250-FcRn) decreased, from 100% to 79.6%. This may be due to the degradation of the antibody through radiolysis and its ability to recognise the antigen on SKRC-52 cells (Table 6).

Table 6: Immunoreactivity of [^{225}Ac]Ac(Macropa-Sq) conjugated antibodies incubated in human serum over seven days.

Immunoreactivity	Day 0 (%)	Day 2 (%)	Day 7 (%)
[^{225}Ac]Ac(MacropaSq-hG250)	99.9	86.0	86.9
Nonspecific binding	4.47	4.07	9.03
[^{225}Ac]Ac(MacropaSq-hG250-FcRn)	100	98.5	79.6
Nonspecific binding	3.64	5.00	5.16

There is a degree of nonspecific binding of both antibodies at each time point; the percentage of nonspecific binding increases for [^{225}Ac]Ac(MacropaSq-hG250) from 4.47 % at day zero to 9.03 % on day seven. Similarly, the nonspecific binding of [^{225}Ac]Ac(MacropaSq-hG250-FcRn) increases from 3.64 % at day zero to 5.16 % on day seven. This is most likely due to radiolysis or proteases degrading the antibody, as would be expected.

4.3.4 [^{225}Ac]Ac(MacropaSq-hG250) Complexes are Stable in Challenge Experiments

[^{225}Ac]Ac(MacropaSq-hG250) was selected for the competition experiments to determine the stability of the radiolabelled conjugate in the presence of a competing trivalent metal, La^{III} and a high affinity metal chelator, ethylenediaminetetraacetic acid (H_4EDTA). An excess of the trivalent metal La^{III} can transchelate actinium, which would cause decomplexation of [^{225}Ac]Ac^{III}. The RCY (measured *via* radioTLC) of the [^{225}Ac]Ac(MacropaSq-hG250) at multiple time points (1 hour, day 1, day 2, and day 7) in the presence of varying excess (5x, 50x, 500x) of La^{III} and H_4EDTA is shown (Table 7).

The data indicate that in the vehicle only (PBS), the radiochemical yield is not affected, with >99% RCY at all time points. The addition of La^{III} and EDTA appears to only have minor effects on the RCY, and the RCY remains above 99% for La^{III} and above 98% for the competition experiments with EDTA. Overall these results indicate that [^{225}Ac]Ac(MacropaSq-hG250) is a highly stable complex and is promising for future *in vivo* work.

Table 7: Competition experiment of [^{225}Ac]Ac(MacropaSq-hG250) over seven days.

Day 0 (RCY = 100 %)	Hour 1	Day 1	Day 2	Day 7
PBS	99.9	99.9	99.7	99.7
PBS + La^{III} (5x)	99.8	99.9	100	99.4
PBS + La^{III} (50x)	99.9	100	99.9	99.4
PBS + La^{III} (500x)	99.9	99.9	99.8	99.2
PBS + H_4EDTA (5x)	98.4	99.2	99.5	99.6
PBS + H_4EDTA (50x)	99.9	100	99.8	99.1

4.3.5 [^{225}Ac]Ac(MacropaSq-hG250) Outperforms [^{225}Ac]Ac(DOTA-NCS-hG250)

We chose to compare the radiolabeling efficiency of H_4DOTA-NCS with H_2MacropaSq. Two samples of H_4DOTA-pBn-NSC-hG250 with different chelator antibody ratios of approximately 1:1 and 3:1 were prepared as described in Chapter Three. The radiolabeling of the H_4DOTA-pBn-NCS-hG250 conjugates with [^{225}Ac]Ac^{III} was performed under multiple conditions in an attempt to optimise the reaction. These results are summarised in the experimental section (Table 10). Conjugates were radiolabelled at different pH (5.5 – 9.0) with different concentrations and temperatures (~22 °C – 60 °C). There were several considerations to make when calculating the appropriate antibody concentration for radiolabeling experiments; the [^{225}Ac]Ac(MacropaSq-mAb) constructs were radiolabelled at concentrations starting at 10^{-6} M. It was estimated that a final antibody concentration of 10^{-5} M (3.7 kBq/µg) would strike an appropriate balance between being of a sufficient concentration to facilitate complexation while avoiding using an excessive quantity of biological sample.

Radiolabeling for 60 minutes gave radiochemical yields for [^{225}Ac]Ac(DOTA-pBn-NCS-hG250) of 10 % for a CAR of 1:1 (in 37 °C, Figure 65, a) and 12.6 % for the CAR of 3:1 (45 °C, Figure 65, a). This is significantly less than reported by Merkx *et al.,*[250] where a labelling efficiency of 99.3% was achieved with a maximum specific activity of 15.7 kBq/µg when the DOTA-conjugated hG250 was incubated with [^{225}Ac]Ac^{III} in Tris buffer (0.1 M, pH

9.0, 37 °C) for 60 minutes. Heating the mixtures to 45°C only marginally improved the radiochemical yield to 12.6 % and is not advised for antibodies. The radiochemical yield plateaued, and even after 180 minutes, it remained relatively low at 15%. This is a limiting factor in using these conjugates in clinical settings, where rapid radiolabelling is advantageous.

[^{225}Ac]Ac(MacropaSq-hG250) (Figure 65, b) far outperforms [^{225}Ac]Ac(DOTA-NCS-hG250) in terms of radiochemical yield (> 99.9 % vs 12.6 %), reaction concentration (10^{-7} M vs 10^{-5} M) and overall radiolabelling time (5 minutes vs 60 minutes) in the same buffer and pH.

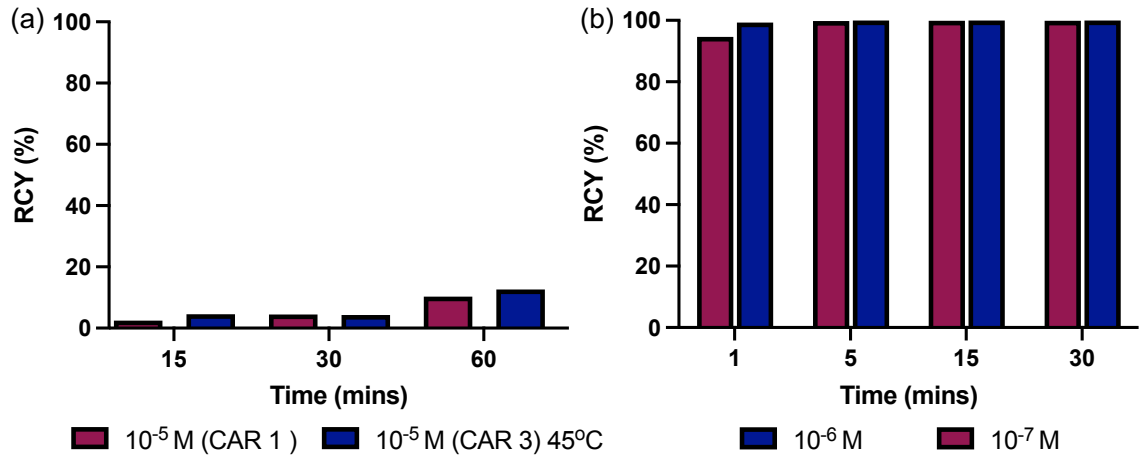

Figure 65: (a) The radiochemical yield of [^{225}Ac]Ac(DOTA-NCS-hG250) and (b) [^{225}Ac]Ac(MacropaSq-hG250) as a function of time at different antibody concentrations in the same buffer and pH (sodium acetate buffer, pH 5.5).

An investigation of existing radiolabelling protocols for [^{225}Ac]Ac(DOTA-mAb) showed many similarities. Due to the reported suboptimal radiolabelling efficiency of using DOTA as a metal chelator for actinium-225, a two-step radiolabelling procedure was commonly employed (see section 2.5.2),[264] where it was necessary to purify the reaction mixtures by size exclusion chromatography. This suffers from the disadvantage of very low specific activity and low yield of the final conjugates, as well as requiring two purification steps. The majority of protocols where DOTA conjugated antibodies were radiolabelled with [^{225}Ac]Ac^{III} used an acetate buffer (ammonium, tetramethyl ammonium or sodium) and slightly

varied pH range (5 – 6.5) and required post-labelling purification with size exclusion chromatography (PD 10)[265-267] or centrifugal filtration.[268, 269]

As these were initial radiochemical investigations using an H_4DOTA chelator, we did not have sufficient actinium-225 nor the antibody conjugates to perform post-labelling purification on actinium constructs with such low radiochemical yields. It is also important to highlight that as actinium-225 is only in the infancy of its development as a radiopharmaceutical, the radionuclide is extremely rare, and losing a minimum of 80% of the radionuclide is not practical.

Radiolabeling experiments were repeated at 60°C in an attempt to achieve quantitative radiolabeling. At 60 °C, there was an increase in radiochemical yield (Table 8). After 15 minutes, the [^{225}Ac]Ac(DOTA-NCS-hG250) formed with a radiochemical yield of 89.2 %, which increases to 98.0 % at 30 minutes and 99.3 % after 60 minutes. After 180 minutes, the RCY decreased to 91.4 %, demonstrating that long heating times, in fact, caused the loss of [^{225}Ac]Ac^{III} from [^{225}Ac]Ac(DOTA-NCS-hG250). Although radioTLC is a useful tool to determine radiochemical yield, it cannot provide important structural information about the antibody conjugates, and merely designates whether the [^{225}Ac]Ac^{III} is incorporated into the antibody. The immunoreactive fraction of the heated [^{225}Ac]Ac(DOTA-NCS-hG250) construct was 90.1% for SKRC-52 cells. Although [^{225}Ac]Ac(DOTA-NCS-hG250) may recognise the CAIX antigen, the tertiary structure of the antibody was likely affected by high temperatures. These temperatures are not compatible with monoclonal antibodies.

Table 8: Radiochemical yield of [^{225}Ac]Ac(DOTA-NCS-hG250) when heated to 60°C.

Time (mins)	[^{225}Ac]Ac(DOTA-NCS-hG250)
15	89.2
30	98.0
60	99.3
180	91.4

4.3.6 [^{225}Ac]Ac(MacropaSq-hG250) is Stable in Human Serum

Serum stability challenge assays were undertaken to compare the kinetic inertness of [^{225}Ac]Ac(MacropaSq-hG250), [^{225}Ac]Ac(MacropaSq-hG250-FcRn) and [^{225}Ac]Ac(DOTA-NCS-hG250) complexes when challenged with an excess of endogenous metal-binding proteins. To achieve a quantitative radiochemical yield of [^{225}Ac]Ac(DOTA-NCS-hG250), the construct was heated to 60°C. All three constructs exhibited radiochemical yields > 99 % at day 0 and were incubated in human serum (Sigma Aldrich) at 37 °C. Samples were analysed by radioTLC (50 mM EDTA mobile phase). When H_4EDTA is in a large excess, any [^{225}Ac]Ac^{III} that has been sequestered by human serum is transchelated by H_4EDTA. The [^{225}Ac]Ac(EDTA) complex travels with the solvent front of the mobile phase (R_f = 1). Both the [^{225}Ac]Ac(MacropaSq-hG250) and [^{225}Ac]Ac(MacropaSq-hG250-FcRn) antibodies retained stability after two days (99.4% and 99.6%). In contrast, 93.9% of the [^{225}Ac]Ac(DOTA-NCS-hG250) complex remained intact after two days. After seven days at 37 °C, 97.8 and 99.5% of the [^{225}Ac]Ac(MacropaSq-hG250) complexes remained intact. The RCY of [^{225}Ac]Ac(DOTA-NCS-hG250) decreased to 89.6% (Figure 66).

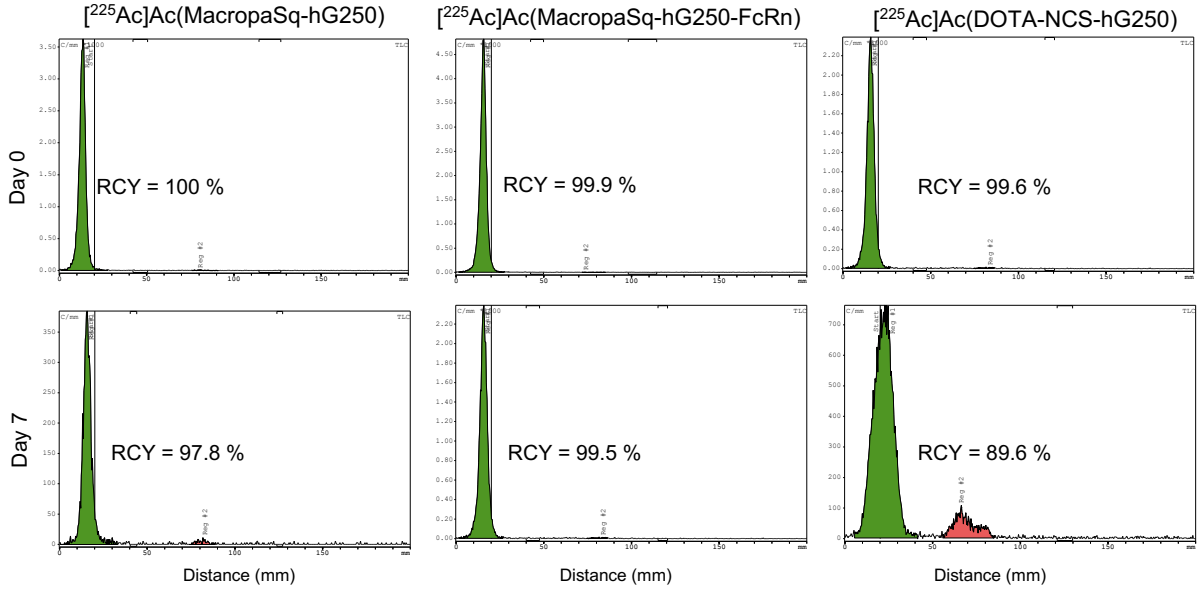

Figure 66: RadioTLC showing radiochemical yield of [^{225}Ac]Ac(MacropaSq-hG250), [^{225}Ac]Ac(MacropaSq-hG250-FcRn) and [^{225}Ac]Ac(DOTA-NCS-hG250) when incubated in human serum at at 37°C over seven days.

The requisite high temperatures and long reaction times needed for radiolabelling [^{225}Ac]Ac^{III} with DOTA show that it is not an ideal chelator, especially for antibody conjugations. The conjugates [^{225}Ac]Ac(MacropaSq-hG250) and [^{225}Ac]Ac(MacropaSq-hG250-FcRn) were more stable in biologically relevant conditions such as human serum when compared to [^{225}Ac]Ac(DOTA-NCS-hG250). After 7 days, more than 97.8% and 99.5% of the actinium remained complexed to H_2MacropaSq conjugated antibodies. The high stability, in combination with the ease of room temperature radiolabelling of H_2MacropaSq, make this chelator ideal for future *in vitro* applications.

4.3.7 [^{225}Ac]Ac(MacropaSq-hG250) and [^{225}Ac]Ac(MacropaSq-hG250-FcRn) Reduce the Viability of SKRC-52 cells

Prior to conducting *in vivo* studies, it is imperative to perform *in vitro* experiments that aim to assess the toxicity of the newly developed conjugates, [^{225}Ac]Ac(MacropaSq-hG250) and [^{225}Ac]Ac(MacropaSq-hG250-FcRn). These experiments allow us to make predictions about the behaviour of these radioimmunoconjugates in more complex biological systems and have significant value in preclinical research. The colorimetric-based MTS assay is derived from the 3-(4,5-dimethylthiazol-2-yl)-5-(3-carboxymethoxyphenyl)-2-(4-sulfophenyl)-2H- tetrazolium compound. Viable cells have the ability to enzymatically reduce the MTS tetrazolium compound, (Figure 67, a) which results in the production of a soluble formazan dye, which can be measured spectrophotometrically, λ = 490 nm (Figure 67, b).

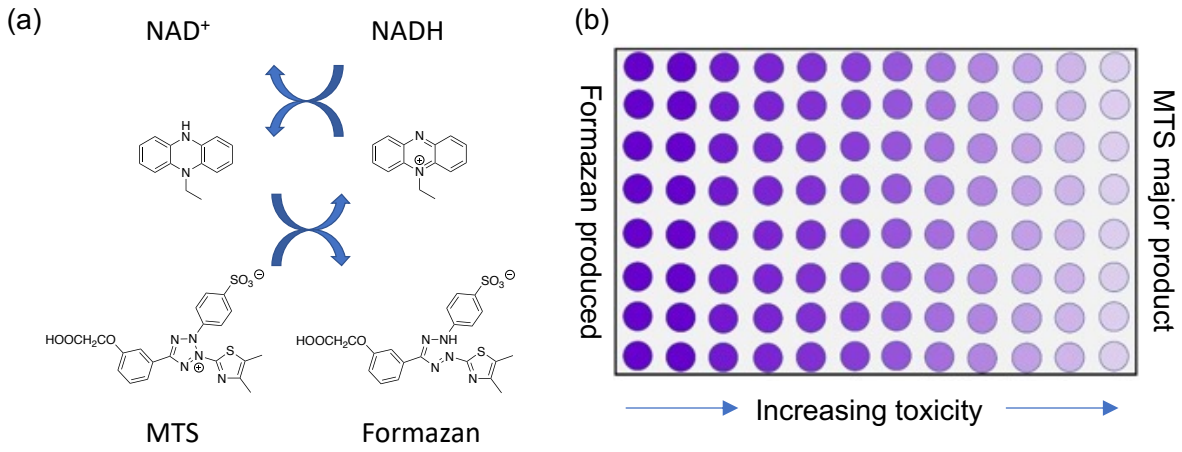

Figure 67: (a) The enzymatic reduction of MTS to Formazan in the presence of living cells, (b) the formazan product is detected colourimetrically (λ = 490 nm).

The MTS assay was used to probe the viability of SKRC-52 cancer cells after exposure to two [^{225}Ac]Ac(MacropaSq-hG250) antibodies. The isotype control, [^{225}Ac]Ac-MacropaSq-IgG was labelled using the same protocol to investigate the effect of non-specific antibody binding. SKRC-52 cells were also exposed to the same activities of 'uncomplexed' [^{225}Ac]Ac^{III} to probe the effect that the radionuclide alone has on overall cell viability (Figure 68). The cell viability, which is determined spectroscopically (n = 3), is measured at decreasing antibody and radioactivity concentrations. The radiolabelling of the antibody conjugates was achieved with a ratio of 1 μg of conjugate for 1 μCi (37 kBq) of actinium-225. Therefore, the antibody concentration (μg/mL) is equivalent to the radioactivity (1 μCi/mL) on the x-axis of the graph. This is possible when the specific activity is 1 μCi/μg of antibody. Therefore, microcuries are used instead of kilobecquerels so that antibody concentration and radioactivity concentration can be plotted on the same graph.

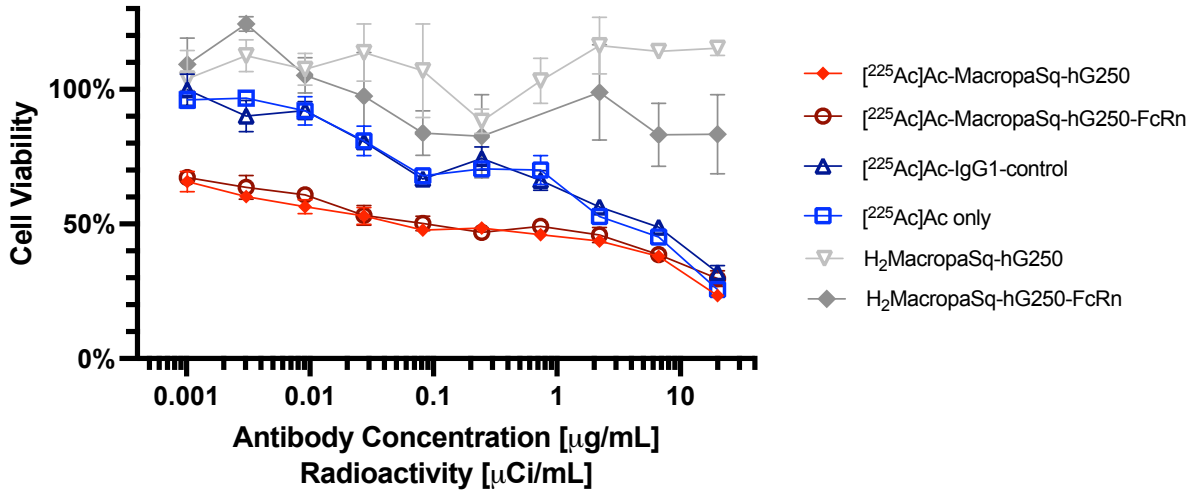

Figure 68: Effect on viability of SKRC-52 cells following incubation with increasing dose of [^{225}Ac]Ac(MacropaSq-hG250), [^{225}Ac]Ac(MacropaSq-hG250-FcRn) as determined by MTS assay.

The highly cytotoxic nature of all [^{225}Ac]Ac^{III} samples is immediately apparent. At the highest concentration of antibody (20 μg/mL, on the right of the graph), and thus highest radioactivity in the samples (20 μCi/mL), only 23.4 % and 32.0 % of SKRC-52 cells are still viable when incubated with [^{225}Ac]Ac(MacropaSq-hG250) and [^{225}Ac]Ac(MacropaSq-hG250-FcRn), respectively. At the same concentration, the [^{225}Ac]Ac(MacropaSq-IgG1) control is comparable, decreasing overall cell viability to 25.7 %. Both [^{225}Ac]Ac(MacropaSq-hG250) antibodies show comparable binding to SKRC-52 cells, as shown in the analysis of the immunoreactive fraction and flow cytometry. Therefore, it was expected that the radioimmunoconjugates would display a similar level of cytotoxicity, which is evident upon comparison of the data.

Interestingly, both the isotype control and uncomplexed [^{225}Ac]Ac^{III} show very similar toxicity towards SKRC-52 cells. Both are binding through 'non-specific' binding and killing the cells. The total volume of each sample (100 μL) is small enough that [^{225}Ac]Ac^{III} is in proximity to the SKRC-52 cells for the entire incubation time whether it is bound or not. The α-emissions from [^{225}Ac]Ac^{III} have a short path length and typically only travel 40 – 90 μm in biological tissue.[3] The decrease in cell viability after exposure to the non-specific controls,

[^{225}Ac]Ac(MacropaSq-IgG1) and [^{225}Ac]Ac^{III}, is caused by non-targeted alpha emissions. This highlights the cytotoxicity of free, circulating [^{225}Ac]Ac^{III}. This assay limitation may underestimate the effect of conjugating actinium-225 to a high-affinity biological target, such as an antibody.

In an MTS assay, the analysis of cold controls, H_2MacropaSq-hG250 and hG250-FcRn, can be challenging, as these controls should not affect the overall cell viability, and therefore, lead to the highest levels of formazan. Consequently, the resultant absorbance levels are the highest in these samples, leading to larger errors and calculated cell viability that may exceed 100 %. This phenomenon is an inherent limitation of colourimetric-based assays. In general, there is no dose-dependent reduction in cell viability when SKRC-52 cells are incubated with hG250 and hG250-FcRn for four days.

This assay is most insightful when SKRC-52 cells are incubated with the lowest concentrations of [^{225}Ac]Ac-MacropaSq-hG250. The results highlight the pronounced impact on cell viability when antibody concentration is 1.01 ng/ mL, and radioactivity in the sample is merely 37.4 Bq/ mL. At these concentrations, the radioactive controls have an overall viability ranging from 96.2% when the cells are exposed to unlabelled [^{225}Ac]Ac^{III}, and 99.9% for [^{225}Ac]Ac(MacropaSq-IgG1). When cells were incubated with parental antibodies hG250 and hG250-FcRn, they had a viability of 103.9% and 109.4%, respectively. In contrast, [^{225}Ac]Ac(MacropaSq-hG250) reduced the overall cell viability to 65.8%. This is a remarkable demonstration of the incredible cytotoxicity of these α-emitting radioimmunoconjugates. At these exceedingly low concentrations, we can see how using a biological targeting vector directed at these cancer cells can have an enormous impact on delivering activity to the cells. [^{225}Ac]Ac(MacropaSq-hG250) is internalised over four days,[270] presumably leading to the internalisation and retention of the radionuclide where the short-range, high-energy emissions

can cause irreparable damage to the cell. Only 3.7 Bq of radioactivity can reduce the overall cell survival by greater than 30 %. This is promising for further *in vivo* studies.

Individual cell lines have different degrees of radiosensitivity toward α radiation. In the case of SKRC-52 cells derived from renal cell carcinoma, [^{225}Ac]Ac(MacropaSq-hG250) and [^{225}Ac]Ac(MacropaSq-hG250-FcRn) specifically kill these cancer cells at becquerel levels *in vitro.*

4.3.8 [^{225}Ac]Ac(MacropaSq-hG250) Inhibits the Ability of SKRC-52 Cells to Form New Colonies

The effect of ionising radiation on the ability of SKRC-52 cells to grow colonies was investigated *in vitro*. This was a preliminary investigation into the effect of the α-emissions on clonogenic survival and a measure of cell reproductive death after treatment with ionising radiation. SKRC-52 cells were incubated with increasing amounts of [^{225}Ac]Ac(MacropaSq-hG250) (0, 0.05, 0.5, 5, and 50 kBq/mL) for 24 hours (Figure 69, a). Samples were then incubated at 37 °C for 12 days, and media was changed every 2 days to assess the ability of SKRC-52 cells to undergo cell division after being exposed to various doses of ionising radiation. This is a model to investigate the effect [^{225}Ac]Ac(MacropaSq-hG250) has on the ability of cancer cells to proliferate. The high cytotoxicity of the antibody construct toward SKRC-52 is immediately apparent. A colony is classified as having greater than 50 cells. [271, 272] The addition of all activity levels (0.05 – 50 kBq / mL) significantly impacts colony formation compared to the untreated control.

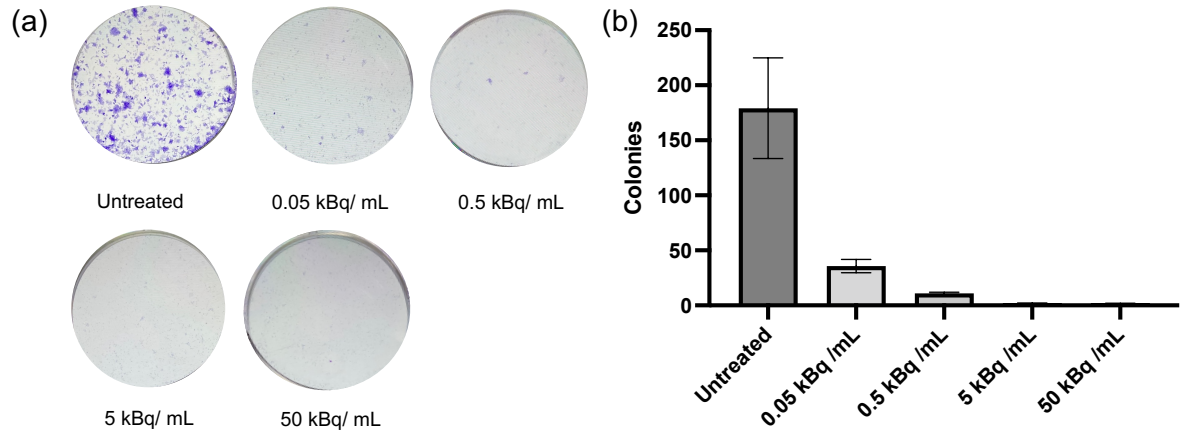

Figure 69: (a) Clonogenic assay performed in six-well plates, with clones produced by SKRC-52 cells. Representative image (n = 6) of colonies formed after seeding 5000 cells, with increasing activity of [^{225}Ac]Ac(MacropaSq-hG250), colonies were stained with crystal violet; (b) a number of colonies incubated for 24 hours with increasing radioactivity of [^{225}Ac]Ac(MacropaSq-hG250) (n = 3).

SKRC-52 cells that were not exposed to [^{225}Ac]Ac(MacropaSq-hG250) grew on average 180 colonies in two weeks (Figure 69, b). Incubation of [^{225}Ac]Ac(MacropaSq-hG250) at a concentration of 0.05 kBq/ mL, the lowest concentration of radioactivity, reduced the number of colonies to 35, an 80% reduction in number of colonies formed. This was significantly reduced with an increase in [^{225}Ac]Ac(MacropaSq-hG250), with the cohorts exposed to 0.5 kBq/ mL, 5 kBq/ mL, and 50 kBq/ mL only having 12, 2, and 1 colonies post-irradiation respectively.

4.3.9 [^{225}Ac]Ac(MacropaSq-hG250) Accumulates in SKRC-52 Tumours in Evaluation of Biodistribution

Understanding the biodistribution of [^{225}Ac]Ac(MacropaSq-hG250) is crucial for maximising therapeutic efficacy and understanding any potential adverse effects. Biodistribution studies provide valuable insight into the distribution and accumulation of the radiopharmaceuticals within different tissues and organs. This makes it possible to evaluate the risks associated with radiation exposure to organs that may be particularly radiosensitive, such as kidneys, and asses the risk of chronic exposure.

The biodistribution of [^{225}Ac]Ac(MacropaSq-hG250) in mice bearing SKRC-52 renal cell carcinoma tumour xenografts was measured over seven days (Figure 70) and is presented

in terms of percentage of injected activity per gram of tissue (% IA g^{-1}). Mice were injected with 14.8 kBq of [^{225}Ac]Ac(MacropaSq-hG250) supplemented with 30 μg of hG250 or 14.8 kBq [^{225}Ac]Ac(MacropaSq-IgG1) (with 30 μg of IgG1). As monoclonal antibodies exhibit biphasic pharmacokinetic behaviour,[231] they are both rapidly distributed throughout the vasculature and interstitial space and can remain in the blood pool for a significant period before being eliminated. The enduring circulation is in part due to the neonatal Fc receptors that prevent antibody catabolism.[231]

As such, the highest uptake is in the blood pool (41.6 ± 5.0 % IA g^{-1}) three hours post-injection (p.i.). Over seven days, the radioactivity in the blood steadily decreased from 23.3 ± 4.3 % IA g^{-1}on day three to 14.8 ± 3.3 % IA g^{-1} on day seven. Highly vascularised organs, such as the lungs and heart, also experienced high uptake of the radiotracer at early time points. The heart uptake decreased from 8.7 ± 1.0 % IA g^{-1} 3 hours p.i. to 5.4 ± 0.08 % IA g^{-1} on day 1. The lungs experienced a similar decrease from 16.4 ± 2.4 % IA g^{-1} 3 hours p.i. to 10.9 ± 1.5 % IA g^{-1} on day 1. There was 2.6 ± 1.3 % IA g^{-1} and 6.6 ± 1.7 % IA g^{-1} in the heart and lungs, respectively, on day seven.

The long circulation of [^{225}Ac]Ac(MacropaSq-hG250) in the blood pool is coupled with a steady increase in localisation of the radiopharmaceutical in the SKRC-52 tumour xenografts. The tumour uptake was 5.3 ± 3.4 % IA g^{-1} 3 hours p.i. The tumour uptake increased over the seven days, with 21.2 ± 6.5 % I A g^{-1} on day three and 21.4 ± 10.1 % IA g^{-1} on day seven. The SKRC-52 tumours exhibited the highest uptake of [^{225}Ac]Ac(MacropaSq-hG250) compared with any other tissue on day seven.

The degree of kidney uptake was highest 3 hours p.i. (12.1 ± 2.1 % IA g^{-1}) and decreased over seven days with a final uptake of 7.0 ± 1.2 % IA g^{-1}. The potential for nephrotoxicity is a particularly important consideration.[53, 56, 57] Similarly, the spleen has persistent uptake throughout the biodistribution study; it increased to a maximum of 12.9 ± 2.6

% IA g^{-1} on day three before there is a decline in the radioactivity in the organ to 8.3 ± 1.8 % IA g^{-1} on day seven. Three days post-injection, the lowest uptake was observed in the small intestine (2.5 ± 0.2 % IA g^{-1}), colon (2.8 ± 0.4 % IA g^{-1}), muscle (1.7 ± 0.3 % IA g^{-1}), bone (3.5 ± 0.7 % IA g^{-1}), and skin (5.9 ± 0.5 % IA g^{-1}).

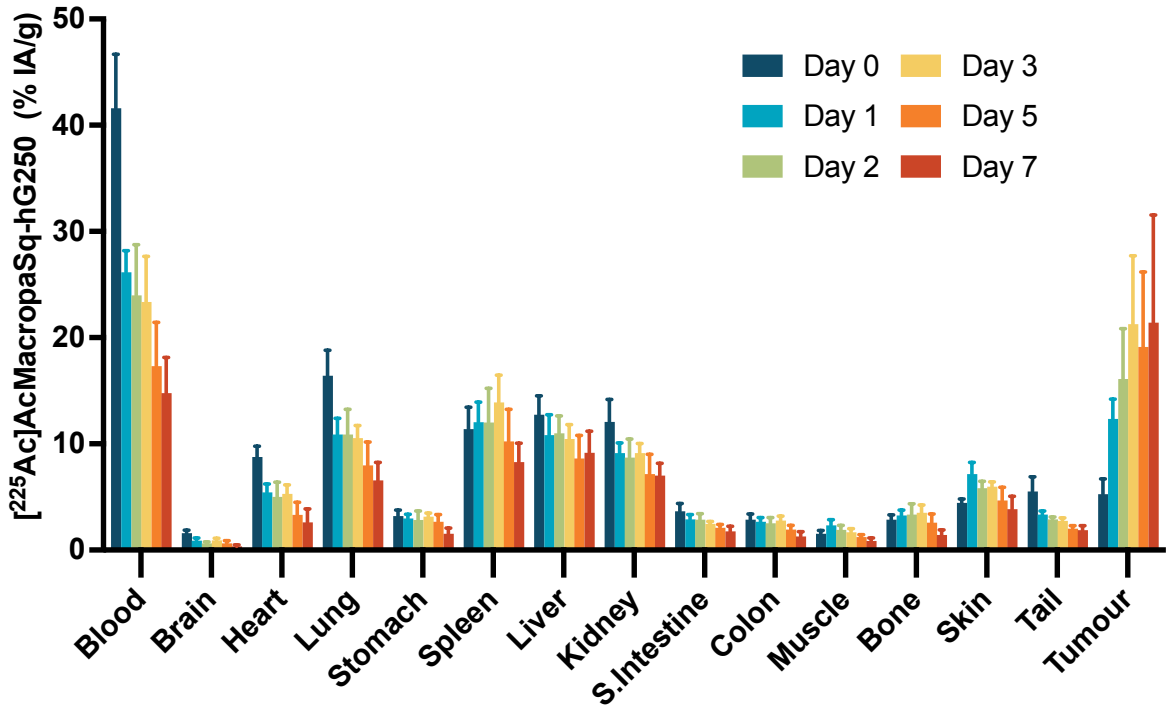

Figure 70: Biodistribution in BALB/c nude mice bearing SKRC-52 tumours (n = 5). Mice were injected with 14.8 kBq of [^{225}Ac]Ac(MacropaSq-hG250) and sacrificed at Days 0, 1, 2, 3, 5, 7.

Non-specific binding and non-specific radiation effects were assessed using an isotype control. Using the same SKRC-52 tumour xenograft model, the uptake of [^{225}Ac]Ac(MacropaSq-IgG1) was investigated 3 hours p.i. and on day three and compared to the uptake of [^{225}Ac]Ac(MacropaSq-hG250) (Figure 71). Interestingly, there was a difference in the overall blood pool distribution between [^{225}Ac]Ac(MacropaSq-hG250) and [^{225}Ac]Ac(MacropaSq-IgG1). The radioactivity in the blood of mice injected with 14.8 kBq of [^{225}Ac]Ac(MacropaSq-IgG1) was 31.3 ± 3.4 % IA g^{-1} three hours p.i. The uptake in the blood rapidly cleared and had reduced to 2.1 ± 1.3 % IA g^{-1} on day three.

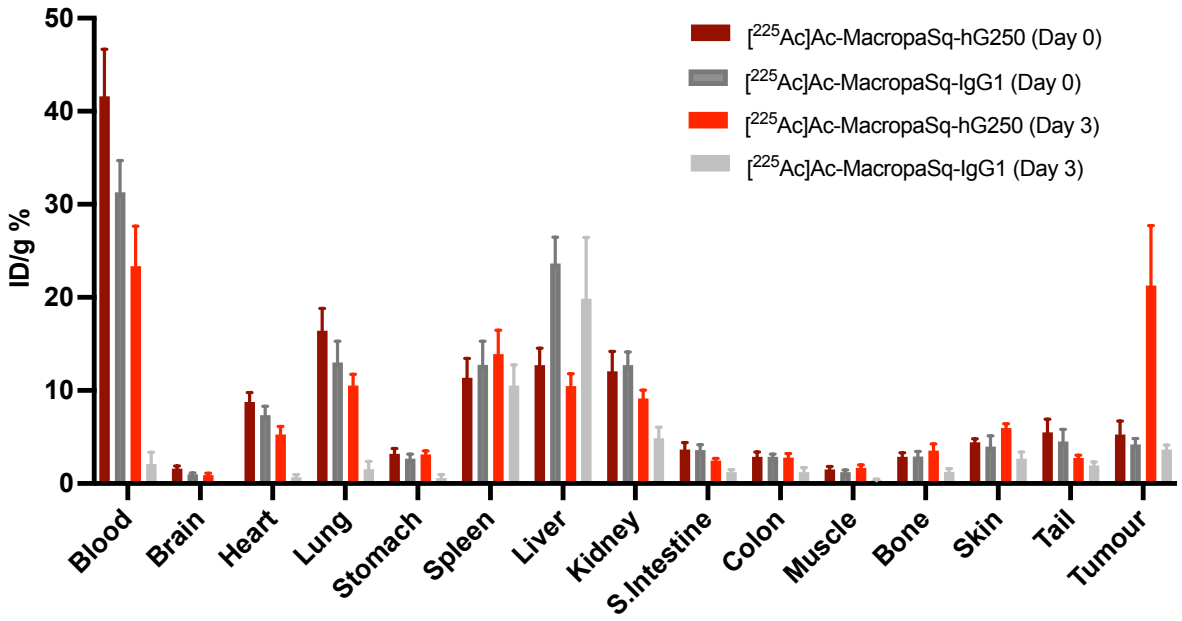

Figure 71: Biodistribution in Balb/c nude mice bearing SKRC-52 tumours (n = 5). Mice were injected with 14.8 kBq (0.4 µCi) of [^{225}Ac]Ac(MacropaSq-IgG1) control and sacrificed at Days 0 and 3.

Another difference between the two antibody constructs was the uptake of radioactivity in the liver. High levels of liver uptake in monoclonal antibodies may be due to IgG processing in the liver or suggest that the antibody had aggregated. Mice that were injected with [^{225}Ac]Ac(MacropaSq-IgG1) exhibited an uptake of 19.8 ± 6.6 % IA g^{-1} on day three. This was almost double the liver uptake in mice that had received [^{225}Ac]Ac(MacropaSq-hG250), which was 10.5 ± 1.3 % IA g^{-1} on the same day. Among the organs with comparable uptake was the spleen (10.5 ± 2.2 % IA g^{-1} on day three). When comparing the two antibody constructs by their whole body distribution, there is lower uptake of [^{225}Ac]Ac(MacropaSq-IgG1) in almost all organs compared to [^{225}Ac]Ac(MacropaSq-hG250). This suggests faster excretion of the isotype control, potentially through the liver. The tumour uptake of the isotype control 3 hours p.i. was 4.2 ± 0.6 % IA g^{-1}. On day three, the tumour uptake of [^{225}Ac]Ac(MacropaSq-IgG1) had reduced to 3.6 ± 0.5 % IA g^{-1}, demonstrating that the antibody control does not appear to have a sustained or specific affinity for the SKRC-52 tumours.

The biodistribution of [^{225}Ac]Ac(MacropaSq-hG250) in different organs is summarised as ratios based on samples collected on day seven p.i. (Table 9). The tumour-to-

blood ratio of [^{225}Ac]Ac(MacropaSq-hG250) was 1.5:1. This can be attributed to the long blood circulation time of [^{225}Ac]Ac(MacropaSq-hG250). The tumour-to-liver ratios showed that [^{225}Ac]Ac(MacropaSq-hG250) had higher tumour uptake with a ratio of 2.3:1. Another metric of radiation localisation in organs of interest is the tumour-to-muscle ratio. [^{225}Ac]Ac(MacropaSq-hG250) had a ratio of 24.6:1. The ratios show high uptake in tumour compared to other organs, indicating a higher likelihood of radiotherapeutic efficacy *in vivo*.

Table 9: Different ratios of [^{225}Ac]Ac(MacropaSq-hG250) in organs of interest at day seven p.i

	Ratio
Tumour: Blood	1.5
Tumour: Liver	2.3
Tumour: Muscle	24.6

The biodistribution of [^{225}Ac]Ac(MacropaSq-hG250) (14.8 kBq) in mice bearing SKRC-52 renal cell carcinoma tumour xenografts showed high uptake in the blood pool, lungs, heart, and spleen at early time points, which gradually decreased over seven days. The highest uptake was observed in the SKRC-52 tumour xenografts with 21.4 ± 10.1 % IA g^{-1} on day seven. The tumour uptake increased throughout the duration of the biodistribution study. The tumour uptake for the IgG-control, [^{225}Ac]Ac(MacropaSq-IgG1) was 3.6 ± 0.5 % IA g^{-1} on day three p.i.

4.3.10 [^{225}Ac]Ac(MacropaSq-hG250) Delays Tumour Growth in Longitudinal Therapy Study

The purpose of this therapy study was to assess the efficacy of the radioimmunoconjugate [^{225}Ac]Ac(MacropaSq-hG250) *in vivo*, and evaluate its ability to selectively target cancers that overexpress the antigen CAIX. These studies provide a foundation for optimising the radioactive dose and building on the understanding of the pharmacokinetic properties and biodistribution of the radioimmunoconjugate. The antitumour effect of the α-emitting radiopharmaceutical, [^{225}Ac]Ac(MacropaSq-hG250), was evaluated in a longitudinal therapy study in the established SKRC-52 tumour xenograft model. Individual tumour volumes of mice

receiving either 14.8 kBq of [^{225}Ac]Ac(MacropaSq-hG250) (with 30 μg of hG250), 14.8 kBq of [^{225}Ac]Ac(MacropaSq-IgG1) (with 30 μg of IgG1) or hG250 only (30 μg) are shown as a function of time (Figure 72, a). The calculated mean tumour volumes across the three cohorts are shown (Figure 72, b). Unlabelled antibodies (hG250 and IgG1) are supplemented in the injection cocktail to reduce non-specific binding due to interactions with neonatal Fc receptors. This generally reduces background as a large excess of unlabelled antibody effectively competes for binding to non-specific targets.

The mean survival time of the isotype control, [^{225}Ac]Ac-MacropaSq-hIgG1 was 17 days p.i. relative to only 10 days for mice that received hG250 (30 μg) alone. The cohort that received a therapeutic dose of [^{225}Ac]Ac(MacropaSq-hG250) (14.8 kBq) experienced significantly longer survival times, and 88 % of the cohort were still alive until 84 days.

On day 84, one mouse in the group receiving [^{225}Ac]Ac(MacropaSq-hG250) was culled as it had reached a tumour volume > 1000 mm^3. Therefore, the cohort's overall tumour volumes were less meaningful after this time, so data presented in Figure 72 are curtailed at this time point. When examining the tumour volumes of the cohort that received [^{225}Ac]Ac(MacropaSq-hG250), 3/5 exhibited a partial response to the treatment. Impressively, 2/5 mice within that cohort experienced a complete response, with tumour volumes unable to be measured in the two mice after day 49 and day 70, respectively.

The investigation into the rate of tumour growth among the three cohorts revealed a notable observation: the administration of [^{225}Ac]Ac(MacropaSq-hG250) (14.8 kBq) resulted in a significant delay in tumour growth. The mean tumour doubling time of mice who received [^{225}Ac]Ac-MacropaSq-hIgG1 was approximately 4 days, or 2.7 days for mice that received hG250 alone. The mean tumour doubling time for the [^{225}Ac]Ac(MacropaSq-hG250) was not achieved in 84 days. Instead, mean tumour doubling of the treatment group occurred at 119 days (total mean volume 264 ± 406 mm^3).

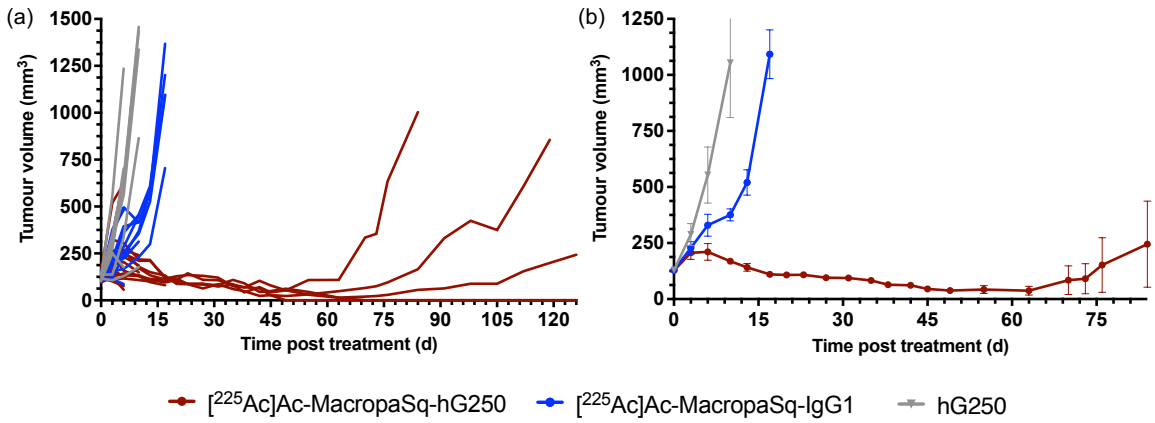

Figure 72: (a) Tumour volume (mm^3) as a function of time post-treatment with [^{225}Ac]Ac(MacropaSq-hG250) (14.8 kBq, 30 µg), [^{225}Ac]Ac(MacropaSq-IgG1) (14.8 kBq, 30 µg) or hG250 (30 µg) in mice with SKRC-52 tumour xenografts.

The Kaplan Meier plot (Figure 73, a) highlights the overall survival of the three cohorts presented as a percentage of survival for the duration of the study. The cohort that received 14.8 kBq of [^{225}Ac]Ac(MacropaSq-hG250) demonstrated an impressive overall survival rate of 88 % throughout the first 84-day study period. Furthermore, 74 % of the cohort remained alive even at 119 days. These findings provide clear evidence that administration of 14.8 kBq of [^{225}Ac]Ac(MacropaSq-hG250) elicits a robust anti-tumour effect without significant off-target toxicity.

Weight loss is a common and often dose-limiting side effect of radiation damage to healthy tissue and indicative of other off-target cytotoxicity.[273] Radiolabelled proteins and peptides primarily affect the liver, kidneys and bone marrow. Ethics approvals advise mice are to be culled when they lose more than 10% of their initial body weight. In this therapy study, there is an initial decline in body weight at early time points in the cohorts that received both radioimmunoconjugates and the parental hG250 antibody alone (Figure 73, b). The most significant difference in initial body weight is at 10 days p.i. for [^{225}Ac]Ac(MacropaSq-hG250), where the body weight drops to 94 % of initial body weight. After day 10, body weight returns to above approximately initial weight levels. Both cohorts of mice that received

[^{225}Ac]AcMacropaSq-hIgG1 and hG250 did not experience significant body weight loss during the remainder of the study (17 days across both groups).

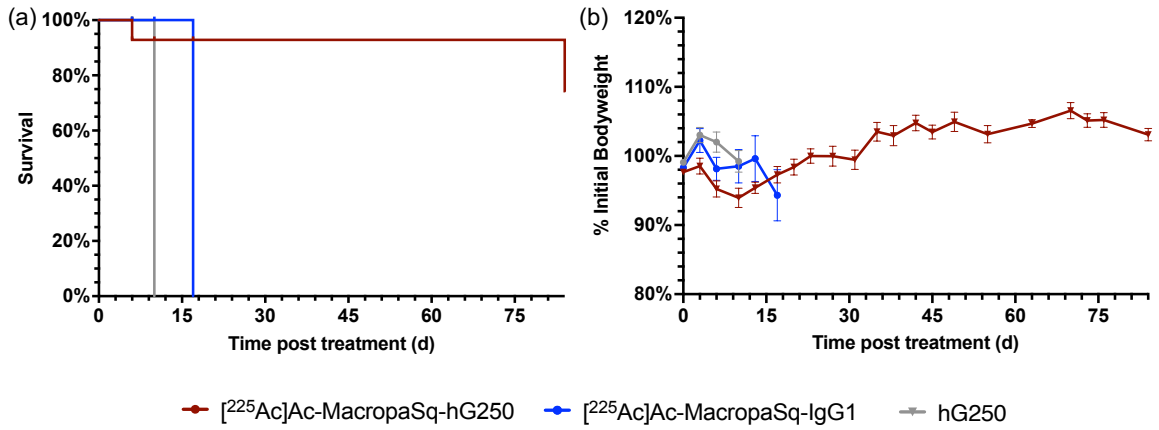

Figure 73: (a) Kaplan Meier plot shows the percentage survival of the cohort as a function of time (days); (b) Percentage body weight change after treatment with [^{225}Ac]Ac(MacropaSq-hG250) (14.8 kBq), [^{225}Ac]AcMacropaSq-hIgG1(14.8 kBq) or hG250(30 µg) over 84 days.

In a separate study using DOTA as a ligand with girentuximab, the complex [^{225}Ac]Ac(DOTA-NCS-hG250) was evaluated by Merkx *et al.*[250] This study showed a sustained delay in tumour growth for cohorts that received either 15, 25 and 50 kBq of [^{225}Ac]Ac(DOTA-NCS-hG250). An investigation of the cytotoxicity of [^{225}Ac]Ac(DOTA-NCS-hG250) showed that there was a dose dependent effect on body weight. In a cohort of non-tumour bearing mice that received 15 kBq, [^{225}Ac]Ac(DOTA-NCS-hG250), 66 % (4/6) mice were culled due to significant weight loss (18.6 ± 3.4%).[250] This significant radiotoxicity and body weight loss raises concerns about the suitability of DOTA as the ligand for [^{225}Ac]Ac^{III}, and warrants further investigation into the degree of potential decomplexation of [^{225}Ac]Ac^{III} from the ligand and the consequent off-target effects. Tumour sections of mice that received either 15 or 25 kBq [^{225}Ac]Ac(DOTA-NCS-hG250), displayed late radiation damage, namely enlarged nuclei, atypical nuclei, and intercellular fibrosis (by hematoxylin and eosin staining). Given that the same antibody, tumour xenograft model and approximately the same dose were used (14.8 kBq vs 15 kBq), it is crucial to determine the extent to which the chelator impacts the overall efficacy of the radioimmunoconjugate. Hematoxylin and eosin staining of

tissue sections collected from the longitudinal study of the antibody conjugate [^{225}Ac]Ac(MacropaSq-hG250) will provide more information of any potential radiation effects, and gauge understanding of the optimal therapeutic dose.

4.3.11 γH2AX Microscopy Determines the Number of Double-Strand Breaks in Actinium-225 Treated Tumour Sections

One notable distinction between conventional β^- radiotherapy and [^{225}Ac]Ac^{III} α therapy is the energy of the particles emitted. The emissions from α particles have a linear energy transfer (LET) of approximately 80 keV/ μm, approximately 400 times greater than β^- particles with a LET in the range of 0.2 keV/ μm. Particle energies of this magnitude are able to cause double-strand breaks in DNA. The LET of α-particles invariably causes more damage to cells in the ionisation path of the α particle. In contrast, emissions from β^- particles typically induce single-strand breaks, which are more 'easily' repaired by various mechanisms in DNA.[274-279]

Eight histones complete the nucleosome with 145 base pairs of DNA. The DNA is tightly packed and held together by these histones, which form chromatin and ensure that DNA transcription cannot occur.[280] There are different types of histones, and they are highly conserved (two of each of H2A, H2B, H3 and H4 which form an octamer; Figure 74, a). When DNA is exposed to ionising radiation, the H2AX histone is phosphorylated at the amino acid residue serine-139 to form γH2AX (Figure 74, b).[280] Serine-139 is four amino acid residues from the C-terminus. This is evolutionarily conserved in organisms from *giardia intestinalis* to humans.[281] The phosphorylation is rapid and occurs within minutes of exposure to ionising radiation and typically reaches a maximal level one hour after irradiation. These foci are proportional to the number of DNA breaks.[282] The phosphorylation of H2AX by kinases such as DNA-dependent kinase and ataxia telangiectasia mutated provide a docking site for enzymes that can repair double-strand breaks in DNA.[283]

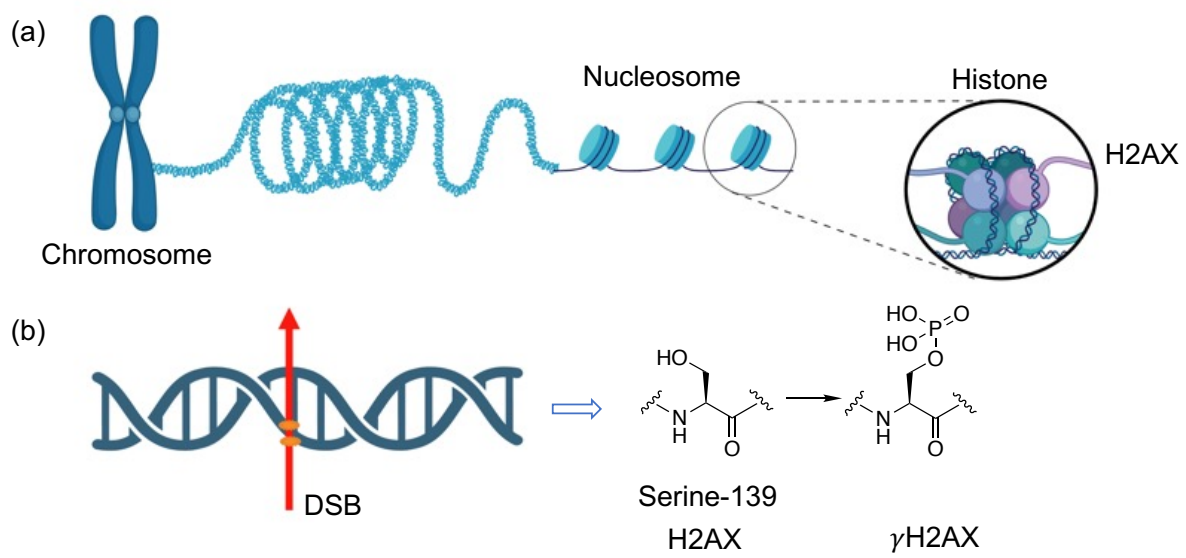

Figure 74: DNA is unravelled, it exists as nucleosomes; 145 base pairs of DNA tightly wrapped around histone proteins. These histones are an octamer of four proteins. One of the proteins is called H2AX; (b) when DNA experiences a double-strand break (DSB), the amino acid residue of H2AX serine-139 is phosphorylated, initiating downstream repair mechanisms.

Due to the signaling of downstream DNA repair factors, the number of foci generally decreases after 24 hours. After this time, the remaining foci presumably represent irreparable double-strand breaks.[283, 284] It is important to quantify the number of double-strand breaks that a radiopharmaceutical can initiate in tumour DNA.[285, 286] Therefore, investigation of the tumours of mice from the longitudinal therapy study would provide insight into the effect of radiation of CAIX positive tumours. Confocal microscopy serves as a valuable tool for realising the impact of radiation on tumours by enabling high-resolution, three-dimensional visualisation of cellular changes within the tumour microenvironment.

Different fluorophore-tagged antibodies and stains provide crucial structural information regarding the overall tumour environment. 4',6-Diamidino-2-phenylindole (DAPI) is a small molecule fluorescent stain that can pass through intact cell membranes and is used to visualise DNA in the nucleus.[287] Upon binding to double-stranded DNA (AT regions), DAPI experiences a 20-fold increase in fluorescence intensity,[288] thus it is used as a nuclear counterstain. Actins are globular proteins that play an essential function in maintaining cell structure.[289] They exist in a monomeric form as G-actin (globular), and polymerise under

physiological conditions into double-helical filaments.[290] The γH2AX foci can be visualized with a commercially available rabbit anti-γH2AX primary antibody raised against phosphorylated serine-134. Incubation of a rat anti-F-actin antibody with tumour sections provides an excellent marker of cell structure. Addition of a goat anti-rat Alexa Fluor 647 fluorescently labelled secondary antibody will then allow for the visualisation of the actin microfilaments. This prevents inaccurate results as there is no cross-reactivity between secondary antibodies used to fluorescently visualise F-actin compared to γH2AX. It is important to ensure no species cross-reactivity, therefore, exclusive rabbit and rat antibodies were used with goat secondary antibodies.

Images were obtained using confocal microscopy of SKRC-52 tumours harvested on day eight post-treatment with either [^{225}Ac]Ac-MacropaSq-hG250, [^{225}Ac]Ac-MacropaSq-IgG1 isotype control or cold hG250 (Figure 75). Three different fluorescent signals associated with the three different fluorophores are used to probe the cellular nucleus (λ_{em} 405 nm), F-actin microfilaments (λ_{em} 648 nm) and the presence of γH2AX phosphorylation (λ_{em} 568 nm) on formalin-fixed, paraffin-embedded tumour sections. Merging the fluorescence signals provides a more complete view of the overall cellular environment after exposure to either 14.8 kBq of ionising radiation or non-radioactive monoclonal antibody alone (30 μg). Examination of the tumour cells exposed to a non-targeted isotype control is also important to evaluate non-specific radiation damage. The investigation of the biodistribution of [^{225}Ac]Ac-MacropaSq-IgG1 determined that this control did not specifically accumulate and internalise within the tumours.

When examining the efficacy of this targeted alpha therapy, the γH2AX stain emerges as a pivotal immunofluorescence staining technique. The γH2AX stain (green) clearly shows the foci, which are indicative of a double-strand break. Tumour sections treated with 14.8 kBq

of [^{225}Ac]Ac(MacropaSq-hG250) show significant DNA damage, evident by the presence of many γH2AX foci, including clustered DNA damage (Figure 75, top panel).

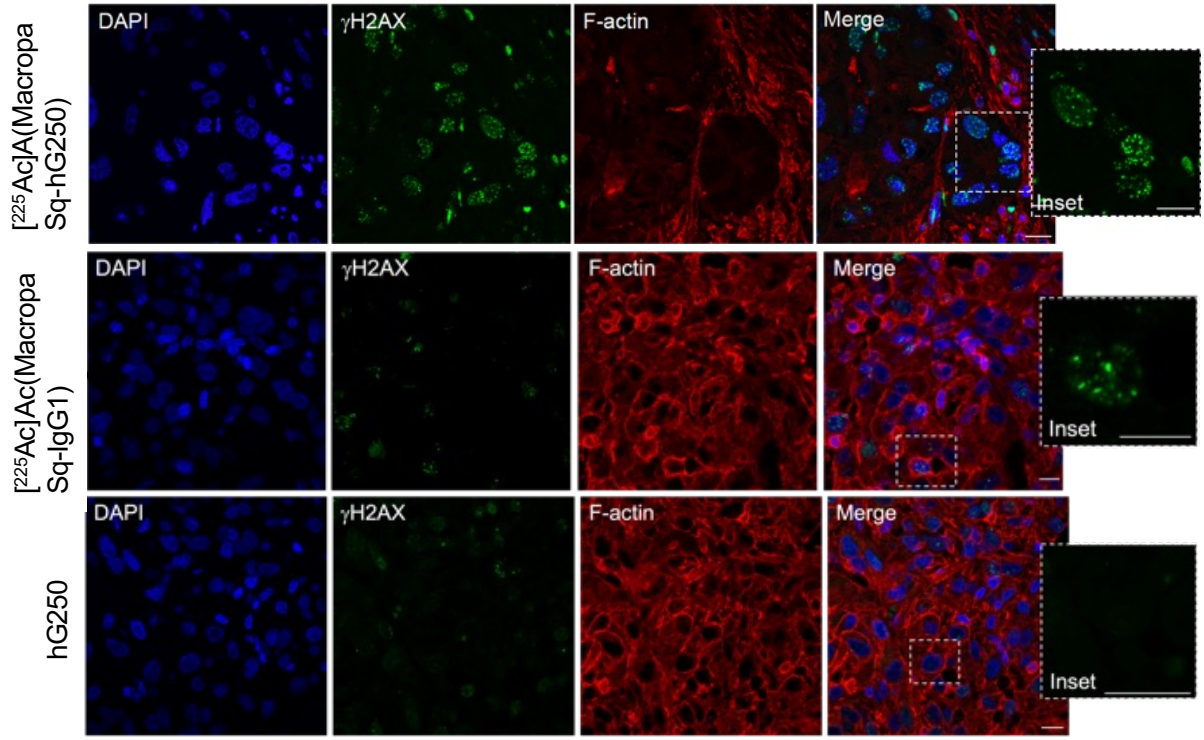

Figure 75: [^{225}Ac]Ac(MacropaSq-G250) induces double-strand DNA breaks in an SKRC-52 tumour model. Confocal microscopy of SKRC-52 tumours harvested on day 8 post-treatment were stained with DAPI (nuclei – blue) and immunostained with antibodies against γH2AX (ds DNA breaks – green) and F-actin (actin – red).

Interestingly, the analysis of tumour sections of mice treated with [^{225}Ac]Ac(MacropaSq-IgG1) also reveals the persistence of γH2AX foci, indicating a level of DNA damage. The observed foci serve as a clear demonstration of the cytotoxicity associated with α particles *in vivo* (Figure 75, middle panel). In this control group, although actinium-225 was not specifically targeted to the CAIX-positive tumour xenografts, there is still irreparable damage at a cellular level. Therefore, quantification of the number of foci per nuclei will allow us to draw conclusions regarding the relative cytotoxicity of the two treatment groups that received actinium-225-based radioimmunoconjugate.

Evaluation of the tumour sections of the mice that received the unlabelled hG250 is visibly different from the tumour sections which were exposed to [^{225}Ac]Ac(MacropaSq-

hG250), or [^{225}Ac]Ac-(MacropaSq-IgG1). Nevertheless, there are a few foci present in tumour sections of mice that were treated with hG250 (Figure 75, bottom panel). This is presumably due to the double-strand breaks that occur as part of the natural cell cycle and apoptosis pathways.[291] Still, the number of foci present in the cold control is visibly fewer than when the tumour xenografts were exposed to an ionising dose of radiation.

Upon examination, the cell morphology of the tumour sections treated with [^{225}Ac]Ac(MacropaSq-hG250) is visibly different (Figure 75, top panel). There are fewer cells, as shown by nuclear counterstaining by DAPI, in tumours of mice eight days after administration of [^{225}Ac]Ac(MacropaSq-hG250). This is a sign that the antibody constructs are killing the SKRC-52 cells. Some smaller nuclei are also present. These result from infiltration of the mice cells into the tumour xenograft. There is also a change in microfilament structure shown by F-actin staining. As the microfilament structure is dynamic and changes with the morphology of the cells, it appears there has been a change in the overall structure of the tumours.

The overall morphology of the cells visualised by the F-actin staining was compared to the tumour volumes from the therapy study. The tumour sections were collected on day 8 post-injection of equal doses of [^{225}Ac]Ac(MacropaSq-hG250), [^{225}Ac]Ac(MacropaSq-IgG1) isotype control or cold hG250 only. Tumour volumes were not measured on day 8 of the therapy study. Instead, it is possible to make comparisons with the tumour volumes as determined from day 10 of the therapy study. The tumour volumes at day 10 of [^{225}Ac]Ac(MacropaSq-hG250) (169.0 ± 42.6 mm^3), [^{225}Ac]Ac-MacropaSq-IgG1 (375.6 ± 76.2 mm^3) and hG250 (1054.1 ± 546.3 mm^3) reflect the significant differences in tumour growth. This is mirrored in the confocal microscopy by the number of cells stained by DAPI and the overall cell architecture visualised by F-actin. Previous research (Dr Laura Ossellame) with γH2AX staining showed that when collecting samples after day 8, the tumour in the cohort that

received [^{225}Ac]Ac(MacropaSq-hG250) were often too small, with few remaining tumour cells available for confocal microscopy. Complex clustered lesions surrounding DNA breaks are evident in several nuclei exposed to [^{225}Ac]Ac(MacropaSq-hG250). These γH2AX foci are difficult to quantify and are not included in the quantitative analysis and comparison between the three treatment groups.[284, 292]

The number of foci per cell nucleus (across a minimum of 36 nuclei for hG250 and [^{225}Ac]Ac(MacropaSq-IgG1) and a minimum of 55 nuclei for [^{225}Ac]Ac(MacropaSq-hG250) was significantly higher in the cohort that received 14.8 kBq of [^{225}Ac]Ac(MacropaSq-hG250) when compared to the cohort that received 14.8 kBq of the [^{225}Ac]Ac(MacropaSq-IgG1) isotype control or unlabelled hG250 (30 µg) (Figure 76). The treatment group had an average of 14.1 ± 1.6 foci per cell nucleus, and the isotype control and cold control had an average of 2.4 ± 0.5 and 5.2 ± 0.8 foci per cell nucleus, respectively. A one-way analysis of variance (ANOVA) determined the difference in both the hG250 and [^{225}Ac]Ac(MacropaSq-hG250) to be statistically significant ($p \leq 0.0001$). The same is true when comparing [^{225}Ac]Ac(MacropaSq-IgG1) ($p \leq 0.0001$).

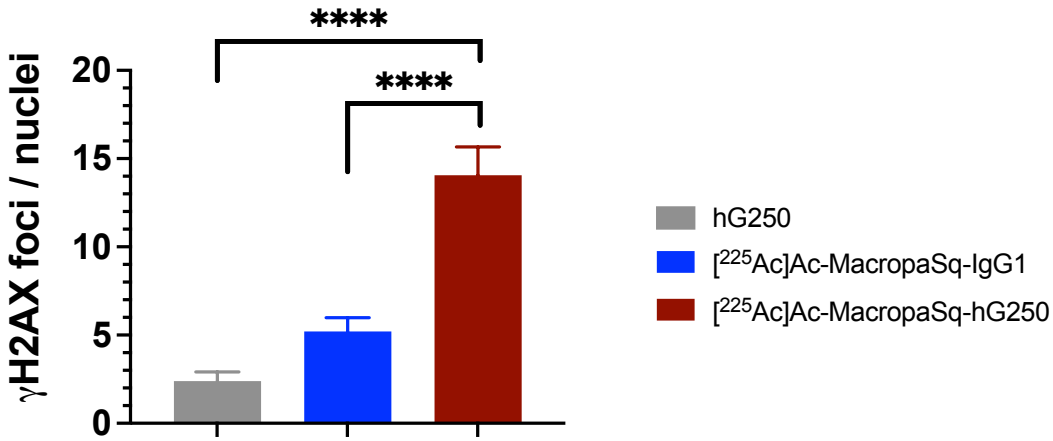

Figure 76: [^{225}Ac]Ac(MacropaSq-hG250) induces double-strand DNA breaks in an SKRC-52 tumour model. Average foci per nuclei from each treatment group (mean ± SEM). Nuclei quantitated for [^{225}Ac]Ac(MacropaSq-hG250) = ≥55. Nuclei quantitated for [^{225}Ac]Ac-MacropaSq-IgG1 and hG250 = ≥36 ****p= ≤0.0001.

γH2AX is a universal marker for detecting double-stranded breaks.[291] Injection of 14.8 kBq of [^{225}Ac]Ac(MacropaSq-hG250) elicited a significant cellular response, as visualised by confocal microscopy. Mice that received 14.8 kBq of [^{225}Ac]Ac(MacropaSq-hG250) were observed to have an average of 14.1 ± 1.6 double-stranded breaks in DNA per cell nuclei. The fact that these breaks were still visualised by γH2AX staining eight days post-injection reflects that these double-strand breaks are likely to be unrepairable. High LET α particles exhibit an extraordinary degree of efficacy. Only 1 – 4 particles are necessary to traverse a nucleus and induce cell death.[27] This damage to SKRC-52 tumour xenografts reflects a 'catastrophic' amount of damage caused by the ionising α radiation delivered within the tumour microenvironment. The evaluation of the therapeutic efficacy of [^{225}Ac]Ac(MacropaSq-hG250) has clearly demonstrated the highly cytotoxic nature of the radioimmunoconjugate.

4.4 Concluding Remarks

The antibody conjugate, H_2MacropaSq-hG250 outlined in Chapter Three, has been radiolabelled with [^{225}Ac]Ac^{III}, to give [^{225}Ac]Ac(MacropaSq-hG250) in quantitative radiochemical yield with a specific activity of 37 MBq/mg. Radiolabelling is rapid and achieved at room temperature in five minutes. Comparison of the conjugate [^{225}Ac]Ac(MacropaSq-hG250) with [^{225}Ac]Ac(DOTA-NCS-hG250) demonstrated that [^{225}Ac]Ac(MacropaSq-hG250) outperforms [^{225}Ac]Ac(DOTA-NCS-hG250) in terms of radiochemical yield (> 99.9 % vs 12.6 %), conjugate concentration in the reaction (10^{-7} M vs 10^{-5} M) and overall radiolabelling time (5 minutes vs 60 minutes) in the same buffer and pH. [^{225}Ac]Ac(MacropaSq-hG250) was shown to be significantly potent against SKRC-52 cell which overexpress CAIX i*n vitro*. Exposure of SKRC-52 cells to [^{225}Ac]Ac(MacropaSq-hG250) significantly reduced the proliferative ability of cells.

An evaluation of the therapeutic efficacy of [^{225}Ac]Ac(MacropaSq-hG250) showed that administration of 14.8 kBq of [^{225}Ac]Ac(MacropaSq-hG250) elicited a strong anti-tumour response in CAIX-positive tumour-bearing mice (SKRC-52). This tumour model was aggressive, and all mice in control cohorts that received an isotype control (14.8 kBq of [^{225}Ac]Ac(MacropaSq-IgG1)) or hG250 alone reached their ethical endpoint after 17 or 10 days, respectively. The radioimmunoconjugate [^{225}Ac]Ac(MacropaSq-hG250) not only delayed the growth of SKRC-52 tumours and increased the mean survival of the mice, but there was no cytotoxicity as measured by excessive body weight loss (> 10%) throughout the study. These promising results highlight the possibility of treating cancer with alpha-emitting actinium-225. Importantly, the protocols and radiochemistry developed in this chapter have the potential to be applied to any validated antibody where targeted radioimmunotherapy with α-emitters may prove particularly advantageous. This underscores the broad scope and potential significance of the radiochemistry developed in this research.

4.5 Experimental

4.5.1 Instrumentation

Radio-radioTLC were analysed using a Raytest Rita-Star TLC scanner. Non-radioactive SE-HPLC was performed on an Agilent 1260 Infinity II HPLC system fitted with a Phenomenex BioSep LC column (5 μm, 300 x 7.8 mm, 290Å), or a Phenomenex Yarra column (3 μm, 300 x 4.6 mm, 290Å) 0.2M phosphate buffer, pH 6.8 as mobile phase. For analysis of radioactive SE-HPLC, samples were collected in 15 second intervals, allowed to reach secular equilibrium with daughter isotopes (>8 hours) and fractions were read on a Perkin Elmer 2470 Automatic Gamma Counter Wizard^2 (30 seconds of counting time). These studies were carried out in a radiochemical facility with appropriate safeguards, protocols, and waste disposal.

4.5.2 Cell culture and tumour models

SKRC-52 was derived from a mediastinal metastasis of a primary RCC. SKRC-52 cells were cultured in RPMI-1640 medium, supplemented with 20% fetal bovine serum (FBS) at 37 °C in a humidified atmosphere with 5% CO_2. Before *in vitro* and *in vivo* experiments, cells were trypsinised and washed with RPMI-1640 supplemented with 20% FBS.

4.5.3 Radiolabelling of H_2MacropaSq Antibodies with Actinium-225

[^{225}Ac]Ac(NO_3)$_3$ was reconstituted in HCl (0.2 M, 50 μL). [^{225}Ac]$AcCl_3$ (25μCi/ 925kBq, 5 μL) was neutralised with $NaCH_3CO_2$ buffer (0.15 M, 45 μL, pH 5.5, stock 1). To a solution of H_2MacropaSq-hG250 (1mg/ mL $NaCH_3CO_2$ buffer, pH 5.5, 10 μL) was added stock 1 (20 μL, 10 μCi/ 370 kBq) and left for 5 minutes. The radiolabelled constructs were used without further purification, RCP, <99% performed *via* radioTLC (Radio detector: raytest RITA, stationary phase glass microfiber chromatography paper impregnated with silica gel, mobile phase: 0.05 M citrate buffer, pH 5.0).

4.5.4 Radiolabelling of H_4DOTA-NSC-hG250 with Actinium-225

Multiple reaction conditions used for radiolabelling. Reactions were heated at either 37°C, 45°C or 60 °C for up to 180 minutes. The following relates to serum stability. [^{225}Ac]$AcCl_3$ was buffered into $NaCH_3CO_2$ (0.15 M, pH 5.5, stock 1). To a solution of H_4DOTA-NSC-hG250 (CAR 1:1, 6mg/ mL, 7 µL +10 µL $NaCH_3CO_2$) and H_4DOTA-NSC-hG250 (CAR 3:1, 1.5 mg/ mL, 25 µL) was added stock 1 (CAR 1: 8µL, 4 µCi/ 148 kBq, CAR 1: 6µL, 3 µCi/ 111 kBq) and heated to 60°C for 60 minutes.

Table 10: Radiolabelling conditions of H_4DOTA-NCS-hG250.

Chelator Antibody Ratio	**1**	**1**	**3**	**3**	**3**
Temperature	**37**	**37**	**37**	**45**	**60**
Conditions	**pH 5.5**	**pH 9.0**	**pH 5.5**	**pH 5.5**	**pH 5.5**
Time (mins)	**10^{-5} M (%)**	**10^{-5} M (%)**	**10^{-5} M (%)**	**10^{-5} M (%)**	**10^{-5} M (%)**
15	2.46	-	-	4.55	89.17
30	4.47	2.63	-	4.29	98.04
60	10.33	3.4	6.09	12.63	99.32
90	-	7.14	12.93	-	-
180	-	-	-	15.46	91.39

4.5.5 Flow Cytometry of hG250 Antibodies and Conjugates

SKRC-52 cells cultured in RPMI media were lifted with trypsin and pelleted *via* gentle centrifugation. Cells were resuspended in fresh media with a final concentration of 1×10^6 cells/ mL. Antibody samples (20 µg) were added and incubated at 4°C for 1 hour before excess antibody was removed *via* centrifugation and washing (x3 PBS). Populations of cells with no fluorescence will have a fluorescence intensity displayed on the histogram at approximately 0.

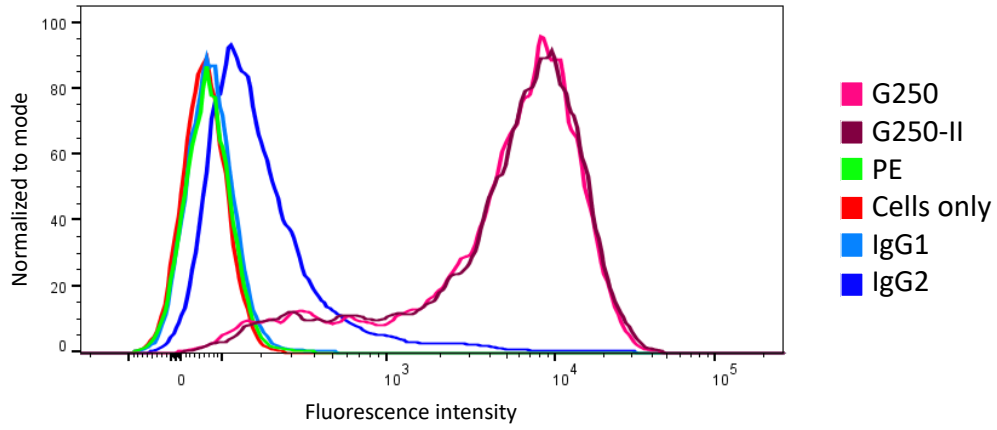

Figure 77: Flow Cytometry of hG250 antibodies against SKRC-52 cells

4.5.6 Lindmo-Scatchard Assay

Lindmo-Scatchard assays were performed as previously described.[293] Briefly, SKRC-52 cells were suspended in centrifuge tubes at concentrations of 5.0, 2.5, 1.25, 0.625, 0.31, 0.15, and 0.07 × 10^6 cells/mL in 500 µL PBS (pH 7.4). Aliquots of either [^{225}Ac]Ac(MacropaSq-hG250) (1µg of radiolabelled conjugate per 150µL of saline) were added to each tube, and the samples were gently shaken for 60 minutes at room temperature. The treated cells were then pelleted via centrifugation (3000 rpm for 5 minutes), re-suspended, and washed twice with cold PBS before removing the supernatant and counting the activity associated with the cell pellet. Self-blocking experiments with the radiolabelled antibody of extremely low specific activity (i.e., 1000-fold excess of unlabelled antibody) were performed as a negative control. The activity data were background-corrected and compared with the total number of counts in appropriate control samples. Immunoreactive fractions were determined by linear regression analysis of a plot of (total/bound) activity against (1/[normalised cell concentration]).

4.5.7 MTS Cell Viability Assay

MTS is performed according to reported protocol.[294-297] Briefly, H_2MacropaSq-hG250, H_2MacropaSq-hG250-FcRn and H_2MacropaSq-IgG_1 control were radiolabelled according to standard procedures (details below). SKRC-52 cells were seeded in a 96-well plate at a density of 1 × 10^3 cells/ 200 µL well 24 hours prior to treatment. The antibodies (3.6 µg) were added

to RPMI media in the cold control dilution plates, and serial dilutions were performed over 10 wells. For all samples containing [^{225}Ac]Ac, 3.6 µCi (133 kBq) was added into the first well and serial dilutions were performed over 10 wells. On the day of treatment, media was replaced on seeded plates with fresh media (50 µL). Then the serially diluted antibody constructs (50 µL) were added to the cells before the plates were incubated for 4 days (37 °C, 5 % CO_2). Following this, MTS reagent (20 µL, Promega CellTiter G3580) was added to the wells and incubated for 120 minutes. The plates were briefly placed on a shaker and absorbance was measured of treated and untreated cells using a plate reader at (OD = 490 nm, reference 650 nm).

Table 11: Details of the MTS assay

SKRC-52	[^{225}Ac]Ac (MacropaSq-hG250)	[^{225}Ac]Ac (MacropaSq-hG250-FcRn)	[^{225}Ac]Ac (MacropaSq-IgG1)
Activity required	15 µCi		
Volume of ***Stock 2***	17 µL (0.88uCi/µL)		
Amount of mAb (1mg/mL)	15µg – 15 µL		
Total volume	32 µL		
Final concentration	0.47 µCi/µL		
Volume	3.6 x 3 – 10.8 µCi = 23 µL total		
RCY (%)	100.00	99.87	99.90
SA (Mbq/mg)	37 MBq	37 MBq	37 MBq
SA (mCi/mg)	1	1	1

Table 12: Results of the MTS assay, including cell viability (%) at different antibody concentrations.

	[^{225}Ac]Ac (MacropaSq-hG250)		[^{225}Ac]Ac (MacropaSq-hG250-FcRn)	
Antibody Conc. (μg/mL)	*Average Cell Viability (%)*	*Error (%)*	*Average Cell Viability (%)*	*Error (%)*
20.00	23.4	0.4	29.8	2.4
6.666	38.0	0.6	38.6	0.2
2.222	43.7	1.2	45.9	2.3
0.740	46.1	1.2	49.2	1.5
0.246	48.5	1.2	46.9	1.6
0.082	47.8	1.0	50.3	2.3
0.027	53.0	2.5	53.3	3.0
0.009	56.4	2.2	60.9	1.4
0.003	60.3	1.6	63.6	3.6
0.001	65.8	3.1	67.3	1.7

	[^{225}Ac]Ac only		[^{225}Ac]Ac(MacropaSq-IgG1)	
Antibody Concentration (μg/mL)	*Average Cell Viability (%)*	*Error (%)*	*Average Cell Viability (%)*	*Error (%)*
20.00	25.7	0.4	32.0	2.1
6.666	45.2	1.6	48.8	1.6
2.222	52.8	2.1	56.3	1.6
0.740	70.1	4.4	66.2	3.0
0.246	70.5	0.8	74.3	3.5
0.082	68.0	2.1	66.8	1.6
0.027	80.9	4.5	80.6	2.2
0.009	92.1	4.3	92.2	2.7
0.003	96.8	1.3	90.1	4.7
0.001	96.2	2.6	99.9	4.8

	hG250		**hG250-FcRn**	
Antibody Conc. (μg/mL)	*Average Cell Viability (%)*	*Error (%)*	*Average Cell Viability (%)*	*Error (%)*
20.00	115.4	2.2	83.4	12.0
6.666	114.2	1.5	83.2	9.5
2.222	116.4	8.6	98.9	14.5
0.740	89.5	20.1	63.0	8.7
0.246	88.3	3.7	82.6	12.6
0.082	107.0	14.2	83.9	6.7
0.027	113.8	8.7	97.5	13.2
0.009	107.5	4.8	105.2	5.4
0.003	112.5	4.9	124.4	2.2
0.001	103.9	8.6	109.4	8.0

4.5.8 Colony Formation (Clonogenic) Assay

Colony forming assays were performed as previously described.[177, 271, 272] Briefly, SKRC-52 cells were seeded in a 6-well plate at a density of 1-5 × 10^3 cells/ 2 mL well 24 hours prior to treatment. H_2MacropaSq-hG250 was radiolabelled and dilutions were prepared according to standard procedure (details below). [^{225}Ac]Ac(MacropaSq-hG250) samples (0.5 mL) were exchanged with media (0.5 mL) for five different final activity concentrations (0, 0.05, 0.5, 5 and 50 kBq/mL) in triplicate. After 24 hours of incubation, the cell culture media was removed, washed with media (2 x 2 mL) and fresh media was added to each well. Plates were then incubated at 37 ◦C for 12 days and re-fed every 2 days, then the cell media was removed, and colonies were stained with 1 mL of 0.5% crystal violet in 50% methanol for 30 min, after which the plates were washed (3 x 2 mL MilliQ) and subsequently air-dried before images were analysed in ImageJ (with colony area plug in).

Table 13: Dilutions used in the clonogenic assay.

Sample	*Concentration*	*Volume of Ac-225*	*Volume of Media*
Reaction 1	1μCi/ 1 ug	27 μL of stock 1	0
Reaction 2	12,280 kBq/mL	43 μL of RXN 1	3.45 mL
2	200 kBq/mL	3 mL of RXN 2	-
3	20 kBq/mL	0.4 mL of RXN 2	3.6 mL
4	2 kBq/mL	0.4 mL of 3	3.6 mL
5	0.2 kBq/mL	0.4 mL of 4	3.6 mL
6	0 kBq/mL	-	4 mL

4.5.9 Biodistribution Study in BALB/c Nude Mice bearing Established SKRC-52 Xenografts

To characterise the biodistribution properties of [^{225}Ac]Ac(MacropaSq-hG250) in mice bearing SKRC-52 renal cell carcinoma tumours BALB/c nude mice with established SKRC-52 tumour xenografts (TV = 155.89 ± 21.47 mm^3) received intravenous injections of [^{225}Ac]Ac(MacropaSq-hG250) (30 μg, 0.4μCi/14.8 kBq, *n* =30) or isotype control [^{225}Ac]Ac-MacropaSq-hIgG1 (30 μg, 0.4μCi/14.8 kBq; *n* = 10 mice). Following injection on day 0 of [^{225}Ac]Ac-MacropaSq-hG250, groups of mice (*n* = 5) were sacrificed by over-inhalation of isoflurane anaesthesia and biodistribution was assessed on Day 0 (3 hrs p.i.) and on day 1, 2, 3, 5, and 7 post injection. Mice injected with isotype control were assessed at day 0 and 3 post injection only. Mice were exsanguinated by cardiac puncture, and tumours and organs [liver, spleen, kidney, muscle, skin, bone (femur), lungs, heart, stomach, brain, small intestines, large intestines, tail, and colon] were collected immediately. All samples were counted in a dual-channel gamma scintillation counter (Wizard, PerkinElmer, Australia). Triplicate standards prepared from the injected material were counted at each time point with tissue and tumour samples enabling calculations to be corrected for the physical decay of the isotope. The tissue

distribution data were calculated as the mean ± SD percent injected activity per gram tissue (%IA g^{-1}) for each construct per time point.

Table 14: Biodistribution data of [^{225}Ac]Ac(MacropaSq-hG250).

	Day 1			**Day 2**			**Day 3**		
	IA g^{-1} *%*	*SD*	*n*	*IA* g^{-1} *%*	*SD*	*n*	*IA* g^{-1} *%*	*SD*	*n*
Blood	41.597	5.072	5	26.157	2.025	5	23.981	4.76	5
Brain	1.604	0.279	5	0.887	0.262	5	0.634	0.143	5
Heart	8.771	1.011	5	5.423	0.813	5	5.016	1.389	5
Lung	16.412	2.394	5	10.888	1.527	5	10.894	2.355	5
Stomach	3.192	0.583	5	2.986	0.397	5	2.834	0.862	5
Spleen	11.378	2.072	5	12.047	1.886	5	12.02	3.205	5
Liver	12.734	1.804	5	10.816	1.932	5	10.987	1.637	5
Kidney	12.07	2.129	5	9.122	0.97	5	8.705	1.749	5
S.Intestine	3.65	0.741	5	2.883	0.467	5	2.859	0.561	5
Colon	2.873	0.515	5	2.673	0.382	5	2.522	0.535	5
Muscle	1.528	0.312	5	2.33	0.542	5	1.91	0.414	5
Bone	2.869	0.437	5	3.274	0.498	5	3.356	1.016	5
Skin	4.441	0.369	5	7.162	1.101	5	5.827	0.654	5
Tail	5.516	1.39	5	3.335	0.356	5	2.895	0.235	5
Tumour	5.272	1.433	5	12.344	1.864	5	16.095	4.767	5

	Day 4			Day 5			Day 7		
	IA g^{-1} *%*	*SD*	*n*	*IA* g^{-1} *%*	*SD*	*n*	*IA* g^{-1} *%*	*SD*	*n*
Blood	23.362	4.282	5	17.32	4.109	5	14.793	3.334	5
Brain	0.918	0.19	5	0.625	0.251	5	0.351	0.137	5
Heart	5.28	0.856	5	3.32	1.196	5	2.624	1.251	5
Lung	10.54	1.2	5	7.976	2.191	5	6.573	1.681	5
Stomach	3.148	0.349	5	2.67	0.684	5	1.544	0.529	5
Spleen	13.899	2.567	5	10.221	3.027	5	8.288	1.788	5
Liver	10.464	1.345	5	8.629	2.176	5	9.149	2.04	5
Kidney	9.143	0.882	5	7.165	1.857	5	7.008	1.156	5
S.Intestine	2.462	0.225	5	2.092	0.33	5	1.777	0.476	5
Colon	2.78	0.432	5	1.924	0.406	5	1.297	0.446	5
Muscle	1.682	0.323	5	1.219	0.238	5	0.871	0.28	5
Bone	3.525	0.734	5	2.594	0.798	5	1.425	0.468	5
Skin	5.96	0.464	5	4.677	1.24	5	3.854	1.227	5
Tail	2.75	0.29	5	2.021	0.28	5	1.891	0.416	5
Tumour	21.26	6.45	5	19.119	7.064	5	21.416	10.134	5

Table 15: Biodistribution of [^{225}Ac]Ac(MacropaSq-IgG1).

	Day 0			Day 3		
Organ	*IA* g^{-1} *%*	*SD*	*n*	*IA* g^{-1} *%*	*SD*	*n*
Blood	31.286	3.407	5	2.095	1.282	5
Brain	0.997	0.155	5	0	0	5
Heart	7.351	0.942	5	0.673	0.286	5
Lung	13.004	2.29	5	1.536	0.834	5
Stomach	2.673	0.486	5	0.585	0.386	5
Spleen	12.745	2.562	5	10.525	2.223	5
Liver	23.642	2.837	5	19.848	6.589	5
Kidney	12.721	1.408	5	4.876	1.168	5
S.Intestine	3.606	0.562	5	1.224	0.278	5
Colon	2.87	0.286	5	1.235	0.479	5
Muscle	1.238	0.231	5	0.297	0.181	5
Bone	2.899	0.545	5	1.267	0.328	5
Skin	3.97	1.145	5	2.66	0.745	5
Tail	4.534	1.299	5	1.945	0.386	5
Tumour	4.194	0.637	5	3.649	0.485	5

4.5.10 *In vivo* Longitudinal Studies with [^{225}Ac]Ac(MacropaSq-hG250)

For the longitudinal therapy study in mice bearing SKRC-52 renal cell carcinoma tumours BALB/c nude mice with established SKRC-52 tumour xenografts received intravenous injections of [^{225}Ac]Ac(MacropaSq-hG250) (30 µg, 0.4µCi/14.8 kBq, *n* =14, mean TV 127.6 ± 23.42 mm^3), isotype control [^{225}Ac]Ac(MacropaSq-IgG1) (30 µg, 0.4uCi/14.8 kBq; *n* = 11 mice, mean TV 129.7 ± 21.98 mm^3) or cold hG250 (30 µg, *n* = 8, mean TV 128.91 ± 13.94 mm^3). Following injection on Day 0 of the three groups, the mice were sacrificed by over-inhalation of isoflurane anaesthesia once they reached their ethical endpoint (tumour volume >1000m^3) or at the following collection time points: 3 mice per group at the time of growth curve separation (when anti-tumour effect becomes apparent), 3 mice per group at the time of hG250 cold control cull due to ethical endpoint + all tissues from hG250 cold control group (n

= 5 remaining), 3 mice from [^{225}Ac]Ac(MacropaSq-hG250) group on the day of [^{225}Ac]Ac-MacropaSq-IgG1) cull due to ethical endpoint + all tissues from [^{225}Ac]Ac(MacropaSq-IgG1) group (n = 5 remaining), and all remaining tissues from [^{225}Ac]Ac(MacropaSq-hG250) at ethical endpoint (n = 5 remaining). The tumour volumes were measured every 3 – 4 days for the first 49 days, then every 3 – 7 days until day 126.

Table 16: Response to targeted alpha therapy with actinium-225.

Study Arm	*Partial Response*	*Complete Response*
hG250	0	0
[^{225}Ac]Ac(MacropaSq-IgG1)	0	0
[^{225}Ac]Ac(MacropaSq-hG250)	3	2

Table 17: Average tumour volumes of mice receiving [^{225}Ac]Ac(MacropaSq-hG250).

Time post treatment (d)	*Tumour Volume (mm^3)*	*SD*	*n*	*Time post treatment (d)*	*Tumour Volume (mm^3)*	*SD*	*n*
0	127.6	23.42	14	49	38.3	26.12	5
3	206.69	110.33	14	55	42.69	39.86	5
6	210.73	140.77	14	63	37.2	44.03	5
10	169.04	42.6	11	70	84.03	142.7	5
13	141.5	47.56	8	73	90.62	150.85	5
17	110.37	16.07	8	76	151.92	272.85	5
20	107.92	15.65	5	84	245.01	429.24	5
23	108.15	28.74	5	91	98.81	158.08	4
27	95.34	25.95	5	98	128.29	201.77	4
31	94.2	19.85	5	105	115.84	177.71	4
35	82.87	17.43	5	112	190.62	287.57	4
38	64.35	19.16	5	119	263.76	405.57	4
42	61.34	29.99	5	126	81.12	140.5	3
45	45.34	21.43	5				

Table 18 Average tumour volumes of mice receiving [^{225}Ac]Ac(MacropaSq-IgG1) and hG250.

	[^{225}Ac]Ac(MacropaSq-IgG1)			**hG250**		
Time post treatment	*Tumour Volume (mm^3)*	*SD*	*n*	*Tumour Volume (mm^3)*	*SD*	*n*
0	129.66	21.98	11	128.91	13.94	8
3	227.81	93.34	11	288.11	139.21	8
6	329.83	163.22	11	553.2	353.17	8
10	375.55	76.2	8	1054.13	546.29	5
13	520.24	127.17	5			
17	1092.35	243.84	5			

4.5.11 γH2AX Confocal Microscopy to Determine the Double-Strand Breaks in Tumour Sections

Formalin fixed, paraffin embedded tumours were dewaxed by two washes in xylene, followed by rehydration in decreasing concentrations of alcohol (two washes in 100% ethanol 5 minutes each, 95% ethanol, 5 minutes and 70% ethanol for 5 minutes). Slides were placed in water before antigen retrieval using citrate buffer, pH 6.0 (Sigma) at 90°C for 20 mins. Slides were left to cool for 1 hour at room temperature, washed with water and blocked with 5% bovine serum albumin (BSA; Sigma) and 5% normal goat serum (Thermo Fisher Scientific) in Tris Buffered Saline with Tween 20 (TBST20; Sigma). Slides were incubated with anti-γH2AX (1:200; Cell Signalling Technologies) and anti-F-actin (1:200; Abcam) primary antibodies in with 5% BSA (Sigma) and 5% normal goat serum (Thermo Fisher Scientific) in TBST20 (Sigma) overnight at 4°C. Primary antibodies were removed by three washes in TBST20, followed by rinsing in water. Primary antibodies were labelled using goat anti-rabbit Alexa Fluor 568 (Thermo Fisher Scientific) and goat anti-rat Alexa Fluor 647 (Abcam) for 1 hour at room temperature. DAPI (1 μg/mL) was used to stain nuclei. Fluoromount-G mounting media (Thermo Fisher Scientific) was used to set slides for microscopy and left overnight at 4°C prior to imaging. γH2AX foci quantitation was performed using GraphPad Prism. A one-way

ANOVA with a Tukey's multiple comparisons test was used. Data is mean ± SEM with >36 nuclei analysed per treatment group. Data were graphed using GraphPad Prism software (Graphpad Software Inc).

5 Adapting [^{225}Ac]Ac(Macropa) for use in Bioorthogonal Click Reactions

Off-target radiotoxicity to healthy tissue dictates the optimal therapeutic dose of radionuclide therapy. The relatively long half-life and highly cytotoxic nature of actinium-225 means that patients are able to tolerate a relatively low dose of radiation. This is highlighted in the severe xerostomia associated with the peptidomimetic [^{225}Ac]Ac(PSMA-617). The toxicity of [^{225}Ac]Ac(PSMA-617) may limit its potential in the clinic.[137, 140] Using monoclonal antibodies as the targeting vector may circumvent the off-target uptake in certain organs, albeit to introduce other complexities associated with using large proteins as therapeutics, namely their poor tumour penetration and long blood pool circulation time of the macrobiomolecule *in vivo*.[298]

Monoclonal antibodies are highly selective for their respective antigens and bind with very high affinity, but their large molecular weight (~ 150 kDa) and interactions of the Fc region mean they often require several days to clear the blood and accumulate in the target tissue. Consequently, radionuclide therapy using full IgG antibodies as targeting vectors has traditionally required the antibodies to be labelled with radionuclides with relatively long radioactive half-lives, such as lutetium-177 ($t_{1/2}$ = 3.27 days) or iodine-131 ($t_{1/2}$ = 8.0 days). This is so that adequate radioactivity can reach the tumour tissue. However, the long circulation times *in vivo* can deleteriously affect healthy tissue.

5.1 Reducing Off-target Toxicity *via* Pretargeted Tetrazine and *Trans*-cyclooctene Click Chemistry

An alternative to using antibodies directly labelled with radionuclides is to use a 'pre-targeting' approach. This involves the administration of an antibody that has been modified with a specific functional group designed to react with an incoming radiolabelled small molecule.

This radiolabelled small molecule is designed for rapid clearance from non-target tissue but is also suitably modified to selectively react with the previously injected modified antibody.

5.2 Leveraging Click Chemistry for *In Vivo* Reactions

The term 'click chemistry' was introduced by Sharpless to stipulate chemical bond-forming reactions that are fast, irreversible, equimolar and lead to stable products in high chemical yields and purity with the generation of inoffensive by-products.[299]

In the years that followed this seminal work that would ultimately result in a Nobel Prize for K. Barry Sharpless, Carolyn Bertozzi and Morten Mendal, there were many new chemical reactions, and their applications were seemingly endless. The copper-catalysed azide–alkyne 1,3-dipolar cycloaddition (CuAAC) is a widely studied and used click reaction. The CuAAC click reaction exhibits rate constants between 10 – 100 M^{-1} s^{-1};[300] however, concerns over the toxicity of copper(I/II) and its applications *in vivo* have motivated efforts to develop 'copper free' variants, such as the strain-promoted [3+2] azide-alkyne cycloaddition (SPAAC).[301-304] The SPAAC reaction activates the alkyne *via* ring strain without a catalyst but these reactions are significantly slower (10^{-2} – 10^{-1} M^{-1} s^{-1}).[305]

A bioorthogonal reaction must display high selectivity between reaction partners, be kinetically fast, catalyst-free and operate at physiological pH and temperature. This term was popularised by Bertozzi,[304] stating that for this reaction to be truly bioorthogonal, it is paramount that the structural perturbation imposed by the conjugation of new functional groups must not disturb any of the native biochemical processes.[306] The potential of one extremely rapid click reaction and its bioorthogonal applications were first recognised by two research groups independently in 2008.[307, 308] The [4+2] cycloaddition, known as the inverse electron demand Diels-Alder reaction (iEDDA) between a 1,2,4,5-tetrazine and a *trans*-cyclooctene (TCO) was reported to display rapid reaction kinetics, high yields and selectivity in aqueous media, with innocuous N_2 released as the only byproduct (Figure 78). This click reaction

displays suitable reaction rates (~10^5 M) and has the potential for *in vivo* applications.[307-309] Tetrazines that are substituted with a methyl group at 6-position (R^1 or R^2) are more stable partners in bioorthogonal cycloadditions, whereas reactions with 6-hydrogen substituted tetrazines are faster, which is a necessity in live cell and *in vivo* applications where dilute concentrations of labelling agents are required.[310]

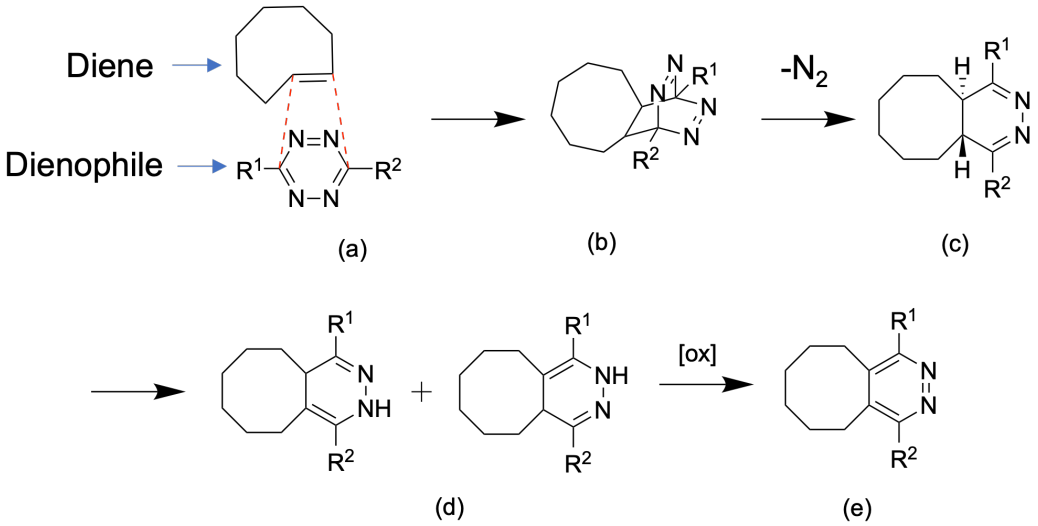

Figure 78: (a) Concerted [4+2] cycloaddition of 1,2,4,5-tetrazine with *trans*-cyclooctene. The highly strained bicyclic adduct (b) is rapidly converted in a retro-Diels–Alder step (upon release of nitrogen) to the corresponding 4,5-dihydro-pyridazine (c) subsequent isomerisation leads to the corresponding 1,4-dihydro-isomers; (d) Electron-rich tetrazines can aromatise to give (e) under ambient conditions.[311]

iEDDA reactions are governed by the energy gap between the highest occupied molecular orbital of the diene and the lowest unoccupied molecular orbital of the dienophile ($HOMO_{dienophile} - LUMO_{diene}$). The reaction is facilitated by electron-withdrawing substituents at the 3- and 6-position (R^1 and R^2) of the tetrazine ring, which acts to lower the LUMO.[306] Consequently, electron-rich dienophiles increase the energy of the HOMO. Therefore, by electronically tuning the cycloaddition partners and manipulating the HOMO – LUMO energy gap it is possible to enhance reaction kinetics. Second order rate constants of up to 3.3×10^6 M^{-1} s^{-1} (25°C, H_2O) are observed.[308, 312]

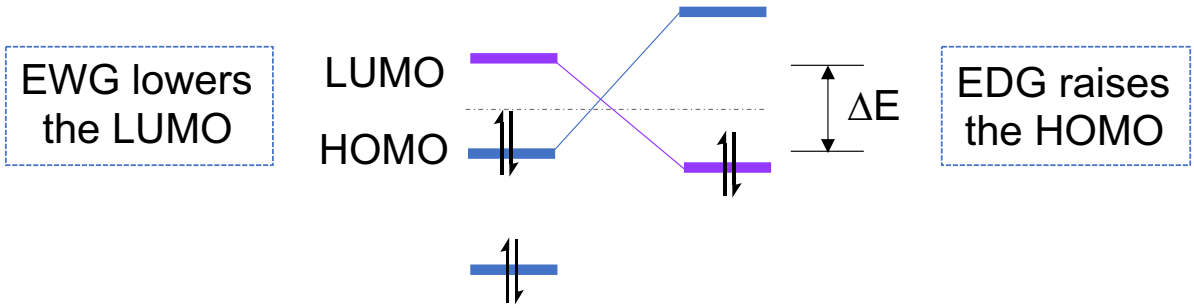

Figure 79: HOMO-LUMO energy gap can be tuned by incorporating an electron donating group (EDG) on the dienophile and electron-withdrawing groups (EWG) on the diene. Adapted from Knall *et al.*[306]

5.3 Harnessing the iEDDA Click Reaction for Antibody Pretargeting

Such 'click reactions' are ideally suited for pretargeted antibody therapy. A pretargeting strategy combines the advantages of antibody selectivity with the favourable pharmacokinetics of small molecule radiolabelled imaging agents and is based on the principle of decoupling the antibody from the radioactivity at the time of injection.[313-316]

A modified antibody, containing a selective small molecule functional group that is stable *in vivo* and reacts with suitable kinetics, reacts with a small molecule radiopharmaceutical containing the corresponding functional group with suitable kinetics. The antibody is administered and allowed to accumulate at the tumour site while excess antibody is excreted slowly. After a suitable period (24 –72 hours in previous research), the small molecule probe is injected and effectively 'clicks' with the modified antibody. This process occurs simultaneously with the rapid excretion of the small molecule radiopharmaceutical.

5.3.1 Pretargeted Radioimmunotherapy with Copper-64/67 Delays Tumour Growth in Murine Models of Cancer

For effective tumour pretargeting, it is necessary that the antibody remains accessible to the incoming 'chaser' radioactive molecules after binding to the target cells. This can be achieved with the use of non-internalising antibodies. One example of a suitable non-internalising antibody compatible with tumour pretargeting is the huA33 antibody, which recognises the A33 antigen, which is present in more than 95% of colorectal cancers. Preclinical

investigations of pretargeting for application of diagnostic imaging using the huA33 antibody were pioneered by Zeglis and Lewis.[313-315, 317-319]

Pretargeted imaging and therapy with copper-64 copper-67 was possible using the huA33 antibody, which was modified to include a *trans*-cyclooctene (Figure 80, a) and a derivative of the ligand MeCOsar that has been modified to include a tetrazine functional group, MeCOSar-Tz (Figure 80, a).[320, 321] *Trans*-cyclooctene functional groups were conjugated to the huA33 antibody to give and an average of in 5.2 ± 0.1 *trans*-cyclooctene groups per antibody and preserved immunoreactivity of 88.9 ± 1.8%. Both [^{64}Cu]CuMeCOSar-Tz and [^{67}Cu]CuMeCOSar-Tz can be prepared in essentially quantitative yield at 37 °C for 20 minutes.

Interestingly, these studies demonstrated that a 1:1 ratio of *trans*-cyclooctene functionalised antibody: radioligand provide superior results compared to using a large excess of either the immunoconjugate or radioligand (Figure 80, b).[322] Therefore, in the design of all *in vivo* pretargeting experiments it was imperative that the molar activity of [$^{64/67}$Cu]CuMeCOSar-Tz was corrected so that there was 0.7 nmol of tetrazine per injection, matching that of huA33-TCO.

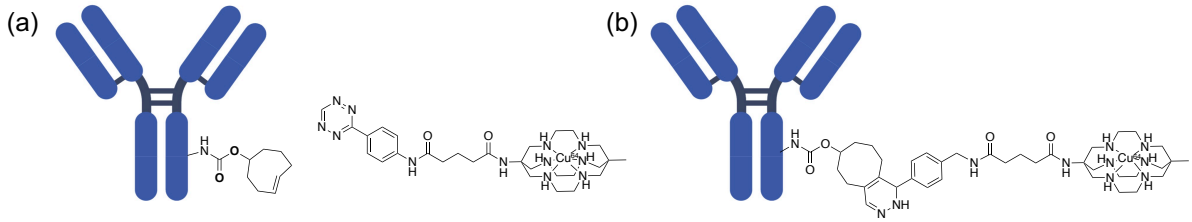

Figure 80: (a) A *trans*-cyclooctene modified antibody is injected into the bloodstream and allowed time to localise at the tumour site, after an appropriate time period when the antibody has reached its optimal biodistribution *in vivo*, a small molecule radioligand is introduced, (b) where it reacts with the modified antibody and excess radioactivity is excreted.

Longitudinal radiotherapy studies were designed around the calculation of the relevant therapeutic indices for the administration of huA33-TCO followed by [^{67}Cu]CuMeCOSar-Tz either 24 or 72 hours later, and compared to that of the directed labelled radioimmunoconjugate. The highest tumour-to-blood ratio (9.7:1) occurred when the

radiotracer was injected at 72 hours, higher than that of the directly labelled conjugate (8.1:1) giving sufficient time for the antibody to accumulate at tumour tissue without the additional burden of excess radiation circulation. The longitudinal radiotherapy study (with SW1222 human colorectal cancer xenografts) was designed to probe the dose dependence of treatment with [^{67}Cu]Cu^{II} (18.5 MBq, 37.0 MBq or 55 MBq) as well as make comparisons to a fractionated dosing regimen (2 x 18.5 MBq) and traditional radioimmunotherapy (18.5 MBq). The inhibition of tumour growth occurred in a dose-dependent manner, with the mean survival time greater than 200 days for those receiving 55 MBq as well as RIT. Importantly this work has not only indicated the *in vivo* feasibility of pretargeted diagnostic imaging and therapy but, by incorporating the positron-emitting radionuclide copper-64, allowed for the assessment of suitability for and prediction of a patient's response to treatment with copper-67. This work demonstrates the incredible selectivity and specificity of the tetrazine *trans*-cyclooctene click reaction and the manner in which a one-to-one stoichiometry of a *trans*-cyclooctene modified antibody and therapeutic copper-67 radioligand produces such a strong dose-dependent inhibition of tumour growth.

5.3.2 Pretargeted Radioimmunotherapy is possible with Actinium-225

Reducing the excess radiation exposure of actinium-225 radiopharmaceuticals was recognised by Poty *et al.* in the development of [^{225}Ac]Ac(DOTA-peg$_7$-Tz) (Figure 81), a metal chelator with an appended 1,2,4,5-tetrazine designed to react with *trans*-cyclooctene functionalised monoclonal antibodies.[323] The iEDDA reaction was first used as a method to increase the radiochemical yield of actinium-225 labelled radioimmunoconjugates, as traditional one- or two-step radiolabelling reactions with isothiocyanates were typically low yielding.[154, 264]

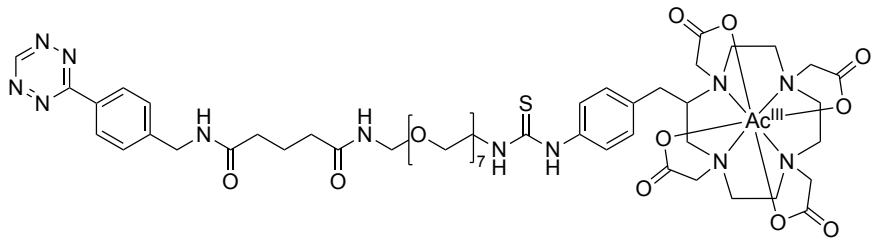

Figure 81: Chemical structure of [^{225}Ac]Ac(DOTA-peg$_7$-Tz).

Using H_4DOTA to form complexes with [^{225}Ac]Ac^{III} meant that the original labelling step proceeded in moderate yields (RCP > 98 %, specific activity 0.17 ± 0.03 MBq μmol^{-1}) and required purification by C18 column. In their work, the purified [^{225}Ac]Ac(DOTA-peg$_7$-Tz) was then reacted with the TCO-modified 5B1 antibody. A second purification step was required, and PD-10 desalting columns purified the [^{225}Ac]Ac-labelled radioimmunoconjugates post 'click' reaction with specific activities between 2.8 – 4.6 ± 0.2 MBq mg^{-1}. The immunoreactivity of the 'clicked' [^{225}Ac]Ac(DOTA-peg$_7$-Tz-5B1) mAb conjugate was 61.3 ± 4.5% for BxPC3 cells. While this is a considerably lower immunoreactivity than expected by one-step radiolabelling, it still confirmed the selectivity of the radioimmunoconjugate for CA19.9.

The therapeutic efficacy of 'chasing' 5B1-TCO modified antibodies with [^{225}Ac]Ac(DOTA-peg$_7$-Tz) (37 kBq) *in vivo* was investigated in an animal model of cancer.[324] There was an increase to the mean survival of the cohort receiving pretargeted treatment, from 28.5 days to 67.5 days. A comparison of the biodistribution of the *in vivo* pretargeted reaction and the directly labelled radioimmunoconjugates with 29.6 ± 6.6 % IA g^{-1} in a tumour model of pancreatic ductal adenocarcinoma showed a statistically significant amount of radioactivity in the blood pool, spleen, liver, and bone. Cerenkov luminescence imaging was used as an imaging modality. The dose of [^{225}Ac]Ac(DOTA-PEG$_7$-Tz) necessary for imaging far surpassed the maximum tolerated dose (MTD) for actinium-225 conjugates (1.9 MBq). This highlights the practical limitations of utilising Cerenkov luminescence imaging instead of

PET/SPECT imaging, but it still demonstrated localisation of activity in BxPC3 tumour xenograft models.

Pretargeted antibody radioimmunotherapy has been successful in preclinical animal models of cancer with [^{225}Ac]Ac^{III}. Poty *et al.* designed a metal chelator, [^{225}Ac]Ac(DOTA-peg$_7$-Tz), that forms complexes with [^{225}Ac]Ac^{III} (Figure 81).[323, 324] In their work, high radiolabelling temperatures and post-labelling purification of the radioligand were necessary.

5.4 Aims

The aim of this chapter is to prepare a ligand with an appended 1,2,4,5-tetrazine to enable radiolabelling with [^{225}Ac]Ac^{III} at room temperature. The ligand, H_2Macropa-Tetrazine, incorporated some core components of H_2MacropaSqOEt (Scheme 9). We elected to use the metal chelator core of compound ***13*** (see section 2.7). The alkyne on the metal chelator reacts with high selectivity with the aliphatic azides and forms a 1,2,3-triazole that is sufficiently stable for *in vivo* work. The same oligo(ethylene glycol) spacer was incorporated into the metal chelator framework. Our previous work, directly radiolabelling Girentuximab with H_2MacropaSqOEt, demonstrated that this small biocompatible linker served as an adequate spacer without significantly increasing the hydrophobicity of both the ligand and the antibody conjugates.

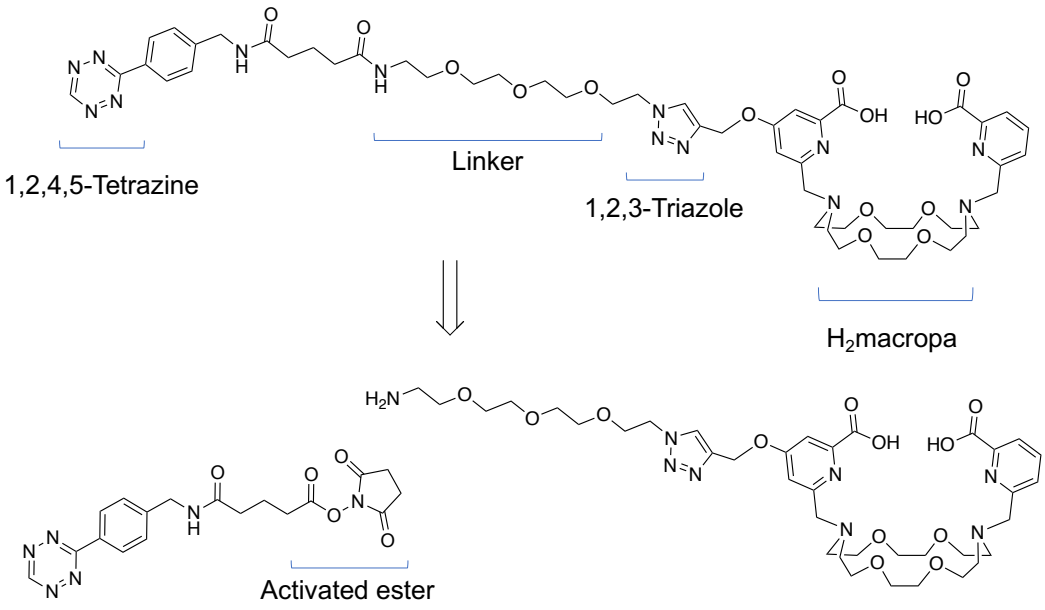

Scheme 9: The retrosynthesis and important components in the ligand design of H_2Macropa-Tetrazine.

5.5 Results and Discussion

5.5.1 Synthesis of a Crown Ether Macrocycle with an Appended Tetrazine, H_2Macropa-Tetrazine

The synthesis of a tetrazine that could be easily incorporated into the macrocycle required the formation of an activated ester (Scheme 10). Activated esters allow for the incorporation of functional groups under mild conditions without the requirement of coupling agents. Incorporating the tetrazine functional group into the ligand, H_2Macropa-Tetrazine in the final synthetic step is preferred due to the known reactivity of 6-hydrogen substituted 1,2,4,5-tetrazines. The compound 4-(1,2,4,5-tetrazin-3-yl)phenyl)methanamine hydrochloride (***22***) was synthesised according to a literature procedure in moderate yields with hydrazine hydrate (20%).[325] The terminal amine was neutralised with base (DIPEA) before the nucleophilic reaction of the amine with glutaric anhydride (76%). An *N*-hydroxysuccinimidyl-activated ester of the carboxylic acid was formed by the reaction of ***22*** with *N*-hydroxysuccinimide and the coupling reagent 1-ethyl-3-(3-dimethylaminopropyl)carbodiimide hydrochloride (EDC.HCl). Compound ***23*** was collected as a pink powder in 65% yield.

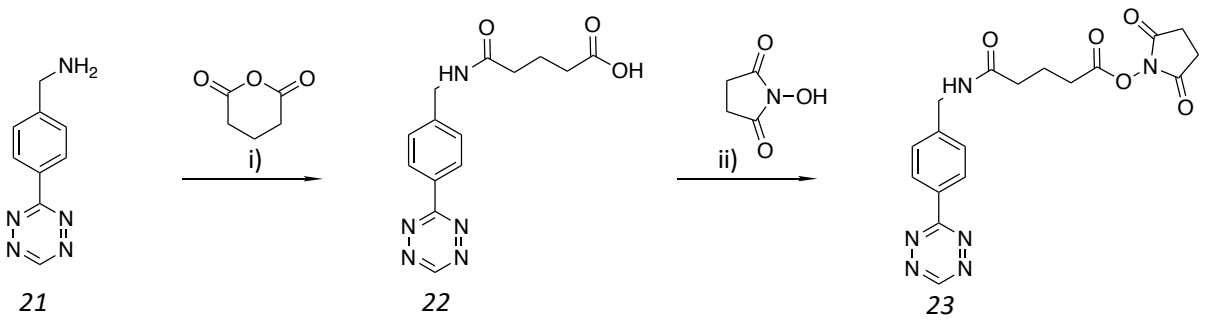

Scheme 10: Synthesis of a 1,2,4,5-tetrazine containing an N-hydroxysuccinimidyl activated ester; (i) DIPEA, dichloromethane, 50°C overnight, 76% (ii) N-hydroxysuccinimide, EDC.HCl and DIPEA, room temperature, 65%.

The reaction of the terminal alkyne on the metal chelator (***12***) with the aliphatic azide on the short oligo(ethylene glycol) chain (***15***) proceeded according to the synthesis of H_2MacropaSqOEt *via* a copper(I) catalysed Huisgen's 1,3-dipolar cycloaddition (Scheme 11, i).[180, 181] The copper(I) species were formed *in situ* with an excess of sodium ascorbate. The catalytic copper was precipitated with excess Na_2S. Without further purification, the esters were hydrolysed (Scheme 11, ii) and compound ***24*** was then purified by semi-preparative HPLC (58 %).

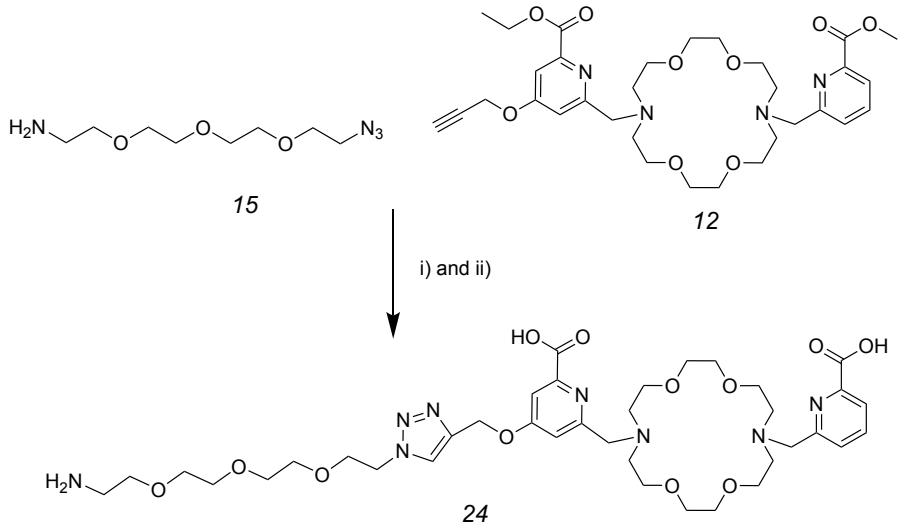

Scheme 11: Synthesis of compound 24. (i) $CuSO_4$, Sodium Ascorbate, DMF: H_20 4:1, (ii) followed by ester hydrolysis with NaOH in MeOH.

In the final synthetic step to install the tetrazine functional group, the NHS ester ***23*** was reacted with the amine of ***24*** in acetonitrile at room temperature (Scheme 12, ii), followed by

immediate purification by HPLC to give the final compound as a pink powder (***26***, H_2Macropa-Tetrazine) in 53 % yield.

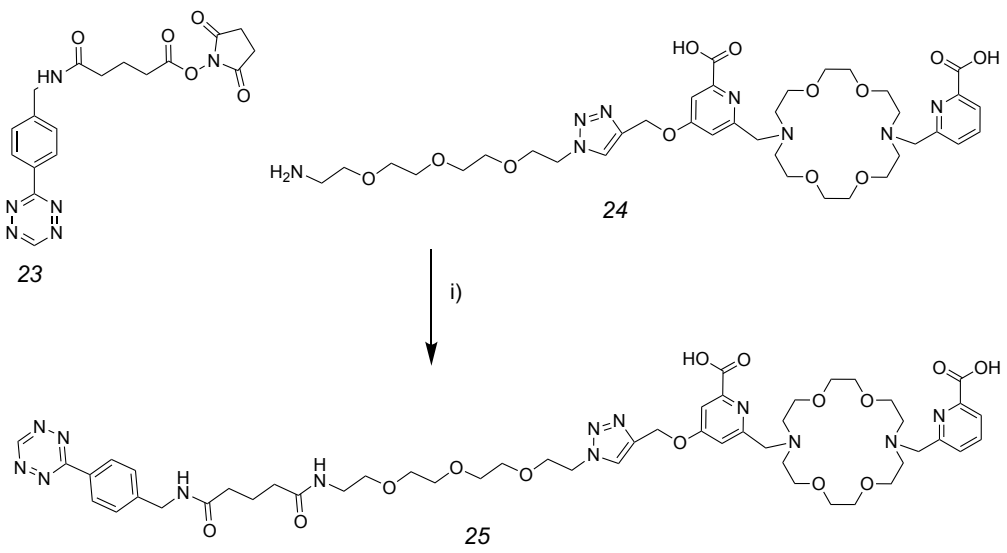

Scheme 12: The synthesis of H_2Macropa-Tetrazine, (i) CH_3CN, 4 hours, purification *via* semi-preparative HPLC, 53%.

Analysis of the ligand H_2Macropa-Tetrazine by RP-HPLC produced a single peak with a retention time of 10.88 minutes (Figure 82, a). High-resolution ESI-MS determined the signal of highest intensity as the doubly protonated adduct, $[M+2H]^{2+}$, m/z = 544.7627. The $[M+3H]^{3+}$ and $[M+H]^{+}$ adducts were also present at m/z = 363.5104 and m/z = 1088.5162, respectively (Figure 82, b).

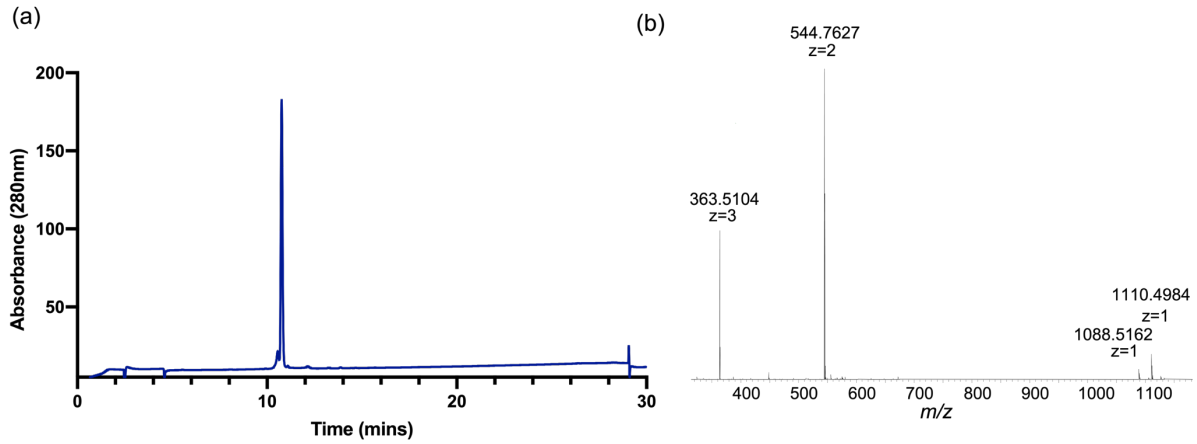

Figure 82: (a) Reverse phase HPLC of H_2Macropa-tetrazine (H_2L^3) showing a single peak at 10.88 minutes (λ = 280 nm), and (b) HR-MS of H_2L^3 showing the singly, doubly and triply protonated adducts.

Analysis of H_2Macropa-Tetrazine by ^{1}H NMR made it possible to assign hydrogen resonances (Figure 83). Notably, there is the characteristic resonance at δ 10.34 ppm that can be attributed to the hydrogen in the 6-position of the tetrazine. There are eight hydrogen environments present in the spectrum which can be attributed to aromatic environments. Of these, there are two doublets which can be assigned to the hydrogen atoms at 29 and 30 that integrate for two and three hydrogens, respectively. The resonance from hydrogen 30 (d, J = 8.1 Hz) integrates for three hydrogens due to the overlapping resonance from hydrogen 13, which has a chemical shift of δ 7.50 ppm. Three resonances assigned to the non-symmetrically substituted picolinate pendant arms can be attributed to hydrogen environments 1, 2 and 3 at δ 7.58 ppm (d, J = 7.6 Hz) δ 7.98 ppm (t, J = 7.7 Hz) and δ 7.93 ppm (d, J = 7.7 Hz, 1H), respectively. A singlet present at δ 8.16 ppm is assigned to the resonance of the hydrogen of the 1,2,3-triazole (15).

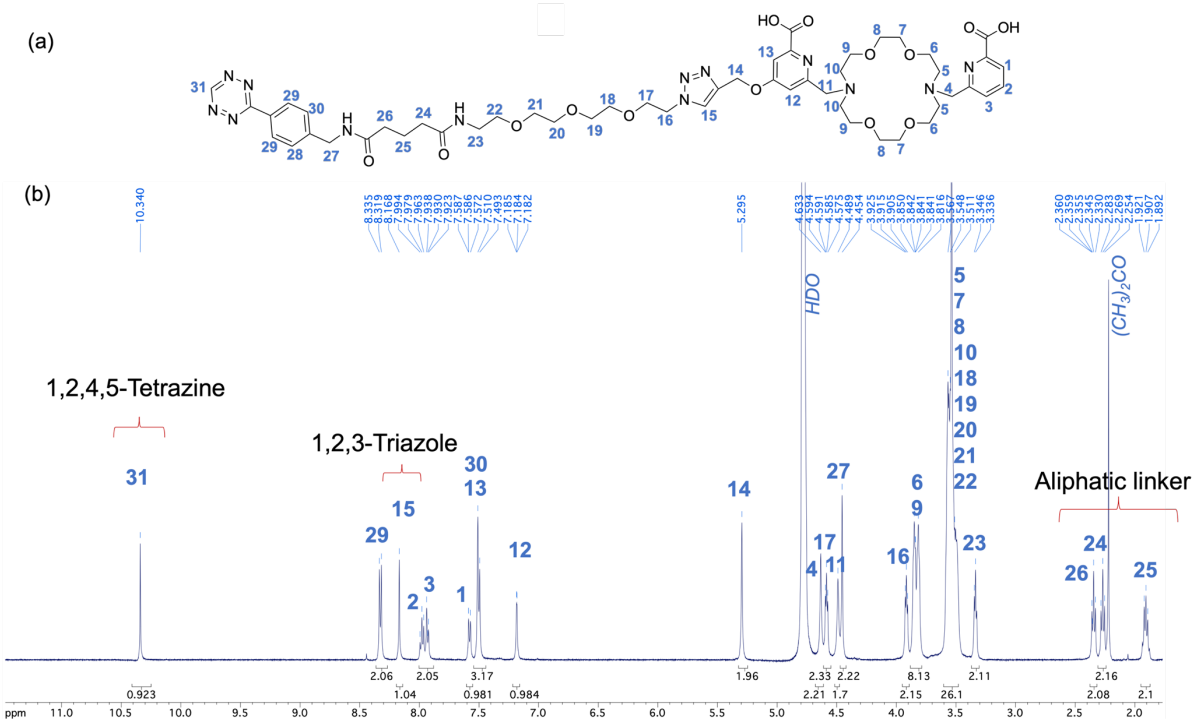

Figure 83: ^{1}H NMR of H_2Macropa-Tetrazine.

There is overlap of the resonances attributed to the methylene groups of the oligo(ethylene)glycol linker (18 – 22) and the diaza-crown ether (5, 7, 8, 10) at δ 3.51– 3.56 ppm, which integrate to 26 hydrogen atoms. The resonance derived from hydrogen

environments 6 and 9 within the macrocycle exhibits two doublets of triplets in an 'AB' split. Further upfield, it is possible to assign the hydrogen environments from the short aliphatic linker between the benzylamine-1,2,4,5-tetrazine which was derived from glutaric anhydride. There are three signals at δ 2.34 ppm (t, J = 7.4 Hz, 2H, 26), δ 2.27 ppm and (t, J = 7.4 Hz, 2H, 24), δ 1.96 – 1.84 ppm (m, 2H, 25) which can be assigned to this linker.

5.5.2 Characterising the Conjugation of *Trans*-cyclooctene to Girentuximab by Native Protein Mass Spectrometry

In this work, *trans*-cyclooctene functional groups were conjugated to monoclonal antibodies with TCO-PEG$_4$-NHS. This activated ester is used for the facile modification of surface lysine resides. The reactivity of TCO towards tetrazines is maintained by incorporating an oligo(ethylene glycol) linker, which will not increase the hydrophobicity of the functional group. The N-hydroxy succinimidyl-activated ester of *trans*-cyclooctene (without any linker) is unsuitable for protein modification.[326] The addition of a relatively short oligo(ethylene glycol) chain also increases the solubility of the TCO ring and prevents steric hindrance of the bulky cycloaddition reaction near the antibody surface. It may also minimise any interactions of the hydrophobic TCO with the external domains of the antibody. Girentuximab was used as a proof-of-concept antibody to investigate if H$_2$Macropa-Tetrazine could react with TCO functionalised antibodies *in vitro* (Figure 84).

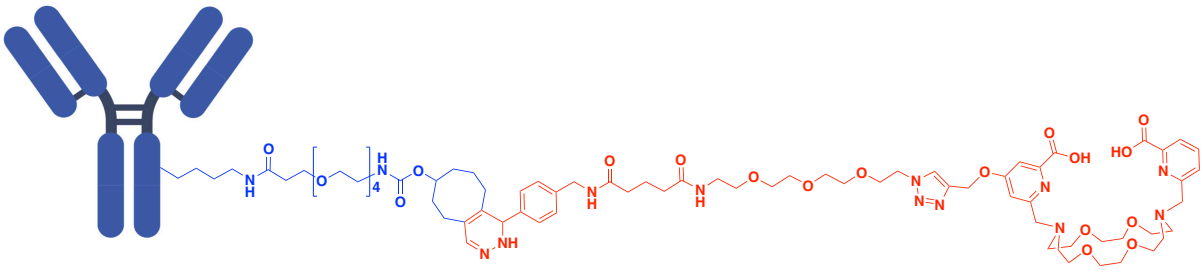

Figure 84: Schematic of TCO-PEG$_4$-hG250, which has undergone an iEDDA reaction with H$_2$Macropa-tetrazine (monoclonal antibody not drawn to scale).

The ‘intact’ deconvoluted mass spectrum of unmodified girentuximab (Figure 85, a) shows the characteristic peaks with a mass of 147 kDa. Incubation of 10 equivalents of TCO-PEG$_4$-NHS ester for 1 hour resulted in the attachment of between 1 and 6 TCO-PEG$_4$ fragments per antibody (Figure 85, b) and excess TCO-PEG$_4$-NHS was removed *via* spin filtration.

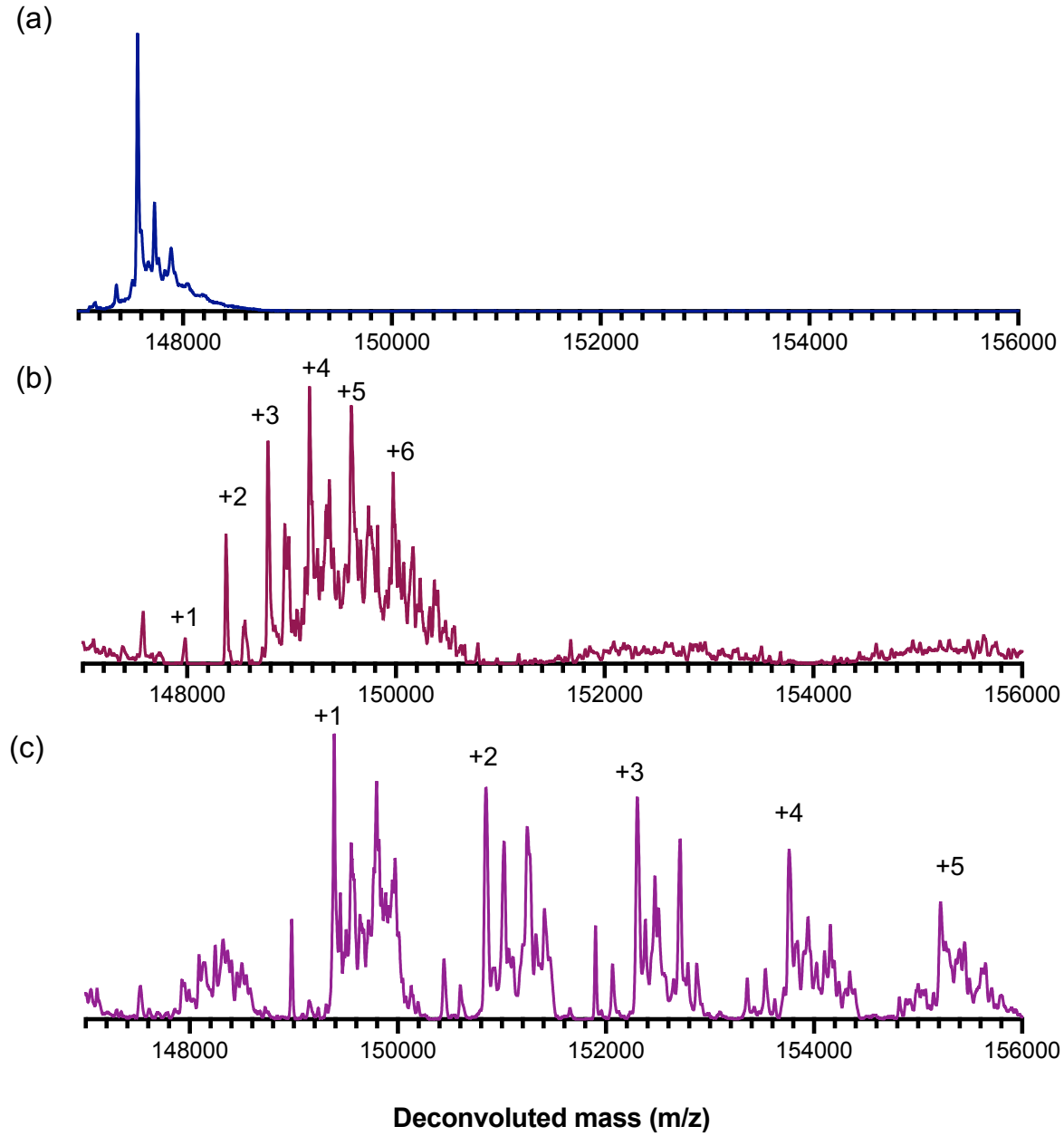

Figure 85: ESI-TOF deconvoluted mass spectra of (a) unmodified Girentuximab (hG250), (b) TCO-Peg$_4$-hG250 showing between 1-6 trans-cyclooctene attachments and (c) H$_2$Macropa-Tz-TCO-Peg$_4$-hG250 showing reaction between the tetrazine and the trans-cyclooctene.

The iEDDA reaction of the TCO functional groups on hG250 was confirmed with the addition of 10 equivalents of H$_2$Macropa-Tetrazine which was reacted for 1 hour to ensure

complete conversion to the clicked dihydropyradizine adduct (Figure 84). It is possible to follow the reaction *via* the change in mass between peaks of the highest intensity in the deconvoluted MS. Before the tetrazine-TCO cycloaddition, peaks were separated by 400 Da, which is equivalent to the reaction between TCO-PEG_4-NHS in the formation of a covalent amide bond to surface lysine residues. After reaction with H_2Macropa-tetrazine, each peak corresponds to a mass difference of 1460 Da, equivalent to the dihydropyradizine clicked product adduct where dinitrogen is evolved (Figure 84, c).

5.5.3 Radiolabelling of H_2Macropa-Tetrazine with Actinium-225

Radiolabelling of H_2Macropa-Tetrazine (H_2L^3) with $[^{225}Ac]Ac^{III}$ was performed using the same conditions as $[^{225}Ac]$Ac(MacropaSq-hG250). Radiochemical experiments were performed with 37 kBq (10 µCi) of neutralised $[^{225}Ac]Ac^{III}$ in $NaCH_3CO_2$ (7.5 µL, 0.15 M) and H_2Macropa-Tetrazine (91 nmol, 1 µL). At a ligand concentration of 1.5 µM, quantitative radiolabelling was achieved within 15 minutes. The resulting radiolabelled construct was used without further purification, and the radiochemical purity (RCP) was found to be greater than 99.9 % using radioTLC (Figure 86, stationary phase of aluminium chromatography paper impregnated with silica gel and a mobile phase of 0.04 M citrate buffer and 10% CH_3OH at a pH of 4.0).

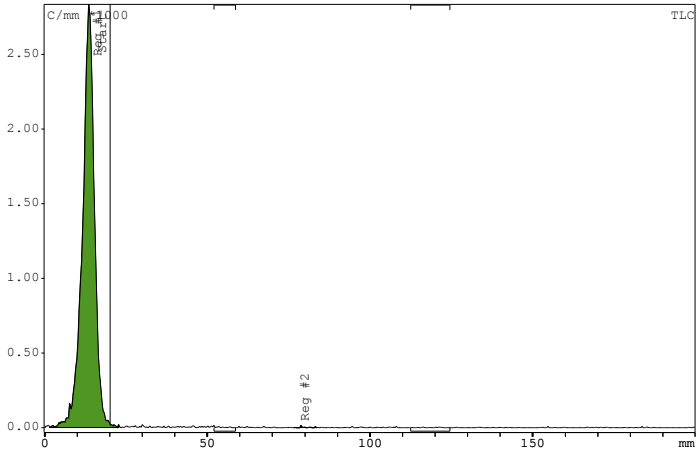

Figure 86: RadioTLC of $[^{225}Ac]$AcMacropa-Tetrazine (91 nmol, 1.5 µM)

The radiochemical synthesis of [^{225}Ac]Ac(Macropa-Tetrazine) has the distinct advantage of rapid, room-temperature labelling. The radiocomplex [^{225}Ac]Ac(Macropa-Tetrazine) does not require post labelling-purification, unlike [^{225}Ac]Ac^{III} complexes derived from tetraaza macrocycles such as H_4DOTA. The development of this new ligand is particularly important due to the highly reactive nature of the 1,2,4,5-tetrazine moiety. The unwanted breakdown of the heterocyclic ring due to excessive heating may decrease potential yield of the reaction. Comparison of the radiolabelling conditions of [^{225}Ac]Ac(Macropa-Tetrazine) and [^{225}Ac]Ac(DOTA-peg$_7$-Tz) highlight some potential advantages with using 'Macropa' based ligand to form complexes with [^{225}Ac]Ac^{III} (Table 19). [^{225}Ac]Ac(Macropa)-based complexes form complexes of quantitative radiochemical yield and purity without the need for purification by C18 column. As such, the final specific activity of [^{225}Ac]Ac(Macropa-Tetrazine) was 0.46 MBq μmol^{-1}, approximately three times greater than complexes derived from [^{225}Ac]Ac(DOTA).

Table 19: Radiolabelling conditions of [^{225}Ac]Ac(Macropa-Tetrazine) and [^{225}Ac]Ac(DOTA-peg$_7$-Tz).

Compound	[^{225}Ac]Ac(Macropa-Tetrazine)	[^{225}Ac]Ac(DOTA-peg$_7$-Tz)
Time	15 minutes	60 minutes
Temperature	RT	37 °C
RCY	> 99.9 %	66 – 96 ± 2%
Purification	N/A	C18
RCP	> 99%	> 98%
Specific Activity	0.46 MBq μmol^{-1}	0.17 ± 0.03 MBq μmol^{-1}

The development of this new ligand is particularly important due to the highly reactive nature of the 1,2,4,5-tetrazine moiety. The unwanted breakdown of the heterocyclic ring due to excessive heating may decrease potential yield of the reaction.

5.6 Conclusions and Future work

The feasibility of utilising the iEDDA to overcome some of the pharmacokinetic limitations of using directly radiolabelled antibodies for radioimmunotherapy has been investigated by others. Poty *et al.* highlighted the incredible selectivity and specificity of the

tetrazine *trans*-cyclooctene click reaction, with excellent localisation of [^{225}Ac]Ac^{III} radiotracers within the tumour environment.[324]

The work in this thesis utilised the 18-membered crown ether macrocycle (H_2Macropa) and developed a new radioligand (H_2Macropa-Tetrazine) with an appended 1,2,4,5-tetrazine. H_2Macropa-Tetrazine can be rapidly radiolabelled at room temperature with [^{225}Ac]Ac^{III} and forms complexes of quantitative radiochemical purity.

The high demand for [^{225}Ac]Ac^{III}, coupled with supply issues of the radionuclide, means that any protocols that can quantitatively incorporate actinium-225 into the targeting vector are of significant benefit, and reducing any post-labelling purification steps is a welcome advantage, which may impact the overall feasibility of using this type of reaction in the future. The conditions for both the radiolabelling with [^{225}Ac]Ac^{III} and the 'click' reaction have been optimised. Future work will involve investigating the potential of the iEDDA reaction between [^{225}Ac]Ac(Macropa-Tetrazine) and TCO-modified antibodies *in vitro*. A future objective of this work will focus on exploring this pretargeted technique in animal models of disease.

5.7 Experimental

5.7.1 (4-(1,2,4,5-tetrazin-3-yl)phenyl)methanamine hydrochloride (20)

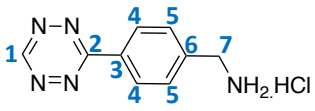

This product was prepared *via* modification of reported literature procedure.[325] 4-(aminomethyl)benzonitrile hydrochloride (168 mg, 1 mmol), formamidine acetate (1040 mg, 10 mmol and $Zn(OTf)_2$ (181 mg, 5% mmol) were dissolved in ethanol (2 mL), then treated with hydrazine *mono*hydrate (2.62 mL, 53 mmol) dropwise and sealed in a microwave reaction vial and stirred at room temperature for 48 hours. $NaNO_2$ (2070 mg, 30 mmol) in H_2O (15 mL) was added slowly to the reaction mixture, followed by the dropwise addition of HCl (1.5M, 30 mL) until the solution reached pH 3 and stopped bubbling, changing colour from yellow to bright red. The reaction mixture extracted into DCM until the organic fractions were colourless and were discarded. The aqueous layer was saturated with NaCl and $NaHCO_3$ and after the bubbling had desisted was extracted into 1:3 IPA:$CHCl_3$ (3 x 50 mL), dried with $MgSO_4$ and taken to dryness under reduced pressure. The resulting precipitate was purified by semi preparative HPLC (Method C), then lyophilised. (45 mg, 0.21 mmol, 20%). R_t : 4.45 minutes (method A, column A). ESI-MS $[M\text{-}Cl+H]^+$: 188.0932 calculated for $(C_9H_{12}N_5)^+$: 188.0931 ^1H NMR (500 MHz, MeOD) δ 10.38 (s, 1H, 1), 8.67 (d, J = 8.5 Hz, 2H, 4), 7.74 (d, J = 8.5 Hz, 2H, 6), 4.27 (s, 2H, 7). ^{13}C NMR (126 MHz, MeOD) δ 167.3 (1), 159.5 (2), 139.2 (6), 134.3 (3), 130.9 (4), 129.8 (5), 43.9 (7).

5.7.2 Tetrazine glutaric acid (21)

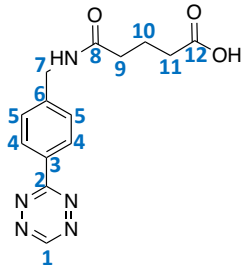

(4-(1,2,4,5-tetrazin-3-yl)phenyl)methanamine hydrochloride (31 mg, 0.139 mmol) and triethyl amine (22 µL, 0.157 mmol) were added to dry DCM (3 mL) under an atmosphere of N_2 to liberate free amine. After 5 minutes glutaric anhydride (18 mg, 0.157 mmol) was added and refluxed at 50 °C overnight. The reaction mixture was taken to dryness under reduced pressure and purified *via* column chromatography (SiO_2, 0-2 % MeOH in CH_2Cl_2). Pure fractions were collected and taken to dryness *in vacuo* to yield a bright pink solid (31 mg, 76%). ESI-MS$[M+H]^+$: 302.1247. calculated for $(C_{14}H_{16}N_5O_3)^+$: 302.1248 R_t: 6.74 min (system A, column A, method A). ^{1}H NMR (500 MHz, MeOD) δ 10.33 (s, 1H, 1), 8.57 (d, J = 8.4 Hz, 2H, 4), 7.57 (d, J = 8.2 Hz, 1H, 5), 4.51 (s, 2H, 7), 2.42 – 2.33 (m, 4H, 8, 11), 1.96 (p, J = 7.4 Hz, 2H, 10). ^{13}C NMR (126 MHz, MeOD) δ 177.00 (12), 175.50 (8), 167.64 (1), 159.26 (2), 145.64 (6), 132.32 (3), 129.34 (4, 5), 49.00, 43.77 (7), 36.09 (9), 34.27 (11), 22.36 (10).

5.7.3 Tetrazine NHS ester (22)

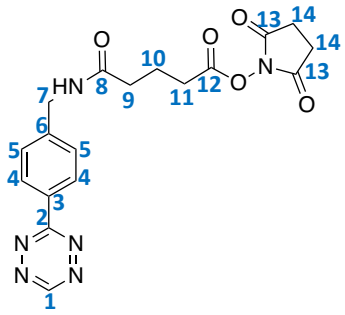

Tetrazine glutaric acid ***21*** (30 mg, 0.1 mmol) was dissolved in dry DCM (3 mL), and DIPEA (100 µL) was added under an atmosphere of N_2. EDC.HCl (23 mg, 0.12 mmol) and N-hydroxy succinimide (13 mg, 0.12 mmol) were added and stirred at room temperate overnight until TLC confirmed no starting material remained. The pink solution was taken to dryness under reduced

pressure and washed with chilled H_2O (3 × 10 mL) to remove excess EDC and lyophilised to give a pink powder (25mg, 65%). ESI-MS $[M+H]^+$: 399.1414 calculated for $(C_{18}H_{19}N_6O_5)^+$:399.1412. R_t: 7.01 min (system A, column A). ^1H NMR (500 MHz, MeOD) δ 10.34 (s, 1H, 1), 8.59 – 8.55 (m, 2H, 4), 7.59 (d, *J* = 8.3 Hz, 2H, 5), 4.53 (s, 2H, 7), 2.86 (s, 4H, 14), 2.77 – 2.70 (m, 2H, 11), 2.46 (t, *J* = 7.4 Hz, 2H, 9), 2.09 (q, *J* = 7.3 Hz, 2H, 10). ^{13}C NMR (126 MHz, MeOD) δ 173.43 (8), 170.44 (12), 168.48 (13), 166.25 (1), 157.86 (2), 144.18 (6), 130.94 (3), 127.99 (5), 127.95 (4), 42.41 (7), 33.92 (9), 29.44 (11), 25.08 (14), 24.87, 20.45 (10).

5.7.4 Compound 23

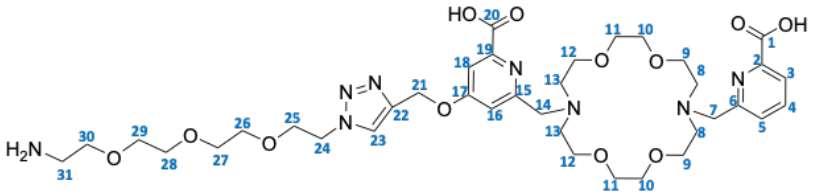

Sodium Ascorbate (1.5 mg, 0.075 mmol, 57 µL in H_2O) and $CuSO_4$ (0.8 mg, 0.003 mmol, 29 µL in H_2O) were combined and allowed time for the copper(II) to reduce to copper(I). Then **12** (20 mg, 0.033 mmol in 250 µL DMF), and azido-3,6,9-trioxaundecan-1-amine (7.5 mg, 0.032 mmol) were added to the reaction mixture and stirred for 1 hour. Na_2S (0.7 mg, in 20 µL H_2O, 0.009 mmol) was added to precipitate the copper species, which formed a black precipitate and was removed *via* centrifugation and taken to dryness under reduced pressure. To a solution of **23** in methanol (450 µL), was added a suspension of NaOH in methanol (50 µL, 3 M), so the final concentration of NaOH was 0.3 M. The reaction mixture was stirred at room temperature for 1 hour, the NaOH was neutralised, and the solvent was removed under reduced pressure. The crude mixture was purified *via* semi-preparative HPLC (method C) to yield a colourless oil (15.2 mg, 58 %). R_t = 7.75 mins (method A, Column B). ESI-MS $[M+2H]^{2+}$: 403.7083, $[M+3H]^{3+}$: 269.1415 calculated for $(C_{37}H_{58}N_8O_{12})^{2+}$: 403.7099 calculated for $(C_{37}H_{59}N_8O_{12})^{3+}$: 269.1412. ^1H NMR (500 MHz, D_2O) δ 8.21 (s, 1H, 23), 7.98 (t, *J* = 7.7 Hz, 1H, 4), 7.93 (dd, *J* = 7.9, 1.1 Hz, 1H, 5), 7.62 – 7.56 (m, 2H, 3, 18), 7.31 (d, *J* = 2.4 Hz, 1H, 16), 5.41 (s, 2H, 21),

4.82 (s, 7H, unknown), 4.74 (s, 5H, unknown), 4.63 (t, *J* = 5.0 Hz, 2H, 25), 4.57 (s, 2H, 7), 4.41 (s, 2H, 14), 3.95 (t, *J* = 5.0 Hz, 2H, 24), 3.81 (dt, *J* = 19.3, 5.0 Hz, 8H, 9, 12), 3.71 (td, *J* = 5.0, 0.9 Hz, 2H, 30), 3.62 – 3.57 (m, 4H, 26, 27), 3.55 (h, *J* = 4.2 Hz, 12H, 10, 11, 28, 29), 3.52 – 3.36 (m, 8H, 8, 13), 3.21 – 3.16 (m, 2H, 31). ^{13}C NMR (126 MHz, D_2O) δ 172.34 (1), 171.28 (17), 171.00 (20), 166.37 (FA), 155.12 (2, 19), 153.57 (6, 15), 142.22 (22), 139.14 (4), 126.14 (3), 125.87 (23), 123.86 (5), 112.66 (16), 109.93 (18), 69.58 (10, 11), 69.55, 69.52, 69.43, 69.38 (26, 27, 28, 29), 68.67 (24), 66.32 (30), 65.32 (9 or 12), 64.53 (9 or 12), 61.19 (21), 58.41 (7), 57.89 (14), 57.55 (8 or 13), 54.76 (8 or 13), 54.24 (unknown), 50.11 (25), 39.06 (31).

5.7.5 H_2Macropa-Tetrazine (24)

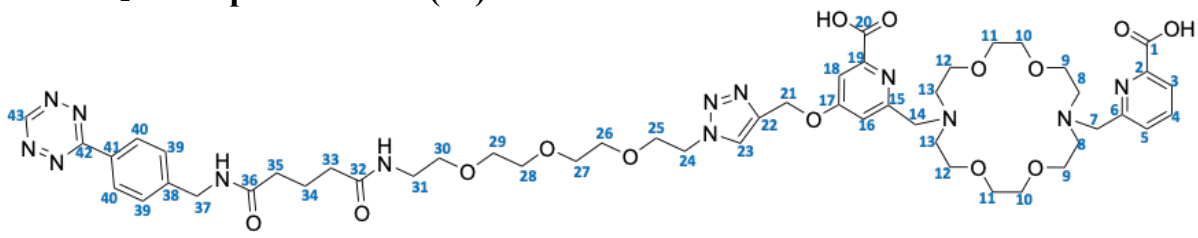

23 (5 mg, 0.006 mmol) and DIPEA (1 μL, 0.006 mmol) were dissolved in CH_3CN (0.5 mL) and left to stir at room temperature for 30 minutes. To this solution was added ***22*** and the pink solution was reacted at 45°C for 1 hour. To the crude solution was added MilliQ (4 mL) and purified by semi-preparative HPLC (Method E). Pure fractions were combined and lyophilised to yield a pink powder (3.5 mg, 53%). R_t = 10.88 mins (method A, column B). ESI-MS $[M+H]^+$: 1088.5162, $[M+2H]^{2+}$: 544.7627, $[M+3H]^{3+}$: 363.5104; calculated for $(C_{51}H_{70}N_{13}O_{14})^+$ 1088.5160, $(C_{51}H_{71}N_{13}O_{14})^+$ 544.7616, $(C_{51}H_{72}N_{13}O_{14})^+$ 363.5210. ^{1}H NMR (500 MHz, D_2O) δ 10.34 (s, 1H, 43), 8.37 – 8.29 (m, 2H, 40), 8.17 (s, 1H, 23), 7.98 (t, *J* = 7.7 Hz, 1H, 4), 7.93 (d, *J* = 7.7 Hz, 1H, 5), 7.58 (d, *J* = 7.6 Hz, 1H, 3), 7.50 (d, *J* = 8.1 Hz, 3H, 19, 39), 7.18 (d, *J* = 2.4 Hz, 1H, 16), 5.30 (s, 2H, 21), 4.63 (s, 2H, 4), 4.58 (t, *J* = 5.0 Hz, 2H, 25), 4.49 (s, 2H, 14), 4.45 (s, 2H, 37), 3.91 (t, *J* = 4.9 Hz, 2H, 24), 3.83 (dt, *J* = 17.1, 4.9 Hz, 8H, 9,

12), 3.62 – 3.46 (m, 26H, 26, 27, 28, 29, 30, 8, 10, 11, 13), 3.34 (t, J = 5.2 Hz, 2H, 31), 2.34 (t, J = 7.4 Hz, 2H, 35), 2.27 (t, J = 7.4 Hz, 2H, 33), 1.96 – 1.84 (m, 2H, 34). ^{13}C NMR (126 MHz, D_2O) δ 175.76 (36), 172.20 (32), 170.63 (17) 166.51 (20), 166.16 (1), 157.35 (43), 154.90 (42), 153.51 (2, 19), 143.62 (6, 15), 142.03 (38), 139.25 (41), 130.16 (22), 128.40 (39), 128.06 (40), 125.96, 125.83 (3), 123.97 (5), 112.49 (16), 110.18 (18), 69.59 (10,11), 69.54, 69.42, 69.35, 68.73, 68.62, (24, 26, 27, 28, 29) 64.78 (9 or 12), 64.29 (9 or 12), 61.30 (21), 58.25 (14), 58.15 (7), 54.55 (13 or 8), 54.23 (8 or 13), 50.09 (25), 42.67 (37), 38.89 (31), 34.80, 34.72 (35), 30.20 (33), 21.72 (34).

5.7.6 Proof of concept *in vitro* 'click' reaction quantified by mass spectrometry.

A solution of TCO-PEG$_4$-NHS ester (7 μL of 5 mg/mL stock solution in DMSO, 10 equivalents) was added to a solution of hG250 (5.04 mg/ mL) in PBS (1x, pH 7.4) and the reaction was incubated in the dark at room temperature for 1 hour. Excess reagents were removed and buffer exchanged (HEPES, 0.1M, pH7.4) *via* spin filtration (50 KDa MW cut off). Analysis by intact protein mass spectrometry determined the chelator antibody ratio (CAR) to be approximately 4, with a mass difference of 401 Dalton between major peaks, indicating that the TCO-peg4-succimidyl ester has attached to surface lysine residues on the antibody. H_2Macropa-Tetrazine (4 μL, 10 equivalents) was added to a solution of hG250-TCO (120μg) in 10 mM HEPES and shaken in the dark for one hour. Excess reagents were removed, and buffer was exchanged ($NaCH_3CO_2$, 10 mM, pH 5.5) *via* spin filtration (50 KDa MW cut off).

5.7.7 Radiolabelling H_2Macropa-Tetrazine

[^{225}Ac]$AcCl_3$ was buffered into $NaCH_3CO_2$ (0.15 M, pH 5.5, stock 1). H_2Macropa-Tetrazine was diluted to a final concentration of 18 μM in MilliQ. H_2Macropa-Tetrazine (5 μL for 7 μM and 1 μL for 1.5 μM) was added to stock 1 (7.5 μL, 1 μCi/ 37 kBq) and left for 15 minutes at room temperature. The radiolabelled constructs were used without further purification, RCP,

> 99% performed *via* radioTLC (stationary phase aluminium chromatography paper impregnated with silica gel, mobile phase: 0.04 M citrate buffer + 10% CH_3OH, pH 4.0).

6 Pre-Targeting Amyloid-β with Antibodies: Toward Antibody Targeted Molecular Imaging of Alzheimer's Disease

Aspects of this work have been published in the journal article titled: Pre-targeting amyloid-β with antibodies for potential molecular imaging of Alzheimer's disease. *Chem. Commun.* **2023,** 59, 2243-2246.[327]

6.1 Introduction

Alzheimer's disease (AD) is a progressive neurodegenerative condition that leads to cognitive and behavioural impairment.[328] The pathology of AD is characterised by the presence of both amyloid-β and tau pathology in the brain.[329-331] The biological impact of amyloid-β plaques and neurofibrillary tau tangles (NFT) is controversial, and these structures may not play a causal role in the pathogenesis of AD; however, the presence of these abnormal protein deposits define AD and form the basis of its differential diagnosis from other dementias.[328, 332]

6.1.1 The Pathology of Alzheimer's Disease

A major component of amyloid-β plaques are aggregated forms of the amyloid-β peptide (Aβ), which is formed by cleavage of the amyloid precursor protein (APP), a type I transmembrane glycoprotein of 695 – 770 amino acids.[333] The gene encoding the amyloid precursor protein (APP) is found on chromosome 21.[330] There are multiple pathways for APP proteolysis, not all of which release the Aβ peptide. APP is cleaved by both α- and β-secretases, which release soluble derivatives of the protein (α-APP and β-APP) and retain the membrane-anchored C-terminal fragments.[334] BACE1, known as beta-site amyloid precursor protein cleaving enzyme 1, is the transmembrane aspartic protease responsible for cleavage of APP forming the cell membrane-bound C-terminal fragment terminal C99; this is then cleaved by γ-secretase generating the Aβ peptide (Figure 87, a, b).[335]

Cleavage of APP leads to the formation of fragments of various lengths, with the 40 amino acid variant ($A\beta_{1-40}$) and 42 amino acid variants ($A\beta_{1-42}$), both being significant. Aβ42 exhibits a higher potential for self-aggregation into oligomers and protofibrils; it is the predominant component of senile plaques.[336] The length of the hydrophobic tail of the Aβ peptide is a crucial factor that determines its aggregation and toxicity,[337, 338] Aggregation of Aβ leads to the formation of oligomers, protofibrils, fibrils and finally, the deposition of extracellular plaques.[333, 339]

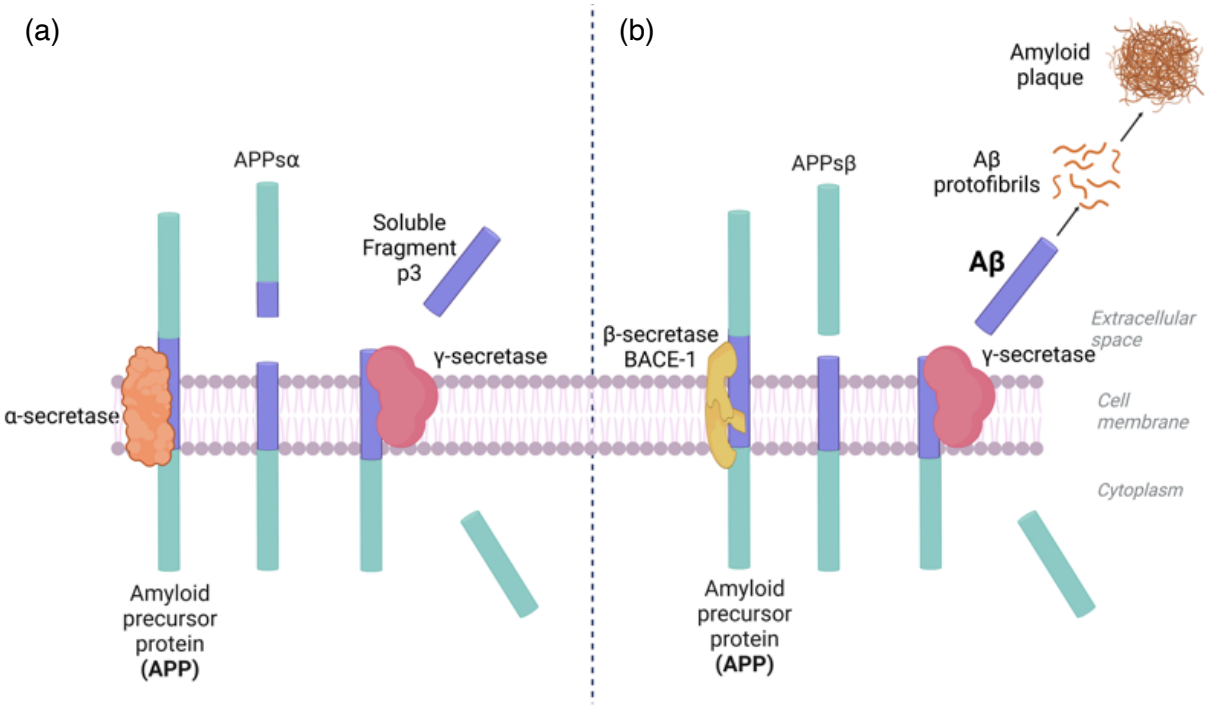

Figure 87: (a) Non-amyloidogenic processing of APP by α-secretase then γ-secretase releasing the p3 soluble fragment; (b) amyloidogenic processing of APP by BACE1 followed by cleavage by γ -secretase, releasing 39-42 amino acid Aβ peptide. Adapted from O'Brien.[335, 340] Created with biorender.com.

Tau pathology in AD involves intracellular deposition of hyperphosphorylated tau protein to form neurofibrillary tangles (NFT), which lead to progressive cytoskeletal changes and disrupts axonal transport.[339] NFT consists of hyperphosphorylated forms of the protein tau, that aggregates inside nerve cell bodies, known as dystrophic neurites; it results in impaired axonal transport and altered synaptic function.[331, 341]

The Aβ peptides aggregate to form plaques due to electrostatic interactions, hydrogen bonding and the π-π stacking of aromatic residues (such as phenylalanine at the 19 and 20 position).[342] The Aβ peptide contains hydrophobic segments in the middle (17-21) and C terminus residues (30-40). The formation of parallel β sheets (Figure 88, a) results in hydrophobic pockets within the structure, to which small conjugated aromatic molecules bind *via* π-π interactions (Figure 88, b).[343]

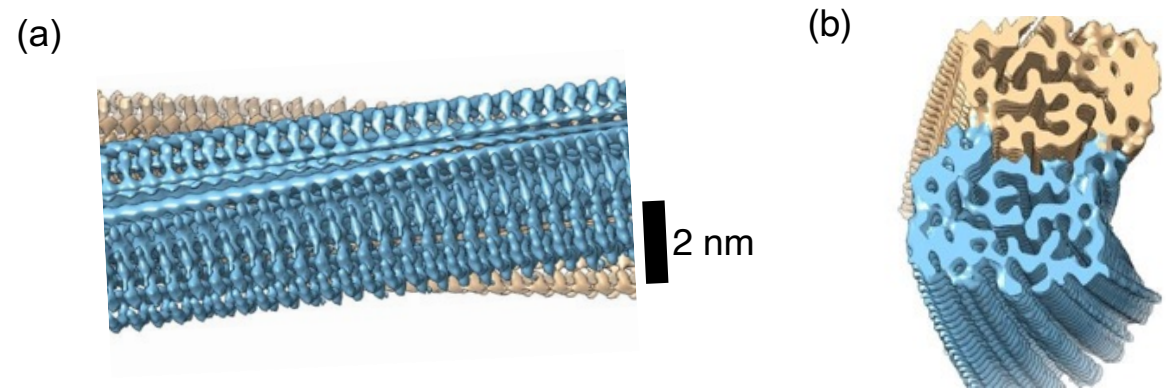

Figure 88: (a) Schematic representation of Aβ monomers sacking to form a cross β-sheet structure; (b) protofilaments twist together in a helical geometry to form protofibrils, which further aggregate into senile plaques.[344]

6.1.2 Diagnostic Imaging of the Amyloid-β Burden

Positron Emission Tomography (PET) imaging using radiolabelled small molecules that bind to amyloid-β plaques can assist in the differential diagnosis of AD.[339] For some patients, amyloid-β burden does not directly correlate with cognitive impairment.[345] This observation has contributed to the conjecture that soluble Aβ fibrils and oligomers, that are thought to be in equilibrium with the insoluble Aβ plaques are neurotoxic species.[346, 347] It is possible that synergistic interactions between amyloid-β plaques and NFT lead to neurotoxicity.[348]

Current approaches for PET imaging of amyloid-β use small molecules radiolabelled with positron-emitting fluorine-18 that bind to insoluble Aβ plaques. These tracers are typically small aromatic, planar and lipophilic molecules, such as derivatives of stilbenes

([^{18}F]Florbetaben, Figure 89, a), styrylpyridines ([^{18}F]Florbetapir, Figure 89, b) or benzothiazoles ([^{18}F]Flutemetamol, Figure 89, c), that bind to insoluble amyloid-β plaques through a combination of hydrophobic and non-covalent interactions but offer little insight into the presence of soluble Aβ fibrils and oligomers.[349] A limitation of using radiolabelled tracers that interact with the β-sheets, such as [^{18}F]Florbetapir, is the lack of selectivity, with no preferential binding interaction to intracellular neurofibrillary tangles, extracellular Aβ plaques, monomers or the soluble oligomeric species, which are increasingly considered neurotoxic.

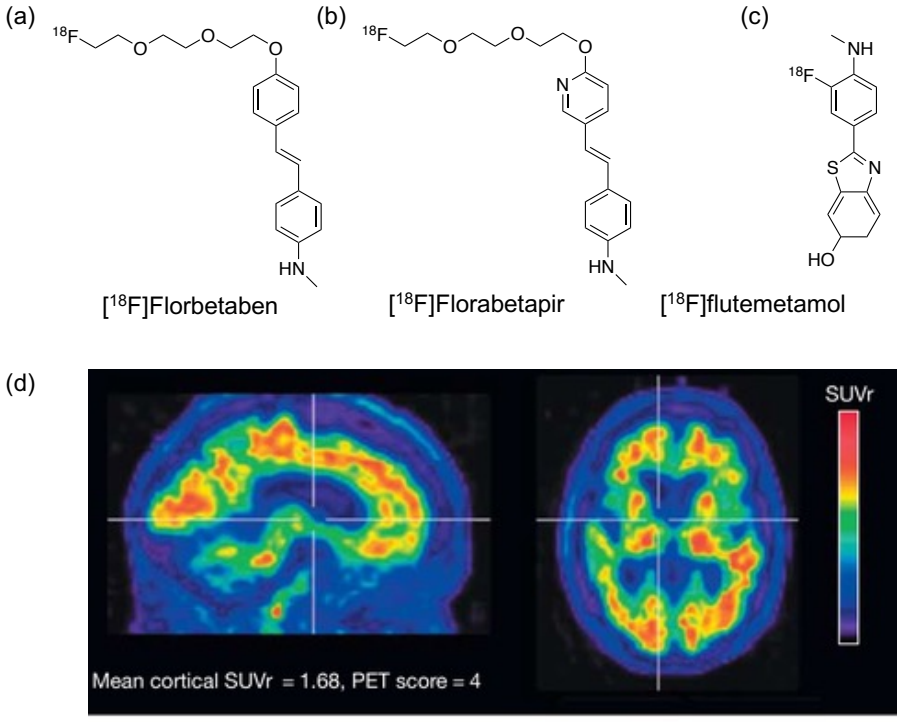

Figure 89: Chemical structure of (a) [^{18}F]Florbetaben, (b) [^{18}F]Florabetapir, (c) [^{18}F]flutemetamol, (d) Sagittal (left) and axial (right) PET image of a patient after administration of [^{18}F]Florabetapir. Maximum colour corresponds to a standard uptake value (SUV, the concentration of the tracer in tissue typically divided by the injected activity and body weight) approximately 2.2.[350]

6.1.3 [^{64}Cu]Cu^{II}-based complexes of *bis*(thiosemicarbazones) are Stable

Alternatively, incorporation of a metal radioisotope such as [^{64}Cu]Cu^{II} *via* metal complexation has proven a promising alternative to traditional radiotracer syntheses.[351] The relatively longer half-life of copper-64 ($t_{1/2}$ = 12.7 hours, 511 keV)[352] and unique decay scheme which combines

electron capture (40%), β^- (40%) and β^+ (19%) decay, makes it possible to image [^{64}Cu]Cu^{II} based radiopharmaceuticals over a longer time period compared to traditional [^{11}C]C or [^{18}F]F tracers.[352-354]

Bis(thiosemicarbazone) ligands form complexes with copper-64 radionuclides that are sufficiently stable for PET imaging applications. The copper(II) *bis*(thiosemicarbazonato) complex diacetyl*bis*(4-methyl-3-thiosemicarbazone) (Cu^{II}(atsm), Figure 90, a) is charge neutral, lipophilic and is capable of crossing the blood-brain barrier allowing PET imaging of the brain in human subjects.[355-357] Previous work in the Donnelly lab focused on modifying the *bis*(thiosemicarbazone) ligand to append substituted stilbenyl functional groups (Figure 90, b). These copper(II) complexes bind to amyloid-β plaques in human brain tissue.[341, 343, 358-361]

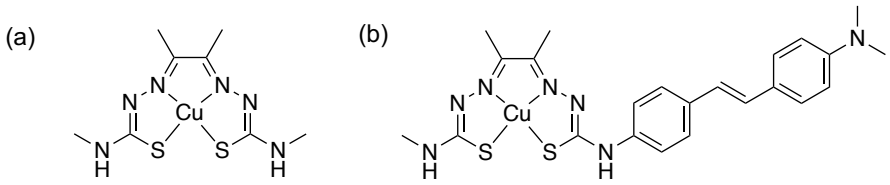

Figure 90: Chemical structure of (a) Cu(atsm), where $R^1 = R^2 = CH_3$; (b) Cu(atsm-stilbene), which binds to amyloid-β plaques.[359]

Copper(II) complexes of *bis*(thiosemicarbazones) are stable ($K_a \sim 10^{18}$), but the reduction of the metal to copper(I) can lead to dissociation from the ligand and transfer of the copper to proteins that have a high affinity for copper(I).[362] Electron donating methyl or ethyl substituents on the backbone of the ligand (R^1 and R^2 in Figure 90, a) yield copper(II) complexes that are more resistant to reduction to copper(I). The nature of the substituents on *bis*(thiosemicarbazone)copper(II) complexes also influences their solubility, lipophilicity, interaction with serum proteins, membrane permeability and ultimately their biodistribution.[363-366]

6.1.4 Monoclonal Antibodies Gain Approval for the Treatment of Alzheimer's Disease

Antibodies can be engineered to have a very high affinity for specific targets and often offer better selectivity than small molecules. Several anti-Aβ antibodies that target different regions or forms of Aβ have been developed, and consequentially, diagnostic imaging with radiolabelled antibodies has the potential to offer insights that complement conventional amyloid-β plaque imaging. For example, aducanumab (Aduhelm) is a recombinant IgG1 antibody that binds to soluble Aβ aggregates and insoluble fibrils in preference to monomers.[367] Aducanumab was approved by the FDA in 2021 for the treatment of AD, although its approval was controversial.[368]

Aducanumab crosses the blood-brain barrier and accumulates in the brain of transgenic mice (Tg2576), which are genetically modified mice that represent a model of amyloid pathology. Administration of a single dose (30 mg kg^{-1}) to Tg2576 transgenic mice resulted in the highest concentration of the antibody in the blood (C_{max}) in the brain of 1,062 ng g^{-1} of tissue.[367] The single administration led to long-term retention with significant quantities of antibody (400–500 ng g^{-1}) detectable three weeks after administration suggesting more than one dose of the monoclonal antibodies should lead to higher concentrations of antibody in the brain. Repeated administration of a suitably modified antibody should lead to concentrations in the brain which can be targeted by a radiolabelled small molecule.

6.1.5 Antibody Pretargeting may Overcome Challenges of Brain ImmunoPET

Developing immunoconjugates as brain imaging agents has been a challenge due to the difficulty of amyloid-specific antibodies to cross the blood-brain barrier (BBB). Nevertheless, the antibodies Aducanumab and BAN2401 have shown promising BBB permeability.[369, 370] These studies confirm that the chronic dosing required, in combination with long circulation

times to reach optimum uptake, is a significant limitation to directly labelling antibodies for brain imaging.

PET imaging with radiolabelled antibodies (immunoPET) has already made a significant impact in the diagnosis of cancer and can be used to plan personalised therapy, but the application of immunoPET to diagnose neurodegenerative diseases presents difficulties. A major challenge is the large molecular weight of radiolabelled antibodies (~150 kDa) that significantly limits their passage across the blood brain barrier. Antibodies typically take several days to clear from the blood and accumulate within the target, which necessitates labelling antibodies with radionuclides with a long radioactive half-life. PET imaging of cancer patients with radiolabelled antibodies normally requires imaging the patient several days after administration to enable sufficient delineation of the signal from the background and accumulate in the tumour. This complicates its clinical implementation.

The selectivity and fast reaction kinetics ($k_2 \sim 10^5$ M^{-1} s^{-1}) of inverse-electron-demand Diels-Alder reactions between electron-deficient tetrazines and strained *trans*-cyclooctene (TCO) derivatives are well suited for *in vivo* pre-targeting (see section 5.3). Pre-targeting of tumours using antibodies modified to incorporate TCO and radiolabelled molecules featuring a tetrazine has been demonstrated in animal models for both PET imaging and radionuclide therapy.[371, 372] Antibodies that do not internalise upon binding to the antigen are best suited to *in vivo* click reactions,[320, 321, 373] so antibodies such as aducanumab that bind to extracellular soluble Aβ aggregates and insoluble fibrils are well suited for pre-targeted PET-imaging.

6.2 Aims

In this chapter, we present an antibody 'pre-target and chase' approach that has the potential to circumvent the technical difficulties associated with immunoPET of the brain (Figure 91). This strategy involves administering an antibody that has been modified to incorporate a functional group poised for a bioorthogonal 'click reaction' with a small molecule radiolabelled tracer

that crosses the BBB. The small molecule tracer is administered after allowing sufficient time and repeated dosing to maximise the accumulation of the antibody at the target site in the brain. In previously investigated models of cancer, the optimal time frame was determined to be between 24 – 72 hours.[374]

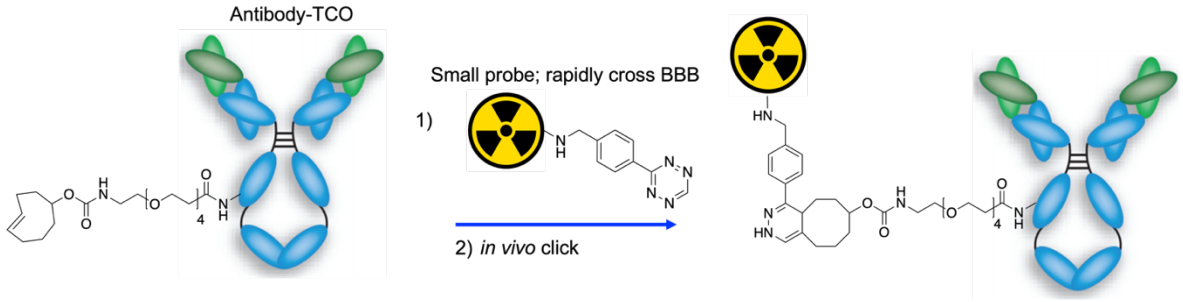

Figure 91: Schematic representation of in vivo inverse-electron-demand Diels-Alder 'click' reaction between tetrazines and strained trans-cyclooctene (TCO). In step 1) the small, radiolabelled probe is administered, and step 2) *in vivo* click between the *trans*-cyclooctene.

In this work, we prepared two ligands with a benzylaminotetrazine (Tz) functional group with either methyl (H_2atsm-Tz) or ethyl (H_2dtse-Tz) groups by selective transamination reactions (Scheme 13).[375, 376] These ligands were designed to form complexes with copper-64 rapidly, at room temperature. We elected to incorporate a 1,2,4,5-tetrazine functional group designed for bioorthogonal *in vivo* click reactions with the TCO-modified antibodies.

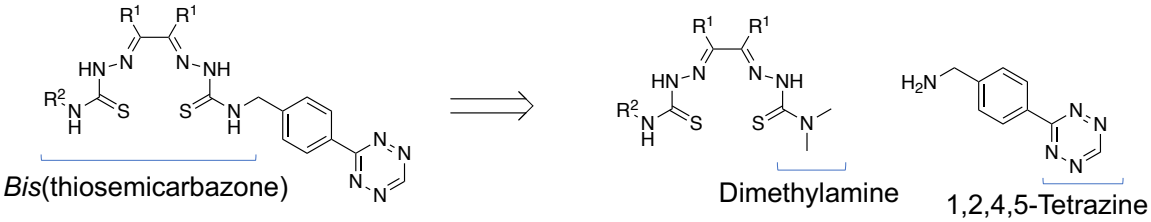

$R^1 = R^2 = CH_3 = H_2$atsm-Tz
$R^1 = R^2 = CH_2CH_3 = H_2$dtse-Tz

Scheme 13: The retrosynthesis and important components in the ligand design of H_2atsm-Tz and H_2dtse-Tz.

The aim of this research project was to develop a proof-of-concept strategy to enable antibody-targeted PET imaging by the preparation of small copper-containing molecules designed to cross the blood brain barrier and react with specifically modified Aβ antibodies.

6.3 Results and Discussion

6.3.1 Previous Work

These ligands and their copper complexes were synthesised and characterised by the PhD candidate before the commencement of the PhD candidature. The cyclic voltammetry of H_2dtse-Tz and Cu(dtse-Tz) was also conducted prior to beginning the PhD study. All other work was conducted as part of the PhD candidature.

6.3.2 Synthesis of Non-symmetrical *Bis*(thiosemicarbazones)

Bis(thiosemicarbazone) ligands are synthesised by condensation reactions between either 2,3-butane dione or 3,4-hexane dione (depending on the desired degree of alkylation on the ligand backbone) and 4-substituted-3-thiosemicarbazides. Non-symmetrical *bis*(thiosemicarbazone) ligands where one limb bears a 4,4′-dimethylthiosemicarbazone, such as **1** and **2** (Scheme 14), react with primary amines to give products in which the amine functional group is incorporated into the ligand.

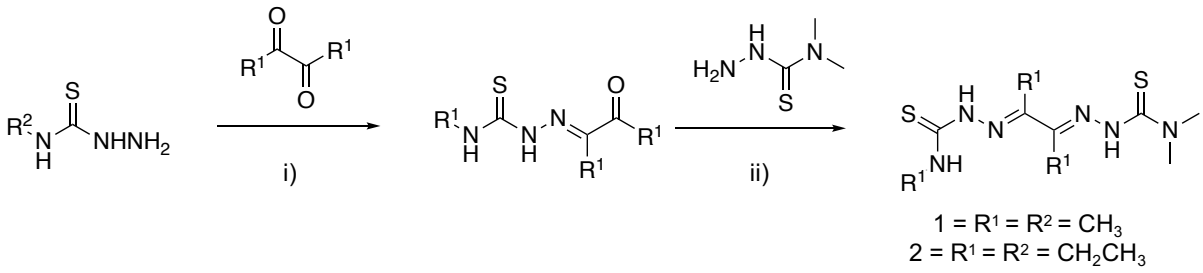

Scheme 14: General synthetic pathway of asymmetric bis(thiosemicarbazones), i) H_2O and HCl (36%); and ii) NN-dimethylformamide, CH_3COOH.

A microwave-assisted transamination of the non-symmetrical *bis*(thiosemicarbazone) ligands (***1*** and ***2***) with a benzylaminotetrazine (Tz, ***3***) and one equivalent of DIPEA to liberate the free amine from the hydrochloride salt proceeded with yields of 64 – 67%. This approach was adopted in lieu of heating to reflux which led to the degradation of the 1,2,4,5-tetrazine moiety, due to its reactivity and instability (Scheme 15). The ligands were purified by

recrystallisation (H_2atsm-Tz) or silica chromatography (H_2dtse-Tz) and characterised by nuclear magnetic resonance, electrospray mass spectrometry, and RP-HPLC.

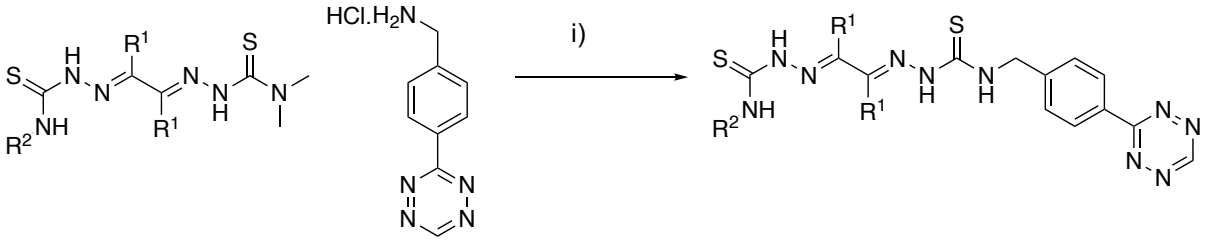

Scheme 15: General synthetic pathway of the ligands H_2atsm-Tz and H_2dtse-Tz; i) CH_3CN, N,N-diisopropylethylamine, using μwave heating (64 –67%). For H_2atsm-tz: $R^1 = R^2 = CH_3$; and for H_2dtse-tz: $R^1 = R^2 = CH_2CH_3$.

6.3.3 Synthesis of copper(II) *bis*(thiosemicarbazone) complexes

The copper complexes, Cu(atsm-Tz) and Cu(dtse-Tz) were formed by the addition of copper (II) acetate hydrate to mixtures of the ligands in N,N-Dimethylformamide (DMF, H_2atsm-Tz) or methanol (H_2dtse-Tz). Acetate ions deprotonate the hydazinic protons on the *bis*(thiosemicarbazone) backbone, and the ligand acts as a dianionic tetradentate N_2S_2 donor, forming charge neutral complexes (Scheme 16).

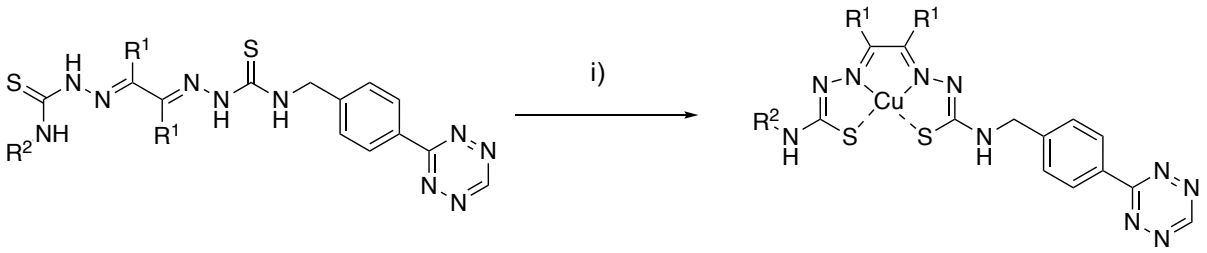

Scheme 16: Copper(II) complexation of H_2atsm-Tz and H2dtse-Tz; i) copper(II) acetate in DMF (Cu(atsm-Tz)) or CH_3OH (Cu(dtse-Tz)) (88%).

The copper(II) complexes, Cu(atsm-Tz) and Cu(dtse-Tz) in (Scheme 16) were characterised by electrospray mass spectrometry and RP-HPLC. Both Cu(atsm-Tz) and Cu(dtse-Tz) have strong absorptions at λ = 495 nm, which is characteristic of metal-ligand-charge transfer transitions. These complexes are both stable to excess glutathione for 24 hours at 37 °C (Figure 92).

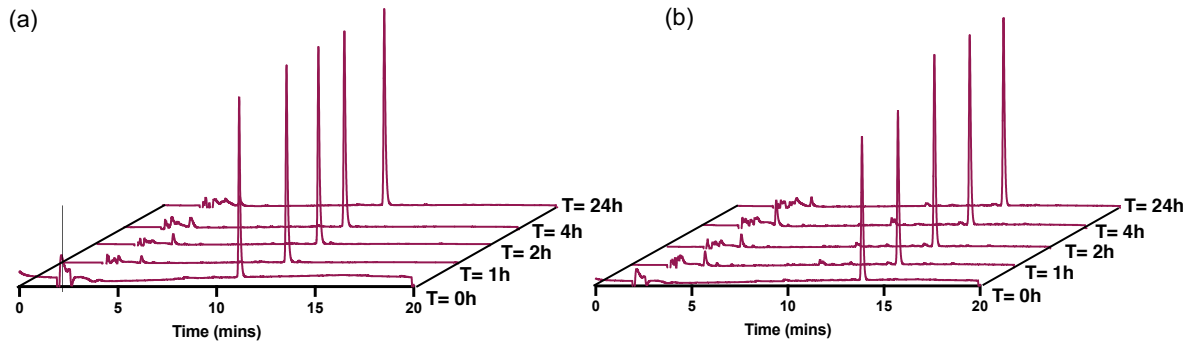

Figure 92: HPLC chromatogram of (a) Cu(atsm-Tz) and (b) Cu(dtse-Tz) incubated with an excess of glutathione in MilliQ /acetonitrile mobile phase containing 0.1% TFA.

For a molecule to be blood brain barrier permeable, it must be small (MW < 600), charge neutral and lipophilic.[360] By increasing the degree of alkylation at the *bis*(thiosemicarbazone) backbone and N-terminus, there was a subtle increase in solubility of the complexes. This may be a result of decreased packing of the large lipophilic complex since the ethyl groups on the ligand backbone inhibit close packing due to the rotation of ethyl groups (R^1) in solution. Nevertheless, this slight increase in solubility may come at a cost of reduced BBB permeability, and both complexes were investigated *in vivo.*

6.3.4 Cyclic Voltammetry of Cu(atsm-Tz) and Cu(dtse-Tz)

Cyclic voltammetry shows that both Cu(atsm-Tz) and Cu(dtse-Tz) undergo a quasi-reversible redox process at $E_{1/2}$ = −1.17 V vs ferricenium/ferrocene (Fc^+/Fc) that can be attributed to a $Cu^{II/I}$ process similar to what is found in Cu(atsm) ($E_m \approx -1.16$ V) (Figure 93, a; Figure 94, a). Each complex also displayed two essentially irreversible and partially overlapping processes at more positive potentials, i.e., E = 0.19 V vs Fc^+/ Fc, which are likely to be due to ligand-based oxidation (Figure 93, b; Figure 94, b).

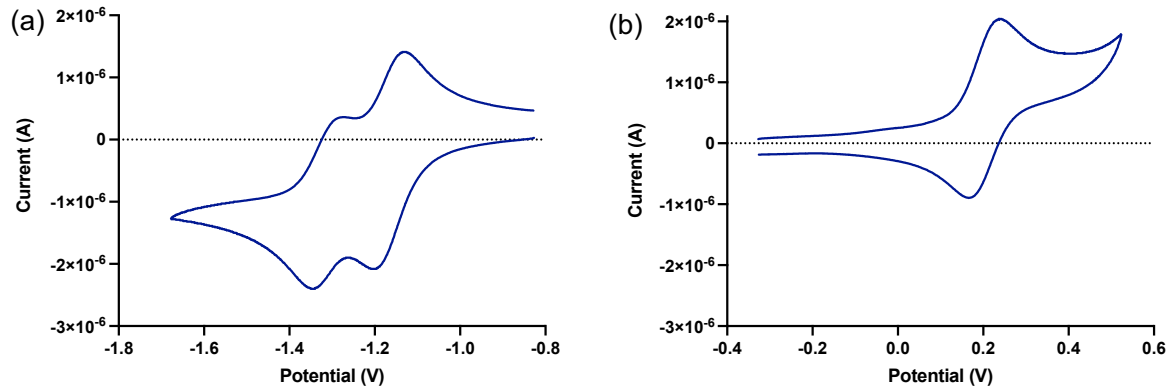

Figure 93: Cyclic voltammetry of Cu(atsm-Tz) (1mM) in DMF (versus Ag/Ag^{+}), referenced to Fc/Fc+ couple E°' = 0V) with $(Bu)_4NPF_6$ supporting electrolyte 0.1M.

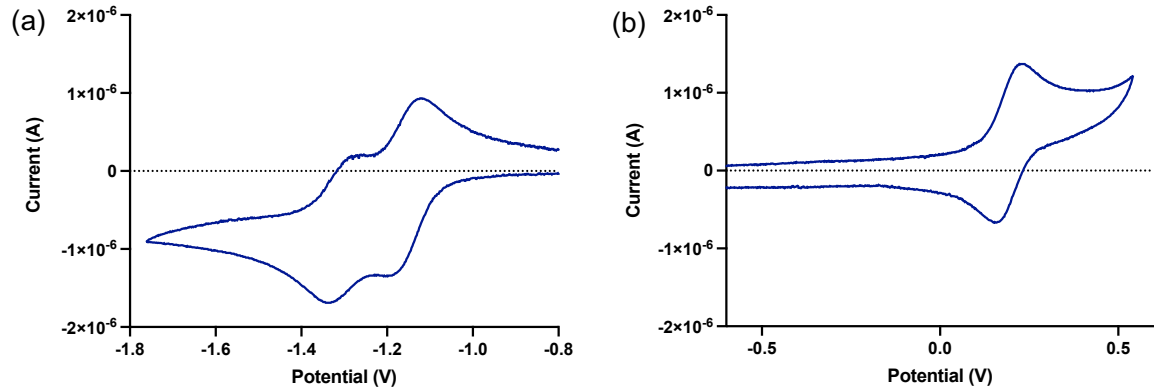

Figure 94: Cyclic voltammetry of Cu(dtse-Tz) (1mM) in DMF (versus Ag/Ag^{+}), referenced to Fc/Fc+ couple E°' = 0V) with $(Bu)_4NPF_6$ supporting electrolyte 0.1M.

The electrochemistry of H_2atsm-Tz and H_2dtse-Tz was investigated to further elucidate whether one of the two reduction processes was ligand-based (Figure 95). Tetrazines that are substituted by heteroatoms or aromatic ring structures can be reversibly reduced in organic solvents due to their electron-deficient character. They are able to accept one electron to give an anion radical (which is stable in the absence of acid).[377] The ligands H_2atsm-Tz and H_2dtse-Tz were shown to have reduction potentials of $E^{\circ\prime}$ = -1.32 V and $E^{\circ\prime}$ = -1.29 V, respectively. Therefore, the second quasi-reversible process at $E_{1/2}$ = -1.32 V in the voltammogram of both Cu(atsm-Tz) and Cu(dtse-Tz) can be attributed to ligand-based processes due to the reduction of the tetrazine functional group. No electrochemical processes were observed for either H_2atsm-Tz or H_2dtse-Tz at positive potentials (oxidation) in the voltammogram.

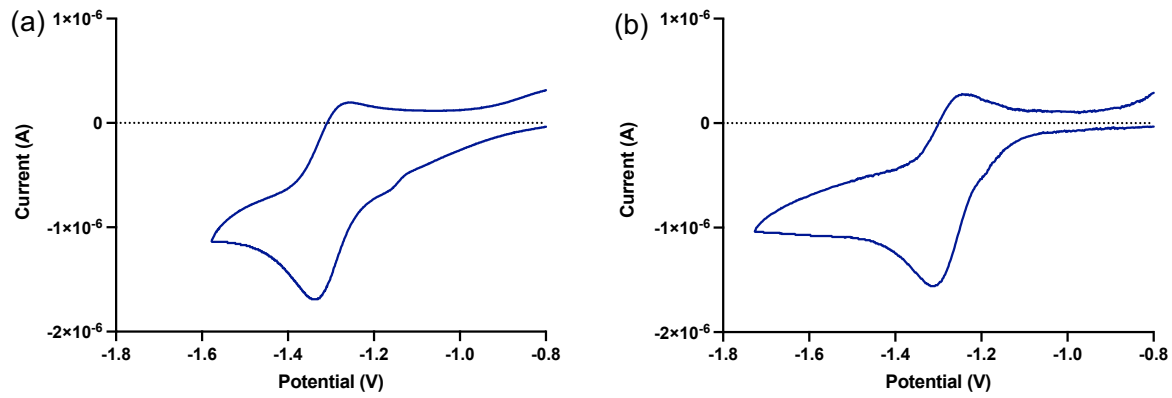

Figure 95: Cyclic voltammetry of (a) H_2atsm-Tz and (b) H_2dtse-Tz (1mM) in DMF (versus Ag/Ag^+), referenced to Fc/Fc+ couple E°' = 0V) with $(Bu)_4NPF_6$ supporting electrolyte 0.1M.

These potentials correlate well with the electron deficiency of the substituent at the 6-position of the tetrazine. For example, H_2dtse-Tz has a higher reduction potential and is more readily reduced than the corresponding complexes where the 1,2,4,5-tetrazine contains a methyl group at the 6-position. Both the $Cu^{II/I}$ and tetrazine reductions occur at potentials that are outside the typical reducing environment encountered in a cellular environment.

6.3.5 X-ray Crystallographic data of $Cu(dtse\text{-}Tz)_2(C_2H_2OS)_3$ and $[Cu(H_2atsm\text{-}Tz)](ClO_4)_2$.

Crystals of Cu(dtse-Tz) suitable for single crystal X-ray crystallography were grown from a concentrated solution of the complex in dimethyl sulfoxide. Characterisation of Cu(dtse-Tz) (Figure 96) by X-ray crystallography confirmed the copper(II) is in a distorted square planar environment with the ligand acting as a N_2S_2 donor. The Cu−N bond and Cu-S bond lengths are similar to those found in Cu(atsm).[378] The double deprotonation of the ligand and the resonance form depicted (Scheme 16) is supported by the short C-N lengths (C3-N2 1.323(5) and C6-N5 1.321(5) Å), which is consistent with partial double bond character.[378] The C-S bond lengths (C3-S1 1.764(4) Å and C6-S2 1.766(4) Å) are also consistent with more 'thiolene-like' than 'thione-like' bonding.[378] The angle of the side chain, defined by the atoms C(10)-N(6)-C(11) is 126.6°; however, this angle is strongly determined by the crystal packing,

hydrogen bonding to adjacent molecules, and to the solvent molecule, dimethyl sulfoxide (omitted from the crystal structure for clarity). The four-coordinate copper atom sits 0.06 Å out of the plane of the N_2S_2 square planar donor system with the distortion from ideal square planar geometry highlighted by the bond angle S(1)-Cu-S(2) of 109.34°.

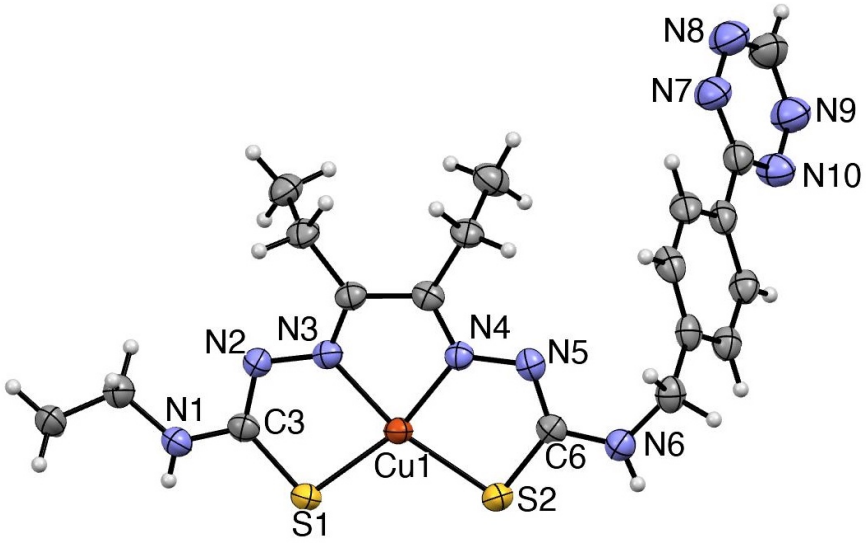

Figure 96: ORTEP representations (with ellipsoids at 50% probability) of the X-ray crystal structure of Cu(dtse-Tz), selected bond lengths (Å): Cu-N3 1.966(3); Cu-N4 1.965(3); Cu-S1 2.2430(11); Cu-S2 2.2453(10).

We were unable to grow single crystals of the charge neutral Cu(atsm-Tz) of sufficient quality for analysis by X-ray crystallography; however, crystals of the dication $[Cu(H_2atsm\text{-}Tz)]^{2+}$, where the *bis*(thiosemicarbazone) ligand is protonated, were grown by the addition of perchloric acid to a mixture of the complex acid in methanol (Figure 97). The most notable differences compared to the structure of charge neutral Cu(dtse-Tz) are the longer C-N bond lengths, C2-N1 1.319(4) Å and C2-N2 1.354(4) Å, and the shorter C-S bond distances, C2-S1 1.712(3) Å and C5 S2 1.709(3) Å) (Figure 97). The copper(II) is 5-coordinate square pyramidal due to a weak axial interaction with the oxygen of a perchlorate anion (Cu-O3 2.505(3) Å) (Figure 97). Despite the change in the degree of protonation of the ligand and the weak interaction between the copper and one perchlorate anion, the Cu-N and Cu-S bond lengths are similar to the charge-neutral Cu(dtse-Tz).[379]

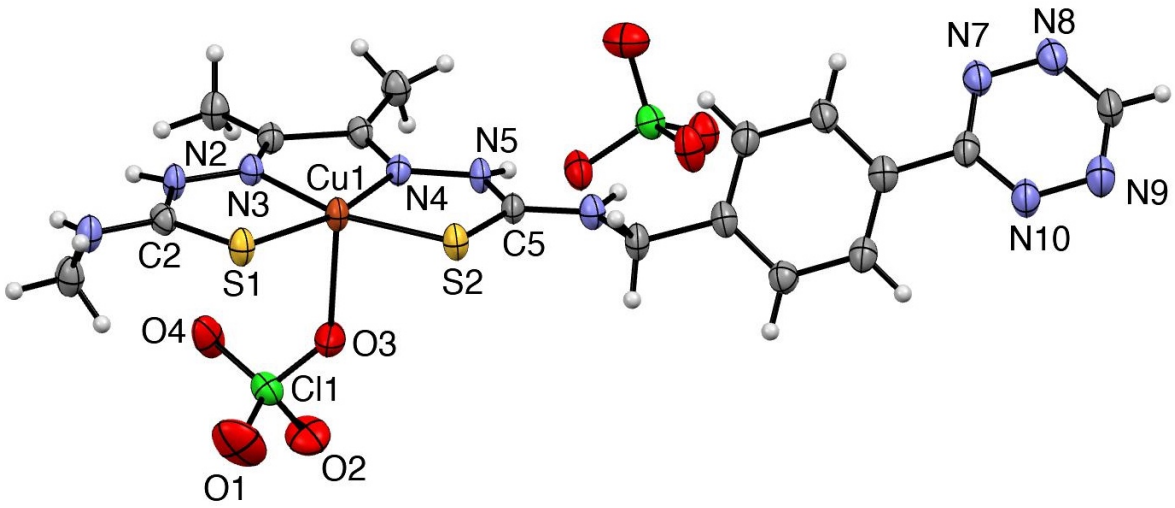

Figure 97: ORTEP representations (with ellipsoids at 50% probability) of the X-ray crystal structure of $[Cu(H_2atsm\text{-}Tz)](ClO_4)_2$ selected bond lengths (Å): Cu-N3 1.968(3); Cu-N4 1.957(3); Cu-S1 2.2413(8); Cu-S2 2.2489(9); Cu-O3 2.505(3).

The structure of $(Cudtse\text{-}Tz)_2.(DMSO)_3$ is characterised by N-H···N hydrogen bonding between the two independent molecules of the ligand in addition to N-H···O hydrogen bonds to the three DMSO solvate molecules (Figure 98). The dihedral angles between the tetrazene rings and the phenyl rings are 2.7(3)° and 12.8(2)° for the two molecules, respectively. The structure of $CuH_2atsm\text{-}Tz.(ClO_4)_2$ is characterised by two sets of N-H···O hydrogen bonds between the two thiourea moieties and the two ClO_4^- anions (Figure 99). One set involves the 'free' ClO_4^- anion, while the second set involves the coordinated ClO_4^- anion resulting in a centrosymmetric dimer. The dihedral angle between the tetrazene ring and the phenyl ring is 26.6(2)°.

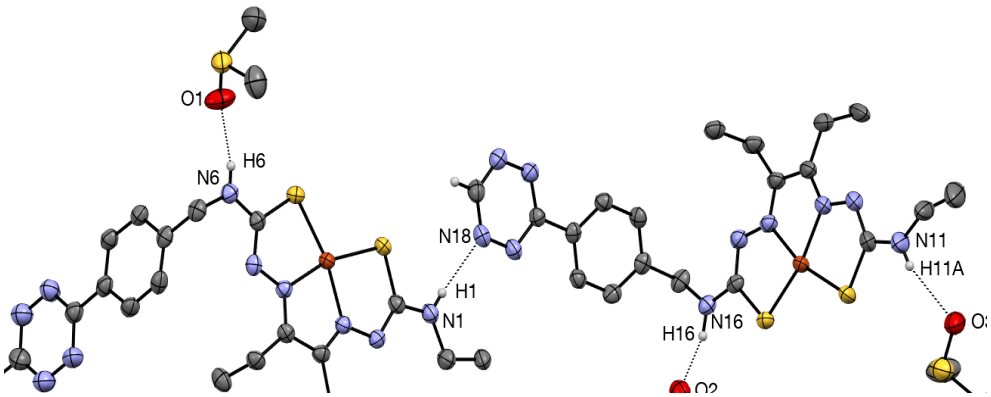

Figure 98: Thermal ellipsoid plot (50% ellipsoids) of the asymmetric unit of Cu(dtse-Tz) showing the hydrogen bonding interaction between the two complexes and with the three molecules of the DMSO solvate: N1-H···N18 (N1···N18 3.000(5) Å, N1-H···N18 173(5)°); N6-H···O1 (N6···O1 2.792(5) Å, N6-H···O1 164(5)°); N16-H···O2 (N16···O2 2.824(5) Å, N16-H···O2 157(5)°); N11-H···O3 (N11···O3 2.986(5) Å, N11-H···O3 153(6)°).

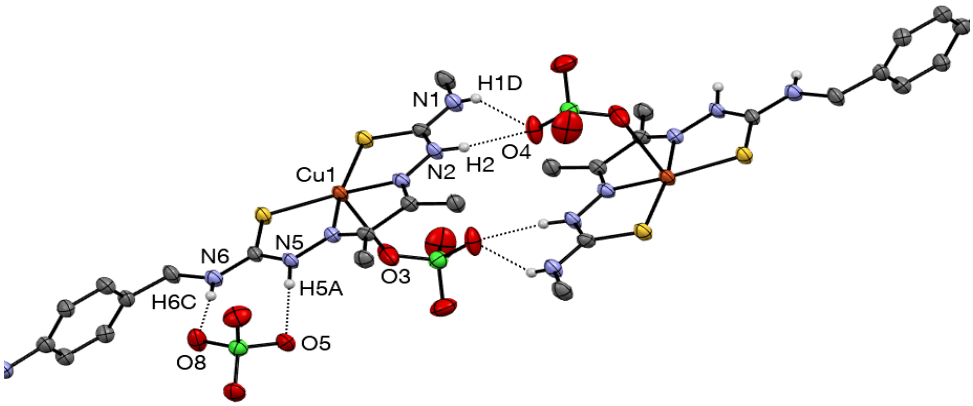

Figure 99: Thermal ellipsoid plot (50% ellipsoids) showing centrosymmetric CuH_2atsm-Tz dimers bridged by N-H···O hydrogen bonds: N1-H···O4 (N1···O4 2.955(5) Å, N1-H···O4 143(5)°); N2-H···O4 (N2···O4 2.731(5) Å, N2-H···O4 157(4)°); N5-H···O5 (N5···O5 2.863(4) Å, N5-H···O5 172(4)°); N6-H···O8: (N6···O8 2.878(4) Å, N6-H···O8 174(4)°); O3-Cu1 2.504(3) Å

Table 20: Crystallographic Data for $Cu(H_2atsm\text{-}Tz)(ClO_4)_2$ and $Cu(dtse\text{-}Tz)(C_2H_2OS)_3$.

	$[Cu(H_2atsm\text{-}Tz)](ClO_4)_2$	**$Cu(dtse\text{-}Tz)_2(C_2H_2OS)_3$**
Empirical Formula	$C_{16}H_{20}Cl_2CuN_{10}O_8S_2$	$C_{44}H_{66}Cu_2N_{20}S_7$
Formula Weight	678.98	1274.66
Crystal System	Triclinic	Monoclinic
Space Group	P $\bar{1}$	P 2_1/n
***a*/Å**	8.0247(2)	17.7445(7)
***b*/Å**	8.5035(3)	8.2723(3)
***c*/Å**	18.5600(6)	37.4544 (13)
α/(°)	78.558(3)	90
β/(°)	87.910(3)	94.522(3)
γ/(°)	89.697(3)	90
***V*/Å^3**	1240.50(7)	5785.5(4)
Z	2	4
Temperature/K	100.0(2)	130.01(10)
λ/Å	1.54184	1.54184
Refinement method	Full-matrix least-squares on F2	
R-Factor/%	4.4	5.93
CCDC	2205696	2205695

6.3.6 Characterising the Conjugation of *Trans*-cyclooctene to Aducanumab and 6E10 by Native Protein Mass Spectrometry.

Trans-cyclooctene is susceptible to isomerisation to unreactive *cis*-cyclooctene, which can reduce the effectiveness of *in vivo* 'click' reactions with TCO and tetrazine biorthogonal partners. One approach to mitigate this limitation is to add as many TCO functional groups as the antibody can tolerate without significantly compromising binding. Most IgG antibodies can accommodate an average of 3 – 4 functional groups without significantly compromising the binding of the antibody to the target.

In this work, TCO functional groups were conjugated to an aducanumab biosimilar through a short hydrophilic polyethylene glycol (TCO-PEG_4) linker. The antibody was reacted with the succinimidyl ester of TCO-PEG_4-CO_2H (10 equivalents) at room temperature for one hour before purification with an ultra-centrifugation filter (molecular weight cut-off 50 kDa). Analysis of the aducanumab-PEG_4-TCO conjugates (aducanumab-TCO, Figure 100, a, b) by 'intact' electrospray mass spectrometry (ESI-MS) revealed an average of four PEG_4-TCO groups per antibody.

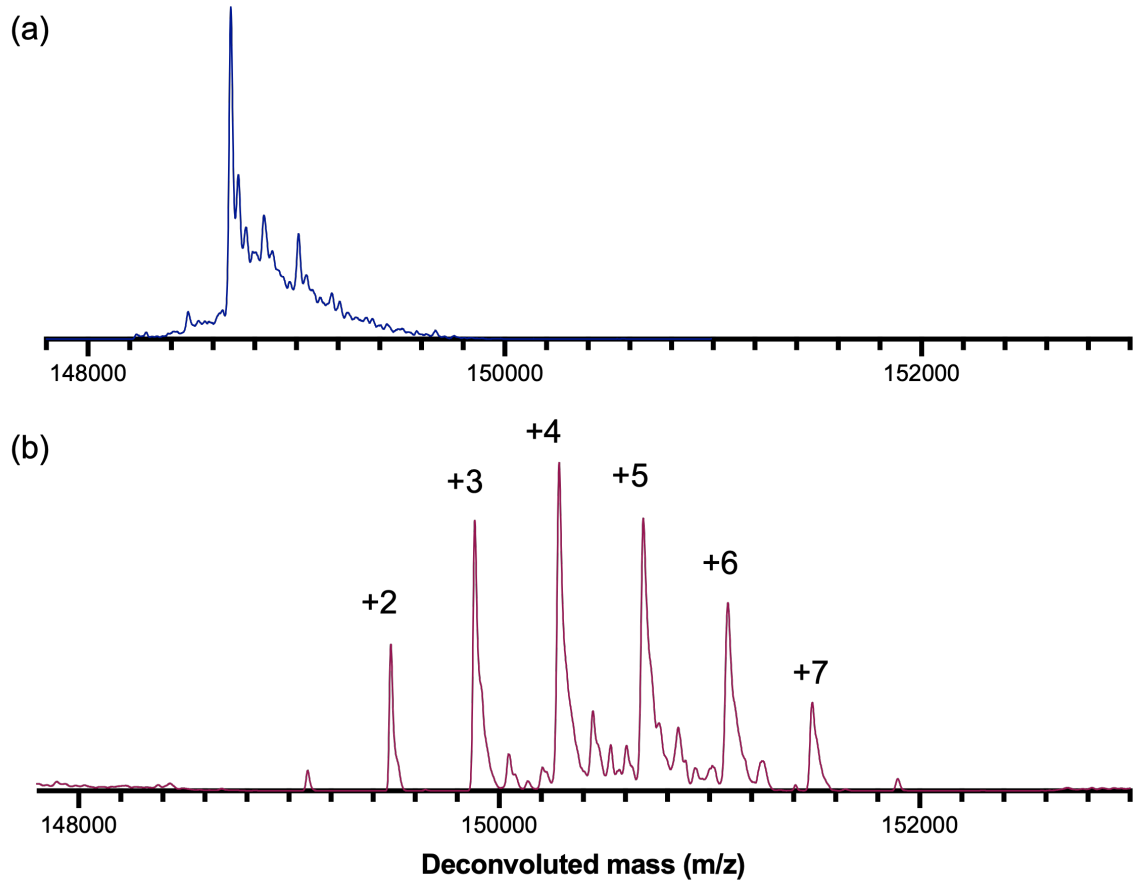

Figure 100: Deconvoluted ESI mass spectra of (a) unconjugated aducanumab and (b) aducanumab-TCO_x conjugate where x = 2 – 7.

We also added TCO functional groups to the 6E10 antibody, a research anti-Aβ monoclonal antibody that was raised against a synthetic peptide corresponding to residues 1-24 of Aβ.[380] Reaction of 6E10 with the *N*-hydroxysuccinimide activated ester of TCO-PEG_4-CO_2H was carried out under the same conditions, and an analysis by intact electrospray mass spectrometry

indicated an average of five PEG_4-TCO groups per antibody (6E10-TCO) (Figure 101, a, b). The more complicated mass spectrum of 6E10-TCO, when compared to aducanumab-TCO, reflects the higher degree of glycosylation.

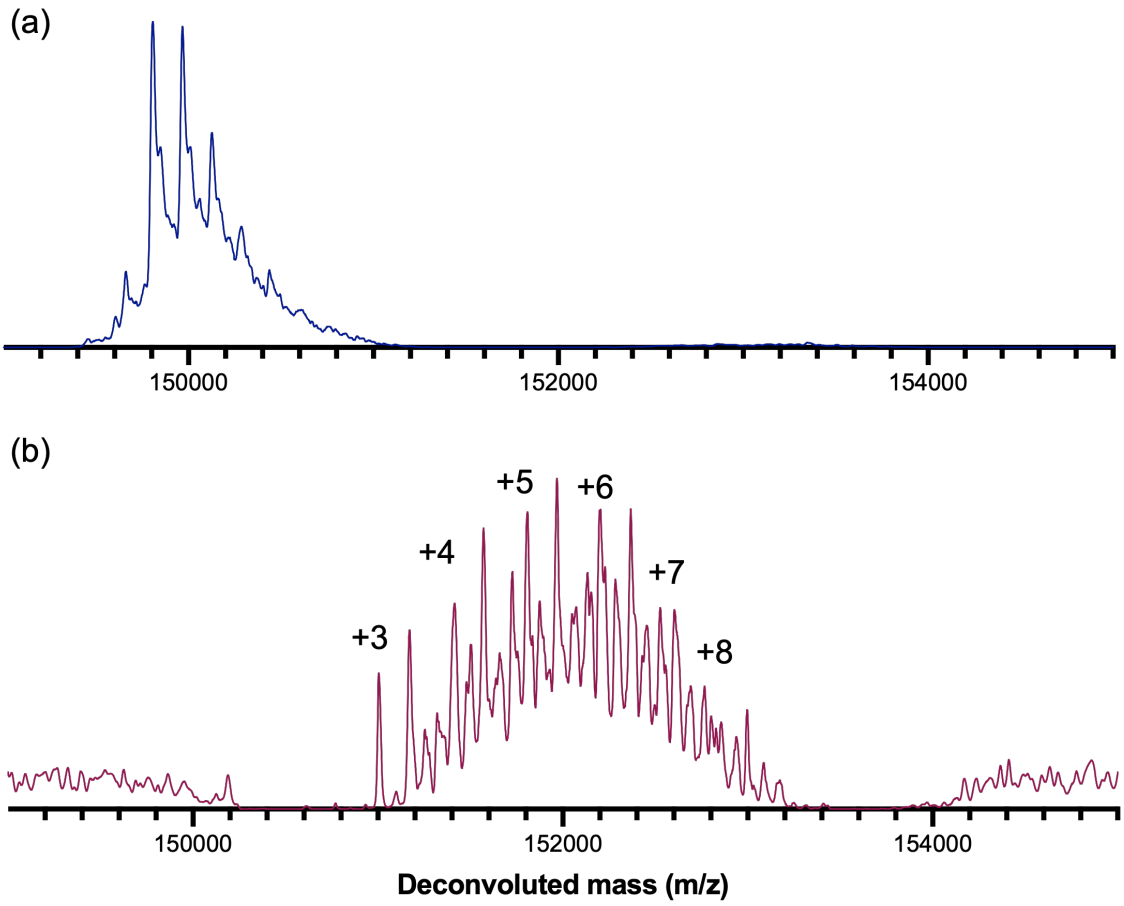

Figure 101: Deconvoluted ESI mass spectra of (a) unconjugated 6E10 and (b) 6E10-TCO_x conjugate where x = 3-8.

The modified 6E10-TCO retained an affinity for Aβ plaques present in post-mortem frontal cortex tissue of subjects with diagnosed AD (Figure 102, a). 6E10 is reactive to amino acids 1-16 of Aβ, and the epitope lies within amino acids 3-8 (EFRHDS). To confirm that the addition of hydrophilic PEG_4-TCO functional groups did not interfere with the antigen binding sites on amyloid plaques or cause aggregation of the protein due to the addition of multiple functional groups, 6E10-PEG_4-TCO was incubated with AD tissue confirmed to have amyloid-β pathology. Visualisation of the plaques was achieved by the addition of a universal secondary

antibody coupled to a polymer backbone containing horse-radish peroxidase enzyme (HRP) and diaminobenzidine (DAB). The chromogenic compound DAB is oxidised in the presence of the HRP enzyme and H_2O_2. Staining showed that conjugation of the antibody with TCO functional groups did not alter binding affinity, and serially stained sections of tissue correlated well to plaque distribution (Figure 102, b).

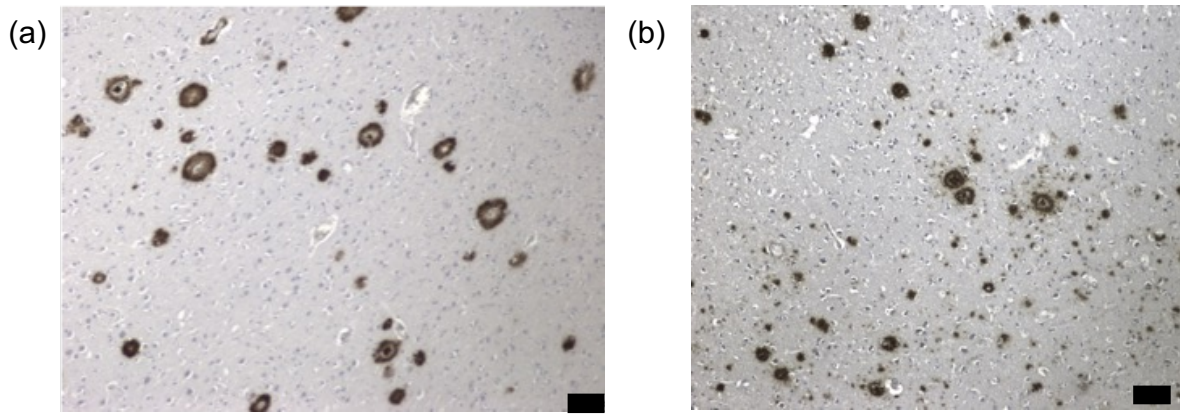

Figure 102: Sections of human brain tissue from an AD-affected subject. (a) Immuno-stained with 6E10-TCO antibody (1:400 dilution), (b) immuno-stained with 6E10 antibody (1:200 dilution). The staining shows that there is the retention of antigen-binding sites and comparable binding between the unmodified 6E10 antibody and the 6E10-TCO conjugate. black scale bar = 100 μm.

Aducanumab-TCO was analysed by size exclusion-HPLC, which showed that there were no significant changes in the retention time of aducanumab-TCO compared to the parental antibodies, with retention times of 8.51 min and 8.61 minutes, respectively. (Figure 103). This indicates that the modifications made to the antibodies did not cause them to aggregate. Typically, protein aggregates are larger and eluted at earlier time points. Therefore, antibody modification did not result in aggregation.

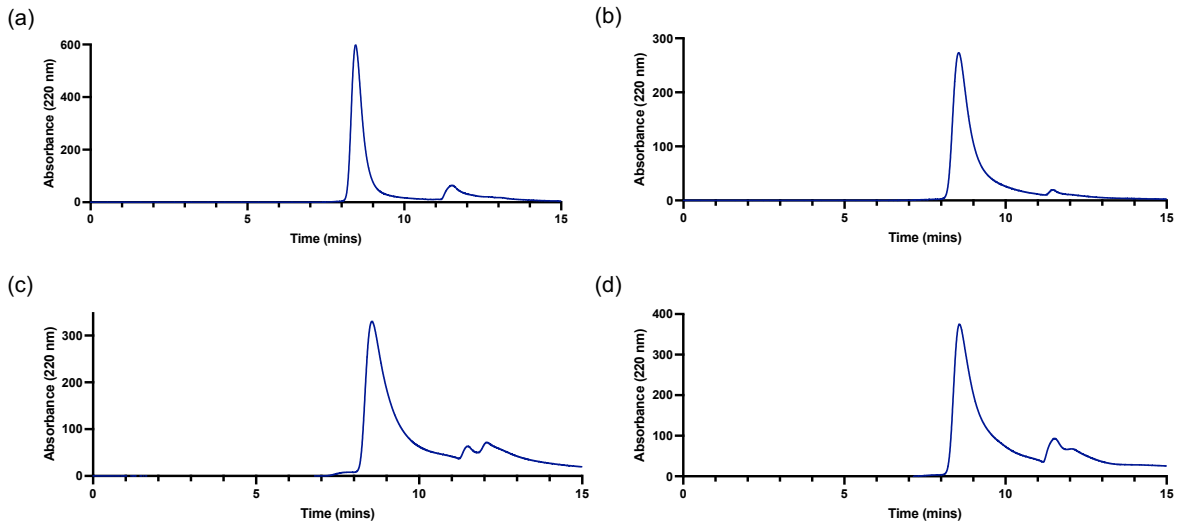

Figure 103: Size exclusion HPLC chromatograms for (a) unmodified Aducanumab, and (b) Aducanumab-TCO, (c) Aducanumab-TCO + Cu(atsm-Tz) click, and (d) Aducanumab-TCO + Cu(dtse-Tz) click. Eluent: 1x PBS pH 7.4, flow rate: 0.35 mL/min, UV detection: 220 nm.

6.3.7 H_2atsm-Tz and H_2dtse-Tz can be Radiolabelled with Copper-64

Both H_2atsm-Tz and H_2dtse-Tz can be radiolabelled with [^{64}Cu]Cu^{II} in sodium acetate buffer (100 mM, pH 5.5) at room temperature in < 30 minutes to give the copper-64 complexes in high radiochemical yield and specific activity (4.2 - 4.6 MBq/nmol). The copper-64 complexes were characterised by comparing their respective HPLC traces (C18 reverse phase column) with their non-radioactive copper complexes. The radio-HPLC traces of [^{64}Cu]Cu(atsm-Tz) and [^{64}Cu]Cu(dtse-Tz) closely matched the non-radioactive copper complexes with retention times of 10.8 and 13.2 minutes, respectively (Figure 104, a, b). The differences in retention times between [^{64}Cu]Cu(atsm-Tz) and [^{64}Cu]Cu(dtse-Tz) are consistent with the increased lipophilicity of [^{64}Cu]Cu(dtse-Tz).

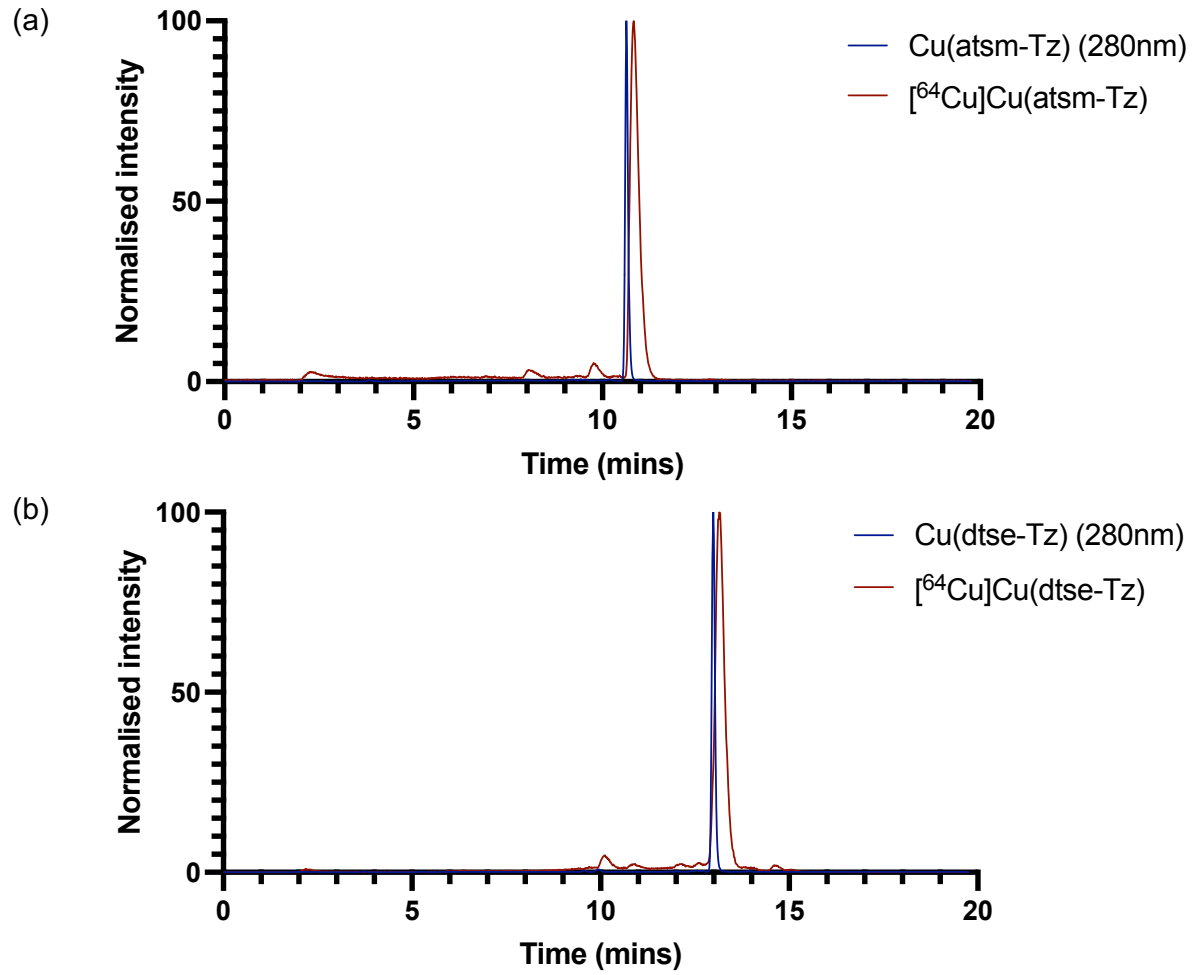

Figure 104: Radio HPLC of (a) [^{64}Cu]Cu(atsm-Tz) (scintillation detector, red trace) Cu(atsm-Tz) (λ = 280 nm, blue trace). Retention time = 10.8 min and 10.6 min, respectively; (b) [^{64}Cu]Cu(dtse-Tz) (scintillation detector, red trace) Cu(dtse-Tz) (λ = 280 nm, blue trace). Retention time = 13.2 min and 13.0 min, respectively.

The octanol-PBS distribution coefficient (LogD) is often used to predict the ability of a compound to cross the blood-brain barrier, with the ideal range often stated to be LogD 1.5 - 3.5. The LogD values of [^{64}Cu]Cu(atsm-Tz) (LogD 1.84) and [^{64}Cu]Cu(dtse-Tz) (LogD 2.17) were consistent with their respective HPLC retention times and slightly higher than the value obtained for [^{64}Cu]Cu(atsm) (LogD 1.56). Both [^{64}Cu]Cu(atsm-Tz) and [^{64}Cu]Cu(dtse-Tz) were stable with respect to a kinetic challenge experiment with biologically relevant amino acid residues, cysteine and histidine. Incubation of the complexes with an excess of cysteine and histidine at 37 °C for 4 hours resulted in minimal loss of copper-64 from the complexes (Figure 105).

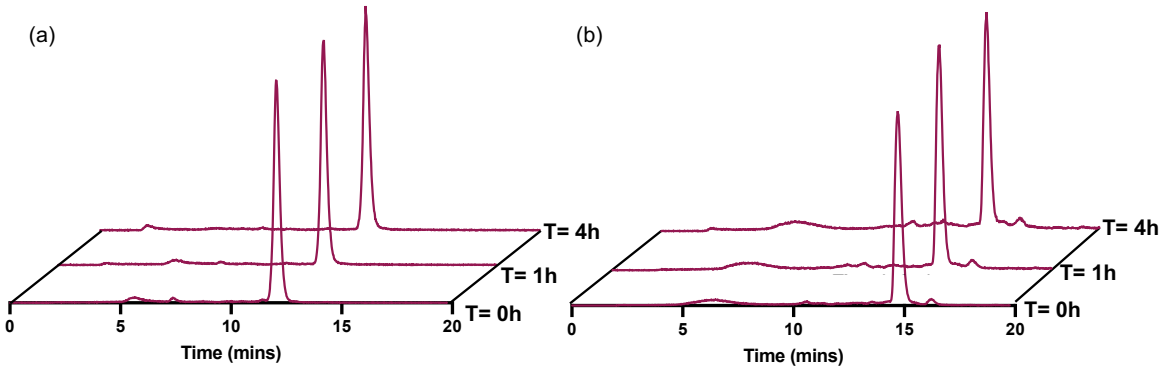

Figure 105: HPLC chromatograms of (a) [^{64}Cu]Cu(atsm-Tz) and (b) [^{64}Cu]Cu(dtse-Tz) at 0, 2, 4 hours incubation times with an excess of cysteine and histidine. 0.05% TFA in the mobile phases instead of 0.1% TFA accounts for the slight shift in the retention times for both copper-64 complexes.

6.3.8 In Vitro 'Click' Reaction with Trans-cyclooctene Functionalised Amyloid-β Antibodies

Radio-thin layer chromatography(radioTLC) was used to monitor the iEDDA click reaction between the monoclonal antibodies 6E10 and Aducanumab, which were modified to contain the *trans*-cyclooctene functional groups and the small radiolabelled probes [^{64}Cu]Cu(atsm-Tz) and [^{64}Cu]Cu(dtse-Tz). Unchelated [^{64}Cu]Cu^{II} stays at the baseline (ethanol mobile phase), while [^{64}Cu]Cu(atsm-Tz) and [^{64}Cu]Cu(dtse-Tz) travel to the solvent front with high radiochemical yield (>95%, Figure 106). Either TCO-aducanumab or TCO-6E10 (~1 equivalent based on the total amount of ligand present, ~3.6 -3.9 × 10^{-10} mol) was added to [^{64}Cu]Cu(atsm-Tz) and [^{64}Cu]Cu(dtse-Tz)] and the mixture was allowed to react for 1 hour at room temperature. Following this, the [^{64}Cu]Cu^{II} complexes were incubated with either unconjugated 6E10 and Aducanumab or TCO-modified antibodies. When the copper-64 complexes with appended tetrazine functional groups were incubated with 6E10-TCO and Aducanumab-TCO, the copper-64 signal remained at the baseline of the radioTLC. Analysis of the reaction mixtures by radioTLC reveals that the majority of the activity is now retained on the baseline, consistent with copper-64 complexes reacting with the TCO-modified antibodies (Figure 106). When unmodified 6E10 and Aducanumab were incubated with both [^{64}Cu]Cu(atsm-Tz) and [^{64}Cu]Cu(dtse-Tz), the radio-signal continued to travel to the solvent

front, indicating the reaction with TCO functionalised antibodies isn't simply a hydrophobic interaction of the constructs to the antibody surface (Figure 108 and Figure 109). Previous research has shown that superior results in imaging are achieved when approximately equimolar amounts of both the tetrazine and trans-cyclooctene are injected *in vivo*[320, 322] Therefore, the copper complexes were incubated with 1 equivalent of antibody conjugate (based on total ligand present in reaction volume) and reacted for 1 hour to give complexes with greater than 68% yield when 3.6 -3.9 × 10^{-10} mol of antibody conjugate was used.

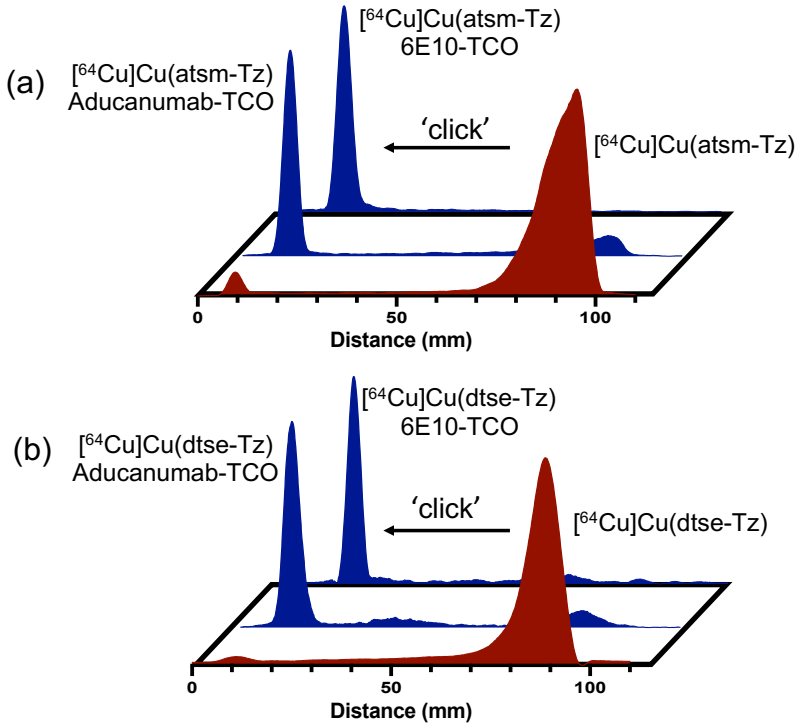

Figure 106: Normalised, smoothed radioTLC traces of (a) [^{64}Cu]Cu(atsm-Tz) and (b) [^{64}Cu]Cu(dtse-Tz) (red) >95% RCY, when reacted with aducanumab-TCO or 6E10-TCO (blue) for 1 h, in 0.1M sodium acetate, pH 5.5, 10^{-6} M.

6.3.9 *In Vivo* Analysis of [^{64}Cu]Cu(atsm-Tz) and [^{64}Cu]Cu(dtse-Tz)

Encouraged by the efficacy of the click reaction, we investigated the potential of the two compounds to cross the blood brain barrier in mice. Following administration of either [^{64}Cu]Cu(atsm-Tz) or [^{64}Cu]Cu(dtse-Tz) to wild type mice by intravenous tail vein injection, the mice were euthanised at 2 and 60 minutes post injection (m.p.i.). Ideally, brain uptake is followed by fast clearance of the AD probe from the brain, which is typical of small molecule

radiopharmaceuticals (Table 21). The radioactivity in each organ was counted and expressed as a percentage of the injected activity normalised to the mass of the organ (% IA g^{-1}). The brain uptake at 2 m.p.i. of [^{64}Cu]Cu(atsm-Tz) was 2.5 ± 0.5 % IA g^{-1}, whilst the brain uptake of [^{64}Cu]Cu(dtse-Tz) was 1.7 ± 0.3 % IA g^{-1}. Both compounds clear from the brain in wild-type mice, with the activity in the brain reducing to 0.78 ± 0.08 % IA $g^{-1}$and 0.41 ± 0.03 % IA g^{-1} at 60 m.p.i. For both compounds, the degree of brain uptake in wild-type mice is slightly higher than for [^{64}Cu]Cu(atsm) (~0.9 ± 0.4% IA g^{-1}).[381]

Table 21: Brain uptake of [^{64}Cu]Cu(atsm-Tz) and [^{64}Cu]Cu(dtse-Tz) at 2 minutes and 60 minutes, expressed as % IA g^{-1}.

	[^{64}Cu]Cu(atsm-Tz) (2 mins) n = 5	[^{64}Cu]Cu(atsm-Tz) (60 mins) n = 6	[^{64}Cu]Cu(dtse-Tz) (2 mins) n = 6	[^{64}Cu]Cu(dtse-Tz) (60 mins) n = 6
Brain	2.48 ± 0.49	0.79 ± 0.08	1.69 ± 0.28	0.41 ± 0.03

In this experiment, with wild-type mice and no TCO-antibody present to 'trap' the tracer it is important that the initial brain uptake is followed by effective clearance (Table 22). Both [^{64}Cu]Cu(atsm-Tz) and [^{64}Cu]Cu(dtse-Tz) have high uptake in the liver (19.8 ± 1.2 % IA $g^{-1}$and 34.5 ± 3.7 % IA g^{-1}respectively at 60 m.p.i.) consistent with hepatobiliary metabolism as would be expected for lipophilic compounds. The initial brain uptake and clearance of [^{64}Cu]Cu(atsm-Tz) was further confirmed by micro-PET imaging, which clearly shows initial brain uptake followed by clearance of the radiotracer (Figure 107).

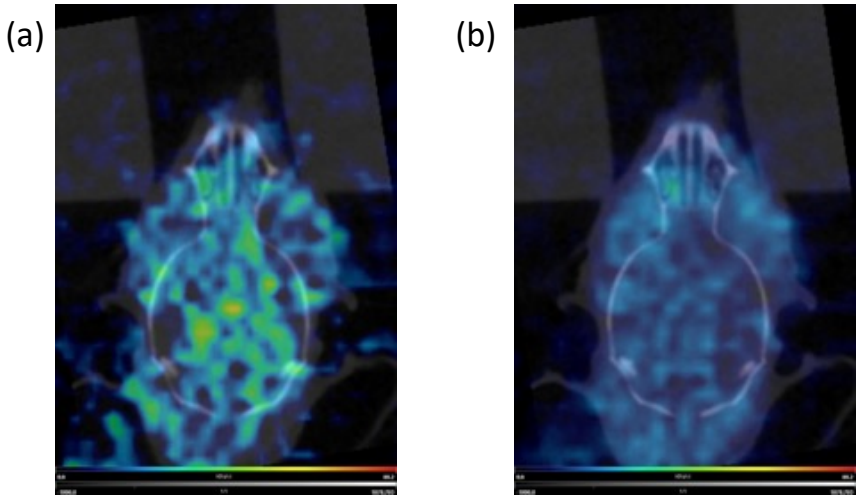

Figure 107: microPET/CT images of the brain region in Balb/c mice at (a) 1-5 m.p.i. and (b) 5-30 m.p.i of [^{64}Cu]Cu(atsm-Tz).

6.4 Concluding Statements and Future Work

A challenge in using radiolabelled antibodies for PET imaging of neurodegenerative diseases is the low amounts of antibody that cross the blood-brain barrier. Continued dosing of antibodies modified for bioorthogonal click reactions has the potential to increase the concentration of antibody present in the brain and allow amyloid pre-targeting. This work explored the application of click chemistry using an antibody pretargeted technique for the visualisation of Aβ plaques. The ligands H_2atsm-Tz and H_2dtse-Tz and their respective Cu^{II} complexes were synthesised and characterised, and their reactivity was studied. Both H_2atsm-Tz and H_2dtse-Tz can be radiolabelled with [^{64}Cu]Cu^{II} to give complexes in high radiochemical yield and specific activity (4.2 - 4.6 MBq/nmol). Preliminary biodistribution studies showed rapid brain uptake of [^{64}Cu]Cu(atsm-Tz) (2.5 ± 0.5 % IA g^{-1}) and [^{64}Cu]Cu(dtse-Tz) (1.7 ± 0.3 % IA g^{-1}) at 2 m.p.i. Both compounds clear from the brain in wild-type mice, with the activity in the brain reducing to 0.78 ± 0.08 % IA $g^{-1}$and 0.41 ± 0.03 % IA g^{-1} at 60 m.p.i.

We modified two antibodies that bind to different types of amyloid-β pathology with TCO functional groups. Chemical modification of the antibodies did not affect the antigen binding site, as demonstrated by immunohistochemical staining. This preliminary work suggests that

pre-targeting amyloid plaques may be feasible, and further investigation of pre-targeted molecular imaging in animal models of amyloid pathology is warranted. Extrapolation of this concept to other antibodies that bind to other proteins of interest in neurodegeneration, such as tau, TDP-4, and α-synuclein, are also worthy of investigation.

6.5 Experimental

6.5.1 Instrumentation

Radioactive analytical HPLC were performed on a Shimadzu SCL-10A VP/LC-10 AT VP system with a Shimadzu SPD-10A VP UV detector followed by a radiation detector (Ortec model 276 photomultiplier base with preamplifier, Ortec 925-SCINT ACE mate preamplifier, BIAS supple and SCA, Bicron 1M 11/2 photomultiplier tube). Column: Phenomenex Luna 5µm C18(2) 150 x 4.6 m 100 A. Gradient elution of Buffer A = 0.05% TFA in H_2O and Buffer B = 0.05% TFA in acetonitrile (5 to 95 % B in A at 15 min, 95 % at 17 min and 5% at 20 min) and detection at 254, and 350 nm.

6.5.2 Diacetyl-4,4-dimethyl-4'-methyl*bis*(thiosemicarbazone) (1)

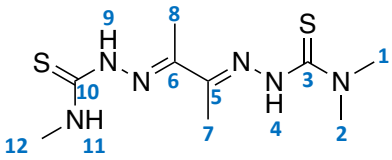

1 was prepared according to a literature procedure.[375] To a solution of diacetyl-*mono*-4-methyl-3-thiosemicabazone (1.19g, 6.89 mmol) in DMF (4 mL) was added 4,4-dimethyl-3-thio-semicarbazide (1.01, 8.40 mmol) and acetic acid (glacial, 5-drops). The solution was stirred for 72 hours, a yellow precipitate formed and H_2O (50mL) was added and the suspension was cooled in an ice bath before the precipitate was collected *via* filtration and washed with H_2O (15 mL), ethanol (2 × 10 mL) and diethyl ether (2 × 10 mL) and dried to yield a light-yellow powder (1.56g, 5.68 mmol, 83%). ESI-MS [M+H$^+$]: 275.1107 calculated for $(C_9H_{19}N_6S_2)^+$: 275.1107. ^{1}H NMR (400 MHz, DMSO-d_6) δ 10.23 (s, 1H, 9), 9.51 (s, 1H, 4), 8.38 (d, J = 4.4 Hz, 1H, 11), 3.27 (s, 6H, 1, 2), 3.02 (d, J = 4.5 Hz, 3H, 12), 2.19, 2.14 (2 x s, 3H; 7, 8). ^{13}C NMR (101 MHz, DMSO) δ 182.1 (10), 178.9 (3), 149.9, 148.5 (5, 6), 42.8 (1, 2), 31.7 (12), 11.9, 11.7 (7, 8).

6.5.3 Diethyl-4,4-dimethyl-4'-ethyl*bis*(thiosemicarbazone) (2)

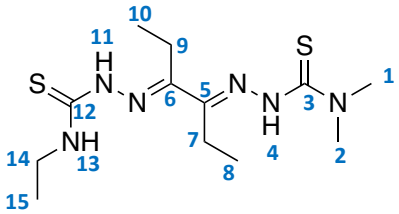

2 was prepared according to an unpublished procedure.[382] diethyl-*mono*-4-ethyl-3-thiosemicabazone (0.510g, 2.37 mmol) and 4,4-dimethyl-3-thiosemicarbazide (0.336g, 2.78 mmol) was dissolved in DMF (3 mL), then acidified with acetic acid (5 drops, glacial) and stirred at room temperature for 72 hours. H_2O (2 mL) was added to aid precipitation; the precipitate was collected *via* filtration, washed with H_2O (2 × 10 mL), cold ethanol (2 × 10 mL) and diethyl ether (2× 10 mL) and dried to yield a bright yellow powder (0.284g, 0.89 mmol, 40%). ESI MS $[M+H]^+$: 317.1579 calculated for $(C_{12}H_{25}N_6S_2)^+$: 317.1577. ^{1}H NMR (400 MHz, DMSO-d_6) δ 10.28 (s, 1H, 11), 9.51 (s, 1H, 4), 8.26 (s, 1H, 13), 3.59 (q, J = 6.8 Hz, 2H, 14), 3.26 (s, 6H, 1, 2), 2.77 (dq, J = 26.9, 7.6 Hz, 4H, 7, 9), 1.12 (t, J = 7.0 Hz, 3H, 15), 0.91 (q, J = 7.3 Hz, 6H, 8, 10).^{13}C NMR (101 MHz, DMSO) δ 182.3 (12), 177.9 (3), 152.7 (6), 151.3 (5), 42.9 (1, 2), 39.0 (14), 17.6, 17.1 (8, 9), 14.8 (15), 11.2, 10.8 (8, 10).

6.5.4 H_2atsm-Tz

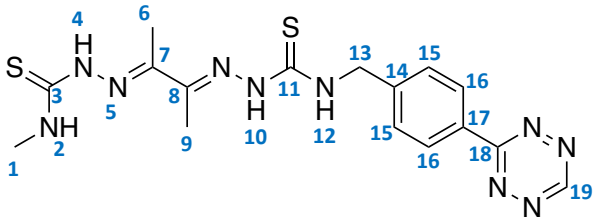

Diacetyl-4,4-dimethyl-4'-methyl*bis*(thiosemicarbazone) (22.0 mg, 0.08 mmol), (4-(1,2,4,5-tetrazin-3-yl)phenyl)methanamine hydrochloride (22.1 mg, 0.096 mmol) and triethyl amine (13 µL, 0.096 mmol) were suspended in acetonitrile (1.5 mL) and irradiated with µwave radiation for 5 minutes at 90°C with high absorbency. Upon cooling, a bright pink precipitate formed and the reaction suspension was centrifuged, washed with acetonitrile (2 x 1 mL), H_2O

(2 x 1 mL), cold ethanol (2 mL), and diethyl ether (2 mL), then dried *in vacuo* to yield a pink powder (21.2 mg, 0.051 mmol, 64%). R_t = 11.65 min (Method B, Column B). ESI MS $[M+H]^+$: 417.1391 calculated for $(C_{16}H_{20}N_{10}S_2)^+$: 417.1392 ^{1}H NMR (500 MHz, DMSO-d_6) δ 10.58 (s, 1H, 19), 10.43 (s, 1H, 3), 10.22 (s, 1H, 10), 9.06 (s, 1H, 12), 8.48 (d, J = 8.4 Hz, 2H, 16), 8.39 (d, J = 4.6 Hz, 1H, 2), 7.60 (d, J = 8.5 Hz, 2H, 15), 4.98 (d, J = 6.3 Hz, 2H, 13), 3.03 (d, J = 4.6 Hz, 3H, 1), 2.25 (d, J = 9.5 Hz, 6H, 6, 9). ^{13}C NMR (126 MHz, DMSO) δ 178.5, 178.3 (3, 11), 165.3 (18), 157.9 (19), 148.6 (7), 147.7 (8), 144.5 (14), 130.1 (17), 127.8 (15), 127.6 (16), 46.6 (13), 31.0 (1), 11.7 (6), 11.6 (9).

6.5.5 Cu(atsm-Tz)

H_2(atsm-Tz) (4.78 mg, 0.011 mmol) and Cu(II)OAc.H_2O (2.59 mg, 0.013 mmol) were dissolved in DMF and allowed to stir at room temperature for 1 hour, before the addition of H_2O. The precipitate was collected *via* centrifugation, and the solid was washed with H_2O, ethanol, and diethyl ether, then taken to dryness *in vacuo* yield a dark red solid. (4.62 mg, 0.009 mmol, 88%). R_t = 10.63 mins (Method B, Column B). ESI MS $[M+H]^+$: 478.0529 calculated for $(C_{16}H_{18}CuN_{10}S_2)^+$: 478.0532.

6.5.6 H_2dtse-Tz

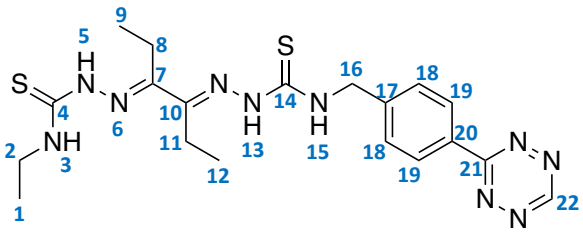

Diethyl-4,4-dimethyl-4'-ethyl*bis*(thiosemicarbazone) (6.44 mg, 0.020 mmol), (4-(1,2,4,5-tetrazin-3-yl)phenyl)methanamine hydrochloride (5.01 mg, 0.022 mmol) and DIPEA (3 µL, 0.023 mmol) were suspended in CH_3CN (1 mL) and irradiated with µwave radiation for 5 minutes at 90°C with high absorbency. Upon cooling, the reaction mixture was taken to dryness under reduced pressure. The precipitate was purified *via* column chromatography (SiO_2, 10 -

40 % ethyl acetate in CH_2Cl_2), and combined fractions were taken to dryness *in vacuo* to yield a bright pink/purple solid. (6.08 mg, 0.013 mmol, 67 %). R_t: 13.15 min (Method B, Column B). ESI MS$[M+H]^+$: 459.1861 calculated for $(C_{19}H_{27}N_{10}S_2)^+$: 459.18. ^{1}H NMR (500 MHz, DMSO-d_6) δ 10.64 (s, 1H, 22), 10.58 (s, 1H, 13), 10.35 (s, 1H, 5), 8.98 (t, J = 6.2 Hz, 1H, 15), 8.48 (d, J = 8.3 Hz, 2H, 19), 8.33 (t, J = 5.8 Hz, 1H, 3), 7.60 (d, J = 8.3 Hz, 2H, 18), 4.99 (d, J = 6.1 Hz, 2H, 16), 3.63 – 3.57 (m, 2H, 2), 2.93 (q, J = 7.3 Hz, 4H, 8, 11), 1.14 (t, J = 7.1 Hz, 3H, 1), 0.92 (dt, J = 14.4, 7.4 Hz, 6H, 9, 12). ^{13}C NMR (126 MHz, DMSO) δ 179.1, 177.9 (4, 14), 165.9 (21), 158.6 (22), 152.0 (7), 151.3 (10), 145.1 (17), 130.8 (20), 128.4 (18), 128.2 (19), 47.2 (16), 39.0 (2), 17.6, 17.4 (8, 11), 14.8 (1), 11.4 (12), 11.3 (9).

6.5.7 Cu(dtseTz)

H_2dtseTz (15.67 mg, 0.034 mmol) and Cu(II)OAc.H_2O (8.37 mg, 0.042 mmol) were suspended in MeOH and allowed to stir at room temp overnight. The suspension was centrifuged and washed with H_2O and ethanol then taken to dryness *in vacuo* to yield a dark red/purple solid. The residue was purified *via* column chromatography to yield a red solid. (15.89 mg, 0.030 mmol, 88%). R_t = 12.98 min (Method B, Column B). ESI MS $[M+H]^+$: 520.1005 calculated for $(C_{19}H_{24}CuN_{10}S_2)^+$: 520.1001.

6.5.8 Conjugation of TCO-PEG$_4$-NHS to aducanumab and 6E10 antibodies

Aducanumab was expressed in CHO cells and purified by Protein A affinity and size exclusion chromatography in PBS (pH 7.4). A solution of TCO-PEG$_4$-NHS ester (7 μL of 5 mg/mL stock solution in DMSO, 10 equivalents) was added to a solution of Aducanumab (5mg/ mL) in PBS (1x, pH 7.4) and the reaction was incubated in the dark at room temperature for 1 hour. Tris-HCl buffer (25 μL, 3M, pH 8.0) was added to quench the reaction and excess reagents were removed and buffer exchanged (HEPES, 0.1M, pH7.4) *via* spin filtration (50 KDa MW cut off). Purified anti-β-amyloid, 1-16 antibody (clone 6E10, purchased from Biolegend, United

States) (30 μg, 1mg/ mL in PBS 1x) was conjugated under the same conditions (10-fold excess of TCO-PEG_4-NHS, 2.5 μL of 1mg/mL anhydrous DMSO.

6.5.9 Immunohistochemistry

Brain tissues isolated from the frontal cortex of AD and healthy control subjects were fixed in 10% formalin/PBS and embedded in paraffin. Serial sections (7 μm) were deparaffinised and treated with 80% formic acid (5 min) and endogenous peroxidase activity was blocked with 3% hydrogen peroxide. The section was then treated with blocking buffer (20% fetal calf serum, 50 mM Tris-HCl, 175 mM NaCl pH 7.4) before incubation with primary antibody to Aβ (6E10 1:200 or 6E10-TCO; 1:400) for one hour at room temperature. Visualization of antibody reactivity was achieved using the LSABTM+ kit (DAKO) and hydrogen-peroxidase-diaminobenzidine (H_2O_2-DAB) to visualise the Aβ deposits and coverslipped with DAKO fluorescent mount. Bright-field images were visualised using a Leica DMIL LED microscope.

6.5.10 Radiochemistry

The copper-64 complexes were prepared by diluting [^{64}Cu]$CuCl_2$ (aq) (0.05M HCl, 20 μL, 50 MBq) with aqueous sodium acetate (0.1 M, pH 5.5 180 μL) to pH 5 or by diluting [^{64}Cu]CII (aq) (H_2O, pH 6, 20 μL, 35 MBq) with aqueous sodium acetate (1M, 2 μL), then H_2atsm-Tz or H_2dtse-Tz in DMSO was added (1mg/ mL, 5 μL) at room temperature for 30 minutes. An aliquot of the reaction solution (1 MBq) was taken for analysis by reverse phase radio-HPLC.

6.5.11 Stability studies with cysteine and histidine.

A solution of cysteine and histidine (5 mM) was added to a solution of both [^{64}Cu]Cu(atsm-Tz) and [^{64}Cu]Cu(dtse-Tz) (4 MBq in 50 uL) and incubated at 37°C. Aliquots of the mixture (12.5 μL) were injected into the HPLC at 0, 2 and 4 hours incubation time.

6.5.12 Stability study with glutathione (GSH).

A solution of Cu(atsm-Tz) and Cu(dtse-Tz) (10 μL, final concentration 0.2 mM) was added to glutathione (GSH, 40 μL, 16 mM) and shaken at 37 °C (20% DMSO total volume). Aliquots

were taken at 1, 2, 4 and 24 hours and diluted, then analysed via RP-HPLC and compared to the unchallenged complexes. Both tetrazine complexes are stable >90% with respect to GSH.

6.5.13 In vitro click reaction with aducanumab-TCO and 6E10-TCO.

The copper-64 complexes were prepared by diluting [^{64}Cu]$CuCl_2$ (aq) (0.05M HCl, 20 µL, 50 MBq) with aqueous sodium acetate (0.1 M, pH 5.5 180 µL) to pH 5 or by diluting [^{64}Cu]Cu^{II} (aq) (H_2O, pH 6, 20 µL, 35 MBq) with aqueous sodium acetate (2 µL, 1M). H_2atsm-Tz or H_2dtse-Tz in DMSO was added (1mg/ mL, 0.5 ug per 10 MBq of [^{64}Cu]Cu^{II}) and the reaction was left at room temperature for 30 minutes. Once TLC had confirmed >95% RCY (radioTLC stationary phase, ethanol mobile phase, free [^{64}Cu]Cu^{2+} Rf = 0 and complex Rf = 1), the copper complexes were added directly into a solution of either aducanumab and aducanumab-TCO with equal molar amounts compared to H_2atsm-Tz and H_2dtse-Tz , or a slight excess of ligands for 6E10 or 6E10-TCO in NaOAc buffer (pH 5.5, 0.1, total volume 100 –125 µL, 6 –16 µM concentration before analysis via TLC under identical conditions.

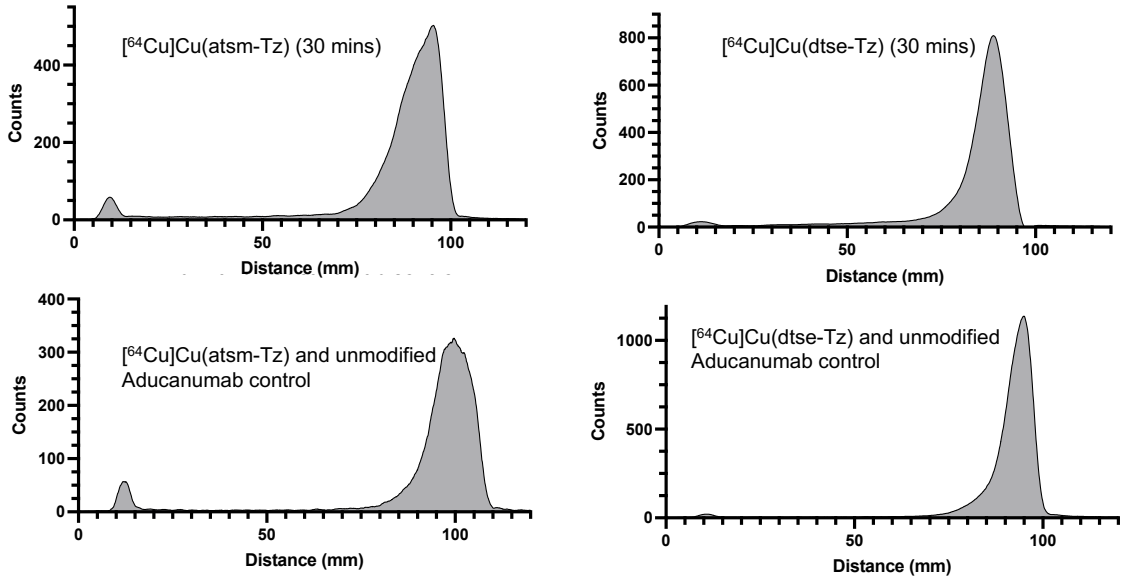

Figure 108: RadioTLC of [^{64}Cu]Cu(atsm-Tz) and [^{64}Cu]Cu(dtse-Tz) incubation with unmodified aducanumab control.

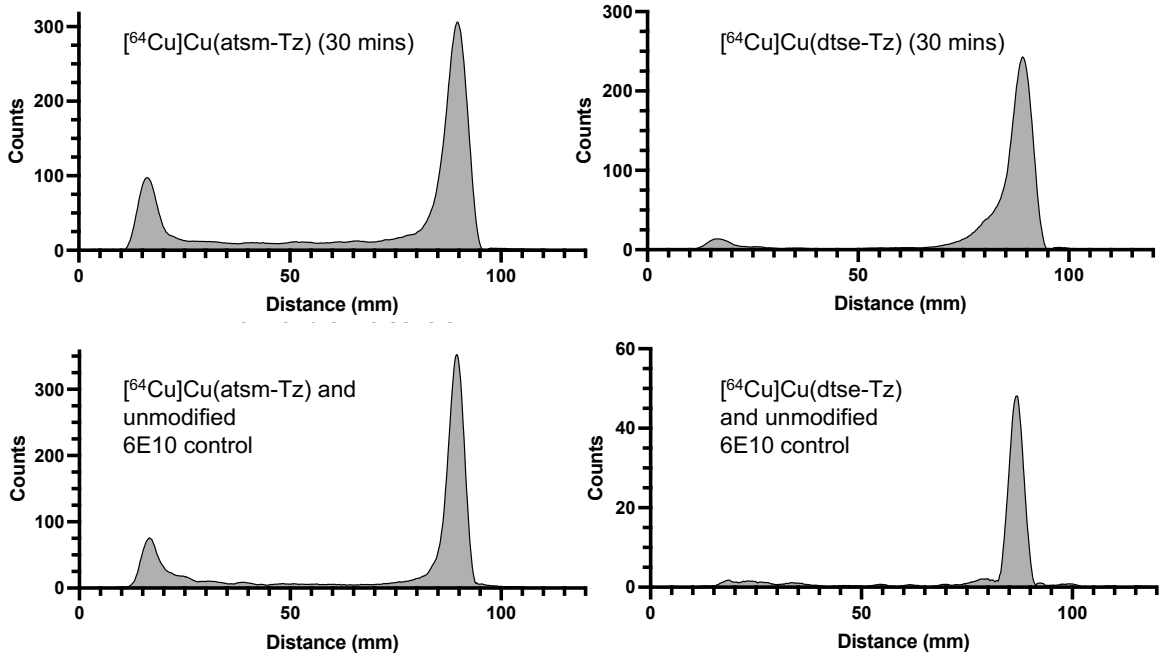

Figure 109: Radio TLC of ^{64}Cu]Cu(atsm-Tz) and [^{64}Cu]Cu(dtse-Tz) incubation with unmodified 6E10 control

6.5.14 PET/CT of [^{64}Cu]Cu(atsm-Tz) and [^{64}Cu]Cu(dtse-Tz) in Balb/c mice

For mouse imaging studies, [^{64}Cu]Cu(atsm-Tz) and [^{64}Cu]Cu(dtse-Tz) complexes were made with a final activity of approximately 3.3 MBq/injection or 6MBq/ injection, respectively. Doses were prepared with a final concentration of DMSO (10%), ethanol (8%) in sodium Acetate buffer (0.1M). Wild-type (WT) mice (n = 6) underwent microPET/computed tomography (CT) imaging on an Inveon PET-CT (Siemens). Mice were anesthetized with isoflurane, catheterized and placed in the PET-CT, and PET listmode data was collected for 1 minute before injection of [^{64}Cu]Cu(atsm-Tz) and [^{64}Cu]Cu(dtse-Tz) via the tail vein. Following the 30 min PET acquisition, mice received a CT scan for co-localisation of the PET signal. The 30-minute list-mode data were histogrammed into 1x60s, 15x1s, 15x15s and 25x60s for kinetic analysis. Image analysis was carried out using PMODv4.2 software (Bruker).

6.5.15 Biodistribution of [^{64}Cu]Cu(atsm-Tz) and [^{64}Cu]Cu(dtse-Tz) in Balb/c mice

This study was performed in strict accordance with the National Health and Medical Research Council (2013) Australian code for the care and use of animals for scientific purposes, 8th edition. Canberra: National Health and Medical Research Council and was approved by the Monash Animal Research Platform (MARP) Animal Ethics Committee of Monash University (Victoria, Australia). To characterise the biodistribution properties of [^{64}Cu]Cu(atsm-Tz) and [^{64}Cu]Cu(dtse-Tz) and their capacity to cross the blood brain barrier, healthy wild type mice (balb/c) received intravenous injections (0.6 – 3.1 MBq in 200 μL) of [^{64}Cu]Cu(atsm-Tz)(*n*= 5 for 2 m.p.i and n=6 at 60 m.p.i)and [^{64}Cu]Cu(dtse-Tz), groups of mice (*n*= 6 per time point) were sacrificed by cervical dislocation and biodistribution was assessed at 2 and 60 minutes post injection. Organs [liver, spleen, kidney, muscle, skin, bone (femur), lungs, heart, stomach, brain, small intestines, large intestines, and tail) were collected immediately. All samples were counted in a Multi-Wiper™ HE γ-radiation well-counter (2008 Laboratory Technologies, Inc.). The tissue distribution data were calculated as the mean ± SD percent injected activity per gram tissue (%IA g^{-1}) for each construct per time point.

Table 22: Biodistribution data for [^{64}Cu]Cu(atsm-Tz), and [^{64}Cu]Cu(dtse-Tz).

	[^{64}Cu]Cu(atsm-Tz) (2 mins) n= 5	[^{64}Cu]Cu(atsm-Tz) (60 mins) n=6	[^{64}Cu]Cu(dtse-Tz) (2 mins) n=6	[^{64}Cu]Cu(dtse-Tz) (60 mins) n=6
Blood	7.27 ± 2.51	1.51 ±0.15	4.29 ± 0.68	0.85 ± 0.05
Urine	1.44 ± 1.04	2.40 ± 0.40	0.06 ± 0.02	0.41 ± 0.10
Bladder	1.91 ± 0.36	1.80 ± 0.14	1.66 ± 0.36	0.92 ± 0.06
Heart	13.18 ± 4.20	1.83 ± 0.13	7.76 ± 0.91	1.57 ± 0.09
Brain	2.48 ± 0.49	0.79 ± 0.08	1.69 ± 0.28	0.41 ± 0.03
Liver	23.93 ±5.71	19.76 ± 1.22	21.99 ± 0.90	34.48 ± 3.73
Kidney	8.07 ± 0.43	4.84 ± 0.35	7.57 ± 0.77	2.86 ± 0.12
Spleen	4.48 ± 1.05	9.40 ±1.48	11.15 ± 1.86	19.74 ± 3.00
Stomach	3.19 ± 0.54	3.54 ± 0.68	2.20 ± 0.20	1.59 ± 0.12
Small Intestine	3.19 ± 0.31	9.85 ± 0.55	2.70 ± 0.32	5.81 ± 0.39
Large Intestine	1.10 ± 0.12	1.42 ± 0.09	0.86 ± 0.12	0.70 ± 0.05
Lungs	18.12 ± 0.14	3.41 ± 0.77	12.79 ± 2.06	12.41± 2.01
Muscle	1.05 ± 0.14	0.84 ± 0.25	0.92 ± 0.12	0.67 ± 0.03
Bone	1.56 ± 0.11	0.95 ± 0.06	2.09 ± 0.42	0.72 ± 0.02
Tail	11.14 ± 2.34	5.79 ± 2.69	3.10 ± 0.56	1.26 ± 0.10

7 Toward Molecular Imaging of PD-L1 Positive Targets with Copper-64 Labelled Peptides

7.1 The Cancer Immunity Cycle

The immune system comprises a series of physical, chemical, and cellular barriers that synergise to passively and actively defend against microbial pathogens. Through the evolution of mechanisms to recognise 'non-self' pathogens, the immune system simultaneously has developed the ability to detect neoantigens generated by malignant transformation, thereby providing a form of immune surveillance capable of detecting and eliminating cancer cells. This has given rise to the concept of 'immune escape' as one of the fundamental hallmarks of cancer cellular biology described by Hanahan and Weinberg in their seminal paper on the underpinnings of tumourigenesis.[383]

As in the defence against microbial pathogens, the immune surveillance and elimination of cancer cells depends on the interaction between the innate and adaptive arms of the immune system. Innate immunity consists of physical epithelial and mucoid barriers, chemical serum factors, natural killer cells and phagocytic cells of myeloid lineage, providing a front-line of defence against microbial invasion. The adaptive immune system by contrast consists of a diverse population of T and B cell lymphocytes capable of expanding and responding to stimulation from a vast array of specific antigenic stimulants. The wide array of targets against which the adaptive immune system can respond is generated by junctional diversity from recombination of the V, D, and J segments of each individual lymphocyte antigen receptor. Activated CD4+ T cells enhance the immune response by providing cytokine co-stimulation to other immune cells, whilst CD8+ T cells contribute to cellular immunity through direct cytotoxic mechanisms. B cell activation by contrast leads to the proliferation of a lymphocyte population capable of secreting large amounts of immunoglobulins with binding specificity for the stimulating antigen, thereby bolstering humoral immunity through the neutralising effects

of these immunoglobulin antibodies. The innate and adaptive immune systems are intimately intertwined in function and localisation, with lymphocyte activation requiring a complex interplay of antigen presentation and stimulation from innate antigen-presenting cells (APC). Whilst B cells are activated by soluble antigens binding the B cell receptor on their cell surface, T cell stimulation requires the T cell receptor to bind antigenic peptides presented within the Major Histocompatibility Complex (MHC) on the cell surface of APCs, together with the appropriate milieu of co-stimulating factors. Inhibitory checkpoints have evolved in conjunction with the immune system to enable tolerance of 'self antigens' and prevent auto-immune attack against autologous tissues. Notwithstanding complex positive and negative selection processes that occur during lymphocyte development within primary lymphoid tissues to select against lymphocytes with self-specificity, peripheral mechanisms also exist to dampen immune responses that may otherwise constitute friendly fire. An important example of this is requirement of appropriate co-stimulation, usually only instigated by the presence of external pathogens, along with the presence of cell-surface signals that serve as inhibitory, negative regulators of immunity.

The immune system plays a crucial role in disease progression and outcomes of cancer. The 'cancer immunity cycle' is a complex network of stimulatory and inhibitory factors and checkpoints that mediate the body's response to cancer.[384, 385] When tumour cells die, neoantigens are released, facilitating the production of peptides that bind to the major histocompatibility complex (MHC) by antigen-presenting cells (APC). T cell receptors (CD4+) recognise these complexes and activate effector T cells, which then infiltrate the tumour microenvironment, recognise, then eliminate cancer cells expressing the tumour antigen.[386] This initiates a cascade of cellular responses leading to apoptosis, further amplifying the cancer cycle as more neo-antigens are released upon cell death (Figure 110). However, inhibitory

checkpoints in place to prevent auto-immune responses may also act as inhibitory regulators against stimulation of cancer-specific immune responses.

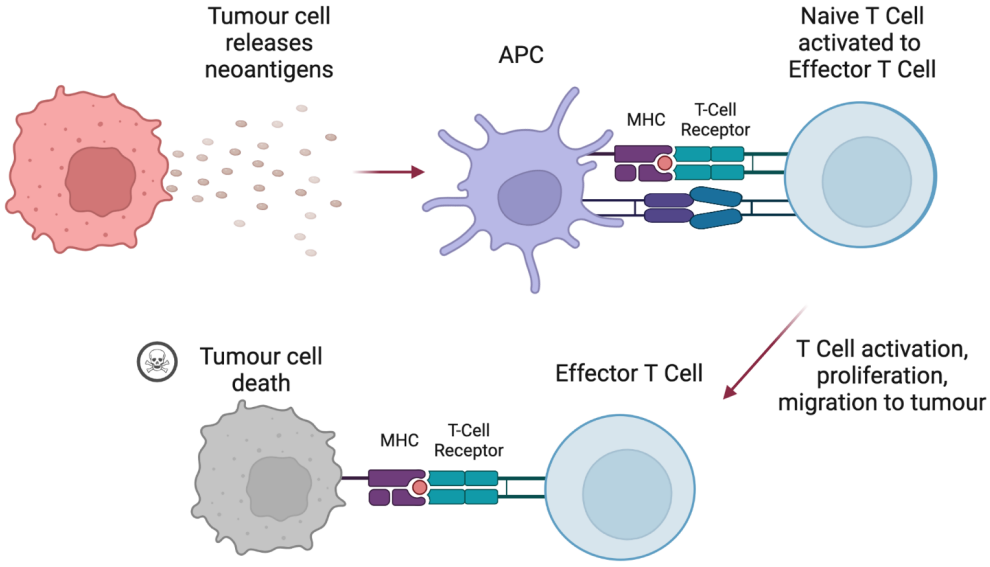

Figure 110: Illustration of the cancer immunity cycle. Adapted from Chen *et al.*[385] Created with biorender.com.

In 2018, James Alison and Tasuku Honjo were awarded the Nobel Prize in Physiology for identifying two pathways pivotal in negative immune regulation. [387, 388] Their seminal work focused on two proteins, cytotoxic T-lymphocyte associated protein 4 (CTLA-4) and programmed cell death-1 (PD-1), which effectively act as 'brakes' on the immune system through different mechanisms. CTLA-4 is an inhibitory checkpoint receptor confined to the expression on T-cells and functioning mainly as a primary immune checkpoint inhibitor, blocking T cells at the initial stage of naive T-cell activation.[389]

7.2 The PD-1 /PD L1 Checkpoint

Programmed cell death-1 (PD-1) is a type 1 transmembrane receptor and member of the CD28/B7 superfamily that negatively regulates the immune system following binding to its two ligands, PD-L1 or PD-L2.[390] PD-1 is expressed on T- and B-lymphocytes, dendritic cells, macrophages, and natural killer cells, with high expression on B cells in peripheral tissue.[391] The interaction between PD-1 and its ligands is important for immunological tolerance *via*

negative regulation of the immune system and is integral later in the cancer immunity cycle. Upon antigen recognition, a T-cell upregulates surface PD-1 expression and produces interferons that induce expression of PD-L1/2 by other cells, which upon binding PD-1 creates a negative feedback loop that limits T-cell activity without the appropriate level of co-stimulating factors to overcome this feedback inhibition.[392] PD-1 expression is often correlated to a poor prognosis and is also a sign of T-cell exhaustion due to chronic infection and cancer (Figure 111).[389]

Tumour cells are engaged in a complex process of maintaining 'balance'. The more somatic mutations that cancer cells acquire, the more likely they are to be targeted by the immune system and elicit an anti-cancer response. Therefore, the release of cancer neoantigens is correlated with increased immunogenicity. Tumour cells are often able to hijack immune checkpoint inhibition mechanisms, evidenced by the fact that PD-L1 is overexpressed in a variety of cancers, such as breast and lung cancer, glioblastoma, melanoma, and lymphoma.[392] This interaction between tumour cells expressing PD-L1 and the PD-1 receptor inhibits T-lymphocyte proliferation and reduces the release of immune-stimulating cytokines. The immune system's ability to detect and destroy tumour cells is subsequently hindered combination of T cell anergy and apoptosis. Immunotherapeutic strategies designed to block the PD-1 and PD-L1 interaction are yielding promising results in the treatment of various cancer type,[384, 391] and there has been a significant investment in the development of novel monoclonal antibodies for immune checkpoint therapy.

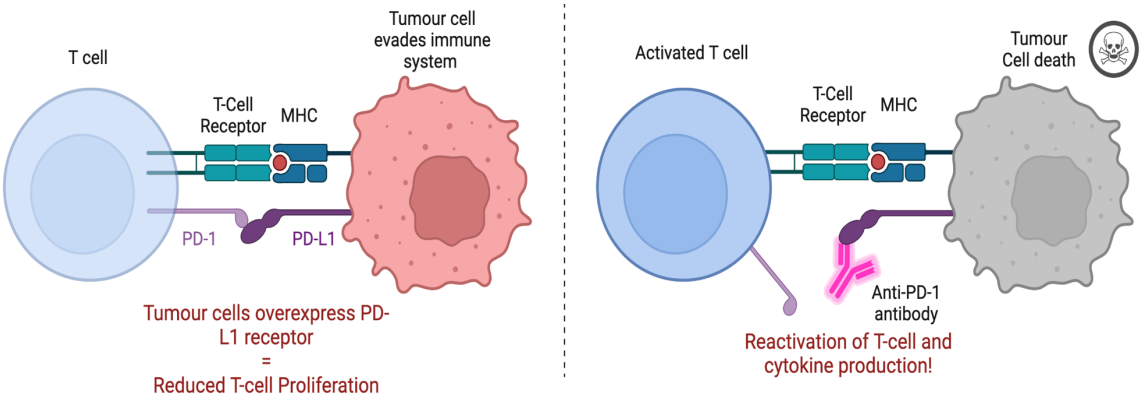

Figure 111: Illustration of PD-1 mediated inhibition of T cells. Prolonged T cell receptor (TCR) activation can result in the upregulation of PD-1. Tumour cells often express PD-L1 and PD-L2, and binding to PD-1 decreases T cell proliferation and survival by inhibition of TCR-mediated positive signalling. PD-1 or PD-L1 antibodies reactive to the immune response.[389] Created with biorender.com

There are several monoclonal antibodies that have received clinical approval for cancer immunotherapy. Pembrolizumab (Keytruda®) and nivolumab (Opdivo®) target the PD-1 receptor on T-cells. Upon binding to PD-1, these antibodies block the interaction between PD-1 and its ligands, thereby inhibiting the immune checkpoint pathway and allowing for an enhanced anti-tumour immune response. Pembrolizumab and nivolumab are approved for the treatment of several types of cancer, including melanoma, NSCLC, head and neck squamous carcinoma, Hodgkin lymphoma, urothelial carcinoma, and gastric cancer, and both antibodies have demonstrated significant clinical benefits and durable response in patients with advanced or metastatic cancer.[393] There have been similar advances in the development of anti-PD-L1 antibodies. The monoclonal antibodies durvalumab (Imfinzi®), atezolizumab (Tecentriq®) and avelumab (Bavencio®) have all received clinical approval and are designed to bind to PD-L1 on tumour cells; thus, inhibiting the interaction with PD-1 and 'rearming' the immune system (Figure 111). Durvalumab is approved for the treatment of unresectable stage III NSCLC and urothelial carcinoma. Similarly, avelumab is approved for advanced urothelial carcinoma and Merkel cell carcinoma. Atezolizumab is approved for NSCLC, SCLC and TNBC.[394-396]

7.3 The Development of Chelators that Form Complexes with Copper

There are two copper radionuclides, copper-64 and copper-67, that are considered a matched pair.[7, 397, 398] Molecules labelled with β^+-emitting copper-64 ($t_{1/2}$ = 12.7 h, β^+ = 17.4%, E_{β^+} (mean) = 278 keV) can be used as companion diagnostic agents to plan the use of radionuclide therapy with the same molecule labelled with β^--emitting copper-67 ($t_{1/2}$ = 61.9 h, β^- = 100%, E_{β^-} (mean) = 141 keV).[352] The lower β^+ emission energy of copper-64 when compared to gallium-68 can lead to PET images with higher resolution and the longer radioactive half-life of copper-64 permits imaging at later time points which can be beneficial in improving tumour-to-background contrast. The β^- emissions of copper-67 have a mean range of 0.2 mm and are appropriate for the treatment of small tumours (~ 5 mm in diameter) and disseminated metastatic disease.[399] The energy of the β^- emissions from copper-67 is similar to the β^- emissions from lutetium-177, but the significantly shorter radioactive half-life of copper-67 (2.58 vs. 6.71 days) provides a higher dose-rate. Copper-67 also has γ emission (185 keV, 49%, and 93 keV, 16%), which can be used for SPECT imaging. Copper-67 can be prepared with linear accelerators at high specific activity (>5.6 MBq/mg) and >99% radionuclide purity.[400] This is a potential advantage when compared to lutetium-177, which is prepared in nuclear reactors. Copper-64 is produced on a cyclotron. The relatively long radioactive half-lives of both copper-64 and copper-67 permit centralised manufacturing and distribution to sites without on-site radiochemistry facilities.

7.3.1 The Chelator Makes the Difference for Copper

The therapeutic potential of copper-67/64 has been known for several decades, and initial experiments used derivatives of the tetraazamacrocycle cyclam to attach the metal to antibodies. Initial biodistribution experiments in mice on an antibody conjugate labelled with [^{64}Cu]Cu^{II} showed high degrees of liver uptake, which was originally attributed to retention of

the ion in the blood pool but is most likely due to dissociation of the [^{64}Cu]Cu^{II} from the chelator.[401] A different cyclam derivative, 4-[(l,4,8,11-tetraazacyclotetradec-l-yl)methyl]benzoic acid was also conjugated to an antibody against the anti-carcinoembryonic antigen (AB35), and the conjugate was radiolabelled with copper-67. Evaluation of this conjugate in a mouse LoVo tumour model demonstrated high tumour uptake (15 ± 3% injected activity/g (IA g^{-1}) after 24 h and 32 ± 7% IA g^{-1} after 96 h).[402] This work was extended to a comparison of the biodistribution of copper-67-labelled AB35 with iodine-125-labelled AB35 in six patients with primary colorectal cancer. The copper-67 conjugate had higher tumour uptake than the radioiodinated antibody but also high non-specific liver and bowel uptake, which was presumably due to some dissociation of the Cu^{II} from the chelator.[403]

The polyaminocarboxylate macrocycle DOTA that is used for gallium-68 and lutetium-177 radiopharmaceuticals forms complexes with [$^{64/67}$Cu]Cu^{II} but the complexes are susceptible to dissociation of the metal ion *in vivo,* leading to high uptake of 'free' [$^{64/67}$Cu]Cu^{II} in the liver and general increased background signal.[404, 405] It has been proposed that the instability of [^{64}Cu]CuDOTA complexes is due to the reduction of Cu^{II} to Cu^{I} *in vivo*.[406] Pioneering research identified that [$^{64/67}$Cu]Cu^{II} complexes with the larger macrocycle, 1,4,8,11-tetraazacyclotetradecane-N,N',N'',N'''-tetraacetic acid (TETA), derived from the 14-membered macrocycle cyclam, are more stable *in vivo*.[404] The TETA chelator was conjugated to a monoclonal antibody (Lym-1) that preferentially targets malignant tissue and this conjugate was evaluated in eleven lymphoma patients leading to tumour regressions despite the fact that patients received doses intended only for SPECT imaging (126 – 477 MBq).[407, 408] Administration of [^{64}Cu]Cu^{II}(TETA-octreotide) (2 x 555 MBq, 1-2 days apart) to tumour bearing rats showed promising radiotherapeutic responses, but dissociation of the [^{64}Cu]Cu^{II} from the chelator *in vivo* led to high levels of radioactivity in the blood, liver and bone marrow

and demonstrated that the metabolic fate of some of the injected [^{64}Cu]Cu^{II} was Cu/Zn superoxide dismutase.[398, 409]

These early studies identified the considerable potential of copper-64 and copper-67 radionuclides for both diagnostic imaging and radionuclide therapy but also identified that a chelator that formed Cu^{II} complexes that were more stable *in vivo* than [Cu(DOTA)]$^{2-}$ and [Cu(TETA)]$^{2-}$ would be preferable. The search for ligands that formed more stable Cu^{II} complexes led to extensive investigations into 'cross-bridged cyclam' (CB-cyclam) ligands and hexaazamacrobicyclic ligands known as sarcophagines. Cross-bridged cyclam ligands and their carboxymethylated derivatives form Cu^{II} complexes that are remarkably kinetically stable but radiolabelling with [^{64}Cu]Cu^{II} requires heating at high temperatures.[410-413] The chemistry of CB-cyclam derivatives and their application to copper radiopharmaceuticals has been reviewed previously and is not discussed in detail here.[414-416] This review will focus on sarcophagine chelators with a focus on the chemistry that has been translated to clinical trials.

7.3.2 'Sarcophagine' Ligands form Stable Complexes with Copper

Macrobicyclic cage amine ligands, known as sarcophagines (Sar = 3,6,10,13,16,19-hexaazabicyclo[6.6.6]icosane), are ligands capable of encapsulating metal ions to form complexes with very high thermodynamic stability. This is due to a combination of factors that include their preorganised three-dimensional structures that restricts the motion of the donor atoms, a lower entropy of complex formation and decreases in the solvation of the donor atoms.[417] The synthesis of sarcophagine ligands was pioneered by Alan Sargeson and co-workers and typically involves assembly of the ligand around a substitutionally inert d^6 low spin Co^{III} template ion.[418] The synthesis of the carbon-capped cage with two exocyclic nitro functional groups, [Co($(NO_2)_2$Sar)]$^{3+}$, involves the one-pot template reaction [Co(en)$_3$]$^{3+}$ (en = 1,2-diaminoethane) with paraformaldehyde and nitromethane. Reduction of the nitro functional groups to primary amines allows isolation of [Co($(NH_2)_2$Sar]$^{3+}$. Extrusion of the Co^{III}

from the ligand is challenging, but reduction of the Co^{III} to the more kinetically labile Co^{II} allows removal of the cation by treatment with either concentrated acids under pressure or by the use of a large excess of cyanide (Figure 112).[419] The free cage amine ligand, $(NH_2)_2$sar, is then capable of forming complexes with a wide range of metal ions.[417]

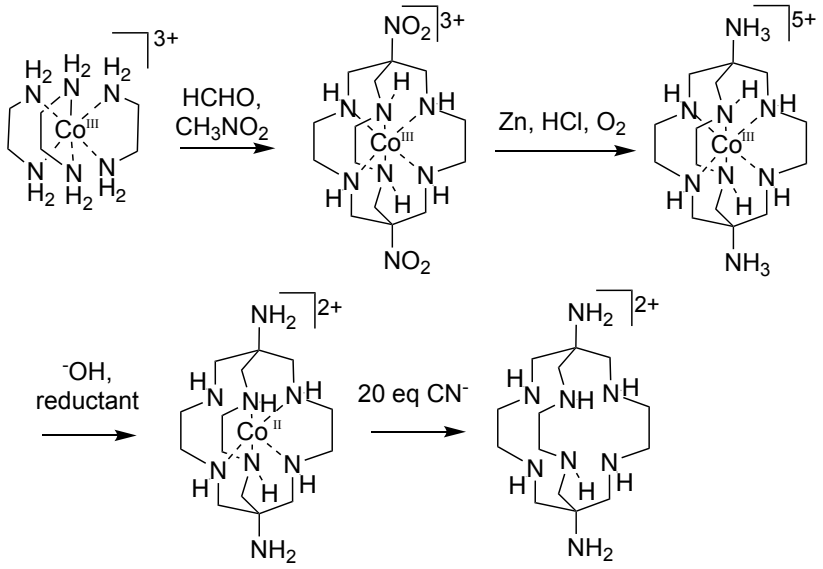

Figure 112: Synthesis of $(NH_2)_2$Sar.

The potential of Sar and $(NH_2)_2$Sar to form very kinetically and thermodynamically stable complexes with $[^{64}Cu]Cu^{II}$ and $[^{67}Cu]Cu^{II}$ was recognised by Sargeson and co-workers, who used $(NH_2)_2$Sar to probe fundamental aspects of cellular copper metabolism in rat hepatocytes and as a potential therapy for Wilson's disease.[420-422] The metal-free $(NH_2)_2$Sar ligand, is able to remove 80% of the bound copper in rat hepatocytes that have been exposed to $[^{67}Cu]Cu^{II}$ and even prevent the incorporation of $[^{67}Cu]Cu^{II}$ into ceruloplasmin.[423] Separate studies demonstrated that $[^{64}Cu][Cu((NH_2)_2Sar)]^{2+}$ was stable for at least 24 hours when challenged with human superoxide dismutase and when incubated in human serum albumin.[424] These studies demonstrated that radiopharmaceuticals that use sarcophagine derivatives to coordinate copper radionuclides were unlikely to release the metal ion to copper-binding metalloproteins.

7.3.3 Bifunctional Sarcophagines allow Conjugation to Antibodies and Peptides

The use of sarcophagine ligands in radiopharmaceuticals requires the ligand framework to be attached to targeting molecules such as peptides or antibodies. Direct coupling reactions of the primary amines of $(NH_2)_2$Sar (Figure 113) to peptides or antibodies using standard coupling techniques are relatively inefficient, so this encouraged the synthesis of 'bifunctional' derivatives where an additional functional group is added to the ligand for reaction with biomolecules. Pioneering work directed at making a bifunctional sarcophagine ligand prepared a variant with an aromatic amine functional group (SarAr, Figure 113).[425] The SarAr ligand readily forms complexes with $[^{57}Co]Co^{II}$, $[^{57}Ni]Ni^{II}$ and $[^{64}Cu]Cu^{II}$ at 'tracer' concentrations of ~ 10^{-6} M, for both the ligand and metal ion, at pH 6-8, at room temperature in 30 minutes. Complexation with $[^{64}Cu]Cu^{II}$ was remarkably fast in the pH range 4-9 with yields >98% at room temperature (10^{-6} M Cu^{II} and SarAr ligand). At pH 3, complexation with Cu^{II} is much slower and requires ~100 minutes to reach completion.[425] The complexation of both $[^{57}Co]Co^{II}$ and $[^{57}Ni]Ni^{II}$ with SarAr is significantly slower than the complexation with $[^{64}Cu]Cu^{II}$. Complexation with $[^{64}Cu]Cu^{II}$ at pH 5 still resulted in high radiochemical yields but for both $[^{57}Co]Co^{II}$ and $[^{57}Ni]Ni^{II}$ radiolabelling at this pH only resulted in 10% labelling after 3 hours.

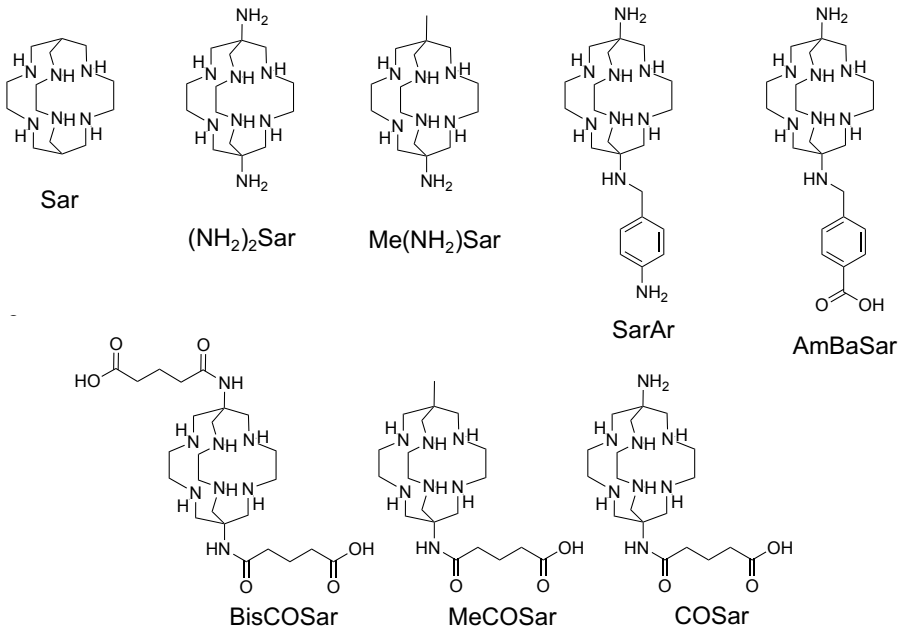

Figure 113: Chemical structures of sarcophagine-based chelators.

The remarkable stability of Cu^{II} complexes of sarcophagine ligands coupled with the ability of SarAr to form complexes in high radiochemical yields with Cu^{II} at tracer concentrations at room temperature demonstrated the significant potential of sarcophagine-based ligands for the development of [$^{64/67}$Cu] Cu^{II}-based radiopharmaceuticals. The ability to radiolabel sarcophagines at room temperature is particularly significant for potential applications with antibody conjugates, as antibodies are often sensitive to heat. This potential advantage was recognised by Smith and Sargeson, who used SarAr to conjugate sarcophagine to the monoclonal B72.3 antibody and its F(ab′)$_2$ fragment. The B72.3 antibody binds to the high-molecular-weight tumour-associated glycoprotein, TAG-72, expressed in a variety of adenocarcinomas.[426] The biodistribution of [^{64}Cu]Cu(SarAr-B72.3) and [^{64}Cu]Cu(SarAr-B72.3-F(ab′)$_2$) was evaluated in nude mice bearing LS174t tumours and revealed excellent tumour uptake consistent with a [^{64}Cu]Cu^{II} complex of high stability *in vivo*. In a separate study, an anti-GD2 monoclonal antibody, 14.G2a, and its chimeric derivative, ch14.18, that target disialogangliosides that are overexpressed on neuroblastoma and melanoma was conjugated to SarAr. The resulting conjugate was radiolabelled with [^{64}Cu]Cu^{II} with high

radiochemical yields and specific activity. Biodistribution studies in mice bearing neuroblastoma (IMR-6, NMB-7) and melanoma (M21) xenografts revealed high tumour uptake (15 – 20% IA g^{-1} of tissue) 24 hours p.i. Importantly, the uptake in the liver was low (5 – 10% IA g^{-1}), consistent with minimal loss of Cu^{II} from the chelate.[427]

The nine amine groups that are present in SarAr have the potential to add complications to coupling reactions with targeting molecules. An alternative approach is to functionalise $(NH_2)_2$Sar with aliphatic carboxylate groups to give derivatives that are ideal for conjugation to peptides with similar amide coupling chemistry to that used to conjugate peptides to DOTA. This is of particular importance when the C-terminus is crucial to biological activity. Initial work aimed at preparing sarcophagine ligands with carboxymethyl functional groups suitable for radiopharmaceutical applications investigated the reactions of $(NH_2)_2$Sar with chloroacetate,[428, 429] the same reaction used to prepare DOTA and TETA from cyclen and cyclam, respectively. A complication in the alkylation of $(NH_2)_2$Sar is that the ligand contains both primary and secondary amine centres leading to the possibility of varying degrees of alkylation and extensive structural isomers. The reaction of free $(NH_2)_2$Sar with chloroacetate does indeed lead to a mixture of products, with the major product involving alkylation of the secondary amine centres rather than the primary amine centres.[430] Metal ion coordination is a useful method to effectively 'protect' the six secondary amine groups and allows essentially selective reactions with the terminal primary amine groups of $(NH_2)_2$Sar. The introduced carboxymethyl arms can be used to introduce peptides and polyamine to the ligand framework,[429] but the removal of the metal ion (either Co^{III} or Cu^{II} used to 'protect' the secondary amines) resulted in intramolecular cyclisation reactions where the carboxymethyl entities reacted with the secondary amine centres of the cage ligand to form cyclic amides.[428, 430]

An improved procedure for the synthesis of mono- and disubstituted derivatives of sarcophagine with carboxylate functional groups is the reaction of glutaric anhydride with $[Cu(NH_2)_2Sar]^{2+}$ (Figure 114, a). The metal-free ligands could be isolated through the reduction of the copper(II) with an excess of sodium sulfide to give COSar ('carboxy'-sarcophagine) and bisCOsar.[431, 432] Although the Cu^{II} complexes of sarcophagines are extremely stable, upon reduction of the metal to Cu^{I} the ion rapidly dissociates from the ligand, presumably because the ligand cannot adjust to the coordination requirements of d^{10} Cu^{I}. Fortunately, the $Cu^{II/I}$ reduction potential is well outside biologically accessible reduction potentials. The copper(II) complex of bisCOSar has been characterised by single crystal X-ray crystallography (Figure 114, b). The copper(II) is six coordinate with a distorted octahedral coordination geometry tending toward trigonal prismatic and octahedral with two Cu-N bonds slightly shorter than the other four consistent with tetragonal compression.

Both COSar and bisCOSar can be conjugated to the targeting peptides Tyr^3-octreotate and bombesin and radiolabelled with $[^{64}Cu]Cu^{II}$ at room temperature and the resulting copper-64 complexes were stable in human serum with respect to dissociation of the metal ion.[431, 432] The two carboxylate functional groups of bisCOsar allow conjugation of two targeting peptides to a single cage amine to produce bivalent agents that have the potential enhanced tumour binding and retention.

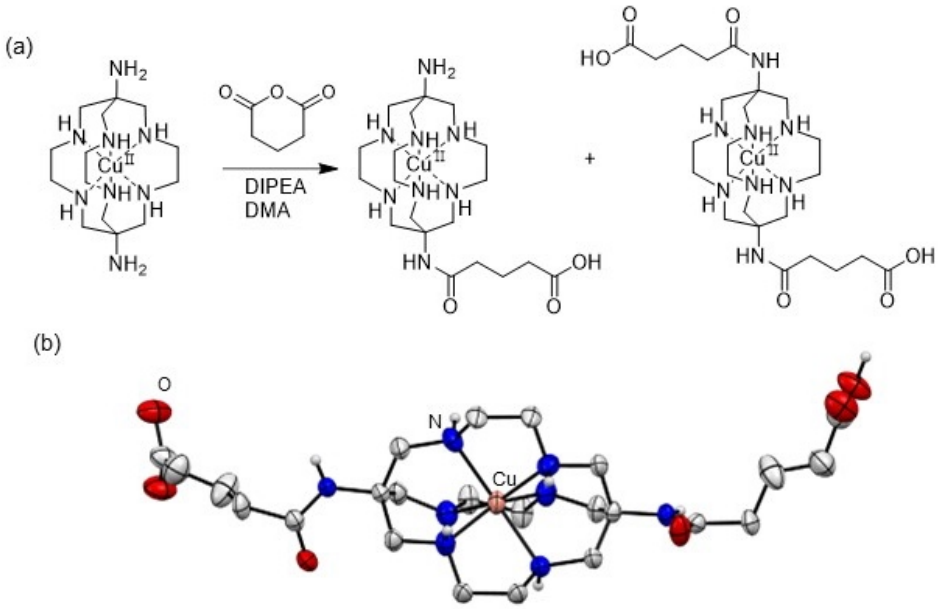

Figure 114: (a) Synthesis of Cu(COSar) and Cu(bisCOSar) (b) ORTEP representation of the cation present in [Cu(bisCOSar)](CF_3SO_3)Cl as determined by X-ray crystallography.[432]

The introduction of carboxylate functional groups to sarcophagine is also possible by either alkylation of $(NH_2)_2$Sar with 4-bromomethylbenzoic acid,[433, 434] or by reductive amination of 4-carboxybenzaldehyde with $[Cu(NH_2)_2Sar]^{2+}$ to give AmBaSar (Figure 113).[96] Introducing aliphatic carboxylic acid functional groups through ring-opening acylation reactions with glutaric anhydride results in the primary amine centres in the apical positions of sarcophagines being converted to amide functional groups that are non-nucleophilic and not protonated at physiological pH, a potential advantage when compared to alkylation reactions with alkyl halides to reductive amination reactions.

The COSar ligand with a single aliphatic carboxylic acid functional group (Figure 113) has an obsolescent apical primary amine that is protonated at physiological pH *in vivo*. This primary amine can also act as potential nucleophilic primary amine, complicating coupling reactions between the carboxylic acid functional group and amines of peptides or proteins. A methyl-capped bifunctional Sar ligand, MeCOSar ('methyl-carboxylate' sarcophagine, Figure 113), can be prepared by analogous ring opening acylation reactions between glutaric anhydride and the methyl-capped sarcophagine, $(CH_3)(NH_2)$Sar (Figure 115).

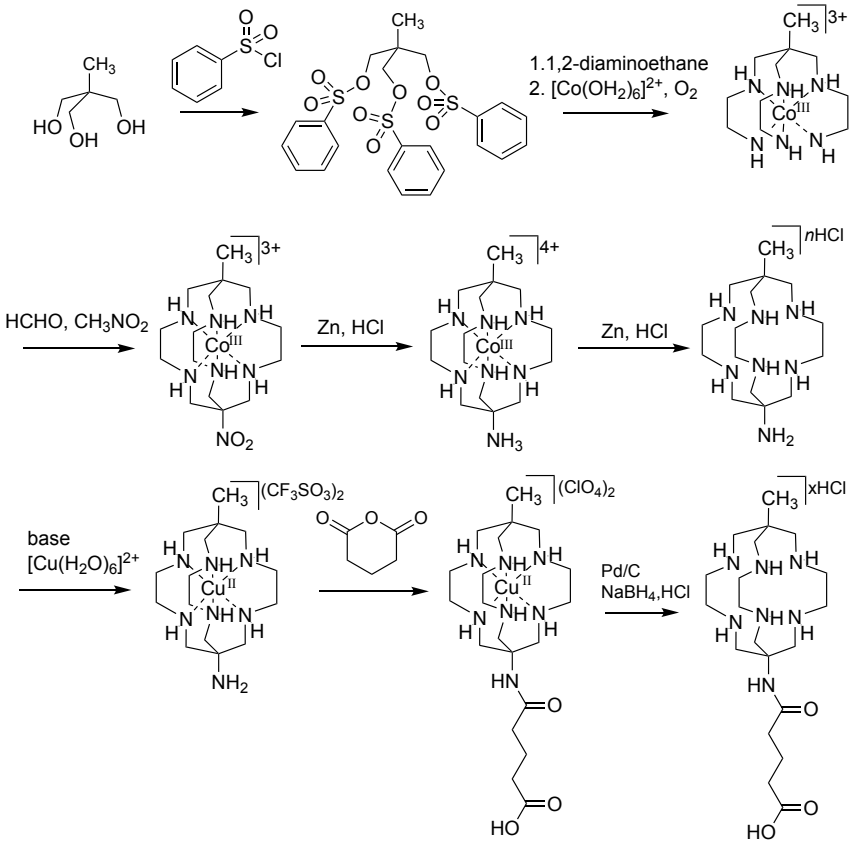

Figure 115: Synthesis of methyl-capped bifunctional Sar ligand, MeCOSar.

The bright blue $[Cu(MeCOSar)]^{2+}$ complex was characterised as the perchlorate salt by single crystal X-ray crystallography (Figure 116, a). The Cu^{II} ion is 6-coordinate and in a distorted octahedral environment with tetragonal elongation resulting in a pair of *trans* Cu–N1, Cu–N5 bonds (2.283(3), 2.337(3) Å) being longer than the other four Cu–N bonds (2.065(3)–2.096(3) Å). The distorted octahedral coordination geometry of the copper(II) reflects the combination of trigonal distortion imposed by the ligand and tetragonal distortion due to the Jahn–Teller effect in the d^9 metal ion. The introduced aliphatic carboxylate functional group extends away from the macro-bicyclic cage and is not involved in intramolecular cyclisation and lactam formation that complicated carboxymethylated sarcophagine derivatives.

7.3.4 Preclinical evaluation of [$^{64/67}$Cu]Cu(SarTATE) shows promise

With a view to make a [$^{64/67}$Cu]Cu-sarcophagine that selectively binds to somatostatin subtype 2 receptors that are over-expressed in neuroendocrine tumours MeCOSar was conjugated to Tyr^3-octreotate to give MeCOSar-Tyr^3-octreotate (SarTATE, Figure 116, b).[435]

SarTATE can be labelled with [^{64}Cu]Cu^{II} at room temperature to give [^{64}Cu]Cu(SarTATE) in high radiochemical purity. The *in vivo* biodistribution of [^{64}Cu]Cu(SarTATE) was compared to [^{64}Cu]Cu(DOTATATE) in mice bearing A427-7 tumours that over-express somatostatin receptor 2. The initial uptake in the SSTR2 positive tumours at 2 hour post-injection (p.i.) was high for both [^{64}Cu]Cu(SarTATE) (31.2 ± 7.5% IA g^{-1}) and [^{64}Cu]Cu(DOTATATE) (27.8 ± 1.8% IA g^{-1}) but tumour retention was significantly higher for [^{64}Cu]Cu(SarTATE). At 24 hour p.i. the activity in the mice administered [^{64}Cu]Cu(SarTATE) was 31.4 ± 8.1% IA g^{-1} whereas the activity in the tumours administered [^{64}Cu]Cu(DOTATATE) reduced to 10.4 ± 1.4 % IA g^{-1}. There was much lower liver uptake following administration of [^{64}Cu]Cu(SarTATE) (3.1 ± 0.8% IA g^{-1} at 2 hours; 1.7 ± 0.4% IA g^{-1} at 24 h) when compared to administration of [^{64}Cu]Cu(DOTATATE) (9.9 ± 1.2% IA g^{-1} at 2 hours; 5.9 ± 0.5% IA g^{-1} at 24 h p.i.). PET imaging in the same mouse model confirmed the high tumour uptake and low background signal following administration of [^{64}Cu]Cu(SarTATE). The very high tumour uptake and retention of [^{64}Cu]Cu(SarTATE) is coupled to lower uptake and better clearance from the liver and spleen as well as lower blood concentration than [^{64}Cu]Cu(DOTATATE).[435] The high liver uptake and slow clearance from the blood seen with [^{64}Cu]Cu(DOTATATE) is most likely due to the release of [^{64}Cu]Cu^{II} from the chelate. [^{64}Cu]Cu(SarTATE) has also been evaluated in a different tumour cell line (AR42J) which has endogenous expression of somatostatin subtype 2a receptor (Figure 116).[436] PET imaging following administration of [^{64}Cu]Cu(SarTATE) showed very high tumour uptake as early as at 1 h p.i., and retention of this uptake led to images at 4 h p.i. with excellent tumour-to-background ratios (Figure 116, c). The high tumour uptake was confirmed by an *ex vivo* biodistribution study (62 ± 2 %IA g^{-1}, 4 h p.i.). The preclinical imaging results with [^{64}Cu]Cu(SarTATE) demonstrated that the improved stability of the sarcophagine chelator when compared to the commonly used DOTA ligand results in better tumour uptake and low uptake in non-target organs. The use of the sarcophagine ligand offers

significant advantages that include the possibility of acquiring PET images at later time points (4 – 24 hours) allowing extra time for clearance of activity from non-target organs. The high tumour uptake [^{64}Cu]Cu(SarTATE) is also associated with high tumour retention supporting investigation of radionuclide therapy with [^{67}Cu]Cu(SarTATE).

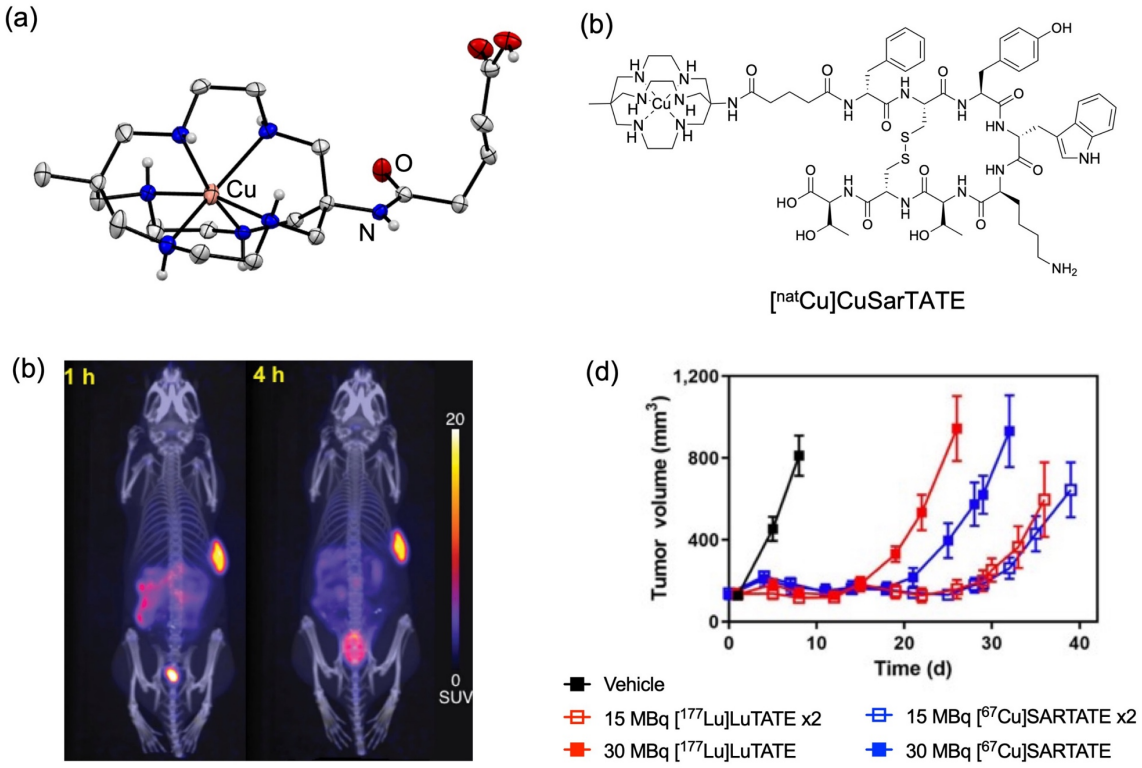

Figure 116: (a) ORTEP representation of the cation present in [Cu^{II}(MeCOSar)]$(ClO_4)_2$·0.5MeCN as determined by X-ray crystallography, thermal ellipsoids shown at 30% probability.[435] (b) Chemical structure of [^{nat}Cu]Cu(SarTATE) (c) PET/CT maximum intensity projection images of AR42J tumour bearing female Balb/c nude mice following injection of [^{64}Cu]Cu(SarTATE) at 1 and 4 h p.i, reproduced with permission.[436] (d) Efficacy of fractionated [^{67}Cu]Cu(SarTATE) PRRT compared to [^{177}Lu]Lu(TATE). Mice were treated with vehicle (day 1), 30 MBq [^{177}Lu]Lu(TATE) (day 1) or 30 MBq [^{67}Cu]Cu(SarTATE) (day 2). For fractionated dosing 15 MBq [^{177}Lu]Lu(TATE) (day 1 + 15) or 15 MBq [^{67}Cu]Cu(SarTATE) on (day 2 + 16) were administered; n = 8 mice/group, reproduced with permission.[436]

The antitumour efficacy of [^{67}Cu]Cu(SarTATE) was evaluated in an AR42J tumour xenograft model.[436] Seven days after a single administration of [^{67}Cu]Cu(SarTATE) (5 MBq), tumour growth was inhibited by 75% compared with a vehicle control (Figure 116, d). The efficacy of fractionated delivery [^{67}Cu]Cu(SarTATE) was assessed by comparing a delivery of 30 MBq of [^{67}Cu]Cu(SarTATE) either as a single intravenous injection or as two 15 MBq fractions 2 weeks apart. The treatment of tumours with two fractions resulted in a significantly

improved survival over delivery as a single fraction (47 vs. 36 days). The efficacy of [^{67}Cu]Cu(SarTATE) was demonstrated to be similar to [^{177}Lu]Lu(DOTATATE) in the same model.[436] The combination of PET imaging with [^{64}Cu]Cu(SarTATE) and radionuclide therapy with [^{67}Cu]Cu(SarTATE) has also been investigated as an intrahepatic model of metastatic neuroblastoma using IMR32 cells in nude mice.[437] PET imaging in this model and *ex vivo* biodistribution confirmed high tumour uptake of [^{64}Cu]Cu(SarTATE) and rapid clearance from other tissues. Radionuclide therapy with a relatively low dose of [^{67}Cu]Cu(SarTATE) (18.5 MBq) was effective when started 2 weeks after tumour cell inoculation. The treatment extended survival by 13 days (30%) compared with the untreated group (mean survival control group 43.0 ± 8.1 days vs. 55.6 ± 9.1 days for the treated group; $p = 0.012$).[437]

7.3.5 [$^{64/67}$Cu]Cu(SarTATE) Moves to Clinical Studies

The high tumour uptake and retention at late time points of [^{64}Cu]Cu(SarTATE) and the animal potential to use the agent for dosimetry planning of therapy with copper-67 justified a first-in-human single-centre open-label, phase 0-1 investigation of [^{64}Cu]Cu(SarTATE) in ten patients with grade 1 or 2 neuroendocrine neoplasia.[354] The PET images showed high retention in tumour deposits and substantial hepatic clearance leading to a significant increase in lesion contrast in the liver (Figure 117, a). Images were acquired at 0.5, 1, 4 and 24 hours after administration of the tracer. Analysis of the respective images and SUV data led to the recommendation of imaging at 4 hours p.i., as it combines the extra time to allow clearance from non-target tissue with the convenience of same-day imaging for the patient. Delayed imaging at 24 hours p.i. is also feasible, leading to a particularly high lesion-to-liver contrast, potentially improving the sensitivity of detection of disease in this organ, which is a major site of metastases in neuroendocrine neoplasia.[354] Similarly, imaging of a gastroenteropancreatic neuroendocrine tumour with nodal and metastatic disease with [^{64}Cu]Cu(SarTATE) showed

clear visualisation of the primary tumour in the gastrointestinal tract, but also metastatic disease (Figure 117, b).

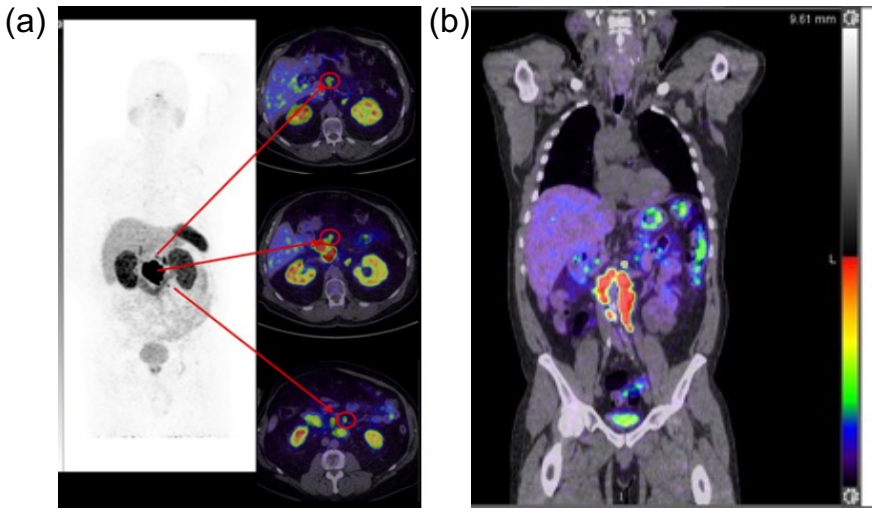

Figure 117: (a) Maximum intensity projection PET/CT images show excellent lesion detection and contrast with [^{64}Cu]Cu(SarTATE) at 4 hours p.i. in a patient with pancreatic primary tumour, (b) Maximum intensity projection PET/CT imaging also shows clear visualisation of primary tumour in the gastrointestinal tract.[354] Images kindly provided by Prof. Rodney J. Hicks.

Expression of somatostatin receptors type 2 receptors (SSTR2) is also a reliable diagnostic biomarker for meningiomas. An open-label, non-randomised phase I safety study with both [^{64}Cu]Cu(SarTATE) and [^{67}Cu]Cu(SarTATE) was completed in adult subjects with meningiomas.[438] This study provided a direct comparison of the tumour uptake and biodistribution of [^{64}Cu]Cu(SarTATE) by PET imaging with that of [^{67}Cu]Cu(SarTATE) with SPECT imaging (Figure 118). The matched pairing was shown by PET and SPECT imaging to have near identical targeting to tumours for guiding therapy, demonstrating an accurate and precise theranostic localisation of the radiopharmaceutical. The volume of the primary lesion in the SPECT images appears greater than in the PET images due to the poorer spatial resolution of SPECT.[438]

Significant advantages of using [^{64}Cu]Cu(SarTATE) include excellent tumour delineation at late time points when compared to imaging with either [^{68}Ga]Ga(DOTATATE) or [^{64}Cu]Cu(DOTATATE). Importantly, it also offers the potential for prospective dosimetry for

therapy with [^{67}Cu]Cu(SarTATE). For radiotheranostics of paediatric cancers, precise prospective dosimetry holds significant importance. Taking this into consideration, a combined imaging and therapy Phase I/IIa clinical trial for the use of [$^{64/67}$Cu]Cu(SarTATE) in paediatric patients with high-risk refractory neuroblastoma is ongoing (NCT04023331) with no safety issues being reported after the administration of up to 175 MBq/kg body weight of [^{67}Cu]Cu(SarTATE).

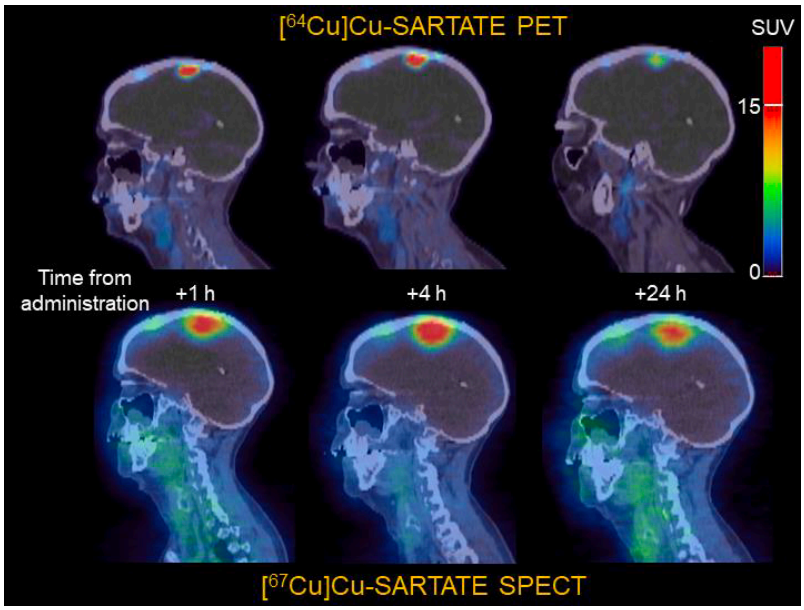

Figure 118: Side by side PET and SPECT at equivalent time points of [^{64}Cu]Cu(SarTATE) and [^{67}Cu]Cu(SarTATE), respectively, shows that changing the radionuclide does not affect tumour targeting.[438]

7.3.6 [$^{64/67}$Cu]CuSar-bombesin used in breast and prostate cancer

Bombesin, a 14-amino-acid peptide (Pyr-Gln-Arg-Leu-Gly-Asn-Gln-Trp-Ala-Val-Gly-His-Leu-Met-NH_2) was first isolated from the skin of frogs. A mammalian bombesin was isolated from porcine non-antral gastric tissue and called gastrin-releasing polypeptide (GRP) because of its role in gastric acid stimulation due to the release of gastrin.[439] There are three receptors for the mammalian bombesin peptides: BB1 (neuromedin-B receptor), BB2 (GRPR), and BB3 (bombesin receptor subtype 3). The gastrin releasing peptide receptor (GRPR – bombesin-2 receptor) is a transmembrane G protein–coupled receptor expressed in the central nervous system, gastrointestinal tract, pancreas and adrenal cortex tissues.[440] GRPR is also

overexpressed in many solid malignancies including prostate, breast, lung, colon, and ovarian cancers. The over-expression of GRPR in such a wide variety of cancers makes it an attractive target for radiotheranostics.[439]

Several peptides based on the N-terminal truncated bombesin(7−14) motif have been identified as GRPR agonists, and radiolabelled variants have been studied extensively. Initial studies with sarcophagine-bombesin conjugates described the synthesis of COSar-bombesin(Lys^3-bombesin(1-14)) and the homobivalent compound bisCOSar-(Lys^3-bombesin(1-14))$_2$, where the peptide is conjugated to the respective COSar and bisCOSar ligands through the amino group of the Lys^3 residue. Both constructs could be radiolabelled with [^{64}Cu]Cu^{II} at room temperature to give the respective complexes in high radiochemical yield and purity. Both [^{64}Cu]CuCOSar-(Lys^3-bombesin(1-14))$_2$ and [^{64}Cu]CubisCOSar-(Lys^3-bombesin(1-14))$_2$ were stable with respect to dissociation of the [^{64}Cu]Cu^{II} from chelator when incubated in human serum, but these constructs were not evaluated *in vivo*. [431, 432] In a separate study, SarAr was conjugated to bombesin(7-14) by a linker formed with succinic acid and 8-aminooctanoic acid.[441] This SarAr conjugate was radiolabelled with [^{64}Cu]Cu^{II} and evaluated in a PC3 xenograft model that overexpresses GRPR. These studies showed the tracer had high tumour uptake but considerable retention of radioactivity in normal tissues.

More recent studies have focused on GRPR antagonists rather than agonists.[442] GRPR antagonists have been identified with favourable pharmacokinetics, increased binding and the significant advantage of no gastrointestinal side effects that complicated the clinical translation of bombesin-based agonists.[439] In general, radiolabelled GRPR antagonists show superior tumour uptake and image contrast when compared to GRPR agonists.[443] A statine-based GRPR antagonist, H-D-Phe-Gln-Trp-Ala-Val-Gly-His-Sta-Leu-NH_2 (BBN, where Sta = statine) is a promising candidate for the targeting of GRPR positive tumours.[444] The molecular nature of the linker between the peptide and the metal chelator is also important for both receptor binding

and metabolic stability. The MeCOSar bifunctional chelator was conjugated to the GRPR antagonist BBN through two different (PEG_2 and PEG_4) oligo(ethylene) molecular linkers to give MeCOSar-PEG_4-BBN (known as Sar-BBN, Figure 119, a) and MeCOSar-PEG_2-BBN (where PEG = polyethyleneglycol).[170] Both conjugates have high affinity for GRPR and could be radiolabelled with [^{64}Cu]Cu^{II} at room temperature to give products in >95% yield and specific activities of ~ 100 MBq/nmol. Both tracers were evaluated in PC3 tumour-bearing mice and both tracers had high tumour uptake. Based on marginally better PET images (Figure 119, b) and cell uptake data, [^{64}Cu]Cu(MeCOSar-PEG_4-BBN) was selected as the most promising of the two candidates. Administration of [^{64}Cu]Cu(Sar-BBN) to the PC3 tumour model resulted in very high tumour uptake (19.6 ± 4.7% IA g^{-1} at 1 hour p.i.), and the tumour uptake remained high at 24 hours p.i. (7.9 ± 1.4% IA g^{-1}). The relatively high levels of GRPR in the pancreas resulted in high radioactivity in this organ at 1-hour p.i. (4.7 ± 2.0% IA g^{-1}) but, in contrast to the tumour, the radioactivity in the pancreas cleared rapidly, dropping to 1.7 ± 0.6% IA g^{-1} at 4 h p.i. and 0.07 ± 0.0% IA g^{-1} at 24 h p.i. Importantly, there was very low liver uptake and fast clearance from blood consistent with the [^{64}Cu]Cu^{II} remaining bound to the sarcophagine chelator *in vivo*. The high tumour uptake and retention of this agent suggested that the copper-67 variant may be of use for radionuclide therapy. Consequently, the therapeutic efficacy [^{67}Cu]Cu(Sar-BBN) was evaluated in PC3 tumour-bearing mice. The mice were administered with 6 × 24 MBq of [^{67}Cu]Cu(Sar-BBN) on days 0, 2, and 4, followed by a drug-free week, then another three injections on days 14, 16, and 18 (Figure 119, c). This fractionated treatment resulted in a 93% reduction in tumour volume on day 19 compared to control mice with no noticeable signs of toxicity.[445]

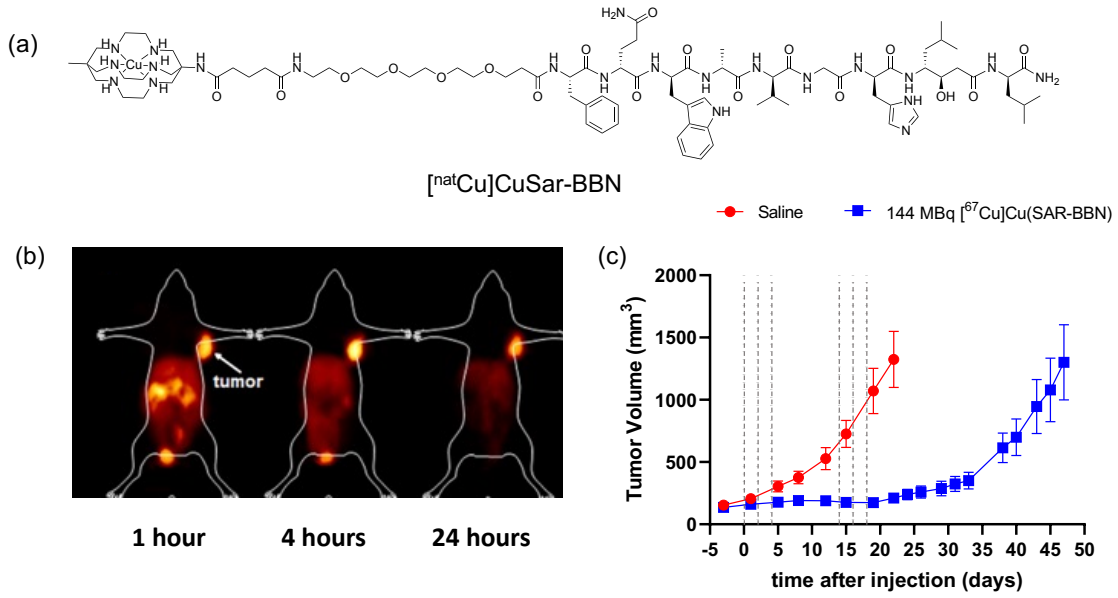

Figure 119: (a) Chemical structure of [^{nat}Cu]Cu(Sar-BBN), (b) MIP of [^{64}Cu]Cu(Sar-BBN) with PC3 tumour xenografts at 1, 4, 24 hours p.i.,[170] (c) Therapeutic results of 6 × 24 MBq of [^{67}Cu]Cu(Sar-BBN) in PC3 tumour-bearing mice (injected on days 0, 2, and 4, then 14, 16, and 18) delayed tumour growth.[445]

The *in vivo* stability of [^{64}Cu]Cu(MeCOSar) complexes combined with the favourable biodistribution profile of [^{64}Cu]Cu(Sar-BBN) resulted in PET images of high contrast in mouse models and supported translation to first-in-human studies. A clinical trial was designed to assess the safety and potential of [^{64}Cu]Cu(Sar-BBN) PET imaging in re-staging oestrogen receptor-positive (ER+), progesterone receptor positive (PR+), human epidermal growth-factor-2-negative (HER2-) breast cancer patients. In this study, patients with metastatic ER+/PR+/HER2- breast cancer underwent PET/CT with [^{64}Cu]Cu(Sar-BBN).[446] The results were extremely encouraging, and it was possible to conclude that the agent appears safe and may have a diagnostic and theranostic utility in subtypes of metastatic ER+/PR+/HER2- breast cancer patients, especially the lobular subtype, with excellent tumour visualisation 24 hours p.i. (Figure 120) .

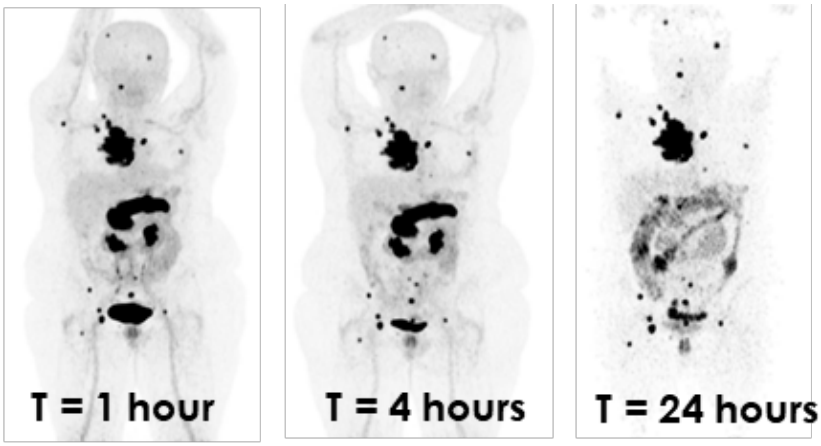

Figure 120: PET images of a patient with ER/PR+ HER2-negative metastatic breast cancer administered with [^{64}Cu]Cu(Sar-BBN) (200 MBq) at 1, 4, 24 hours p.i. Reproduced with permission.[446]

[^{64}Cu]Cu(Sar-BBN) is also currently being investigated as an imaging agent in PSMA-negative prostate cancer in a phase IIA clinical trial (NCT05613842). This study will involve patients presenting with progression of biopsy-proven prostate cancer who require imaging for staging/re-staging of their disease. The participants enrolled will be further sub-stratified into two groups; one group of men with hormone-sensitive disease (cohort A) and a second group of men with castrate-resistant disease being considered for [^{177}Lu]Lu(PSMA-617) therapy (Cohort B).

The GRPR antagonist BBN was also investigated as a potential diagnostic imaging agent using the CB-cyclam derivative, CB-TE2A. The peptide complex 4,11-bis(carboxymethyl)-1,4,8,11-tetraazabicyclo(6.6.2)hexadecane-PEG$_4$-BBN, [^{64}Cu]Cu(CB-TE2A-AR06) was selected for its high stability and increased tumour uptake compared with the corresponding [^{64}Cu]Cu(NODAGA) complexes (containing the chelator [1,4,7-triazacyclononan-1-yl-4,7-bis(tBu-ester)]-1,5-pentanedioic acid). A first-in-human study of four patients with newly diagnosed, untreated prostate cancer who were administered 184 ± 51 MBq of [^{64}Cu]Cu(CB-TE2A-AR06). In 3/4 patients, there was clear visualisation of prostate cancer, highlighting the advantages of diagnosing PSMA-negative prostate cancer with a GRPR antagonist.[447]

7.4 Imaging Immune Checkpoint Regulators

Over a decade of research has focused on the development of antibodies, peptides, peptidomimetics, and small molecules to interact at the PD-1/PD-L1 interface and elicit an anti-cancer response. Building on this body of work, the specificity and selectively of these cancer immunotherapeutics to interact with the PD-1/PD-L1 immune checkpoint pathway have also been explored as potential diagnostic imaging agents.

7.4.1 Diagnostic Imaging of PD-L1 Positive Tumours with Antibodies

Incorporating positron (β^+) or gamma (γ) emitting radionuclides into clinically approved antibodies makes it possible to monitor the variable expression of PD-L1 on the surface of tumours over time.[448, 449] An advantage of imaging tumours overexpressing PD-L1 is the ability to modulate predictive biomarkers. This results in better patient selection for immunotherapy with clinically approved antibodies. Expression of these receptors is a highly conserved mechanism to evade immune-mediated destruction[384, 450] The transient expression or heterogenous expression of PD-L1 means that therapy may not be as efficacious. Diagnostic imaging with PD-1 or PD-L1 antibodies has focused on using the positron-emitting radionuclide zirconium-89 ($t_{1/2}$ = 3.27 days) and aims to better stratify/identify patients that are most likely to benefit from immunotherapy with high PD-L1 expression[448, 449, 451-453]

Antibodies offer high specificity and can be engineered to recognise specific cell surface antigens. This specificity allows for the precise targeting of cancer cells, and these qualities have been harnessed for targeted immunotherapy. That being said, there are disadvantages to using antibodies as targeting vectors for diagnostic imaging. There is also an extensive cost associated with the production of the biological agents, and they often suffer from poor tumour permeability and potential immunogenicity or 'off-target effects'. The long circulation time of monoclonal antibodies *in vivo* can cause high background signals when

directly labelled with imaging agents.[307] This requires antibodies to be labelled with relatively long-lived radionuclides, which increases patient radiation dose to healthy tissue.[454]

Therefore, research has focused on the development of peptides as targeting agents. Validated, optimised peptides such as octreotate (see section 1.2.1) maintain a high binding affinity while offering potential advantages associated with molecules of a smaller size and ease of synthesis. There is also the potential to incorporate multiple targeting or biodistribution altering functionalities, such as albumin binders. Peptides typically have more rapid uptake in target tissue that is coupled with faster clearance from non-target tissue.[455] On the other hand, these relatively smaller molecules have a reduced specificity when compared to monoclonal antibodies and without extensive optimisation, they have a significantly reduced biological half-life.

The monoclonal antibodies discussed above have demonstrated significant clinical benefit and are important therapeutic oncologic interventions.[456] Unfortunately, there are low response rates and low targeting with varied patient outcomes between individuals.[457] This means the patient response for immunotherapy is typically only 10 – 40%.[458]

7.4.2 Peptides that Interact with PD-1/ PD-L1 Show Promise in Preclinical Therapy Studies

Although monoclonal antibodies have shown an excellent ability to target immune checkpoint proteins, there has been a significant investment in the discovery of small molecule, peptide and peptidomimetic compounds that are able to reactivate the immune response.[459-461]

Initial investigation of the peptide with the sequence FPNWSLRPMNQM containing only L-amino acid residues was rapidly catabolised and consequently failed to show any PD-L1 activity. Instead, peptide inhibitors of PD-L1 containing only D-amino acid residues, such as the lead compound, ^{D}PPA-1, with the sequence NYSKPTDRQYHF were shown to be highly resistant to proteolysis.[462] These peptides retained a strong binding affinity to PD-L1 (0.51 μM) and no degradation of the D-peptide was observed after 24 hours in 10 % human serum.

When conjugated to the near-infrared fluorophore (Cy5.5), ^{D}PPA-1 accumulated at the site of tumour tissue, increasing survival time of mice bearing CT26 tumour xenografts by nearly 50 % in mice treated with ^{D}PPA-1.

The biotechnology company Aurigene has made a significant investment in developing peptides and peptidomimetics based on a tri-or tetrapeptide sequence with a conserved serine, asparagine motif in combination with either hydrazine or urea moieties. Examination of the patent literature highlighted a large number of amino acid residue combinations, including derivatisation and cyclisation between residues. These peptidomimetics were screened for their ability to increase the ability of these peptidomimetics to restore splenocyte proliferation, including T-lymphocytes, B-lymphocytes and natural killer cells.[463, 464]

Work by Liu *et al.* discovered anti-PD-L1 peptide inhibitors designed to block the PD-1/PD-L1 interaction with high affinity *via* biopanning a phage display library that represents billions (10^9) of different peptide sequences.[465, 466] The binding affinities of the selected peptides towards human PD-L1 protein and albumin were measured using SPR and were calculated to be 366 ± 150 nM for CLP002 and 117 ± 80 nM for CLP003.[465, 467]

Peptide Name	Amino Acid Sequence
CLP002	WHRSYYTWNLNT
CLP003	WHFSYNWRWLPP

The lead compound, CLP002, showed the greatest blocking efficiency of the PD-1/PD-L1 binding interaction (85% with an IC_{50} of 2.17 μM). These peptides shown to enhance the activation of T cells and promote the production of pro-inflammatory cytokines. When CLP002 was derivatised to contain the fluorophore Cy5 (λ_{ex} 649 nm, λ_{em} 666 nm) was incubated with tumour spheroids, CLP002 was able to penetrate more deeply when compared to a PD-L1 antibody (up to 250 μm, Figure 121, a). In an animal model of CT26 colorectal tumour xenografts, CLP002 and CLP003 (2mg/kg) significantly inhibited tumour growth (Figure 121, b and c). Continued work has focused on stabilising the linear peptide CLP002 by cyclisation

through two cysteine residues. Upon cyclisation, there was up to a 34-fold in improvement in the ability to block the PD-1/PD-1 interaction, coupled with a significant improvement in the anti-tumour effect.[452] Cyclisation aims to reduce degradation by effectively making the peptide sequences 'unrecognisable' to proteases.[468]

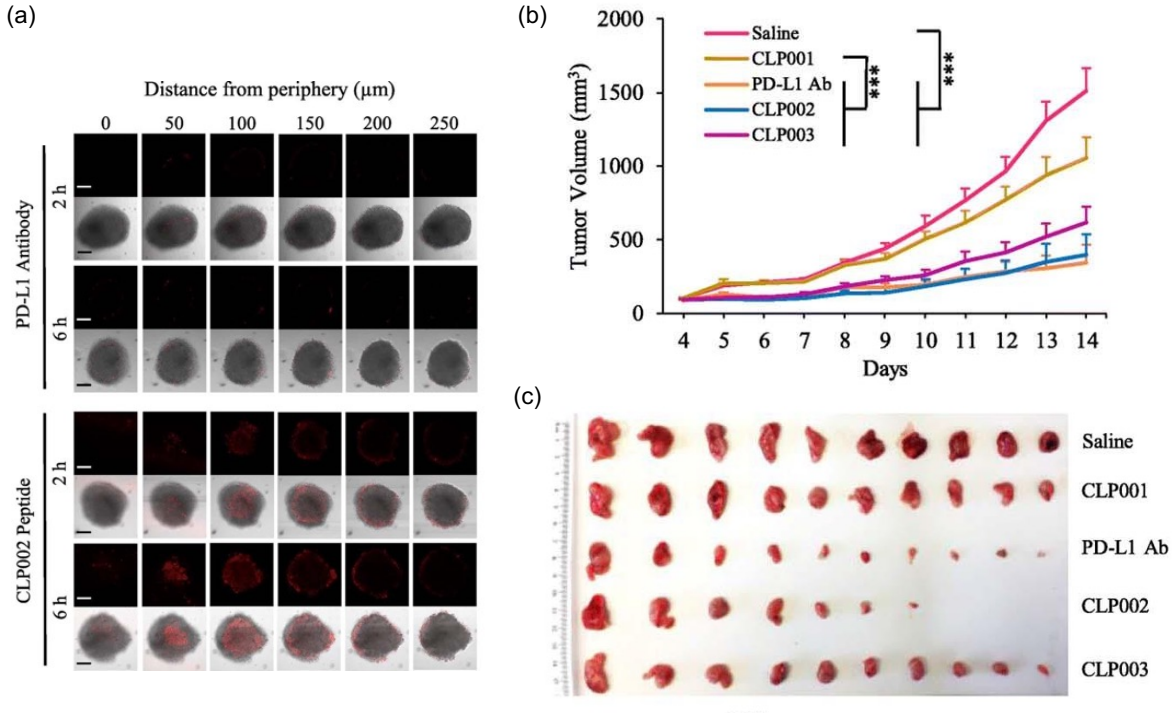

Figure 121: (a) A comparison of the 3D spheroid penetration (MDA-MB-231 cells) of CLP002 peptide and anti-PD-L1 antibody. (BioXcell, 29E.2A3). Cy5-labelled peptide and antibody were incubated with the tumour spheroids (~ 700 μm) for 2 and 6 h, followed by confocal microscopy analysis to evaluate tumour penetration (z -stacked confocal images of the spheroids (50 μm; scale bar = 200 μm); (b) CT26 tumour-bearing Balb/C mice (n = 10) were intraperitoneally injected with the anti-PD-L1 peptides (2 mg/Kg) daily for a total of 10 injections and the anti-mouse PD-L1 antibody (10 mg/Kg) every other day for a total of 5 injections. Tumour volume measured over time and represented as the mean ± SE (n = 10). and (c). Image of tumours harvested at day 14.[465]

7.4.3 Diagnostic Imaging of PD-L1 positive NSCLC Tumours with [^{68}Ga]GaNOTA-WL12

Extensive research has focused on developing peptides that interact with the PD-/PD-L1 pathway to reactivate the immune system for immunotherapy. However, has been relatively limited exploration of these peptides in the context of diagnostic imaging.

One of the first examples of peptides that have been investigated as a potential diagnostic imaging agent is the 14-amino-acid cyclic peptide, WL12. WL12 is a highly

optimised, macrocyclic peptide containing unnatural amino acids and has undergone a series of N-methylations of amide bonds to increase its biological stability. The metal chelators DOTAGA (where DOTA has been modified to contain a glutaric acid: 1,4,7,10-tetrakis(carboxymethyl)-1,4,7,10-tetraazacyclododecane glutaric acid)[469] and NOTA (2,2′,2”-(1,4,7-triazacyclononane-1,4,7-triyl)triacetic acid) were appended to allow for diagnostic imaging using the β^+-emitting radionuclides [^{64}Cu]Cu^{II} and [^{68}Ga]Ga^{II}.[470-473] Both [^{68}Ga]Ga(NOTA-WL12) (Figure 122, a) and [^{64}Cu]Cu(DOTAGA-WL12) have demonstrated high *in vitro* PD-L1 binding affinity (IC_{50} = 2.9 nM for [^{64}Cu]Cu(DOTAGA-WL12) and excellent localisation in hPD-L1 positive CHO tumour xenografts (Figure 122, b). This research culminated in a first-in-human clinical trial to evaluate the efficacy of [^{68}Ga]GaNOTA-WL12 in diagnosing advanced non-small cell lung cancer (NSCLC). This translation into the clinic was consistent preclinical imaging resulted, and demonstrated excellent tumour visualisation, especially in the lungs, with a tumour-to-lung ratio of 4.45 ± 1.89:1 at 1 hour p.i. (Figure 122, c).[472]

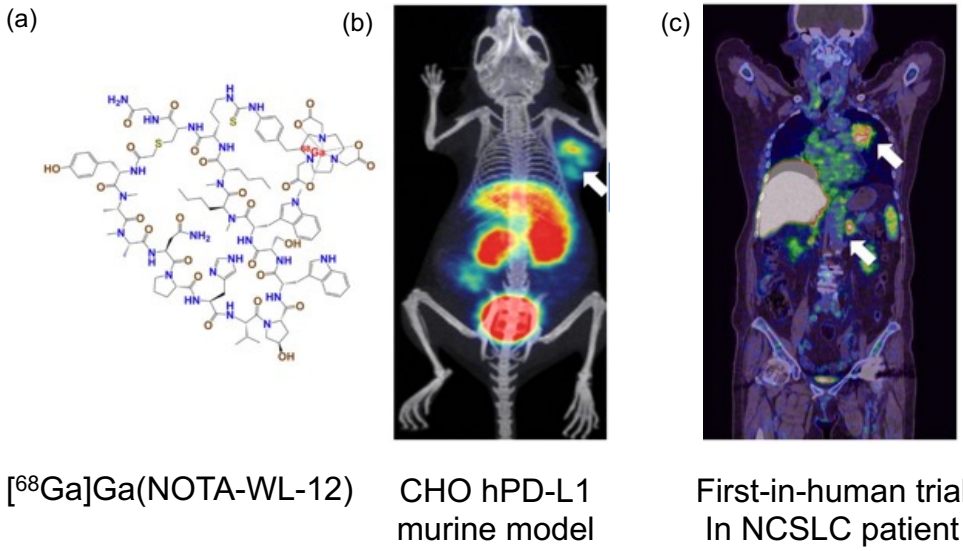

Figure 122: (a) Chemical structure of [^{68}Ga]Ga-NOTA-WL12; (b) [^{68}Ga]Ga-NOTA-WL12 has been investigated preclinically in mice bearing PD-L1 positive tumour xenografts (CHO) and showed clear tumour uptake. (c) Recently, [^{68}Ga]Ga-NOTA-WL12 has been used to image patients with PD-L1 positive non-small cell Lung Cancer.[472]

7.5 Aims

In this chapter, we focus on the development of peptides that may serve as diagnostic imaging agents of PD-L1 positive tumours. We elected to use the positron emitting radionuclide, $[^{64}Cu]Cu^{II}$ as it offers favorable characteristics for molecular imaging. Incorporating $[^{64}Cu]Cu^{II}$ provides the distinct advantage of monitoring the clearance kinetics of the radiotracer to 24 hours post-injection, where extended radioligand distribution and dosimetry estimations are not feasible with more short-lived radionuclides such as $[^{68}Ga]Ga^{II}$.

The utilisation of MeCOSar as a ligand for $[^{64/67}Cu]Cu^{II}$ radionuclides offers particular advantages for stable complex formation. The ability of MeCOSar to form complexes with the 'matched pair' of $[^{64/67}Cu]Cu^{II}$ radionuclides at room temperature with rapid complexation kinetics results in the formation of complexes with exceptional stability.[435] MeCOSar has been successfully conjugated to a range of peptides and peptidomimetics. As such, this versatile chelator has been translated from preclinical research to clinical trials. The outcome of these clinical investigations designates MeCOSar based radiopharmaceuticals as exceptional diagnostic imaging and successful therapeutic agents in NETs and prostate cancer. Consequently, we elected to use MeCOSar based chelators in the design of imaging agents that aim to diagnose PD-L1 positive cancers.

Peptides have emerged as attractive alternatives to antibodies for diagnostic imaging due to several fundamental advantages. Peptides are more cost-effective and relatively easier to synthesise, which has significant implications for their availability. Moreover, peptides exhibit enhanced tumour penetration and rapid biodistribution, which may contribute to improved imaging. We chose to develop molecular imaging agents based on peptides developed by Liu *et al.*[465] and peptidomimetic compounds developed by Aurigene.[464] Our focus on the peptide CLP003 was driven by its demonstrated ability to bind to PD-L1 at

nanomolar concentrations (117 ± 80 nM), while tri-peptidomimetics such as SN-NH-CO-NH-K were shown to restore splenocyte proliferation (Table 23).

Table 23: Amino acid sequence of peptides investigated in this work.

Peptide Name	Amino Acid Sequence
CLP003	WHFSYNWRWLPP
SNuKK	SN-NH-CO-NH-KK

To evaluate if these molecules bind to cells that overexpress the PD-L1 receptor, we first aimed to synthesise two fluorescent variants of CLP003 and SN-NH-CO-NH-K that contained fluorescein isothiocyanate and probed their binding in PD-L1-positive cells (HCC-827). Following this, by combining the favourable imaging qualities of [^{64}Cu]Cu^{II}, the superior stability of [^{64}Cu]Cu^{II} complexes with MeCOSar and the targeting capabilities, we aim to develop novel diagnostic imaging agents for PD-L1.

7.6 Results and Discussion

7.6.1 Synthesis of the Fluorescent Peptide, FITC-CLP003

Fluorescent peptides make it possible to assess binding to receptors that are overexpressed on the surface of cells, such as PD-L1, by flow cytometry. Standard solid-phase peptide synthesis protocols were followed to produce the linear protected peptide using HATU/DIPEA coupling for all amino acids. The amino acid sequence of CLP003 displays a repeated WHxSY motif. The peptide contains several hydrophobic residues in the sequence. Therefore, a small oligo(ethylene glycol) chain (PEG) was used as a linker between the peptide and the fluorescence molecule, fluorescein isothiocyanate (FITC). Based on the work with sarcophagine-BBN, [^{64}Cu]Cu(Sar-BBN)[170] we elected to incorporate the same 'PEG_4' linker between MeCOSar and the peptide CLP003.

The N-terminal Fmoc group of Fmoc-NH-CLP003 was deprotected, and the linker Fmoc-NH-PEG_4-CO_2H was installed under the same reaction conditions. Synthesis of NH_2-PEG_4-CLP003 on 2-chlorotrityl (2CT) resin afforded the corresponding peptide, which was

purified by semi-preparative HPLC and isolated in 12 % yield. The isolated compound was analysed by RP-HPLC and showed a single peak corresponding to the peptide NH_2-PEG_4-CLP003 with a retention time of 12.56 min.

A fluorescent derivative of NH_2-PEG_4-CLP003 was synthesised to investigate the *in vitro* binding to PD-L1 positive cells. The reaction of the isothiocyanate functional group of fluorescein with the terminal amine of the peptide forms a thiourea bond. Purification by semi-preparative HPLC yielded the fluorescent peptide FITC-PEG_4-CLP003, which was isolated in 30 % yield (Scheme 17).

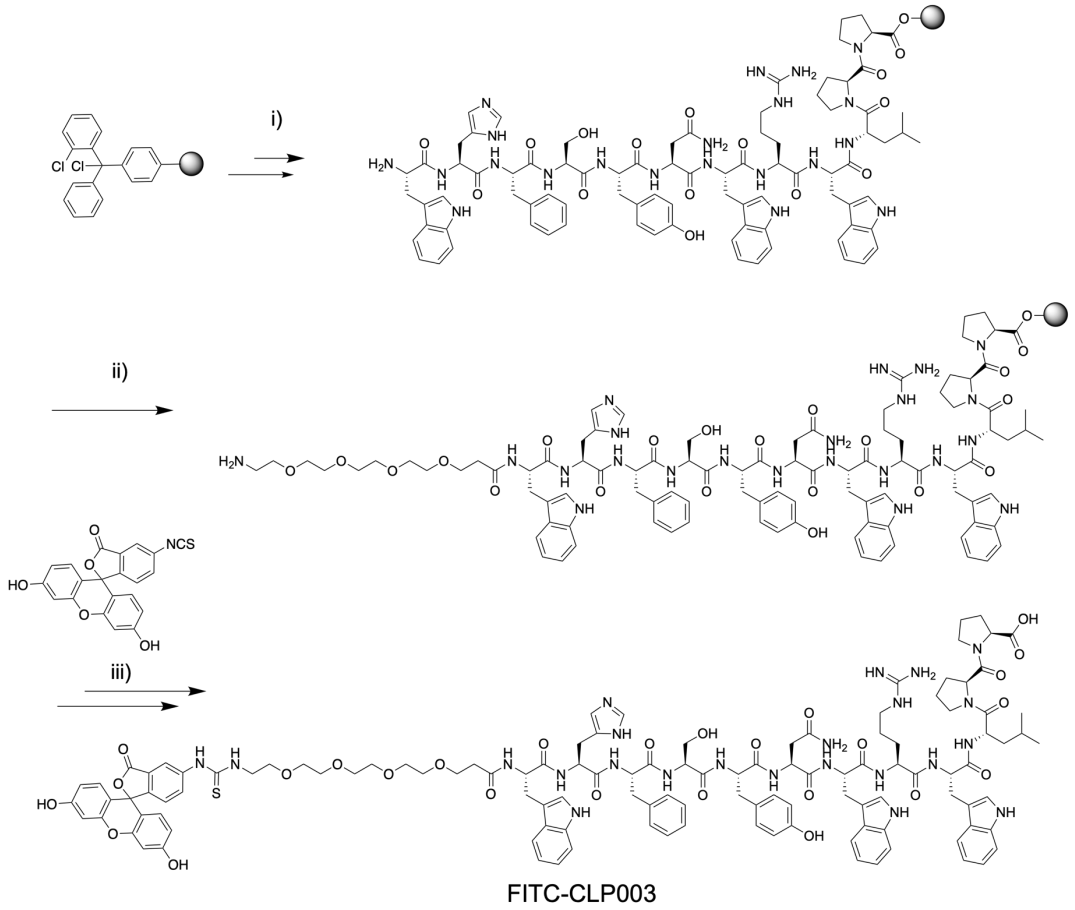

Scheme 17: Chemical structure the fluorescently labelled peptide FITC-CLP003. Relevant amino acid residue protecting groups omitted for clarity. i) Sequential SPPS on resin with HATU/DIPEA; deprotection of Fmoc protecting groups with Piperidine (20%) in DMF/NMP; ii) Fmoc-PEG_4-OH, HATU/DIPEA; Piperidine (20%) in DMF/NMP followed by cleavage with TFA/TIPS/DODT/H_2O (92.5: 2.5: 2.5: 2.5). FITC and NH_2-PEG_4-CLP003 (DMF, RT), to give FITC-PEG_4-CLP003, FITC-CLP003 (30 %).

Analysis by RP-HPLC showed a single peak corresponding to the peptide FITC-CLP003 at 14.47 min. High-resolution ESI-MS determined the signal of highest intensity as the triply protonated adduct, $[M+3H]^{3+}$, m/z = 776.0082 with a smaller peak corresponding to the doubly protonated adduct $[M+2H]^{2+}$ m/z = 1163.5017 (Figure 123).

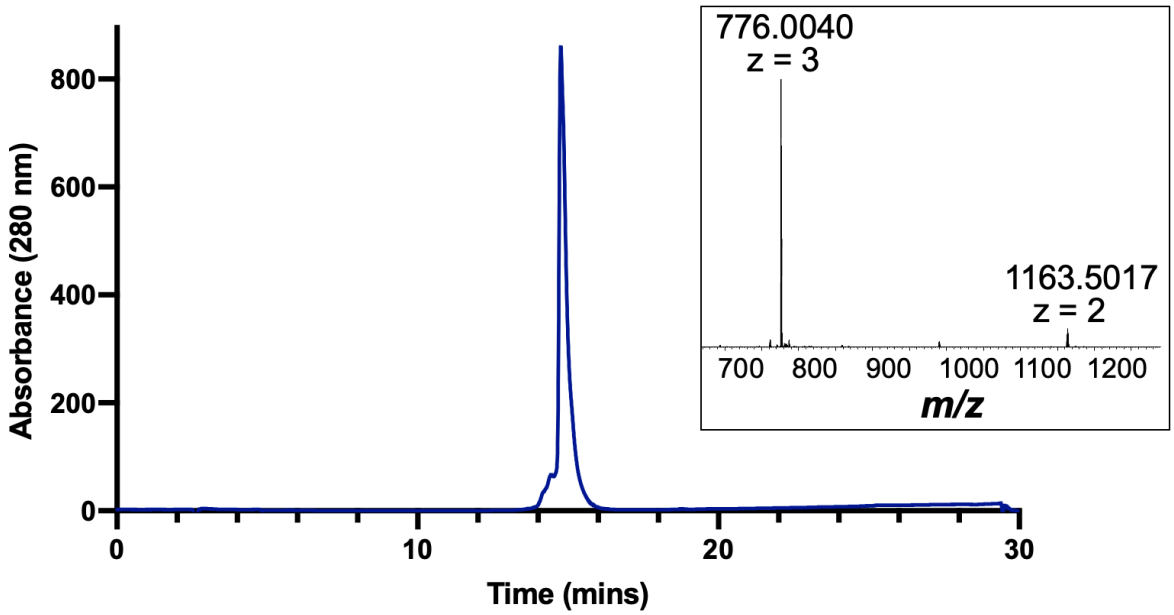

Figure 123: RP-HPLC of compound FITC-CLP003**,** showing a single peak (R_t = 14.47 min, column B, method A) with an inset of the HR-MS of compound FITC-CLP003.

7.6.2 Synthesis of a Fluorescent Peptidomimetic, FITC-SNuKK

Based on the proposed structures from research at Aurigene,[464] we also chose to investigate the binding of a tripeptidomimetic that contains both a serine-hydrazido-asparagine (Ser-CO-NH-NH-CO-Asn) with an adjacent asparagine-ureido-lysine (Asn-NH-CO-NH-Lys) pharmacophore (Figure 124, a). To easily incorporate a fluorophore into the amino acid sequence, we elected to include an additional C-terminal lysine residue. The bioorthogonal lysine protecting groups (N-Allyloxycarbonyl (Alloc) versus tert-butoxycarbonyl (Boc)) allows for the facile deprotection of the ε-amine of the C-terminal lysine to install the fluorescein isothiocyanate (Figure 124, b, blue arrow).

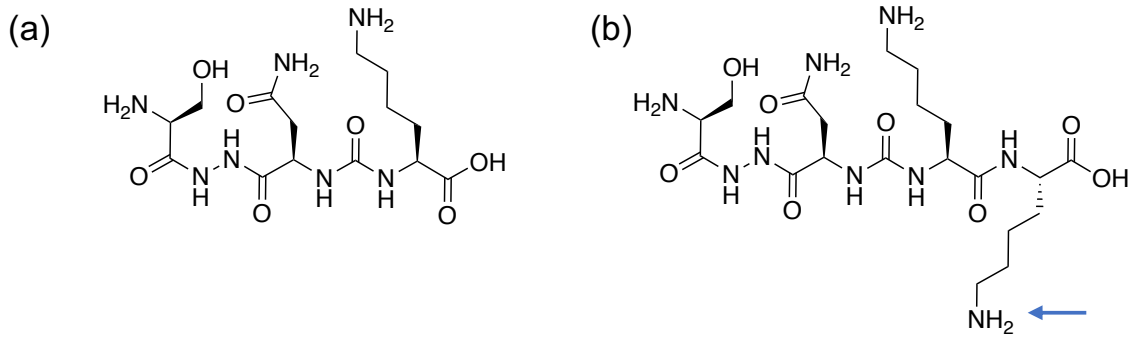

Figure 124: Chemical structure of (a) the peptidomimetic from Aurigene and (b) the peptidomimetic compound with a C-terminal lysine for functionalisation with fluorophore and metal chelators.

The synthesis of FITC-SNuKK proceeded on 2-chlorotrityl resin in five steps (Figure 125). Sequential coupling and deprotection of Lys(Boc)-Lys(Alloc)-2CT was followed by formation of the Asn-NH-CO-NH-Lys motif. Carbonyldiimidazole was reacted with the N-terminal lysine ε-amine before an excess of N-Asn(Trt)-OH was introduced into the reaction mixture.

To install a serine residue *via* a hydrazide moiety on resin, Boc-H-Ser(tBu)-$NHNH_2$ was synthesised *via* the initial esterification of the carboxylic acid with methyl iodide. Nucleophilic attack of the ester by hydrazine hydrate gave the corresponding acyl hydrazide. The reaction of the compound on resin with Boc-H-Ser(tBu)-$NHNH_2$ in the presence of standard (HATU/DIPEA) coupling reagents proceeded at room temperature. The alloc protecting group of the C-terminal lysine was removed with catalytic tetrakis(triphenylphosphine)palladium(0), before reaction with fluorescein isothiocyanate. Cleavage of the peptide and purification by RP-HPLC yielded a characteristic orange compound which was isolated as a single peak with a retention time of 7.21 minutes in 8 % yield. High-resolution ESI-MS determined the signal of highest intensity as the doubly protonated adduct, $[M+2H]^{2+}$, m/z = 462.1710. The $[M+3H]^{3+}$ and $[M+H]^{+}$ adducts were also present at m/z = 308.4499 and m/z = 923.3345, respectively.

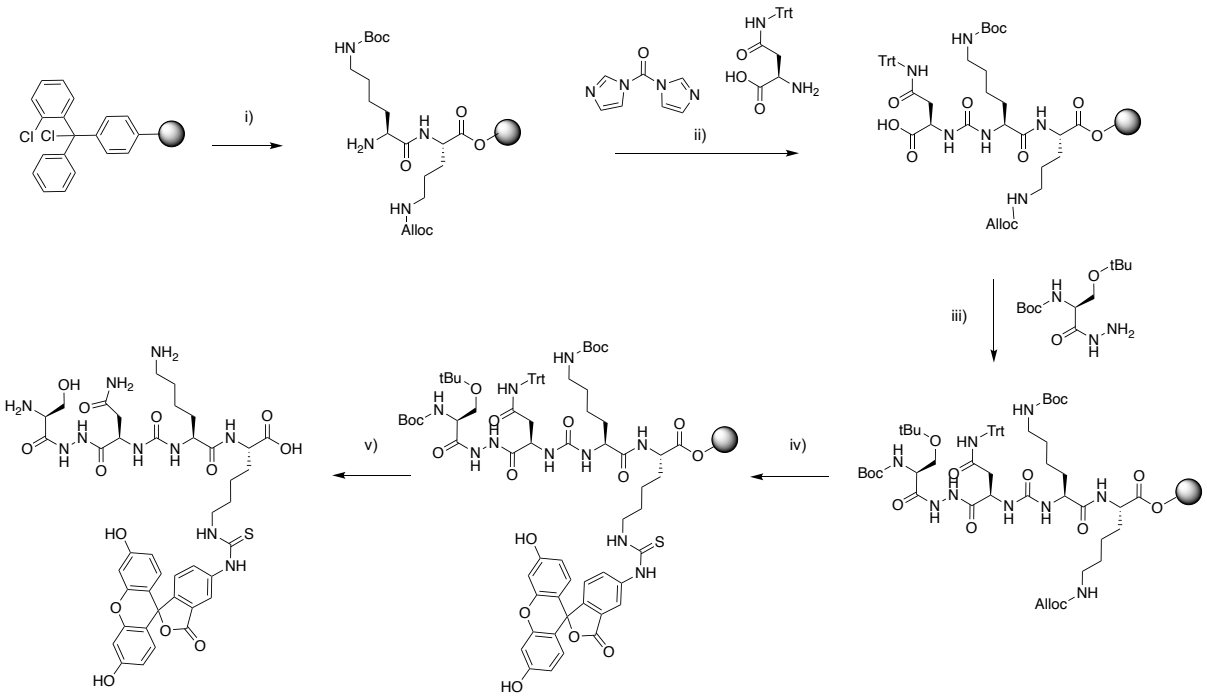

Figure 125: Synthesis of FITC-SNuKK. i) Fmoc-Lys(Alloc)-OH, HATU/DIPEA; Piperidine (20%) in DMF/NMP, Fmoc-Lys(Boc)-OH, HATU/DIPEA; Piperidine (20%) in DMF/NMP ii) carbonyldiimidazole, H-Asn(Trt)-OH iii) Boc-Ser(tBu)-NHNH$_2$ HATU/DIPEA iv) Pd(PPh$_3$)$_4$, morpholine, dichloromethane then fluorescein isothiocyanate v) TFA/TIPS/DODT/H$_2$O (92.5: 2.5: 2.5: 2.5)

7.6.3 Flow Cytometry of a Fluorescently Labelled Peptide and Peptidomimetic

To investigate the efficacy of these newly synthesised peptides in binding to the PD-L1 receptor, flow cytometry was used. HCC-827 cells are derived from epithelial adenocarcinoma and exhibit high levels of PD-L1 expression on the cell surface. The fluorophore FITC has an excitation maximum at $\lambda = 495$ nm and an emission maximum at $\lambda = 519$ nm and exhibits high absorptivity and an excellent quantum yield ($\phi = 0.92$) with suitable aqueous solubility for *in vitro* work.[474]

In the first instance, to probe the binding of the fluorescent compounds towards HCC-827, a higher concentration was used of the fluorescent peptides (25 μM). Propidium iodide staining acts as a negative control, which is indicative of no binding (Figure 126, a). There is binding of both fluorescent peptides to HCC-827 cells (Figure 126, b). At the same concentration (25 μM), there is slightly higher binding of FITC-SNuKK than FITC-CLP003

for HCC-827 cells. These results are consistent with binding to PD-L1 and as a result, enabled us to pursue developing peptide compounds that could be radiolabelled with [^{64}Cu]Cu^{II}.

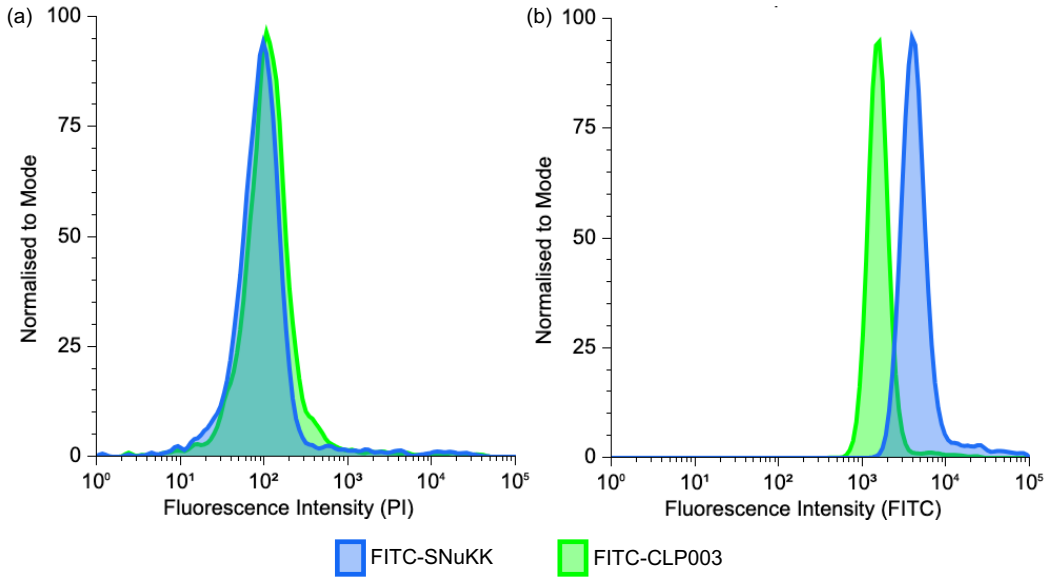

Figure 126: Flow Cytometry showing the (a) fluorescence intensity propidium iodide (PI) of FITC-SNuKK and FITC-CLP003 against HCC-827 cells; (b) the fluorescence intensity (FITC) of FITC-SNuKK and FITC-CLP003 against HCC-827 cells.

7.6.4 Synthesis of a Peptide that Contains the Copper Chelator, MeCOSar

In this work, the peptide CLP003 was also modified to contain the sarcophagine cage amine ligand (MeCOSar) through the same small oligo(ethyl glycol) linker for the modification of fluorescent peptides. There was difficulty purifying the SNuKK peptidomimetic after cleavage in conditions that would retain the Boc, tert-butyl and triphenylmethyl (trityl) protecting groups (15% HFIP in dichloromethane). The coupling reaction of the NHS ester of MeCOSar in solution was not successful, and therefore only NH_2-PEG_4-CLP003 was further developed as a peptide-complex to bind [^{64}Cu]Cu^{II}. Reaction of the NHS-ester of MeCOSar with amine of NH_2-PEG_4-CLP003 afforded the compound, MeCOSar-PEG_4-CLP003 (Sar-CLP003, Scheme 18).

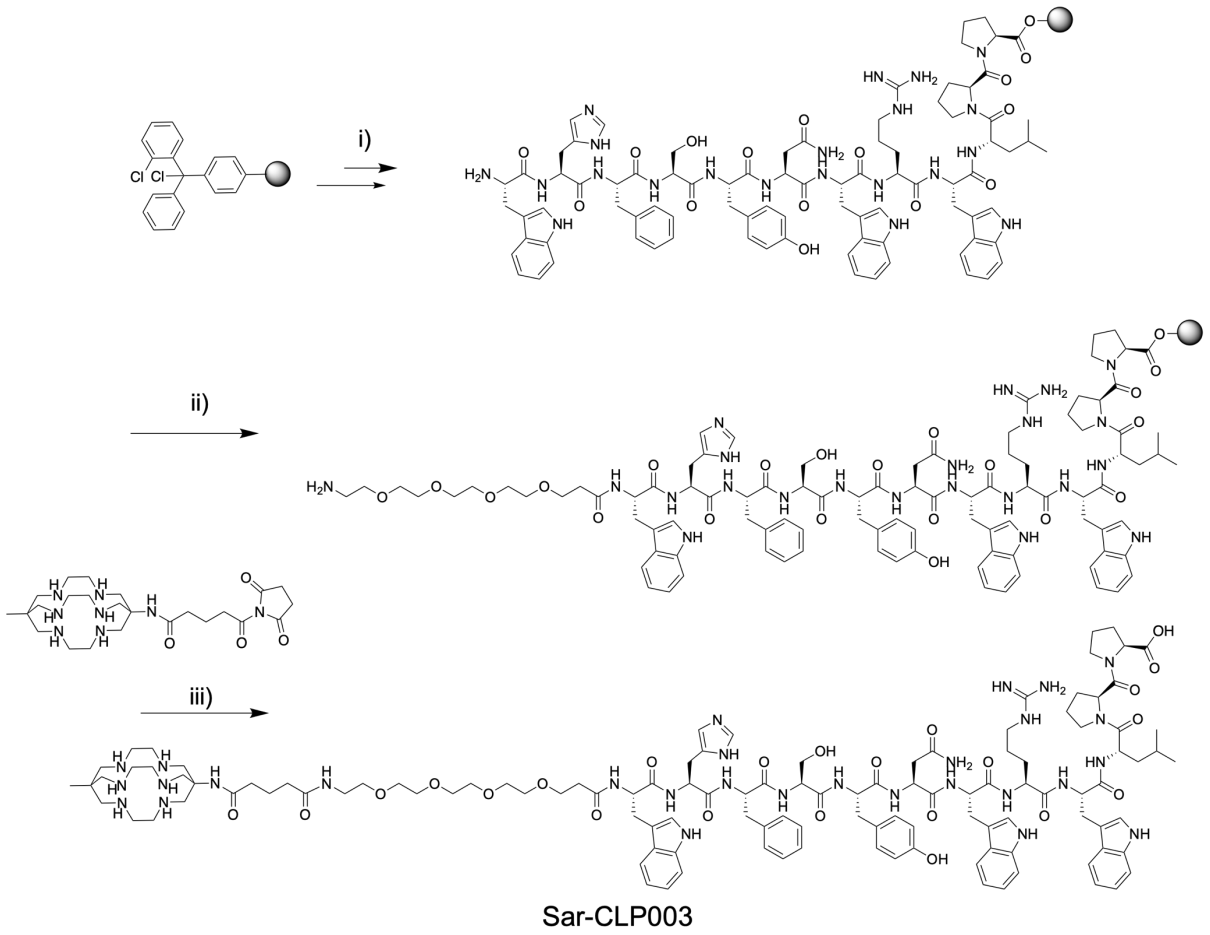

Scheme 18: Synthesis of Sar-CLP003 on 2CT resin. Relevant amino acid residue protecting groups omitted for clarity. i) Sequential SPPS on resin with HATU/DIPEA; deprotection of Fmoc protecting groups with Piperidine (20%) in DMF/NMP; ii) Fmoc-PEG_4-OH, HATU/DIPEA; Piperidine (20%) in DMF/NMP followed by cleavage with TFA/TIPS/DODT/H_2O (92.5: 2.5: 2.5: 2.5). MeCOSar-NHS and NH_2-PEG_4-CLP003 (DMF, RT), to give MeCOSar-PEG_4-CLP003, Sar-CLP003 (63 %).

Sar-CLP003 was purified by semi-preparative HPLC and gave the corresponding ligand peptide in 63 % yield. Analysis by RP-HPLC yielded a single peak with a retention time of 8.59 mins (Figure 127, method B) High-resolution ESI-MS determined the signal of highest intensity as the triply protonated adduct, $[M+3H]^{3+}$, m/z = 782.7627 with two smaller peaks corresponding to the $[M+4H]^{4+}$ and $[M+2H]^{2+}$ adducts with m/z values of 587.3244 and 1173.6401, respectively.

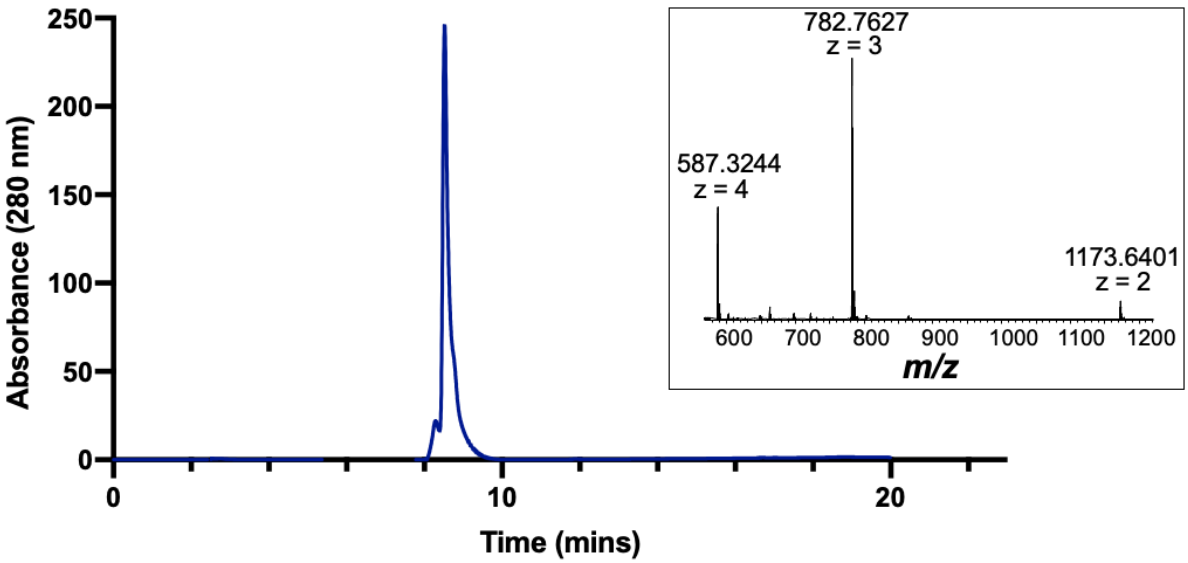

Figure 127: RP-HPLC of compound Sar-CLP003**,** showing a single peak (R_t = 8.59 min, column B, method B) with an inset of the HR-MS of compound Sar-CLP003.

7.6.5 Radiolabelling of Peptides with Copper-64

Sar-CLP003 can be radiolabelled with [^{64}Cu]Cu^{II} in $NaCH_3CO_2$ buffer (100 mM, pH 5.5) at room temperature in under 20 minutes to give the corresponding [^{64}Cu]Cu^{II} complex in high radiochemical yield and specific activity (23.5 MBq/nmol). [^{64}Cu]Cu(Sar-CLP003) was characterised by comparing the respective HPLC trace (C18 reverse phase column) with the non-radioactive analogue (Figure 128). Analysis of the complex [^{64}Cu]Cu(Sar-CLP003) gave a single peak with a retention time of 8.22 minutes, that matched the non-radioactive [^{nat}Cu]Cu(Sar-CLP003) (8.41 mins).

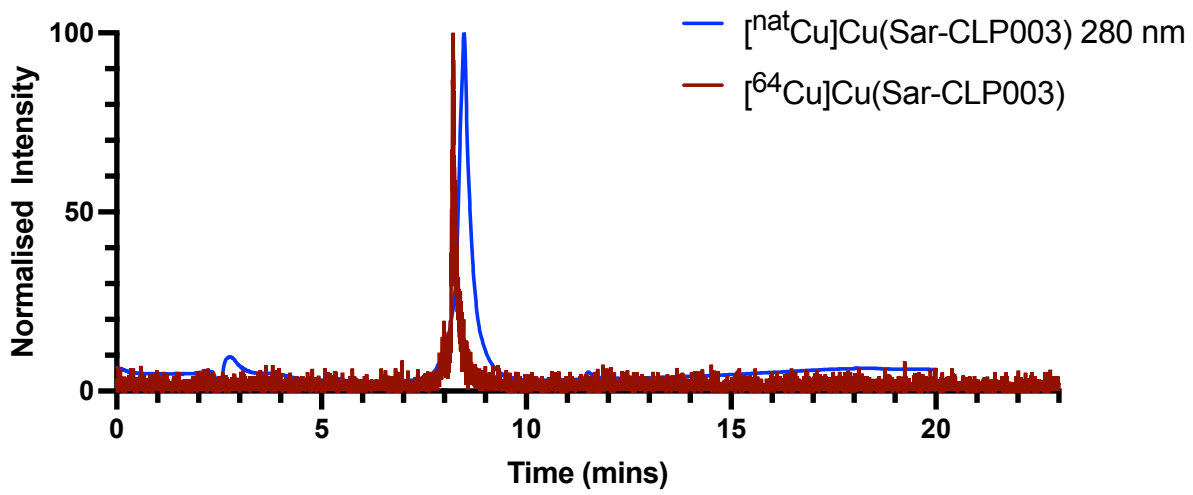

Figure 128: Radio HPLC of [^{64}Cu]Cu(Sar-CLP003) (scintillation detector, red line) and [^{nat}Cu]Cu(Sar-CLP003) (λ = 280 nm, blue line). Retention time = 8.23 min and 8.41 min, respectively.

7.6.6 Investigating the Stability of [^{64}Cu]Cu(Sar-CLP003) in human serum

A serum stability challenge assay was undertaken to compare the kinetic inertness of the sarcophagine complex with [^{64}Cu]Cu^{II}. [^{64}Cu]Cu(Sar-CLP003) was radiolabelled with a radiochemical yield > 99% (time = 0 min) and was incubated in excess human serum (Sigma Aldrich) at 37°C. Samples were analysed by radioTLC (Table 24; 50 mM EDTA mobile phase) and RP-HPLC. The peptide sequence of CLP003 only contain L-amino acid residues. Therefore, the proteolysis of the peptide is likely to be rapid.

Analysis of the serum-peptide mixture at 15, 30, 60 and 120 mins would determine the fraction of [^{64}Cu]Cu^{II} retained in the sarcophagine. Separation of the relative radioactive fractions can be achieved by radioTLC. When EDTA is in a large excess, any [^{64}Cu]Cu^{II} that has been sequestered by human serum is transchelated by EDTA. The [^{64}Cu]Cu(EDTA) complex travels with the solvent front of the mobile phase (R_f = 1), while [^{64}Cu]Cu^{II} that remains in a coordination complex with the sarcophagine will stay at the baseline (R_f = 0), allowing for the quantitative determination of the potential degree of decomplexation. For the complex [^{64}Cu]Cu(Sar-CLP003), over 120 minutes, there is minimal decomplexation. After 120 minutes, 99.2 % of [^{64}Cu]Cu^{II} remains complexed.

Table 24: Radiochemical yield (%) calculated by radioTLC of [^{64}Cu]Cu(SarCLP003) up to 120 minutes incubation time with an excess of human serum.

Time (mins)	[^{64}Cu]CuMecosar-CLP003 (%)
0	100
15	99.7
30	99.2
60	99.6
120	99.2

The overall radioactivity was measured in the soluble and insoluble portions of the serum challenge after the proteins were precipitated out with an organic solvent (CH_3CN). Between 14 – 29 % of the total radioactivity remains in the insoluble proteins, which varied slightly across four time points (Table 25). Whether this indicates that the [^{64}Cu]Cu^{II} had been sequestered by the serum proteins or the peptide complex precipitated out of the serum mixture before addition of CH_3CN, is unclear.

The soluble fractions of the serum stability challenge were also analysed by RP-HPLC (Figure 129). When [^{64}Cu]CuMecosar-CLP003 was incubated with an excess of serum, there is an immediate breakdown of the peptide complex. After 15 minutes at 37°C, only 29.4 % of the peptide remained intact, which significantly declined to 15.4 % after 30 minutes. After 60 and 120 minutes, new peaks formed with a different retention time of 8.02 minutes, and there were negligible amounts of radioactivity at the retention times corresponding to the [^{64}Cu]Cu(Sar-CLP003) (Figure 129, blue arrow). As indicated, radioTLC shows that [^{64}Cu]Cu^{II} is not being removed from the cage. Therefore, it is likely that the proteolysis occurs at the amide bond either between the cage and the oligo(ethylene glycol) chain or alternatively between the linker and the peptide. The retention time of the cleaved signal in the RP-HPLC is difficult to distinguish between the [^{64}Cu]CuMeCOSar or free [^{64}Cu]Cu^{II}, but the results of the radioTLC suggest that decomplexation from the sarcophagine cage is not occurring. Comparison between the percentage of the complex by radioTLC shows there is still 99.2 % of the activity retained at the baseline (R_f = 0), indicating that the [^{64}Cu]Cu^{II} is still

encapsulated by the ligand. These stability studies highlight that [^{64}Cu]Cu(Sar-CLP003) is highly susceptible to proteolytic degradation.

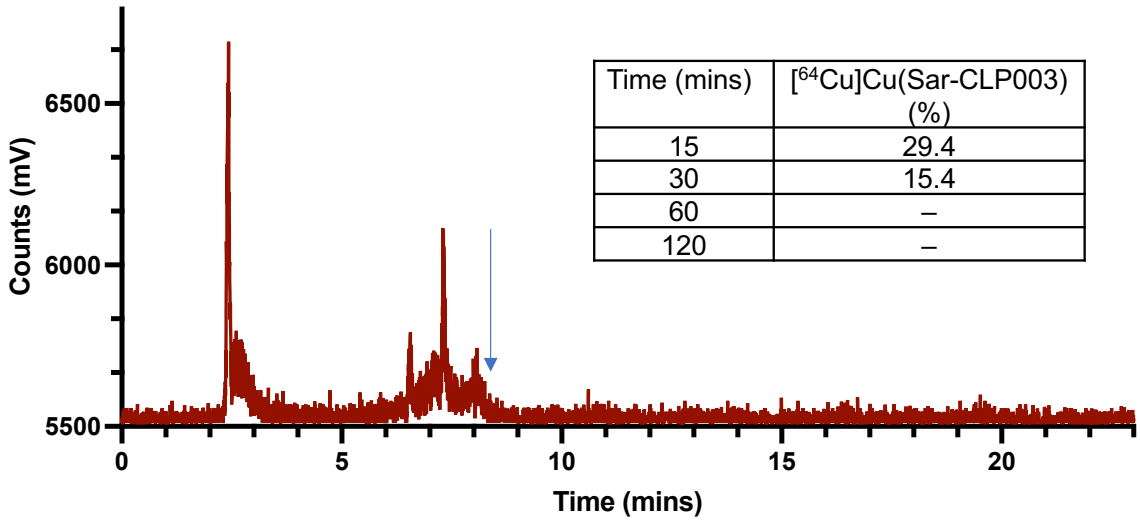

Time (mins)	[^{64}Cu]Cu(Sar-CLP003) (%)
15	29.4
30	15.4
60	–
120	–

Figure 129: Radio HPLC of [^{64}Cu]Cu(Sar-CLP003) after 120 min incubation with human serum with an inset of the radiochemical yield (%) calculated by RP-HPLC of [^{64}Cu]Cu(Sar-CLP003) up to 120 minutes incubation time with an excess of human serum. Blue arrow represents the retention time of [^{64}Cu]Cu(Sar-CLP003), 8.21 mins.

Peptides that are investigated preclinically and clinically often are optimised through a series of modifications, namely D-amino acid residue substitution, cyclisation, or N-methylation, similar to the peptide WL12 (Figure 122). In this preliminary investigation, the linear peptide [^{64}Cu]Cu(Sar-CLP003) containing only natural amino acids is likely to be prone to degradation. Nevertheless, this study represents the initial study to investigate the behaviour of these peptides within a model that simulates a biological environment.

7.6.7 Investigating the Stability of [^{64}Cu]Cu(Sar-CLP003) in a Cysteine and Histidine Challenge

The stability of [^{64}Cu]Cu(Sar-CLP003) was also investigated in a challenge assay with cysteine and histidine (Figure 130). Both of these amino acids are 'biologically nucleophilic' and can coordinate [^{64}Cu]Cu^{II}. Incubation of the peptide complex [^{64}Cu]Cu(Sar-CLP003) in 5 mM of cysteine or histidine at 37°C, resulted in minimal decomplexation of [^{64}Cu]Cu^{II}. After 4 hours, 95.7 % and 98.7 % of the complex remained intact with an excess of cysteine and histidine,

respectively. After heating at 37 °C for six hours, the samples of the cysteine and histidine challenge were combined and analysed by RP-HPLC, which showed a single peak with a retention time of 8.4 minutes and minimal degradation of [^{64}Cu]Cu(Sar-CLP003) (Figure 130).

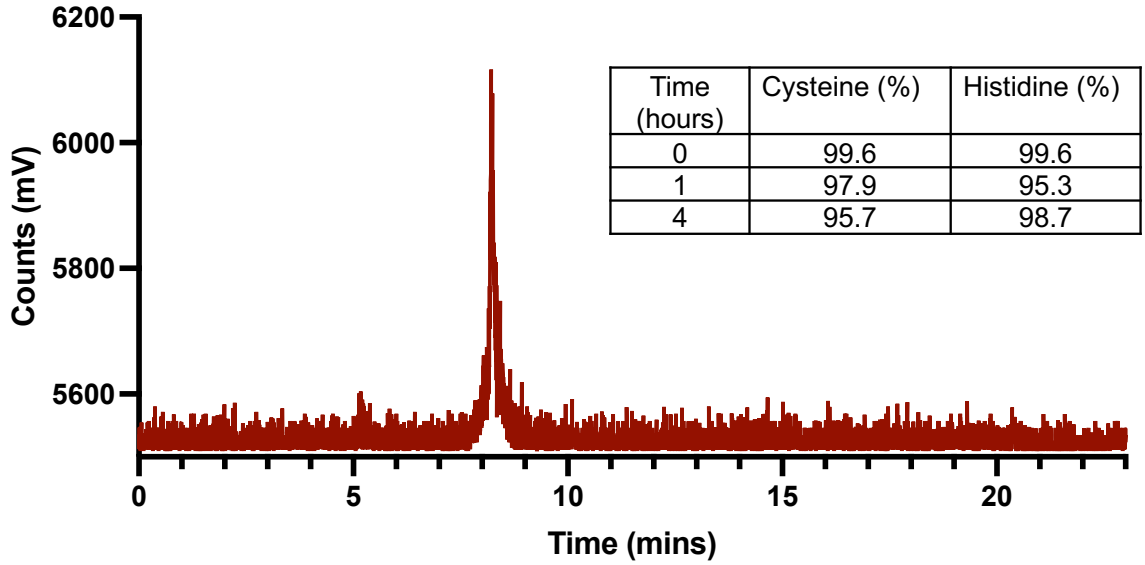

Time (hours)	Cysteine (%)	Histidine (%)
0	99.6	99.6
1	97.9	95.3
4	95.7	98.7

Figure 130: Radio HPLC of [^{64}Cu]Cu(Sar-CLP003) after incubation with cysteine and histidine (5 mM, 6 hours) with an inset of radiochemical yield (%) calculated by radioTLC of [^{64}Cu]Cu(Sar-CLP003) at 0, 1, 4 hours incubation time with an excess of cysteine and histidine.

7.7 Concluding remarks and Future work

When the peptide CLP003 and peptidomimetic SN-NH-CO-NH-KK were modified to contain a fluorophore, they were shown to bind to cells that overexpress PD-L1 on their surface.

To enable radiolabelling with [^{64}Cu]Cu^{II}, the sarcophagine ligand MeCOSar was incorporated into the peptide sequence of CLP003 through N-terminal modification, facilitated by a small oligo(ethylene glycol) linker. [^{64}Cu]Cu(Sar-CLP003) was radiolabelled in quantitative yield with high specific activity (23.5 MBq/nmol). As is the case with peptides that contain natural amino acids, proteolysis in human serum is rapid.

We acknowledge that this is only a preliminary investigation of the radiochemistry of the peptide complex [^{64}Cu]Cu(Sar-CLP003).We envisage that optimising the peptide sequence to improve the biodistribution and pharmacokinetic qualities will be necessary to proceed in future experiments. This could be achieved by substitution with D-amino acid residues or

peptide cyclisation. Increasing the circulation *in vivo* this could also be facilitated by the addition of albumin binders. This chapter highlights the promise of using a [^{64}Cu]Cu^{II}-based peptide as a molecular targeting agent for PD-L1 positive tumours.

7.8 Experimental

7.8.1 General procedure for peptide synthesis

Peptides were synthesised on a Biotage manual peptide synthesiser (0.2-0.3 mmol scale) using standard Fmoc-protected chemistry. Fmoc groups were removed (20% piperidine in DMF with 0.1M Oxyma, 15 minutes), and the peptides were cleaved with cleavage reagents (92.5/2.5/2.5/2.5 trifluoroacetic acid/triisoprpyl silane/DODT/H_2O) and purified by semi-preparative HPLC. Semipreparative RP- HPLC (Agilent 1260 Infinity II Preparative LC System with mass detector on a Kinetex EVO C18 column, 100Å, 150 x 4.5 mm, 5 μm) with a 7 mL/min flow rate. Gradient elution of Buffer B = 0.1% FA in H_2O and Buffer B= 0.1% FA in acetonitrile. Method H (10 to 95% B in A at 35 min, 95 % B in A at 36 min, 10 % B at 40 min) and detection at 280 nm and 254 nm.

7.8.2 NH_2-PEG_4-CLP003

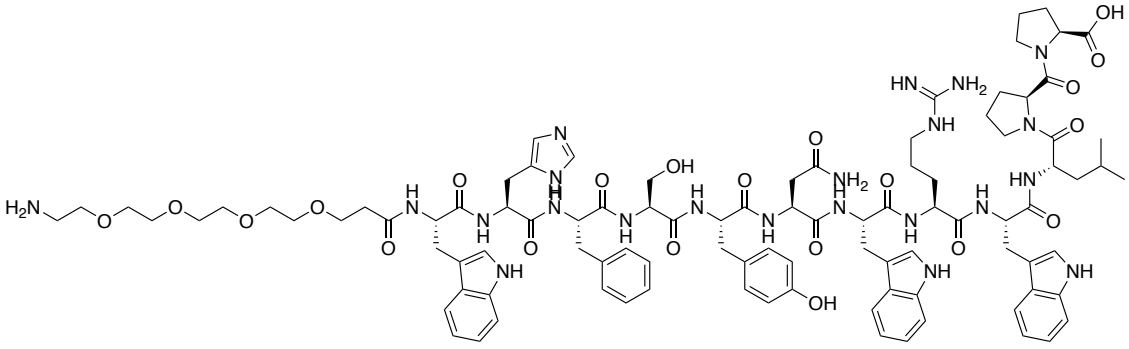

Fmoc-NH_2-PEG_4-COOH (3 eq, 159 mg, 0.3 mmol) was reacted with the peptide according to standard amine coupling procedure with HATU (5 eq, 190 mg, 0.5 mmol) and DIPEA (10 eq, 175 μL, 1 mmol) in DMF (5 mL) overnight. N-terminal Fmoc was removed, and the peptide was cleaved. The TFA reside was evaporated under a stream of N_2 before cold diethyl ether (10 mL) was added to precipitate the peptide, and the solid was centrifuged and washed (10mL) with diethyl ether purified by high-performance liquid chromatography (Method H). Pure fractions were combined and lyophilised to yield a white powder (23 mg, 12%). R_t = 12.56

mins (method A, column B). ESI-MS $[M+2H]^{2+}$: 968.9818, $[M+3H]^{3+}$:646.3243 calculated for $(C_{97}H_{128}N_{22}O_{21})^{2+}$: 968.9823, calculated for $(C_{97}H_{120}N_{22}O_{21})^{3+}$:646.3240.

7.8.3 FITC-PEG$_4$-CLP003

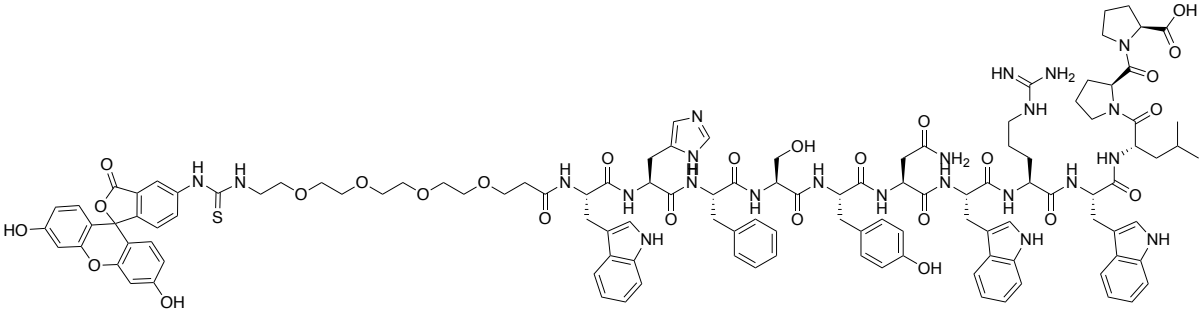

NH_2-PEG$_4$-CLP003 (5 mg, 0.0025 mmol) was dissolved in DMF before fluorescein isothiocyanate (1.1 mg, 0.0028 mmol) was added to the reaction mixture and incubated in the absence of light overnight. Cold diethyl ether (10 mL) was added to precipitate the peptide and the solid was centrifuged and washed (10mL) with diethyl ether and purified by high-performance liquid chromatography (Method H). Pure fractions were combined and lyophilised to yield a bright yellow powder (1.8 mg, 30 %). R_t = 14.47 mins (method A, column B). ESI-MS: $[M+2H]^{2+}$: 1163.5017, $[M+3H]^{3+}$: 776.0040, calculated for $(C_{118}H_{139}N_{23}O_{26})^{2+}$: 1163.5002 calculated for $(C_{118}H_{140}N_{23}O_{26})^{3+}$: 776.0036.

7.8.4 Boc-Ser(tBu)-NH-NH$_2$

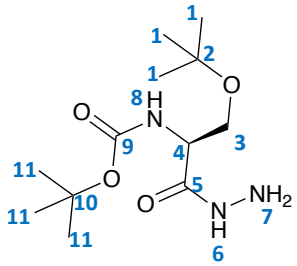

Boc-Ser(tBu)-OH (1.4 g, 6.1 mmol) was dissolved in dry DMF (15 mL) and K_2CO_3 (1.05g, 7.6 mmol) was added under an atmosphere of N_2. To this solution was added iodomethane dropwise (0.4 mL) and stirred at room temperature for 2 hours before volatiles were removed *in vacuo*. The resulting residue was partitioned between ethyl acetate and H_2O and washed with H_2O (2 x 50 mL) and brine (1 x 50 mL). Organic fractions were dried over $MgSO_4$, filtered,

and taken to dryness under reduced pressure to yield a yellow oil which crystallised overnight (1.3g). The crystals were dissolved in methanol (10 mL) and hydrazine hydrate (2 mL) was added to the reaction and stirred overnight. The volatiles were removed *in vacuo* and the resulting colourless oil was partitioned between ethyl acetate and H_2O and washed with H_2O (1 x 50 mL), HCl (0.01 M, 50 mL), saturated $NaHCO_3$ solution (1 x 50 mL) and brine (1 x 50 mL). Organic fractions were dried over $MgSO_4$, filtered, and taken to dryness under reduced pressure to yield a white crystalline solid (0.7g, 43%). ESI-MS: $[M+H]^+$: 276.1806, $[M+Na]^+$: 298.1625, $[M\text{-}tBu]^+$: 220.1181. ^{1}H-NMR (500 MHz; $CDCl_3$): δ 7.99 (s, 1H, 6), 5.48 (d, J = 5.9 Hz, 1H, 8), 4.14 (s, 1H, 4), 3.90 (s, 2H, 7), 3.66 (dd, J = 8.8, 4.0 Hz, 1H, 3), 3.34 (t, J = 7.7 Hz, 1H, 3), 1.37 (s, 9H, 11), 1.09 (s, 9H, 1). ^{13}C NMR (126 MHz; $CDCl_3$): δ 171.6 (2, 10), 155.6 , 80.1, 73.9, 61.8 (3) 53.7 (4), 28.4 (11), 27.5 (1).

7.8.5 FITC-SNuKK

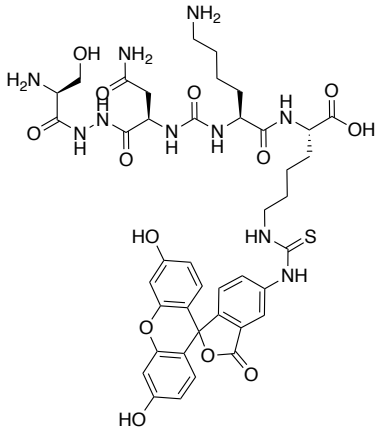

This product was prepared *via* standard Fmoc SPPS. Fmoc-Lys(Alloc)-OH was loaded onto 2-chlorotrityl resin (0.83 mmol/g) according to standard protocols. The Fmoc protecting group was then removed, as described above. A solution of Fmoc-Lys(Boc)-OH (1.4 g, 3.8 mmol), HATU (1.5 g, 3.8 mmol) and DIPEA (1.4 mL, 8 mmol) in dimethylformamide and N-methylpyrrolidine (4:1, 25 mL) was incubated at room temperature for 5 min before being added to the pre swelled, resin-bound Lysine(alloc) (2.3 g, 1.9 mmol). The mixture was incubated for 5 h at room temperature. The resin was isolated by filtration and washed with

N,N-dimethylformamide, dichloromethane and diethyl ether. The Fmoc protecting group was then removed, as described above.

The dipeptide Lys(Boc)-Lys(alloc)-2CT (0.95 g, 0.8 mmol) was swelled in dichloromethane. CDI (0.65 g, 4.15 mmol) and DIPEA (0.7 mL, 4.15 mmol) were added to the resin in DMF: NMP (4:1, 20 mL) and left for 1 hour. The resin was isolated by filtration and resuspended in a solution of H-Asn(Trt)-OH (0.62 g, 1.6 mmol) and left to stir overnight. The resin was isolated by filtration and washed with N,N-dimethylformamide, dichloromethane and diethyl ether. Boc-Ser(tBu)-NH-NH_2 (0.225g, 0.83 mmol), HATU (0.315 g, 0.83 mmol), DIPEA (0.3 mL, 1.6 mmol) was added to the resin (0.5 g, 0.41 mmol) and shaken overnight before isolated as above. The alloc functional group on resin was removed with catalytic tetrakis(triphenyl)phosphine palladium(0) (0.1 eq) and morpholine (5 eq) in dichloromethane (10 mL).

SNuKK-2CT resin (100 mg, 0.083 mmol), fluorescein isothiocyanate (30 mg, 0.083 mmol) and DIPEA (30 μL, 0.16 mmol) were shaken overnight in the absence of light, before the resin was isolated and washed as above. The peptide was cleaved according to standard procedures, and the crude mixture was purified by semi-preparative HPLC (Method D). Pure fractions were lyophilised to yield a bright orange powder (8 % yield). R_t = 7.21 min (method A, column B). ESI-MS: $[M+H]^+$: 923.3345, $[M+2H]^{2+}$: 462.1710, $[M+3H]^{3+}$: 308.4499, calculated for $(C_{41}H_{51}N_{10}O_{13}S)^+$: 923.3353 calculated for $(C_{41}H_{52}N_{10}O_{13}S)^{2+}$: 462.1713 calculated for $(C_{41}H_{53}N_{10}O_{13}S)^{3+}$: 308.4499.

7.8.6 Sar-CLP003

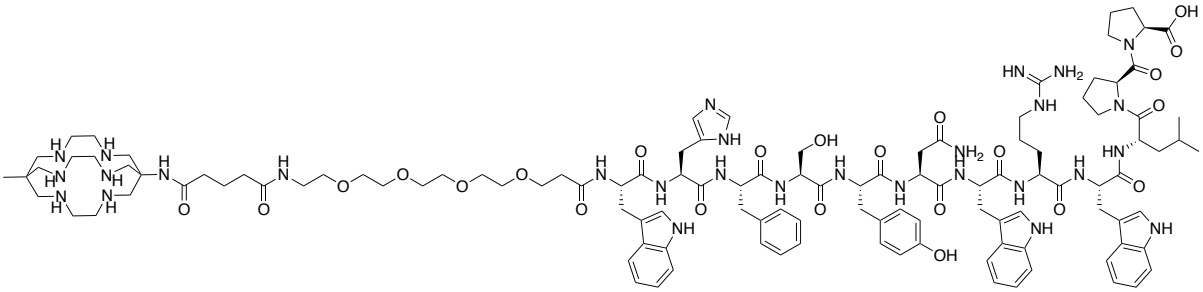

MeCOSar-NHS (1.37 mg, 0.0026 mmol) in DMF (30 µL, 50mg/ mL) was added to the solution of NH_2-Peg_4-CLP003 (4.6 mg, 0.0023 mmol) in DMF and shaken at room temperature for four hours. Cold diethyl ether (5 mL) was added to precipitate the peptide, and the solid was centrifuged and washed (3 mL) with diethyl ether then purified *via* semi-preparative HPLC (Method H). Pure fractions were combined and lyophilised to yield a colourless powder (3.30 mg, 63%). R_t = 8.59 minutes (method B, column B). ESI-MS $[M+2H]^{2+}$: 1173.6401 $[M+3H]^{3+}$:782.7627 $[M+4H]^{4+}$: 587.3244 calculated for $(C_{117}H_{166}N_{29}O_{23})^{2+}$: 1173.6404 calculated for $(C_{117}H_{167}N_{29}O_{23})^{3+}$: 782.7628, calculated for $(C_{117}H_{168}N_{29}O_{23})^{4+}$: 587.0720.

7.8.7 Flow cytometry of fluorescent PD-L1 peptides

HCC-827 and LNCaP cells cultured in RPMI media were lifted with trypsin and pelleted *via* gentle centrifugation. 'Stained' cells were resuspended in either the labelling solution (200 µL 1:200, FITC-CLP003 and FITC-SNuKK with 1:100 CD45:2 APC-047) and 'unstained' cells were suspended in PBS + 2% FBS with a final concentration of 1 × 10^6 cells/ mL. Samples were incubated in the absence of light on ice for 1 hour before excess peptide was removed *via* centrifugation and washing (3 min @ 1000 RPM), then the supernatant was removed, and the cells were resuspended in PI buffer (300 µL). Populations of cells with no fluorescence will have a fluorescence intensity displayed on the histogram at approximately 10^2.

7.8.8 Radiolabelling of Sar-CLP003

The $[^{64}Cu]Cu^{II}$ complexes were prepared by neutralising $[^{64}Cu]CuCl_2$ (aq) (0.05M HCl, 18 µL, 30 MBq) with NaOH (11 µL, 0.1 M) with aqueous sodium acetate (1 M, pH 3.5 µL) to a final

pH 5.5. An aliquot of [^{64}Cu]Cu^{II} (10 MBq in 13µL) was reacted with Sar-CLP003 (1µl, 1 mg/ mL in Milli Q) at room temperature for 20 minutes. An aliquot of the reaction solution (1 MBq) was taken for analysis by radio TLC and RP radio-HPLC (5 –100% in 15 min, 100% in 17 mins, in 5% to 23 mins).

7.8.9 Stability of [^{64}Cu]Cu(Sar-CLP003) in human serum

[^{64}Cu]Cu(Sar-CLP003) (7 MBq in 9.5 µL) was incubated with human serum albumin (100 µL, Sigma Aldrich) at 37 °C. At time points of 15, 30, 60 and 120 mins, 1 µL of the reaction mixture was monitored by RadioTLC (mobile phase: 10 mM EDTA in PBS 1x), then 20 µL of the serum solution was removed, CH_3CN (60 µL) was added to the serum to precipitate proteins, and the resultant mixture was centrifuged for 5 min. After this, the clear supernatant was removed, and the CH_3CN wash was repeated (60 µL) before analysis *via* HPLC. Radioactivity was counted in both the soluble and insoluble fractions.

Table 25: The percentage of radioactivity in soluble and insoluble fractions of human serum.

Time (mins)	Portion	[^{64}Cu]Cu(Sar-CLP003) (%)
15	Insoluble	29
	Soluble	**69**
30	Insoluble	18
	Soluble	**80**
60	Insoluble	17
	Soluble	**82**
120	Insoluble	14
	Soluble	**76**

7.8.10 Stability studies with cysteine and histidine

[^{64}Cu]Cu(Sar-CLP003) (3 MBq in 15 µL per reaction) was incubated with either a solution of cysteine and histidine (final concentration of 5 mM) and incubated at 37°C. Aliquots of the mixture (2 µL) were analysed by radio TLC at 0, 1 and 4 hours incubation time. The soluble fractions were combined and analysed by RP- HPLC at 6 hours.

8 Conclusions, Challenges and Future Opportunities

The individual achievements within this thesis have been highlighted in the conclusions in each chapter. These final concluding remarks aim to summarise the overall contribution that this work provides to the field of radionuclide therapy and diagnostic imaging, the challenges associated with research in this field and the future opportunities that aim to build on this body of work.

Targeted radionuclide therapy of cancers is possible, provided sufficient radiation can be selectively delivered to the active sites of disease. Diagnostic PET imaging allows the selection of patients most likely to respond to radionuclide therapy and can also provide insight into the molecular responses to treatment. The potential to selectively target tumour cells with either α- or β^--emitting radionuclides whilst minimising adverse effects is a potential advantage when compared to conventional chemotherapy. The clinical approval of two lutetium-177 containing radiopharmaceuticals, [^{177}Lu]Lu(DOTATATE) and [^{177}Lu]Lu(PSMA-617), approved for the treatment of somatostatin receptor-positive neuroendocrine tumours and metastatic castrate resistant prostate cancer, respectively have shown the feasibility of radionuclide therapy. These approaches have the potential to assist many patients, but there are still some challenges and limitations that are impeding widespread adoption in clinical cancer care. In part these challenges stem from difficulty in production of relevant therapeutic radionuclides, the limited scope of indications these agents are approved to treat and the burden of radiation dose that patients receive. Nevertheless, these clinical approvals highlight the impact that the development of suitable molecular agents can have on the field. The work in this thesis builds on the chemistry, biochemistry and biology of countless research groups in the search for better treatments of cancer.

The emerging potential of radionuclide therapy with α-emitting actinium-225 has stimulated significant interest in developing chemistry to enable the selective delivery of actinium to tumours. The high particle energy and energy transfer of α-emission delivers high doses of radioactivity, capable of causing double-stranded breaks in DNA. Therefore, there is significant interest in developing bifunctional chelators that form stable complexes with [^{225}Ac]Ac^{III} that can be easily conjugated to monoclonal antibodies for targeted alpha therapy of cancer.

The work in Chapters, Two, Three and Four highlight such a development. The new bifunctional ligand H_2MacropaSqOEt was used to chemically modify monoclonal antibodies that target CAIX. These antibody conjugates were radiolabelled with [^{225}Ac]Ac^{III}, and [^{225}Ac]Ac(MacropaSq-hG250) was evaluated in a murine model of cancer. The research presented in these three chapters highlight the future potential of targeted alpha therapy with monoclonal antibodies. We believe this work will have the most impact in targeting hypoxic tumours. Targeting the metalloenzyme CAIX, which plays an integral role in stabilising hypoxia within the tumour microenvironment may offer a solution to classical radioresistant tumours. In this regard, [^{225}Ac]Ac^{III}-based radio-immunotherapeutic agents such as [^{225}Ac]Ac(MacropaSq-hG250) may be successful in cases where β^--emitting radiopharmaceuticals are not.

Future work with [^{225}Ac]Ac(MacropaSq-hG250) will explore optimising the treatment strategy to ensure that maximal efficacy is achieved with the smallest radiation dose. Fractionated dosing has proven to be more effective than a single intravenous injection.[475] This technique is routine in external beam radiation therapy and relies on the principle that delivering the same cumulative radiation in multiple-dose fractions allows healthy tissue sufficient recovery time.[41, 436] It is important to state that a fractionated dosing regimen introduces new challenges, which should be highlighted. As Australia currently does not

produce actinium-225 suitable for radiopharmaceutical use, the shipment of actinium-225 into Australia is a significant undertaking and poses several challenges. The scarcity of this rare radioisotope is a significant contributing factor to the imbalance in the supply of actinium-225. Although actinium-225 has a relatively long half-life (9.9 days), multiple shipments would be necessary to fractionate the doses of [^{225}Ac]Ac(MacropaSq-hG250) to achieve a comparable cumulative dose. Nevertheless, using fractionated doses of [^{225}Ac]Ac(MacropaSq-hG250) may produce a more sustained delay in tumour growth. Administering doses of [^{225}Ac]Ac(MacropaSq-hG250) in fractions may better target all cells in different stages of the cell cycle, including the radioresistant cells that go into cell cycle senescence as a protective mechanism. Multimodality therapy, where [^{225}Ac]Ac(MacropaSq-hG250) could be used in combination with other chemotherapeutic or immunotherapeutic agents may further enhance the anti-tumour effect of [^{225}Ac]Ac(MacropaSq-hG250). These are exciting alternative protocols to further improve the efficacy of an already successful treatment strategy for a model of cancer that overexpresses CAIX on the tumour surface.

Despite the challenges associated targeted therapy with [^{225}Ac]Ac^{III}, the findings presented in this thesis provide promising insights for the further developments of the conjugate, [^{225}Ac]Ac(MacropaSq-hG250). When evaluated in murine model of cancer that overexpresses CAIX, mice that received 14.8 kBq of [^{225}Ac]Ac(MacropaSq-hG250) exhibited a significant delay in tumour growth. Notably, three out of five mice (60 %) exhibited a partial response to the treatment while two out of five mice (40%) experienced a complete response, with tumour volumes unable to be measured in the two mice after day 70. Examination of the SK-RC52 tumour of mice that received [^{225}Ac]Ac(MacropaSq-hG250) (14.8 kBq) were observed to have an average of 14.1 ± 1.6 double-strand breaks in DNA per cell nuclei. This damage to SKRC-52 tumour xenografts reflects a ‘catastrophic’ amount of damage caused by

the ionising α radiation delivered within the tumour microenvironment, highlighting the impact of [^{225}Ac]Ac(MacropaSq-hG250) to treat cancers that overexpress the enzyme CAIX.

The work in Chapter Five focuses on the concept of antibody-based pre-targeting. This is another exciting alternative strategy to increase therapeutic efficacy and reduce the burden of radiation on patients. The synthesis of [^{225}Ac]Ac(Macropa-Tetrazine) was a preliminary investigation into the possibilities of pre-targeted α therapy, and future work will involve exploring the potential of the iEDDA reaction between [^{225}Ac]Ac(Macropa-Tetrazine) and TCO-modified antibodies. A future objective of this work would involve translating this pretargeted radio-immunotherapeutic technique in animal models of disease.

The focus of Chapter Six focused on developing a [^{64}Cu]Cu^{II}-based diagnostic imaging agent for Alzheimer's disease. Utilising the same iEDDA reaction previously explored, this work focused on the development of an antibody 'pre-target and chase' approach which as the potential to circumvent the technical difficulties associated with immunoPET of the brain. This preliminary work suggests that pre-targeting amyloid plaques may be feasible, and further investigation of pre-targeted molecular imaging in animal models of amyloid pathology is warranted.

The work in Chapter Seven focused on the development of a new peptide-based imaging agent for the diagnosis of PD-L1-positive tumours. Peptides have emerged as attractive alternatives to antibodies for diagnostic imaging. The preclinical success of peptides that incorporate the theranostic matched pair of diagnostic and therapeutic radionuclides [$^{64/67}$Cu]Cu^{II}, [$^{64/67}$Cu]Cu(SarTATE) and [$^{64/67}$Cu]Cu(Sar-BBN) offers an exciting alternative to clinically approved [^{68}Ga]Ga^{II} and [^{177}Lu]Lu^{III}-based molecular agents. The design of our peptide, [^{64}Cu]Cu(Sar-CLP003), drew on these preclinic and clinical achievements as well as the peptide sequence CLP003 by Liu *et al.*[465] This chapter explored the [^{64}Cu]Cu^{II} radiochemistry and stability of this compound. Future work will build on this preliminary

investigation to optimise peptide stability and evaluate the binding efficacy of [^{64}Cu]Cu(Sar-CLP003) in PD-L1-positive models. Another potential advantage of incorporating [^{64}Cu]Cu^{II}-MeCOSar in the synthesis of [^{64}Cu]Cu(Sar-CLP003) is the capacity to translate this diagnostic molecular target into a companion therapeutic, [^{67}Cu]Cu(Sar-CLP003), and offers the potential to provide a theranostic matched pair of agents. Whether targeting cancers that evade the immune system with radionuclide therapy may cause off-target effects remains to be seen, but this simply highlights the ease with which translating the peptide [^{64}Cu]Cu(Sar-CLP003) into [^{67}Cu]Cu(Sar-CLP003) could be achieved. Instead, this final chapter offers a preliminary investigation into targeting PD-L1-positive tumours.

The work described in the seven chapters of this thesis features both therapeutic ([^{225}Ac]Ac^{III}) and diagnostic ([^{64}Cu]Cu^{II}) radionuclides and is dedicated to developing different radioactive metal complexes that can be incorporated into antibodies, small molecules and peptides. The overarching theme of this work relates to the progression of new radiopharmaceuticals designed to better diagnose or treat various malignancies, such as renal cancer, Alzheimer's disease and cancers that are associated with suppression of the immune system, known as immune checkpoint inhibitors with a view to progress these new radioactive metal complexes and conjugates in preclinical work.

9 References

1. Sgouros, G.; Bodei, L.; McDevitt, M. R.; Nedrow, J. R. Radiopharmaceutical therapy in cancer: clinical advances and challenges. *Nat. Rev. Drug. Discov.* **2020,** 19, 589-608.

2. L'Annunziata, M. F. Chapter 4 - Alpha Radiation. In *Radioactivity (Second Edition)*, L'Annunziata, M. F., Ed. Elsevier: Boston, 2016; pp 123-134.

3. Franken, N. A.; Hovingh, S.; Ten Cate, R.; Krawczyk, P.; Stap, J.; Hoebe, R.; Aten, J.; Barendsen, G. W. Relative biological effectiveness of high linear energy transfer α-particles for the induction of DNA-double-strand breaks, chromosome aberrations and reproductive cell death in SW-1573 lung tumour cells. *Oncol. Rep.* **2012,** 27, 769-74.

4. Milenic, D. E.; Brady, E. D.; Brechbiel, M. W. Antibody-targeted radiation cancer therapy. *Nat. Rev. Drug. Discov.* **2004,** 3, 488-99.

5. Seidl, C. Radioimmunotherapy with α-particle-emitting radionuclides. *Immunotherapy* **2014,** 6, 431-58.

6. Kiess, A. P.; Minn, I.; Chen, Y.; Hobbs, R.; Sgouros, G.; Mease, R. C.; Pullambhatla, M.; Shen, C. J.; Foss, C. A.; Pomper, M. G. Auger Radiopharmaceutical Therapy Targeting Prostate-Specific Membrane Antigen. *J. Nucl. Med.* **2015,** 56, 1401-1407.

7. Qaim, S.; Scholten, B.; Neumaier, B. New developments in the production of theranostic pairs of radionuclides. *J. Radioanal. Nucl. Chem.* **2018,** 318.

8. Rahmim, A.; Zaidi, H. PET versus SPECT: strengths, limitations and challenges. *Nucl. Med. Commun.* **2008,** 29, 193-207.

9. Ametamey, S. M.; Honer, M.; Schubiger, P. A. Molecular Imaging with PET. *Chem. Rev.* **2008,** 108, 1501-1516.

10. Valk, P. E. Positron emission tomography clinical practice. In Springer: London, 2006.

11. Smith, S. V.; Jones, M.; Holmes, V. *Production and Selection of Metal PET Radioisotopes for Molecular Imaging*. IntechOpen: 2011.

12. Frangos, S.; Buscombe, J. R. Why should we be concerned about a “g”? *Eur. J. Nucl. Med. Mol. Imaging* **2019,** 46, 519-519.

13. Savvas, F.; Evanthia, G.; John, B.; Ioannis, I. Theragnostics: A Neologism That Generates Schism—The Hellenic Thesis. *J. Nucl. Med.* **2021,** 62, 880.

14. Hertz, S.; Roberts, A.; Evans, R. D. Radioactive Iodine as an Indicator in the Study of Thyroid Physiology. *Proc. Soc. Exp. Biol. Med.* **1938,** 38, 510-513.

15. Hertz, S.; Roberts, A. Application of radioactive iodine in therapy of Graves' disease. *J. Clin. Investig.* **1942,** 21.

16. Seidlin, S. M.; Marinelli, L. D.; Oshry, E. RADIOACTIVE IODINE THERAPY: Effect on Functioning Metastases of Adenocarcinoma of the Thyroid. *JAMA* **1946,** 132, 838-847.

17. Bodei, L.; Herrmann, K.; Schöder, H.; Scott, A. M.; Lewis, J. S. Radiotheranostics in oncology: current challenges and emerging opportunities. *Nat. Rev. Clin. Oncol.* **2022,** 19, 534-550.

18. Hengartner, M. O. The biochemistry of apoptosis. *Nature* **2000,** 407, 770-6.

19. Kaufmann, S. H.; Earnshaw, W. C. Induction of apoptosis by cancer chemotherapy. *Exp. Cell Res.* **2000,** 256, 42-9.

20. Kaina, B. DNA damage-triggered apoptosis: critical role of DNA repair, double-strand breaks, cell proliferation and signaling. *Biochem. Pharmacol.* **2003,** 66, 1547-54.

21. Kassis, A. I. Therapeutic radionuclides: biophysical and radiobiologic principles. *Semin. Nucl. Med.* **2008,** 38, 358-66.

22. Dowd, S. B.; Tilson, E. R. *Practical radiation protection and applied radiobiology*. 2nd ed.; W.B. Saunders: Philadelphia, 1999; p xvi, 352 p.

23. Pouget, J. P.; Lozza, C.; Deshayes, E.; Boudousq, V.; Navarro-Teulon, I. Introduction to radiobiology of targeted radionuclide therapy. *Front. Med.* **2015,** 2, 12.

24. Nias, A. H. W. *An introduction to radiobiology*. Wiley: Chichester ; New York, 1990; p ix, 346 p.

25. Bolus, N. E. Basic Review of Radiation Biology and Terminology. *J. Nucl. Med. Technol.* **2017,** 45, 259-264.

26. Adumeau, P.; Vivier, D.; Sharma, S. K.; Wang, J.; Zhang, T.; Chen, A.; Agnew, B. J.; Zeglis, B. M. A Site-Specifically Modified Imaging-Enabled Antibody-Drug Conjugate for Therapy and ImmunoPET. *Mol. Pharm.* **2018**.

27. Kassis, A. I.; Harris, C. R.; Adelstein, S. J.; Ruth, T. J.; Lambrecht, R.; Wolf, A. P. The in vitro radiobiology of astatine-211 decay. *Radiat. Res.* **1986,** 105, 27-36.

28. Charlton, D. E.; Kassis, A. I.; Adelstein, S. J. A comparison of experimental and calculated survival curves for V79 cells grown as monolayers or in suspension exposed to alpha irradiation from ^{212}Bi distributed in the growth medium. *Radiat. Prot. Dosimetry* **1994,** 52, 311-315.

29. Chan, P. C.; Lisco, E.; Lisco, H.; Adelstein, S. J. The radiotoxicity of iodine-125 in mammalian cells II. A comparative study on cell survival and cytogenetic responses to 125IUdR, 131TUdR, and 3HTdR. *Radiat. Res.* **1976,** 67, 332-43.

30. Haberkorn, U.; Giesel, F.; Morgenstern, A.; Kratochwil, C. The Future of Radioligand Therapy: α, β, or Both? *J. Nucl. Med.* **2017,** 58, 1017.

31. Frühwald, M. C.; O'Dorisio, M. S.; Pietsch, T.; Reubi, J. C. High Expression of Somatostatin Receptor Subtype 2 (sst2) in Medulloblastoma: Implications for Diagnosis and Therapy. *Pediatr. Res.* **1999,** 45, 697-708.

32. Patel, Y. C. Somatostatin and its receptor family. *Front. Neuroendocrinol.* **1999,** 20, 157-98.

33. Moertel, C. L.; Reubi, J. C.; Scheithauer, B. S.; Schaid, D. J.; Kvols, L. K. Expression of somatostatin receptors in childhood neuroblastoma. *Am. J. Clin. Pathol.* **1994,** 102, 752-6.

34. Weckbecker, G.; Lewis, I.; Albert, R.; Schmid, H. A.; Hoyer, D.; Bruns, C. Opportunities in somatostatin research: biological, chemical and therapeutic aspects. *Nat. Rev. Drug. Discov.* **2003,** 2, 999-1017.

35. Hocart, S. J.; Jain, R.; Murphy, W. A.; Taylor, J. E.; Coy, D. H. Highly potent cyclic disulfide antagonists of somatostatin. *J. Med. Chem.* **1999,** 42, 1863-71.

36. Bass, R. T.; Buckwalter, B. L.; Patel, B. P.; Pausch, M. H.; Price, L. A.; Strnad, J.; Hadcock, J. R. Identification and characterization of novel somatostatin antagonists. *Mol. Pharmacol.* **1996,** 50, 709-15.

37. Fani, M.; Nicolas, G. P.; Wild, D. Somatostatin Receptor Antagonists for Imaging and Therapy. *J. Nucl. Med.* **2017,** 58, 61s-66s.

38. De Jong, M.; Breeman, W. A.; Kwekkeboom, D. J.; Valkema, R.; Krenning, E. P. Tumor imaging and therapy using radiolabeled somatostatin analogues. *Acc. Chem. Res.* **2009,** 42, 873-80.

39. Bakker, W. H.; Albert, R.; Bruns, C.; Breeman, W. A.; Hofland, L. J.; Marbach, P.; Pless, J.; Pralet, D.; Stolz, B.; Koper, J. W.; et al. [^{111}In-DTPA-D-Phe1]-octreotide, a potential radiopharmaceutical for imaging of somatostatin receptor-positive tumors: synthesis, radiolabeling and in vitro validation. *Life Sci* **1991,** 49, 1583-91.

40. Anderson, C. J.; Pajeau, T. S.; Edwards, W. B.; Sherman, E. L.; Rogers, B. E.; Welch, M. J. In vitro and in vivo evaluation of copper-64-octreotide conjugates. *J. Nucl. Med.* **1995,** 36, 2315-25.

41. Lewis, J. S.; Lewis, M. R.; Cutler, P. D.; Srinivasan, A.; Schmidt, M. A.; Schwarz, S. W.; Morris, M. M.; Miller, J. P.; Anderson, C. J. Radiotherapy and dosimetry of ^{64}Cu-TETA-Tyr3-octreotate in a somatostatin receptor-positive, tumor-bearing rat model. *Clin Cancer Res* **1999,** 5, 3608-16.

42. Sprague, J. E.; Peng, Y.; Sun, X.; Weisman, G. R.; Wong, E. H.; Achilefu, S.; Anderson, C. J. Preparation and Biological Evaluation of Copper-64–Labeled Tyr3-Octreotate Using a Cross-Bridged Macrocyclic Chelator. *Clin. Cancer. Res.* **2004,** 10, 8674.

43. Maecke, H. R.; Riesen, A.; Ritter, W. The molecular structure of indium-DTPA. *J. Nucl. Med.* **1989,** 30, 1235-9.

44. Kostelnik, T. I.; Orvig, C. Radioactive Main Group and Rare Earth Metals for Imaging and Therapy. *Chem. Rev.* **2019,** 119, 902-956.

45. De Jong, M.; Valkema, R.; Jamar, F.; Kvols, L. K.; Kwekkeboom, D. J.; Breeman, W. A.; Bakker, W. H.; Smith, C.; Pauwels, S.; Krenning, E. P. Somatostatin receptor-targeted radionuclide therapy of tumors: preclinical and clinical findings. *Semin. Nucl. Med.* **2002,** 32, 133-40.

46. Anthony, L. B.; Woltering, E. A.; Espenan, G. D.; Cronin, M. D.; Maloney, T. J.; McCarthy, K. E. Indium-111-pentetreotide prolongs survival in gastroenteropancreatic malignancies. *Semin. Nucl. Med.* **2002,** 32, 123-32.

47. Valkema, R.; De Jong, M.; Bakker, W. H.; Breeman, W. A.; Kooij, P. P.; Lugtenburg, P. J.; De Jong, F. H.; Christiansen, A.; Kam, B. L.; De Herder, W. W.; Stridsberg, M.; Lindemans, J.; Ensing, G.; Krenning, E. P. Phase I study of peptide receptor radionuclide therapy with [In-DTPA]octreotide: the Rotterdam experience. *Semin. Nucl. Med.* **2002,** 32, 110-22.

48. L'Annunziata, M. F. Chapter 2 - Beta Radiation. In *Radioactivity*, L'Annunziata, M. F., Ed. Elsevier Science B.V.: Amsterdam, 2007; pp 119-140.

49. Chakravarty, R.; Dash, A.; Pillai, M. R. Availability of yttrium-90 from strontium-90: a nuclear medicine perspective. *Cancer Biother. Radiopharm.* **2012,** 27, 621-41.

50. Montaña, R. L.; González, I. H.; Ramirez, A. A.; Garaboldi, L.; Chinol, M. Yttrium-90 -- current status, expected availability and applications of a high beta energy emitter. *Curr. Radiopharm.* **2012,** 5, 253-63.

51. Imhof, A.; Brunner, P.; Marincek, N.; Briel, M.; Schindler, C.; Rasch, H.; Mäcke, H. R.; Rochlitz, C.; Müller-Brand, J.; Walter, M. A. Response, survival, and long-term toxicity after therapy with the radiolabeled somatostatin analogue [^{90}Y-DOTA]-TOC in metastasized neuroendocrine cancers. *J Clin Oncol* **2011,** 29, 2416-23.

52. Melis, M.; Krenning, E. P.; Bernard, B. F.; Barone, R.; Visser, T. J.; de Jong, M. Localisation and mechanism of renal retention of radiolabelled somatostatin analogues. *Eur. J. Nucl. Med. Mol. Imaging* **2005,** 32, 1136-43.

53. Behr, T. M.; Goldenberg, D. M.; Becker, W. Reducing the renal uptake of radiolabeled antibody fragments and peptides for diagnosis and therapy: present status, future prospects and limitations. *Eur. J. Nucl. Med.* **1998,** 25, 201-12.

54. Delpassand, E. S.; Tworowska, I.; Esfandiari, R.; Torgue, J.; Hurt, J.; Shafie, A.; Núñez, R. Targeted α-Emitter Therapy with ^{212}Pb-DOTAMTATE for the Treatment of Metastatic SSTR-Expressing Neuroendocrine Tumors: First-in-Humans Dose-Escalation Clinical Trial. *J. Nucl. Med.* **2022,** 63, 1326.

55. Shah, M. H.; Goldner, W. S.; Halfdanarson, T. R.; Bergsland, E.; Berlin, J. D.; Halperin, D.; Chan, J.; Kulke, M. H.; Benson, A. B.; Blaszkowsky, L. S.; Eads, J.; Engstrom, P. F.; Fanta, P.; Giordano, T.; He, J.; Heslin, M. J.; Kalemkerian, G. P.; Kandeel, F.; Khan, S. A.; Kidwai, W. Z.; Kunz, P. L.; Kuvshinoff, B. W.; Lieu, C.; Pillarisetty, V. G.; Saltz, L.; Sosa, J. A.; Strosberg, J. R.; Sussman, C. A.; Trikalinos, N. A.; Uboha, N. A.; Whisenant, J.; Wong, T.; Yao, J. C.; Burns, J. L.; Ogba, N.; Zuccarino-Catania, G. NCCN Guidelines Insights: Neuroendocrine and Adrenal Tumors, Version 2.2018. *J Natl Compr Canc Netw* **2018,** 16, 693-702.

56. Rolleman, E. J.; Valkema, R.; de Jong, M.; Kooij, P. P.; Krenning, E. P. Safe and effective inhibition of renal uptake of radiolabelled octreotide by a combination of lysine and arginine. *Eur. J. Nucl. Med. Mol. Imaging.* **2003,** 30, 9-15.

57. Bergsma, H.; Konijnenberg, M. W.; van der Zwan, W. A.; Kam, B. L.; Teunissen, J. J.; Kooij, P. P.; Mauff, K. A.; Krenning, E. P.; Kwekkeboom, D. J. Nephrotoxicity after PRRT with ^{177}Lu-DOTA-octreotate. *Eur. J. Nucl. Med. Mol. Imaging.* **2016,** 43, 1802-11.

58. Bodei, L.; Kidd, M.; Paganelli, G.; Grana, C. M.; Drozdov, I.; Cremonesi, M.; Lepensky, C.; Kwekkeboom, D. J.; Baum, R. P.; Krenning, E. P.; Modlin, I. M. Long-term tolerability of PRRT in 807 patients with neuroendocrine tumours: the value and limitations of clinical factors. *Eur. J. Nucl. Med. Mol. Imaging* **2015,** 42, 5-19.

59. Velikyan, I. Continued rapid growth in ^{68}Ga applications: update 2013 to June 2014. *J. Label. Compd. Radiopharm.* **2015,** 58, 99-121.

60. Heppeler, A.; André, J. P.; Buschmann, I.; Wang, X.; Reubi, J.-C.; Hennig, M.; Kaden, T. A.; Maecke, H. R. Metal-Ion-Dependent Biological Properties of a Chelator-Derived Somatostatin Analogue for Tumour Targeting. *Eur. J. Chem.* **2008,** 14, 3026-3034.

61. Aime, S.; Barge, A.; Botta, M.; Fasano, M.; Danilo Ayala, J.; Bombieri, G. Crystal structure and solution dynamics of the lutetium(III) chelate of DOTA. *Inorganica Chim. Acta* **1996,** 246, 423-429.

62. Heppeler, A.; Froidevaux, S.; Mäcke, H. R.; Jermann, E.; Béhé, M.; Powell, P.; Hennig, M. Radiometal-Labelled Macrocyclic Chelator-Derivatised Somatostatin Analogue with Superb Tumour-Targeting Properties and Potential for Receptor-Mediated Internal Radiotherapy. *Eur. J. Chem.* **1999,** 5, 1974-1981.

63. Lewis, J. S.; Lewis, M. R.; Srinivasan, A.; Schmidt, M. A.; Wang, J.; Anderson, C. J. Comparison of Four ^{64}Cu-Labeled Somatostatin Analogues in Vitro and in a Tumor-Bearing Rat Model: Evaluation of New Derivatives for Positron Emission Tomography Imaging and Targeted Radiotherapy. *J. Nucl. Med.* **1999,** 42, 1341-1347.

64. Hicks, R. J. Use of molecular targeted agents for the diagnosis, staging and therapy of neuroendocrine malignancy. *Cancer Imaging* **2010,** 10 Spec no A, S83-S91.

65. Henze, M.; Dimitrakopoulou-Strauss, A.; Milker-Zabel, S.; Schuhmacher, J.; Strauss, L. G.; Doll, J.; Mäcke, H. R.; Eisenhut, M.; Debus, J.; Haberkorn, U. Characterization of ^{68}Ga-DOTA-D-Phe1-Tyr3-octreotide kinetics in patients with meningiomas. *J. Nucl. Med.* **2005,** 46, 763-769.

66. Hofman, M. S.; Kong, G.; Neels, O. C.; Eu, P.; Hong, E.; Hicks, R. J. High management impact of Ga-68 DOTATATE (GaTate) PET/CT for imaging neuroendocrine and other somatostatin expressing tumours. *J. Med. Imaging. Radiat. Oncol.* **2012,** 56, 40-7.

67. Kong, G.; Hofman, M. S.; Murray, W. K.; Wilson, S.; Wood, P.; Downie, P.; Super, L.; Hogg, A.; Eu, P.; Hicks, R. J. Initial Experience With Gallium-68 DOTA-Octreotate PET/CT and Peptide Receptor Radionuclide Therapy for Pediatric Patients With Refractory Metastatic Neuroblastoma. *J. Pediatr. Hematol. Oncol.* **2016,** 38.

68. Strosberg, J.; El-Haddad, G.; Wolin, E.; Hendifar, A.; Yao, J.; Chasen, B.; Mittra, E.; Kunz, P. L.; Kulke, M. H.; Jacene, H.; Bushnell, D.; O'Dorisio, T. M.; Baum, R. P.; Kulkarni, H. R.; Caplin, M.; Lebtahi, R.; Hobday, T.; Delpassand, E.; Van Cutsem, E.; Benson, A.; Srirajaskanthan, R.; Pavel, M.; Mora, J.; Berlin, J.; Grande, E.; Reed, N.; Seregni, E.; Öberg, K.; Lopera Sierra, M.; Santoro, P.; Thevenet, T.; Erion, J. L.; Ruszniewski, P.; Kwekkeboom, D.; Krenning, E. Phase 3 Trial of ^{177}Lu-Dotatate for Midgut Neuroendocrine Tumors. *N. Engl. J. Med.* **2017,** 376, 125-135.

69. Hofman, M. S.; Lau, W. F. E.; Hicks, R. J. Somatostatin Receptor Imaging with ^{68}Ga DOTATATE PET/CT: Clinical Utility, Normal Patterns, Pearls, and Pitfalls in Interpretation. *RadioGraphics* **2015,** 35, 500-516.

70. Kwekkeboom, D. J.; Teunissen, J. J.; Bakker, W. H.; Kooij, P. P.; de Herder, W. W.; Feelders, R. A.; van Eijck, C. H.; Esser, J.-P.; Kam, B. L.; Krenning, E. P. Radiolabeled

Somatostatin Analog [^{177}Lu-DOTA0,Tyr3]Octreotate in Patients With Endocrine Gastroenteropancreatic Tumors. *J. Clin. Oncol.* **2005,** 23, 2754-2762.

71. Valkema, R.; Pauwels, S.; Kvols, L. K.; Barone, R.; Jamar, F.; Bakker, W. H.; Kwekkeboom, D. J.; Bouterfa, H.; Krenning, E. P. Survival and Response After Peptide Receptor Radionuclide Therapy With [^{90}Y-DOTA0,Tyr3]Octreotide in Patients With Advanced Gastroenteropancreatic Neuroendocrine Tumors. *Semin. Nucl. Med.* **2006,** 36, 147-156.

72. Sabet, A.; Ezziddin, K.; Pape, U.-F.; Reichman, K.; Haslerud, T.; Ahmadzadehfar, H.; Biersack, H.-J.; Nagarajah, J.; Ezziddin, S. Accurate assessment of long-term nephrotoxicity after peptide receptor radionuclide therapy with 177Lu-octreotate. *Eur. J. Nucl. Med. Mol. Imaging.* **2014,** 41, 505-510.

73. Beauregard, J.-M.; Hofman, M. S.; Kong, G.; Hicks, R. J. The tumour sink effect on the biodistribution of ^{68}Ga-DOTA-octreotate: implications for peptide receptor radionuclide therapy. *Eur. J. Nucl. Med. Mol. Imaging* **2012,** 39, 50-56.

74. Deppen, S. A.; Blume, J.; Bobbey, A. J.; Shah, C.; Graham, M. M.; Lee, P.; Delbeke, D.; Walker, R. C. ^{68}Ga-DOTATATE compared with ^{111}In-DTPA-octreotide and conventional imaging for pulmonary and gastroenteropancreatic neuroendocrine tumors: a systematic review and meta-analysis. *J. Nucl. Med.* **2016,** 57, 872-878.

75. Hennrich, U.; Benešová, M. [^{68}Ga]Ga-DOTA-TOC: The First FDA-Approved ^{68}Ga-Radiopharmaceutical for PET Imaging. *Pharmaceuticals* **2020,** 13.

76. Kashyap, R.; Hofman, M. S.; Michael, M.; Kong, G.; Akhurst, T.; Eu, P.; Zannino, D.; Hicks, R. J. Favourable outcomes of ^{177}Lu-octreotate peptide receptor chemoradionuclide therapy in patients with FDG-avid neuroendocrine tumours. *Eur. J. Nucl. Med. Mol. Imaging* **2015,** 42, 176-185.

77. Kong, G.; Hicks, R. J. Peptide Receptor Radiotherapy: Current Approaches and Future Directions. *Curr. Treat. Options Oncol.* **2019,** 20, 77.

78. Kong, G.; Grozinsky-Glasberg, S.; Hofman, M. S.; Akhurst, T.; Meirovitz, A.; Maimon, O.; Krausz, Y.; Godefroy, J.; Michael, M.; Gross, D. J.; Hicks, R. J. Highly favourable outcomes with peptide receptor radionuclide therapy (PRRT) for metastatic rectal neuroendocrine neoplasia (NEN). *Eur. J. Nucl. Med. Mol. Imaging* **2019,** 46, 718-727.

79. Lapidus, R. G.; Tiffany, C. W.; Isaacs, J. T.; Slusher, B. S. Prostate-specific membrane antigen (PSMA) enzyme activity is elevated in prostate cancer cells. *Prostate* **2000,** 45, 350-4.

80. Kratochwil, C.; Afshar-Oromieh, A.; Kopka, K.; Haberkorn, U.; Giesel, F. L. Current Status of Prostate-Specific Membrane Antigen Targeting in Nuclear Medicine: Clinical

Translation of Chelator Containing Prostate-Specific Membrane Antigen Ligands Into Diagnostics and Therapy for Prostate Cancer. *Semin. Nucl. Med.* **2016,** 46, 405-418.

81. Israeli, R. S.; Powell, C. T.; Fair, W. R.; Heston, W. D. Molecular cloning of a complementary DNA encoding a prostate-specific membrane antigen. *Cancer. Res.* **1993,** 53, 227-30.

82. Fair, W. R.; Israeli, R. S.; Heston, W. D. Prostate-specific membrane antigen. *Prostate* **1997,** 32, 140-8.

83. Davis, M. I.; Bennett, M. J.; Thomas, L. M.; Bjorkman, P. J. Crystal structure of prostate-specific membrane antigen, a tumor marker and peptidase. *Proc. Natl. Acad. Sci. U. S. A.* **2005,** 102, 5981-6.

84. Jackson, P. F.; Cole, D. C.; Slusher, B. S.; Stetz, S. L.; Ross, L. E.; Donzanti, B. A.; Trainor, D. A. Design, synthesis, and biological activity of a potent inhibitor of the neuropeptidase N-acetylated alpha-linked acidic dipeptidase. *J. Med. Chem.* **1996,** 39, 619-22.

85. Foss, C. A.; Mease, R. C.; Fan, H.; Wang, Y.; Ravert, H. T.; Dannals, R. F.; Olszewski, R. T.; Heston, W. D.; Kozikowski, A. P.; Pomper, M. G. Radiolabeled Small-Molecule Ligands for Prostate-Specific Membrane Antigen: In vivo Imaging in Experimental Models of Prostate Cancer. *Clin. Cancer. Res.* **2005,** 11, 4022-4028.

86. Kozikowski, A. P.; Nan, F.; Conti, P.; Zhang, J.; Ramadan, E.; Bzdega, T.; Wroblewska, B.; Neale, J. H.; Pshenichkin, S.; Wroblewski, J. T. Design of Remarkably Simple, Yet Potent Urea-Based Inhibitors of Glutamate Carboxypeptidase II (NAALADase). *J. Med. Chem.* **2001,** 44, 298-301.

87. Afshar-Oromieh, A.; Babich, J. W.; Kratochwil, C.; Giesel, F. L.; Eisenhut, M.; Kopka, K.; Haberkorn, U. The Rise of PSMA Ligands for Diagnosis and Therapy of Prostate Cancer. *J. Nucl. Med.* **2016,** 57, 79s-89s.

88. Lütje, S.; Heskamp, S.; Cornelissen, A. S.; Poeppel, T. D.; van den Broek, S. A.; Rosenbaum-Krumme, S.; Bockisch, A.; Gotthardt, M.; Rijpkema, M.; Boerman, O. C. PSMA Ligands for Radionuclide Imaging and Therapy of Prostate Cancer: Clinical Status. *Theranostics* **2015,** 5, 1388-401.

89. Kopka, K.; Benešová, M.; Bařinka, C.; Haberkorn, U.; Babich, J. Glu-Ureido-Based Inhibitors of Prostate-Specific Membrane Antigen: Lessons Learned During the Development of a Novel Class of Low-Molecular-Weight Theranostic Radiotracers. *J. Nucl. Med.* **2017,** 58, 17s-26s.

90. Afshar-Oromieh, A.; Haberkorn, U.; Eder, M.; Eisenhut, M.; Zechmann, C. M. [68Ga]Gallium-labelled PSMA ligand as superior PET tracer for the diagnosis of prostate cancer: comparison with ^{18}F-FECH. *Eur. J. Nucl. Med. Mol. Imaging* **2012,** 39, 1085-6.

91. Eplattenier, F. L.; Murase, I.; Martell, A. E. New Multidentate Ligands. VI. Chelating Tendencies of N,N′-Di(2-hydroxybenzyl)ethylenediamine-N,N′-diacetic Acid. *J. Am. Chem. Soc.* **1967,** 89, 837-843.

92. Larsen, S. K.; Jenkins, B. G.; Memon, N. G.; Lauffer, R. B. Structure-affinity relationships in the binding of unsubstituted iron phenolate complexes to human serum albumin. Molecular structure of iron(III) N, N'-bis(2-hydroxybenzyl)ethylenediamine-N,N'-diacetate. *Inorg. Chem.* **1990,** 29, 1147-1152.

93. Tsionou, M. I.; Knapp, C. E.; Foley, C. A.; Munteanu, C. R.; Cakebread, A.; Imberti, C.; Eykyn, T. R.; Young, J. D.; Paterson, B. M.; Blower, P. J.; Ma, M. T. Comparison of macrocyclic and acyclic chelators for gallium-68 radiolabelling. *RSC Advances* **2017,** 7, 49586-49599.

94. Schuhmacher, J.; Klivényi, G.; Hull, W. E.; Matys, R.; Hauser, H.; Kalthoff, H.; Schmiegel, W. H.; Maier-Borst, W.; Matzku, S. A bifunctional HBED-derivative for labeling of antibodies with ^{67}Ga, ^{111}In and ^{59}Fe. Comparative biodistribution with ^{111}In-DPTA and ^{131}I-labeled antibodies in mice bearing antibody internalizing and non-internalizing tumors. *International Journal of Radiation Applications and Instrumentation. Part B. Nuclear Medicine and Biology* **1992,** 19, 809-824.

95. Eder, M.; Neels, O.; Müller, M.; Bauder-Wüst, U.; Remde, Y.; Schäfer, M.; Hennrich, U.; Eisenhut, M.; Afshar-Oromieh, A.; Haberkorn, U.; Kopka, K. Novel Preclinical and Radiopharmaceutical Aspects of [^{68}Ga]Ga-PSMA-HBED-CC: A New PET Tracer for Imaging of Prostate Cancer. *Pharmaceuticals* **2014,** 7, 779-96.

96. Mume, E.; Asad, A.; Di Bartolo, N. M.; Kong, L.; Smith, C.; Sargeson, A. M.; Price, R.; Smith, S. V. Synthesis of hexa aza cages, SarAr-NCS and AmBaSar and a study of their metal complexation, conjugation to nanomaterials and proteins for application in radioimaging and therapy. *Dalton Trans.* **2013,** 42, 14402-14410.

97. Afshar-Oromieh, A.; Malcher, A.; Eder, M.; Eisenhut, M.; Linhart, H. G.; Hadaschik, B. A.; Holland-Letz, T.; Giesel, F. L.; Kratochwil, C.; Haufe, S.; Haberkorn, U.; Zechmann, C. M. PET imaging with a [^{68}Ga]gallium-labelled PSMA ligand for the diagnosis of prostate cancer: biodistribution in humans and first evaluation of tumour lesions. *Eur. J. Nucl. Med. Mol. Imaging.* **2013,** 40, 486-495.

98. Afshar-Oromieh, A.; Zechmann, C. M.; Malcher, A.; Eder, M.; Eisenhut, M.; Linhart, H. G.; Holland-Letz, T.; Hadaschik, B. A.; Giesel, F. L.; Debus, J.; Haberkorn, U. Comparison of PET imaging with a ^{68}Ga-labelled PSMA ligand and ^{18}F-choline-based PET/CT for the diagnosis of recurrent prostate cancer. *Eur. J. Nucl. Med. Mol. Imaging.* **2014,** 41, 11-20.

99. Hennrich, U.; Eder, M. [^{68}Ga]Ga-PSMA-11: The First FDA-Approved ^{68}Ga-Radiopharmaceutical for PET Imaging of Prostate Cancer. In *Pharmaceuticals*, 2021; Vol. 14.

100. Carlucci, G.; Ippisch, R.; Slavik, R.; Mishoe, A.; Blecha, J.; Zhu, S. ^{68}Ga-PSMA-11 NDA Approval: A Novel and Successful Academic Partnership. *J. Nucl. Med.* **2021,** 62, 149-155.

101. Jackson, J. A.; Hungnes, I. N.; Ma, M. T.; Rivas, C. Bioconjugates of Chelators with Peptides and Proteins in Nuclear Medicine: Historical Importance, Current Innovations, and Future Challenges. *Bioconjug. Chem.* **2020,** 31, 483-491.

102. Fallah, J.; Agrawal, S.; Gittleman, H.; Fiero, M. H.; Subramaniam, S.; John, C.; Chen, W.; Ricks, T. K.; Niu, G.; Fotenos, A.; Wang, M.; Chiang, K.; Pierce, W. F.; Suzman, D. L.; Tang, S.; Pazdur, R.; Amiri-Kordestani, L.; Ibrahim, A.; Kluetz, P. G. FDA Approval Summary: Lutetium Lu 177 Vipivotide Tetraxetan for Patients with Metastatic Castration-Resistant Prostate Cancer. *Clin. Cancer. Res.* **2023,** 29, 1651-1657.

103. Benešová, M.; Schäfer, M.; Bauder-Wüst, U.; Afshar-Oromieh, A.; Kratochwil, C.; Mier, W.; Haberkorn, U.; Kopka, K.; Eder, M. Preclinical Evaluation of a Tailor-Made DOTA-Conjugated PSMA Inhibitor with Optimized Linker Moiety for Imaging and Endoradiotherapy of Prostate Cancer. *J. Nucl. Med.* **2015,** 56, 914.

104. Benešová, M.; Bauder-Wüst, U.; Schäfer, M.; Klika, K. D.; Mier, W.; Haberkorn, U.; Kopka, K.; Eder, M. Linker Modification Strategies To Control the Prostate-Specific Membrane Antigen (PSMA)-Targeting and Pharmacokinetic Properties of DOTA-Conjugated PSMA Inhibitors. *J. Med. Chem.* **2016,** 59, 1761-1775.

105. Sartor, O.; de Bono, J.; Chi, K. N.; Fizazi, K.; Herrmann, K.; Rahbar, K.; Tagawa, S. T.; Nordquist, L. T.; Vaishampayan, N.; El-Haddad, G.; Park, C. H.; Beer, T. M.; Armour, A.; Pérez-Contreras, W. J.; DeSilvio, M.; Kpamegan, E.; Gericke, G.; Messmann, R. A.; Morris, M. J.; Krause, B. J. Lutetium-177-PSMA-617 for Metastatic Castration-Resistant Prostate Cancer. *N. Engl. J. Med.* **2021,** 385, 1091-1103.

106. Fendler, W. P.; Reinhardt, S.; Ilhan, H.; Delker, A.; Böning, G.; Gildehaus, F. J.; Stief, C.; Bartenstein, P.; Gratzke, C.; Lehner, S.; Rominger, A. Preliminary experience with dosimetry, response and patient reported outcome after ^{177}Lu-PSMA-617 therapy for metastatic castration-resistant prostate cancer. *Oncotarget* **2017,** 8, 3581-3590.

107. Violet, J.; Jackson, P.; Ferdinandus, J.; Sandhu, S.; Akhurst, T.; Iravani, A.; Kong, G.; Kumar, A. R.; Thang, S. P.; Eu, P.; Scalzo, M.; Murphy, D.; Williams, S.; Hicks, R. J.; Hofman, M. S. Dosimetry of ^{177}Lu-PSMA-617 in Metastatic Castration-Resistant Prostate Cancer: Correlations Between Pretherapeutic Imaging and Whole-Body Tumor Dosimetry with Treatment Outcomes. *J. Nucl. Med.* **2019,** 60, 517.

108. Hofman, M. S.; Violet, J.; Hicks, R. J.; Ferdinandus, J.; Ping Thang, S.; Akhurst, T.; Iravani, A.; Kong, G.; Ravi Kumar, A.; Murphy, D. G.; Eu, P.; Jackson, P.; Scalzo, M.; Williams, S. G.; Sandhu, S. [^{177}Lu]-PSMA-617 radionuclide treatment in patients with metastatic castration-resistant prostate cancer (LuPSMA trial): a single-centre, single-arm, phase 2 study. *Lancet Oncol.* **2018,** 19, 825-833.

109. Hennrich, U.; Eder, M. [^{177}Lu]Lu-PSMA-617 (Pluvicto(TM)): The First FDA-Approved Radiotherapeutical for Treatment of Prostate Cancer. *Pharmaceuticals* **2022,** 15.

110. Wong, C. H.; Siah, K. W.; Lo, A. W. Estimation of clinical trial success rates and related parameters. *Biostatistics* **2019,** 20, 273-286.

111. Kirby, H. W. The Discovery of Actinium. *Isis* **1971,** 62, 290-308.

112. Ferrier, M. G.; Batista, E. R.; Berg, J. M.; Birnbaum, E. R.; Cross, J. N.; Engle, J. W.; La Pierre, H. S.; Kozimor, S. A.; Lezama Pacheco, J. S.; Stein, B. W.; Stieber, S. C.; Wilson, J. J. Spectroscopic and computational investigation of actinium coordination chemistry. *Nat. Commun.* **2016,** 7, 12312.

113. Fried, S.; Hagemann, F.; Zachariasen, W. H. The Preparation and Identification of Some Pure Actinium Compounds1. *J. Am. Chem. Soc.* **1950,** 72, 771-775.

114. Farr, J. D.; Giorgi, A. L.; Bowman, M. G.; Money, R. K. The crystal structure of actinium metal and actinium hydride. *J. Inorg. Nucl. Chem.* **1961,** 18, 42-47.

115. Weigel, F.; Hauske, H. The lattice constants of actinium(III) oxalate deca-hydrate. *J Less-Common Met.* **1977,** 55, 243-247.

116. Teo, B. K. EXAFS: Basic Principles and Data Analysis. In *Inorganic Chemistry Concepts*, Springer Berlin Heidelberg,: Berlin, Heidelberg, 1986; pp 1 online resource (xviii, 349 pages).

117. Hummer, A. A.; Rompel, A. The use of X-ray absorption and synchrotron based micro-X-ray fluorescence spectroscopy to investigate anti-cancer metal compounds in vivo and in vitro. *Metallomics* **2013,** 5, 597-614.

118. McCleverty, J. A.; Meyer, T. *Comprehensive coordination chemistry. 2, From biology to nanotechnology*. Elsevier: 2003; Vol. 2, p 10 volumes (8000 pages).

119. Stor, J. NEXAFS Spectroscopy. In *Springer Ser. Surf. Sci.*, Springer Berlin Heidelberg,: Berlin, Heidelberg, 1992; pp 1 online resource (xv, 403 pages).

120. Ferrier, M. G.; Stein, B. W.; Batista, E. R.; Berg, J. M.; Birnbaum, E. R.; Engle, J. W.; John, K. D.; Kozimor, S. A.; Lezama Pacheco, J. S.; Redman, L. N. Synthesis and Characterization of the Actinium Aquo Ion. *ACS. Cent. Sci.* **2017,** 3, 176-185.

121. Thierer, L. M.; Tomson, N. C. The Actinium Aqua Ion: A Century in the Making. *ACS. Cent. Sci.* **2017,** 3, 153-155.

122. Morss, L. R.; Edelstein, N. M.; Fuger, J.; Katz, J. J. The chemistry of the actinide and transactinide elements. In 3rd ed.; Springer,: Dordrecht, 2006; pp 1 online resource (5 v. (xvii, 3474, 157 p.)).

123. Apostolidis, C.; Molinet, R.; Rasmussen, G.; Morgenstern, A. Production of Ac-225 from Th-229 for targeted alpha therapy. *Anal. Chem.* **2005,** 77, 6288-91.

124. Zielinska, B.; Apostolidis, C.; Bruchertseifer, F.; Morgenstern, A. An Improved Method for the Production of Ac-225/Bi-213 from Th-229 for Targeted Alpha Therapy. *Solvent Extr. Ion Exch.* **2007,** 25, 339-349.

125. Robertson, A. K. H.; Ramogida, C. F.; Schaffer, P.; Radchenko, V. Development of ^{225}Ac Radiopharmaceuticals: TRIUMF Perspectives and Experiences. *Curr. Radiopharm.* **2018,** 11, 156-172.

126. Engle, W. J. The Production of Ac-225. *Curr. Radiopharm.* **2018,** 11, 173-179.

127. Apostolidis, C.; Molinet, R.; McGinley, J.; Abbas, K.; Möllenbeck, J.; Morgenstern, A. Cyclotron production of Ac-225 for targeted alpha therapy. *Appl. Radiat. Isot.* **2005,** 62, 383-387.

128. Robertson, A. K. H.; McNeil, B. L.; Yang, H.; Gendron, D.; Perron, R.; Radchenko, V.; Zeisler, S.; Causey, P.; Schaffer, P. ^{232}Th-Spallation-Produced ^{225}Ac with Reduced ^{227}Ac Content. *Inorg. Chem.* **2020,** 59, 12156-12165.

129. Kelly, J. M.; Amor-Coarasa, A.; Sweeney, E.; Wilson, J. J.; Causey, P. W.; Babich, J. W. A suitable time point for quantifying the radiochemical purity of ^{225}Ac-labeled radiopharmaceuticals. *EJNMMI Radiopharm. Chem.* **2021,** 6, 38.

130. Luo, Y.-R. *Comprehensive handbook of chemical bond energies*. CRC Press: Boca Raton, 2007; p 1655 p.

131. De Kruijff, R. M.; Wolterbeek, H. T.; Denkova, A. G. A Critical Review of Alpha Radionuclide Therapy—How to Deal with Recoiling Daughters? In *Pharmaceuticals*, 2015; Vol. 8, pp 321-336.

132. Roscher, M.; Bakos, G.; Benešová, M. Atomic Nanogenerators in Targeted Alpha Therapies: Curie's Legacy in Modern Cancer Management. In *Pharmaceuticals*, 2020; Vol. 13.

133. Khabibullin, A. R.; Karolak, A.; Budzevich, M. M.; McLaughlin, M. L.; Morse, D. L.; Woods, L. M. Structure and properties of DOTA-chelated radiopharmaceuticals within the ^{225}Ac decay pathway. *Medchemcomm* **2018,** 9, 1155-1163.

134. Whitmire, K. H. Bismuth: Inorganic Chemistry. In *Encyclopedia of Inorganic and Bioinorganic Chemistry*, 2014; pp 1-32.

135. Rahbar, K.; Ahmadzadehfar, H.; Kratochwil, C.; Haberkorn, U.; Schäfers, M.; Essler, M.; Baum, R. P.; Kulkarni, H. R.; Schmidt, M.; Drzezga, A.; Bartenstein, P.; Pfestroff, A.; Luster, M.; Lützen, U.; Marx, M.; Prasad, V.; Brenner, W.; Heinzel, A.; Mottaghy, F. M.; Ruf, J.; Meyer, P. T.; Heuschkel, M.; Eveslage, M.; Bögemann, M.; Fendler, W. P.; Krause, B. J. German Multicenter Study Investigating ^{177}Lu-PSMA-617 Radioligand Therapy in Advanced Prostate Cancer Patients. *J. Nucl. Med.* **2017,** 58, 85-90.

136. Delker, A.; Fendler, W. P.; Kratochwil, C.; Brunegraf, A.; Gosewisch, A.; Gildehaus, F. J.; Tritschler, S.; Stief, C. G.; Kopka, K.; Haberkorn, U.; Bartenstein, P.; Boning, G. Dosimetry for ^{177}Lu-DKFZ-PSMA-617: a new radiopharmaceutical for the treatment of metastatic prostate cancer. *Eur. J. Nucl. Med. Mol. Imaging.* **2016,** 43, 42-51.

137. Kratochwil, C.; Bruchertseifer, F.; Rathke, H.; Hohenfellner, M.; Giesel, F. L.; Haberkorn, U.; Morgenstern, A. Targeted alpha-Therapy of Metastatic Castration-Resistant Prostate Cancer with ^{225}Ac-PSMA-617: Swimmer-Plot Analysis Suggests Efficacy Regarding Duration of Tumor Control. *J. Nucl. Med.* **2018,** 59, 795-802.

138. Kelly, J. M.; Amor-Coarasa, A.; Ponnala, S.; Nikolopoulou, A.; Williams, C., Jr.; Thiele, N. A.; Schlyer, D.; Wilson, J. J.; DiMagno, S. G.; Babich, J. W. A Single Dose of ^{225}Ac-RPS-074 Induces a Complete Tumor Response in an LNCaP Xenograft Model. *J. Nucl. Med.* **2019,** 60, 649-655.

139. Morgenstern, A.; Apostolidis, C.; Kratochwil, C.; Sathekge, M.; Krolicki, L.; Bruchertseifer, F. An Overview of Targeted Alpha Therapy with ^{225}Actinium and ^{213}Bismuth. *Curr. Radiopharm.* **2018,** 11, 200-208.

140. Kratochwil, C.; Bruchertseifer, F.; Giesel, F. L.; Weis, M.; Verburg, F. A.; Mottaghy, F.; Kopka, K.; Apostolidis, C.; Haberkorn, U.; Morgenstern, A. ^{225}Ac-PSMA-617 for PSMA-Targeted alpha-Radiation Therapy of Metastatic Castration-Resistant Prostate Cancer. *J. Nucl. Med.* **2016,** 57, 1941-1944.

141. Sathekge, M.; Bruchertseifer, F.; Knoesen, O.; Reyneke, F.; Lawal, I.; Lengana, T.; Davis, C.; Mahapane, J.; Corbett, C.; Vorster, M.; Morgenstern, A. ^{225}Ac-PSMA-617 in chemotherapy-naive patients with advanced prostate cancer: a pilot study. *Eur. J. Nucl. Med. Mol. Imaging.* **2019,** 46, 129-138.

142. Langbein, T.; Chaussé, G.; Baum, R. P. Salivary Gland Toxicity of PSMA Radioligand Therapy: Relevance and Preventive Strategies. *J. Nucl. Med.* **2018,** 59, 1172-1173.

143. Pearson, R. G. Hard and Soft Acids and Bases. *J. Am. Chem. Soc.* **1963,** 85, 3533-3539.

144. Schaeffer, L. Chapter 14 - The Role of Functional Groups in Drug–Receptor Interactions. In *The Practice of Medicinal Chemistry (Fourth Edition)*, Wermuth, C. G.; Aldous, D.; Raboisson, P.; Rognan, D., Eds. Academic Press: San Diego, 2008; pp 359-378.

145. Thiele, N. A.; Wilson, J. J. Actinium-225 for Targeted alpha Therapy: Coordination Chemistry and Current Chelation Approaches. *Cancer Biother. Radiopharm.* **2018,** 33, 336-348.

146. Davis, I. A.; Glowienka, K. A.; Boll, R. A.; Deal, K. A.; Brechbiel, M. W.; Stabin, M.; Bochsler, P. N.; Mirzadeh, S.; Kennel, S. J. Comparison of ^{225}actinium chelates: tissue distribution and radiotoxicity. *Nucl. Med. Biol.* **1999,** 26, 581-589.

147. Xu, H.; Baidoo, K. E.; Wong, K. J.; Brechbiel, M. W. A novel bifunctional maleimido CHX-A" chelator for conjugation to thiol-containing biomolecules. *Bioorg. Med. Chem. Lett.* **2008,** 18, 2679-83.

148. Stein, B. W.; Morgenstern, A.; Batista, E. R.; Birnbaum, E. R.; Bone, S. E.; Cary, S. K.; Ferrier, M. G.; John, K. D.; Pacheco, J. L.; Kozimor, S. A.; Mocko, V.; Scott, B. L.; Yang, P. Advancing Chelation Chemistry for Actinium and Other +3 f-Elements, Am, Cm, and La. *J. Am. Chem. Soc.* **2019,** 141, 19404-19414.

149. Benetollo, F.; Bombieri, G.; Calabi, L.; Aime, S.; Botta, M. Structural Variations Across the Lanthanide Series of Macrocyclic DOTA Complexes: Insights into the Design of Contrast Agents for Magnetic Resonance Imaging. *Inorg. Chem.* **2003,** 42, 148-157.

150. Smith, R. M.; Martell, A. E. Critical stability constants: Second Supplement. In Springer, Ed. Plenum.: New York ; London, 1989; Vol. 6, p 643.

151. Borchardt, P. E.; Yuan, R. R.; Miederer, M.; McDevitt, M. R.; Scheinberg, D. A. Targeted actinium-225 in vivo generators for therapy of ovarian cancer. *Cancer. Res.* **2003,** 63, 5084-90.

152. Escorcia, F. E.; Henke, E.; McDevitt, M. R.; Villa, C. H.; Smith-Jones, P.; Blasberg, R. G.; Benezra, R.; Scheinberg, D. A. Selective killing of tumor neovasculature paradoxically improves chemotherapy delivery to tumors. *Cancer Res.* **2010,** 70, 9277-86.

153. Ballangrud, A. s. M.; Yang, W.-H.; Palm, S.; Enmon, R.; Borchardt, P. E.; Pellegrini, V. A.; McDevitt, M. R.; Scheinberg, D. A.; Sgouros, G. Alpha-Particle Emitting Atomic Generator (Actinium-225)-Labeled Trastuzumab (Herceptin) Targeting of Breast Cancer Spheroids: Efficacy versus HER2/neu Expression. *Clinical Cancer Research* **2004,** 10, 4489-4497.

154. Maguire, W. F.; McDevitt, M. R.; Smith-Jones, P. M.; Scheinberg, D. A. Efficient 1-step radiolabeling of monoclonal antibodies to high specific activity with ^{225}Ac for alpha-particle radioimmunotherapy of cancer. *J. Nucl. Med.* **2014,** 55, 1492-8.

155. Atallah, E. L.; Orozco, J. J.; Craig, M.; Levy, M. Y.; Finn, L. E.; Khan, S. S.; Perl, A. E.; Park, J. H.; Roboz, G. J.; Tse, W.; Begna, K. H.; Mawad, R.; Rizzieri, D. A.; Berger, M. S.; Jurcic, J. G. A Phase 2 Study of Actinium-225 (^{225}Ac)-Lintuzumab in Older Patients with Untreated Acute Myeloid Leukemia (AML) - Interim Analysis of 1.5 μci/Kg/Dose. *Blood* **2018,** 132, 1457.

156. Atallah, E.; Berger, M.; Jurcic, J.; Roboz, G.; Tse, W.; Mawad, R.; Rizzieri, D.; Begna, K.; Orozco, J.; Craig, M.; Yair Levy, M.; Finn, L.; Sharif, K.; Perl, A.; Park, J. A Phase 2 Study of Actinium-225 [^{225}Ac]-lintuzumab in Older Patients with Untreated Acute Myeloid Leukemia (AML). *J. Med. Imaging Radiat. Sci.* **2019,** 50, S37.

157. Rosenblat, T. L.; McDevitt, M. R.; Carrasquillo, J. A.; Pandit-Taskar, N.; Frattini, M. G.; Maslak, P. G.; Park, J. H.; Douer, D.; Cicic, D.; Larson, S. M.; Scheinberg, D. A.; Jurcic, J. G. Treatment of Patients with Acute Myeloid Leukemia with the Targeted Alpha-Particle Nanogenerator Actinium-225-Lintuzumab. *Clin. Cancer Res.* **2022,** 28, 2030-2037.

158. Tagawa, S. T.; Sun, M.; Sartor, A. O.; Thomas, C.; Singh, S.; Bissassar, M.; Fernandez, E.; Niaz, M. J.; Ho, B.; Vallabhajosula, S.; Babich, J.; Molina, A. M.; Sternberg, C. N.; Nanus, D. M.; Osborne, J.; Bander, N. H. Phase I study of ^{225}Ac-J591 for men with metastatic castration-resistant prostate cancer (mCRPC). *J. Clin. Oncol.* **2021,** 39, 5015-5015.

159. Roca-Sabio, A.; Mato-Iglesias, M.; Esteban-Gomez, D.; Toth, E.; de Blas, A.; Platas-Iglesias, C.; Rodriguez-Blas, T. Macrocyclic receptor exhibiting unprecedented selectivity for light lanthanides. *J. Am. Chem. Soc.* **2009,** 131, 3331-41.

160. Thiele, N. A.; Brown, V.; Kelly, J. M.; Amor-Coarasa, A.; Jermilova, U.; MacMillan, S. N.; Nikolopoulou, A.; Ponnala, S.; Ramogida, C. F.; Robertson, A. K. H.; Rodriguez-Rodriguez, C.; Schaffer, P.; Williams, C., Jr.; Babich, J. W.; Radchenko, V.; Wilson, J. J. An Eighteen-Membered Macrocyclic Ligand for Actinium-225 Targeted Alpha Therapy. *Angew. Chem., Int. Ed.* **2017,** 56, 14712-14717.

161. Hu, A.; Simms, M. E.; Kertesz, V.; Wilson, J. J.; Thiele, N. A. Chelating Rare-Earth Metals (Ln^{3+}) and $^{225}Ac^{3+}$ with the Dual-Size-Selective Macrocyclic Ligand Py2-Macrodipa. *Inorg. Chem.* **2022,** 61, 12847-12855.

162. Kadassery, K. J.; King, A. P.; Fayn, S.; Baidoo, K. E.; MacMillan, S. N.; Escorcia, F. E.; Wilson, J. J. H2BZmacropa-NCS: A Bifunctional Chelator for Actinium-225 Targeted Alpha Therapy. *Bioconjug. Chem.* **2022,** 33, 1222-1231.

163. Thiele, N. A.; Woods, J. J.; Wilson, J. J. Implementing f-Block Metal Ions in Medicine: Tuning the Size Selectivity of Expanded Macrocycles. *Inorg. Chem.* **2019,** 58, 10483-10500.

164. Hu, A.; MacMillan, S. N.; Wilson, J. J. Macrocyclic Ligands with an Unprecedented Size-Selectivity Pattern for the Lanthanide Ions. *J. Am. Chem. Soc.* **2020,** 142, 13500-13506.

165. Hu, A.; Brown, V.; MacMillan, S. N.; Radchenko, V.; Yang, H.; Wharton, L.; Ramogida, C. F.; Wilson, J. J. Chelating the Alpha Therapy Radionuclides $^{225}Ac^{3+}$ and $^{213}Bi^{3+}$ with 18-Membered Macrocyclic Ligands Macrodipa and Py-Macrodipa. *Inorg. Chem.* **2022,** 61, 801-806.

166. Hu, A.; Aluicio-Sarduy, E.; Brown, V.; MacMillan, S. N.; Becker, K. V.; Barnhart, T. E.; Radchenko, V.; Ramogida, C. F.; Engle, J. W.; Wilson, J. J. Py-Macrodipa: A Janus Chelator Capable of Binding Medicinally Relevant Rare-Earth Radiometals of Disparate Sizes. *J. Am. Chem. Soc.* **2021,** 143, 10429-10440.

167. Fiszbein, D. J.; Brown, V.; Thiele, N. A.; Woods, J. J.; Wharton, L.; MacMillan, S. N.; Radchenko, V.; Ramogida, C. F.; Wilson, J. J. Tuning the Kinetic Inertness of Bi^{3+} Complexes: The Impact of Donor Atoms on Diaza-18-Crown-6 Ligands as Chelators for ^{213}Bi Targeted Alpha Therapy. *Inorg. Chem.* **2021,** 60, 9199-9211.

168. Vosjan, M. J. W. D.; Perk, L. R.; Visser, G. W. M.; Budde, M.; Jurek, P.; Kiefer, G. E.; van Dongen, G. A. M. S. Conjugation and radiolabeling of monoclonal antibodies with zirconium-89 for PET imaging using the bifunctional chelate p-isothiocyanatobenzyl-desferrioxamine. *Nat. Protoc.* **2010,** 5, 739-743.

169. Hu, A.; Wilson, J. J. Advancing Chelation Strategies for Large Metal Ions for Nuclear Medicine Applications. *Acc. Chem. Res.* **2022,** 55, 904-915.

170. Gourni, E.; Del Pozzo, L.; Kheirallah, E.; Smerling, C.; Waser, B.; Reubi, J.-C.; Paterson, B. M.; Donnelly, P. S.; Meyer, P. T.; Maecke, H. R. Copper-64 Labeled Macrobicyclic Sarcophagine Coupled to a GRP Receptor Antagonist Shows Great Promise for PET Imaging of Prostate Cancer. *Mol. Pharm.* **2015,** 12, 2781-2790.

171. Plesner, B.; Fee, C. J.; Westh, P.; Nielsen, A. D. Effects of PEG size on structure, function and stability of PEGylated BSA. *Eur. J. Pharm. Biopharm.* **2011,** 79, 399-405.

172. Boros, E.; Holland, J. P. Chemical aspects of metal ion chelation in the synthesis and application antibody-based radiotracers. *J. Label. Compd. Radiopharm.* **2018,** 61, 652-671.

173. Guillou, A.; Earley, D. F.; Klingler, S.; Nisli, E.; Nüesch, L. J.; Fay, R.; Holland, J. P. The Influence of a Polyethylene Glycol Linker on the Metabolism and Pharmacokinetics of a ^{89}Zr-Radiolabeled Antibody. *Bioconjug. Chem.* **2021,** 32, 1263-1275.

174. Rudd, S. E.; Roselt, P.; Cullinane, C.; Hicks, R. J.; Donnelly, P. S. A desferrioxamine B squaramide ester for the incorporation of zirconium-89 into antibodies. *ChemComm* **2016,** 52, 11889-11892.

175. Storer, R. I.; Aciro, C.; Jones, L. H. Squaramides: physical properties, synthesis and applications. *Chem. Soc. Rev.* **2011,** 40, 2330-46.

176. Pauling, L. The nature of the chemical bond. Application of results obtained from the quantum mechanics and from a theory of paramagentic susceptibility to the structure of molecules. *J. Am. Chem. Soc.* **1931,** 53, 1367-1400.

177. Reissig, F.; Bauer, D.; Zarschler, K.; Novy, Z.; Bendova, K.; Ludik, M. C.; Kopka, K.; Pietzsch, H. J.; Petrik, M.; Mamat, C. Towards Targeted Alpha Therapy with Actinium-225: Chelators for Mild Condition Radiolabeling and Targeting PSMA-A Proof of Concept Study. *Cancers* **2021,** 13.

178. Tietze, L. F.; Arlt, M.; Beller, M.; Gl üsenkamp, K.-H.; Jähde, E.; Rajewsky, M. F. Anticancer Agents, 15. Squaric Acid Diethyl Ester: A New Coupling Reagent for the Formation of Drug Biopolymer Conjugates. Synthesis of Squaric Acid Ester Amides and Diamides. *Chem. Ber.* **1991,** 124, 1215-1221.

179. Lim, N. C.; Morton, M. D.; Jenkins, H. A.; Brückner, C. Squaric Acid N-Hydroxylamides: Synthesis, Structure, and Properties of Vinylogous Hydroxamic Acid Analogues. *J. Org. Chem.* **2003,** 68, 9233-9241.

180. Rostovtsev, V. V.; Green, L. G.; Fokin, V. V.; Sharpless, K. B. A stepwise huisgen cycloaddition process: copper(I)-catalyzed regioselective "ligation" of azides and terminal alkynes. *Angew. Chem., Int. Ed.* **2002,** 41, 2596-9.

181. Tornøe, C. W.; Christensen, C.; Meldal, M. Peptidotriazoles on solid phase: [1,2,3]-triazoles by regiospecific copper(i)-catalyzed 1,3-dipolar cycloadditions of terminal alkynes to azides. *J. Org. Chem.* **2002,** 67, 3057-64.

182. Chen, R.; Yan, Q.-Q.; Hu, S.-J.; Guo, X.-Q.; Zhou, L.-P.; Sun, Q.-F. Dinuclear mono-bridged or polymeric lanthanide complexes from one ligand: structural transformation and chiral induction. *Dalton Trans.* **2023,** 52, 37-43.

183. Chen, R.; Yan, Q.-Q.; Hu, S.-J.; Guo, X.-Q.; Cai, L.-X.; Yan, D.-N.; Zhou, L.-P.; Sun, Q.-F. Dinuclear helicate or mononuclear pincer lanthanide complexes from one ligand: stereo-controlled assembly and catalysis. *Org. Chem. Front.* **2021,** 8, 2576-2582.

184. Thijssen, E. H.; La Joie, R.; Wolf, A.; Strom, A.; Wang, P.; Iaccarino, L.; Bourakova, V.; Cobigo, Y.; Heuer, H.; Spina, S.; VandeVrede, L.; Chai, X.; Proctor, N. K.; Airey, D. C.; Shcherbinin, S.; Duggan Evans, C.; Sims, J. R.; Zetterberg, H.; Blennow, K.; Karydas, A. M.; Teunissen, C. E.; Kramer, J. H.; Grinberg, L. T.; Seeley, W. W.; Rosen, H.; Boeve, B. F.; Miller, B. L.; Rabinovici, G. D.; Dage, J. L.; Rojas, J. C.; Boxer, A. L.; Forsberg, L.; Knopman, D. S.; Graff-Radford, N.; Grossman, M.; Huey, E. H.; Onyike, C.; Kaufer, D.; Roberson, E.; Ghoshal, N.; Weintraub, S.; Appleby, B.; Litvan, I.; Kerwin, D.; Mendez, M.; Bordelon, Y.; Coppola, G.; Ramos, E. M.; Tartaglia, M. C.; Hsiung, G.-Y.; MacKenzie, I.; Domoto-Reilly, K.; Foroud, T.; Dickerson, B. C.; Advancing, R.; Treatment for Frontotemporal Lobar Degeneration, i. Diagnostic value of plasma phosphorylated tau181 in Alzheimer's disease and frontotemporal lobar degeneration. *Nat. Med.* **2020,** 26, 387-397.

185. Feldman, A. K.; Colasson, B.; Fokin, V. V. One-Pot Synthesis of 1,4-Disubstituted 1,2,3-Triazoles from In Situ Generated Azides. *Org. Lett.* **2004,** 6, 3897-3899.

186. Ferreirós-Martínez, R.; Esteban-Gómez, D.; Tóth, É.; de Blas, A.; Platas-Iglesias, C.; Rodríguez-Blas, T. Macrocyclic Receptor Showing Extremely High Sr(II)/Ca(II) and Pb(II)/Ca(II) Selectivities with Potential Application in Chelation Treatment of Metal Intoxication. *Inorg. Chem.* **2011,** 50, 3772-3784.

187. Gracia, S.; Arrachart, G.; Marie, C.; Chapron, S.; Miguirditchian, M.; Pellet-Rostaing, S. Separation of Am (III) by solvent extraction using water-soluble H(4)tpaen derivatives. *Tetrahedron* **2015,** 71, 5321-5336.

188. Mato-Iglesias, M.; Roca-Sabio, A.; Pálinkás, Z.; Esteban-Gómez, D.; Platas-Iglesias, C.; Tóth, É.; de Blas, A.; Rodríguez-Blas, T. Lanthanide Complexes Based on a 1,7-Diaza-12-crown-4 Platform Containing Picolinate Pendants: A New Structural Entry for the Design of Magnetic Resonance Imaging Contrast Agents. *Inorg. Chem.* **2008,** 47, 7840-7851.

189. Froidevaux, S.; Heppeler, A.; Eberle, A. N.; Meier, A. M.; Hausler, M.; Beglinger, C.; Behe, M.; Powell, P.; Macke, H. R. Preclinical comparison in AR4-2J tumor-bearing mice of four radiolabeled 1,4,7,10-tetraazacyclododecane-1,4,7,10-tetraacetic acid-somatostatin analogs for tumor diagnosis and internal radiotherapy. *Endocrinology* **2000,** 141, 3304-12.

190. Tarasenko, E. A.; Beletskaya, I. P. Poly(ethylene glycol)-supported chiral pyridine-2,6-bis(oxazoline): synthesis and application as a recyclable ligand in Cu-I-catalyzed

enantioselective direct addition of terminal alkynes to imines. *Mendeleev Commun.* **2016,** 26, 477-479.

191. Theodorou, V.; Skobridis, K.; Tzakos, A. G.; Ragoussis, V. A simple method for the alkaline hydrolysis of esters. *Tetrahedron Lett.* **2007,** 48, 8230-8233.

192. Supuran, C. T. Carbonic anhydrases: novel therapeutic applications for inhibitors and activators. *Nat. Rev. Drug Discov.* **2008,** 7, 168-181.

193. Wykoff, C. C.; Beasley, N. J.; Watson, P. H.; Turner, K. J.; Pastorek, J.; Sibtain, A.; Wilson, G. D.; Turley, H.; Talks, K. L.; Maxwell, P. H.; Pugh, C. W.; Ratcliffe, P. J.; Harris, A. L. Hypoxia-inducible expression of tumor-associated carbonic anhydrases. *Cancer. Res.* **2000,** 60, 7075-83.

194. Pastorekova, S.; Zatovicova, M.; Pastorek, J. Cancer-associated carbonic anhydrases and their inhibition. *Curr. Pharm. Des.* **2008,** 14, 685-98.

195. Fukumura, D.; Jain, R. K. Tumor microenvironment abnormalities: causes, consequences, and strategies to normalize. *J. Cell. Biochem.* **2007,** 101, 937-49.

196. Svastová, E.; Hulíková, A.; Rafajová, M.; Zat'ovicová, M.; Gibadulinová, A.; Casini, A.; Cecchi, A.; Scozzafava, A.; Supuran, C. T.; Pastorek, J.; Pastoreková, S. Hypoxia activates the capacity of tumor-associated carbonic anhydrase IX to acidify extracellular pH. *FEBS Lett* **2004,** 577, 439-45.

197. Swietach, P.; Vaughan-Jones, R. D.; Harris, A. L. Regulation of tumor pH and the role of carbonic anhydrase 9. *Cancer Metastasis Rev.* **2007,** 26, 299-310.

198. Potter, C. P.; Harris, A. L. Diagnostic, prognostic and therapeutic implications of carbonic anhydrases in cancer. *Br. J. Cancer* **2003,** 89, 2-7.

199. Oosterwijk, E.; Debruyne, F. M.; Schalken, J. A. The use of monoclonal antibody G250 in the therapy of renal-cell carcinoma. *Semin. Oncol.* **1995,** 22, 34-41.

200. Opavský, R.; Pastoreková, S.; Zelník, V.; Gibadulinová, A.; Stanbridge, E. J.; Závada, J.; Kettmann, R.; Pastorek, J. Human MN/CA9 gene, a novel member of the carbonic anhydrase family: structure and exon to protein domain relationships. *Genomics* **1996,** 33, 480-7.

201. Pastorek, J.; Pastorekova, S. Hypoxia-induced carbonic anhydrase IX as a target for cancer therapy: from biology to clinical use. *Semin. Cancer Biol.* **2015,** 31, 52-64.

202. Innocenti, A.; Pastorekova, S.; Pastorek, J.; Scozzafava, A.; De Simone, G.; Supuran, C. T. The proteoglycan region of the tumor-associated carbonic anhydrase isoform IX acts as anintrinsic buffer optimizing CO2 hydration at acidic pH values characteristic of solid tumors. *Bioorg. Med. Chem. Lett.* **2009,** 19, 5825-8.

203. Brahimi-Horn, M. C.; Bellot, G.; Pouysségur, J. Hypoxia and energetic tumour metabolism. *Curr. Opin. Genet. Dev.* **2011,** 21, 67-72.

204. Gatenby, R. A.; Gillies, R. J. Why do cancers have high aerobic glycolysis? *Nat. Rev. Cancer* **2004,** 4, 891-9.

205. Ames, S.; Andring, J. T.; McKenna, R.; Becker, H. M. CAIX forms a transport metabolon with monocarboxylate transporters in human breast cancer cells. *Oncogene* **2020,** 39, 1710-1723.

206. Ames, S.; Pastorekova, S.; Becker, H. M. The proteoglycan-like domain of carbonic anhydrase IX mediates non-catalytic facilitation of lactate transport in cancer cells. *Oncotarget* **2018,** 9, 27940-27957.

207. Jamali, S.; Klier, M.; Ames, S.; Barros, L. F.; McKenna, R.; Deitmer, J. W.; Becker, H. M. Hypoxia-induced carbonic anhydrase IX facilitates lactate flux in human breast cancer cells by non-catalytic function. *Sci. Rep.* **2015,** 5, 13605.

208. Mboge, M. Y.; Chen, Z.; Khokhar, D.; Wolff, A.; Ai, L.; Heldermon, C. D.; Bozdag, M.; Carta, F.; Supuran, C. T.; Brown, K. D.; McKenna, R.; Frost, C. J.; Frost, S. C. A non-catalytic function of carbonic anhydrase IX contributes to the glycolytic phenotype and pH regulation in human breast cancer cells. *Biochem J* **2019,** 476, 1497-1513.

209. Alterio, V.; Hilvo, M.; Di Fiore, A.; Supuran, C. T.; Pan, P.; Parkkila, S.; Scaloni, A.; Pastorek, J.; Pastorekova, S.; Pedone, C.; Scozzafava, A.; Monti, S. M.; De Simone, G. Crystal structure of the catalytic domain of the tumor-associated human carbonic anhydrase IX. *Proc. Natl. Acad. Sci. U. S. A.* **2009,** 106, 16233-8.

210. Hilvo, M.; Baranauskiene, L.; Salzano, A. M.; Scaloni, A.; Matulis, D.; Innocenti, A.; Scozzafava, A.; Monti, S. M.; Di Fiore, A.; De Simone, G.; Lindfors, M.; Jänis, J.; Valjakka, J.; Pastoreková, S.; Pastorek, J.; Kulomaa, M. S.; Nordlund, H. R.; Supuran, C. T.; Parkkila, S. Biochemical characterization of CA IX, one of the most active carbonic anhydrase isozymes. *J. Biol. Chem.* **2008,** 283, 27799-27809.

211. De Simone, G.; Supuran, C. T. Carbonic anhydrase IX: Biochemical and crystallographic characterization of a novel antitumor target. *Biochim. Biophys. Acta* **2010,** 1804, 404-9.

212. Holthöfer, H.; Miettinen, A.; Paasivuo, R.; Lehto, V. P.; Linder, E.; Alfthan, O.; Virtanen, I. Cellular origin and differentiation of renal carcinomas. A fluorescence microscopic study with kidney-specific antibodies, antiintermediate filament antibodies, and lectins. *Lab Invest.* **1983,** 49, 317-26.

213. Ljungberg, B.; Campbell, S. C.; Choi, H. Y.; Jacqmin, D.; Lee, J. E.; Weikert, S.; Kiemeney, L. A. The epidemiology of renal cell carcinoma. *Eur. Urol.* **2011,** 60, 615-21.

214. Ljungberg, B.; Cowan, N. C.; Hanbury, D. C.; Hora, M.; Kuczyk, M. A.; Merseburger, A. S.; Patard, J. J.; Mulders, P. F.; Sinescu, I. C. EAU guidelines on renal cell carcinoma: the 2010 update. *Eur. Urol.* **2010,** 58, 398-406.

215. Cairns, P. Renal cell carcinoma. *Cancer Biomark* **2010,** 9, 461-73.

216. Bedke, J.; Stenzl, A. Immunotherapeutic strategies for the treatment of renal cell carcinoma: where are we now? *Expert Rev. Anticancer Ther.* **2013,** 13, 1399-1408.

217. Clifford, S. C.; Prowse, A. H.; Affara, N. A.; Buys, C. H.; Maher, E. R. Inactivation of the von Hippel-Lindau (VHL) tumour suppressor gene and allelic losses at chromosome arm 3p in primary renal cell carcinoma: evidence for a VHL-independent pathway in clear cell renal tumourigenesis. *Genes Chromosomes Cancer* **1998,** 22, 200-9.

218. Ciechanover, A. The ubiquitin-proteasome pathway: on protein death and cell life. *Embo J.* **1998,** 17, 7151-60.

219. Hekman, M. C. H.; Rijpkema, M.; Aarntzen, E. H.; Mulder, S. F.; Langenhuijsen, J. F.; Oosterwijk, E.; Boerman, O. C.; Oyen, W. J. G.; Mulders, P. F. A. Positron Emission Tomography/Computed Tomography with ^{89}Zr-girentuximab Can Aid in Diagnostic Dilemmas of Clear Cell Renal Cell Carcinoma Suspicion. *Eur. Urol.* **2018,** 74, 257-260.

220. Huang, L. E.; Gu, J.; Schau, M.; Bunn, H. F. Regulation of hypoxia-inducible factor 1alpha is mediated by an O_2-dependent degradation domain via the ubiquitin-proteasome pathway. *Proc. Natl. Acad. Sci. U. S. A.* **1998,** 95, 7987-92.

221. Wang, G. L.; Jiang, B. H.; Rue, E. A.; Semenza, G. L. Hypoxia-inducible factor 1 is a basic-helix-loop-helix-PAS heterodimer regulated by cellular O_2 tension. *Proc. Natl. Acad. Sci. U. S. A.* **1995,** 92, 5510-4.

222. Krieg, M.; Haas, R.; Brauch, H.; Acker, T.; Flamme, I.; Plate, K. H. Up-regulation of hypoxia-inducible factors HIF-1alpha and HIF-2alpha under normoxic conditions in renal carcinoma cells by von Hippel-Lindau tumor suppressor gene loss of function. *Oncogene* **2000,** 19, 5435-43.

223. Vaupel, P. The role of hypoxia-induced factors in tumor progression. *Oncologist* **2004,** 9 Suppl 5, 10-7.

224. Shi, Y. H.; Fang, W. G. Hypoxia-inducible factor-1 in tumour angiogenesis. *World J. Gastroenterol.* **2004,** 10, 1082-7.

225. Low, G.; Huang, G.; Fu, W.; Moloo, Z.; Girgis, S. Review of renal cell carcinoma and its common subtypes in radiology. *World J. Radiol.* **2016,** 8, 484-500.

226. Schroeder, H. W., Jr.; Cavacini, L. Structure and function of immunoglobulins. *J. Allergy Clin. Immunol.* **2010,** 125, S41-52.

227. Moser, M.; Leo, O. Key concepts in immunology. *Vaccine* **2010,** 28 Suppl 3, C2-13.

228. Murali, R.; Greene, M. I. Structure based antibody-like peptidomimetics. *Pharmaceuticals* **2012,** 5, 209-35.

229. Roopenian, D. C.; Akilesh, S. FcRn: the neonatal Fc receptor comes of age. *Nat. Rev. Immunol.* **2007,** 7, 715-25.

230. Chan, A. C.; Carter, P. J. Therapeutic antibodies for autoimmunity and inflammation. *Nat. Rev. Immunol.* **2010,** 10, 301-16.

231. Gill, K. L.; Machavaram, K. K.; Rose, R. H.; Chetty, M. Potential Sources of Inter-Subject Variability in Monoclonal Antibody Pharmacokinetics. *Clin. Pharmacokinet.* **2016,** 55, 789-805.

232. Uemura, H.; Nakagawa, Y.; Yoshida, K.; Saga, S.; Yoshikawa, K.; Hirao, Y.; Oosterwijk, E. MN/CA IX/G250 as a potential target for immunotherapy of renal cell carcinomas. *Br. J. Cancer* **1999,** 81, 741-746.

233. Grabmaier, K.; Vissers, J. L. M.; De Weijert, M. C. A.; Oosterwijk-Wakka, J. C.; Van Bokhoven, A.; Brakenhoff, R. H.; Noessner, E.; Mulders, P. A.; Merkx, G.; Figdor, C. G.; Adema, G. J.; Oosterwijk, E. Molecular cloning and immunogenicity of renal cell carcinoma-associated antigen G250. *Int. J. Cancer* **2000,** 85, 865-870.

234. Oosterwijk, E.; Ruiter, D. J.; Hoedemaeker, P. J.; Pauwels, E. K.; Jonas, U.; Zwartendijk, J.; Warnaar, S. O. Monoclonal antibody G 250 recognizes a determinant present in renal-cell carcinoma and absent from normal kidney. *Int. J. Cancer* **1986,** 38, 489-94.

235. Leibovich, B. C.; Sheinin, Y.; Lohse, C. M.; Thompson, R. H.; Cheville, J. C.; Zavada, J.; Kwon, E. D. Carbonic anhydrase IX is not an independent predictor of outcome for patients with clear cell renal cell carcinoma. *J. Clin. Oncol.* **2007,** 25, 4757-64.

236. Oosterwijk-Wakka, J. C.; Boerman, O. C.; Mulders, P. F.; Oosterwijk, E. Application of monoclonal antibody G250 recognizing carbonic anhydrase IX in renal cell carcinoma. *Int. J. Mol. Sci.* **2013,** 14, 11402-23.

237. Surfus, J. E.; Hank, J. A.; Oosterwijk, E.; Welt, S.; Lindstrom, M. J.; Albertini, M. R.; Schiller, J. H.; Sondel, P. M. Anti-renal-cell carcinoma chimeric antibody G250 facilitates antibody-dependent cellular cytotoxicity with in vitro and in vivo interleukin-2-activated effectors. *J. Immunother. Emphasis Tumor Immunol.* **1996,** 19, 184-91.

238. Bleumer, I.; Knuth, A.; Oosterwijk, E.; Hofmann, R.; Varga, Z.; Lamers, C.; Kruit, W.; Melchior, S.; Mala, C.; Ullrich, S.; De Mulder, P.; Mulders, P. F.; Beck, J. A phase II trial of

chimeric monoclonal antibody G250 for advanced renal cell carcinoma patients. *Br. J. Cancer* **2004,** 90, 985-90.

239. Merkx, R. I. J.; Lobeek, D.; Konijnenberg, M.; Jiménez-Franco, L. D.; Kluge, A.; Oosterwijk, E.; Mulders, P. F. A.; Rijpkema, M. Phase I study to assess safety, biodistribution and radiation dosimetry for ^{89}Zr-girentuximab in patients with renal cell carcinoma. *Eur. J. Nucl. Med. Mol. Imaging.* **2021,** 48, 3277-3285.

240. Muselaers, C. H.; Boers-Sonderen, M. J.; van Oostenbrugge, T. J.; Boerman, O. C.; Desar, I. M.; Stillebroer, A. B.; Mulder, S. F.; van Herpen, C. M.; Langenhuijsen, J. F.; Oosterwijk, E.; Oyen, W. J.; Mulders, P. F. Phase 2 Study of Lutetium 177-Labeled Anti-Carbonic Anhydrase IX Monoclonal Antibody Girentuximab in Patients with Advanced Renal Cell Carcinoma. *Eur. Urol.* **2016,** 69, 767-70.

241. Siebels, M.; Rohrmann, K.; Oberneder, R.; Stahler, M.; Haseke, N.; Beck, J.; Hofmann, R.; Kindler, M.; Kloepfer, P.; Stief, C. A clinical phase I/II trial with the monoclonal antibody cG250 (RENCAREX®) and interferon-alpha-2a in metastatic renal cell carcinoma patients. *World J. Urol.* **2011,** 29, 121-6.

242. Stillebroer, A. B.; Boerman, O. C.; Desar, I. M.; Boers-Sonderen, M. J.; van Herpen, C. M.; Langenhuijsen, J. F.; Smith-Jones, P. M.; Oosterwijk, E.; Oyen, W. J.; Mulders, P. F. Phase 1 radioimmunotherapy study with lutetium 177-labeled anti-carbonic anhydrase IX monoclonal antibody girentuximab in patients with advanced renal cell carcinoma. *Eur. Urol.* **2013,** 64, 478-85.

243. Belldegrun, A. S.; Chamie, K.; Kloepfer, P.; Fall, B.; Bevan, P.; Störkel, S.; Wilhelm, O.; Pantuck, A. J. ARISER: A randomized double blind phase III study to evaluate adjuvant cG250 treatment versus placebo in patients with high-risk ccRCC—Results and implications for adjuvant clinical trials. *J. Clin. Oncol.* **2013,** 31, 4507-4507.

244. Chamie, K.; Donin, N. M.; Klöpfer, P.; Bevan, P.; Fall, B.; Wilhelm, O.; Störkel, S.; Said, J.; Gambla, M.; Hawkins, R. E.; Jankilevich, G.; Kapoor, A.; Kopyltsov, E.; Staehler, M.; Taari, K.; Wainstein, A. J. A.; Pantuck, A. J.; Belldegrun, A. S. Adjuvant Weekly Girentuximab Following Nephrectomy for High-Risk Renal Cell Carcinoma: The ARISER Randomized Clinical Trial. *JAMA Oncol.* **2017,** 3, 913-920.

245. Muselaers, C. H.; Oosterwijk, E.; Bos, D. L.; Oyen, W. J.; Mulders, P. F.; Boerman, O. C. Optimizing lutetium 177-anti-carbonic anhydrase IX radioimmunotherapy in an intraperitoneal clear cell renal cell carcinoma xenograft model. *Mol. Imaging* **2014,** 13, 1-7.

246. Cheal, S. M.; Punzalan, B.; Doran, M. G.; Evans, M. J.; Osborne, J. R.; Lewis, J. S.; Zanzonico, P.; Larson, S. M. Pairwise comparison of ^{89}Zr- and ^{124}I-labeled cG250 based on

positron emission tomography imaging and nonlinear immunokinetic modeling: in vivo carbonic anhydrase IX receptor binding and internalization in mouse xenografts of clear-cell renal cell carcinoma. *Eur. J. Nucl. Med. Mol. Imaging.* **2014,** 41, 985-94.

247. Stillebroer, A. B.; Franssen, G. M.; Mulders, P. F.; Oyen, W. J.; van Dongen, G. A.; Laverman, P.; Oosterwijk, E.; Boerman, O. C. ImmunoPET imaging of renal cell carcinoma with ^{124}I- and ^{89}Zr-labeled anti-CAIX monoclonal antibody cG250 in mice. *Cancer Biother. Radiopharm.* **2013,** 28, 510-5.

248. van Oostenbrugge, T.; Mulders, P. Targeted PET/CT imaging for clear cell renal cell carcinoma with radiolabeled antibodies: recent developments using girentuximab. *Curr. Opin. Urol.* **2021,** 31, 249-254.

249. Verhoeff, S. R.; van Es, S. C.; Boon, E.; van Helden, E.; Angus, L.; Elias, S. G.; Oosting, S. F.; Aarntzen, E. H.; Brouwers, A. H.; Kwee, T. C.; Heskamp, S.; Hoekstra, O. S.; Verheul, H.; van der Veldt, A. A. M.; de Vries, E. G. E.; Boerman, O. C.; van der Graaf, W. T. A.; Oyen, W. J. G.; van Herpen, C. M. L. Lesion detection by [^{89}Zr]Zr-DFO-girentuximab and [(18)F]FDG-PET/CT in patients with newly diagnosed metastatic renal cell carcinoma. *Eur. J. Nucl. Med. Mol. Imaging.* **2019,** 46, 1931-1939.

250. Merkx, R. I. J.; Rijpkema, M.; Franssen, G. M.; Kip, A.; Smeets, B.; Morgenstern, A.; Bruchertseifer, F.; Yan, E.; Wheatcroft, M. P.; Oosterwijk, E.; Mulders, P. F. A.; Heskamp, S. Carbonic Anhydrase IX-Targeted α-Radionuclide Therapy with ^{225}Ac Inhibits Tumor Growth in a Renal Cell Carcinoma Model. *Pharmaceuticals* **2022,** 15.

251. Staudacher, A. H.; Liapis, V.; Brown, M. P. Therapeutic targeting of tumor hypoxia and necrosis with antibody α-radioconjugates. *Antibody Therapeutics* **2018,** 1, 55-63.

252. Raju, M. R.; Eisen, Y.; Carpenter, S.; Inkret, W. C. Radiobiology of alpha particles. III. Cell inactivation by alpha-particle traversals of the cell nucleus. *Radiat. Res.* **1991,** 128, 204-9.

253. Wulbrand, C.; Seidl, C.; Gaertner, F. C.; Bruchertseifer, F.; Morgenstern, A.; Essler, M.; Senekowitsch-Schmidtke, R. Alpha-particle emitting ^{213}Bi-anti-EGFR immunoconjugates eradicate tumor cells independent of oxygenation. *PLoS One* **2013,** 8, e64730.

254. McCombs, J. R.; Owen, S. C. Antibody drug conjugates: design and selection of linker, payload and conjugation chemistry. *Aaps j* **2015,** 17, 339-51.

255. Boylan, N. J.; Zhou, W.; Proos, R. J.; Tolbert, T. J.; Wolfe, J. L.; Laurence, J. S. Conjugation site heterogeneity causes variable electrostatic properties in Fc conjugates. *Bioconjug. Chem.* **2013,** 24, 1008-16.

256. Wakankar, A. A.; Feeney, M. B.; Rivera, J.; Chen, Y.; Kim, M.; Sharma, V. K.; Wang, Y. J. Physicochemical stability of the antibody-drug conjugate Trastuzumab-DM1: changes due to modification and conjugation processes. *Bioconjug. Chem.* **2010,** 21, 1588-95.

257. Acchione, M.; Kwon, H.; Jochheim, C. M.; Atkins, W. M. Impact of linker and conjugation chemistry on antigen binding, Fc receptor binding and thermal stability of model antibody-drug conjugates. *MAbs* **2012,** 4, 362-72.

258. Sharma, S. K.; Glaser, J. M.; Edwards, K. J.; Khozeimeh Sarbisheh, E.; Salih, A. K.; Lewis, J. S.; Price, E. W. A Systematic Evaluation of Antibody Modification and ^{89}Zr-Radiolabeling for Optimized Immuno-PET. *Bioconjug. Chem.* **2021,** 32, 1177-1191.

259. Chari, R. V. Targeted cancer therapy: conferring specificity to cytotoxic drugs. *Acc. Chem. Res.* **2008,** 41, 98-107.

260. Engvall, E.; Jonsson, K.; Perlmann, P. Enzyme-linked immunosorbent assay. II. Quantitative assay of protein antigen, immunoglobulin G, by means of enzyme-labelled antigen and antibody-coated tubes. *Biochim. Biophys. Acta* **1971,** 251, 427-34.

261. Engvall, E.; Perlmann, P. Enzyme-linked immunosorbent assay (ELISA). Quantitative assay of immunoglobulin G. *Immunochemistry* **1971,** 8, 871-4.

262. Reen, D. J. Enzyme-Linked Immunosorbent Assay (ELISA). In *Basic Protein and Peptide Protocols*, Walker, J. M., Ed. Humana Press: Totowa, NJ, 1994; pp 461-466.

263. Coenen, H. H.; Gee, A. D.; Adam, M.; Antoni, G.; Cutler, C. S.; Fujibayashi, Y.; Jeong, J. M.; Mach, R. H.; Mindt, T. L.; Pike, V. W.; Windhorst, A. D. Open letter to journal editors on: International Consensus Radiochemistry Nomenclature Guidelines. *Ann. Nucl. Med.* **2018,** 32, 236-238.

264. McDevitt, M. R.; Ma, D.; Simon, J.; Frank, R. K.; Scheinberg, D. A. Design and synthesis of 225Ac radioimmunopharmaceuticals. *Appl. Radiat. Isot.* **2002,** 57, 841-7.

265. Cortez, A.; Josefsson, A.; McCarty, G.; Shtekler, A. E.; Rao, A.; Austin, Z.; Nedrow, J. R. Evaluation of [^{225}Ac]Ac-DOTA-anti-VLA-4 for targeted alpha therapy of metastatic melanoma. *Nucl. Med. Biol.* **2020,** 88-89, 62-72.

266. Pruszynski, M.; D'Huyvetter, M.; Bruchertseifer, F.; Morgenstern, A.; Lahoutte, T. Evaluation of an Anti-HER2 Nanobody Labeled with ^{225}Ac for Targeted α-Particle Therapy of Cancer. *Mol. Pharm.* **2018,** 15, 1457-1466.

267. De Veirman, K.; Puttemans, J.; Krasniqi, A.; Ertveldt, T.; Hanssens, H.; Romao, E.; Hose, D.; Goyvaert, C.; Vlummens, P.; Muyldermans, S.; Breckpot, K.; Bruchertseifer, F.; Morgenstern, A.; D'Huyvetter, M.; Devoogdt, N. CS1-specific single-domain antibodies

labeled with Actinium-225 prolong survival and increase CD8+ T cells and PD-L1 expression in Multiple Myeloma. *OncoImmunology* **2021,** 10, 2000699.

268. Dawicki, W.; Allen, K. J. H.; Jiao, R.; Malo, M. E.; Helal, M.; Berger, M. S.; Ludwig, D. L.; Dadachova, E. Daratumumab-225Actinium conjugate demonstrates greatly enhanced antitumor activity against experimental multiple myeloma tumors. *OncoImmunology* **2019,** 8, 1607673.

269. Sudo, H.; Tsuji, A. B.; Sugyo, A.; Harada, Y.; Nagayama, S.; Katagiri, T.; Nakamura, Y.; Higashi, T. FZD10-targeted α-radioimmunotherapy with ^{225}Ac-labeled OTSA101 achieves complete remission in a synovial sarcoma model. *Cancer Sci.* **2022,** 113, 721-732.

270. Basaco, T.; Pektor, S.; Bermudez, J. M.; Meneses, N.; Heller, M.; Galván, J. A.; Boligán, K. F.; Schürch, S.; von Gunten, S.; Türler, A.; Miederer, M. Evaluation of Radiolabeled Girentuximab In Vitro and In Vivo. *Pharmaceuticals* **2018,** 11.

271. Franken, N. A.; Rodermond, H. M.; Stap, J.; Haveman, J.; van Bree, C. Clonogenic assay of cells in vitro. *Nat. Protoc.* **2006,** 1, 2315-9.

272. Guda, K.; Natale, L.; Markowitz, S. D. An improved method for staining cell colonies in clonogenic assays. *Cytotechnology* **2007,** 54, 85-8.

273. Workman, P.; Aboagye, E. O.; Balkwill, F.; Balmain, A.; Bruder, G.; Chaplin, D. J.; Double, J. A.; Everitt, J.; Farningham, D. A. H.; Glennie, M. J.; Kelland, L. R.; Robinson, V.; Stratford, I. J.; Tozer, G. M.; Watson, S.; Wedge, S. R.; Eccles, S. A.; An ad hoc committee of the National Cancer Research, I. Guidelines for the welfare and use of animals in cancer research. *Br. J. Cancer* **2010,** 102, 1555-1577.

274. Cannan, W. J.; Pederson, D. S. Mechanisms and Consequences of Double-Strand DNA Break Formation in Chromatin. *J. Cell. Physiol.* **2016,** 231, 3-14.

275. Christmann, M.; Tomicic, M. T.; Roos, W. P.; Kaina, B. Mechanisms of human DNA repair: an update. *Toxicology* **2003,** 193, 3-34.

276. Collis, S. J.; DeWeese, T. L.; Jeggo, P. A.; Parker, A. R. The life and death of DNA-PK. *Oncogene* **2005,** 24, 949-61.

277. Haber, J. E. Partners and pathwaysrepairing a double-strand break. *Trends Genet.* **2000,** 16, 259-64.

278. Rich, T.; Allen, R. L.; Wyllie, A. H. Defying death after DNA damage. *Nature* **2000,** 407, 777-83.

279. Smith, G. C.; Jackson, S. P. The DNA-dependent protein kinase. *Genes Dev.* **1999,** 13, 916-34.

280. Redon, C.; Pilch, D.; Rogakou, E.; Sedelnikova, O.; Newrock, K.; Bonner, W. Histone H2A variants H2AX and H2AZ. *Curr. Opin. Genet. Dev.* **2002,** 12, 162-9.

281. Pilch, D. R.; Sedelnikova, O. A.; Redon, C.; Celeste, A.; Nussenzweig, A.; Bonner, W. M. Characteristics of gamma-H2AX foci at DNA double-strand breaks sites. *Biochem Cell Biol* **2003,** 81, 123-9.

282. Rogakou, E. P.; Boon, C.; Redon, C.; Bonner, W. M. Megabase chromatin domains involved in DNA double-strand breaks in vivo. *J. Cell. Biol.* **1999,** 146, 905-16.

283. Firsanov, D. V.; Solovjeva, L. V.; Svetlova, M. P. H2AX phosphorylation at the sites of DNA double-strand breaks in cultivated mammalian cells and tissues. *Clin. Epigenetics* **2011,** 2, 283-297.

284. Nakamura, A. J.; Rao, V. A.; Pommier, Y.; Bonner, W. M. The complexity of phosphorylated H2AX foci formation and DNA repair assembly at DNA double-strand breaks. *Cell Cycle* **2010,** 9, 389-97.

285. Graf, F.; Fahrer, J.; Maus, S.; Morgenstern, A.; Bruchertseifer, F.; Venkatachalam, S.; Fottner, C.; Weber, M. M.; Huelsenbeck, J.; Schreckenberger, M.; Kaina, B.; Miederer, M. DNA double strand breaks as predictor of efficacy of the alpha-particle emitter Ac-225 and the electron emitter Lu-177 for somatostatin receptor targeted radiotherapy. *PLoS One* **2014,** 9, e88239.

286. Ivashkevich, A.; Redon, C. E.; Nakamura, A. J.; Martin, R. F.; Martin, O. A. Use of the gamma-H2AX assay to monitor DNA damage and repair in translational cancer research. *Cancer Lett.* **2012,** 327, 123-33.

287. Tarnowski, B. I.; Spinale, F. G.; Nicholson, J. H. DAPI as a useful stain for nuclear quantitation. *Biotech Histochem* **1991,** 66, 297-302.

288. Kapuscinski, J. Interactions of nucleic acids with fluorescent dyes: spectral properties of condensed complexes. *J. Histochem. Cytochem.* **1990,** 38, 1323-1329.

289. Goldblum, J. R.; Folpe, A. L.; Weiss, S. W.; Enzinger, F. M.; Weiss, S. W. *Enzinger and Weiss's soft tissue tumors*. 6th ed.; Saunders/Elsevier: Philadelphia, PA, 2014; p xiv, 1155 p.

290. Hansen, M. D. H.; Kwiatkowski, A. V. Chapter One - Control of Actin Dynamics by Allosteric Regulation of Actin Binding Proteins. In *Int. Rev. Cell Mol. Biol.*, Jeon, K. W., Ed. Academic Press: 2013; Vol. 303, pp 1-25.

291. Bonner, W. M.; Redon, C. E.; Dickey, J. S.; Nakamura, A. J.; Sedelnikova, O. A.; Solier, S.; Pommier, Y. GammaH2AX and cancer. *Nat. Rev. Cancer* **2008,** 8, 957-67.

292. Meyer, B.; Voss, K. O.; Tobias, F.; Jakob, B.; Durante, M.; Taucher-Scholz, G. Clustered DNA damage induces pan-nuclear H2AX phosphorylation mediated by ATM and DNA-PK. *Nucleic Acids Res.* **2013,** 41, 6109-18.

293. Lindmo, T.; Boven, E.; Cuttitta, F.; Fedorko, J.; Bunn, P. A., Jr. Determination of the immunoreactive fraction of radiolabeled monoclonal antibodies by linear extrapolation to binding at infinite antigen excess. *J. Immunol. Methods.* **1984,** 72, 77-89.

294. Barltrop, J. A.; Owen, T. C.; Cory, A. H.; Cory, J. G. 5-(3-carboxymethoxyphenyl)-2-(4,5-dimethylthiazolyl)-3-(4-sulfophenyl)tetrazolium, inner salt (MTS) and related analogs of 3-(4,5-dimethylthiazolyl)-2,5-diphenyltetrazolium bromide (MTT) reducing to purple water-soluble formazans As cell-viability indicators. *Bioorg. Med. Chem. Lett.* **1991,** 1, 611-614.

295. Cory, A. H.; Owen, T. C.; Barltrop, J. A.; Cory, J. G. Use of an aqueous soluble tetrazolium/formazan assay for cell growth assays in culture. *Cancer Commun* **1991,** 3, 207-12.

296. Ishiyama, M.; Shiga, M.; Sasamoto, K.; Mizoguchi, M.; He, P.-g. A New Sulfonated Tetrazolium Salt That Produces a Highly Water-Soluble Formazan Dye. *Chem. Pharm. Bull.* **1993,** 41, 1118-1122.

297. Tominaga, H.; Ishiyama, M.; Ohseto, F.; Sasamoto, K.; Hamamoto, T.; Suzuki, K.; Watanabe, M. A water-soluble tetrazolium salt useful for colorimetric cell viability assay. *Anal. Chem.* **1999,** 36, 47-50.

298. Kitson, S. L.; Cuccurullo, V.; Moody, T. S.; Mansi, L. Radionuclide antibody-conjugates, a targeted therapy towards cancer. *Curr. Radiopharm.* **2013,** 6, 57-71.

299. Kolb, H. C.; Finn, M. G.; Sharpless, K. B. Click Chemistry: Diverse Chemical Function from a Few Good Reactions. *Angew. Chem., Int. Ed.* **2001,** 40, 2004-2021.

300. Presolski, S. I.; Hong, V.; Cho, S. H.; Finn, M. G. Tailored ligand acceleration of the Cu-catalyzed azide-alkyne cycloaddition reaction: practical and mechanistic implications. *J. Am. Chem. Soc.* **2010,** 132, 14570-6.

301. Oliveira, B. L.; Guo, Z.; Bernardes, G. J. L. Inverse electron demand Diels-Alder reactions in chemical biology. *Chem. Soc. Rev.* **2017,** 46, 4895-4950.

302. Presolski, S. I.; Hong, V. P.; Finn, M. G. Copper-Catalyzed Azide-Alkyne Click Chemistry for Bioconjugation. *Curr .Protoc. Chem. Biol.* **2011,** 3, 153-162.

303. Lewis, W. G.; Magallon, F. G.; Fokin, V. V.; Finn, M. G. Discovery and characterization of catalysts for azide-alkyne cycloaddition by fluorescence quenching. *J. Am. Chem. Soc.* **2004,** 126, 9152-3.

304. Agard, N. J.; Prescher, J. A.; Bertozzi, C. R. A strain-promoted [3 + 2] azide-alkyne cycloaddition for covalent modification of biomolecules in living systems. *J. Am. Chem. Soc.* **2004,** 126, 15046-7.

305. Dommerholt, J.; Rutjes, F.; van Delft, F. L. Strain-Promoted 1,3-Dipolar Cycloaddition of Cycloalkynes and Organic Azides. *Top Curr Chem (Cham)* **2016,** 374, 16.

306. Knall, A. C.; Slugovc, C. Inverse electron demand Diels-Alder (iEDDA)-initiated conjugation: a (high) potential click chemistry scheme. *Chem. Soc. Rev.* **2013,** 42, 5131-42.

307. Devaraj, N. K.; Weissleder, R.; Hilderbrand, S. A. Tetrazine-based cycloadditions: application to pretargeted live cell imaging. *Bioconjug. Chem.* **2008,** 19, 2297-9.

308. Blackman, M. L.; Royzen, M.; Fox, J. M. Tetrazine ligation: fast bioconjugation based on inverse-electron-demand Diels-Alder reactivity. *J. Am. Chem. Soc.* **2008,** 130, 13518-9.

309. Devaraj, N. K.; Weissleder, R. Biomedical applications of tetrazine cycloadditions. *Acc. Chem. Res.* **2011,** 44, 816-27.

310. Karver, M. R.; Weissleder, R.; Hilderbrand, S. A. Synthesis and evaluation of a series of 1,2,4,5-tetrazines for bioorthogonal conjugation. *Bioconjug. Chem.* **2011,** 22, 2263-70.

311. Selvaraj, R.; Fox, J. M. An efficient and mild oxidant for the synthesis of s-tetrazines. *Tetrahedron Lett.* **2014,** 55, 4795-4797.

312. Taylor, M. T.; Blackman, M. L.; Dmitrenko, O.; Fox, J. M. Design and synthesis of highly reactive dienophiles for the tetrazine-trans-cyclooctene ligation. *J. Am. Chem. Soc.* **2011,** 133, 9646-9.

313. Zeglis, B. M.; Sevak, K. K.; Reiner, T.; Mohindra, P.; Carlin, S. D.; Zanzonico, P.; Weissleder, R.; Lewis, J. S. A pretargeted PET imaging strategy based on bioorthogonal Diels-Alder click chemistry. *J. Nucl. Med.* **2013,** 54, 1389-96.

314. Zeglis, B. M.; Mohindra, P.; Weissmann, G. I.; Divilov, V.; Hilderbrand, S. A.; Weissleder, R.; Lewis, J. S. Modular strategy for the construction of radiometalated antibodies for positron emission tomography based on inverse electron demand Diels-Alder click chemistry. *Bioconjug. Chem.* **2011,** 22, 2048-59.

315. Zeglis, B. M.; Brand, C.; Abdel-Atti, D.; Carnazza, K. E.; Cook, B. E.; Carlin, S.; Reiner, T.; Lewis, J. S. Optimization of a Pretargeted Strategy for the PET Imaging of Colorectal Carcinoma via the Modulation of Radioligand Pharmacokinetics. *Mol. Pharm.* **2015,** 12, 3575-87.

316. Rossin, R.; Verkerk, P. R.; van den Bosch, S. M.; Vulders, R. C.; Verel, I.; Lub, J.; Robillard, M. S. In vivo chemistry for pretargeted tumor imaging in live mice. *Angew. Chem. Int. Ed. Engl.* **2010,** 49, 3375-8.

317. Meyer, J. P.; Houghton, J. L.; Kozlowski, P.; Abdel-Atti, D.; Reiner, T.; Pillarsetty, N. V.; Scholz, W. W.; Zeglis, B. M.; Lewis, J. S. (18)F-Based Pretargeted PET Imaging Based on Bioorthogonal Diels-Alder Click Chemistry. *Bioconjug. Chem.* **2016,** 27, 298-301.

318. Meyer, J. P.; Adumeau, P.; Lewis, J. S.; Zeglis, B. M. Click Chemistry and Radiochemistry: The First 10 Years. *Bioconjug. Chem.* **2016,** 27, 2791-2807.

319. Houghton, J. L.; Membreno, R.; Abdel-Atti, D.; Cunanan, K. M.; Carlin, S.; Scholz, W. W.; Zanzonico, P. B.; Lewis, J. S.; Zeglis, B. M. Establishment of the In Vivo Efficacy of Pretargeted Radioimmunotherapy Utilizing Inverse Electron Demand Diels-Alder Click Chemistry. *Mol. Cancer. Ther.* **2017,** 16, 124-133.

320. Keinanen, O.; Fung, K.; Brennan, J. M.; Zia, N.; Harris, M.; van Dam, E.; Biggin, C.; Hedt, A.; Stoner, J.; Donnelly, P. S.; Lewis, J. S.; Zeglis, B. M. Harnessing ^{64}Cu/^{67}Cu for a theranostic approach to pretargeted radioimmunotherapy. *Proc. Natl. Acad. Sci. U. S. A.* **2020,** 117, 28316-28327.

321. Keinänen, O.; Brennan, J. M.; Membreno, R.; Fung, K.; Gangangari, K.; Dayts, E. J.; Williams, C. J.; Zeglis, B. M. Dual Radionuclide Theranostic Pretargeting. *Mol. Pharm.* **2019,** 16, 4416-4421.

322. van Duijnhoven, S. M. J.; Rossin, R.; van den Bosch, S. M.; Wheatcroft, M. P.; Hudson, P. J.; Robillard, M. S. Diabody Pretargeting with Click Chemistry In Vivo. *J. Nucl. Med.* **2015,** 56, 1422-1428.

323. Poty, S.; Membreno, R.; Glaser, J. M.; Ragupathi, A.; Scholz, W. W.; Zeglis, B. M.; Lewis, J. S. The inverse electron-demand Diels-Alder reaction as a new methodology for the synthesis of ^{225}Ac-labelled radioimmunoconjugates. *ChemComm* **2018,** 54, 2599-2602.

324. Poty, S.; Carter, L. M.; Mandleywala, K.; Membreno, R.; Abdel-Atti, D.; Ragupathi, A.; Scholz, W. W.; Zeglis, B. M.; Lewis, J. S. Leveraging Bioorthogonal Click Chemistry to Improve ^{225}Ac-Radioimmunotherapy of Pancreatic Ductal Adenocarcinoma. *Clin. Cancer Res.* **2019,** 25, 868-880.

325. Maggi, A.; Ruivo, E.; Fissers, J.; Vangestel, C.; Chatterjee, S.; Joossens, J.; Sobott, F.; Staelens, S.; Stroobants, S.; Van Der Veken, P.; Wyffels, L.; Augustyns, K. Development of a novel antibody-tetrazine conjugate for bioorthogonal pretargeting. *Org. Biomol. Chem.* **2016,** 14, 7544-51.

326. Rahim, M. K.; Kota, R.; Haun, J. B. Enhancing reactivity for bioorthogonal pretargeting by unmasking antibody-conjugated trans-cyclooctenes. *Bioconjug. Chem.* **2015,** 26, 352-60.

327. Morgan, K. A.; de Veer, M.; Miles, L. A.; Kelderman, C. A. A.; McLean, C. A.; Masters, C. L.; Barnham, K. J.; White, J. M.; Paterson, B. M.; Donnelly, P. S. Pre-targeting

amyloid-β with antibodies for potential molecular imaging of Alzheimer's disease. *Chem. Commun.* **2023,** 59, 2243-2246.

328. Dubois, B.; Villain, N.; Frisoni, G. B.; Rabinovici, G. D.; Sabbagh, M.; Cappa, S.; Bejanin, A.; Bombois, S.; Epelbaum, S.; Teichmann, M.; Habert, M.-O.; Nordberg, A.; Blennow, K.; Galasko, D.; Stern, Y.; Rowe, C. C.; Salloway, S.; Schneider, L. S.; Cummings, J. L.; Feldman, H. H. Clinical diagnosis of Alzheimer's disease: recommendations of the International Working Group. *Lancet Neurol.* **2021,** 20, 484-496.

329. Knopman, D. S.; Amieva, H.; Petersen, R. C.; Chételat, G.; Holtzman, D. M.; Hyman, B. T.; Nixon, R. A.; Jones, D. T. Alzheimer disease. *Nat. Rev. Dis.* **2021,** 7, 33.

330. Hardy, J.; Selkoe, D. J. The amyloid hypothesis of Alzheimer's disease: progress and problems on the road to therapeutics. *Science* **2002,** 297, 353-6.

331. Selkoe, D. J.; Hardy, J. The amyloid hypothesis of Alzheimer's disease at 25 years. *EMBO Mol. Med.* **2016,** 8, 595-608.

332. Jack, C. R.; Bennett, D. A.; Blennow, K.; Carrillo, M. C.; Dunn, B.; Haeberlein, S. B.; Holtzman, D. M.; Jagust, W.; Jessen, F.; Karlawish, J.; Liu, E.; Molinuevo, J. L.; Montine, T.; Phelps, C.; Rankin, K. P.; Rowe, C. C.; Scheltens, P.; Siemers, E.; Snyder, H. M.; Sperling, R.; Elliott, C.; Masliah, E.; Ryan, L.; Silverberg, N. NIA-AA Research Framework: Toward a biological definition of Alzheimer's disease. *Alzheimer's & Dementia* **2018,** 14, 535-562.

333. Panza, F.; Lozupone, M.; Logroscino, G.; Imbimbo, B. P. A critical appraisal of amyloid-β-targeting therapies for Alzheimer disease. *Nat. Rev. Neurol.* **2019,** 15, 73-88.

334. Wolfe, M. S.; Xia, W.; Ostaszewski, B. L.; Diehl, T. S.; Kimberly, W. T.; Selkoe, D. J. Two transmembrane aspartates in presenilin-1 required for presenilin endoproteolysis and gamma-secretase activity. *Nature* **1999,** 398, 513-7.

335. O'Brien, R. J.; Wong, P. C. Amyloid precursor protein processing and Alzheimer's disease. *Annu. Rev. Neurosci.* **2011,** 34, 185-204.

336. Schenk, D.; Barbour, R.; Dunn, W.; Gordon, G.; Grajeda, H.; Guido, T.; Hu, K.; Huang, J.; Johnson-Wood, K.; Khan, K.; Kholodenko, D.; Lee, M.; Liao, Z.; Lieberburg, I.; Motter, R.; Mutter, L.; Soriano, F.; Shopp, G.; Vasquez, N.; Vandevert, C.; Walker, S.; Wogulis, M.; Yednock, T.; Games, D.; Seubert, P. Immunization with amyloid-beta attenuates Alzheimer-disease-like pathology in the PDAPP mouse. *Nature* **1999,** 400, 173-7.

337. Masters, C. L.; Beyreuther, K. Alzheimer's disease. *BMJ* **1998,** 316, 446-8.

338. Beyreuther, K.; Masters, C. L. Amyloid precursor protein (APP) and beta A4 amyloid in the etiology of Alzheimer's disease: precursor-product relationships in the derangement of neuronal function. *Brain Pathol* **1991,** 1, 241-51.

339. Hansson, O. Biomarkers for neurodegenerative diseases. *Nat. Med.* **2021,** 27, 954-963.
340. Thinakaran, G.; Koo, E. H. Amyloid precursor protein trafficking, processing, and function. *J. Biol. Chem.* **2008,** 283, 29615-9.
341. Hayne, D. J.; Lim, S.; Donnelly, P. S. Metal complexes designed to bind to amyloid-beta for the diagnosis and treatment of Alzheimer's disease. *Chem. Soc. Rev.* **2014,** 43, 6701-15.
342. Cukalevski, R.; Boland, B.; Frohm, B.; Thulin, E.; Walsh, D.; Linse, S. Role of aromatic side chains in amyloid beta-protein aggregation. *ACS Chem. Neurosci.* **2012,** 3, 1008-16.
343. Hickey, J. L.; Lim, S. C.; Hayne, D. J.; Paterson, B. M.; White, J. M.; Villemagne, V. L.; Roselt, P.; Binns, D.; Cullinane, C.; Jeffery, C. M.; Price, R. I.; Barnham, K. J.; Donnelly, P. S. Diagnostic Imaging Agents for Alzheimer's Disease: Copper Radiopharmaceuticals that Target Aβ Plaques. *J. Am. Chem. Soc.* **2013,** 135, 16120-16132.
344. Gremer, L.; Scholzel, D.; Schenk, C.; Reinartz, E.; Labahn, J.; Ravelli, R. B. G.; Tusche, M.; Lopez-Iglesias, C.; Hoyer, W.; Heise, H.; Willbold, D.; Schroder, G. F. Fibril structure of amyloid-beta(1-42) by cryo-electron microscopy. *Science* **2017,** 358, 116-119.
345. Villemagne, V. L.; Doré, V.; Burnham, S. C.; Masters, C. L.; Rowe, C. C. Imaging tau and amyloid-β proteinopathies in Alzheimer disease and other conditions. *Nat. Rev. Neurol.* **2018,** 14, 225-236.
346. Yang, T.; Li, S.; Xu, H.; Walsh, D. M.; Selkoe, D. J. Large Soluble Oligomers of Amyloid β-Protein from Alzheimer Brain Are Far Less Neuroactive Than the Smaller Oligomers to Which They Dissociate. *J. Neurosci.* **2017,** 37, 152.
347. Wang, Z.-X.; Tan, L.; Liu, J.; Yu, J.-T. The Essential Role of Soluble Aβ Oligomers in Alzheimer's Disease. *Mol. Neurobiol.* **2016,** 53, 1905-1924.
348. Busche, M. A.; Hyman, B. T. Synergy between amyloid-β and tau in Alzheimer's disease. *Nat. Neurosci.* **2020,** 23, 1183-1193.
349. Zhu, L.; Ploessl, K.; Kung, H. F. PET/SPECT imaging agents for neurodegenerative diseases. *Chem. Soc. Rev.* **2014,** 43, 6683-6691.
350. Clark, C. M.; Schneider, J. A.; Bedell, B. J.; Beach, T. G.; Bilker, W. B.; Mintun, M. A.; Pontecorvo, M. J.; Hefti, F.; Carpenter, A. P.; Flitter, M. L.; Krautkramer, M. J.; Kung, H. F.; Coleman, R. E.; Doraiswamy, P. M.; Fleisher, A. S.; Sabbagh, M. N.; Sadowsky, C. H.; Reiman, E. P.; Zehntner, S. P.; Skovronsky, D. M. Use of florbetapir-PET for imaging beta-amyloid pathology. *JAMA* **2011,** 305, 275-83.

351. Holland, J. P.; Aigbirhio, F. I.; Betts, H. M.; Bonnitcha, P. D.; Burke, P.; Christlieb, M.; Churchill, G. C.; Cowley, A. R.; Dilworth, J. R.; Donnelly, P. S.; Green, J. C.; Peach, J. M.; Vasudevan, S. R.; Warren, J. E. Functionalized bis(thiosemicarbazonato) complexes of zinc and copper: synthetic platforms toward site-specific radiopharmaceuticals. *Inorg. Chem.* **2007,** 46, 465-85.

352. Blower, P. J.; Lewis, J. S.; Zweit, J. Copper radionuclides and radiopharmaceuticals in nuclear medicine. *Nucl. Med. Biol.* **1996,** 23, 957-980.

353. Blower, P. J. A nuclear chocolate box: the periodic table of nuclear medicine. *Dalton Trans.* **2015,** 44, 4819-4844.

354. Hicks, R. J.; Jackson, P.; Kong, G.; Ware, R. E.; Hofman, M. S.; Pattison, D. A.; Akhurst, T. A.; Drummond, E.; Roselt, P.; Callahan, J.; Price, R.; Jeffery, C. M.; Hong, E.; Noonan, W.; Herschtal, A.; Hicks, L. J.; Hedt, A.; Harris, M.; Paterson, B. M.; Donnelly, P. S. ^{64}Cu-SARTATE PET Imaging of Patients with Neuroendocrine Tumors Demonstrates High Tumor Uptake and Retention, Potentially Allowing Prospective Dosimetry for Peptide Receptor Radionuclide Therapy. *J. Nucl. Med.* **2019,** 60, 777-785.

355. Ikawa, M.; Okazawa, H.; Arakawa, K.; Kudo, T.; Kimura, H.; Fujibayashi, Y.; Kuriyama, M.; Yoneda, M. PET imaging of redox and energy states in stroke-like episodes of MELAS. *Mitochondrion* **2009,** 9, 144-148.

356. Ikawa, M.; Okazawa, H.; Kudo, T.; Kuriyama, M.; Fujibayashi, Y.; Yoneda, M. Evaluation of striatal oxidative stress in patients with Parkinson's disease using [^{62}Cu]ATSM PET. *Nucl. Med. Biol.* **2011,** 38, 945-951.

357. Ikawa, M.; Okazawa, H.; Tsujikawa, T.; Matsunaga, A.; Yamamura, O.; Mori, T.; Hamano, T.; Kiyono, Y.; Nakamoto, Y.; Yoneda, M. Increased oxidative stress is related to disease severity in the ALS motor cortex: A PET study. *Neurology* **2015,** 84, 2033-2039.

358. Lim, S.; Paterson, B. M.; Fodero-Tavoletti, M. T.; O'Keefe, G. J.; Cappai, R.; Barnham, K. J.; Villemagne, V. L.; Donnelly, P. S. A copper radiopharmaceutical for diagnostic imaging of Alzheimer's disease: a bis(thiosemicarbazonato)copper(II) complex that binds to amyloid-β plaques. *Chem. Commun.* **2010,** 46, 5437-5439.

359. Noor, A.; Hayne, D. J.; Lim, S.; Van Zuylekom, J. K.; Cullinane, C.; Roselt, P. D.; McLean, C. A.; White, J. M.; Donnelly, P. S. Copper Bis(thiosemicarbazonato)-stilbenyl Complexes That Bind to Amyloid-β Plaques. *Inorg. Chem.* **2020,** 59, 11658-11669.

360. Acevedo, K. M.; Hayne, D. J.; McInnes, L. E.; Noor, A.; Duncan, C.; Moujalled, D.; Volitakis, I.; Rigopoulos, A.; Barnham, K. J.; Villemagne, V. L.; White, A. R.; Donnelly, P. S. Effect of Structural Modifications to Glyoxal-bis(thiosemicarbazonato)copper(II) Complexes

on Cellular Copper Uptake, Copper-Mediated ATP7A Trafficking, and P-Glycoprotein Mediated Efflux. *J. Med. Chem.* **2018,** 61, 711-723.

361. McInnes, L. E. Copper-based Radiopharmaceuticals for Diagnostic Imaging of Alzheimer's Disease. The University of Melbourne, 2018.

362. Xiao, Z.; Donnelly, P. S.; Zimmermann, M.; Wedd, A. G. Transfer of Copper between Bis(thiosemicarbazone) Ligands and Intracellular Copper-Binding Proteins. Insights into Mechanisms of Copper Uptake and Hypoxia Selectivity. *Inorg. Chem.* **2008,** 47, 4338-4347.

363. Mathias, C. J.; Bergmann, S. R.; Green, M. A. Species-Dependent Binding of Copper(II) Bis(Thiosemicarbazone) Radiopharmaceuticals to Serum Albumin. *J. Nucl. Med.* **1995,** 36, 1451.

364. Basken, N. E.; Mathias, C. J.; Lipka, A. E.; Green, M. A. Species dependence of [64Cu]Cu-Bis(thiosemicarbazone) radiopharmaceutical binding to serum albumins. *Nucl. Med. Biol.* **2008,** 35, 281-286.

365. Price, K. A.; Crouch, P. J.; Volitakis, I.; Paterson, B. M.; Lim, S.; Donnelly, P. S.; White, A. R. Mechanisms Controlling the Cellular Accumulation of Copper Bis(thiosemicarbazonato) Complexes. *Inorg. Chem.* **2011,** 50, 9594-9605.

366. Paterson, B. M.; Cullinane, C.; Crouch, P. J.; White, A. R.; Barnham, K. J.; Roselt, P. D.; Noonan, W.; Binns, D.; Hicks, R. J.; Donnelly, P. S. Modification of Biodistribution and Brain Uptake of Copper Bis(thiosemicarbazonato) Complexes by the Incorporation of Amine and Polyamine Functional Groups. *Inorg. Chem.* **2019,** 58, 4540-4552.

367. Sevigny, J.; Chiao, P.; Bussiere, T.; Weinreb, P. H.; Williams, L.; Maier, M.; Dunstan, R.; Salloway, S.; Chen, T.; Ling, Y.; O'Gorman, J.; Qian, F.; Arastu, M.; Li, M.; Chollate, S.; Brennan, M. S.; Quintero-Monzon, O.; Scannevin, R. H.; Arnold, H. M.; Engber, T.; Rhodes, K.; Ferrero, J.; Hang, Y.; Mikulskis, A.; Grimm, J.; Hock, C.; Nitsch, R. M.; Sandrock, A. The antibody aducanumab reduces Abeta plaques in Alzheimer's disease. *Nature* **2016,** 537, 50-6.

368. Mullard, A. Landmark Alzheimer's drug approval confounds research community. *Nature* **2021,** 594, 309-310.

369. Logovinsky, V.; Satlin, A.; Lai, R.; Swanson, C.; Kaplow, J.; Osswald, G.; Basun, H.; Lannfelt, L. Safety and tolerability of BAN2401--a clinical study in Alzheimer's disease with a protofibril selective Abeta antibody. *Alzheimers Res. Ther.* **2016,** 8, 14.

370. Tucker, S.; Moller, C.; Tegerstedt, K.; Lord, A.; Laudon, H.; Sjodahl, J.; Soderberg, L.; Spens, E.; Sahlin, C.; Waara, E. R.; Satlin, A.; Gellerfors, P.; Osswald, G.; Lannfelt, L. The murine version of BAN2401 (mAb158) selectively reduces amyloid-beta protofibrils in brain and cerebrospinal fluid of tg-ArcSwe mice. *J. Alzheimer's Dis.* **2015,** 43, 575-88.

371. Rossin, R.; Läppchen, T.; van den Bosch, S. M.; Laforest, R.; Robillard, M. S. Diels–Alder Reaction for Tumor Pretargeting: In Vivo Chemistry Can Boost Tumor Radiation Dose Compared with Directly Labeled Antibody. *J. Nucl. Med.* **2013,** 54, 1989.

372. Rossin, R.; Renart Verkerk, P.; van den Bosch, S. M.; Vulders, R. C. M.; Verel, I.; Lub, J.; Robillard, M. S. In Vivo Chemistry for Pretargeted Tumor Imaging in Live Mice. *Angew. Chem., Int. Ed.* **2010,** 49, 3375-3378.

373. Altai, M.; Membreno, R.; Cook, B.; Tolmachev, V.; Zeglis, B. M. Pretargeted Imaging and Therapy. *J. Nucl. Med.* **2017,** 58, 1553.

374. Sarrett, S. M.; Keinänen, O.; Dayts, E. J.; Dewaele-Le Roi, G.; Rodriguez, C.; Carnazza, K. E.; Zeglis, B. M. Inverse electron demand Diels–Alder click chemistry for pretargeted PET imaging and radioimmunotherapy. *Nat. Protoc.* **2021,** 16, 3348-3381.

375. Paterson, B. M.; Karas, J. A.; Scanlon, D. B.; White, J. M.; Donnelly, P. S. Versatile New Bis(thiosemicarbazone) Bifunctional Chelators: Synthesis, Conjugation to Bombesin(7-14)-NH_2, and Copper-64 Radiolabeling. *Inorg. Chem.* **2010,** 49, 1884-1893.

376. Buncic, G.; Donnelly, P. S.; Paterson, B. M.; White, J. M.; Zimmermann, M.; Xiao, Z.; Wedd, A. G. A Water-soluble bis(thiosemicarbazone) ligand. A sensitive probe and metal buffer for zinc. *Inorg. Chem.* **2010,** 49, 3071-3073.

377. Audebert, P.; Miomandre, F.; Clavier, G.; Vernieres, M. C.; Badre, S.; Meallet-Renault, R. Synthesis and properties of new tetrazines substituted by heteroatoms: towards the world's smallest organic fluorophores. *Chemistry* **2005,** 11, 5667-73.

378. Cowley, A. R.; Dilworth, J. R.; Donnelly, P. S.; Labisbal, E.; Sousa, A. An Unusual Dimeric Structure of a Cu(I) Bis(thiosemicarbazone) Complex: Implications for the Mechanism of Hypoxic Selectivity of the Cu(II) Derivatives. *J. Am. Chem. Soc.* **2002,** 124, 5270-5271.

379. Blower, P. J.; Castle, T. C.; Cowley, A. R.; Dilworth, J. R.; Donnelly, P. S.; Labisbal, E.; Sowrey, F. E.; Teat, S. J.; Went, M. J. Structural trends in copper(II) bis(thiosemicarbazone) radiopharmaceuticals. *Dalton Trans.* **2003**, 4416-4425.

380. Baghallab, I.; Reyes-Ruiz, J. M.; Abulnaja, K.; Huwait, E.; Glabe, C. Epitomic Characterization of the Specificity of the Anti-Amyloid Aβ Monoclonal Antibodies 6E10 and 4G8. *J. Alzheimer's Dis.* **2018,** 66.

381. Fodero-Tavoletti, M. T.; Villemagne, V. L.; Paterson, B. M.; White, A. R.; Li, Q.-X.; Camakaris, J.; O'Keefe, G.; Cappai, R.; Barnham, K. J.; Donnelly, P. S. Bis (thiosemicarbazonato) Cu-64 Complexes for Positron Emission Tomography Imaging of Alzheimer's Disease. *J. Alzheimer's Dis.* **2010,** 20, 49-55.

382. Szostak, K. Synthesis of new bis(thiosemicarbazone) ligands and their metal complexes. The University of Melbourne, 2017.

383. Hanahan, D.; Weinberg, R. A. Hallmarks of cancer: the next generation. *Cell* **2011,** 144, 646-74.

384. Chen, D. S.; Irving, B. A.; Hodi, F. S. Molecular pathways: next-generation immunotherapy--inhibiting programmed death-ligand 1 and programmed death-1. *Clin. Cancer Res.* **2012,** 18, 6580-7.

385. Chen, Daniel S.; Mellman, I. Oncology Meets Immunology: The Cancer-Immunity Cycle. *Immunity* **2013,** 39, 1-10.

386. Tay, R. E.; Richardson, E. K.; Toh, H. C. Revisiting the role of CD4+ T cells in cancer immunotherapy—new insights into old paradigms. *Cancer Gene Therapy* **2021,** 28, 5-17.

387. Leach, D. R.; Krummel, M. F.; Allison, J. P. Enhancement of antitumor immunity by CTLA-4 blockade. *Science* **1996,** 271, 1734-6.

388. Ishida, Y.; Agata, Y.; Shibahara, K.; Honjo, T. Induced expression of PD-1, a novel member of the immunoglobulin gene superfamily, upon programmed cell death. *The EMBO Journal* **1992,** 11, 3887-3895.

389. Buchbinder, E. I.; Desai, A. CTLA-4 and PD-1 Pathways: Similarities, Differences, and Implications of Their Inhibition. *Am. J. Clin. Oncol.* **2016,** 39, 98-106.

390. Lazar-Molnar, E.; Yan, Q.; Cao, E.; Ramagopal, U.; Nathenson, S. G.; Almo, S. C. Crystal structure of the complex between programmed death-1 (PD-1) and its ligand PD-L2. *Proc. Natl. Acad. Sci. U. S. A.* **2008,** 105, 10483-8.

391. Jia, L.; Zhang, Q.; Zhang, R. PD-1/PD-L1 pathway blockade works as an effective and practical therapy for cancer immunotherapy. *Cancer Biol. Med.* **2018,** 15, 116-123.

392. Zak, K. M.; Kitel, R.; Przetocka, S.; Golik, P.; Guzik, K.; Musielak, B.; Domling, A.; Dubin, G.; Holak, T. A. Structure of the Complex of Human Programmed Death 1, PD-1, and Its Ligand PD-L1. *Structure* **2015,** 23, 2341-2348.

393. Ribas, A.; Wolchok, J. D. Cancer immunotherapy using checkpoint blockade. *Science* **2018,** 359, 1350-1355.

394. Wolchok, J. D.; Chiarion-Sileni, V.; Gonzalez, R.; Rutkowski, P.; Grob, J. J.; Cowey, C. L.; Lao, C. D.; Wagstaff, J.; Schadendorf, D.; Ferrucci, P. F.; Smylie, M.; Dummer, R.; Hill, A.; Hogg, D.; Haanen, J.; Carlino, M. S.; Bechter, O.; Maio, M.; Marquez-Rodas, I.; Guidoboni, M.; McArthur, G.; Lebbe, C.; Ascierto, P. A.; Long, G. V.; Cebon, J.; Sosman, J.; Postow, M. A.; Callahan, M. K.; Walker, D.; Rollin, L.; Bhore, R.; Hodi, F. S.; Larkin, J.

Overall Survival with Combined Nivolumab and Ipilimumab in Advanced Melanoma. *N. Engl. J. Med.* **2017,** 377, 1345-1356.

395. Robert, C.; Schachter, J.; Long, G. V.; Arance, A.; Grob, J. J.; Mortier, L.; Daud, A.; Carlino, M. S.; McNeil, C.; Lotem, M.; Larkin, J.; Lorigan, P.; Neyns, B.; Blank, C. U.; Hamid, O.; Mateus, C.; Shapira-Frommer, R.; Kosh, M.; Zhou, H.; Ibrahim, N.; Ebbinghaus, S.; Ribas, A. Pembrolizumab versus Ipilimumab in Advanced Melanoma. *N. Engl. J. Med.* **2015,** 372, 2521-32.

396. Robert, C.; Soria, J. C.; Eggermont, A. M. Drug of the year: programmed death-1 receptor/programmed death-1 ligand-1 receptor monoclonal antibodies. *Eur J Cancer* **2013,** 49, 2968-71.

397. Connett, J. M.; Anderson, C. J.; Guo, L. W.; Schwarz, S. W.; Zinn, K. R.; Rogers, B. E.; Siegel, B. A.; Philpott, G. W.; Welch, M. J. Radioimmunotherapy with a ^{64}Cu-labeled monoclonal antibody: a comparison with 67Cu. *Proc. Natl. Acad. Sci. U. S. A.* **1996,** 93, 6814-8.

398. Anderson, C. J.; Jones, L. A.; Bass, L. A.; Sherman, E. L.; McCarthy, D. W.; Cutler, P. D.; Lanahan, M. V.; Cristel, M. E.; Lewis, J. S.; Schwarz, S. W. Radiotherapy, toxicity and dosimetry of copper-64-TETA-octreotide in tumor-bearing rats. *J. Nucl. Med.* **1998,** 39, 1944-51.

399. Novak-Hofer, I.; Schubiger, P. A. Copper-67 as a therapeutic nuclide for radioimmunotherapy. *Eur. J. Nucl. Med. Mol. Imaging* **2002,** 29, 821-30.

400. Mou, L.; Martini, P.; Pupillo, G.; Cieszykowska, I.; Cutler, C. S.; Mikołajczak, R. ^{67}Cu Production Capabilities: A Mini Review. *Molecules* **2022,** 27, 1501.

401. Morphy, J. R.; Parker, D.; Kataky, R.; Harrison, A.; Eaton, M. A. W.; Millican, A.; Phipps, A.; Walker, C. Towards tumour targeting with copper-radiolabelled macrocycle–antibody conjugates. *J. Chem. Soc., Chem. Commun.* **1989**, 792-794.

402. Smith-Jones, P. M.; Fridrich, R.; Kaden, T. A.; Novak-Hofer, I.; Siebold, K.; Tschudin, D.; Maecke, H. R. Antibody labeling with copper-67 using the bifunctional macrocycle 4-[(1,4,8,11-tetraazacyclotetradec-1-yl)methyl]benzoic acid. *Bioconjug. Chem.* **1991,** 2, 415-21.

403. Delaloye, A. B.; Delaloye, B.; Buchegger, F.; Vogel, C. A.; Gillet, M.; Mach, J. P.; Smith, A.; Schubiger, P. A. Comparison of copper-67- and iodine-125-labeled anti-CEA monoclonal antibody biodistribution in patients with colorectal tumors. *J. Nucl. Med.* **1997,** 38, 847-53.

404. Jones-Wilson, T. M.; Deal, K. A.; Anderson, C. J.; McCarthy, D. W.; Kovacs, Z.; Motekaitis, R. J.; Sherry, A. D.; Martell, A. E.; Welch, M. J. The in vivo behavior of copper-64-labeled azamacrocyclic complexes. *Nucl. Med. Biol.* **1998,** 25, 523-530.

405. Chen, X.; Hou, Y.; Tohme, M.; Park, R.; Khankaldyyan, V.; Gonzales-Gomez, I.; Bading, J. R.; Laug, W. E.; Conti, P. S. Pegylated Arg-Gly-Asp peptide: ^{64}Cu labeling and PET imaging of brain tumor alphavbeta3-integrin expression. *J. Nucl. Med.* **2004,** 45, 1776-83.

406. Heroux, K. J.; Woodin, K. S.; Tranchemontagne, D. J.; Widger, P. C. B.; Southwick, E.; Wong, E. H.; Weisman, G. R.; Tomellini, S. A.; Wadas, T. J.; Anderson, C. J.; Kassel, S.; Golen, J. A.; Rheingold, A. L. The long and short of it: the influence of N-carboxyethyl versusN-carboxymethyl pendant arms on in vitro and in vivo behavior of copper complexes of cross-bridged tetraamine macrocycles. *Dalton Trans.* **2007**, 2150-2162.

407. DeNardo, S. J.; DeNardo, G. L.; Kukis, D. L.; Shen, S.; Kroger, L. A.; DeNardo, D. A.; Goldstein, D. S.; Mirick, G. R.; Salako, Q.; Mausner, L. F.; Srivastava, S. C.; Meares, C. F. ^{67}Cu-2IT-BAT-Lym-1 pharmacokinetics, radiation dosimetry, toxicity and tumor regression in patients with lymphoma. *J. Nucl. Med.* **1999,** 40, 302-10.

408. O'Donnell, R. T.; DeNardo, G. L.; Kukis, D. L.; Lamborn, K. R.; Shen, S.; Yuan, A.; Goldstein, D. S.; Carr, C. E.; Mirick, G. R.; DeNardo, S. J. A clinical trial of radioimmunotherapy with ^{67}Cu-2IT-BAT-Lym-1 for non-Hodgkin's lymphoma. *J. Nucl. Med.* **1999,** 40, 2014-20.

409. Bass, L. A.; Wang, M.; Welch, M. J.; Anderson, C. J. In vivo transchelation of copper-64 from TETA-octreotide to superoxide dismutase in rat liver. *Bioconjug. Chem.* **2000,** 11, 527-32.

410. Weisman, G. R.; Rogers, M. E.; Wong, E. H.; Jasinski, J. P.; Paight, E. S. Cross-bridged cyclam. Protonation and lithium cation (Li^+) complexation in a diamond-lattice cleft. *J. Am. Chem. Soc.* **1990,** 112, 8604-8605.

411. Weisman, G. R.; Wong, E. H.; Hill, D. C.; Rogers, M. E.; Reed, D. P.; Calabrese, J. C. Synthesis and transition-metal complexes of new cross-bridged tetraamine ligands. *Chem. Commun.* **1996**, 947-948.

412. J. Hubin, T.; M. McCormick, J.; R. Collinson, S.; H. Busch, D.; W. Alcock, N. Ultra rigid cross-bridged tetraazamacrocycles as ligands—the challenge and the solution. *Chem. Commun.* **1998**, 1675-1676.

413. Wong, E. H.; Weisman, G. R.; Hill, D. C.; Reed, D. P.; Rogers, M. E.; Condon, J. S.; Fagan, M. A.; Calabrese, J. C.; Lam, K.-C.; Guzei, I. A.; Rheingold, A. L. Synthesis and Characterization of Cross-Bridged Cyclams and Pendant-Armed Derivatives and Structural

Studies of Their Copper(II) Complexes. *Journal of the American Chemical Society* **2000,** 122, 10561-10572.

414. Wadas, T. J.; Wong, E. H.; Weisman, G. R.; Anderson, C. J. Coordinating Radiometals of Copper, Gallium, Indium, Yttrium, and Zirconium for PET and SPECT Imaging of Disease. *Chem. Rev.* **2010,** 110, 2858-2902.

415. Shokeen, M.; Anderson, C. J. Molecular Imaging of Cancer with Copper-64 Radiopharmaceuticals and Positron Emission Tomography (PET). *Acc. Chem. Res.* **2009,** 42, 832-841.

416. Paterson, B. M.; Donnelly, P. S. Chapter Five - Macrocyclic Bifunctional Chelators and Conjugation Strategies for Copper-64 Radiopharmaceuticals. In *Adv. Inorg. Chem.*, van Eldik, R.; Hubbard, C. D., Eds. Academic Press: 2016; Vol. 68, pp 223-251.

417. Gahan, L. R.; Harrowfield, J. M. Sepulchrate: Four decades on. *Polyhedron* **2015,** 94, 1-51.

418. Geue, R. J.; Hambley, T. W.; Harrowfield, J. M.; Sargeson, A. M.; Snow, M. R. Metal ion encapsulation: cobalt cages derived from polyamines, formaldehyde, and nitromethane. *J. Am. Chem. Soc.* **1984,** 106, 5478-5488.

419. Bottomley, G. A.; Clark, I. J.; Creaser, II; Engelhardt, L. M.; Geue, R. J.; Hagen, K. S.; Harrowfield, J. M.; Lawrance, G. A.; Lay, P. A.; Sargeson, A. M.; See, A. J.; Skelton, B. W.; White, A. H.; Wilner, F. R. The Synthesis and Structure of Encapsulating Ligands: Properties of Bicyclic Hexamines. *Aus. J. Chem.* **1994,** 47, 143-179.

420. McArdle, H. J.; Gross, S. M.; Creaser, I.; Sargeson, A. M.; Danks, D. M. Effect of chelators on copper metabolism and copper pools in mouse hepatocytes. *Am. J. Physiol.* **1989,** 256, G667-72.

421. McArdle, H. J.; Mercer, J. F.; Sargeson, A. M.; Danks, D. M. Effects of cellular copper content on copper uptake and metallothionein and ceruloplasmin mRNA levels in mouse hepatocytes. *J. Nutr.* **1990,** 120, 1370-5.

422. Sargeson, A. M. The potential for the cage complexes in biology. *Coord. Chem. Rev.* **1996,** 151, 89-114.

423. Bingham, M. J.; Sargeson, A. M.; McArdle, H. J. Characterization of intracellular copper pools in rat hepatocytes using the chelator diamsar. *Am. J. Physiol. Gastrointest. Liver Physiol.* **1997,** 272, G1400-G1407.

424. Zarschler, K.; Kubeil, M.; Stephan, H. Establishment of two complementary in vitro assays for radiocopper complexes achieving reliable and comparable evaluation of in vivo stability. *RSC Adv.* **2014,** 4, 10157-10164.

425. Di Bartolo, N. M.; Sargeson, A. M.; Donlevy, T. M.; Smith, S. V. Synthesis of a new cage ligand, SarAr, and its complexation with selected transition metal ions for potential use in radioimaging. *Dalton. Trans.* **2001**, 2303-2309.

426. Di Bartolo, N.; Sargeson, A. M.; Smith, S. V. New ^{64}Cu PET imaging agents for personalised medicine and drug development using the hexa-aza cage, SarAr. *Org. Biomol. Chem.* **2006,** 4, 3350-3357.

427. Voss, S. D.; Smith, S. V.; DiBartolo, N.; McIntosh, L. J.; Cyr, E. M.; Bonab, A. A.; Dearling, J. L. J.; Carter, E. A.; Fischman, A. J.; Treves, S. T.; Gillies, S. D.; Sargeson, A. M.; Huston, J. S.; Packard, A. B. Positron emission tomography (PET) imaging of neuroblastoma and melanoma with ^{64}Cu-SarAr immunoconjugates. *Proc. Natl. Acad. Sci. U. S. A.* **2007**, 1-5.

428. Donnelly, P. S.; Harrowfield, J. M.; Skelton, B. W.; White, A. H. Carboxymethylation of Cage Amines: Control of Alkylation by Metal Ion Coordination. *Inorg. Chem.* **2000,** 39, 5817-5830.

429. Donnelly, P. S.; Harrowfield, J. M. Synthesis with coordinated ligands: biomolecule attachment to cage amines. *J. Chem. Soc., Dalton Trans.* **2002**, 906-913.

430. Donnelly, P. S.; Harrowfield, J. M.; Skelton, B. W.; White, A. H. Carboxymethylated Cage Amines: Coordination and Lactamization. *Inorg. Chem.* **2001,** 40, 5645-5652.

431. Ma, M. T.; Karas, J. A.; White, J. M.; Scanlon, D.; Donnelly, P. S. A new bifunctional chelator for copper radiopharmaceuticals: a cage amine ligand with a carboxylate functional group for conjugation to peptides. *Chemical Communications* **2009**, 3237-3239.

432. Ma, M. T.; Cooper, M. S.; Paul, R. L.; Shaw, K. P.; Karas, J. A.; Scanlon, D.; White, J. M.; Blower, P. J.; Donnelly, P. S. Macrobicyclic Cage Amine Ligands for Copper Radiopharmaceuticals: A Single Bivalent Cage Amine Containing Two Lys^3-bombesin Targeting Peptides. *Inorg. Chem.* **2011,** 50, 6701-6710.

433. Liu, S.; Li, Z.; Yap, L.-P.; Huang, C.-W.; Park, R.; Conti, P. S. Efficient Preparation and Biological Evaluation of a Novel Multivalency Bifunctional Chelator for ^{64}Cu Radiopharmaceuticals. *Eur. J. Chem.* **2011,** 17, 10222-10225.

434. Liu, S.; Li, D.; Huang, C.-W.; Yap, L.-P.; Park, R.; Shan, H.; Li, Z.; Conti, P. S. The Efficient Synthesis and Biological Evaluation of Novel Bi-Functionalized Sarcophagine for ^{64}Cu Radiopharmaceuticals. *Theranostics* **2012,** 2, 589-596.

435. Paterson, B. M.; Roselt, P.; Denoyer, D.; Cullinane, C.; Binns, D.; Noonan, W.; Jeffery, C. M.; Price, R. I.; White, J. M.; Hicks, R. J.; Donnelly, P. S. PET imaging of tumours with a 64Cu labeled macrobicyclic cage amine ligand tethered to Tyr3-octreotate. *Dalton. Trans.* **2014,** 43, 1386-1396.

436. Cullinane, C.; Jeffery, C. M.; Roselt, P. D.; van Dam, E. M.; Jackson, S.; Kuan, K.; Jackson, P.; Binns, D.; van Zuylekom, J.; Harris, M. J.; Hicks, R. J.; Donnelly, P. S. Peptide Receptor Radionuclide Therapy with ^{67}Cu-CuSarTATE Is Highly Efficacious Against a Somatostatin-Positive Neuroendocrine Tumor Model. *J. Nucl. Med.* **2020,** 61, 1800-1805.

437. Dearling, J. L. J.; van Dam, E. M.; Harris, M. J.; Packard, A. B. Detection and therapy of neuroblastoma minimal residual disease using [$^{64/67}$Cu]Cu-SARTATE in a preclinical model of hepatic metastases. *EJNMMI Res.* **2021,** 11, 20.

438. Bailey, D. L.; Willowson, K. P.; Harris, M.; Biggin, C.; Aslani, A.; Lengkeek, N. A.; Stoner, J.; Eslick, M. E.; Marquis, H.; Parker, M.; Roach, P. J.; Schembri, G. P. ^{64}Cu Treatment Planning and ^{67}Cu Therapy with Radiolabelled SARTATE ([^{64}Cu/^{67}Cu]MeCOSAR-Octreotate) in Subjects with Unresectable Multifocal Meningioma – Initial Results for Human Imaging, Safety, Biodistribution and Radiation Dosimetry. *J. Nucl. Med.* **2022**, jnumed.122.264586.

439. Baratto, L.; Duan, H.; Mäcke, H.; Iagaru, A. Imaging the Distribution of Gastrin-Releasing Peptide Receptors in Cancer. *J. Nucl. Med.* **2020,** 61, 792-798.

440. Bratanovic, I. J.; Zhang, C.; Zhang, Z.; Kuo, H. T.; Colpo, N.; Zeisler, J.; Merkens, H.; Uribe, C.; Lin, K. S.; Bénard, F. A Radiotracer for Molecular Imaging and Therapy of Gastrin-Releasing Peptide Receptor-Positive Prostate Cancer. *J. Nucl. Med.* **2022,** 63, 424-430.

441. Lears, K., A ; Ferdani, R.; Liang, K.; Zheleznyak, A.; Andrews, R.; Sherman, C., D; Achilefu, S.; Anderson, C., J; Rogers, B., E. In Vitro and In Vivo Evaluation of ^{64}Cu-Labeled SarAr-Bombesin Analogs in Gastrin-Releasing Peptide Receptor–Expressing Prostate Cancer. *J. Nucl. Med.* **2011,** 52, 470.

442. Cescato, R.; Maina, T.; Nock, B.; Nikolopoulou, A.; Charalambidis, D.; Piccand, V.; Reubi, J. C. Bombesin receptor antagonists may be preferable to agonists for tumor targeting. *J. Nucl. Med.* **2008,** 49, 318-26.

443. Mansi, R.; Nock, B. A.; Dalm, S. U.; Busstra, M. B.; van Weerden, W. M.; Maina, T. Radiolabeled Bombesin Analogs. In *Cancers*, 2021; Vol. 13.

444. Mansi, R.; Wang, X.; Forrer, F.; Waser, B.; Cescato, R.; Graham, K.; Borkowski, S.; Reubi, J. C.; Maecke, H. R. Development of a potent DOTA-conjugated bombesin antagonist for targeting GRPr-positive tumours. *Eur. J. Nucl. Med. Mol. Imaging* **2011,** 38, 97-107.

445. Huynh, T. T.; van Dam, E. M.; Sreekumar, S.; Mpoy, C.; Blyth, B. J.; Muntz, F.; Harris, M. J.; Rogers, B. E. Copper-67-Labeled Bombesin Peptide for Targeted Radionuclide Therapy of Prostate Cancer. In *Pharmaceuticals*, 2022; Vol. 15.

446. Wong, K.; Sheehan-Dare, G.; Nguyen, A.; Ho, B.; Liu, V.; Lee, J.; Brown, L.; Dear, R.; Chan, L.; Sharma, S.; Malaroda, A.; Smith, I.; Lim, E.; Emmett, L. ^{64}Cu-SAR-Bombesin PET-CT Imaging in the Staging of Estrogen/Progesterone Receptor Positive, HER2 Negative Metastatic Breast Cancer Patients: Safety, Dosimetry and Feasibility in a Phase I Trial. In *Pharmaceuticals*, 2022; Vol. 15.

447. Wieser, G.; Mansi, R.; Grosu, A. L.; Schultze-Seemann, W.; Dumont-Walter, R. A.; Meyer, P. T.; Maecke, H. R.; Reubi, J. C.; Weber, W. A. Positron emission tomography (PET) imaging of prostate cancer with a gastrin releasing peptide receptor antagonist--from mice to men. *Theranostics* **2014,** 4, 412-9.

448. Hegi-Johnson, F.; Rudd, S. E.; Wichmann, C.; Akhurst, T.; Roselt, P.; Trinh, J.; John, T.; Devereux, L.; Donnelly, P. S.; Hicks, R.; Scott, A. M.; Steinfort, D.; Fox, S.; Blyth, B.; Parakh, S.; Hanna, G. G.; Callahan, J.; Burbury, K.; MacManus, M. ImmunoPET: IMaging of cancer imMUNOtherapy targets with positron Emission Tomography: a phase 0/1 study characterising PD-L1 with ^{89}Zr-durvalumab (MEDI4736) PET/CT in stage III NSCLC patients receiving chemoradiation study protocol. *BMJ Open* **2022,** 12, e056708.

449. MacManus, M.; Rudd, S.; Roselt, P.; Wichmann, C.; Callahan, J.; John, T.; Scott, A.; Donnelly, P.; Hanna, G.; Hegi-Johnson, F. P1.10-02 ImmunoPET: A Phase 0/1 Study Characterising PD-L1 with ^{89}Zr-Durvalumab (MEDI4736) PET/CT in Stage III NSCLC Patients Receiving Chemoradiation. *J. Thorac. Oncol.* **2022,** 17, S107-S108.

450. Broos, K.; Lecocq, Q.; Raes, G.; Devoogdt, N.; Keyaerts, M.; Breckpot, K. Noninvasive imaging of the PD-1:PD-L1 immune checkpoint: Embracing nuclear medicine for the benefit of personalized immunotherapy. *Theranostics* **2018,** 8, 3559-3570.

451. Bensch, F.; van der Veen, E. L.; Lub-de Hooge, M. N.; Jorritsma-Smit, A.; Boellaard, R.; Kok, I. C.; Oosting, S. F.; Schröder, C. P.; Hiltermann, T. J. N.; van der Wekken, A. J.; Groen, H. J. M.; Kwee, T. C.; Elias, S. G.; Gietema, J. A.; Bohorquez, S. S.; de Crespigny, A.; Williams, S.-P.; Mancao, C.; Brouwers, A. H.; Fine, B. M.; de Vries, E. G. E. 89Zr-atezolizumab imaging as a non-invasive approach to assess clinical response to PD-L1 blockade in cancer. *Nat. Med.* **2018,** 24, 1852-1858.

452. Fetse, J.; Zhao, Z.; Liu, H.; Mamani, U.-F.; Mustafa, B.; Adhikary, P.; Ibrahim, M.; Liu, Y.; Patel, P.; Nakhjiri, M.; Alahmari, M.; Li, G.; Cheng, K. Discovery of Cyclic Peptide Inhibitors Targeting PD-L1 for Cancer Immunotherapy. *J. Med. Chem.* **2022,** 65, 12002-12013.

453. Moroz, A.; Lee, C.-Y.; Wang, Y.-h.; Hsiao, J. C.; Sevillano, N.; Truillet, C.; Craik, C. S.; Fong, L.; Wang, C.-I.; Evans, M. J. A Preclinical Assessment of ^{89}Zr-atezolizumab

Identifies a Requirement for Carrier Added Formulations Not Observed with ^{89}Zr-C4. *Bioconjug. Chem.* **2018,** 29, 3476-3482.

454. Devaraj, N. K.; Upadhyay, R.; Haun, J. B.; Hilderbrand, S. A.; Weissleder, R. Fast and sensitive pretargeted labeling of cancer cells through a tetrazine/trans-cyclooctene cycloaddition. *Angew. Chem., Int. Ed.* **2009,** 48, 7013-6.

455. Vlieghe, P.; Lisowski, V.; Martinez, J.; Khrestchatisky, M. Synthetic therapeutic peptides: science and market. *Drug Discov. Today* **2010,** 15, 40-56.

456. Pardoll, D. M. The blockade of immune checkpoints in cancer immunotherapy. *Nat. Rev. Cancer* **2012,** 12, 252-264.

457. Brown, Z. J.; Yu, S. J.; Heinrich, B.; Ma, C.; Fu, Q.; Sandhu, M.; Agdashian, D.; Zhang, Q.; Korangy, F.; Greten, T. F. Indoleamine 2,3-dioxygenase provides adaptive resistance to immune checkpoint inhibitors in hepatocellular carcinoma. *Cancer Immunology, Immunotherapy* **2018,** 67, 1305-1315.

458. Kuai, R.; Yuan, W.; Son, S.; Nam, J.; Xu, Y.; Fan, Y.; Schwendeman, A.; Moon, J. J. Elimination of established tumors with nanodisc-based combination chemoimmunotherapy. *Sci. Adv.* 4, eaao1736.

459. Zhan, M. M.; Hu, X. Q.; Liu, X. X.; Ruan, B. F.; Xu, J.; Liao, C. From monoclonal antibodies to small molecules: the development of inhibitors targeting the PD-1/PD-L1 pathway. *Drug Discov. Today* **2016,** 21, 1027-36.

460. Chen, T.; Li, Q.; Liu, Z.; Chen, Y.; Feng, F.; Sun, H. Peptide-based and small synthetic molecule inhibitors on PD-1/PD-L1 pathway: A new choice for immunotherapy? *Eur. J. Med. Chem.* **2019,** 161, 378-398.

461. Konstantinidou, M.; Zarganes-Tzitzikas, T.; Magiera-Mularz, K.; Holak, T. A.; Domling, A. Immune Checkpoint PD-1/PD-L1: Is There Life Beyond Antibodies? *Angew. Chem., Int. Ed.* **2018,** 57, 4840-4848.

462. Chang, H.-N.; Liu, B.-Y.; Qi, Y.-K.; Zhou, Y.; Chen, Y.-P.; Pan, K.-M.; Li, W.-W.; Zhou, X.-M.; Ma, W.-W.; Fu, C.-Y.; Qi, Y.-M.; Liu, L.; Gao, Y.-F. Blocking of the PD-1/PD-L1 Interaction by a D-Peptide Antagonist for Cancer Immunotherapy. *Angew. Chem., Int. Ed.* **2015,** 54, 11760-11764.

463. Sasikumar, P.; Ramachandra, M.; Naremaddepalli, S. Immunomodulating peptidomimetic derivatives. *WO2015036927A1. Geneva: WIPO* **2015**.

464. Sasikumar, P.; Ramachandra, M.; Naremaddepalli, S. Peptidomimetic compounds as immunomodulators. *Aurigene Discovery Technologies Limited* **2013**.

465. Liu, H.; Zhao, Z.; Zhang, L.; Li, Y.; Jain, A.; Barve, A.; Jin, W.; Liu, Y.; Fetse, J.; Cheng, K. Discovery of low-molecular weight anti-PD-L1 peptides for cancer immunotherapy. *J. Immunother. Cancer* **2019,** 7, 270.

466. Qin, B.; Tai, W.; Shukla, R. S.; Cheng, K. Identification of a LNCaP-specific binding peptide using phage display. *Pharm. Res.* **2011,** 28, 2422-34.

467. Li, Q.; Quan, L.; Lyu, J.; He, Z.; Wang, X.; Meng, J.; Zhao, Z.; Zhu, L.; Liu, X.; Li, H. Discovery of peptide inhibitors targeting human programmed death 1 (PD-1) receptor. *Oncotarget* **2016,** 7, 64967-64976.

468. Roxin, Á.; Zheng, G. Flexible or fixed: a comparative review of linear and cyclic cancer-targeting peptides. *Future Med. Chem.* **2012,** 4, 1601-18.

469. Eisenwiener, K. P.; Powell, P.; Mäcke, H. R. A convenient synthesis of novel bifunctional prochelators for coupling to bioactive peptides for radiometal labelling. *Bioorg. Med. Chem. Lett.* **2000,** 10, 2133-5.

470. Chatterjee, S.; Lesniak, W. G.; Miller, M. S.; Lisok, A.; Sikorska, E.; Wharram, B.; Kumar, D.; Gabrielson, M.; Pomper, M. G.; Gabelli, S. B.; Nimmagadda, S. Rapid PD-L1 detection in tumors with PET using a highly specific peptide. *Biochem. Biophys. Res. Commun.* **2017,** 483, 258-263.

471. Kumar, D.; Lisok, A.; Dahmane, E.; McCoy, M.; Shelake, S.; Chatterjee, S.; Allaj, V.; Sysa-Shah, P.; Wharram, B.; Lesniak, W. G.; Tully, E.; Gabrielson, E.; Jaffee, E. M.; Poirier, J. T.; Rudin, C. M.; Gobburu, J. V. S.; Pomper, M. G.; Nimmagadda, S. Peptide-based PET quantifies target engagement of PD-L1 therapeutics. *J. Clin. Investig.* **2019,** 129, 616-630.

472. Xin, Z.; Jinquan, J.; Xue, Y.; Teli, L.; Jin, D.; Sridhar, N.; Martin, G. P.; Hua, Z.; Jun, Z.; Zhi, Y.; Nan, L. First-in-Humans Evaluation of a PD-L1–Binding Peptide PET Radiotracer in Non–Small Cell Lung Cancer Patients. *J. Nucl. Med.* **2022,** 63, 536.

473. De Silva, R. A.; Kumar, D.; Lisok, A.; Chatterjee, S.; Wharram, B.; Venkateswara Rao, K.; Mease, R.; Dannals, R. F.; Pomper, M. G.; Nimmagadda, S. Peptide-Based ^{68}Ga-PET Radiotracer for Imaging PD-L1 Expression in Cancer. *Mol. Pharm.* **2018,** 15, 3946-3952.

474. Zhang, X.-F.; Zhang, J.; Liu, L. Fluorescence Properties of Twenty Fluorescein Derivatives: Lifetime, Quantum Yield, Absorption and Emission Spectra. *J. Fluoresc.* **2014,** 24, 819-826.

475. Schaue, D.; Ratikan, J. A.; Iwamoto, K. S.; McBride, W. H. Maximizing Tumor Immunity With Fractionated Radiation. *Int. J. Radiat. Oncol. Biol. Phys.* **2012,** 83, 1306-1310.

Appendices

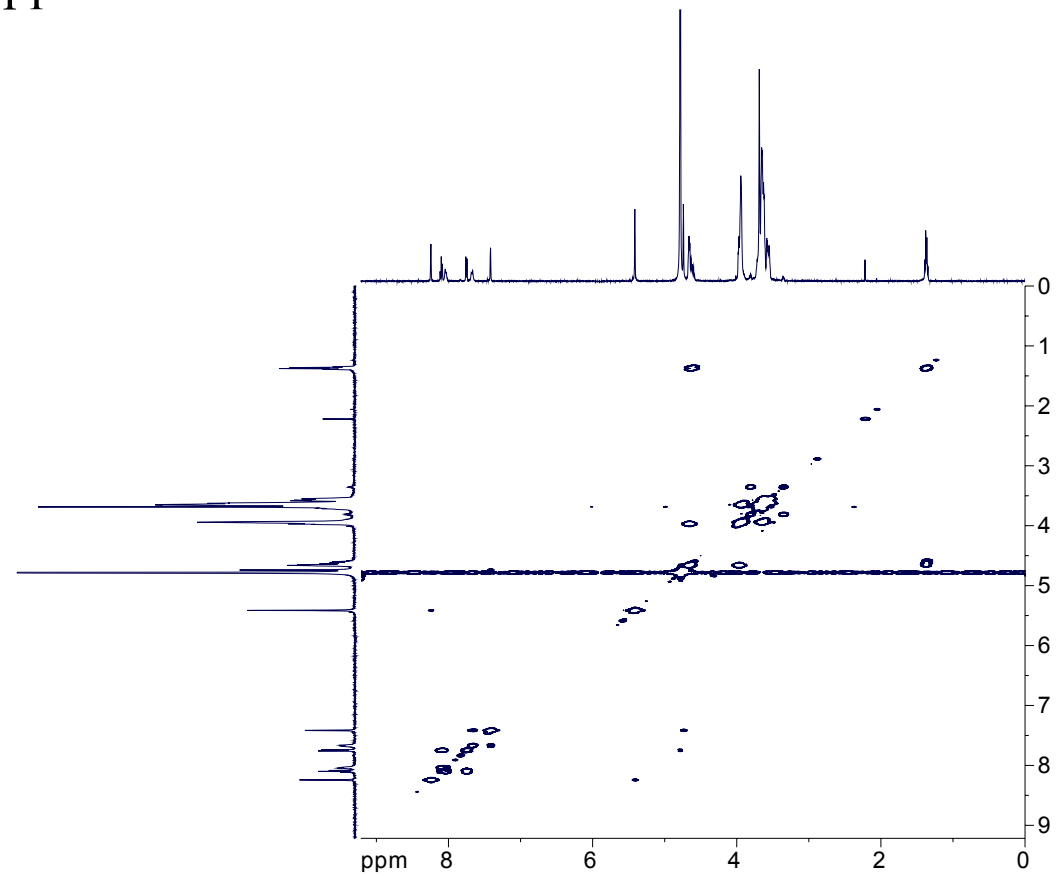

Appendix 1: 2D Correlation Spectroscopy (COSY) of H_2MacropaSqOEt.

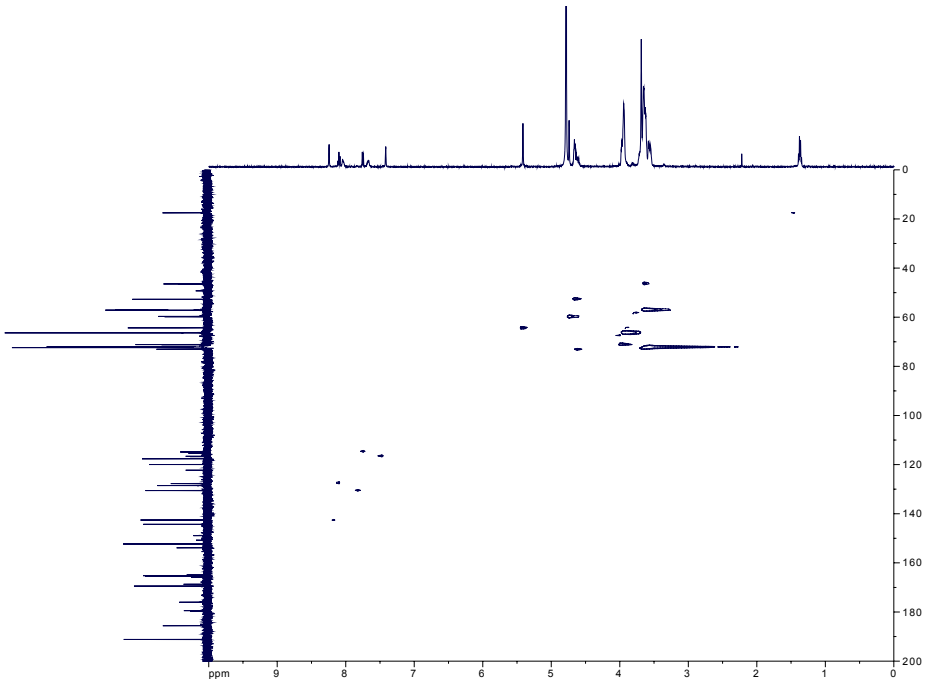

Appendix 2: Heteronuclear Single Quantum Coherence (HSQC) of H_2MacropaSqOEt.

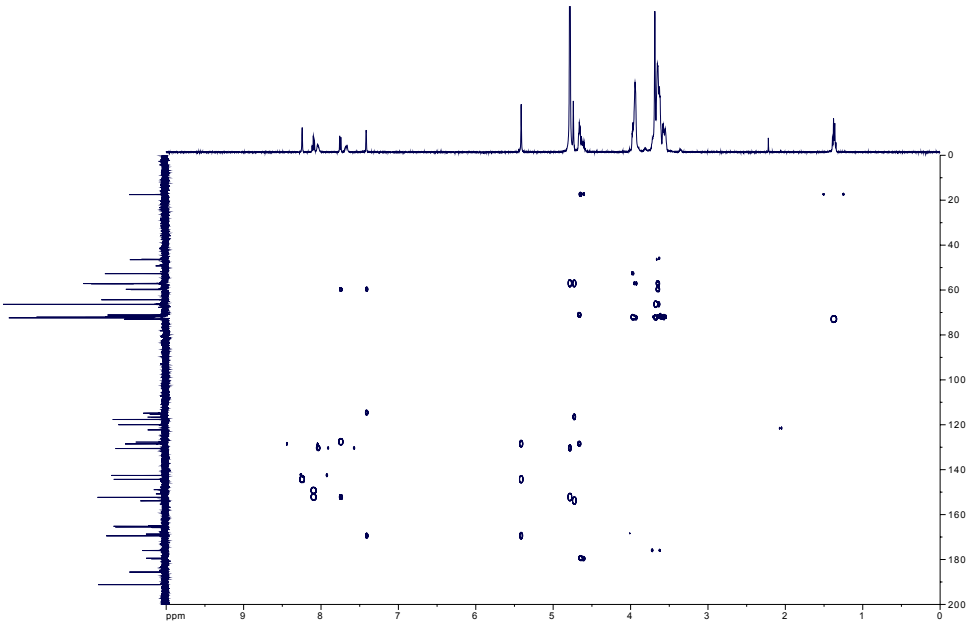

Appendix 3: Heteronuclear Multiple Bond Correlation (HMBC) of H_2MacropaSqOEt.

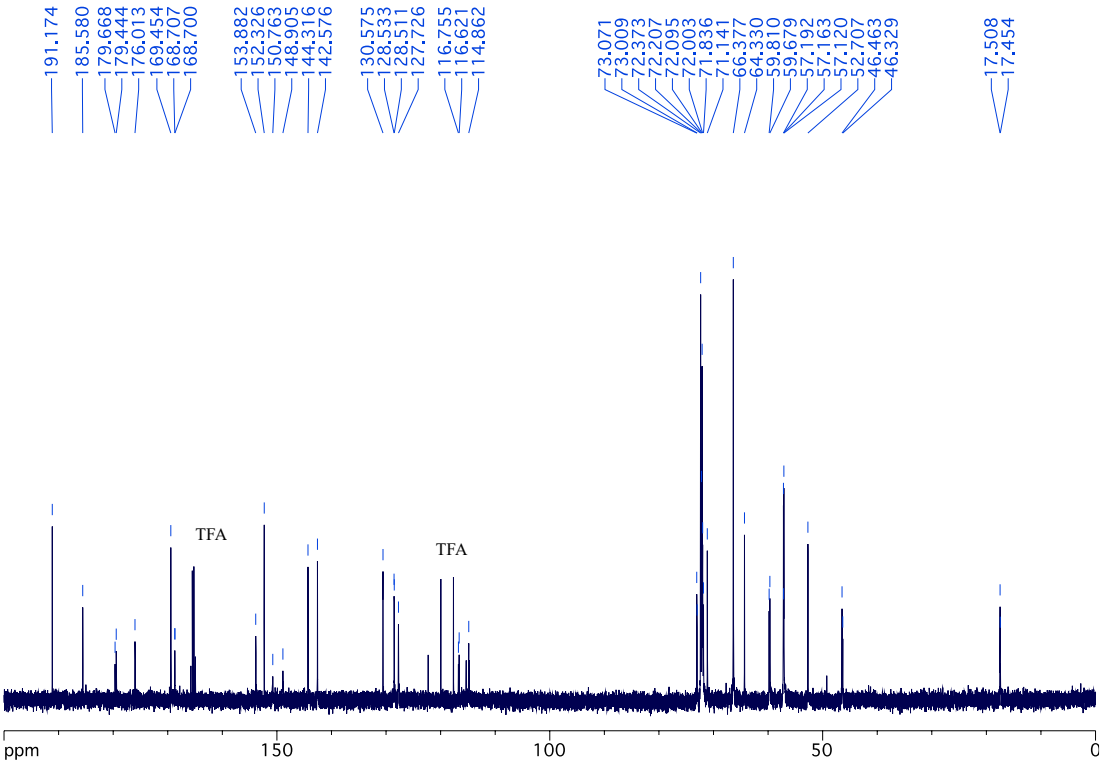

Appendix 4: ^{13}C NMR of H_2MacropaSqOEt.

Volume 59
Number 16
25 February 2023
Pages 2171–2330

ChemComm

Chemical Communications

rsc.li/chemcomm

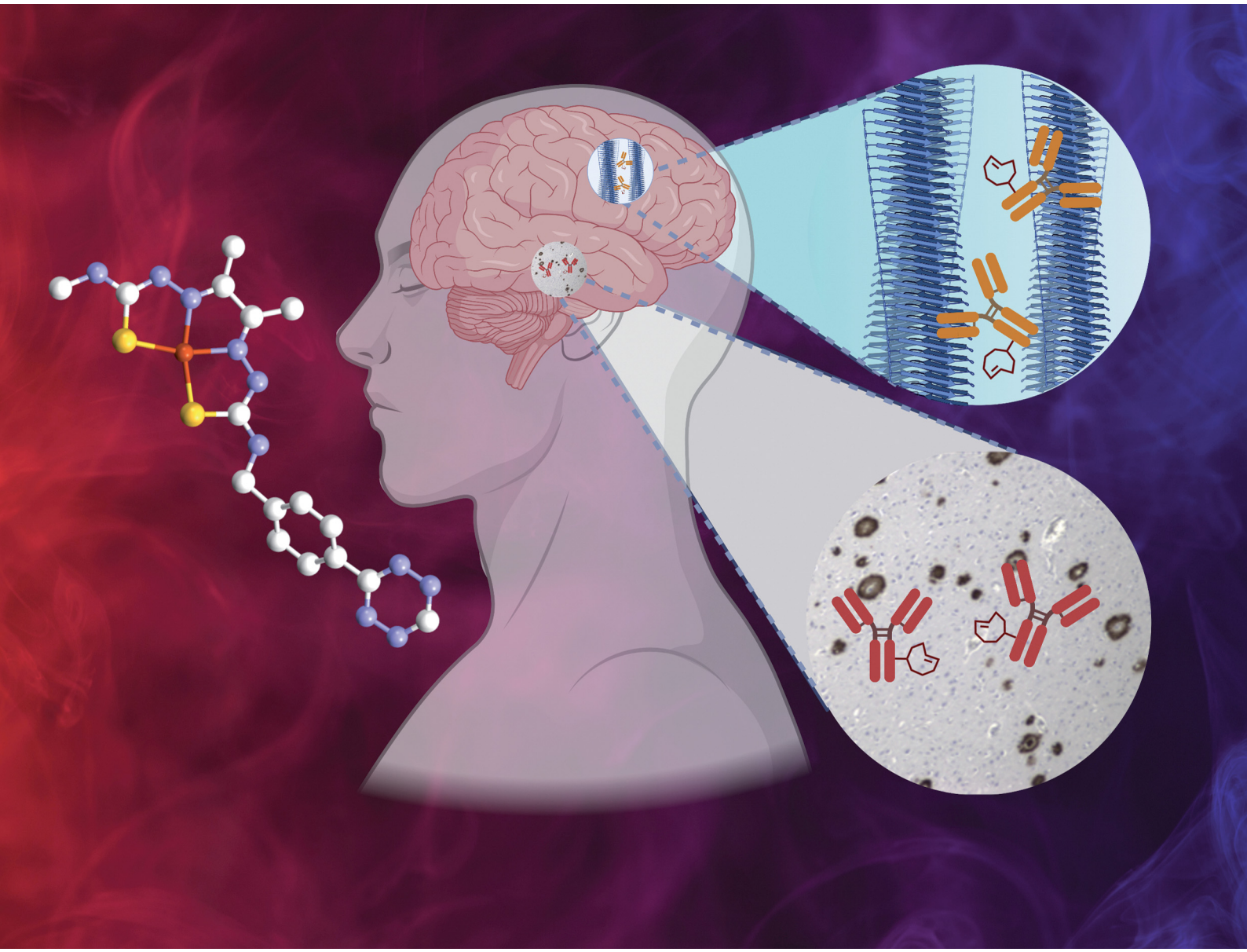

ISSN 1359-7345

ROYAL SOCIETY OF CHEMISTRY

COMMUNICATION

Paul S. Donnelly *et al.*

Pre-targeting amyloid-β with antibodies for potential molecular imaging of Alzheimer's disease

ChemComm

COMMUNICATION

View Article Online
View Journal | View Issue

Published on 17 January 2023. Downloaded by The University of Melbourne Libraries on 7/20/2023 11:34:51 PM.

Check for updates

Cite this: *Chem. Commun.*, 2023, **59**, 2243

Received 16th December 2022,
Accepted 16th January 2023

DOI: 10.1039/d2cc06850h

rsc.li/chemcomm

Pre-targeting amyloid-β with antibodies for potential molecular imaging of Alzheimer's disease†

Katherine A. Morgan,[a] Michael de Veer,[b] Luke A. Miles,[c] Cormac A. A. Kelderman,[d] Catriona A. McLean,[c] Colin L. Masters,[c] Kevin J. Barnham,[c] Jonathan M. White,[a] Brett M. Paterson[bd] and Paul S. Donnelly*[a]

With the aim of developing the concept of pretargeted click chemistry for the diagnosis of Alzheimer's disease two antibodies specific for amyloid-β were modified to incorporate *trans*-cyclooctene functional groups. Two bis(thiosemicarbazone) compounds with pendant 1,2,4,5-tetrazine functional groups were prepared and radiolabelled with positron emitting copper-64. The new copper-64 complexes rapidly react with the *trans*-cyclooctene functionalized antibodies in a bioorthogonal click reaction and cross the blood–brain barrier in mice.

Alzheimer's disease (AD) is a progressive neurodegenerative condition that leads to cognitive and behavioural impairment. The pathology of AD is characterised by the presence of both amyloid-β and tau pathology in the brain.[1] The biological impact of amyloid-β plaques and neurofibrillary tau tangles is controversial, but the presence of these abnormal protein deposits define AD and form the basis of its differential diagnosis from other dementias.[2,3] A major component of amyloid-β plaques are aggregated forms of the amyloid-β peptide (Aβ) which is formed by cleavage of the amyloid precursor protein (APP).[4] Cleavage of APP leads to the formation of fragments of various lengths with the 40 amino acid variant ($A\beta_{1-40}$) and 42-amino acid variant, $A\beta_{1-42}$, both being significant. Aggregation of Aβ leads to the formation of oligomers, protofibrils, fibrils and finally the deposition of extracellular plaques.[4,5]

Positron Emission Tomography (PET) imaging using radiolabelled small molecules that bind to amyloid-β plaques can assist in differential diagnosis of AD.[5] For some patients, amyloid-β burden does not directly correlate with cognitive impairment.[6] This dichotomy has contributed to the theory that soluble Aβ fibrils and oligomers are the neurotoxic species.[7] Current approaches for PET imaging of amyloid-β use small molecules radiolabelled with positron-emitting fluorine-18 that bind to insoluble Aβ plaques through a combination of hydrophobic and non-covalent interactions but offer little insight into the presence of soluble Aβ fibrils and oligomers.[8]

Several anti-Aβ antibodies that target different regions or forms of Aβ have been developed. For example, aducanumab (Aduhelm) is a recombinant IgG1 antibody that binds to soluble Aβ aggregates and insoluble fibrils in preference to monomers.[9] Aducanumab was approved by the FDA in 2021 for the treatment of AD, although the approval was controversial.[10] Diagnostic imaging with radiolabelled antibodies has the potential to offer new insight when compared to conventional amyloid-β plaque imaging. PET imaging with radiolabelled antibodies (immunoPET) has already made a significant impact in the diagnosis of cancer, but the application of immunoPET to diagnose neurodegenerative diseases is challenging. The large molecular weight of radiolabelled antibodies (~150 kDa) significantly limits their passage across the blood brain barrier.

In this work, we present an antibody 'pre-target and chase' approach that has the potential to circumvent these challenges (Fig. 1). The strategy involves administering an antibody that has been modified to incorporate a functional group poised for a bioorthogonal 'click reaction' with a small molecule radiolabelled tracer that crosses the blood–brain barrier (BBB). The small molecule tracer is administered after allowing sufficient time and repeated dosing to maximise the accumulation of the antibody at the target site in the brain.

Aducanumab crosses the blood–brain barrier and accumulates in the brain of transgenic mice (Tg2576) that are a model of amyloid pathology. Administration of a single dose (30 mg kg^{-1}) to Tg2576 transgenic mice resulted in a C_{max} in brain of 1,062 ng g^{-1} of tissue.[9] Repeated administration of a suitably modified antibody should lead to concentrations in the brain that could be targeted by a radiolabelled small molecule.

The selectivity and fast reaction kinetics ($k_2 \sim 10^5$ M^{-1} s^{-1}) of inverse-electron-demand Diels–Alder reactions between

[a] *School of Chemistry and Bio21 Molecular Science and Biotechnology Institute, University of Melbourne, Melbourne, Victoria, 3010, Australia. E-mail: pauld@unimelb.edu.au*
[b] *Monash Biomedical Imaging, Monash University, Clayton, Victoria 3800, Australia*
[c] *The Florey Institute of Neuroscience and Mental Health, University of Melbourne, Melbourne, Victoria, 3010, Australia*
[d] *School of Chemistry, Monash University, Clayton, Victoria 3800, Australia*

† Electronic supplementary information (ESI) available. CCDC 2205695–2205696. For ESI and crystallographic data in CIF or other electronic format see DOI: https://doi.org/10.1039/d2cc06850h

Published on 17 January 2023. Downloaded by The University of Melbourne Libraries on 7/20/2023 11:34:51 PM.

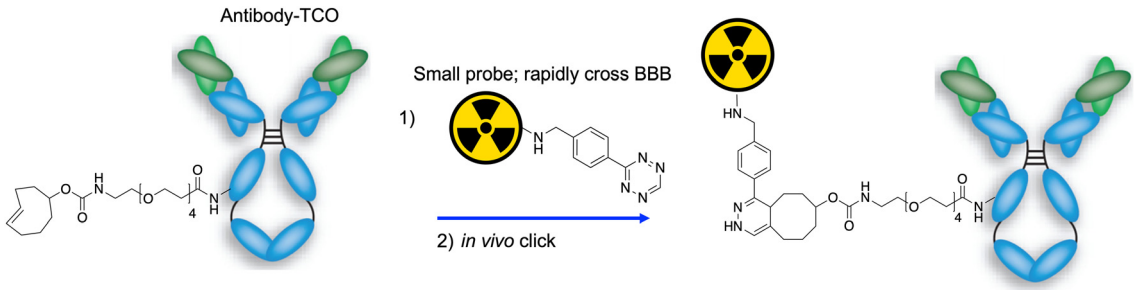

Fig. 1 Schematic representation of *in vivo* inverse-electron-demand Diels–Alder 'click' reaction between tetrazines and strained *trans*-cyclooctene (TCO) with a polyethylene glycol linker (PEG_4).

electron-deficient tetrazines and strained *trans*-cyclooctene (TCO) derivatives are well suited for *in vivo* pre-targeting (Fig. 1). Pre-targeting of tumours using antibodies modified to incorporate TCO and radiolabelled molecules featuring a tetrazine react selectively, even in the complex reaction environment encountered *in vivo*, as demonstrated in animal models for PET imaging.[11,12] Antibodies that do not internalise upon binding to the antigen are best suited to *in vivo* click reactions,[12] so antibodies such as aducanumab that bind to extracellular soluble Aβ aggregates and insoluble fibrils are well suited for pre-targeted PET-imaging.

In this work, TCO functional groups were conjugated to an aducanumab biosimilar through a short hydrophilic polyethylene glycol (TCO-PEG_4) linker. The antibody was reacted with the succinimidyl ester of TCO-PEG_4-CO_2H (10 equivalents) at room temperature for one hour before purification with an ultra-centrifugation filter (MWCO 50 kDa). Analysis of the aducanumab-PEG_4-TCO conjugates (aducanumab-TCO, Fig. 2a) by intact electrospray ionisation mass spectrometry (ESI-MS) revealed an average of four PEG_4-TCO groups per antibody. We also added TCO functional groups to the 6E10 antibody, a research anti-Aβ monoclonal antibody that was raised against a synthetic peptide corresponding to residues 1–24 of Aβ.[13] Reaction of 6E10 with the *N*-hydroxysuccinimide activated ester of TCO-PEG_4-CO_2H under the same conditions and analysis by intact electrospray mass spectrometry indicated an average of five PEG_4-TCO groups per antibody (6E10-TCO) (Fig. 2b). The more complicated mass spectrum of 6E10-TCO when compared to aducanumab-TCO presumably reflects a higher degree of glycosylation. The modified 6E10-TCO (1 : 400) retained affinity for Aβ plaques present in post-mortem frontal cortex tissue of subjects with diagnosed AD (Fig. 2c) and behaved in the same way as parental 6E10 (1 : 200, ESI,† Fig. S18). This assay could not be used to demonstrate the retention of affinity of the aducanumab-TCO conjugate as the antibody binds to soluble Aβ aggregates. Both aducanumab-TCO and 6E10-TCO were also analysed by size exclusion-HPLC, and the chromatograms were similar to the unmodified antibodies with no evidence of aggregation (ESI,† Fig. S17).

Copper-64 is a positron-emitting radionuclide that can be used for PET imaging.[14] The copper(II) bis(thiosemicarbazonato) complex diacetylbis(4-methyl-3-thiosemicarbazone) (Cu(atsm), Fig. 3a) is charge neutral, lipophilic and is capable of crossing the blood–brain barrier allowing PET imaging of the brain in human subjects.[15] In previous work, we modified the *bis*(thiosemicarbazone) ligand to append substituted stilbenyl functional groups. These copper(II) complexes bound to amyloid-β plaques in human brain tissue.[16,17] In this work, we prepared copper complexes with *bis*(thiosemicarbazone) ligands incorporating a tetrazine functional group (Fig. 3b) designed for bioorthogonal *in vivo* click reactions with the TCO-modified antibodies. Copper(II) complexes of *bis*(thiosemicarbazones) are stable ($K_a \sim 10^{18}$),[18,19] but reduction of the metal to copper(I) can lead to dissociation from the ligand and transfer of the copper to proteins. Electron donating methyl or ethyl substituents on the backbone of the ligand (R in Fig. 3b) give copper(II) complexes that are more resistant to reduction to copper(I) and can also influence their biodistribution.[20] Two ligands with a benzylaminotetrazine (Tz) functional group with either methyl (H_2atsm-Tz) or ethyl (H_2dtse-Tz) groups were prepared by selective transamination reactions.[21] The copper(II) complexes, Cu(atsm-Tz) and Cu(dtse-Tz) (Fig. 3b), were characterised by electrospray ionisation mass spectrometry and reversed-phase HPLC. Cyclic voltammetry shows that both Cu(atsm-Tz) and Cu(dtse-Tz) undergo a quasi-reversible redox process at $E_{1/2} = -1.15$ V *vs.* ferricenium/ferrocene

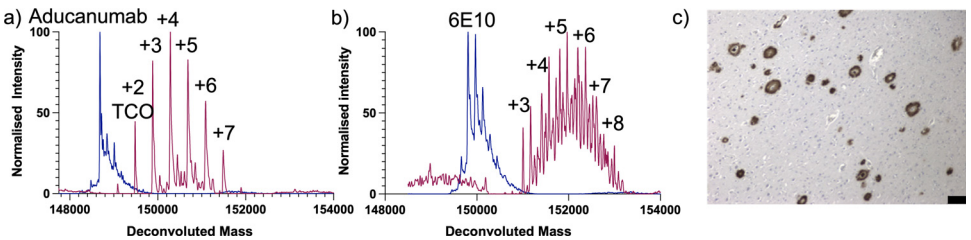

Fig. 2 Deconvoluted ESI mass spectra of (a) unconjugated aducanumab (blue) and aducanumab-TCO_x conjugate where x = 2–7 (red); (b) unconjugated 6E10 (blue) and 6E10-TCO_x conjugate where x = 3–8 (red) and (c) section of human brain tissue from AD affected subject immuno-stained with 6E10-TCO antibody; black scale bar = 100 μm.

 This journal is © The Royal Society of Chemistry 2023

Published on 17 January 2023. Downloaded by The University of Melbourne Libraries on 7/20/2023 11:34:51 PM.

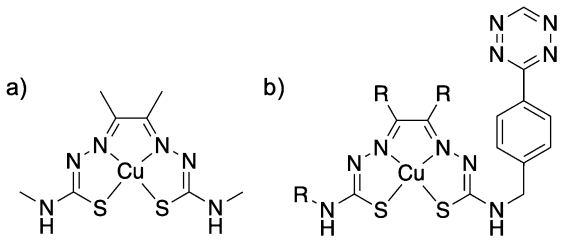

Fig. 3 (a) Cu(atsm); (b) Cu(atsm-Tz): R = CH_3; Cu(dtse-Tz): R = CH_2CH_3 (this work).

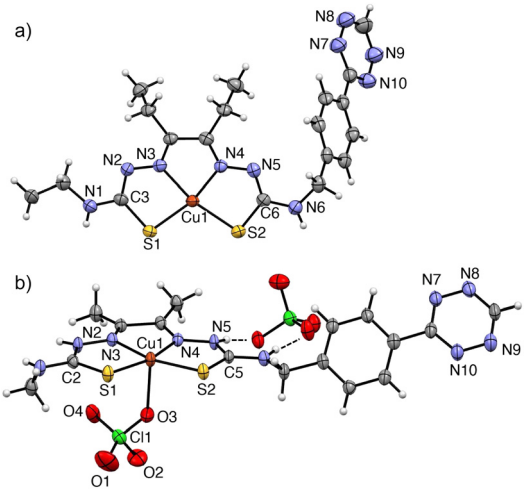

Fig. 4 ORTEP representations (ellipsoids at 50% probability) of the X-ray crystal structures of: (a) $(Cu(dtse\text{-}Tz)_2(DMSO)_3$, solvent omitted for clarity, bond lengths (Å): Cu–N3 1.966(3); Cu–N4 1.965(3); Cu–S1 2.2430(11); Cu–S2 2.2453(10). (b) $[Cu(H_2atsm\text{-}Tz)](ClO_4)_2$ selected bond lengths (Å): Cu–N3 1.968(3); Cu–N4 1.957(3); Cu–S1 2.2413(8); Cu–S2 2.2489(9); Cu–O3 2.505(3).

(Fc^+/Fc) that can be attributed to a $Cu^{II/I}$ process similar to what is found in Cu(atsm) ($E_m \approx -1.16$ V). A second quasi-reversible process at $E_{1/2} = -1.32$ V is attributed to reduction of the tetrazine functional group. Both the $Cu^{II/I}$ and tetrazine reductions occur at potentials that are outside the typical reducing environment encountered in most cells. Each complex also displayed two essentially irreversible and partially overlapping processes at more positive potentials, *i.e.*, $E = 0.19$ V *vs.* Fc^+/Fc which are likely to be due to ligand-based oxidation. Characterisation of Cu(dtse-Tz) by X-ray crystallography (Fig. 4a) confirmed the copper(II) is in a distorted square planar environment with the ligand acting as a N_2S_2 donor. The Cu–N and Cu–S bond lengths are similar to those found in Cu(atsm).[22] The double deprotonation of the ligand and the resonance form depicted (Fig. 3b) is supported by the short C–N lengths (C3–N2 1.323(5) and C6–N5 1.321(5) Å) consistent with partial double bond character.[22] The C–S bond lengths (C3–S1 1.764(4) and C6–S2 1.766(4) Å) are also consistent with more 'thiolate-like' than 'thione-like' bonding.[22] The asymmetric unit contains two independent molecules that interact through hydrogen bonding ($N\text{–}H\cdots N_{tetrazine}$) as well $N\text{–}H\cdots O$ hydrogen bonds to the three DMSO solvent molecules. Crystals of protonated $[Cu(H_2atsm\text{-}Tz)]^{2+}$, where the bis(thiosemicarbazone) ligand is protonated, were grown by the addition of perchloric acid to a mixture of the complex in methanol (Fig. 4b). The most notable differences when comparing to the structure of charge neutral Cu(dtse-Tz) are the longer C–N bond lengths, C2–N1 1.319(4) Å and C2–N2 1.354(4) Å and the shorter C–S bond distances, C2–S1 1.712(3) Å and C5 S2 1.709(3) Å) (Fig. 4b). The copper(II) is 5-coordinate square pyramidal due to a weak axial interaction with the oxygen of a perchlorate anion (Cu–O3 2.505(3) Å) (Fig. 4b). Despite the change in degree of protonation of the ligand the Cu–N and Cu–S bond lengths are similar to the charge neutral Cu(dtse-Tz).

Both ligands can be radiolabelled with $[^{64}Cu]^{2+}$ in sodium acetate buffer (100 mM, pH 5.5) at room temperature in <30 minutes to give the copper-64 complexes in high radiochemical yield and specific activity (4.2–4.6 MBq $nmol^{-1}$, ESI,† Fig. S19 and S20). The copper-64 complexes were characterised by comparing their respective HPLC traces with their non-radioactive analogues. The octanol-PBS distribution coefficient ($\log D$) is often used to predict a compounds ability to cross the blood–brain barrier with the ideal range often stated to be $\log D$ 1.5–3.5. The $\log D$ values of $[^{64}Cu]Cu(atsm\text{-}Tz)$ ($\log D$ 1.84) and $[^{64}Cu]Cu(dtse\text{-}Tz)$ ($\log D$ 2.17) were consistent with their respective HPLC retention times and slightly higher than the value obtained for $[^{64}Cu]Cu(atsm)$ ($\log D$ 1.56). Both $[^{64}Cu]Cu(atsm\text{-}Tz)$ and $[^{64}Cu]Cu(dtse\text{-}Tz)$ were stable with respect to a kinetic challenge experiment with excess of cysteine and histidine at 37 °C for 4 hours, as well as the presence of glutathione (16 mmol L^{-1}) for 24 hours (ESI,† Fig. S13, S14 and S21).

Both the initial radiolabelling reactions and the click reactions were analysed by radio-thin layer chromatography (radio-TLC). Unchelated copper-64 stays at the baseline (ethanol mobile phase), while $[^{64}Cu]Cu(atsm\text{-}Tz)$ and $[^{64}Cu]Cu(dtse\text{-}Tz)$ travel to the solvent front (Fig. 5). Either TCO-aducanumab or TCO-6E10 ($\sim$1 equivalent based on the total amount of ligand present with respect to the antibody, $\sim 3.6\text{–}3.9 \times 10^{-10}$ mol, 10^{-6} mol L^{-1}) were added to $[^{64}Cu]Cu(atsm\text{-}Tz)$ and $[^{64}Cu]Cu(dtse\text{-}Tz)$] and the mixture was allowed to react for 1 hour at room temperature. Analysis of the reaction mixtures by radio-TLC reveals that the majority ($>68\%$) of the activity is now retained on the baseline, consistent with copper-64 complexes reacting with the TCO-modified antibodies (Fig. 5). When unmodified 6E10 and aducanumab were incubated with both $[^{64}Cu]Cu(atsm\text{-}Tz)$ and $[^{64}Cu]Cu(dtse\text{-}Tz)$, the radioactive signal remained unchanged, consistent with no reaction occurring (ESI,† Fig. S21 and S22).

Encouraged by the efficacy of the click reaction we investigated the potential of the two compounds to cross the blood brain barrier in mice. Following administration of either $[^{64}Cu]Cu(atsm\text{-}Tz)$ or $[^{64}Cu]Cu(dtse\text{-}Tz)$ to wild type mice by intravenous tail vein injection, the mice were euthanised at 2 and 60 minutes post injection (m.p.i.). The radioactivity in each organ was counted and expressed as a percentage of the injected activity normalised to the mass of the organ (% IA g^{-1}). The brain uptake at 2 m.p.i. of $[^{64}Cu]Cu(atsm\text{-}Tz)$ was $2.5 \pm 0.5\%$ IA g^{-1} whilst the brain uptake of $[^{64}Cu]Cu(dtse\text{-}Tz)$ was $1.7 \pm 0.3\%$ IA g^{-1}. Both compounds clear from the brain in wild type mice with the activity in the brain reducing to $0.78 \pm 0.08\%$ IA g^{-1} and $0.41 \pm 0.03\%$ IA g^{-1} at 60 m.p.i. In this

Published on 17 January 2023. Downloaded by The University of Melbourne Libraries on 7/20/2023 11:34:51 PM.

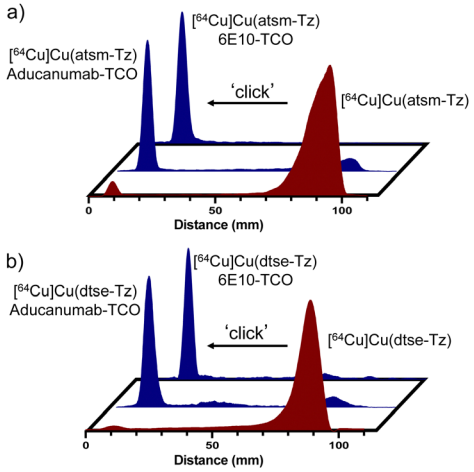

Fig. 5 Normalised, smoothed radio-TLC traces of (a) [^{64}Cu]Cu(atsm-Tz) and (b) [^{64}Cu]Cu(dtse-Tz) (red) >95% RCY, when reacted with aducanumab-TCO or 6E10-TCO (blue) for 1 h, in 0.1M NaOAc, pH 5.5, 10^{-6} M.

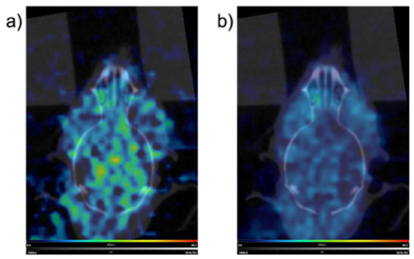

Fig. 6 PET/CT images of brain region in Balb/c mouse at (a) 1–5 m.p.i. and (b) 5–30 m.p.i of [^{64}Cu]Cu(atsm-Tz).

experiment, with wild type mice and no TCO-antibody present to 'trap' the tracer it is important that the initial brain uptake is followed by effective clearance. For both compounds, the degree of brain uptake in wild type mice is slightly higher than for [^{64}Cu]Cu(atsm) ($\sim 0.9 \pm 0.4\%$ IA g^{-1}).[23] Both [^{64}Cu]Cu(atsm-Tz) and [^{64}Cu]Cu(dtse-Tz) have high uptake in the liver ($20.8 \pm 1\%$ IA g^{-1} and $34 \pm 4\%$ IA g^{-1} respectively at 60 m.p.i.) consistent with hepatobiliary metabolism as expected for lipophilic compounds. The initial brain uptake and clearance of [^{64}Cu]Cu(atsm-Tz) was further confirmed by micro-PET imaging, which clearly shows initial brain uptake followed by clearance of the radiotracer (Fig. 6).

A challenge in using radiolabelled antibodies for PET imaging of neurodegenerative diseases is the low amounts of antibody that cross the blood-brain barrier. Continued dosing of antibodies modified for bioorthogonal click reactions has the potential to increase the concentration of antibody present in the brain and allow amyloid pre-targeting. This work explores this concept, by modifying two antibodies that bind to amyloid-β with TCO functional groups. We also prepared two new copper-64 complexes with tetrazine functional groups that that cross the blood–brain barrier. These new copper-64 complexes react *via* bioorthogonal click chemistry with the modified TCO-antibodies. This work suggests that pre-targeting amyloid plaques may be feasible and further investigation of this concept in animal models of amyloid pathology is warranted. Extrapolation of this concept to other antibodies that bind to other proteins of interest in neurodegeneration such as tau, TDP-4 and α-synuclein could be worthy of investigation.

The Australian Research; Council; Australian Cancer Research Foundation; Victorian Brain Bank Network; Bio21 Mass Spectrometry and Proteomics Facility; National Imaging Facility (a NCRIS facility) and Monash Biomedical Imaging are all acknowledged.

Conflicts of interest

The authors declare no conflicts of interest.

References

1 D. S. Knopman, H. Amieva, R. C. Petersen, G. Chételat, D. M. Holtzman, B. T. Hyman, R. A. Nixon and D. T. Jones, *Nat. Rev. Dis. Primers*, 2021, **7**, 33.
2 B. Dubois, N. Villain, G. B. Frisoni, G. D. Rabinovici, M. Sabbagh, S. Cappa, A. Bejanin, S. Bombois, S. Epelbaum, M. Teichmann, M.-O. Habert, A. Nordberg, K. Blennow, D. Galasko, Y. Stern, C. C. Rowe, S. Salloway, L. S. Schneider, J. L. Cummings and H. H. Feldman, *Lancet Neurol.*, 2021, **20**, 484–496.
3 C. R. Jack, D. A. Bennett, K. Blennow, M. C. Carrillo, B. Dunn, S. B. Haeberlein, D. M. Holtzman, W. Jagust, F. Jessen, J. Karlawish, E. Liu, J. L. Molinuevo, T. Montine, C. Phelps, K. P. Rankin, C. C. Rowe, P. Scheltens, E. Siemers, H. M. Snyder, R. Sperling, C. Elliott, E. Masliah, L. Ryan and N. Silverberg, *Alzheimers. Demen.*, 2018, **14**, 535–562.
4 F. Panza, M. Lozupone, G. Logroscino and B. P. Imbimbo, *Nat. Rev. Neurol.*, 2019, **15**, 73–88.
5 O. Hansson, *Nat. Med.*, 2021, **27**, 954–963.
6 V. L. Villemagne, V. Doré, S. C. Burnham, C. L. Masters and C. C. Rowe, *Nat. Rev. Neurol.*, 2018, **14**, 225–236.
7 T. Yang, S. Li, H. Xu, D. M. Walsh and D. J. Selkoe, *J. Neurosci.*, 2017, **37**, 152.
8 L. Zhu, K. Ploessl and H. F. Kung, *Chem. Soc. Rev.*, 2014, **43**, 6683–6691.
9 J. Sevigny, P. Chiao, T. Bussière, P. H. Weinreb, L. Williams, M. Maier, R. Dunstan, S. Salloway, T. Chen, Y. Ling, J. O'Gorman, F. Qian, M. Arastu, M. Li, S. Chollate, M. S. Brennan, O. Quintero-Monzon, R. H. Scannevin, H. M. Arnold, T. Engber, K. Rhodes, J. Ferrero, Y. Hang, A. Mikulskis, J. Grimm, C. Hock, R. M. Nitsch and A. Sandrock, *Nature*, 2016, **537**, 50–56.
10 A. Mullard, *Nature*, 2021, **594**, 309–310.
11 R. Rossin, P. Renart Verkerk, S. M. van den Bosch, R. C. M. Vulders, I. Verel, J. Lub and M. S. Robillard, *Angew. Chem., Int. Ed.*, 2010, **49**, 3375–3378.
12 M. Altai, R. Membreno, B. Cook, V. Tolmachev and B. M. Zeglis, *J. Nucl. Med.*, 2017, **58**, 1553.
13 I. Baghallab, J. M. Reyes-Ruiz, K. Abulnaja, E. Huwait and C. Glabe, *J. Alzheimer's. Dis.*, 2018, **66**, 1235–1244.
14 P. J. Blower, *Dalton Trans.*, 2015, **44**, 4819–4844.
15 M. Ikawa, H. Okazawa, K. Arakawa, T. Kudo, H. Kimura, Y. Fujibayashi, M. Kuriyama and M. Yoneda, *Mitochondrion*, 2009, **9**, 144–148.
16 S. Lim, B. M. Paterson, M. T. Fodero-Tavoletti, G. J. O'Keefe, R. Cappai, K. J. Barnham, V. L. Villemagne and P. S. Donnelly, *Chem. Commun.*, 2010, **46**, 5437–5439.
17 A. Noor, D. J. Hayne, S. Lim, J. K. Van Zuylekom, C. Cullinane, P. D. Roselt, C. A. McLean, J. M. White and P. S. Donnelly, *Inorg. Chem.*, 2020, **59**, 11658–11669.
18 Z. Xiao, P. S. Donnelly, M. Zimmermann and A. G. Wedd, *Inorg. Chem.*, 2008, **47**, 4338–4347.
19 D. A. Winkelmann, Y. Bermke and D. H. Petering, *Bioinorg. Chem.*, 1974, **3**, 261–277.
20 C. J. Mathias, S. R. Bergmann and M. A. Green, *J. Nucl. Med.*, 1995, **36**, 1451.
21 B. M. Paterson, J. A. Karas, D. B. Scanlon, J. M. White and P. S. Donnelly, *Inorg. Chem.*, 2010, **49**, 1884–1893.
22 A. R. Cowley, J. R. Dilworth, P. S. Donnelly, E. Labisbal and A. Sousa, *J. Am. Chem. Soc.*, 2002, **124**, 5270–5271.
23 M. T. Fodero-Tavoletti, V. L. Villemagne, B. M. Paterson, A. R. White, Q.-X. Li, J. Camakaris, G. O'Keefe, R. Cappai, K. J. Barnham and P. S. Donnelly, *J. Alzheimer's. Dis.*, 2010, **20**, 49–55.

 This journal is © The Royal Society of Chemistry 2023